Synthesis and Vectorial Functionalisation of N-Heterocycles for Fragment-based Drug Discovery

ELIZABETH VICTORIA BEDWELL

Synthesis and Vectorial Functionalisation of *N*-Heterocycles for Fragment-based Drug Discovery

Author

Elizabeth V. Bedwell

Supervisor

Prof. Patrick G. Steel

A thesis presented for the degree of

Doctor of Philosophy

Department of Chemistry

December 2024

Abstract

Fragment-based drug discovery (FBDD) is a well established method of finding and developing biologically active molecules. Nitrogen heterocycles are a common motif found in many commercial drug compounds and are therefore valuable inputs for FBDD. However, the range of nitrogen heterocycles in common usage remains limited and novel scaffolds offer a much needed source of molecular diversity. This project advances two complementary areas of FBDD - exploring key heterocyclic cores representing unexplored region of chemical space and developing new synthetic methodology to support fragment elaboration.

The first heterocyclic cores of interest were the 5-halo-*1H*-pyrazolo[3,4-c]pyridines (**77** and **185**), accessed in two steps from the corresponding 6-halo-5-methylpyridin-3-amine. Complimentary methods of late-stage functionalisation enabled elaboration along the major growth-vectors. *N*-alkylation and nitrogen protection strategies decorated *N*-1 and *N*-2 on the pyrazole ring, while the *C*-3 vector was accessed by a tandem C-H borylation and Suzuki-Miyaura cross-coupling, the *C*-5 vector was accessed by Buchwald-Hartwig amination, and the *C*-7 vector was accessed by a *turbo*-Grignard metalation strategy. These methods can be used individually or in sequences to generate an elaborated library of compounds. Biological characterisation of this library sort to exemplify the pharmaceutical value of the pyrazolo[3,4-c]pyridine core. Unfortunately, both crystal soaking and thermal shift assays were challenged by the limited aqueous solubility of the heterocycles, so were unable to verify results of the virtual screening.

The second heterocyclic cores of interest, the semi-saturated azabenzolactams (**241**, **242**, **243**, and **244**), were designed to incorporate more sp^3 character to improve aqueous solubility. A multi-step synthetic route was established to afford four analogues starting from the respective halo-cyanopyridine. The saturated part of these ring systems opens new possibilities for functionalisation, with a particular site of interest being *C*-α to the amine nitrogen. This led to an in-depth study developing methodology for the α-functionalisation of cyclic amines.

This methodology study established a route of C-H activation by electrochemical oxidation followed by reaction with phenylzinc. By first performing a boron-to-zinc transmetalation of commercial aryl boronic acids, the scope of this transformation was extended to include substitution by other aryl groups. Variation in ring size, protecting group, morpholines, and benzo-fused systems were all tolerated, while future work will see the application of this methodology to more drug-like cores, including the azabenzolactams.

Contents

List of Tables

Abbreviations

(c) $\log P$	(calculated) partition coefficient of water/octanol
ACT	4-acetamido-2,2,6,6-tetramethyl-piperidinedin-1-oxyl
ADMET	Absorption, distribution, metabolism, excretion, and toxicity
ARC	Aromatic ring count
CBS	Cystathionine β-synthase
CGL	Cystathionine γ-lyase
COD	1,5-cyclooctadiene ligand
CS	Cysteine Synthase
dba	Dibenzylideneacetone
DCE	Dichloroethane solvent
DCM	Dichloromethane solvent
DDQ	2,3-dichloro-5,6-dicyanobenzoquinone
DFS	Differential scanning fluorimetry
DFT	Density Functional Theory
DMAc	Dimethylacetamide solvent
DMAD	Dimethyl acetylenedicarboxylate
DME	1,2-Dimethoxy ethane solvent
dppf	1,1'-Bis(diphenylphosphino)ferrocene ligand
dr	Diastereomeric ratio
dtbpy	4,4'-Di-tert-butyl-2,2'-dipyridyl ligand
ee	Enantiomeric excess
ESI	Electrospray ionisation
FBDD	Fragment-based drug discovery
Fsp^3	sp^3 fraction
GCMS	Gas chromatography mass spectrometry
GSE	General solubility equation
HAC	Heavy atom count
HMBC	Heteronuclear multiple-bond correlation spectroscopy
HOMO	Highest occupied molecular orbital
HONTO	Highest occupied natural transition orbital
HRMS	High-resolution mass spectrometry
HTS	High throughput screening
IPTG	Isopropyl β-D-1-thiogalactopyranoside
ITC	Isothermal calorimetry

JAK	Janus kinase
JCF	Joseph C Foster
LAmB	Liposomal amphotericin B
LCMS	Liquid chromatography mass spectrometry
LE	Ligand efficiency
LSF	Late-stage functionalisation
LUMO	Lowest unoccupied molecular orbital
LUNTO	Lowest unoccupied natural transition orbital
MD	Molecular dynamics
MELK	Maternal embryonic leucine zipper kinase
MF	Miltefosine
MP	Methyl pyruvate
mp	Melting point
Ms	Methanesulfonyl group
MS	Metabolic stability
MTBE	Methyl tert-butyl ether solvent
MW	Microwave
MYL	Mingyu Lou
NBS	N-bromo succinimide
NMP	N-methyl pyrrolidone
NMR	Nuclear magnetic resonance
NOE	Nuclear overhauser effect
Nrot	Number of rotatable bonds
NTD	Neglected tropical disease
OLEDs	Organic light-emitting diodes
PCET	Proton-coupled electron transfer
Pd/C	Palladium on carbon
PDB	Protein data bank
pin	Pinocol ligand
PLQY	Photoluminescence quantum yield
RPA	Replication protein A
rt	Room temperature
SAR	Structure activity relationship
SAT	Serine acetyltransferase
SEM	2-(trimethylsilyl)ethoxymethyl group
SET	Single electron transfer

SM	Starting material
SPR	Surface plasmon resonance
TADF	Thermally activated delayed fluorescence
TBAF	Tetrabutylammonium fluoride
TFA	Trifluoroacetic acid
TFE	Trifluoroethanol
THF	Tetryhydrofuran solvent
THP	Tetrahydropyran group
TIPS	Triisopropylsilyl group
TMP	2,2,6,6-tetramethylpiperidine
TPSA	Topological polar surface area
TsCl	4-toluenesulfonyl chloride
VEHICLe	Virtual exploratory heterocycle library
WHO	World Health Organisation

Declaration

The work in this thesis was carried out by the author in the Department of Chemistry at Durham University between October 2021 and December 2024, except for work carried out by collaborators who are acknowledged below and where relevant in the text. No part of this work has been submitted for any other degree at this or another university.

Collaborator Contributions

Molecular dynamics refinement of the *Leishmania major* protein model was performed by André Berndt Penteado, Universidade São Paulo. Crystals of *Leishmania infantum* Cysteine Synthase were generated by Dr Kate Sowerby, Durham University. Photoluminescence data was collected by Ruth Pollard and Dr Marc Etherington, Northumbria University. PLQY and fluorescence lifetimes were determined by Ruth Pollard, Northumbria University, and Dr Chris Hogg, University of York. Density functional theory calculations were conducted by Dr Antonio Prlj, Institut Ruder Bošković. The pH titration analysis was carried out by Laura Duncan, Durham University. Small molecule single X-ray crystal structures were solved by Dr Toby Blundell, Durham University.

Statement of Copyright

Acknowledgements

Firstly, thanks to my funding body, the EPSRC, for their financial support, without which this work would not have been possible. Thanks to my primary supervisor Prof Patrick Steel for his advice and guidance throughout the PhD. Thank you for allowing me to follow this project in the many unexpected directions that gave me the opportunity to learn new skills in different areas of science.

Further thanks to Prof Giuliano Clososki, Prof Flavio Emery, and Prof Gustavo Trossini for welcoming me into their research groups and for giving me the opportunity to experience chemistry research at Universidade São Paulo. Thank you also to everyone who welcomed me to Brazil, showed me the delights of Ribeirão Preto and São Paulo, and put up with my terrible Portuguese. I learned so much in those three months and have made memories that will stay with me for life.

Thank you to Prof Ehmke Pohl and Dr Stefanie Pohl for teaching me the magic of cell cultures and protein expression. Thank you also to Dr Marc Etherington for introducing me to the wonders of photophysics. I am grateful to you all for giving me the opportunity to explore beyond the synthetic chemistry lab.

To the Durham University analytical services: Thank you Dr Juan Aguilar, Eric Hughes, Peter Stokes, and Dr Aileen Congreve for your assistance with compound isolation and characterisation. Thank you for never backing down from a challenge and for being an endless source of creative problem solving.

To the members of CG001, past and present: I am extremely grateful to have had this opportunity to work alongside you, I have learnt so much from you all. Thank you to Jonathan, Victor, and Jaime, for welcoming me so warmly and for showing me the ropes, and to Boye for being a true constant of CG001. To Exe, thank you for putting up with my endless questioning, your seemingly endless knowledge and suggestions have given me hope of salvaging even the most problematic reactions. To Felipe and Adolfo, thank you for bringing some Brazilian sunshine to the North East and for teaching us some very important rules for life. To Sinthujah, thank you for sharing this journey with me and I wish you well for your final year.

To the JAGW group: I feel incredibly lucky to have shared a lab and then an office with you. Thank you for being a dependable source of friendship and biscuits.

To all my other Durham friends, Harry, Marc, and the Northern Navigators: Thank you for reminding me there is a world outside the chemistry lab. Thank you for keeping me running through the cold winters and for keeping me going with home-baked cakes, good cheese, and so many pancakes. Also to my family and friends back home: Thank you for supporting me from afar and for always cheering me on, even if you didn't always understand what I was complaining about.

Finally, Paul, if I detailed every way you have supported me over the last 3 years, this thesis would surely be twice as long. Instead I will simply say thank you for being there always, even when there was 200 or 6,000 miles away.

Chapter 1

Introduction

This thesis has two discrete sections which take different approaches to advance fragment-based drug discovery efforts. Chapter 2 presents work accessing the pyrazolo[3,4-c]pyridine core and synthetic efforts to explore its subsequent functionalisation in generating an elaborated fragment library. An additional feature of the pyrazolo[3,4-c]pyridine cores is presented in Chapter 3, with the exploration of its photoluminescence properties. This work was carried out in collaboration with physicists at Northumbria University. Attempts to demonstrate the medicinal chemistry potential of this fragment are then described in Chapter 4.

The second section of the thesis focuses on more saturated fragments and Chapter 5 describes the synthesis of the azabenzolactam cores. This chapter also details the synthetic methodology development for the functionalisation of cyclic amines. Finally, Chapter 7 presents the experimental and analytical data to support all of these discussions.

The remainder of this chapter discusses the background to the project, reviewing ideas of fragment-based drug discovery, chemical space, and late-stage functionalisation.

1.1 Fragment-based Drug Discovery

1.1.1 Overview

Fragment-based drug discovery (FBDD) is a well-established method of finding and developing biologically active molecules that compliments the high-throughput screening (HTS) approaches traditionally favoured by the pharmaceutical industry. The fundamental difference between these approaches is the lower molecular weight and lower complexity of molecules used in FBDD. Fragments typically comply to the Rule-of-Three: adapted from Lipinski's Rule-of-Five, this defines fragments as molecules with a molecular weight ≤ 300 Da, ≤ 3 hydrogen bond donors, ≤ 3 hydrogen bond acceptors, and a $c\log P \leq 3$.[1,2]

The use of fragments leads to better sampling of chemical space, so smaller libraries can be used compared to HTS. Their small size results in fewer yet higher quality interactions of fragment hits because binding groups are less hindered by the reduced bulk of the molecule. Therefore, FBDD puts more emphasis on the efficiency of the binding interaction, measured with metrics such as ligand efficiency (LE) which divides the binding free energy of the ligand ($-\Delta G$) by its heavy atom count (HAC) [Equation 1.1].[3]

$$LE = \frac{-\Delta G}{HAC} \tag{1.1}$$

More sensitive biophysical screening techniques are required in FBDD in response to the relative weakness of target-hit interactions, typically 0.1-10 mM, compared to those of HTS hits, typically 1-100 μM [Figure 1.1.1.1]. Techniques such as Differential Scanning Fluorimetry (DSF), ligand-observed NMR, Surface Plasmon Resonance (SPR), and Isothermal Calorimetry (ITC) are used in various combinations and often X-ray crystallography is employed to elucidate structural information. Furthermore, to ensure a robust and comprehensive search for hits, fragment screening cascades employ orthogonal biophysical techniques for the preliminary screen, validation, and characterisation of fragments.[4]

The reduced throughput of these more sensitive methods is offset by the smaller size of fragment libraries compared to HTS. A recent study of commercially available libraries confirmed that a fragment library of fewer than 2,000 fragments is sufficient to represent the chemical diversity of all fragment-sized molecules.[5] Fragment libraries may be general (eg. OTAVAChemicals general fragment library),[6] focused on a particular characteristic (eg. LifeChemicals 3D fragment library),[7] or target-oriented based on known ligands (eg. *KinFragLib* Kinase Fragment Library).[8]

Due to low starting molecular weights, fragment hits have more scope for elaboration to improve potency and specificity without the lead compounds becoming overly large. This is advantageous for oral and topical drug-delivery because lipophilic compounds with low molecular weight have better oral bioavailability and

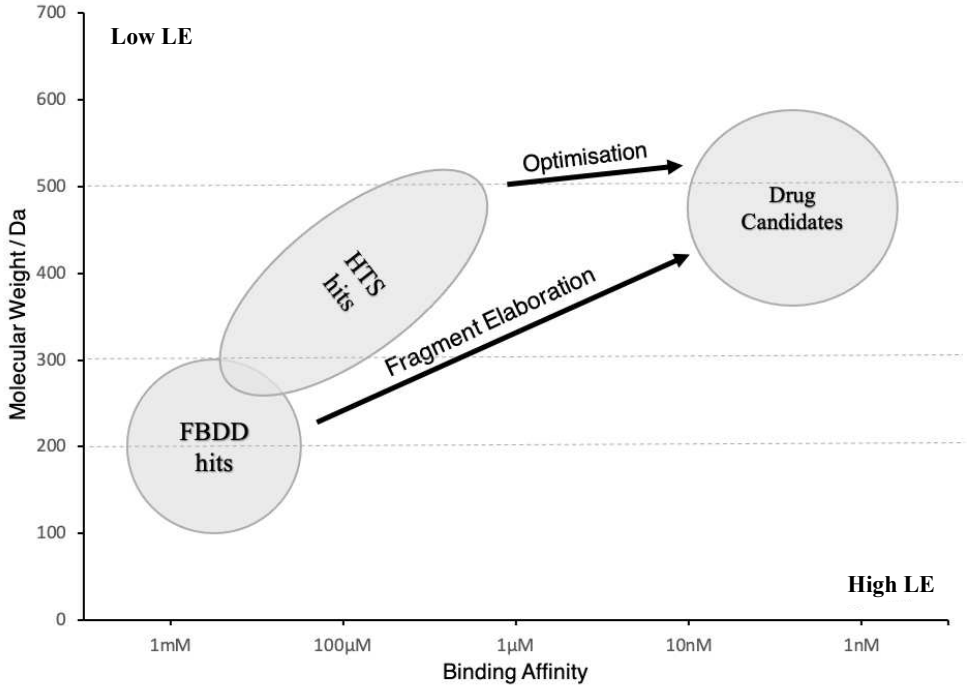

Figure 1.1.1.1: Graphical representation of the relative sizes and binding affinity ranges of FBDD hits, HTS hits, and drug candidates.

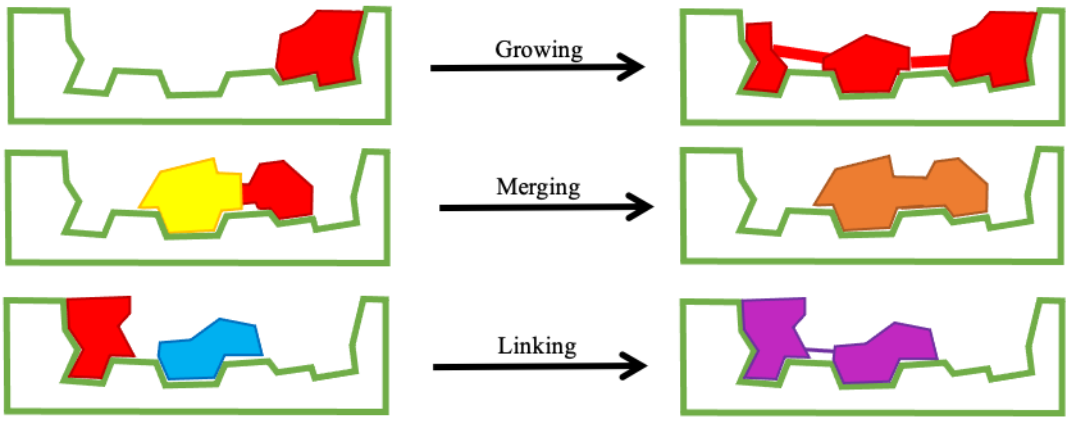

Figure 1.1.1.2: Cartoon of the basic fragment elaboration strategies: growing, merging, and linking.

better skin-permeability. Improvements to other drug-like properties can also be addressed as fragments are developed into potent inhibitors. Elaboration may be through fragment growing, fragment merging, fragment linking, or any combination of these methods [Figure 1.1.1.2].

1.1.2 Fragment Elaboration Strategies

Fragment growing incorporates additional functionality via stepwise chemical synthesis to engage new binding interactions with a protein target. It is the most accessible and, therefore, most common method of fragment elaboration as it requires identification of only one fragment hit. This strategy was exemplified by Kirsh *et al.* in the optimisation of hits targeting the DNA-binding domain of the latency-associated nuclear antigen of Kaposi's sarcoma-associated herpesvirus.[9] Structure-activity relationships were guided by a fluorescence-polarisation based assay and copper-catalysed triazole formation was used to grow imidazole **1** into triazole **2** (IC_{50} = 17 mM, LE = 0.33) [Scheme 1.1.2.1.a].

Fragment merging is the least common method of fragment elaboration because it requires the identification of two or more fragment hits with overlapping moieties that can be merged into a single more potent molecule. Furthermore, it is often dependent on structural information to guide the merging which may not be available. In an example reported by Markert *et al.*, tetrazole fragment **3** (IC_{50} = 4.5 mM, LE = 0.47) and diaryl ether fragment **4** (IC_{50} = 8.8 mM, LE = 0.47) were identified through DSF screening [Scheme 1.1.2.1.b]. X-ray crystal structure analysis, following co-crystallisation with leukotriene A4 hydrolase, guided fragment merging to afford tetrazole **5** (IC_{50} = 4.0 nM, LE = 0.53). As is commonly the case, further optimisation followed the merging step to generate the lead compound.[10]

Fragment linking requires the identification of two fragments binding to distinct regions of the target protein that can be joined by a chemical linker to generate a more potent inhibitor. Theoretically, this should be the most efficient way to improve binding affinity due to what is known as the superadditivity effect.[11] However, like fragment merging, it is often dependent on structural information to guide the design of the linker, so its applications are limited. One example, reported by Frank *et al.*, targeted the N-terminal domain of Replication Protein A (RPA70N) by linking fragment hits **6** (K_D = 1.4 mM, LE = 0.26) and **7** (K_D = 580 μM, LE = 0.22), identified through NMR-based screening [Scheme 1.1.2.1.c].[12] Linked compound **8** (K_D = 20 μM, LE = 0.18) had a much improved binding affinity compared to the individual fragments, although the lower LE shows that the new binding position was sub-optimal. This arises when the chemical linker prevents the molecule from finding the preferred binding pose of the original fragments, hence the interactions with the protein are weakened. The authors addressed this through further optimisation of the linker guided by X-ray crystal structure analysis, which restored the ligand efficiency and further improved the binding affinity.

These examples and many others demonstrate the established methodology of FBDD and how it continues to develop novel treatment strategies. There are currently seven FDA-approved drugs that started from fragment-based approaches. The first, Vemurafenib,[13,14] was approved in 2011 to treat mutant BRAF in skin cancer patients, and the most recent, Capivasertib,[15,16] was approved in 2023 to treat certain breast cancer patients. Nevertheless, many important biological targets remain intractable with no known ligands. Advances in screening techniques enable detection of increasingly weak

interaction in the hopes of establishing new starting hits and *in silico* screening allows for rapid virtual chemical database searches. However, it remains a significant possibility that the key to unlocking these targets lies in molecular scaffolds that have yet to be explored.

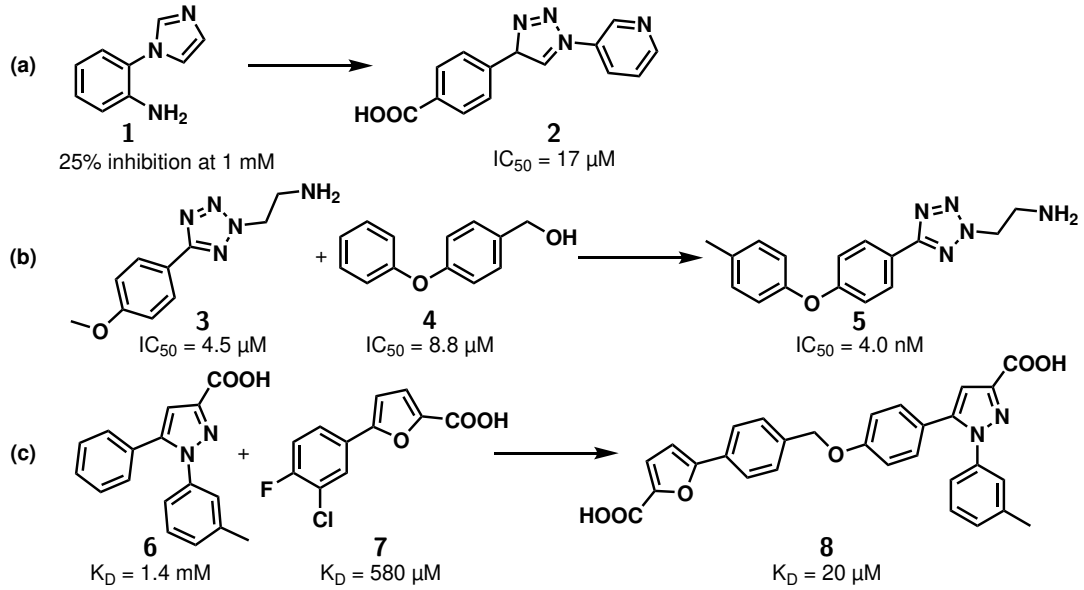

Scheme 1.1.2.1: Structure and IC_{50} or K_D data of examples fragment-based drug discovery regimes targeting **a)** the DNA-binding domain of latency-associated nuclear antigen via fragment growing,[9] **b)** Leukotriene A4 hydrolase via fragment merging,[10] and **c)** Replication Protein A via fragment linking.[12]

1.1.3 Limitations of FBDD

A typical FBDD programme begins by screening a fragment library against a particular biological target of interest to find promising starting molecules. The subsequent structure-activity relationship (SAR) analysis and fragment elaboration requires a collection of analogues with new binding groups introduced at different positions around the fragment core. The most desirable growth vectors are dictated by the potential binding interactions with each protein target, often identified by structural information from X-ray crystallography.

If commercial analogues are not available, diverse syntheses may be required to produce the necessary structural diversity in compounds to be tested by a drug-discovery regime. In this way, the chemical synthesis required during fragment elaboration is often the rate-limiting step in FBDD programmes.[12] Progress may stall while new synthetic routes are established, or promising fragment hits may be down-prioritised due to synthetic intractability [see reference[17] for examples]. These complications discourage the adoption of novel molecular scaffolds and encourage "scaffold hopping" to more established fragment cores. This undermines the advantages that fragment screening offers for efficient sampling of chemical space and has limited current research within small "islands" of chemical similarity.

1.2 Chemical Space

Chemical space describes an exhaustive collection of all possible molecules. Construction principles and boundary conditions are then introduced to define specific subsets that are useful and usable.[18] These space descriptors typically include constraints on molecular weight, numbers of specific heteroatoms (eg. O, N, F, Cl, S), ring size, and chain length.[19] Depending on its purpose, a chosen chemical space may also be defined by rules such as chemical feasibility, measured biological activity, or metal-binding ability. The size of a given chemical space depends on the boundary condition descriptors, and as the number of experimental or computational descriptors increases, so does the number of possible valid chemical spaces.[20]

The concept of a drug-like chemical space is of great interest and there have been many attempts to define it.[21–23] Generally, it is defined by constraints of physicochemical parameters including molecular weight, partition coefficient of water/octanol ($\log P$), number of hydrogen bond donors and acceptors, number of rotatable bonds (NRot), and topological polar surface areas (TPSA) to reflect already approved drug compounds. A widely quoted estimate of the size of drug-like chemical space suggests it contains 10^{60} molecules,[24] although estimates vary from 10^{12} to 10^{180} molecules.[25] The present number of reported chemicals is only 2×10^8 molecules and the difference between these figures represents areas of unexplored molecular structures that could unlock as yet undruggable biological targets and enable access to novel intellectual property.[26]

Early methods to enumerate areas of chemical space relied on synthetic combinatorial chemistry; the systematic combination of various sets of chemical building blocks through repetitive covalent bond-forming reactions. These combinatorial chemical libraries can be screened concurrently, and individual hit molecules are later identified by genetic tags (DNA-encoded libraries),[27] fluorescent-activation of beads (one bead, one compound),[28] or chemical means (mass spectrometry or NMR spectroscopy).[29,30]

To meet demands for larger and larger compound collections, electronic compound databases have been generated from the systematic combination of virtual building blocks according to robust organic syntheses, the largest being the Enamine REAL database.[31] The REAL database contains 6.75 billion compounds for virtual screening, and once hits are identified they can be purchased from Enamine directly. However, the sequential screening of molecules in virtual libraries of this size requires extreme computing power and extensive analysis to produce meaningful starting points for new drug-discovery programmes. The development of new cheminformatics tools and virtual combinatorial processes have since made it easier to generate ultra-large virtual libraries of compounds, the largest of which is "eXplore" containing over 4.9 trillion compounds.[32]

A major drawback of these commercial libraries, however, is that the need for simplicity and commercial availability limits the diversity in these collections. For example, there are known molecular scaffolds,

such as cubane or prismane, that are often discounted in chemical space enumerations due to noncompliance of their unusual, highly strained systems with standard chemical feasibility descriptors.[33] Another example is that "eXplore", generated from combinations of building blocks using only 45 common reactions in one or two-step syntheses, fails to adequately represent certain functionalised heterocycles and other (oligo-)nucleotide analogues due to their relatively complex, and often specially tailored, syntheses.[33] This is a major drawback due to the prevalence of heterocycles in drug compounds and natural products. Therefore, despite the ever-increasing size of available compound libraries, there are still significant gaps in the compound diversity being introduced to the drug discovery pipeline.

1.2.1 "Rings of the Future"

In an attempt to explore new areas of chemical space relevant to medicinal chemistry, the 2009 publication from Pitt *et al.* introduced the "virtual exploratory heterocyclic library (VEHICLe)".[34] This computer generated compound library aimed to enumerate the under-utilised areas of chemical space with a focus on heterocyclic scaffolds. This set of 24,847 possible small heteroaromatic ring systems included over 3,000 synthetically tractable, yet largely unpublished, molecules. After the application of several chemical-feasibility filters, this was refined to a set of 232 heteroaromatic bicyclic systems from which 22 "Rings of the Future" were chosen by the authors [Figure 1.2.1.1]. These were presented as a challenge for chemists to establish new synthetic routes and methods of functionalisation.

Of these 22 heterocycles, synthetic routes to 16 have been reported, including 10 which have been isolated in their bicyclic form and 6 which exist in polycyclic forms. A further 4 have appeared in industrial patents with no explicit synthesis. Of the 2 remaining heterocycles, **P20** appears in a DFT study of the hydrogen bonding strength of heterocycles,[35] while **P3** remains elusive [Figure 1.2.1.1]. The

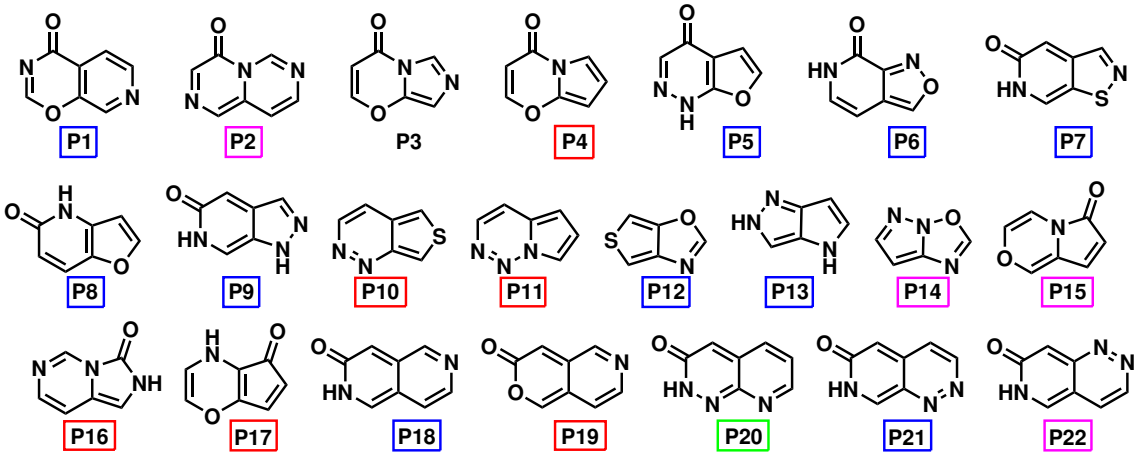

Figure 1.2.1.1: Structures of the 22 "Rings of the Future" labelled as in the 2009 publication.[34]
Blue = reported synthetic route to bicyclic scaffold, Red = reported synthetic route to polycyclic form, Purple = structure in patent with no reported synthesis, Green = included in DFT study

syntheses and applications of these "Rings of the Future" are briefly discussed below.

Several of the heterocycles had, in fact, been reported prior to the 2009 publication. For example, anti-fungal agents reported in 2008 contained cyclopenta[b][1,4]oxazin-5-(*4H*)-one **P17** as a substructure of the tricyclic phosphate ester **9** [Scheme 1.2.1.1]. The fused tricyclic system was formed via the cyclisation reaction between an indanmonoxime **10** and the Wittig-Horner reagent, diethyl(cyanomethyl)phosphonate, under basic conditions.[36]

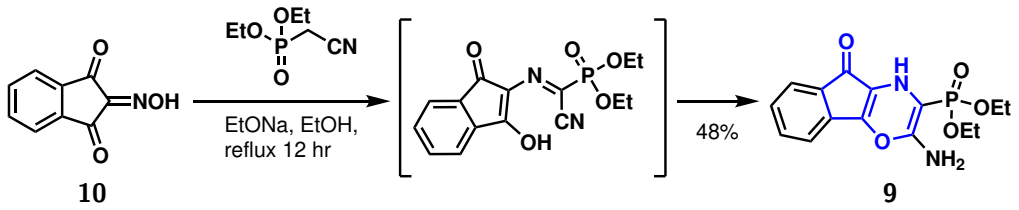

Scheme 1.2.1.1: Structure of anti-fungal agents containing benzo-fused cyclopenta[b][1,4]oxazin-5(*4H*)-one **P17** scaffold.[36]

The **P10** heterocycle had also been reported prior to 2009 as part of some tricyclic compounds derived from the intramolecular diazo coupling reaction of thiazole **11** in the presence of $NaNO_2$, under acidic conditions [Scheme 1.2.1.2].[37] Subsequent modifications to this approach have improved reaction scope but no pharmaceutical applications have yet been explored.[38,39]

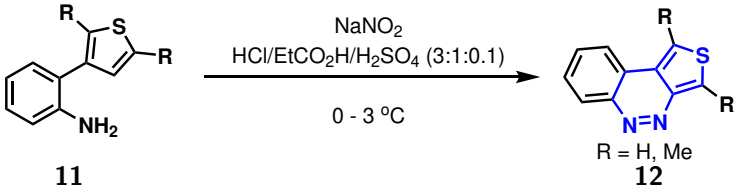

Scheme 1.2.1.2: Synthesis of thieno[3,4-c]cinnolines (tricyclic compounds containing the **P10** scaffold) via intramolecular diazo coupling reactions.[37]

The **P4** scaffold was first identified in 1999 as a substructure of Streptopyrrole XR587 **13** isolated from Streptomyces and with potential antibacterial activity [Figure 1.2.1.2].[40] Later studies have evaluated its potential as a histidine kinase inhibitor in salmonella.[41] The **P4** scaffold was also a substructure of the benzoxazino[3,2-a]indol-12-ones **14** synthesised by Xia *et al.* via intramolecular Cu catalysed C-N coupling, which has shown potential activity against multiple biological targets [Figure 1.2.1.2].[42] There has yet to be a reported synthesis of the isolated scaffold, but the **P4** motif was included in a 2024 patent for compounds targeting neurodegenerative, degenerative and metabolic disorders.[43]

The pyrrolo[1,2-c][1,2,3]triazine **P11** scaffold was reported by Cirrincione *et al.* in 1999 as a substructure of a library of indolo[1,2-*c*]benzo[1,2,3]triazines which demonstrated antibacterial activity against *Streptococcus* and *Staphylococcus*. The indolobenzotriazine structure was synthesized via

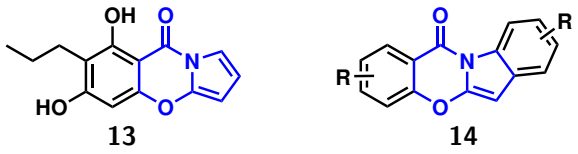

Figure 1.2.1.2: Literature examples of the **P4** scaffold.[40,42]

diazotization of variously substituted 2-(2-aminophenyl)indoles **15** with $NaNO_2$ in acetic acid, followed by an intramolecular coupling reaction of the diazonium group with the indole nitrogen of **16** to afford the triazine product **17** [Scheme 1.2.1.3]. The authors note a necessity to protect the 3 position of the indole to prevent cyclization into the indolo[3,2-*c*]cinnoline system, indicating the complexity of this synthetic route.[44] A series of compounds with this general structure are now commercially available from multiple suppliers.

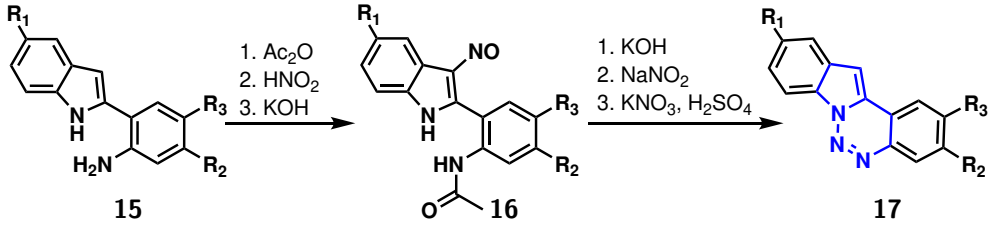

Scheme 1.2.1.3: Synthesis of antibacterial agents containing the pyrrolo[1,2-c][1,2,3]triazine core **P11** scaffold.[44]

Also prior to the 2009 publication, Crum *et al.* reported compound **18** as a close analogue of the **P1** scaffold with an additional carbonyl at the *C*-2 position [Figure 1.2.1.3].[45] More recently Slowinski *et al.* employed an intramolecular O-arylation to access compound **19** with 24 examples,[46] while Le Falher *et al.* used Stille and Sonogashira coupling reactions to access another 23 examples of polyfunctionalised compound **20** for use as fluorescent probes [Figure 1.2.1.3].[47]

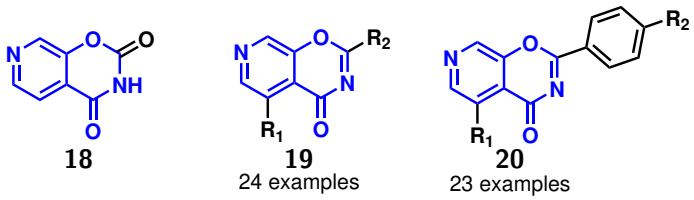

Figure 1.2.1.3: Literature examples of the **P1** scaffold.[45–47]

In 2008, a 5-carboxylate derivative of the **P13** scaffold was identified by Sparey *et al.* through an HTS campaign targeting the D-amino acid oxidase enzyme.[48] However, it showed complete loss of activity compared to the parent compound so was not progressed. Here the pyrrolo[3,2-c]pyrazole bicyclic system was accessed through an intramolecular thermal cyclisation of the SEM-protected pyrazole **21**

[Scheme 1.2.1.4]. This methodology was used later in the formation of the benzo-fused scaffold, pyrazolo[4,3-b]indole in the development of methionine aminopeptidase-2 inhibitors. This time the heterocyclic scaffold was developed from an indazole hit identified in a fragment screen.[49] Synthetic routes to other more substituted pyrrolo[3,2-c]pyrazoles and pyrazolo[4,3-b]indoles later emerged, using Cu and Ru metal catalysed C-N coupling reactions to form the cyclic systems.[50,51]

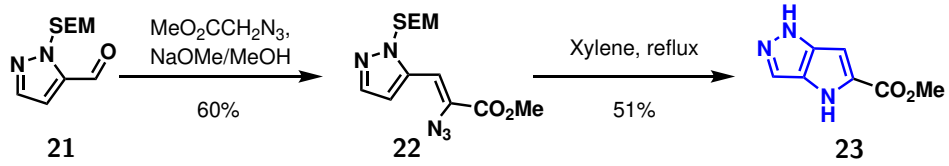

Scheme 1.2.1.4: Synthesis of pyrrolo[3,2-c]pyrazole **P13** scaffold via intramolecular cyclisation.[48]

Multiple benzo-fused variants have been reported for the **P8** scaffold. These have demonstrated biological activity as endothelin antagonists and as promising antibacterial and anti-fungal agents.[52,53] For this scaffold, the distinct bicyclic core *4H,5H*-furo[3,2-b]pyridine-5-one has also been synthesised [Scheme 1.2.1.5]. Fu *et al.* described a route to the 6-phenyl compound **24** via Cu catalysed condensation of 3-bromo-2-furaldehyde **25** with 2-phenylacetamide **26**, although this form has not been used in any pharmaceutical applications thus far.[54]

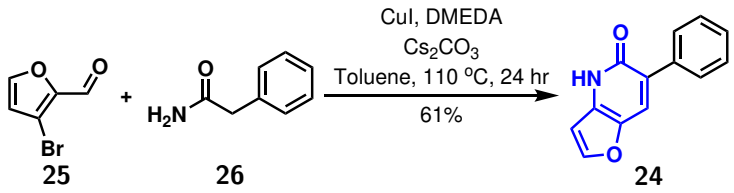

Scheme 1.2.1.5: Synthesis of **P8** scaffold containing 6-phenyl-*4H,5H*-furo[3,2-b]pyridine-5-one via Cu catalysed condensation reaction.[54]

Unusually, the **P19** motif only appears as a substructure of the tetracyclic *5H*-pyrano[2,3,4,5-lmn]-phenanthridin-5-one **27**. This was first observed in 1968 as an unexpected product of the oxidation of 2'-cyano biphenyl-2-carboxylic acid **28** with persulfate.[55] The authors proposed this reaction proceeded via the radical pathway illustrated in Scheme 1.2.1.6. This same compound was later identified as a minor component of *Cymbopogon winterianus* essential oil and as a constituent of dissolved organic matter collected from glacier thaw.[56,57]

More of the "Rings of the Future" have been reported since 2009, including one work stimulated primarily by the original paper that was reported by Keserü *et al.* in 2016. A synthetic route from furan **29** to the *C*-3 substituted furo[2,3-c]pyridazine-4-one **30** based on scaffold **P5** was described offering good yield over 6 steps, albeit with limited substituent options [Scheme 1.2.1.7a].[58] In the same year, the Keserü group also reported the first synthesis of *C*-3 substituted derivatives of the **P6** scaffold [Scheme 1.2.1.7.b]. This

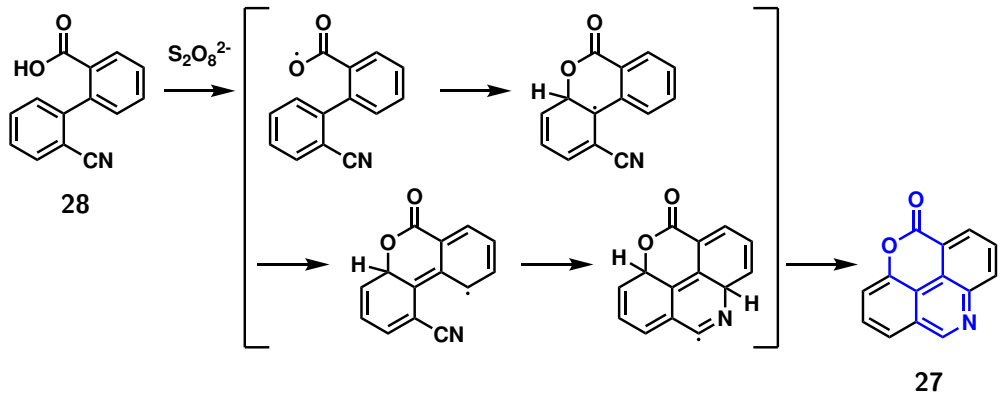

Scheme 1.2.1.6: Proposed radical mechanism for the formation of tetracycle **27** containing the **P19 scaffold**.[55]

employed a ring opening and closing sequence of the isoxazole **31**. This intermediate can be made from the commercially available propiophenones which offers broader scope for other functionalised derivatives, although no pharmaceutical applications of either scaffold have yet been reported.[59]

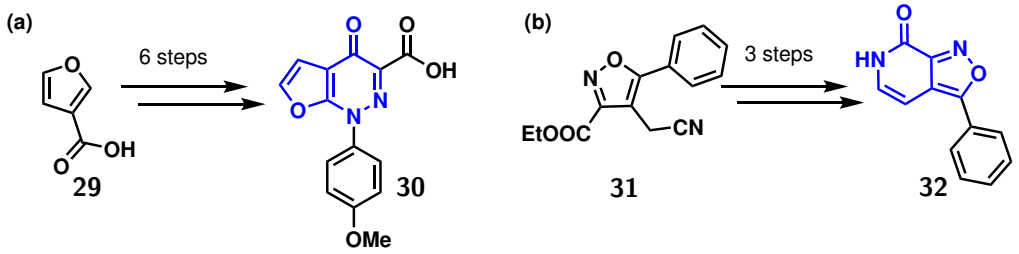

Scheme 1.2.1.7: Synthetic routes to **a)** compounds containing the **P5** scaffold and **b)** compounds containing the **P6** scaffold.[58,59]

The *6H*-[1,2]thiazolo[5,4-c]pyridine-5-one **P7** ring was central to a small library of herbicides reported by Selby *et al*. The *N*-methylated core in structure **33** was synthesised via the condensation of an α-keto ester **34** and a *N*-methyl-1-isothiazol-5-yl-methanamine **35** followed by cyclisation in concentrated sulfuric acid [Scheme 1.2.1.8].[60]

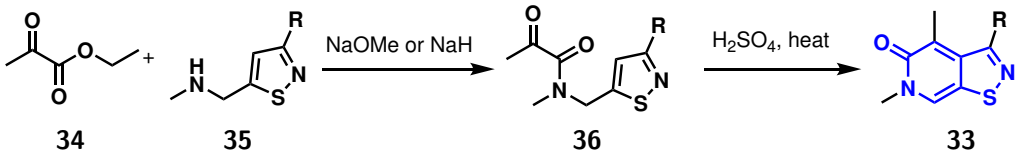

Scheme 1.2.1.8: Synthesis of *6H*-[1,2]thiazolo[5,4-c]pyridine-5-one **P7** scaffold-based library of herbicidal compounds **33**.[60]

As these heterocyclic scaffolds are finding more industrial applications, they are increasingly reported in the patent literature. For example, the **P12** scaffold has found uses in electrochromic materials, organic semiconductors, and conjugated polymers showing this heterocycle possesses unusual electronic

properties.[61–63] The preparation of 2-methylthieno[3,4-d][1,3]oxazole **37** was reported by Otake *et al.* in a 2011 patent for electrochromic materials starting from oxazole **38** [Scheme 1.2.1.9].[61] Subsequent bromination with NBS generated 6-bromo-2-methylthieno[3,4-d][1,3]oxazole **39** to be used in Stille cross-coupling reactions in the generation of 2-methylthieno[3,4-d][1,3]oxazole **40**.

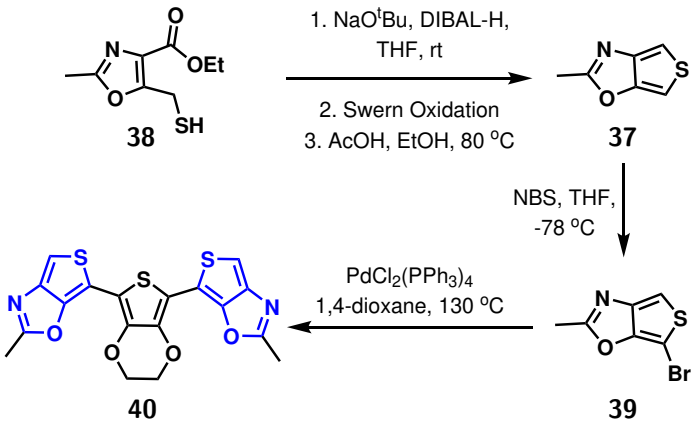

Scheme 1.2.1.9: Stille cross-coupling of compounds containing the **P12** scaffold.[61]

The pyrazolo[1,5-b]isoxazole **P14** scaffold appears only in tetracyclic pyrido- and benzo-fused compounds **41** and **42** described by a Konica Minolta research group in a 2016 patent for blue phosphorescent Ir(III) and Pt(II) complexes [Figure 1.2.1.4.a].[64] Similarly, the 2*H*-imidazol[1,5-c]pyrimidine-3-one **P16** scaffold appears only in tricyclic systems such as the imidazo-fused compounds **43** described by the Nissan Chemical Corporation in a 2015 patent for Janus kinase inhibitors [Figure 1.2.1.4.b].[65]

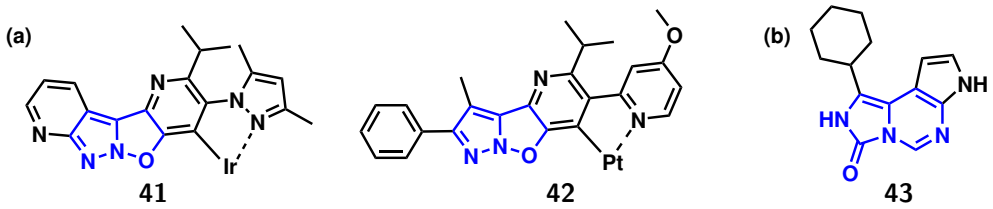

Figure 1.2.1.4: Literature examples of the **P14** and **P16** scaffolds.[64,65]

Another scaffold that appears in the patent literature is **P21**, an intermediate in the synthesis of HPK1 antagonists [Scheme 1.2.1.10]. Here the pyridazine ring was introduced in the starting material **44** and the pyridine ring was introduced through a condensation of the 1,5-dicarbonyl **45** with ammonia to afford **46**. The pyrido[3,4-c]pyridazine core was retained in final compound **47** with the oxygen at the 6-position replaced by a 4-methylpyridine ring.[66]

Some of the heterocycles that appear in recent industrial patents were reported without an explicit description of their synthesis. The **P2** scaffold, for example, only made an appearance in 2024 in a patent for lysine-specific demethylase 1 inhibitors [Figure 1.2.1.5].[67] In the same year, **P22** was reported as an

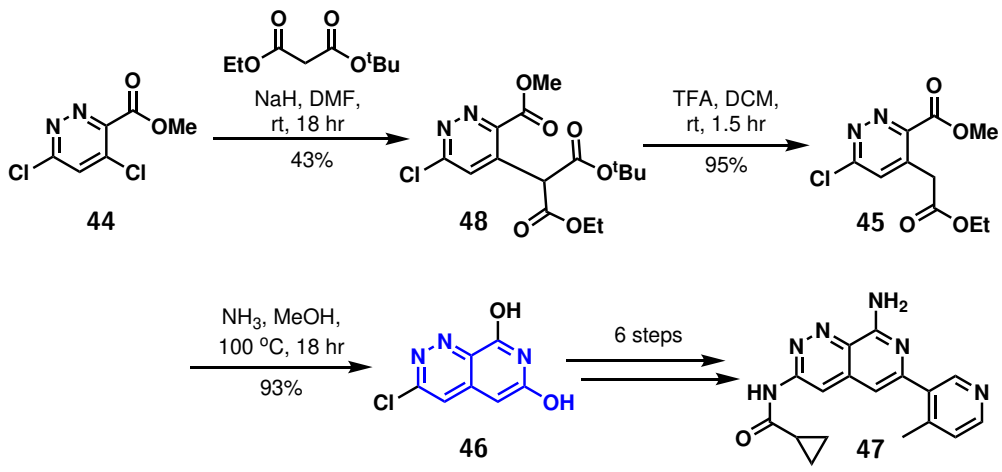

Scheme 1.2.1.10: Synthesis of HPK1 antagonists via an intermediate based on the **P21** scaffold.[66]

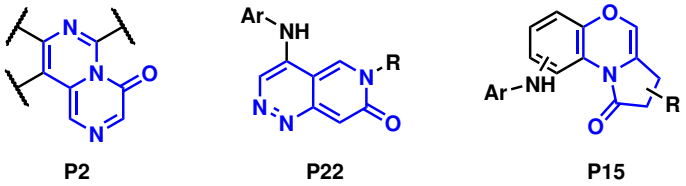

Figure 1.2.1.5: Scaffolds **P2**, **P22**, and **P15** are covered by industrial patents.[67–69]

inhibitor of the SOS1-KRAS protein-protein interaction covered by a patent from Wangshi Wisdom Tech [Figure 1.2.1.5].[68] The **P15** scaffold has also only been included in a recent patent, appearing as a part of a series of tricyclic phosphatidylinositol phosphate kinase inhibitors [Figure 1.2.1.5].[69]

A 3-amino derivative of the **P18** scaffold was reported in a Cancer Research Technology patent in 2014 as an efficient monopolar spindle 1 inhibitor, synthesised from the azaisoquinolinol tautomer of the **P18** heterocycle.[70] Diphenyl-substituted derivatives of the same scaffold had been previously reported in 2013 by Li *et al.* who found the 6 vs 7 position of the aza-nitrogen had a marked effect on the UV-vis and fluorescence spectra. The two heterocycles were synthesised via an intermolecular [4+2] cycloaddition then retro-Diels-Alder reaction.[71] A novel synthetic route was later reported by Silva Júnior *et al.* to afford the parent unsubstituted 2,3-dihydro-2,6-naphthyridin-3-one **49**.[72] *N*-oxidation then *O*-ethylation of ethyl 2-(pyridine-3-yl)acetate **50**, followed by nucleophilic addition of cyanide, generated an ethyl 2-(4-cyanopyridin-3-yl)acetate intermediate **51**. Intramolecular lactam formation proceeded spontaneously following reduction of the cyano group to form the second ring in **52**. Oxidation over activated charcoal then gave the desired heterocycle [Scheme 1.2.1.11].

In the same paper, Silva Júnior *et al.* also reported a route to the parent unsubstituted *1H*-pyrazolo[3,4-c]pyridine-5-ol heterocycle **P9**.[72] The synthetic route to this heterocyclic system was first reported in 1980 by Chapman and Hurst, as discussed in more detail in the next chapter.[73]

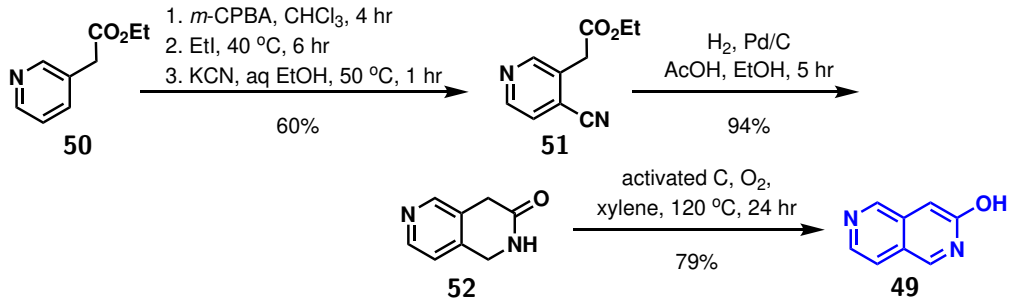

Scheme 1.2.1.11: Synthesis of the **P18** scaffold.[72]

1.2.1.1 Conclusion

The original "Rings of the Future" were designed to promote the exploration of new areas of chemical space. Currently, 21 of the 22 highlighted heterocycles have been reported elsewhere in the literature. Only a few of these acknowledge the original publication, so even if Pitt *et al.* did not inspire a lot of research directly, the authors at least predicted valuable potential scaffolds. However, the authors did not achieve the desired novelty in their hand-picked selection as nine of these had already been reported prior to the 2009 publication. Of these nine, only **P9** and **P13**, were reported as the bicyclic structure with the rest appearing as a substructure of a tri- or tetracyclic scaffold. The fused rings likely increased the chemical feasibility of these scaffolds by improving the synthetic stability and offering different synthetic routes. For example, the additional benzene ring in **12** facilitated the diazo coupling that generated the **P10** scaffold and a route to the bicyclic system has not yet been reported.[37]

Many of the scaffolds that were only reported more recently have appeared in industrial patents. These examples show an increasing awareness of the value of new heterocycle motifs for establishing new intellectual property. The inclusion of structures without a reported synthesis could also indicate an increasing belief in the accessibility of these scaffolds which are not yet widely reported.

Finally, 12 of these heterocycle cores have found use or have been tested against biological targets in a wide range of applications. To develop potent compounds, many analogues are required for screening. However, nearly all of the structures described here had the molecular diversity introduced prior to the ring-forming step. For example, the additional *C*-3 substituents on compound **17**, based on **P11**, were necessary to facilitate the formation of the desired heterocycle, while the *C*-3 substituents of compounds **33**, based on **P7**, were present in the starting thiazole.[44,60] Also in the case of compound **46**, based on **P21**, an additional chlorine atom was included to enable the introduction of different amide substituents.[66] These examples highlight that a major obstacle of using uncommon heterocyclic scaffolds for biological testing is the challenge generating analogues that enable the exploration of chemical space around the chosen core.

1.2.2 Late-stage Functionalisation

Late-stage functionalisation (LSF) is the concept of chemically modifying a compound that has already undergone several steps of synthesis. This enables the formation of focused libraries of compounds generated from a common intermediate.[74] LSF plays an important role in drug development, particularly during hit-to-lead and lead optimisation. Rapid synthesis of a focused library of analogues is used to generate valuable SAR that guides optimisation of lead compounds without returning to *de novo* syntheses. This is particularly useful in fragment-based drug discovery, introduced in Section 1.1, where low molecular weight fragments are elaborated by the addition of new substituents. SAR analysis can identify which positions are the best to functionalise to most effectively enhance biological activity.

LSF has historically relied on intermediates with preinstalled handles that can be combined by various metal-catalysed cross-coupling reactions. SGX Pharmaceuticals capitalised on this by designing a fragment library for X-ray crystallographic screening in which many of the compounds contain one or more bromine atoms. The heavy bromine atoms not only facilitate fragment location during structure elucidation, but also provide a synthetic handle for easy fragment elaboration. This fact was exploited by Antonysamy *et al.* in the development of Janus kinase 2 (JAK-2) inhibitors.[75] The primary screen selected fragments **53** and **54** and the crystal structures revealed a channel in the protein accessible by modifications at *C*-5 or *C*-6. The bromine handle enabled modification through two analogous Suzuki-Miyaura cross-coupling strategies: by reaction of **53** directly with a range of aryl boronic acids, or by the inverted reaction replacing the bromine with a Bpin group and reacting this intermediate with the appropriate aryl bromide. Two rounds of SAR by cross-coupling identified *C*-5 was the best position for elaboration, and compound **55** was selected as the lead candidate [Figure 1.2.2.1].

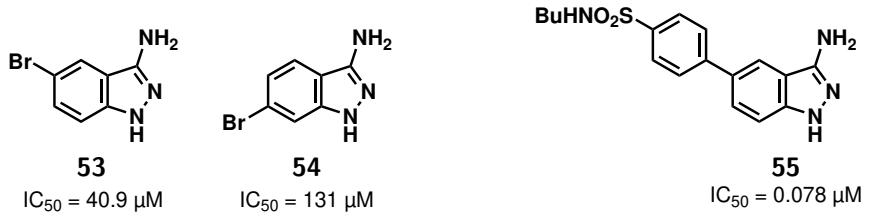

Figure 1.2.2.1: Fragment elaboration by Suzuki-Miyaura cross-coupling of bromine-contain fragments.

Other synthetic handles that enable synthetic transformations include carboxylic acids, aldehydes, and amines. However, the problem of using such chemical building blocks is that the reactive groups are often not suitable for biological screening. One route to address this was presented by Maly *et al.* who masked the reactive aldehyde handles in their fragment library by replacing them with an *O*-methyl oxime.[76] Once hit compounds were identified, the unmasked aldehyde was used as a synthetic handle to link two binding elements together by condensation with an *O,O'*-diaminoalkanediol linker. This strategy was used in a combinatorial library approach to c-Src inhibitors, identifying final compound **56** [Scheme 1.2.2.1].

While this approach can clearly be used to identify potent inhibitors, there is a major drawback. To be effective, the synthetic handle cannot be involved in protein binding and must be available for synthetic modification. This clashes with the concept of fragments offering low molecular weight compounds with high ligand efficiency. Furthermore, this approach is limited by the need for synthetic handles to be in a suitable direction for fragment elaboration as dictated by the protein structure.

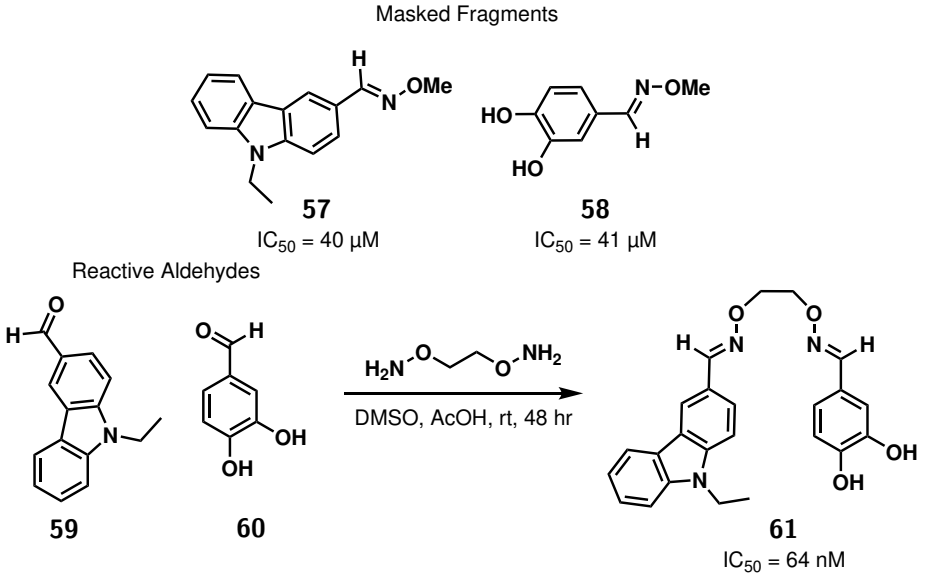

Scheme 1.2.2.1: Masked fragments protect reactive synthetic handles during screening.

To overcome these challenges, there are now increasingly methods of LSF that target C-H bonds directly. Goldman and Goldberg describe the C-H bond as "the un-functional group" and, due to its ubiquity and relative inertness, describe its activation as "the most broadly applicable and powerful class of transformations in organic synthesis".[77] The most important aspect of any method of LSF is that it can be applied selectively in the presence of many other functional groups.[74] This selectivity becomes harder when the functional group being targeted is as common as the C-H bond. As such, there are two broad strategies to achieve C-H bond selectivity: (1) guided reactions that rely on directing groups or steric interaction within the substrate to achieve C–H selectivity, and (2) innate reactions that rely on the intrinsic difference in reactivity of the C–H bonds.[78] Examples of both strategies are given below.

A common directing group strategy is to exploit the coordination of sp^2 nitrogen atoms with a metal catalyst, for example in the late-stage fluorination of the commercial herbicide Diflufenican **62** [Scheme 1.2.2.2].[79] This strategy can also be applied even when no pyridine ring is present in the substrate by introducing a removable pyridine directing group. This was exemplified by Lou *et al.* for the regioselective Pd-catalysed C-H fluorination of 2-phenyoxyl nicotinate derivatives **63** [Scheme 1.2.2.3].[79] Removable pyridine directing groups have also been reported for the C-H activation of phenols to introduce alkenyl,[80] aryl,[81] boryl,[82] acyl,[83] and silyl groups.[84] Pd is the most common transition metal

catalyst but Ru and Cu are also used in these transformations. The ability to temporarily introduce the pyridine directing group is a useful strategy to control regioselectivity, however the requirements for additional synthetic steps are undesirable. This challenge is avoided by utilising intrinsic differences in C-H bond reactivity within a substrate.[85]

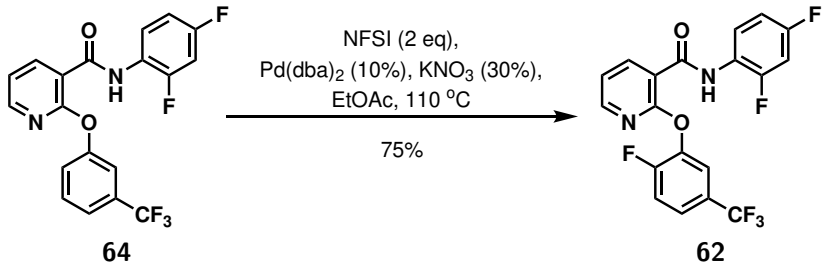

Scheme 1.2.2.2: Pyridine directing group for the regioselective fluorination of diflufenican **62**.[79]

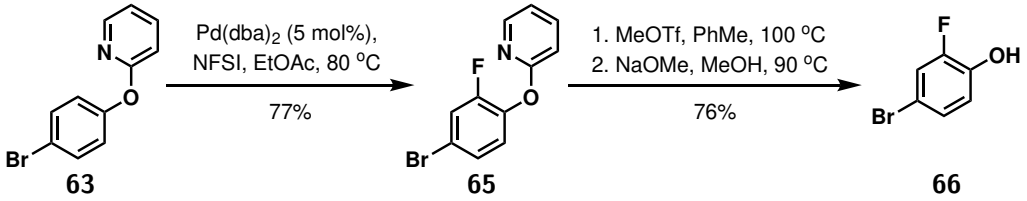

Scheme 1.2.2.3: Literature example of a removable pyridine directing group used for the regioselective fluorination of 2-phenyoxyl nicotinate derivatives.[79]

An early example of this intrinsic selectivity was reported by Fujiwara and Moritani in the arylation of olefins, wherein electron-donating groups favoured *para*-C-H activation but electron-withdrawing groups favoured *meta*-C-H activation [Scheme 1.2.2.4.a and b].[86,87] Altering the electronic nature of ring substituents was also proven to control the C-H selectivity in the Ir-catalysed borylation of substituted arenes.[88] In this case, π-electron acceptors favoured *para*-C-H borylation while π-electron donors favoured *meta*-C-H borylation [Scheme 1.2.2.4.c and d]. The reverse selectivities demonstrated by these two methods highlight differences in the reaction mechanisms. The Fujiwara-Moritani reaction proceeds by an electrophilic metalation mechanism, so obeys typical S_EAr selectivities, meanwhile Ir-catalysed borylation correlated better with C-H acidities. The Fujiwara-Moritani reaction has since been used in the synthesis of many biologically relevant compounds, including an intramolecular Fujiwara-Moritani-type coupling in one reported synthesis of codeine [Scheme 1.2.2.5].[89]

During hit-to-lead elaboration, the most desirable growth vectors are dictated by the protein structure and it is often necessary to employ complimentary methods of LSF to access multiple positions around the fragment core. This makes it advantageous to have different synthetic strategies available that offer orthogonal selectivities. As demonstrated by these examples, small changes in the electronic and steric properties can have a big influence on the outcome of reactions and this is further complicated when

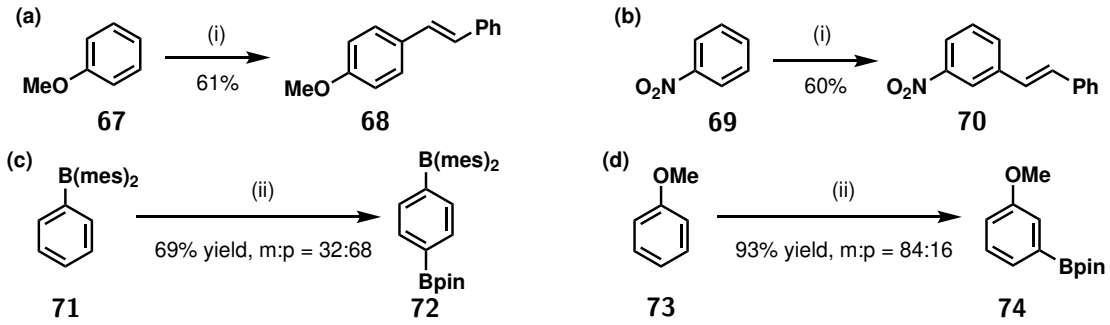

Scheme 1.2.2.4: Comparing the regioselectivity of the Fujiwara-Moritani-type arylation of olefins to the regioselectivity of the Ir-catalysed borylation of substituted arenes.

Conditions: (i) Styrene, $Pd(OAc)_2$, AcOH, 110 °C. (ii) $[Ir(OMe)cod]_2$, B_2pin_2, dtbpy, MTBE, rt, 16 hr.

mes = mesityl = 2,4,6-$Me_3C_6H_2$. The *meta* yields for borylation combined mono- and bis-borylated products.

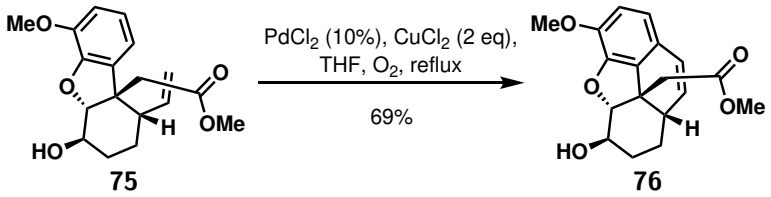

Scheme 1.2.2.5: Late-stage application of an intramolecular Fujiwara-Moritani-type coupling in a reported synthesis of codeine.[89]

heteroatoms are introduced. There is still a need to explore methods of LSF to understand reaction selectivities, expand the functional group tolerances, and develop new methodology for the functionalisation of uncommon substrates.

1.3 Project Objectives

As discussed previously, nitrogen heterocycles have a privileged place in FBDD as they are prevalent in bioactive natural products, pharmaceuticals, and agrochemicals. Heteroatoms facilitate strong polar interactions with the target proteins and they enable modification of the physicochemical properties of a drug candidate. As such they are common motifs in fragment libraries. Despite this, there is limited variation in the range of heterocycles that are represented in commercial drug compounds. New heterocyclic cores, therefore, offer a route to explore new areas of chemical space that could unlock elusive therapeutic targets.

To address this opportunity, the first aim of this project was to develop novel fragment libraries based on under-represented nitrogen heterocycles to explore new areas of chemical space. A subsidiary aim was to demonstrate their value to future drug discovery programmes by exploring the biological activity of the fragments against an exemplary protein target.

The biggest challenge of working with heterocyclic fragments is the synthetic chemistry of fragment elaboration. Synthetic methods of accessing decorated heterocycles often involve *de novo* construction of the aromatic ring so new synthetic routes must be derived for each new compound. The required optimisation can be laborious and costly, while the range of tolerated functionalities may be limited by the conditions of heterocyclic formation. These synthetic challenges limit the structural diversity of compounds that can be rapidly generated for further testing.

Therefore, a second objective was to develop methods for the functionalisation of nitrogen heterocycles. The ambition for this methodology was that it should be regioselective with a broad reaction scope, so efforts focused on strategies for the C-H activation of aromatic and aliphatic systems.

Chapter 2

Exploring the Pyrazolo[3,4-c]pyridine Scaffold

The many advantages that nitrogen heterocycles offer FBDD have already been discussed, explaining their attraction to medicinal chemists. The main drawback is that synthetic methods of accessing heterocycles often involves construction of the aromatic ring, so new synthetic routes must be derived and optimised for each new compound. This is time and resource expensive and therefore impractical for commercial drug discovery programmes.

For a new heterocyclic scaffold to be widely recognised it must overcome three hurdles. Firstly, the synthesis must be robust, efficient, and from cheap starting materials so large amounts of material can be easily generated. Secondly, synthetic routes must be established to enable functionalisation along as many growth vectors as possible. This methodology should have a broad reaction scope to facilitate SAR analysis and fragment elaboration. Specifically, the development of synthetic chemistry that utilises C-H functionalisation strategies in the presence of heteroatoms and heterocycles is most valuable. Finally, the heterocycle needs to show activity against a biological target of interest to exemplify its utility to medicinal chemistry research.

The following chapters outline the work taking a *1H*-pyrazolo[3,4-c]pyridine scaffold through these three stages to establish its potential as a new heterocycle of interest for FBDD.

2.1 The *1H*-Pyrazolo[3,4-c]pyridine

The pyrazolo[3,4-c]pyridine was identified as a heterocycle of interest due to its favourable characteristics for FBDD. 'Drug-like' molecules are defined by properties that include compound size, polarity, and water solubility, while a good drug candidate balances potency with absorption, distribution, metabolism, excretion, and toxicity (ADMET).[90] Numerous sets of drug-likeness guidelines have been proposed to aid early stages of drug discovery in an effort to improve attrition rates. The original, and most well-known, being Lipinski's Rule-of-Five for good oral bioavailability.[2] As described in Section 1.1, a similar yet more restrictive Rule-of-Three defines a good fragment. Table 2.1 shows that 5-chloro-*1H*-pyrazolo[3,4-c]pyridine **77** meets all of the criteria for an acceptable fragment and so would be a suitable starting point for FBDD.

Table 2.1: Comparing 5-chloro-*1H*-pyrazolo[3,4-c]pyridine with the criteria for drug-like compounds.

Compound Property	**Ro3 Criteria**	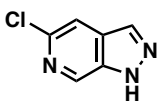 **77**
Molecular Weight	$\leq$ 300 Da	153.5 Da
No. H-bond Acceptors	$\leq$ 3	3
No. H-bond Donors	$\leq$ 3	1
$c\log P$[91]	$\leq$ 3	1.55
TPSA[5]	$\leq$ 60 Å^2	41.6 Å^2

The idea that the pyrazolo[3,4-c]pyridine scaffold is a good fragment and a promising pharmacophore for future drug molecules is supported by the following examples of its use in reported compounds of biological interest.

2.1.1 Medicinal Chemistry Applications of the Pyrazolo[3,4-c]pyridine

Since it was first reported in 1980, the pyrazolo[3,4-c]pyridine core has begun to emerge as a potential scaffold in drug discovery programmes, sometimes serendipitously through rational optimisation of a related scaffold, and occasionally through targeted compound screenings. This section outlines examples of pyrazolo[3,4-c]pyridine derivatives in the literature.

The pyrazolo[3,4-c]pyridine heterocycle has attracted attention as a potential analogue of purine **78** which is a core scaffold of ATP, NAD^+, and the nucleotide bases guanine and adenine [Figure 2.1.1.1]. The therapeutic potential of many purine derivatives has already been realised for several biological targets, showing anti-inflammatory, anti-viral, and anti-cancer potential.[92] This broad range of

applications stems from the prevalence of purine-based biological compounds and, subsequently, the variety of cellular proteins that contain purine-binding pockets.

The pyrazolo[3,4-c]pyridine core was chosen due to its similarity to purine in the development of anti-cancer agents.[92] A series of 3,7-disubstituted derivatives were generated and the most promising target, compound **79**, showed good activity against both MIA PaCa-2 and ovarian SCOV3 cancer cell-lines with micromolar and nanomolar activity [Figure 2.1.1.1]. Elsewhere, pyrazolo[3,4-c]pyridine **80**, was prepared in a series of *C*-nucleosides structurally related to guanine.[93] The pyrazolo[3,4-c]pyridines were designed for anti-viral activity, although they showed low selectivity for the virus when compared with host cytotoxicity. Modified 4-deaza analogues of formycins A and B, compounds **81** and **82**, containing the pyrazolo[3,4-c]pyridine core have also been investigated as potential nucleoside antibiotics and useful probes for chemical and biological studies of formycin activity [Figure 2.1.1.1].[94,95]

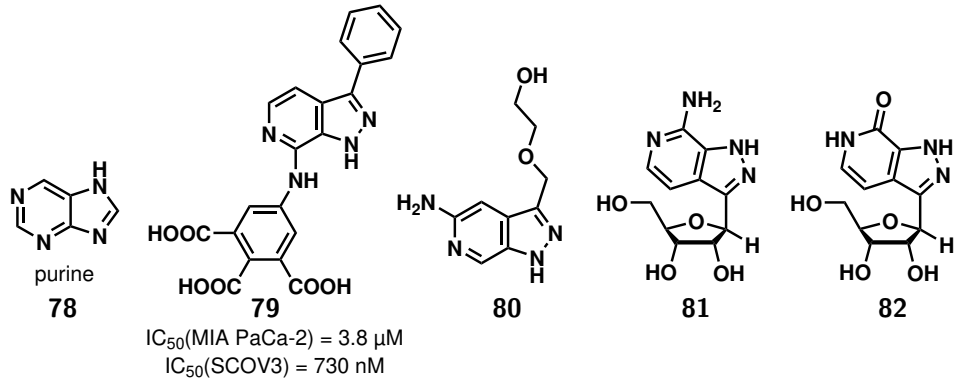

Figure 2.1.1.1: Literature examples of pyrazolo[3,4-c]pyridine containing compounds chosen for its structural similarity to nucleosides.[92–95]

Pyrazolo[3,4-c]pyridines have also appeared in several potent kinase inhibitors. For example, compound **83** showed good activity (IC_{50} = 0.33 μM) against maternal embryonic leucine zipper kinase (MELK)[96] and compound **84** was identified as a potent (IC_{50} = 14 nM), selective, and orally bioavailable (F = 70% in mouse) inhibitor of protein kinase B (Akt)[97] [Figure 2.1.1.2]. The kinase inhibition activity was also evaluated for pyrazolo[3,4-c]pyridines **85** and **86**.[98] In this example, docking calculations with GSK3β identified the importance of the hydrogen bonding interactions between the nitrogen atoms on the pyrazole ring and the D133 carbonyl of the kinase hinge region. This observation was supported by an experimentally measured drop in potency if either nitrogen was methylated. It is interesting to note that kinase inhibitors **83** and **84** also exhibit the unsubstituted pyrazole nitrogen atoms, although no *N*-substituted analogues were tested against Akt for SAR analysis.

Applications of pyrazolo[3,4-c]pyridines to other biological targets include the pursuit of GPR119 agonists. Pyrazolo[3,4-c]pyridine **87** was identified through *in silico* ligand-based pharmacophore modelling.[99] Subsequent elaboration to improve potency and optimise metabolic stability (MS) afforded

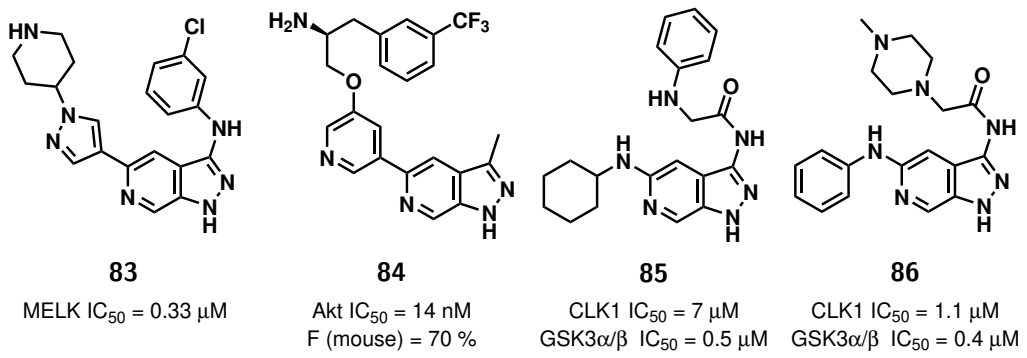

Figure 2.1.1.2: Literature examples of pyrazolo[3,4-c]pyridine based kinase inhibitors.[96–98]

the final compound **88** with $c\log P$ 2.25, and EC_{50} = 4 nM against GPR119 [Figure 2.1.1.3]. The pyrazolo[3,4-c]pyridine scaffold was also identified as an inhibitor of human cystathionine β-synthase (CBS), this time through a screening by an enzymatic activity assay.[100] Compound **89** was measured to have an IC_{50} value of 11 μM and competition experiments with s-adenosylmethionine confirmed **89** as an orthosteric CBS inhibitor [Figure 2.1.1.3].

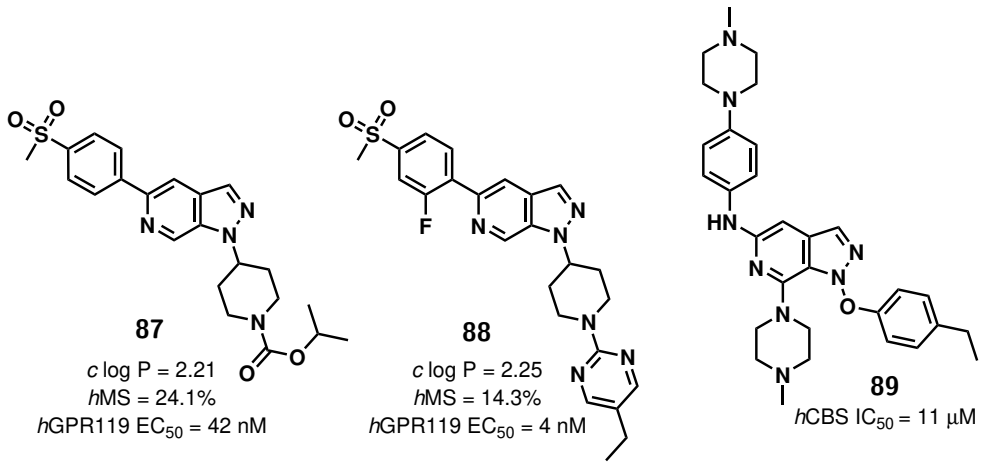

Figure 2.1.1.3: Literature examples of pyrazolo[3,4-c]pyridines with activity against *h*GPR119 and *h*CBS.[99,100]

The MELK inhibitor **83** was tested alongside a series of *1H*-pyrazolo[3,4-b]pyridine derivatives including **90**, which ultimately proved more potent [Figure 2.1.1.4].[96] This heterocyclic scaffold has so far received more attention than the *1H*-pyrazolo[3,4-c]pyridine scaffold, and is central to many compounds showing anti-cancer, anti-microbial, and anti-viral activity as explored in a recent review by Atukuri.[101] Other close analogues that also have proven biological activity are pyrazolo[4,3-c]pyrazole **91** as a potential therapy for Alzheimer's disease,[102] and pyrazolo[4,3-c]pyridine **92** as an antibacterial [Figure 2.1.1.4].[103] These examples show the value of these small nitrogen heterocyclic cores and the potential of the pyrazolo[3,4-c]pyridine.

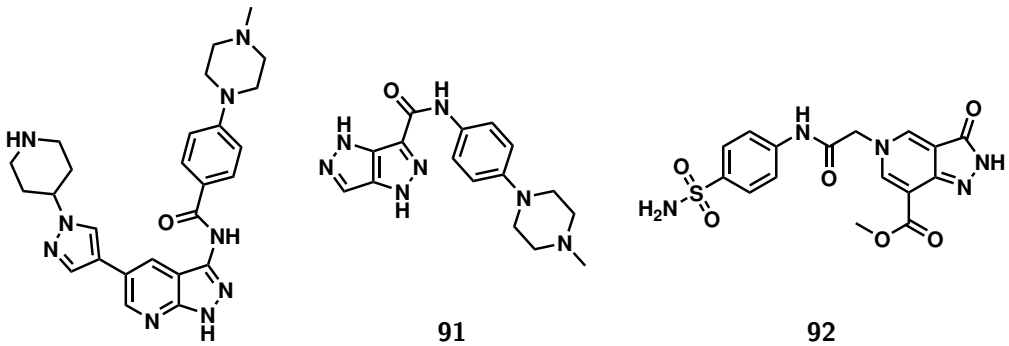

Figure 2.1.1.4: Biologically active compounds containing heterocyclic scaffolds as close analogues to the pyrazolo[3,4-c]pyridine.[96,102,103]

2.1.2 Reported Synthetic Routes to Pyrazolo[3,4-c]pyridines

The first reported synthetic preparation of the pyrazolo[3,4-c]pyridine scaffold was adapted from the Huisgen indazole synthesis by Chapman and Hurst.[73] In this report, nitrosylation of 3-amino-4-methylpyridine **93** by nitrosyl chloride in acetic acid was followed by rearrangement of intermediate **94** to give a mixture of the *N*-1 and *N*-2 acetylated products [Scheme 2.1.2.1.a]. This generated a series of 5- and 7-substituted pyrazolo[3,4-c]pyridines **95**, but was generally limited by poor versatility and scalability.

This route has since been adapted to replace the highly toxic nitrosyl chloride gas with either sodium nitrite [Scheme 2.1.2.1.b][72] or amyl nitrite [Scheme 2.1.2.1.c and Scheme 2.1.2.1.d],[104,105] improving safety and scalability. This approach forms the pyrazolo[3,4-c]pyridine scaffold by cyclisation of the pyrazole ring onto an existing pyridine. The key step is formation of the N-N bond by nitrosylation of an acetylated 3-aminopyridine (eg. **96**). This mechanism can tolerate a range of substituents around the pyridine ring including larger alkyl groups in place of the 4-methyl (eg. **97**). It is therefore the most common approach to form the substituted heterocycle, applied in most of the examples reported above.

Heller and Natarajan took a different approach, forming the bicyclic system by Ni or Pd catalysed annulation of 4-iodopyrazolecarboximines **98** with various alkynes **99** [Scheme 2.1.2.1.e].[106] This route offers a lot of versatility in terms of substituents, but showed variable regioselectivity, thought to be due to competing electronic and steric factors, and relies on expensive metal catalysts. Furthermore, formation of the parent pyrazolecarboximines was low yielding which limits the potential to scale-up this reaction.

In a third synthetic route, formation of the pyrazole ring occurs between hydrazine and 4-acetyl-5-fluoropyridine **100**. The ketone was introduced into this intermediate by *ortho*-lithiation, followed by reaction with an aldehyde, then MnO_2 oxidation [Scheme 2.1.2.1.f]. Variation in the

aldehyde enables diversity at the 3-position, although certain groups such as furan were not tolerated. Diversity could also be introduced into the ring through substituted hydrazines, although this opportunity was not explored by the authors.[107]

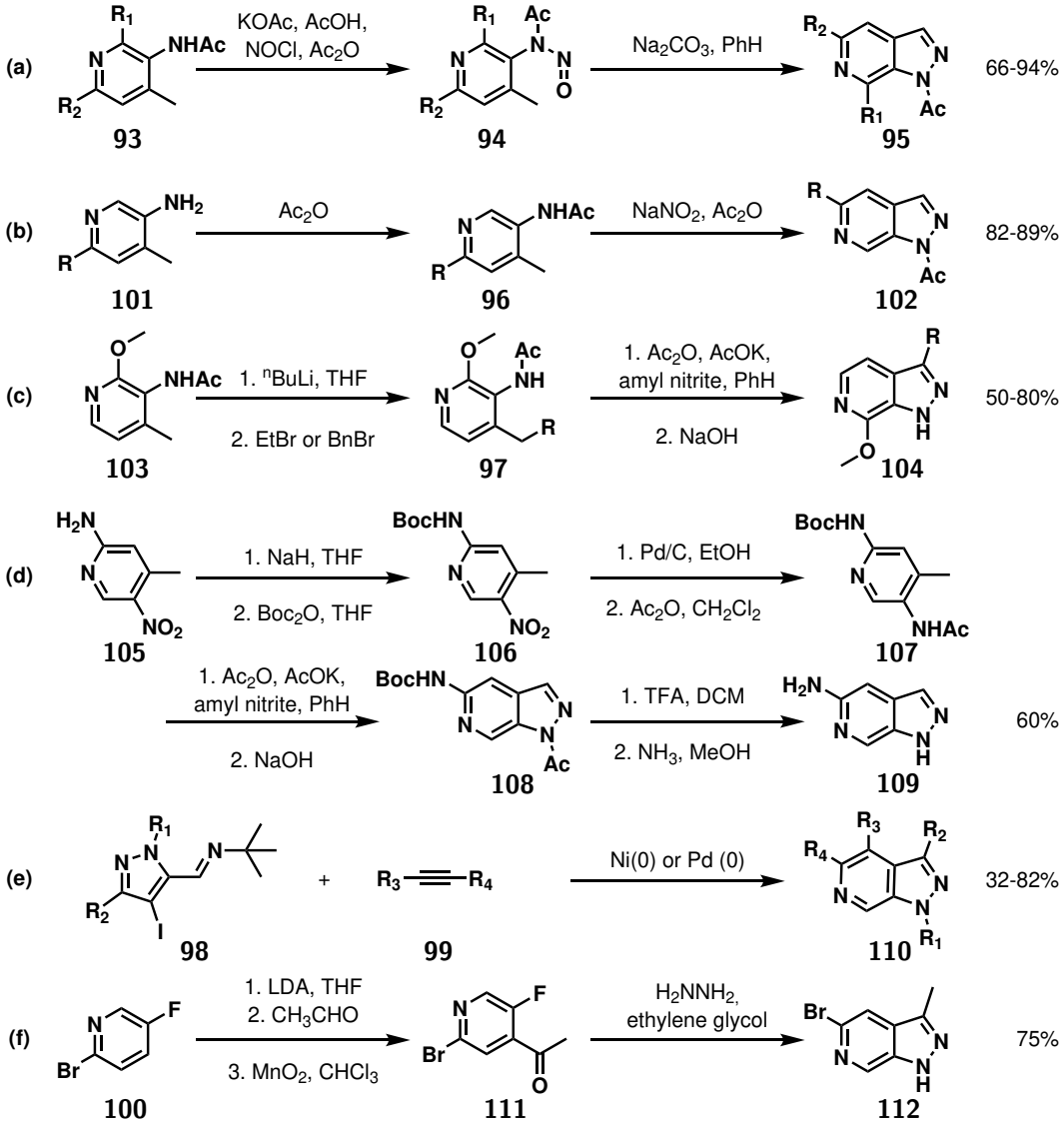

Scheme 2.1.2.1: Previously reported syntheses of compounds containing the pyrazolo[3,4-c]pyridine scaffold.[72,73,104–107]

In summary, there are three different approaches to the synthesis of the pyrazolo[3,4-c]pyridine scaffold. Only one of these starts from a substituted pyrazole ring, forming the pyridine half of the scaffold through a catalysed annulation with various alkynes. However, this method was limited by poor regioselectivity, expensive catalysts, and limited scalability. The other two approaches start instead from a substituted pyridine ring. In one approach the N-N bond is introduce by way of hydrazine condensation with a corresponding pyridinyl-ketone. This route was generally high yielding but is limited by the

requirements of the substituent at the 3-position. The final approach forms the N-N bond by nitrosylation of an acetylated 3-aminopyridine. This approach is the one most commonly reported in the literature as it allows for the greatest variation in substituent pattern. This route was the starting point of the synthetic work outlined in the next section.

2.2 Results and Discussion

2.2.1 Scaffold Synthesis

The first synthetic objective was to devise an efficient route to the parent 5-chloro-*1H*-pyrazolo[3,4-c]pyridine **77**. As discussed in Section 2.1, there are a few reported procedures to generate this scaffold with various substitution patterns. In order to facilitate the development of late-stage functionalisation chemistry, a minimally substituted scaffold was desired, so the metal catalysed annulation [Scheme 2.1.2.1.e] and the hydrazine based approach [Scheme 2.1.2.1.f] were not suitable. Therefore, the scaffold synthesis was based on the adapted Huisgen indazole approach, in particular building on previous work reported by Silva Junior *et al.* [Scheme 2.2.1.1].[72]

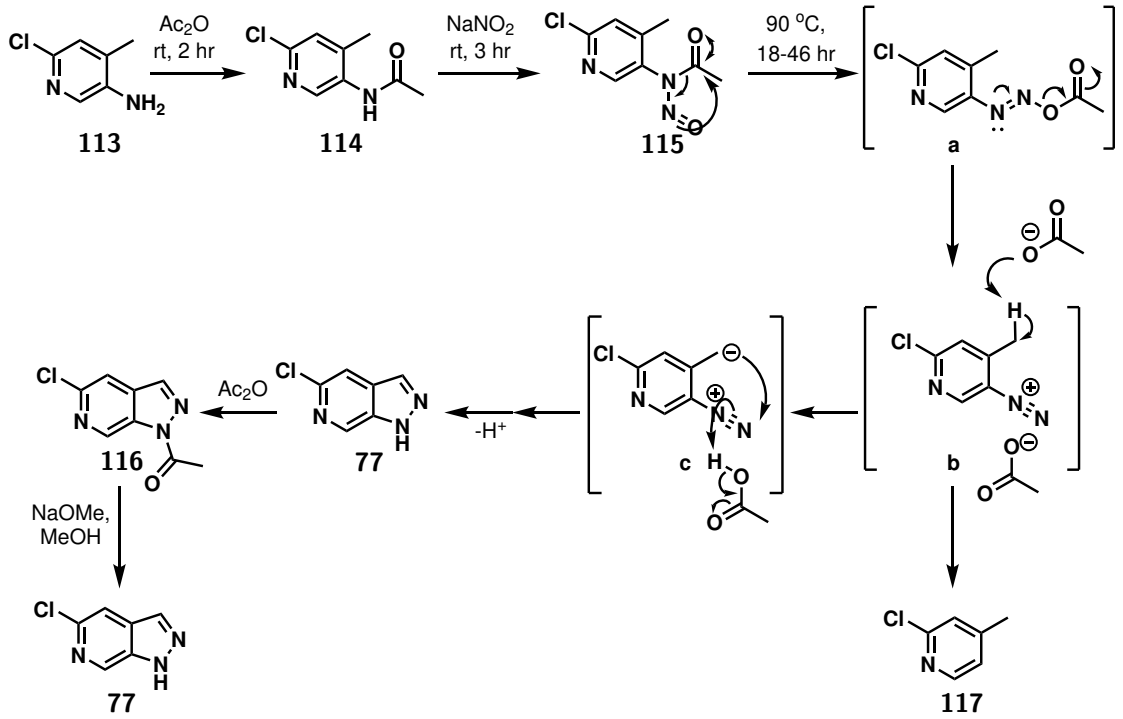

Scheme 2.2.1.1: Reported synthetic route to generate 1'-(5-chloro-*1H*-pyrazolo[3,4-c]pyridin-1-yl)ethan-1'-one **116** from 6-chloro-4-methylpyridin-3-amine **113**.[72] **117** was collected as a side product when reaction was quenched before complete conversion.

Initial conditions were taken directly from the procedure reported by Silva Júnior *et al.* starting from 6-chloro-4-methylpyridin-3-amine **113** [Scheme 2.2.1.1].[72] Following this precedent, stirring in Ac_2O saw rapid acetylation to afford **114**, observed by a peak in the LCMS at m/z = 185.09 corresponding to the $[M]^+$ ion. Subsequent heating overnight at 90 °C with $NaNO_2$ generated a black crude product from which the desired azaindole **116** was isolated as white needle-like crystals by chromatography. This reaction afforded good yields on a small scale [Table 2.2, entry 1] and was feasible on a gram scale [Table 2.2, entry 2].

However, there were reports of runaway exotherms from previous attempts to scale up the reaction.[108] Moreover, the high boiling point and low volatility of Ac_2O was problematic for the work-up on larger scales. Even after excess solvent was hydrolysed to the more volatile acetic acid (boiling point of AcOH = 117.9 °C compared to Ac_2O = 139.5 °C) it required extended heating under reduced pressure to concentrate the crude solid product. Furthermore, analysis of the crude ^{1}H NMR spectra implied the coloured impurities were a result of decomposition of the acetic anhydride, so reducing its excess was desirable. A series of reactions were conducted in search of a suitable co-solvent for the reaction.

Similar transformations have been reported in solvent mixtures of equal parts DCM and Ac_2O, yet the use of DCM was not suitable here as its boiling point was too low. Instead DCE was selected as a potential co-solvent, being similarly polar and aprotic to DCM and offering a higher boiling point to enable heating the reaction to 90 °C. The reaction performed in Ac_2O:DCE 1:1 afforded efficient conversion to the desired product, as seen by the characteristic singlet in the ^{1}H NMR spectrum at 2.81 ppm corresponding to the CH_3 group on the acetyl [Table 2.2, entry 3]. However, there was still a large excess of Ac_2O to remove so the work-up was still challenging.

To test the limits of the requirement for Ac_2O in the reaction, stoichiometric quantities were trialled. This reaction required 1,4-dioxane as the bulk solvent to enable sufficient heating of the reaction mixture [Table 2.2, entry 4]. Complete conversion to intermediate **114** was observed, though as expected, this step proceeded more slowly than in previous reactions. The desired product **116** was seen by LCMS analysis of the reaction mixture, however, even after the addition of more $NaNO_2$ and heating for 48 hours, the nitrosylation and cyclisation did not go to completion. The reaction stalled after 25% of species **115** had reacted, resulting in a mixture of **114**, **116**, **77**, and **117**.

Table 2.2: Conditions trialled for generating the pyrazolo[3,4-c]pyridine scaffold.

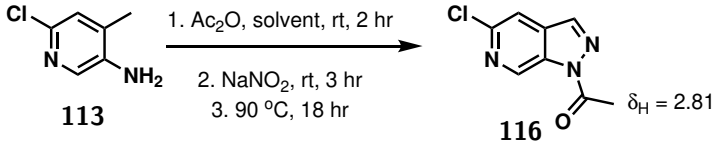

113 **116**

Entry	Mass of SM /g	Co-solvent	SM concentration	Ac_2O equivalents	Yield
1	0.20	-	0.14 M	75.5	65%
2	1.00	-	0.28 M	37.8	79%
3	0.50	DCE	0.2 M	24.2	Quantitative[a]
4	0.50	1,4-dioxane	0.25 M	2.00	20%
5	0.50	DCE	0.25 M	10.0	95%
6	5.00	DCE	0.25 M	10.0	96%

SM = starting material, 6-chloro-4-methylpyridin-3-amine. [a] = determined from ^{1}H NMR spectrum of crude product.

A balance was found in 10 equivalents of Ac_2O with DCE as the co-solvent, enabling efficient reaction

conversion and affording a product with no need for further purification [Table 2.2, entry 5]. These conditions were used for the larger scale reaction, generating the desired 1'-(5-chloro-*1H*-pyrazolo[3,4-c]pyridin-1-yl)ethan-1'-one **116** in good yield (96%) [Table 2.2, entry 6].

Deacetylation of 1'-(5-chloro-*1H*-pyrazolo[3,4-c]pyridin-1-yl)ethan-1'-one **116** proceeded easily in MeOH and more rapidly with addition of NaOMe to afford the 5-chloro-*1H*-pyrazolo[3,4-c]pyridine **77** in good yield [Scheme 2.2.1.1]. Once a route to the chlorine scaffold was successfully established, attention turned to accessing the different growth vectors around the core.

2.2.2 Accessing *C*-3: C-H Borylation

2.2.2.1 Ir Borylation and Suzuki-Miyaura Cross-coupling

The Suzuki-Miyaura cross-coupling reaction is one of the most frequently used synthetic reactions in drug discovery programmes. It enables the formation of sp^2-sp^2 carbon bonds between an organoboron and an organohalide using palladium catalysis.[109] Organoboron reagents were typically accessed from aryl halides via Miyaura borylation or reaction with a Grignard reagent.[110] However, the additional steps to protect sensitive groups against harsh reaction conditions and the requirements for pre-functionalised carbon centres made these methods undesirable. Direct C-H borylation has since been achieved through several catalytic pathways including by Ir, Rh, Fe, Zn, and Ru.[110–113] Ir-catalysis is the preferred method of borylation of aromatic C-H bonds because the reaction is broadly tolerant and enables functionalisation of both carbo- and heterocyclic substrates.[114] The general mechanism for C-H borylation of benzene is outlined in Scheme 2.2.2.1.

The C-H regioselectivity of carbocyclic aromatic compounds is primarily driven by steric factors due to the congested [Ir(Ar)H$(Bpin)_3$(dtbpy)] intermediate complex (**II**) which forms after the oxidative addition of the arene [Figure 2.2.2.1].[115] This is exemplified in the work of Ishiyama *et al.* in Figure 2.2.2.1; arene substrates with a variety of functional groups consistently show preference for reaction at the least hindered position when treated with B_2pin_2 in the presence of $[Ir(COD)(OMe)]_2$.[116] Compared to 1,2-dichlorobenzene **118** and 1,3-dichlorobenzene **119**, the reduced yield of 1,4-dichlorobenzene **120** reflects the decreased reactivity of the sterically hindered C-H bonds *ortho* to chlorine. Meanwhile, the regioselectivity of heteroaromatic compounds is more heavily dependent on electronic factors.[114] Borylation of electron-poor arenes occurs more quickly than for electron-rich arenes. However, the higher electron density of heterocyclic compounds appears to lend itself to Ir-catalysed borylation. In particular, electron-rich 5-membered rings exhibit increased reactivity compared with arenes. This can be seen in the preference for indoles **121** and **122** to react exclusively on the heteroaromatic ring [Figure 2.2.2.1].[117] Furthermore, reaction is consistently favoured at the site *ortho* to the heteroatom due to the greater C-H acidity. Notably, steric effects are still prevalent as evidenced by the reaction of *N*-TIPS-indole **122** at *C*-3 rather than *C*-2 due to the steric bulk of the silyl group [Figure 2.2.2.1].

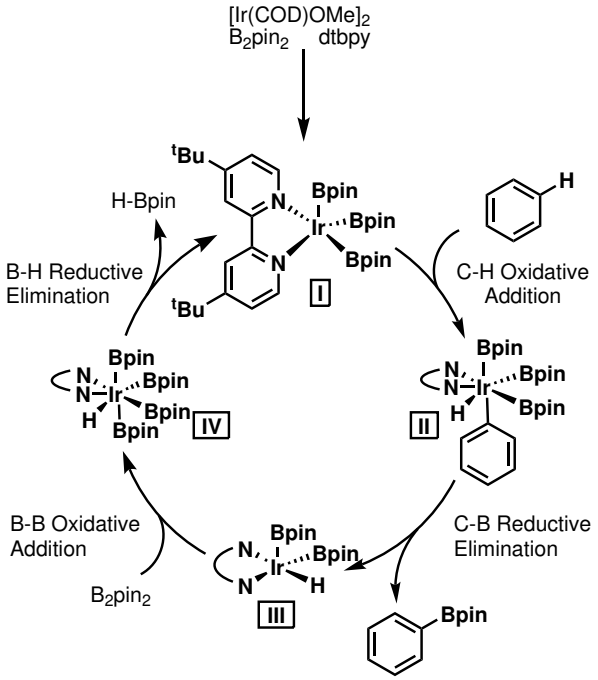

Scheme 2.2.2.1: Mechanism of Ir-catalysed borylation of (hetero)aromatic compounds.

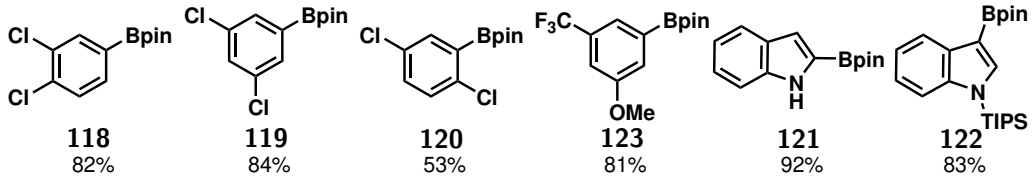

Figure 2.2.2.1: Examples of the regioselectivity of C-H borylation.[116,117]

Compared to indole, pyridine shows notably slow reaction kinetics for C-H borylation even with strongly forcing conditions. This has been attributed to the coordination of the basic azinyl nitrogen to the active Ir(III) triboryl complex (**I**) which prevents the oxidative addition and slows the rate of reaction. Pyridine also shows unexpected regioselectivity as borylation occurs at *C*-3 and *C*-4 [Table 2.3, entry 1 & 2]. This reflects repulsive interactions between the azinyl nitrogen lone pair and the developing negative charge on the *ortho*-carbon during the C-H activation step.

Ortho-borylation is also limited by a low-energy pathway for protodeborylation.[118] Protodeborylation describes the decomposition pathway where the boron group is lost and replaced by a hydrogen atom, regenerating the starting material. This is a widely reported phenomenon for which acid and base mediated mechanisms have been proposed.[119] The rate of protodeborylation is enhanced by a basic nitrogen centre, polarised NC-H bonds, or C-X σ^* antibonding orbitals that can stabilise an ylide intermediate formed during C-B fragmentation. Metal-catalysed mechanisms have also been proposed so the presence of metal salts could enhance boronate ester decomposition.[120]

Fortunately, in most cases the reactivity of nitrogen heterocycles can be restored by preventing coordination through steric hinderance by a *C*-2 substituent or by reducing the basicity of the azinyl nitrogen with a nearby azole nitrogen and an electron withdrawing protecting group [Table 2.3].[121] Similar trends have been observed in other aromatic azinyl systems including pyrimidine [Table 2.3, entry 3 & 4], imidazoles [Table 2.3, entry 5 & 6], and indazoles [Table 2.3, entry 7 to 9].

Table 2.3: Iridium catalysed borylation of pyridine, pyrimidine, imidazole, and (aza-)indazaole.

Entry	Product	Yield	Entry	Product	Yield
1	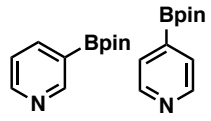	42%[a] 33:67	2	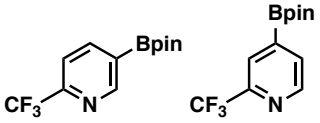	83%[a] 1:1
3	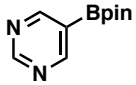	14%[b]	4	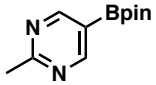	70%[b]
5	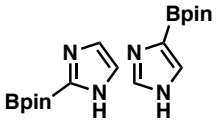	0%[c]	6	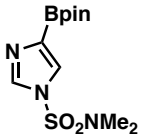	82% [c]
7	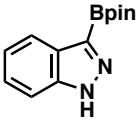	0%[d]	8	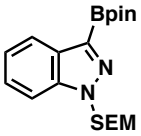	63%[d]
9	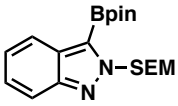	100%[d]	10	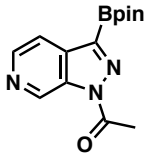	0%[e]

[a] $[Ir(COD)Cl]_2$ 0.5 mol%, dtbpy 3.0 mol%, B_2pin_2 1eq, octane, 100 °C.[117]
[b] $[Ir(COD)OMe]_2$ 0.5 mol%, tmphen 1.0 mol%, B_2pin_2 1eq, THF, rt.[114]
[c] $[Ir(COD)OMe]_2$ 0.5 mol%, dtbpy 3.0 mol%, B_2pin_2 1eq, Et_2O, rt.[114]
[d] $[Ir(COD)OMe]_2$ 0.5 mol%, dtbpy 3.0 mol%, B_2pin_2 1eq, MTBE, rt[121]
[e] $[Ir(COD)OMe]_2$ 2.5 mol%, dtbpy 5.0 mol%, B_2pin_2 1eq, MTBE, 80 °C.[121]

In conclusion, Ir-catalysed borylation appears as an attractive method for C-H activation of aromatic substrates. This method is particularly attractive for the functionalisation of heterocycles as the heteroatoms facilitate greater control of regioselectivity by exerting electronic control. Pyridine-like nitrogen atoms can pose a problem for C-H borylation [Table 2.3, entry 10], but this can be easily overcome by the inclusion of an *ortho* substituent. This methodology was, therefore, a promising route to access the first growth vector on the pyrazolo[3,4-c]pyridine core. Based on the selectivities illustrated in

Table 2.3, this borylation methodology was expected to target the *C*-3 site on the pyrazole ring.

Aromatic boronic esters are versatile intermediates for several synthetic transformations including Pd-catalysed Suzuki-Miyaura cross-coupling. Reaction conditions have been previously established in the Steel group for reliable and high yielding borylation and Suzuki-Miyaura cross-coupling using a tandem reaction approach. These conditions have been shown effective with a range of heteroaromatic substrates and tolerate a range of protecting groups. Hence this two-step synthetic sequence formed the basis for exploring this methodology applied to the pyrazolo[3,4-c]pyridine [Scheme 2.2.2.2]. Borylation of unprotected indazoles was previously attempted without success [Table 2.3, entry 7], so it was clear that a protecting group strategy would be required.

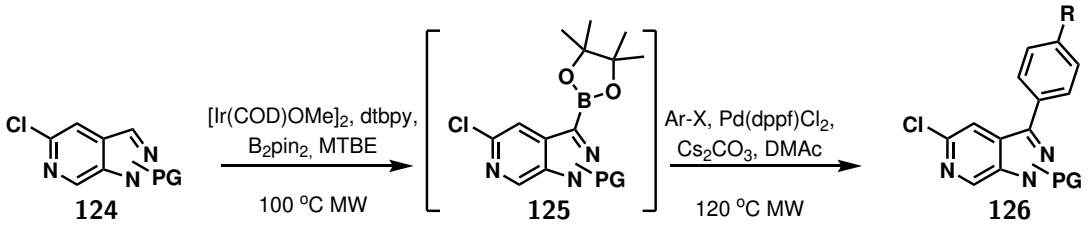

Scheme 2.2.2.2: General procedure for the tandem borylation and Suzuki-Miyaura cross-coupling reaction.

The next section describes the reaction optimisation undertaken to successfully functionalise the pyrazolo[3,4-c]pyridine. The first phase was driven by the search for a compatible protection strategy.

2.2.2.2 Acetyl Protection

With the *N*-1 acylated scaffold already in hand from the synthesis in Scheme 2.2.1.1, the borylation of compound **116** was explored using conditions previously optimised in the Steel group; Ir-catalysed borylation by treatment with $[Ir(COD)OMe]_2$ (2.5 mol%), dtbpy (5 mol%), and B_2pin_2 (1.10 eq), in MTBE [Scheme 2.2.2.2]. Reaction progress was monitored with GCMS analysis and, after 60 minutes at 100 °C, full conversion to boronate ester **128** was confirmed by the appearance of a peak at m/z = 321.2 corresponding to the $[M]^+$ ion. Compared to the previously reported reaction in Table 2.3, entry 10, this showed the successful application of a 2-halopyridine group to block Ir coordination.

Suzuki-Miyaura cross-coupling was then attempted for the reaction between the boronate ester **128** and methyl 4-iodobenzoate, again building on conditions previously developed in the Steel group with $Pd(dppf)Cl_2$ (2.5 mol%) and Cs_2CO_3 (2.00 eq) in DMAc. Unfortunately, the cross-coupling reaction with **128** was unsuccessful with no product mass seen by GCMS. Furthermore, instead of regeneration of the starting material **116**, as expected in the occurrence of protodeborylation, no meaningful mass could be recovered, consistent with an alternate decomposition pathway. The acetyl protected compound was unstable to the cross-coupling conditions so alternative nitrogen-protecting strategies were pursued.

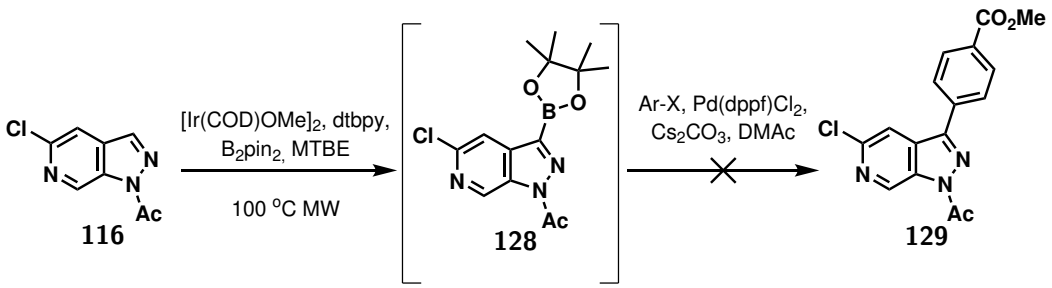

Scheme 2.2.2.3: Borylation and attempted cross-coupling rection of the acetylated substrate.

2.2.2.3 Methanesulfonyl Protection

An electron withdrawing protecting group was desired because electron-poor heterocycles are borylated faster due to the lower basicity of the azinyl nitrogen reducing coordination to the Ir-catalyst. This behaviour was previously demonstrated in the borylation of protected indazoles and pyrazoles.[121] The methanesulfonyl group (Ms) was, therefore, a promising alternative to acyl-protection.

An Ms protecting group was installed through deprotonation by NaH and S_N2 reaction with MsCl in THF [Scheme 2.2.2.4]. This afforded the *N*-1 protected isomer **130** in good yield of 92% without need of further purification. Unfortunately, no borylation of **130** was seen after 30 minutes at 120 °C. Furthermore, this protecting group proved less useful than hoped due to evidence of migration to *C*-3, seen by the loss of the signal corresponding to 3-*H* (8.31 ppm) in the ^{1}H NMR spectrum. This behaviour has been reported elsewhere by Silva Júnior *et al.* and others.[122–124] Attempts were made to inhibit migration by lowering the reaction temperature, yet at room temperature there was no formation of the boronate ester even after 24 hours. An alternative protection strategy was explored instead.

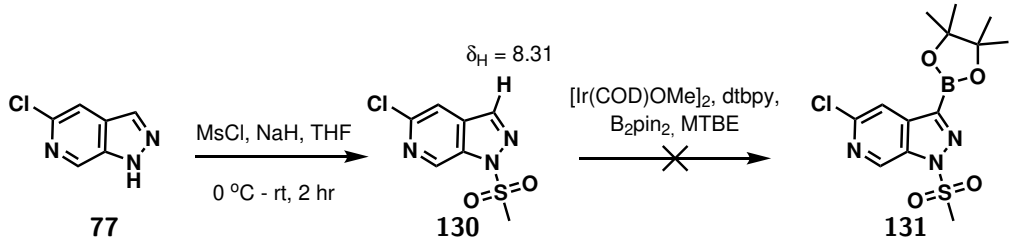

Scheme 2.2.2.4: Installation of the methanesulfonyl protecting group and attempted C-H borylation

2.2.2.4 Tetrahydropyran Protection

The tetrahydropyran (THP) protecting group is commonly employed in the protection of indazoles in other palladium catalysed reactions, so was expected to be stable to the Suzuki-Miyaura cross-coupling conditions.[125] Furthermore, the ether oxygen in the THP group of the *N*-2-THP isomer compound **132** was well positioned to direct *ortho*-borylation to the *C*-3 position,[115] presenting this as a promising strategy.

The THP protecting group was installed under mildly acidic conditions with 3,4-dihydropyran and *p*-toluenesulfonic acid [Scheme 2.2.2.5].[125] According to previous reports for the reaction with indazole, the *N*-2 isomer **132** was expected as the kinetic product and *N*-1 isomer **133** was the expected thermodynamic product. After 90 minutes, LCMS analysis showed complete conversion of the starting material and a mixture of the two products as expected. However, extended heating for 3 hours saw no change in the isomeric composition and the two products had to be separated by column chromatography. The main isomer, with a yield of 66% compared to 14%, had the THP group on the *N*-2 site as confirmed by NOE signals between 3-*H* (8.19 ppm) and 1'-*H* (5.73 ppm).

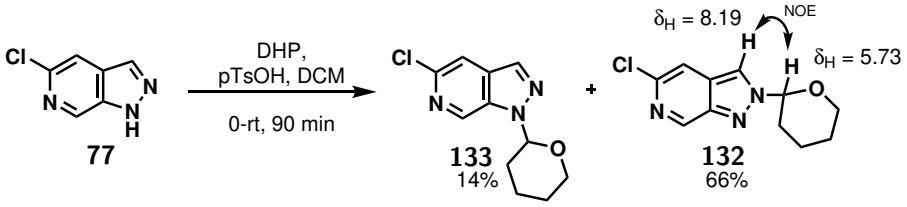

Scheme 2.2.2.5: Installation of the tetrahydropyran protecting group.

Application of the general borylation procedure to compound **132** saw efficient conversion to the 3-boronate ester **134**, determined by observation of a peak at m/z = 363.2 in the GCMS spectrum of the crude intermediate. However, rapid protodeborylation prevented formation of the cross-coupled product and only the starting material was recollected [Scheme 2.2.2.6]. Similar observations have since been made by other members of the Steel group, so it is thought that the size of the *ortho*-THP group is too big to allow efficient transmetalation to the palladium catalyst.

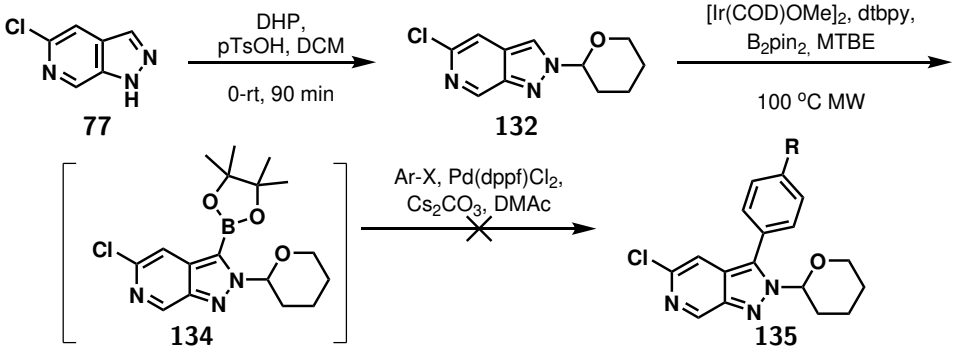

Scheme 2.2.2.6: Installation of the tetrahydropyran protecting group and attempted borylation/cross-coupling reactions.

2.2.2.5 2-(Trimethylsilyl)ethoxymethyl Protection

A 2-(trimethylsilyl)ethoxymethyl (SEM) protection strategy was explored as the linear chain offered a reduced steric bulk. Two routes were pursued to install the SEM group in the hopes that a regioselective

protection strategy could be found.

The first route followed the same procedure as with the methansulfonyl protection, deprotection by NaH then S_N2 reaction with SEM-Cl in THF, giving rapid conversion of the starting material at room temperature. This favoured formation of the *N*-1-SEM isomer giving a 3:2 ratio of products with 74% overall yield. The *N*-1 regioisomer was distinguished by a cross-peak in the HMBC NMR spectrum between *C*-7a (137.1 ppm) and the first CH_2 of the SEM chain (5.87 ppm) and by NOE signals between 7-*H* (8.90 ppm) and the first CH_2 of the SEM chain (5.87 ppm) [Figure 2.2.2.2].

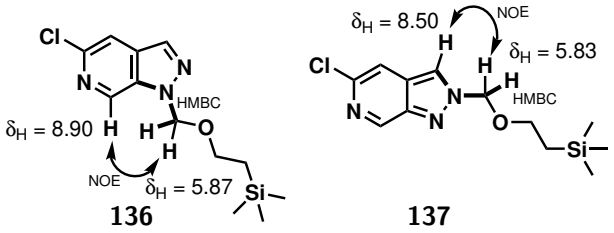

Figure 2.2.2.2: Regiochemistry of the 2-(trimethylsilyl)ethoxymethyl protecting group.

The second route instead employed the organic base *N,N*-dicyclohexylmethylamine with SEM-Cl in THF. This route favoured formation of the *N*-2-SEM isomer giving 1:2 ratio of products with 65% overall yield [Scheme 2.2.2.7]. The *N*-2 regioisomer was distinguished by a cross-peak in the HMBC NMR spectrum between *C*-3 (123.9 ppm) and the first CH_2 of the SEM chain (5.85 ppm) and by NOE signals between 3-*H* (8.50 ppm) and the first CH_2 of the SEM chain (5.83 ppm) [Figure 2.2.2.2].

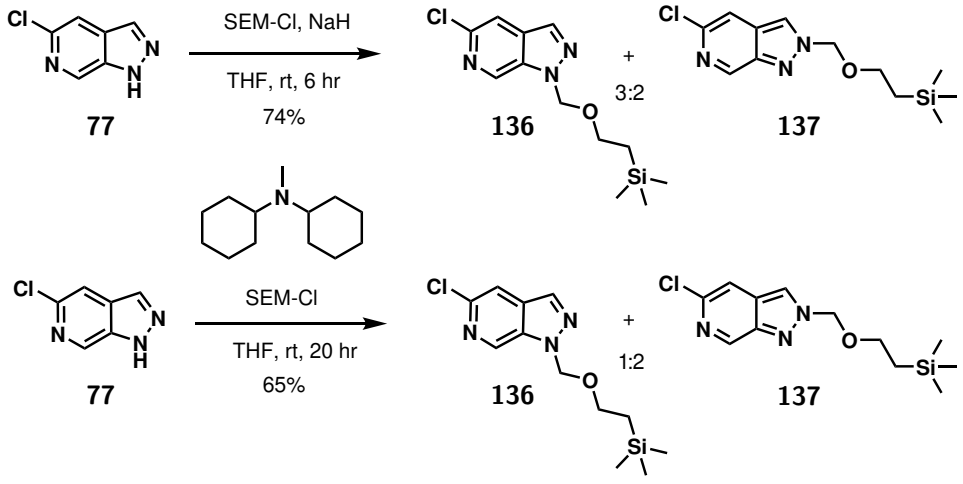

Scheme 2.2.2.7: Installation of the 2-(trimethylsilyl)ethoxymethyl protecting group.

Scheme 2.2.2.7 summarises the product ratios achieved by the two SEM protection approaches. The observed selectivity was consistent with the reported reactivity of indazole for which the major product is dictated by which nitrogen atom has a greater electron density, subtly influenced by the substituents

around the ring, the solvent, and the acid/base conditions employed.[126] In the case of indazole, the hard NaH base fully deprotonates the substrate and the negative charge sits almost completely on the *N*-1 atom whereas reactions without base or under milder basic conditions (as with *N,N*-dicyclohexylmethylamine) favour reaction on *N*-2.[127] NMR studies have confirmed that, like indazole, pyrazolo[3,4-c]pyridine resides almost exclusively as the *1H*-conformer so its reactivity was expected to follow the same pattern.[105] Complete selectivity was challenging, yet by careful choice of base, predominant formation of either the *N*-1 or *N*-2 isomer could be achieved.

Fortunately, the isomers were easily separated by chromatography ($Rf_{\mathbf{136}} = 0.49$, $Rf_{\mathbf{137}} = 0.32$ in EtOAc:Pet Ether 40-60 1:4), so both the *N*-1-SEM isomer **136** and *N*-2-SEM isomer **137** were successfully isolated. Conditions for the borylation and Suzuki-Miyaura cross-coupling reaction of these substrates could then be explored.

Borylation under standard conditions proceeded as expected for both the *N*-1-SEM and *N*-2-SEM protected compounds **136** and **137**, affording boronate esters **138** and **139** as seen by a peak at m/z = 409.2 in the GCMS spectra. Suzuki-Miyaura cross-coupling reactions with *N*-1-SEM boronate ester **138** were also successful and the 3-(4-(trifluoromethyl)phenyl) substituted product was collected in 56% yield over the two steps [Scheme 2.2.2.8]. These conditions became General Procedure A; treatment of an *N*-1-SEM substrate with $[Ir(COD)OMe]_2$ (2.5 mol%), dtbpy (5 mol%), and B_2pin_2 (1.10 eq) in MTBE, heated at 100 °C in a microwave reactor to form the crude boronate ester, followed by reaction with the chosen aryl halide, $Pd(dppf)Cl_2$ (2.5 mol%), and Cs_2CO_3 (2.00 eq) in DMAc, heated at 120 °C in a microwave reactor to give the arylated product.

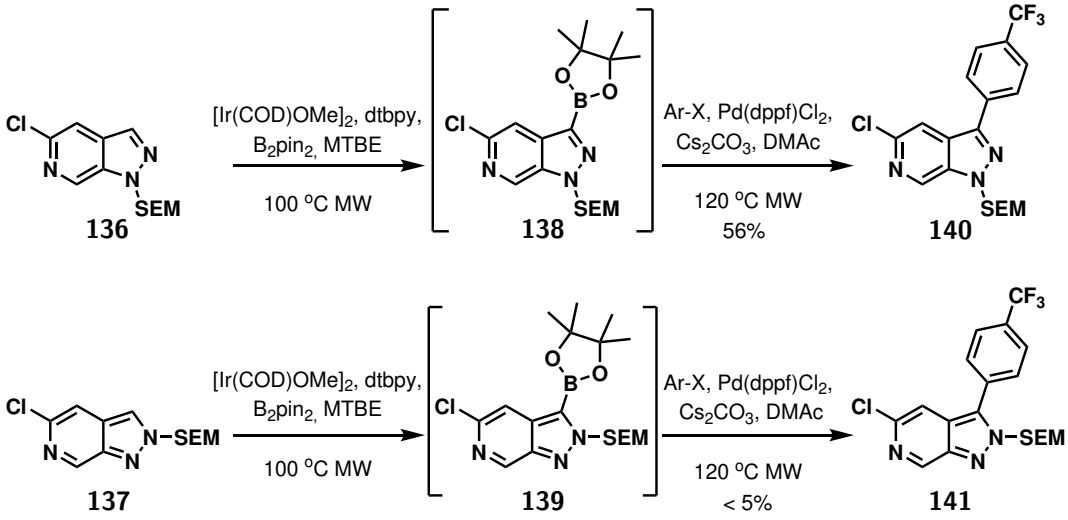

Scheme 2.2.2.8: Example borylation and cross-coupling reactions of **136** and **137** by general procedure A.

Application of the cross-coupling conditions to the *N*-2-SEM boronate ester **139** afforded small amounts of the desired arylated product **141**. However, as with the THP group, increased steric demands of the

N-2 intermediate saw much lower conversion [Scheme 2.2.2.8]. It was assumed that the increased steric congestion at *C*-3 decreased the rate of transmetalation leading to enhanced protodeborylation.

One method reported to overcome undesirable protodeborylation is by generating organometal species *in situ* using a CuCl additive.[128] Mechanistic investigations of Suzuki-Miyaura cross-coupling reactions of electron deficient 2-heterocyclic boronates suggests copper has an active role in the catalytic cycle, with evidence of a 2-pyridyl copper species intermediate **IV** forming prior to the transmetalation to palladium [Scheme 2.2.2.9]. The rate of the two-stage transmetalation process is now more competitive relative to the rate of protodeborylation, allowing for more efficient generation of the diaryl complex **III** ready to form the coupled product after reductive elimination.

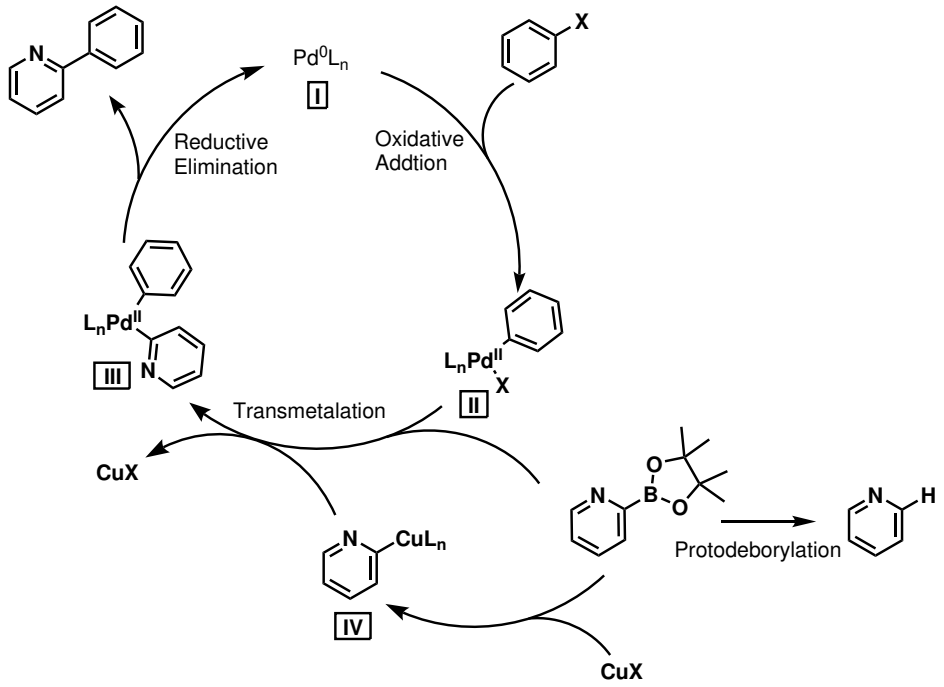

Scheme 2.2.2.9: Proposed mechanism for CuX involvement in the Suzuki-Miyaura cross-coupling of aryl halides and 2-pyridylboronate esters.

This information prompted the inclusion of a CuCl additive to enhance the rate of transmetalation and encourage cross-coupling over protodeborylation. Halving the equivalents of Cs_2CO_3 also helped improve the reaction by facilitating better reaction stirring, especially on larger scales. The modified standard conditions (general procedure B) involved Ir-catalysed borylation by treatment with $[Ir(COD)OMe]_2$ (2.5 mol%), dtbpy (5 mol%), and B_2pin_2 (1.10 eq), in MTBE followed by Suzuki-Miyaura cross-coupling reaction with $Pd(OAc)_2$ (2.5 mol%), dppf (5 mol%), CuCl (1.00 eq), and Cs_2CO_3 (1.00 eq) in DMAc. Although protodeborylation was still evident, more efficient conversion of *N*-2-SEM boronate ester **139** to the desired product was seen in reaction with the CuCl additive in reaction than without. The presence of Ir remaining from the C-H borylation step was thought to be a culprit due to metal-mediated

protodeborylation, so attempts were made to remove it by Celite filtration of the crude reaction mixture. GCMS analysis of the crude boronate ester before and after filtration confirmed that this had no detrimental effects, and the additional exposure to air and moisture did not itself cause protodeborylation. However, there was no significant improvement in yield of the cross-coupling reaction, so this procedure was not permanently adopted [Scheme 2.2.2.10].

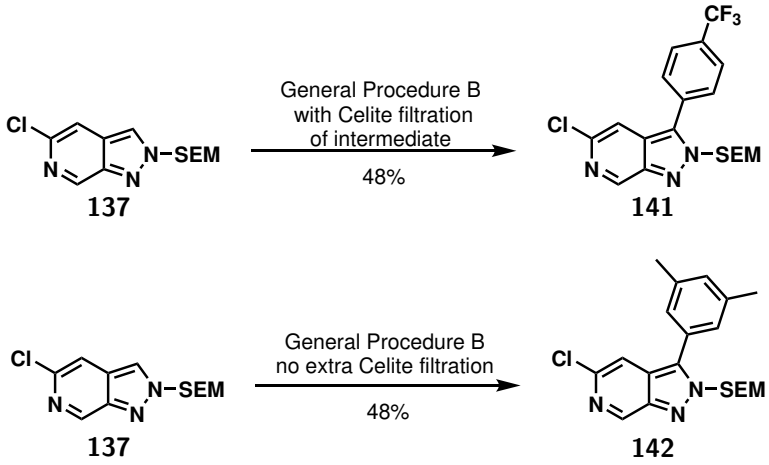

Scheme 2.2.2.10: Testing the effects of Celite filtration of the boronate ester intermediate on overall product generation. General procedure B; 1. $[Ir(COD)OMe]_2$ (2.5 mol%), dtbpy (5 mol%), B_2pin_2 (1.10 eq), MTBE, 100 °C MW, 30 min. 2. $Pd(OAc)_2$ (2.5 mol%), dppf (5 mol%), CuCl (1.00 eq), Cs_2CO_3 (1.00 eq) DMAc, 120 °C MW, 2 hrs.

Another factor that impacted the success of cross-coupling reactions of *N*-2-SEM isomer **137** was its inherent stability to purification; both cross-coupled products and regenerated starting material were notably more prone to decomposition on the silica than their corresponding *N*-1-SEM isomers. Decomposition to unknown species during purification by flash column chromatography limited the amount of pure product that could be isolated after each reaction. In these cases, the application of reverse phase chromatography with a C18 column improved the final yields.

Reaction conditions with the CuCl additive were attempted with *N*-1-SEM isomer **136** as well, to explore if the rate and efficiency of this reaction could also be improved. Instead, a surprising side product was isolated with cross-coupling occurring at position 7 as well, affording bisarylated compound **143** [Scheme 2.2.2.11]. Its structure was confirmed by loss of both the 7-*H* (8.92 ppm) and 3-*H* (8.04 ppm) signals in the ^{1}H NMR spectrum while HRMS found m/z = 572.1351 and $C_{26}H_{25}N_3OSi^{35}ClF_6$ requires M = 572.1360.

Generation of the disubstituted product could have implied a C-H activation reaction facilitated by the CuCl metal. This was disproven by a trial reaction of unsubstituted *N*-1-SEM substrate **136** with $Pd(dppf)Cl_2$, CuCl, 4-bromobenzotrifluoride, and DMAc at 100 °C for 3 hours. There was no conversion of the starting

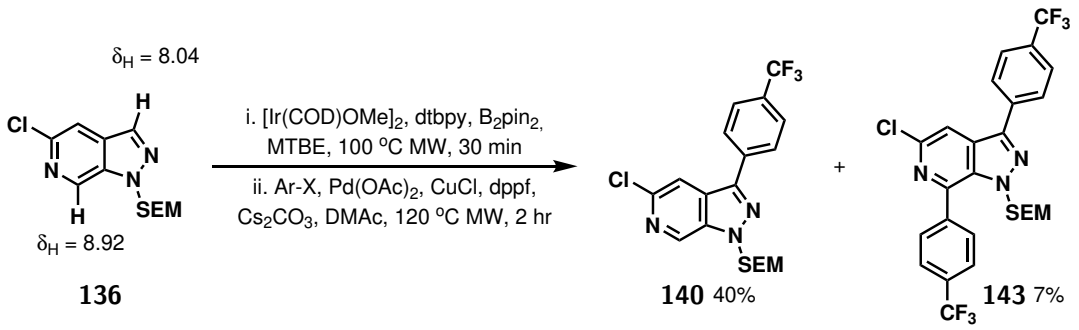

Scheme 2.2.2.11: General procedure B applied to *N*-1-SEM isomer **136** with 4-bromobenzotrifluoride led to generation of disubstituted product **143**.

material. Under the general reaction conditions, formation of the diboronate ester may sometimes be observed by GCMS analysis of the crude reaction mixture with a peak at m/z = 535.3, but only in very small amounts. The limited borylation of *C*-7 was likely due to the decreased reactivity of the α-azinyl position, as explained in Section 2.2.2 pyridine preferentially reacts *meta* to the azinyl nitrogen. This reduced reactivity, coupled with the increased steric hindrance at *C*-7, explains why no disubstituted product is seen without the CuCl additive.

Following these observations, the CuCl additive was only included for the reactions of the *N-2*-SEM substrate. Together these two general procedures enabled both *N-1*- and *N-2*-SEM protected pyrazolo[3,4-c]pyridine substrates to undergo the borylation/cross-coupling reaction with a range of aryl bromide and iodide coupling partners to afford the desired products in yields of 31 - 60% [Figure 2.2.2.3].

2.2.2.6 Summary

During the optimisation of the *C*-3 borylation and Suzuki-Miyaura cross-coupling reaction sequence, several nitrogen protection strategies were trialled [Table 2.4]. Unlike in reactions of indazole, where *N*-1 or *N*-2 can be selectively functionalised, reactions of *1H*-pyrazolo[3,4-c]pyridine **77** generally returned a mixture of isomers. The selectivity of indazole is controlled by which nitrogen has the greater negative charge and is correspondingly more nucleophilic. One possible explanation for the decreased regioselectivity offered by the pyrazolo[3,4-c]pyridine is that the additional aza-nitrogen increases the stability of the *2H*-pyrazolo[3,4-c]pyridine resonance form so the charge is more evenly distributed across the two nitrogen atoms. A more comparable nucleophilicity would explain the product ratios observed in THP protection [Table 2.4, entry 2], and both routes to SEM protection [Table 2.4, entry 3 & 4].

The interesting exception to the mixed regioselectivity, was the reaction with methanesulfonyl chloride which afforded Ms protection selectively at *N*-1 [Table 2.4, entry 1]. This reaction proceeded more quickly than installation of the SEM or THP protecting groups owing to the highly electrophilic sulfur centre.

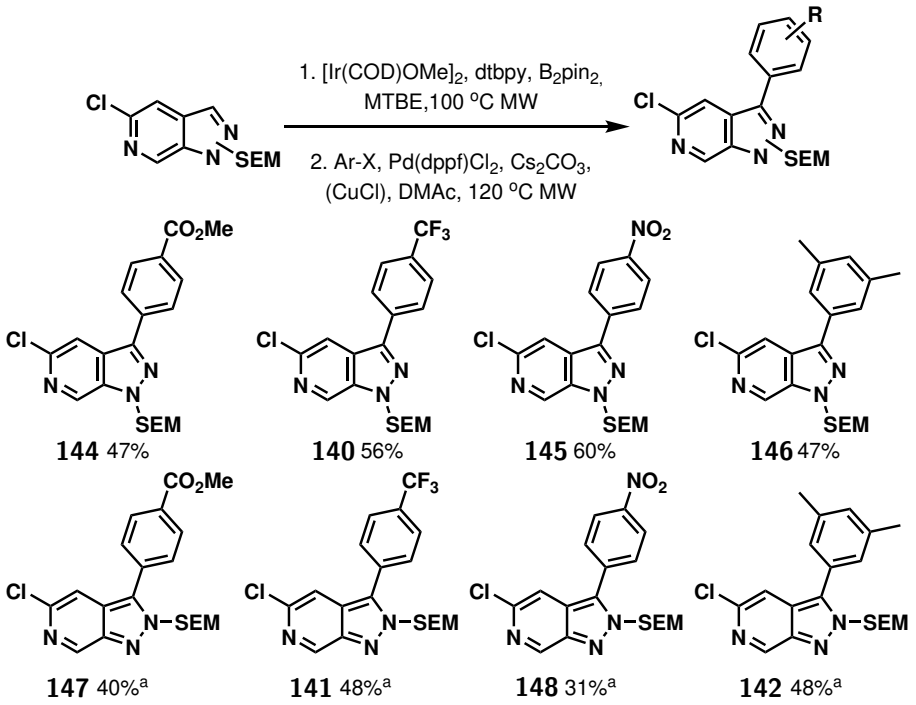

Figure 2.2.2.3: Tandem C-H borylation and Suzuki-Miyaura cross-coupling. Conditions: 1. $[Ir(COD)OMe]_2$, dtbpy, B_2pin_2, MTBE, 100 °C, MW, 2. Ar-X, $Pd(dppf)Cl_2$, Cs_2CO_3, DMAc, 120 °C, MW. [a]additional CuCl.

Table 2.4: *N*-1 and *N*-2 functionalisation of 5-chloropyrazolo[3,4-c]pyridines.

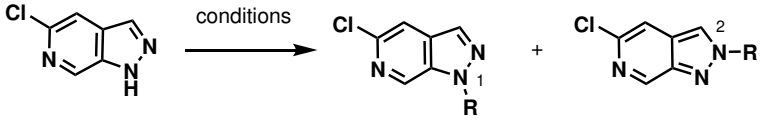

Entry	Reaction Conditions	R =	Yield *N*1	Yield *N*2	Borylation	Cross-coupling
1	MsCl, NaH, THF, 0 °C - rt, 2 hr	-Ms	92% **130**	0% **149**	✗	✗
2	DHP, *p*TsOH, DCM, rt, 4 hr	-THP	14% **133**	66% **132**	✓	✗
3	SEMCl, NaH, THF, 0 °C - rt, 6 hr	-SEM	45% **136**	29% **137**	✓	✓
4	SEMCl, Cy_2MeN, THF, 0 °C - rt, 18 hr	-SEM	21% **136**	44% **137**	✓	✓

This reactivity could account for the increased selectivity observed forming *N*-1-Ms **130** under kinetic control. An alternative explanation is that the *N*-1 isomer was formed under thermodynamic control. As for indazole, the *N*-1 isomer of the pyrazolo[3,4-c]pyridine was expected to be the thermodynamic product. In the reaction with THP, extended heating saw no change in the product isomer ratio. However, the Ms-

migration to *C*-3 (during the attempted borylation reaction) implies the N-S bond is relatively weak, so the greater motility of the Ms group could allow for an N-to-N migration affording the thermodynamic product exclusively. Further exploration of the relative rates of formation of the *N*-Ms products under different temperatures and pH conditions is necessary to determine the full mechanism.

As discussed in Section 2.2.2, sterics are known to effect the outcome of C-H borylation reactions of *N*-heterocycles. However, as this study indicates, reaction sterics are also an important consideration for the Suzuki-Miyaura cross-coupling. The impact on reaction progress was especially evident for the *N*-2 protected substrates in which the *ortho* protecting group hindered transmetalation to the Pd-catalyst. The linear chain of the *N*-2-SEM group was more viable than the THP series. However, the increased steric congestion at *C*-3 compared to the *N*-1-SEM isomer, still limited product generation. This challenge was overcome by the addition of a CuCl additive, and a range of 3-aryl *N*-2-SEM product were isolated.

Together the 3-aryl *N*-1-SEM and *N*-2 SEM products have demonstrated that Ir-catalysed C-H borylation and Suzuki-Miyaura cross-coupling was a viable strategy to access the *C*-3 growth vector on the pyrazolo[3,4-c]pyridine.

2.2.3 Accessing *C*-7: Metalation Strategies

2.2.3.1 Nucleophilic Attack and Oxidation of 2-chloropyridines

With routes to functionalise the *C*-3 position on the pyrazole ring established, it was necessary to explore directions for functionalisation around the pyridine ring. Given the many possible outcomes that could be realised for a 2-chloropyridine derivative, the reaction between the substrate and ^{n}BuLi was explored. It could reasonably be expected to observe (1) lithium-halogen exchange of the 5-chloro substituent, (2) nucleophilic attack of $^{n}Bu^{-}$ anion, or (3) direct lithiation of a C-H bond [Scheme 2.2.3.1].

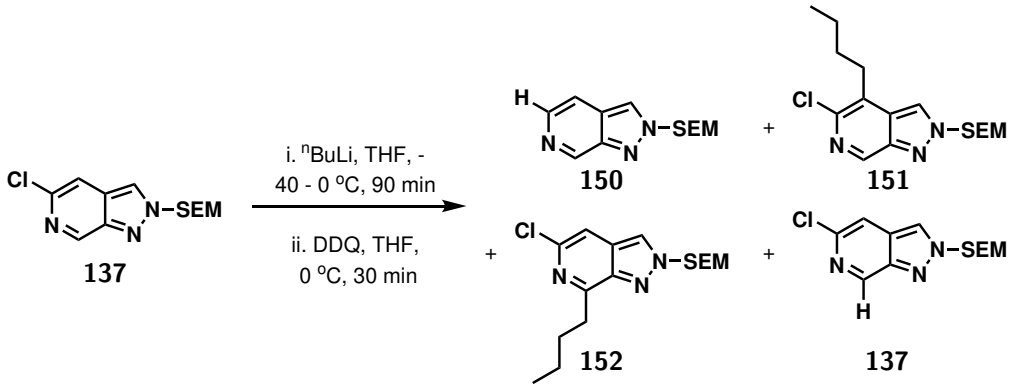

Scheme 2.2.3.1: ^{n}BuLi reaction with *N*-2-SEM isomer **137**, of the possible products only **152** was identified.

Inspiration for this approach came from the literature procedure for the installation of an ^{n}Butyl group at *C*-2 of 4,6-dichloropyrimidine **153** through nucleophilic attack by ^{n}BuLi and subsequent oxidation by 2,3-

dichloro-5,6-dicyanobenzoquinone (DDQ) to afford 2-butyl-4,6-dichloropyrimine **154** in 53% yield.[129] To encourage reactivity on the pyridine ring, this attempt was focused on the *N*-2-SEM isomer **137** for which the conjugation pattern favoured nucleophilic attack at *C*-4 or *C*-7.

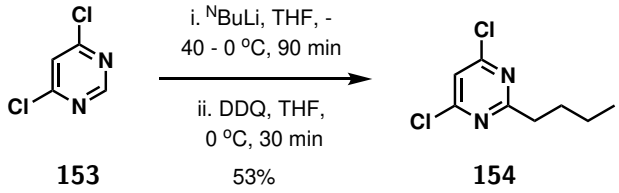

153 53% **154**

Scheme 2.2.3.2: Reaction of 4,6-dichloropyrimidine through nucleophilic attack by ^{n}BuLi.

First, ^{n}BuLi (1.10 eq) was added to a solution of compound **137** in anhydrous THF at -40 °C under nitrogen. The reaction was brought up to 0 °C then quenched with aqueous acetic acid. A solution of DDQ (1.10 eq) in THF was added for the oxidation step, before the reaction mixture was treated with cold NaOH [Scheme 2.2.3.1]. LCMS analysis of the crude reaction mixture indicated the formation of a product with a peak at m/z = 340.31 which corresponded to the addition of a butyl group. This was identified as 7-butyl-pyrazolo[3,4-c]pyridine **152** by the cross peaks in the HMBC NMR spectrum between *C*-7 (157.1 ppm) and the first two CH_2 groups on the butyl chain (3.58 and 2.22 ppm). However, this product was isolated in very poor yield (2.5%) indicating that this reaction sequence was not a promising starting point for accessing the pyridine ring and attention turned elsewhere.

2.2.3.2 Direct Metalation

Regioselective deproto-metalation has been previously reported for a broad range of aromatic and heteroaromatic compounds with the mixed magnesium-lithium 2,2,4,4-tetramethylpiperidine (TMP) bases or in some cases mixed zinc-lithium TMP bases.[130–132] The generated organomagnesium species is a *turbo*-Grignard reagent, it cannot be isolated but reacts quickly with a range of electrophiles.

The regioselectivity of this reaction depends on the relative acidity of the aromatic protons around the ring, as well as being influenced by coordination of the TMP-base to nitrogen lone pairs. For example, Balkenhohl *et al.* neatly showed control of the regioselectivity of the reaction between pyrazolo[1,5-a]pyridine **155** and TMP-bases [Scheme 2.2.3.3]. Here, the addition of $BF_3{\cdot}OEt_2$ changes the selectivity from *C*-9 to *C*-3 because Lewis acid coordination to the nitrogen lone pair prevents the metal-directing effects.[132] The strong regioselectivity and broad functional group tolerance made this an attractive route for functionalisation of the substrate.

TMPMgCl·LiCl was prepared by the addition of freshly distilled TMPH to a cooled solution of isopropyl-MgCl·LiCl in THF and stirring for 48 hours under an inert atmosphere in the absence of light [Scheme 2.2.3.4]. TMPMgCl·LiCl is extreme sensitivity to air, light, and moisture, so must be freshly prepared before each series of reactions and stored below 0 °C in a dry inert atmosphere away from light.

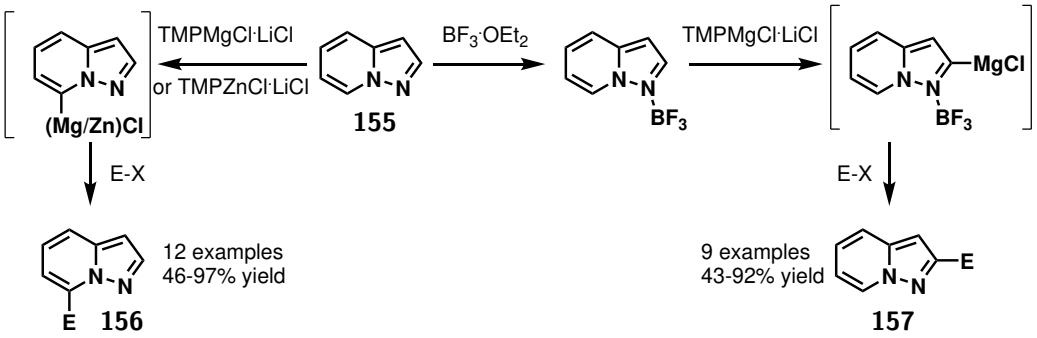

Scheme 2.2.3.3: Regioselective functionalization of the pyrazolo[1,5-a]pyridine scaffold using Mg- and Zn-TMP bases (TMP =2,2,6,6-tetramethylpiperidyl) in the presence or absence of $BF_3 \cdot OEt_2$ taken from the literature.[132]

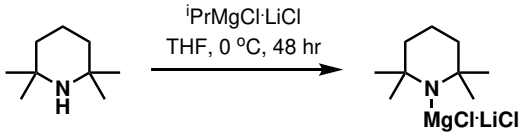

Scheme 2.2.3.4: Preparation of TMPMgCl·LiCl.

The *turbo*-Grignard reagents were explored by treating *N*-1-SEM **136** with freshly prepared TMPMgCl·LiCl and quenching with a simple I_2 electrophile. Although preliminary tests were low yielding, crude ^{1}H NMR spectra showed loss of the 7-*H* signal at 8.92 ppm indicating the desired selectivity had been achieved, so this methodology was tested further. Conditions for the deproto-metalation were optimised for reaction with I_2 and the generation of 5-chloro-7-iodo-1-((2-(trimethylsilyl)ethoxy)methyl)-1H-pyrazolo[3,4-c]pyridine **158** was monitored by GCMS with the peak at m/z = 409.0 for the $[M]^+$ ion of the product.

Initial trials conducted at -78 °C showed small amounts of product formation and increasing the reaction time and base equivalents had a positive effect [Table 2.5, entry 1 & 2]. Conditions were explored increasing the temperature further, but reactions at room temperature and 0 °C were unsuccessful. A lower temperature was necessary to stabilise the *turbo*-Grignard intermediate long enough to add the electrophile. A good balance was found in reactions at -40 °C with yields increasing above 70%. Optimal conditions were found in a 1 hour reaction with 2 equivalents of TMPMgCl·LiCl at -40 °C followed by a 1 hour reaction with the electrophile at room temperature [Table 2.5, entry 9].

This methodology was extended by exploring trapping of the intermediate organomagnesium species with other electrophiles. Reaction with diphenyl disulfide gave compound **159** in 50% yield, reaction with 4-chlorobenzaldehyde and benzaldehyde gave compounds **160** and **161** in 48% and 66% yield respectively, and reaction with DMF gave compound **162** in 49% yield [Figure 2.2.3.1]. The scope of this reaction could be extended further as stirring the intermediate organomagnesium with a solution of $ZnCl_2$ enabled transmetalation to the aryl zinc reagent. The utility of the resulting organozinc reagents was demonstrated

Table 2.5: Metalation with TMPMgCl·LiCl.

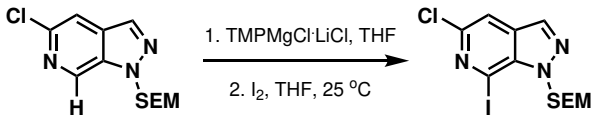

136 158

Entry	Base eq	Temperature	Time with base /min	Time with I_2 /min	Yield
1	1.2	-78 °C	15	120	16%
2	1.5	-78 °C	30	120	35%
3	2.0	0 °C	120	60	0%
4	2.0	0 °C	120	1080	0%
5	2.0	25 °C	300	60	0%
6	2.0	25 °C	1080	60	0%
7	2.0	-40 °C	15	60	77%[a]
8	2.0	-40 °C	30	60	70%[a]
9	2.0	-40 °C	60	60	81%[a]
10	2.0	-40 °C	120	60	0%[a]
11	2.0	-40 °C	60	180	59%[a]

[a] = yield calculated from GCMS

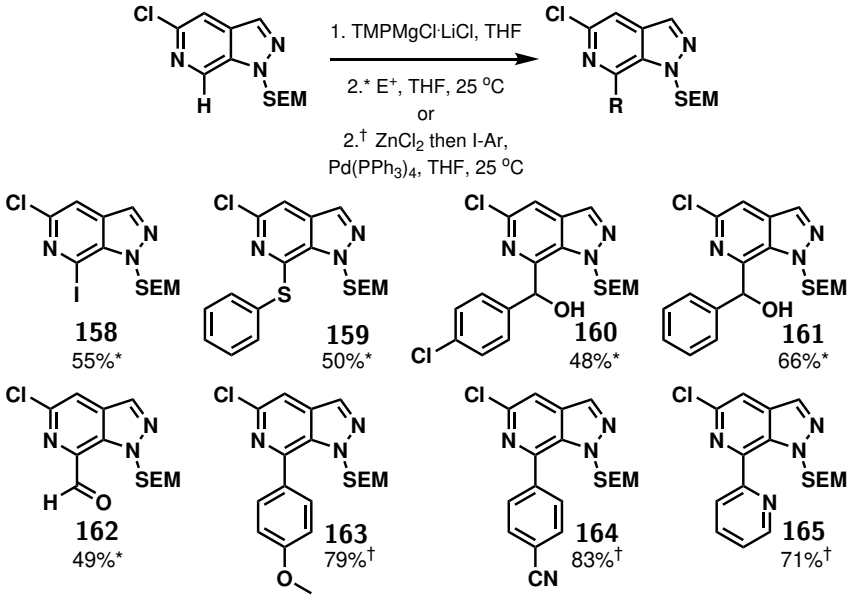

Figure 2.2.3.1: Metalation with TMPMgCl·LiCl followed by reaction with an electrophile or by transmetalation with $ZnCl_2$ for Negishi cross-coupling. Conditions*: 1. TMPMgCl·LiCl, THF, -40 °C, 2. E^+, THF, 25 °C or Conditions†: 1. TMPMgCl·LiCl, THF, -40 °C, 2. $ZnCl_2$ then I-Ar, $Pd(PPh_3)_4$, THF, 25 °C.

through Negishi cross-coupling reactions. After treatment with TMPMgCl·LiCl, a solution of $ZnCl_2$ was added to the reaction mixture followed by the addition of a Pd-catalyst and an aryl iodide. This cross-coupling afforded the desired 7-aryl products with high yields for electron-rich, electron-poor, and hetero-aryl coupling partners [Figure 2.2.3.1].

The *turbo*-Grignard methodology was also explored for the *N*-2-SEM-protected compound **137**. Treatment of **137** with the TMPMgCl·LiCl base led to metalation at *C*-3 instead of *C*-7, evidenced by the loss of the 3-*H* peak at 8.14 ppm in the ^{1}H NMR spectrum [Scheme 2.2.3.5]. The 3-iodo product **166** was isolated in 11% yield. This was surprising as regioselectivity was expected to be controlled by the metal directing effects of the pyridine nitrogen, and so follow the preferences observed for the *N*-1 analogue. As highlighted in Scheme 2.2.3.3, the regioselectivity of this methodology depends on competing electronic and metal-directing effects of the nitrogen lone pairs and any protecting groups. The preference for reaction at *C*-3 was likely due to coordination of the metal with the adjacent SEM group. As this vector was comprehensively accessed through C-H borylation in Section 2.2.2, this methodology was not pursued further here.

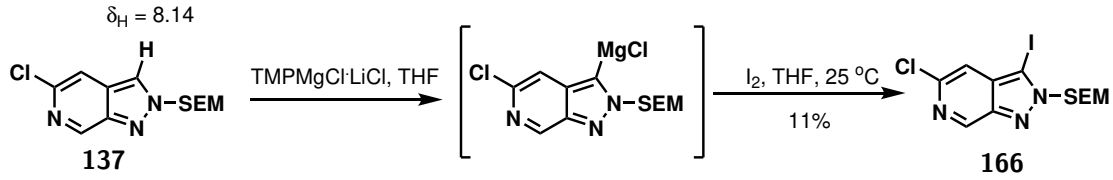

Scheme 2.2.3.5: Reaction of **137** with TMPMgCl·LiCl leading to metalation at *C*-3.

2.2.3.3 Summary

Initial attempts at accessing the *C*-7 site on the pyrazolo[3,4-c]pyridine scaffold with ^{n}BuLi were largely unsuccessful, likely due to the competing reaction pathways between nucleophilic attack, lithium-halogen exchange, and direct lithiation. Focusing on the direct metalation pathway enabled a more targeted approach to explore reaction methodology and success was found on moving to a mixed magnesium-lithium base, TMPMgCl·LiCl. Reaction optimisation demonstrated that the efficiency of the magnesiation step was highly temperature dependent due to the instability of the organomagnesium. After treatment with $ZnCl_2$ the resulting aryl zinc reagents were more stable, corresponding to high yields in the Negishi cross-coupling reactions.

The *C*-7 regioselectivity of the reaction with *N*-1-SEM **136** was initially believed to be due to metal-directing effects of the pyridine nitrogen. However, the preference for *N*-2-SEM **137** to react at *C*-3 indicate that metal-coordination to the SEM protecting group was likely also involved. It is possible that a larger, less coordinating group would have blocked the *C*-3 position and favoured reaction at *C*-7, although other protection strategies were not explored at this time.

Use of the *N*-1-SEM protection strategy meant this methodology was a viable route to access the *C*-7 growth

vector on the pyrazolo[3,4-c]pyridine ring and enabled the installation of a range of substituents through reaction with different electrophiles. The versatility of the methodology was further exemplified through transmetalation to the aryl zinc reagents which facilitated the Negishi cross-coupling reactions.

2.2.4 Accessing *C*-5: Displacement of the Halogen

2.2.4.1 Suzuki-Miyaura Cross-coupling in Aqueous Conditions

As discussed in Section 2.2.2, aryl chlorides are common reagents in metal-catalysed coupling reactions, so the C-X bond was a possible route to access the *C*-5 position.[133,134] In the previous Suzuki-Miyaura reactions, where the pyrazolo[3,4-c]pyridine was the organoboron reagent, no self-coupling was observed so new reaction conditions were explored to unlock the reactivity of the 5-chloro position.

Suzuki-Miyaura cross-coupling reactions in aqueous solvents are an attractive alternative to organic solvents as water is cheaper and less toxic, and organic products can be easily isolated. Several methods of Suzuki-Miyaura cross-couplings in aqueous or organic/aqueous solvent mixtures have been reported with a range of Pd catalysts and aqueous bases.[135] For this substrate, a $Pd(PPh_3)_4$ catalyst with Na_2CO_3 in an aqueous/DME solution was chosen.

Before attempting this transformation on the 5-chloro-1-methanesulfonyl-*1H*-pyrazolo[3,4-c]pyridine **130**, reaction conditions were first tested on a simpler substrate, 2-chloropyridine **167**, with 4-fluorophenyl boronic acid. After 15 hours at reflux the cross-coupled 2-(4'-fluorophenyl)pyridine **168** was isolated in good yield (70%) [Scheme 2.2.4.1].

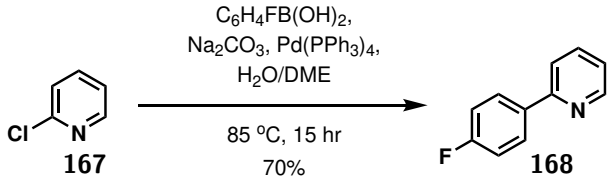

Scheme 2.2.4.1: Test conditions for Suzuki-Miyaura cross-coupling reaction of 2-chloropyridine **167** in aqueous/DME solvent system.

After a successful trial reaction, the same conditions were applied to the Ms-protected compound **130**. The Ms-protection strategy was chosen because electron withdrawing groups promote oxidative addition of aryl halides. Unfortunately, no cross-coupling was observed and instead the deprotected 5-chloro*1H*-pyrazolo[3,4-c]pyridine **77** was isolated.

The absence of successful cross-coupling was somewhat unsurprising as aryl chlorides are known to be less reactive towards oxidative addition. Therefore, instead of exploring this methodology further, attention turned to the formation of C-N bonds as a means of incorporating an additional H-bond acceptor into the molecule.

2.2.4.2 Nucleophilic Aromatic Substitution

Nucleophilic aromatic substitution of the 5-chloro site was expected to proceed directly with a range of nucleophiles. The substitution of *ortho*-halogen substituents on pyridine rings by basic nucleophiles is a well-established transformation. The reaction proceeds by an S_NAr mechanism with the pyridine nitrogen stabilising the build-up of negative charge on the reacting carbon, so this site was expected to be very reactive. Table 2.6 outlines the attempted nucleophilic aromatic substitution reactions trialled on a range of protected and unprotected 5-chloropyrazolo[3,4-c]pyridine scaffolds.

Table 2.6: Exploring the nucleophilic aromatic substitution of 5-chloropyrazolo[3,4-c]pyridines.

Entry	Electrophile	Nucleophile	Conditions	Outcome
1	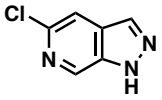	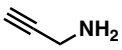	50 °C, 18 hr	SM recollected
2			120 °C MW, 1 hr	SM recollected
3			120 °C MW, 2.5 hr	Decomposition
4	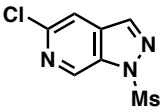	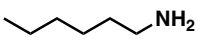	50 °C, 5 hr	SM recollected
5			100 °C, 3 hr	SM recollected
6			130 °C, 18 hr[a]	Decomposition
7	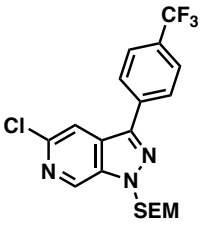		Cs_2CO_3 (3.0 eq), MeCN, 82 °C, 6 hr	SM recollected
8			Cs_2CO_3 (3.0 eq), DMF, 153 °C, 52 hr[a], 1 hr	SM recollected
9	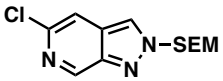		Neat, 120 °C, 30 min	Decomposition

[a] Reaction stopped after loss of protecting group was observed

Despite the anticipated lability of the chloropyridine, multiple attempts under increasingly forcing conditions saw little success. Outcomes varied from loss of the nitrogen protecting groups to complete decomposition of the starting materials. This site proved resistant to nucleophilic attack.

The low reactivity of the 5-chloro position has been reported elsewhere, including by Silva Júnior *et al.* who saw no reaction using a range of acid- and base-catalysed conditions.[72] Also Giannouli *et al.* performed a nucleophilic aromatic substitution by aniline or 3,4,5-trimethoxyaniline on the 5,7-dichloro derivative

169 with reaction exclusively at the 7-position in 93% yield, which further attests the stability of the 5-chloro substituent [Scheme 2.2.4.2.a].[92] The low reactivity of the 5 position was likely due to the electron donating effects of the *para*-amine (*N*-1) which decreases the electrophilicity of this position.

Successful nucleophilic substitution at the 5-chloro position has been reported, demonstrated by Sklepari *et al.* in the preparation of pyrazolo[3,4-c]pyridine based kinase inhibitors [Scheme 2.2.4.2.b].[98] In this case the substrates included a nitro group at *C*-3, so this strongly electron withdrawing group could have overcome the electron donating effects of *N*-1 to facilitate the reaction. The yields of these reactions were modest and the authors note a lack of success with weaker nucleophiles like aniline, which shows that even with the electron withdrawing effects of the 3-nitro group, nucleophilic substitution was a challenging functionalisation strategy.

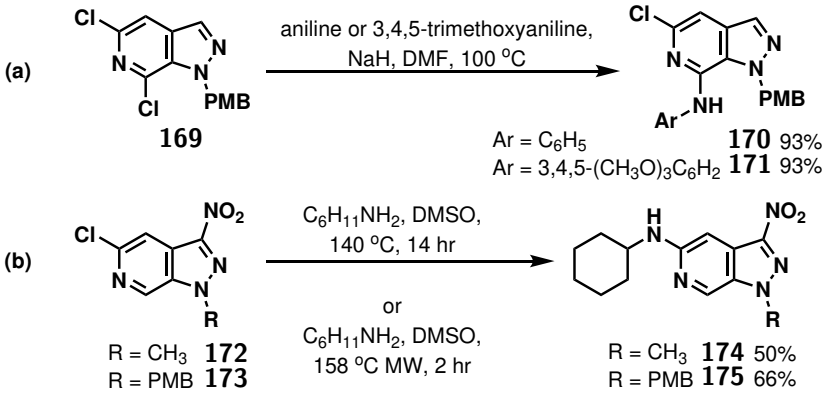

Scheme 2.2.4.2: Nucleophilic aromatic substitution of **a)** 5,7-dichloro-1-(4'-methoxybenzyl)-*1H*-pyrazolo[3,4-c]pyridine **169** and **b)** 5-chloro-3-nitro-pyrazolo[3,4-c]pyridines **172** and **173**.

The 5-fluoro analogue appeared as an attractive strategy to generate a more reactive substrate. The increased polarity of the C-F bond makes fluoride an ideal leaving group, favouring the S_NAr reaction and increasing the rate of reaction compared to the corresponding chloride substrate.

Formation of the fluorine scaffold was attempted using the previously optimised conditions for scaffold synthesis, starting from 6-fluoro-4-methylpyridin-3-amine **176**. Unfortunately, the increased lability of the 5-fluoro position in **177** corresponded to decreased product stability and the C-F was displaced *in situ* by acetic acid present in the reaction mixture, affording 1-acetyl-*1H*-pyrazolo[3,4-c]pyridin-5-yl acetate **178** as the major product. Methods were then explored to try to control this reaction. Unfortunately, decreasing the reaction temperature was not a viable solution as it was necessary to reach 90 °C to promote the cyclisation step that formed the bicyclic system in **177**. Reducing reaction time was also unsuccessful as monitoring of reaction progress by TLC showed that the C-F displacement reaction proceeded faster than the cyclisation reaction. Quenching the reaction after 4 hours already afforded 1-acetyl-*1H*-pyrazolo[3,4-c]pyridin-5-yl acetate **178** in 46% yield compared to 24% yield for 1'-(5-fluoro-*1H*-pyrazolo[3,4-c]pyridin-1-yl)ethan-1'-one **177** [Scheme 2.2.4.3]. The 5-fluoro scaffold

was therefore deemed an unsuitable substrate and alternative strategies to a controlled functionalisation of the *C*-5 position were explored.

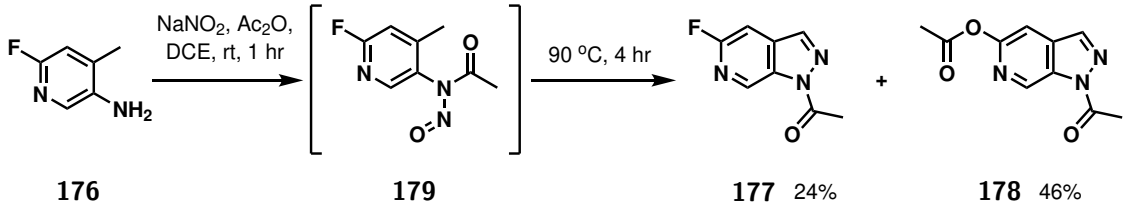

Scheme 2.2.4.3: Synthesis of 1'-(5-fluoro-*1H*-pyrazolo[3,4-c]pyridin-1-yl)ethan-1'-one **177**.

2.2.4.3 Buchwald-Hartwig Amination of 5-chloropyrazolo[3,4-c]pyridines

Carbon-carbon bond formation by Suzuki-Miyaura cross-coupling was not a viable strategy to access this growth vector. Fortunately, Pd-catalysis can also be used to promote the formation of C-N bonds. During the 1990s a series of reports by Buchwald and Hartwig described the use of Pd-catalysis to promote nucleophilic substitution by amines at vinyl or aryl carbon centres. The Buchwald-Hartwig amination has proven to be a valuable route to accessing aromatic amines utilised in the synthesis of several pharmaceuticals and natural products. [136]

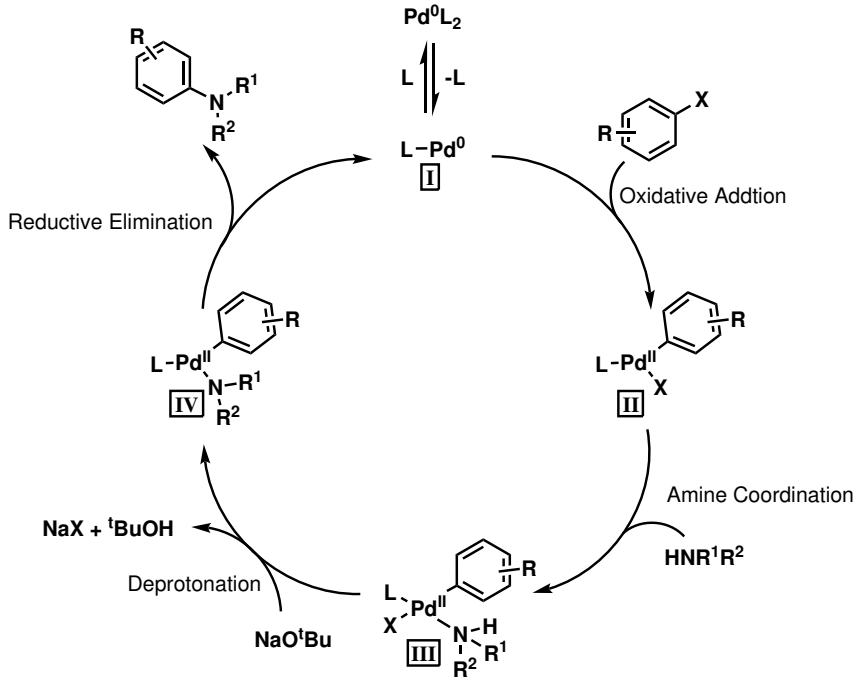

Scheme 2.2.4.4: General mechanism of Buchwald-Hartwig amination

The basic reaction set-up requires an organohalide, an amine coupling partner, a base, and a Pd-catalyst and ligand system. The mechanism is outlined in Scheme 2.2.4.4. The Pd-catalyst is usually added as

a precatalyst which enters the catalytic cycle through ligand dissociation to a coordinatively unsaturated Pd(0) (**I**). The first step is oxidative addition of the arylhalide, followed by coordination of the amine to the Pd(II) complex (**III**). The base, usually NaO^{t}Bu, then eliminates HX giving the extremely reactive aryl-Pd(II) amido system (**IV**). The C-N bond is quickly formed by reductive elimination which releases the product and regenerates the active Pd(0) species (**I**).

A vast array of possible conditions exists in the literature, varying base, ligand, solvent, and reaction time depending on the substrate requirements. Conditions for the reaction of the pyrazolo[3,4-c]pyridine scaffold were based on the amine coupling of a series of 5-bromoindazoles reported by Slade *et al.*.[125] The reported conditions used a combination of $Pd_2(dba)_3$, *rac*-BINAP, and NaO^{t}Bu in THF at 55 °C. When applied to THP-protected bromo-indazole **180**, this approach afforded the desired amine product **181** in 88% yield [Scheme 2.2.4.5].

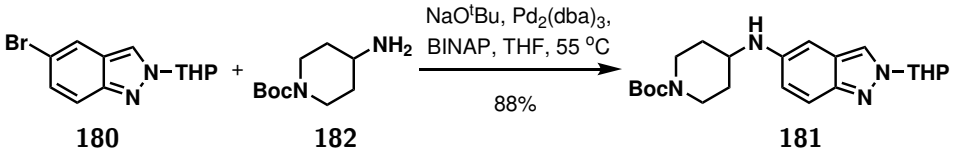

Scheme 2.2.4.5: Literature example of the Buchwald-Hartwig amination of 5-bromo-2-(tetrahydro-*2H*-pyran-2-yl)-*2H*-indazole **180**.[125]

These same conditions were applied directly to the chlorine analogue **132** as a preliminary test [Scheme 2.2.4.6], and the desired amine product was collected in 7% yield. Whilst very low, this yield was more than had been recovered from any previous attempts to access this position, highlighting this as a promising methodology.

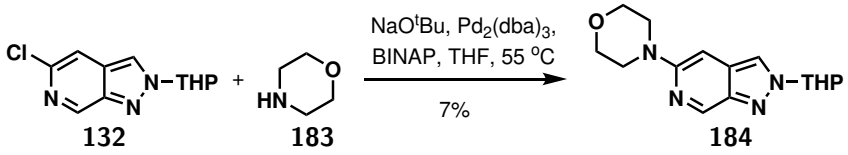

Scheme 2.2.4.6: Trial Buchwald-Hartwig amination of 5-chloro-2-(tetrahydro-*2H*-pyran-2-yl)-*2H*-indazole **132**.

It was clear that the reactivity of the substrate had to be increased. For the organohalide coupling partner, reactivity depends on the rate of oxidative addition to the Pd-catalyst. Aryl iodides are the most reactive, followed by bromides, and tosylates, then chlorides.[134] Due to the availability of the starting materials, the bromide analogue was selected.

2.2.4.4 Formation of the Bromide Scaffold

Pleasingly, the previously optimised conditions that afforded the chlorine analogue were directly transferable to the bromine analogue. Synthesis of compound **185** was straightforward and could be

performed on multigram scale with yields of 81% across the two steps [Scheme 2.2.4.7].

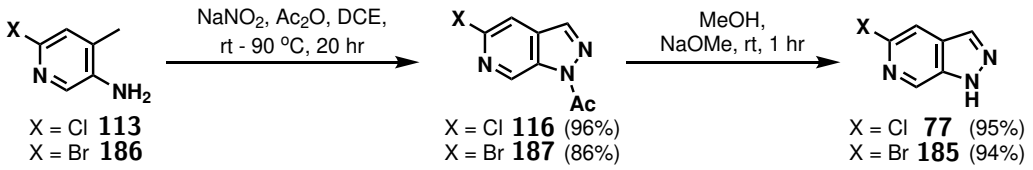

Scheme 2.2.4.7: Synthesis of 5-chloro-*1H*-pyrazolo[3,4-c]pyridine **77** and 5-bromo-*1H*-pyrazolo[3,4-c]pyridine **185**.

Subsequently, the protecting conditions that were previously successful for the chlorine analogue **77** were also viable for the bromine analogue. Introduction of the SEM group afforded a mixture of *N*-1 isomer **188** and *N*-2 isomer **189** with the major isomer being controlled by the choice of base [Table 2.7, entry 3 & 4]. In contrast to the chlorine analogue, THP protection of the bromine scaffold was much more selective. Variation in reaction time enabled the *N*-1 isomer **190** or the *N*-2 isomer **191** to be produced selectively [Table 2.7 , entry 1 & 2] with longer reaction times favouring the thermodynamically more stable *N*-1 protected product.

Table 2.7: Selective *N*-1 and *N*-2 functionalisation of 5-bromopyrazolo[3,4-c]pyridines.

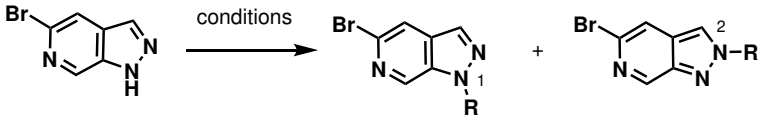

Entry	Reaction Conditions	R =	Yield *N*-1	Yield *N*-2
1	SEMCl, Cy_2MeN, THF, 0 °C - rt, 18 hr	-SEM	18% **188**	32% **189**
2	SEMCl, NaH, THF, 0 °C - rt, 6 hr	-SEM	47% **188**	26% **189**
3	DHP, *p*-TsOH, DCM, rt, 2 hr	-THP	6% **190**	75% **191**
4	DHP, *p*-TsOH, DCM, rt, 22 hr	-THP	82% **190**	0% **191**

2.2.4.5 Buchwald-Hartwig Amination of 5-bromopyrazolo[3,4-c]pyridines

With the *N*-protected 5-bromopyrazolo[3,4-c]pyridine scaffolds now in hand, attention returned to the Buchwald-Hartwig amination. The same conditions that had been attempted with the chlorine analogue were then applied to 5-bromo-2-(tetrahydro-2*H*-pyran-2-yl)-2*H*-pyrazolo[3,4-*c*]pyridine **191**. In this case, a combination of $Pd_2(dba)_3$ (5 mol%), *rac*-BINAP (0.12 eq), and NaO^tBu (3.00 eq) in THF at 55 °C, was successful at installing the morpholine ring in 62% yield [Scheme 2.2.4.8]. The scope of this reaction was then explored for different classes of amines. While there are commercially available ligands that have been finely tuned to enhance the reactivity of specific classes of amines,[137,138] BINAP proved a good general ligand returning successful coupling reactions with primary, secondary, and aromatic amines [Figure 2.2.4.1]. A common challenge of primary amine couplings is preventing further arylation of the

product. This challenge was avoided for the formation of compound **192** by the slight excess of the amine (1.10 eq) used in the general procedure. The reaction between morpholine and 5-bromopyrazolo[3,4-c]pyridine was also explored for various protection group strategies, which revealed the reaction of *N*-1-SEM isomer **188** as the most successful affording **193** in 97% yield.

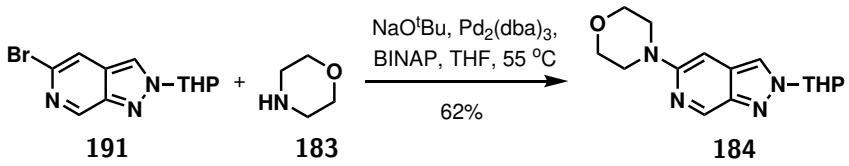

Scheme 2.2.4.8: Buchwald-Hartwig amination of 5-bromopyrazolo[3,4-c]pyridine **191** with morpholine.

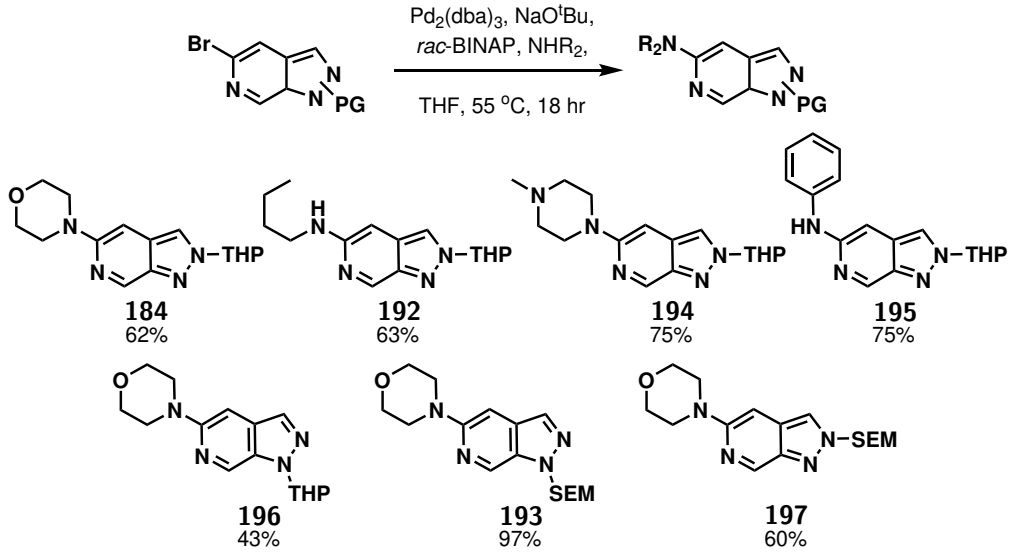

Figure 2.2.4.1: Buchwald-Hartwig amination of 5-bromopyrazolo[3,4-c]pyridine by treatment with $Pd_2(dba)_3$ (5 mol%), NaO^{t}Bu (3.00 eq), and *rac*-BINAP (0.12 eq) in THF with a range of amines and protecting group strategies.

Overall, Buchwald-Hartwig amination had enabled this growth vector to be furnished with a range of amines. Replacing chlorine for bromine had increased the reactivity of the substrate sufficiently to enable access to the *C*-5 position. This same modification might also prove an effective strategy to facilitate the aqueous Suzuki-Miyaura cross-coupling that was unsuccessful for the chlorine analogue. However, this methodology was not explored further and instead attention turned to accessing other growth vectors.

2.2.5 Accessing *C*-4: Dearomatisation-Rearomatisation for *meta*-substitution

The next position around the pyridine ring was *C*-4, *meta* to the pyridine nitrogen and adjacent to the halogen substituent. There are many methods of pyridine functionalisation using both transition-metal catalysed and non-catalysed approaches. However, these are mostly limited to the *ortho*- and

para-positions due to strong electronic influence from the nitrogen as a π-acceptor, σ-donor, and a metal directing group.[139,140]

Meta-functionalisation of pyridines has largely been achieved through Ir-catalysed borylation which was not viable for this substrate as Ir-catalysed C-H activation was shown to target the *C*-3 position.[121] There are other routes to *meta*-functionalisation that utilise Pd-catalysts. These were also not applicable here, though, as they required strong metal directing groups[141] or were intolerant to *ortho*-substituents.[142]

One attractive method that does not rely on transition metal catalysts was to generate a redox-stable dearomatised pyridine intermediate by treatment with dimethyl acetylenedicarboxylate (DMAD) and methyl pyruvate (MP) [Scheme 2.2.5.1]. In recent work, Cao and co-workers demonstrated that this dearomatised pyridine intermediate was susceptible to both radical and ionic methods of functionalisation, furnishing a range of *meta*-functionalised pyridine, quinoline and isoquinoline products.[139] The challenge of this method was in generating a dearomatised intermediate stable enough to undergo radical addition or electrophilic halogenation while able to be rearomatised under specific yet mild conditions.

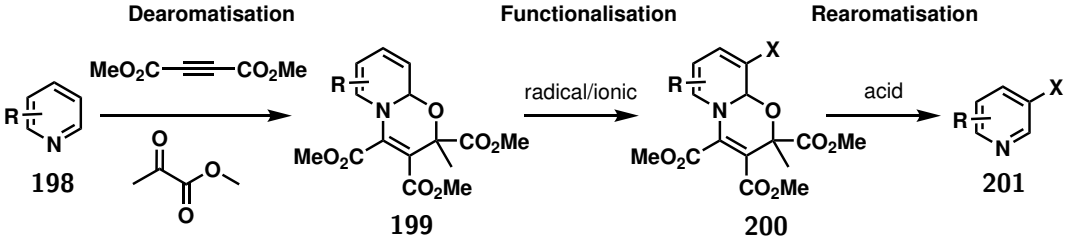

Scheme 2.2.5.1: Literature example of *meta*-pyridine functionalisation using a dearomatisation-rearomatisation approach by reaction with DMAD and MP.[139]

When applied to the 1-(5-chloro-1*H*-pyrazolo[3,4-*c*]pyridin-1-yl)ethan-1-one **116**, the dearomatisation step proceeded very slowly and with significant breakdown of the DMAD, observed through the appearance of a signal in the LCMS trace with m/z = 525.26. When additional DMAD was added over the extended reaction time of 57 hours, the dearomatised intermediate **202** was isolated in 20% yield with 80% of the starting material being recovered. This intermediate was bench stable and remained unaltered after 2 weeks in $CDCl_3$ so was an attractive intermediate to work with.

Before proceeding with optimisation of the dearomatisation reaction step, the viability of the functionalisation and rearomatisation reaction sequence was tested with *N*-bromo succinimide (NBS). After treatment with NBS, the 4-Br intermediate **203** was observed by a peak in the LCMS trace with m/z = 518.08. However, after the addition of HCl, intermediate **203** was lost to an unidentifiable mixture. None of the desired product **204**, the dearomatised intermediate **202**, or the original starting material **116** were recovered. This was attributed to the reduced aromaticity of the pyrazolo[3,4-c]pyridine ring

system compared to pyridine being a smaller driving force for rearomatisation.

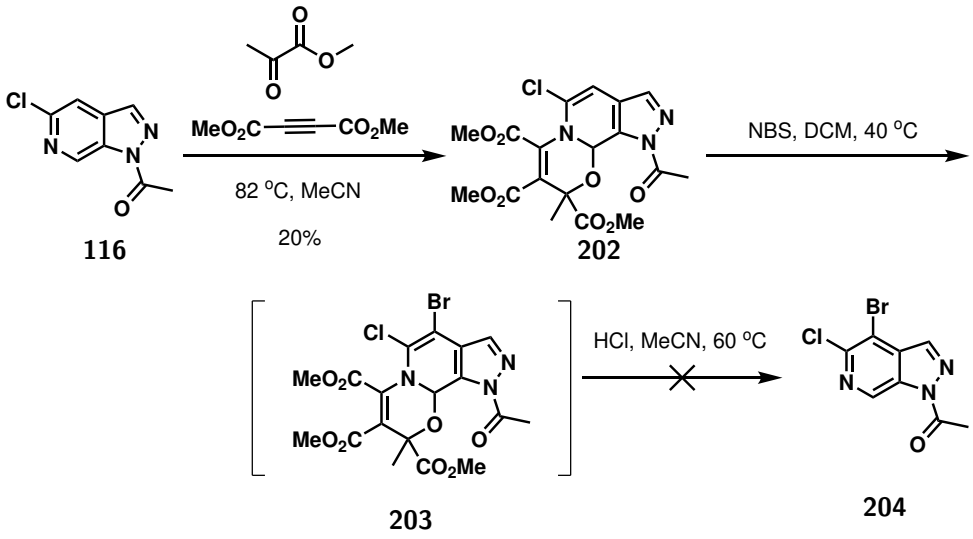

Scheme 2.2.5.2: Proposed method of dearomatisation-rearomatisation to access the *C*-4 position of compound **116**.

Further optimisation by isolating the 4-Br intermediate **203** and separating the functionalisation and rearomatisation steps were not explored at this time. Overall, due to the low yields and long reaction times of the dearomatisation step and the lack of success with the functionalisation-rearomatisation sequence, this approach for *meta*-functionalisation was abandoned.

2.2.6 *N*-alkylation Strategies

As discussed in Section 1.1, the nitrogen atoms add a lot of value to the fragment scaffolds. The *H*-bonding ability enables modification of lipophilicity and polarity and they facilitate strong polar interactions with the target protein. Analysis by Chessari *et al*. highlights the important role of heteroatoms in fragment-protein binding with 93% of the 125 case-studies containing at least one direct heteroatom-mediated polar interaction.[17] Furthermore, the polar interactions were highly conserved through the fragment-to-lead elaboration showing that the heteroatoms are not always viable points for synthetic growth.

Thus far, the nitrogen atoms in the pyrazole ring have only been functionalised when a protection strategy was necessary to prevent undesirable involvement in other reactions. However, their alkylation is also an obvious route to access another growth vector around the core. The two adjacent nitrogen atoms in the pyrazole ring of the scaffold presents a great opportunity to functionalise one to extend the molecule, while leaving the other less encumbered and more available for *H*-bonding. Alkyl groups with low steric bulk are most desirable in this case. Alkylation of the pyrazolo[3,4-c]pyridine was achieved by treatment with NaH followed by an alkyl halide, affording the corresponding *N*-alkylated species as mixtures of isomers that could be separated by column chromatography [Table 2.8].

Table 2.8: Selective *N*-1 and *N*-2 alkylation of 5-halo-*1H*-pyrazolo[3,4-c]pyridines.

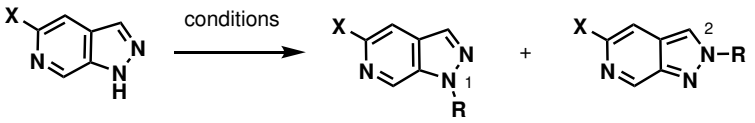

Entry	X =	Reaction Conditions	R =	Yield *N*-1	Yield *N*-2
1	Br	MeI, NaH, THF, 0 °C - rt, 1 hr	-Me	36% **205**	50% **206**
2	Cl	MeI, NaH, THF, 0 °C - rt, 1 hr	-Me	31% **207**	42% **208**
3	Cl	PrI, NaH, THF, 0 °C - rt, 24 hr	-Pr	27% **209**	35% **210**

This was an efficient route to generate usable amounts of both *N*-alkylated isomers in near equal ratios by a single reaction. At the early stages of drug discovery this would be a useful transformation to quickly generate two close analogues for screening. However, returning a mixture of isomers at a late stage of a synthetic sequence could be a disappointing loss of material. A method to generate a single alkylated isomer was therefore desirable. A two-step methylation and SEM-deprotection approach was proposed to preserve the regioselectivity already achieved during the installation of the SEM protection group.

Treatment of the *N*-2-SEM isomer **141** with trimethoxonium tetrafluoroborate saw direct conversion to the *N*-1-methylated product **211** precipitating from the reaction mixture [Scheme 2.2.6.1]. The methyl-salt was not isolated and could not be observed by LCMS analysis of the reaction, indicating that loss of the SEM group was rapid upon *N*-methylation. This could have been promoted by the $[BF_4]^-$ ions present in the reaction mixture.

In the case of **140**, methylation by trimethoxonium tetrafluoroborate saw the formation of intermediate methyl salt **212** as a white precipitate. This was isolated and identified by a new peak observed in the ^{1}H NMR spectrum (3H singlet at 4.64 ppm) corresponding to the *N*-methyl group. Trifluoroacetic acid (TFA) was added to the reaction mixture to promote SEM-deprotection to generate the methylated product. However, following the addition of TFA, compound **211** was isolated instead and *N*-2-methylated **213** was not observed [Scheme 2.2.6.1].

This result was confirmed by reaction of compound **145**, the same methyl transfer occurred in this reaction generating compound **214**. These observations were confirmed by the NOE signal between 7-*H* (9.85 ppm) and N-CH_3 (4.35 ppm) in the final products [Scheme 2.2.6.1]. The formation of the *N*-1 regioisomer from both the *N*-1- and *N*-2-SEM substrate indicates this was the thermodynamically more stable isomer, which is in agreement with observations of analogous reactions with indazoles.[125]

During the progress of the SEM-deprotection, only the methyl salt and the 1-methyl product were observed which indicated that methyl migration was either involved in the SEM-deprotection mechanism or occurred rapidly thereafter. A possible mechanism for the N-to-N methyl migration is by a [1,5] sigmatropic rearrangement that can take place suprafacially [Scheme 2.2.6.2]. However, further

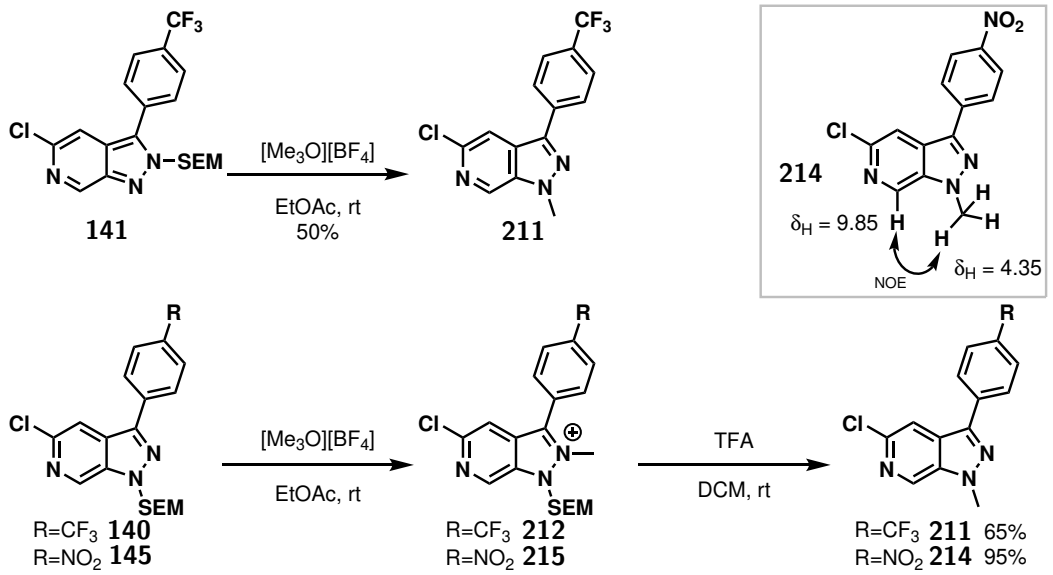

Scheme 2.2.6.1: *N*-methylation and SEM-deprotection of *N*-2-SEM **141** and *N*-1-SEM **140** and **145** cross-coupled products.

evidence is required to confirm this mechanism. For example, it was assumed that methylation occurred on the unsubstituted nitrogen to be in line with the reaction of **141**, but it is also possible that *ipso*-methylation occurred giving the *N*-1-methyl products directly upon SEM-deprotection. Additional evidence for the mechanism could be generated by testing the acid and base stability of *N*-2-metheylated **206** and **208**. Although further investigation into possible mechanisms were not undertaken at this time.

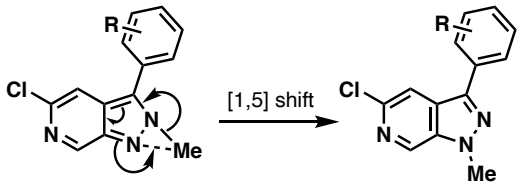

Scheme 2.2.6.2: Suggested mechanism for the N-to-N methyl migration.

During the methylation reaction of **145**, some interesting observations were also made of the collected *N*-1-methyl product **214**. The reaction initially formed a white solid that NMR analysis revealed existed as the trifluroacetate salt due to the characteristic quartet at 158.5 ppm in the ^{13}C NMR spectrum and the peak at -76.3 in the ^{19}F NMR spectrum. Fortunately, the TFA could be removed by stirring with NH_3 in MeOH then washing with minimal H_2O to afford a bright yellow solid which was very insoluble in aqueous and organic solvents, even DMSO. Addition of a small amount of TFA to the DMSO solution, lowering it to pH < 3, immediately turned the yellow solution colourless and dramatically increased the compound's solubility [Figure 2.2.6.1].

The effects of the acid were investigated by analysis of the ^{1}H NMR spectra in the presence and absence

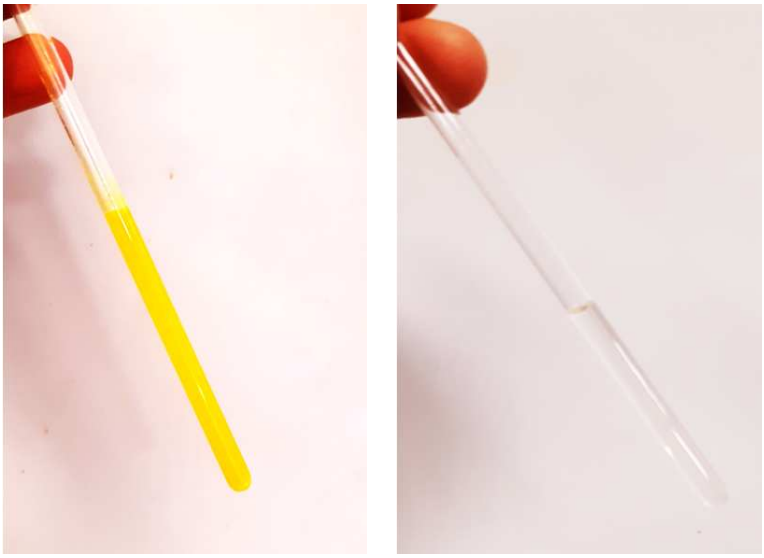

Figure 2.2.6.1: DMSO solution of compound **214** before and after addition of TFA.

of TFA. Upon the addition of TFA, the peaks for the main core protons moved down field and the peaks for the protons on the nitrobenzene coalesced. This is believed to be due to the disruption of the conjugated π system upon protonation of the pyridine nitrogen. These observations were only made for the *para*-nitrobenzene substituted substrate **214**, not the *para*-trifluoromethylbenzene **211** which indicate the importance of the nitro-group extending the conjugation system. These observations prompted a deeper investigation into the physical chemical properties of these scaffolds and the effects of protonation on the conjugated π system. The experiments, results, and discussions of this work is discussed in detail in Chapter 3.

Overall, late-stage alkylation by an *N*-methylation and SEM-deprotection strategy was a valid route to the *N*-1 product from either SEM-isomer. A greater range of *N*-alkylation products were accessible by treatment with an alkyl halide. While the yields of this approach were limited by the need to separate the two products, this was easily done by column chromatography.

2.2.7 Multi-step Sequences

While individual elaboration along each growth vector is a valuable tool to explore fragment space, it is likely that a full optimisation will require multiple growth vectors to be accessible. As a final aspect it was, therefore, necessary to demonstrate how these functionalisation strategies could be combined to emulate a hit-to-lead pathway common to medicinal chemistry development.

Using, for example, a combination of *C*-3 borylation, Suzuki-Miyaura cross-coupling with either 1-bromo-4-trifluoromethylbenzene or 1-iodo-4-nitrobenzene and *N*-methylation/SEM-deprotection afforded the desired products **211** and **214** in yields of 37% and 57% across the two steps

[Scheme 2.2.7.1]. A second sequence combined *C*-3 borylation, Suzuki-Miyaura cross-coupling with 1-bromo-4-trifluoromethylbenzene and *C*-7 TMPMgCl·LiCl metalation with electrophilic trapping by I_2 to give **216** in 37% yield across the two steps. The C-I bond is then a good handle to add a further variety of additional functionality to this position if desired.

Finally, extensions to more elaborate three-vector functionalisation sequences are also possible. Exemplified in Scheme 2.2.7.2, a three-step sequence takes fragment **185** to compound **217** by *N*-methylation, Buchwald-Hartwig amination with morpholine, and C-H borylation and Suzuki-Miyaura cross-coupling with 1-iodo-3,5-dimethylbenzene. Importantly, despite the increasing complexity of the substrate, in each of these sequences the yield of each step was comparable to that of the individual reactions obtained earlier. Other sequences of elaboration are possible and the chemistry here explored could be combined in many ways to realise an expansive library of heterocyclic compounds.

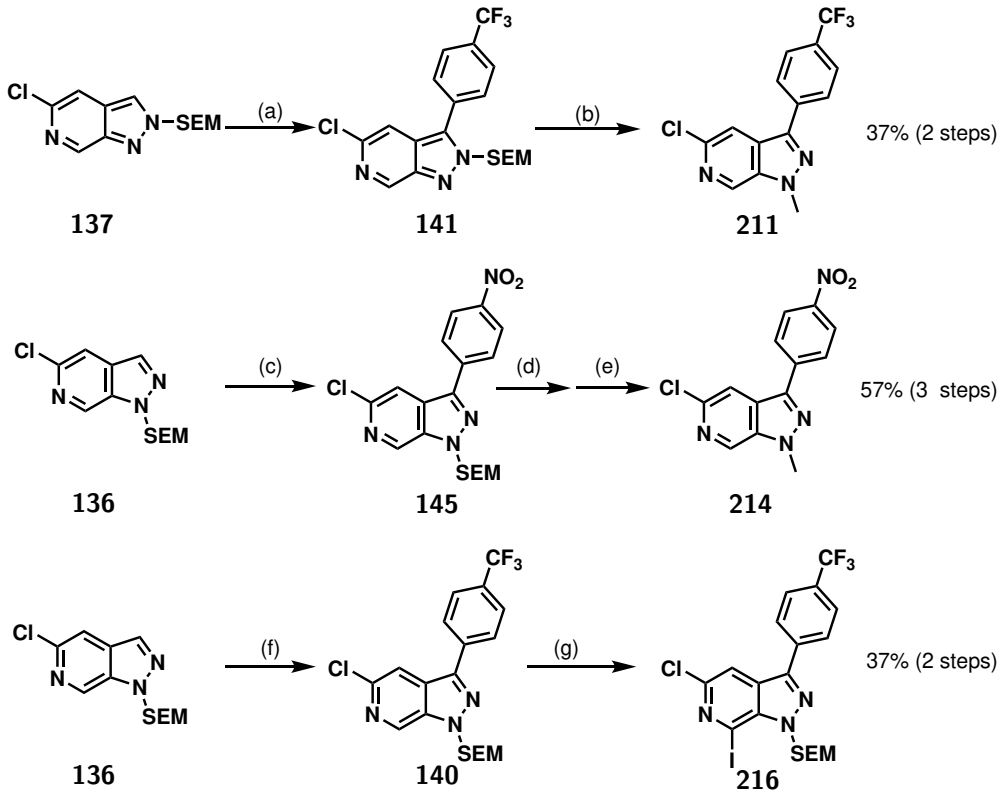

Scheme 2.2.7.1: Multi-vector elaboration sequences.

C-3 borylation, Suzuki-Miyaura cross-coupling with a tandem *N*-methylation/SEM-deprotection, conditions: (a) 1. $[Ir(COD)OMe]_2$, dtbpy, B_2pin_2, MTBE, 100 °C MW, 2. $C_7H_4F_3Br$, $Pd(dppf)Cl_2$, Cs_2CO_3, CuCl, DMAc, 120 °C MW, (b) $[Me_3O][BF_4]$, EtOAc, rt, 18 hr.

C-3 borylation, Suzuki-Miyaura cross-coupling with a tandem *N*-methylation/SEM-deprotection, conditions: (c) 1. $[Ir(COD)OMe]_2$, dtbpy, B_2pin_2, MTBE, 100 °C MW, 2. ArX, $Pd(dppf)Cl_2$, Cs_2CO_3, DMAc, 120 °C MW, (d) $[Me_3O][BF_4]$, EtOAc, rt, 6 hr, (e) TFA, DCM, rt, 20 hr.

C-3 borylation, Suzuki-Miyaura cross-coupling with C-7 TMPMgCl·LiCl metalation and electrophilic trapping with iodine, conditions: (f) 1. $[Ir(COD)OMe]_2$, dtbpy, B_2pin_2, MTBE, 100 °C MW, 2. $C_7H_4F_3Br$, $Pd(dppf)Cl_2$, Cs_2CO_3, DMAc, 120 °C MW, (g) 1. TMPMgCl·LiCl, THF, -40 °C, 30 min 2. I_2, THF, rt, 1 hr.

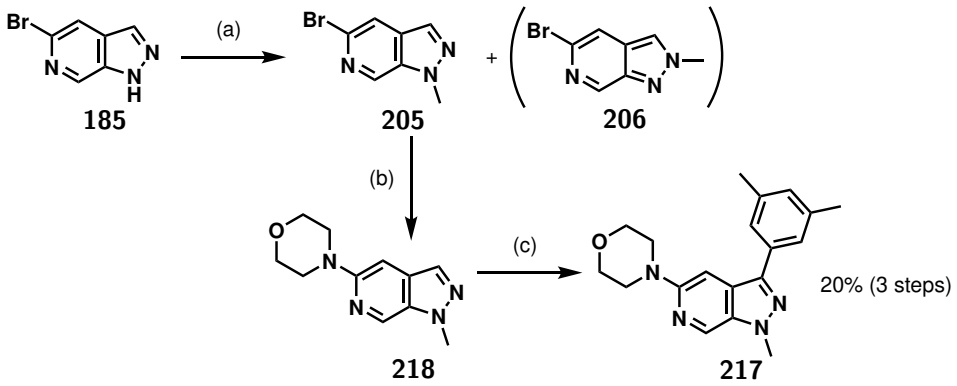

Scheme 2.2.7.2: Multi-vector elaboration sequences.

N-methylation, Buchwald-Hartwig amination, and C-3 borylation, Suzuki-Miyaura cross-coupling, conditions: (a) MeI, NaH, THF, rt, 45 min, (b) $Pd_2(dba)_3$, NHR_2, NaO^tBu, *rac*-BINAP, THF, 55 °C, 18 hr, (c) 1. $[Ir(COD)OMe]_2$, dtbpy, B_2pin_2, MTBE, 100 °C MW 30 min 2. C_8H_9I, $Pd(dppf)Cl_2$, Cs_2CO_3, DMAc, 120 °C MW 2 hr.

2.3 Conclusions

In summary, this portion of work has developed efficient synthetic routes to 5-halo-*1H*-pyrazolo[3,4-c]pyridine scaffolds and demonstrated how these compounds can be selectively elaborated along multiple reaction vectors.

5-Chloro-*1H*-pyrazolo[3,4-c]pyridine **77** was generated on a multigram scale after optimisation of the reported conditions for the small-scale reaction.[72] Introduction of DCE as a co-solvent reduced the hazards and practical challenges of working with large amounts of Ac_2O and cleaned up the reaction to be an efficient synthetic route to the heterocycle of interest **77** without need for further purification. The robustness of these conditions was demonstrated in their easy application to generate the bromine analogue **185**.

During the exploration of vectorial functionalisation, the inspiration for several strategies came from reported examples of indazole and pyridine. The reactivity of the pyrazolo[3,4-c]pyridine was expected to mirror these common heterocycles due to the structural similarity between them. However, this was frequently not the case, for example in the reduced regioselectivity of introducing nitrogen protecting groups. A possible explanation is that the stabilising effects of the additional nitrogen in the pyridine ring mean the electron density is more evenly distributed across the pyrazole nitrogen atoms giving them a more comparable nucleophilicity and giving rise to a mixture of isomers.

In medicinal chemistry the ability to generate two close analogues in one step is useful to test structure-activity relationships, although it would be desirable to have a regioselective route to afford efficient production of one analogue on scale. Already the choice of base had an influence on the major isomer generated in the SEM protection, and reaction time influenced the major isomer in the THP protection of the bromine analogue. These observation imply that greater selectivity could be possible with further exploration of more acid/base conditions.

The proximity of multiple nitrogen atoms also challenged reactivity at the 5-halogen position. The electron donating effects of the *para*-nitrogen reduced the electrophilicity of the C-X bond and prevented a successful S_NAr approach. This was overcome by moving to a Pd-catalysed cross-coupling strategy, and Buchwald-Hartwig amination afforded a range of aromatic amines in good yields. One possibility to extend this reactivity further would be to exchange the coupling partner to facilitate the formation of a carbon-carbon bond instead. The 5-bromo position has been demonstrated as susceptible to Pd-catalysts which opens a range of possible reactions for future exploration, including the much discussed Suzuki-Miyaura cross-coupling.

The most versatile strategy explored for the elaboration of the pyrazolo[3,4-c]pyridine was the direct metalation by TMPMgCl·LiCl. Once conditions for magnesiation had been optimised, the resulting

turbo-Grignard reagent could be trapped by a range of electrophiles introducing a variety of substituents. Furthermore, the opportunity for transmetalation to an organozinc reagent afforded a range of arylated products via Negishi cross-coupling. The surprising regioselectivity of *N*-2-SEM **137** indicated that the arrangement of heteroatoms in scaffold **77** influences the possible outcomes of metalation more than expected. Whilst already a versatile strategy for functionalisation at *C*-7, these observations indicate potential for extending its application to other positions on the ring. There is also the potential to develop a protection group strategy to control the regioselectivity. However, there was no further investigation into the effects of the nitrogen protecting groups at this time.

Finally, the most challenging position to access was *C*-4 on the pyridine ring. A complex dearomatisation-rearomatisation approach was trialled, however, the instability of the tricyclic system meant this strategy was not feasible. The many challenges of *meta*-functionalisation of pyridine means this position remains elusive. As discussed, the most common method of *meta*-functionalisation of pyridine is by Ir-catalysed C-H activation. However, this methodology had been shown to primarily target the *C*-3 site on the pyrazolo[3,4-c]pyridine ring. The application of successive rounds of Ir-catalysed C-H activation could be a route to this position but this would likely be challenged by the increasing steric congestion of a position with two *ortho*-substituents. The multi-step procedure of installing a blocking group is also undesirable for a late-stage fuctionalisation strategy. Furthermore, the evidence of a secondary borylation event already occurring at *C*-7 indicates that, even after blocking *C*-3, *C*-4 borylation might not be favourable. More work is needed to develop a robust method to access this position, although the directing effects of the proximal halogen suggest other metalation strategies could be possible.

The synthetic work undertaken to explore the vectorial functionalisation of the pyrazolo[3,4-c]pyridine is best exemplified in the multi-vector elaboration sequences exemplified in Scheme 2.2.7.1 and Scheme 2.2.7.2. Overall, the late-stage functionalisation sequences described here provide practical routes for the introduction of structural diversity required for fragment-elaboration and demonstrate the possibilities of the 5-halo-pyrazolo[3,4-c]pyridine scaffold.

Chapter 3

Photophysical Characterisation of Methylated Pyrazolo[3,4-c]pyridines

As discussed in Section 2.2.6 compound **214** exhibited unusual behaviour at low pH with sudden changes in colour and solubility. This was believed to be due to changes in the conjugated π-system upon protonation of one of the ring nitrogen atoms. To develop a greater understanding of this behaviour, a series of photophysics experiments were designed to explore the physicochemical properties of the pyrazolo[3,4-c]pyridine scaffold. These experiments, along with the density functional theory calculations to support their interpretation, are the topic of the following chapter.

3.1 Introduction to Photoluminescence

3.1.1 Excitation and Relaxation

When exposed to a source of electromagnetic radiation, an orbital electron absorbs the energy of an incident photon and becomes excited to a higher energy level. The electronic ground state of most molecules is a singlet state, S_0, with a notable exception being molecular oxygen which has a triplet ground state, T_0. Absorption of a photon causes excitation to an excited electronic state with the same spin multiplicity, so for a molecule with a singlet ground state the excited state is denoted S_n where $n \geq 1$. When the molecule then returns to its ground state, there are multiple pathways by which it can dissipate energy. Photoluminescence describes the decay processes by which the substance emits light.[143]

When a molecule is excited to a higher electronic state, $n > 1$, the simplest way to lose energy is by vibrational relaxation, denoted by a black curved arrow in Figure 3.1.1.1. This is a rapid non-radiative process and energy is lost to the environment as heat. As the vibrational energy levels can overlap for different electronic states, it is also possible for a molecule to transition to a lower electronic state by this mechanism. This transition is then called internal conversion, denoted by a dark grey curved arrow in Figure 3.1.1.1. Vibrational relaxation and internal conversion occur on very rapid time-scales so form at least part of most decay pathways.

Molecules in the first singlet excited state, S_1, can also relax to the ground state, S_0, by radiative pathways through emission of a photon. The energy of the emitted photon is usually lower than the absorbed radiation, corresponding to a longer wavelength of light. If this relaxation happens directly from S_1 to S_0, the accompanying emission is called fluorescence.[144] This pathway is indicated by a green arrow in Figure 3.1.1.1. Fluorescence decay happens on fast timescales ($<$10 ns) so fluorescent materials stop glowing almost immediately when the source of radiation is removed.

Another possible pathway is by intersystem crossing, when a molecule in one vibrational energy level of an excited electronic state moves to a higher vibrational energy level of a lower energy electronic state with a different spin. For example, a molecule in the first singlet excited state, S_1, could undergo intersystem crossing to an excited triplet state, T_1. This non-radiative transition is indicated by a curved light grey arrow in Figure 3.1.1.1. Importantly, the spin is no longer paired with the singlet ground state, S_0. Electronic transitions between states with different spin are formally "forbidden" under strict symmetry rules, but can still occur in quantum mechanics. When the molecule relaxes from an excited triplet state to the ground singlet state (T_1 to S_0), the accompanying emission of a photon is called phosphorescence, indicated by a red arrow in Figure 3.1.1.1.[144] Because this transition is formally "forbidden", it is kinetically unfavourable and happens on a longer time scale than fluorescence (μs to ms).[145]

These radiative decay pathways are analysed in the experiments detailed later in this chapter.

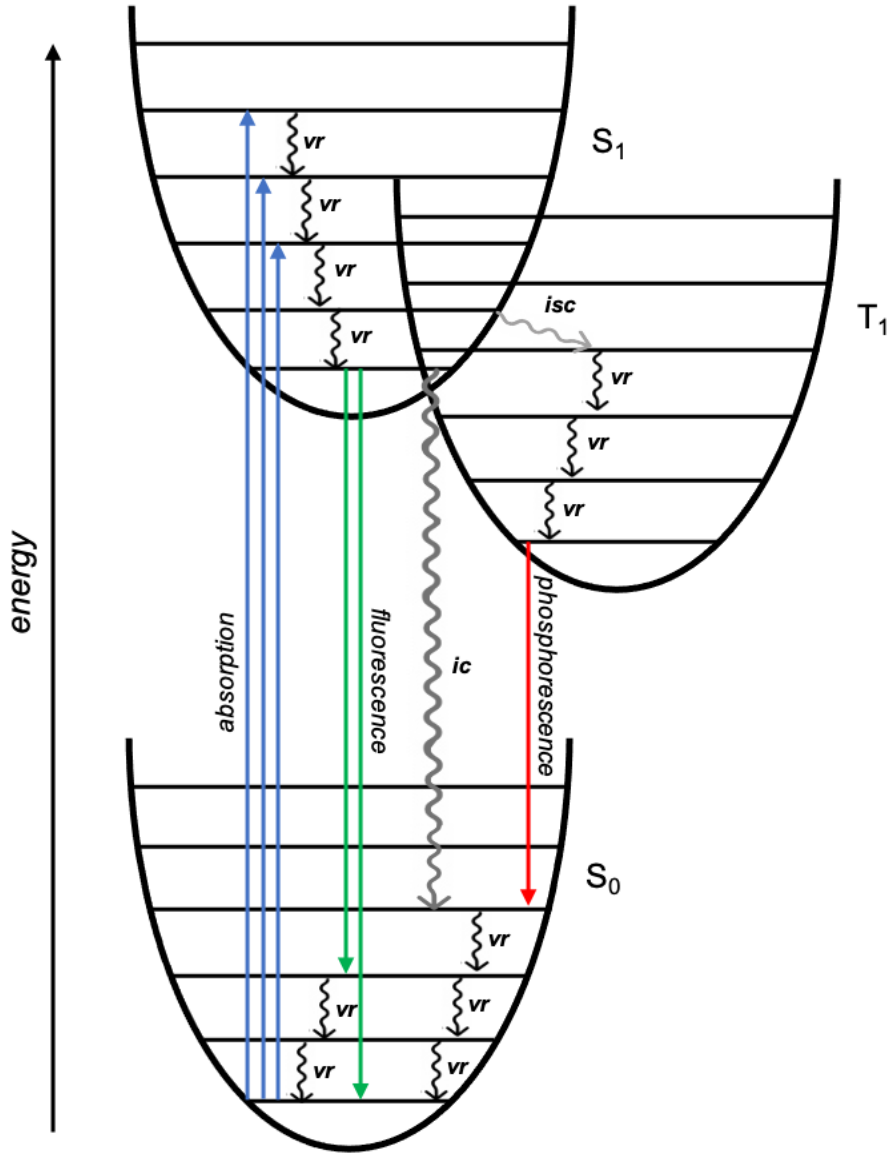

Figure 3.1.1.1: Schematic representation of electronic energy states under the harmonic approximation. ***vr*** = vibrational relaxation, ***ic*** = internal conversion, ***isc*** = intersystem crossing

3.1.2 Methods of Photophysical Characterisation

Photophysical characterisation of a compound involves three types of spectroscopic experimentation. Firstly, UV-Vis absorption spectroscopy measures the wavelengths of light that are absorbed by a chemical compound exposed to white light. The specific wavelengths of light which are absorbed correspond to photons with energy equal to the energy of an excited state of the compound. Secondly, excitation spectroscopy measures the intensity of emission at a fixed wavelength while the wavelength of the excitation radiation is varied. After correcting for variations in the source intensity, the excitation spectrum of a given sample should be nearly identical to its absorbance spectrum. The excitation spectrum is useful for selecting the best wavelength at which to excite the sample for quantitative or qualitative analysis. This excitation wavelength is also used in the third type of photoluminescence experiment, emission spectroscopy. To obtain an emission spectrum, a sample is excited at a single wavelength and the intensity of emitted radiation is monitored across a range of wavelengths. Each excited species has the potential to emit light via either fluorescence or phosphorescence which correspond to the excited singlet and triplet states respectively.

More information about the nature of a molecule's photoluminescence comes from recording the luminescence lifetime. The lifetime depends on how long a molecule remains in the excited state before emission occurs and dictates how long a sample continues to emit after the source of radiation is removed.[146] It is determined by a method of time-correlated single-photon counting in which a sample is repeatedly excited by a large number of rapid laser pulses and the time delay of each single-photon emission is recorded.[147] This data generates a histogram showing the probability distribution for emission of a single-photon following excitation from which the lifetime can be determined. As fluorescence typically occurs on a faster time-scale to phosphorescence, the photoluminescence lifetime can help distinguish these decay pathways.

A final important factor of photoluminescence is measuring the efficiency of the luminescence process, expressed as the photoluminescence quantum yield (PLQY). Quantum yield measures the ratio of the number of photons emitted to the number of photons absorbed, and can be expressed as a percentage or a fraction from 0 to 1.[148] The quantum yield depends on the relative rates of radiative decay (ie. fluorescence and phosphorescence) versus non-radiative decay (ie. vibrational relaxation, internal conversion, and intersystem crossing). Quantum yield is an important consideration for the rational design of fluorescent molecules used as fluorescent dyes or imaging probes as compounds with high quantum yields are desirable. Quinine sulfate, the salt formed from quinine in concentrated sulfuric acid, is a common photoluminescence standard with a PLQY of 54% at room temperature.[149]

3.1.3 Applications of Fluorescent Molecules

Fluorescent molecules have been used in numerous applications such as organic light-emitting diodes (OLEDs), laser applications, and fluorescent dyes.[150–152] Small organic molecules are particularly relevant to applications of biological imaging probes. A fluorescent probe describes a compound that combines or interacts with a biological component (eg. enzyme, cell receptor, antibody, etc) in such a way to cause a detectable physicochemical change with a measurable or quantifiable output. They come in two classes; bioactive molecules with intrinsic fluorescence properties, or conjugate molecules containing a fluorophore linked to a biologically active warhead. Fluorescent small molecules are an attractive technique for biological imaging due to their relative low cost, ease of use, and quantitative sensitivity.[153] Their uses range from studying the function of biological molecules in their cellular environment, to *in vivo* labelling of target cells.[153–155]

A challenge of using fluorescent probes in biological systems is that measured changes in fluorescence intensity can be caused by many factors not relevant to the studied system including background fluorescence, changes in excitation intensity, and variation in effective cell thickness in the optical beam.[154] The errors caused by these factors can be reduced by the use of ratiometric measurements - recording the fluorescence intensity at two wavelengths and calculating the change in ratio. For this technique to be effective, there needs to be some change in the photoluminescence of the probe molecule upon interaction with its target.

This strategy was put to good use in the analysis of amyloid fibril formation using the fluorescent JC-1 probe [Figure 3.1.3.1].[156] When excited by radiation at 490 nm, JC-1 fluoresces at different wavelengths depending on the fibrillation state of α-sinuclein to which it is bound: 590 nm indicates monomers, 560 nm indicates oligomeric intermediates, and 538 nm indicates fibrillar forms. Measuring the changing ratios at these wavelengths enabled real-time analyses of the formation of amyloid fibrils which could be a useful diagnostic tool for neurodegenerative diseases.

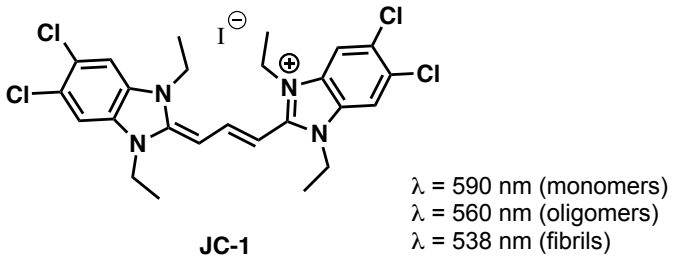

Figure 3.1.3.1: Fluorescent probe **JC-1** 5,5',6,6'-tetrachloro-1,1',3,3'-tetraethylbenzimidazolyl carbocyanine iodide.

Another emerging strategy to improve the sensitivity of fluorescence-based probes is to use materials exhibiting thermally activated delayed fluorescence (TADF). TADF materials are designed to have a small

singlet-triplet energy gap which reduces the energy barrier for reverse intersystem crossing. This means that thermal energy alone is sufficient to promote a triplet state molecule into a higher energy singlet state by reverse intersystem crossing. TADF molecules, therefore, have a two-stage emission profile. The first stage is fluorescence directly from the first excited singlet state, S_1, which occurs on the order of < 10 ns. The second stage occurs after reverse intersystem crossing from the triplet excited state, T_1, and is therefore delayed, occurring on the order of μs to ms. In comparison, the background fluorescence from a typical biological system is complete in < 100 ns. Therefore, time-resolved fluorescence imaging with TADF probes removes the background noise and enables the study of biological systems with improved sensitivity. An additional benefit of TADF molecules is that, by promoting the fluorescence decay from singlet and triplet excited states, higher quantum yields can be achieved. This further enhances the sensitivity of the fluorescence imaging.

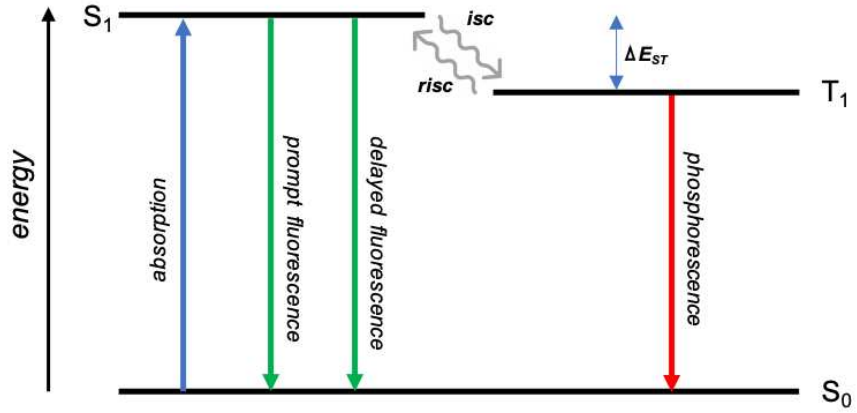

Figure 3.1.3.2: Simplified Jablonski diagram of thermally activated delayed fluorescence (TADF).
isc = intersystem crossing (t = ns), ***risc*** = reverse intersystem crossing (t = μs), ΔE_{ST} = Energy gap between S_1 and T_1

In a recent example, TADF probes, including compound **219**, were incorporated into water-soluble polymer dots which enabled the immunofluorescent labelling of SK-BR3 human breast-cancer cells [Figure 3.1.3.3].[155] Here structure-property relationship analysis identified that the TADF behaviour arose from low-energy rotation around the donor-acceptor linker. When the molecular geometry limits the overlap between the HOMO and LUMO, this minimises the exchange energy and reduces the singlet-triplet energy gap, facilitating the reverse intersystem crossing required for TADF.[157] This behaviour was not expected from calculations based on ground-state geometries which instead predicted a large singlet-triplet energy gap. This shows how difficult these behaviours are to predict and that a greater understanding of structure-property relationships is required. This understanding is necessary to improve the rational design of molecules that display desirable fluorescent properties for bioimaging applications.

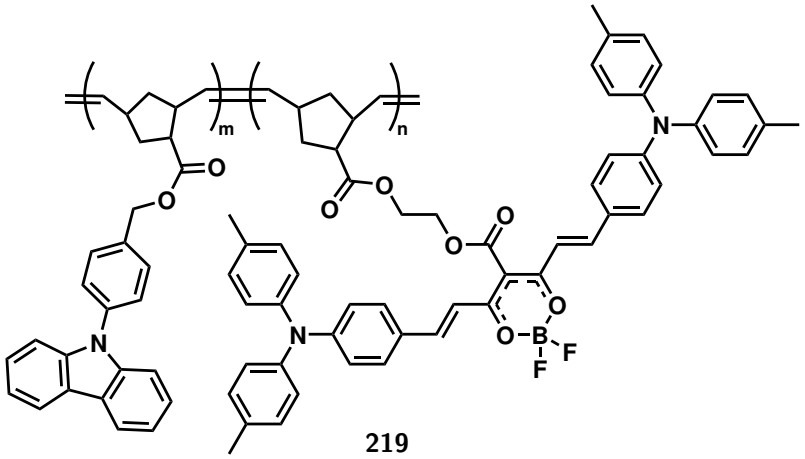

219

Figure 3.1.3.3: Structure of the boron-difluoride-curcuminoid-based polymer **219** exhibiting TADF for use as a biological imaging probe.

3.1.4 Protonation vs Methylation of Aromatic Nitrogens

It is well established in the literature that the protonation of nitrogen-containing compounds modulates their photophysical behaviour, often causing a redshift in photoluminescence.[155,158–161] This phenomenon was first observed in the 1950s when Krumholz recorded a distinct redshift in the absorption of polynuclear pyridine compounds upon moving to acidic conditions.[158] This was corroborated by Nakamoto in 1960 while researching 2,2'-bipyridine **220** and 2,2',2"-terpyridine **221** [Figure 3.1.4.1].[159] These compounds also displayed a redshift in absorbance of around 25 nm upon protonation in acidic aqueous solution.

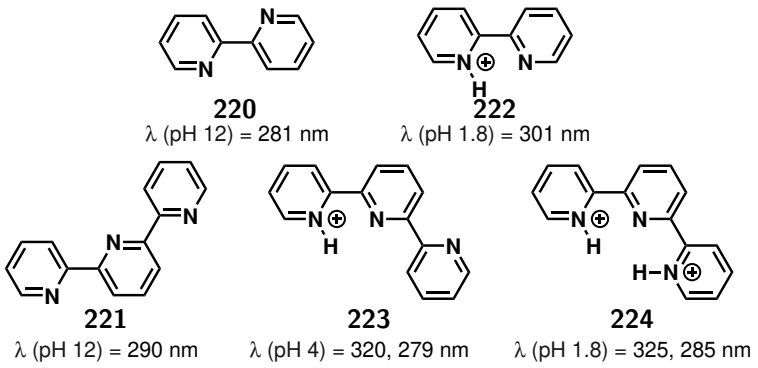

Figure 3.1.4.1: Structures of 2,2'-bipyridine and 2,2',2"-terpyridine.

More interesting behaviour may be exhibited by compounds containing nitrogen atoms in different hybridisation states. For example, Tripathi *et al*. conducted a detailed study of the photophysics and spectroscopy of 9-aminoacridine [Figure 3.1.4.2].[162] Careful control of the pH of aqueous solvents enabled the analysis of the neutral **225**, singly-protonated **226**, and doubly-protonated **227** species. In this case, the first protonation occurs on the aniline nitrogen, this prevents delocalisation of the amine

lone pair, reducing the effective conjugation of the ring and causing a blueshift in the emission spectrum. The second protonation then occurs on the pyridine-like nitrogen which reduces the electron density in the ring causing a significant redshift of 40 nm. These observations demonstrate the complex influences of nitrogen lone pairs on photophysical behaviour.

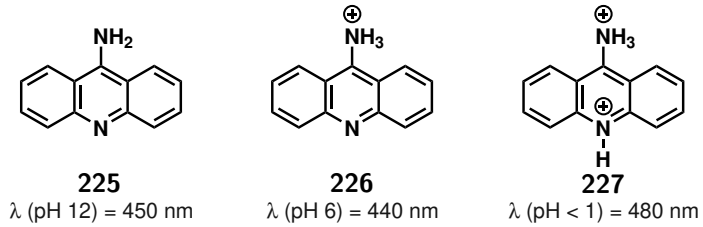

225 λ (pH 12) = 450 nm

226 λ (pH 6) = 440 nm

227 λ (pH < 1) = 480 nm

Figure 3.1.4.2: Structure of 9-aminoacridine.

The challenge of interpreting the effects of *N*-protonation is that the transient nature of the protonated compounds can make it hard to determine their precise chemical structure. This is especially true if there are multiple possible protonation sites in the molecule. Furthermore, if the nitrogen pK_a values are too similar it can be hard or impossible to generate each protonated species in turn with compounds instead existing in dynamic equilibrium mixtures of different protonation states.[160] A mixture of species complicates the recorded spectra and limits the possible analysis of the resulting photophysics. To overcome the challenges of analysing protonated molecules, researchers in the Etherington group have been exploring the photophysical effects of nitrogen methylation.[161]

In their investigation, Turley *et al.* considered quinine **228** as a model substrate. Quinine contains two nitrogen atoms, the tertiary sp^3 amine in the quinuclidine (N1) and the sp^2 quinoline (N2) [Scheme 3.1.4.1].[161] Under increasingly acidic aqueous conditions, protonation occurs at N1 (pK_a = 8.6) then N2 (pK_a = 4.2) in turn.[163] Quinine is only weakly emissive under basic conditions because the emission is quenched by a through-space charge transfer between the quinuclidine N1 lone pair and the quinoline chromophore.[164] Then when the quinuclidine N1 is protonated, the charge transfer pathway is lost and the efficiency of the local excitation of the quinoline chromophore increases to 22%. The second protonation further enhances emission and quinine bisulfate fluoresces blue with high PLQY of 55% under strong acidic conditions.

N1-methylated quinine **229**, under neutral conditions, displayed the same behaviour as the singly protonated quinine: a single peak in the emission spectra corresponding to the local excitation of the quinoline ring and no evidence of the charge transfer state. The emission spectrum of the doubly methylated quinine **230** also showed the same behaviour as the doubly protonated quinine: a single peak in the emission spectrum with no evidence of the charge transfer state but now with a significant redshift of the emission wavelength. This redshift occurs because trapping the sp^2 lone pair stabilises the LUMO and decreases the HOMO-LUMO energy gap. The observed behaviour of the singly-methylated and

doubly-methylated quinines parallels the behaviour of successive protonations. Therefore, these experiments prove that quaternisation of aromatic nitrogen atoms by methylation has a comparable impact on the compound's photoluminescence to that seen by protonation.

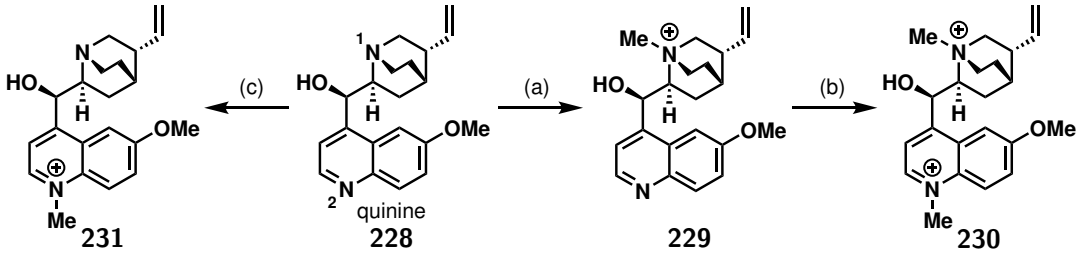

Reagents and conditions: **(a)** 1. MeI, rt, 3 d; 2. $AgBF_4$, MeCN, 60 °C, 10 min; **(b)** 1. MeI, MeCN, 100 °C, 4 hr; 2. $AgBF_4$, MeOH, rt, 10 min; **(c)** 1. allyl bromide, CH_2Cl_2, rt, 16 hr; 2. MeI, MeCN, 100 °C, 3 hr; 3. barbituric acid, $Pd(PPh_3)_4$ (5 mol%), DMSO, 40 °C, 16 hr, 4. diisopropylaminomethyl polystyrene, MeOH, rt, 1 hr; 5. $AgBF_4$, MeOH, rt, 10 mins.

Scheme 3.1.4.1: Structures of methylated quinine analogues.

Methylation offers several advantages over protonation as it generates a synthetic compound that can be isolated and interrogated more comprehensively. The site of methylation can then be assigned more conclusively, for example by NOE NMR spectroscopy or X-ray diffraction analysis of single crystals. Additional advantages of methylation over protonation include the ability to isolate the compound and ensure the whole sample is a single species. This is important in accurately determining a compound's luminescence efficiency (the PLQY). Furthermore, methylated salts have greater solvent tolerances than protonated species making them useful in more versatile applications.

Turley *et al.* demonstrated another advantage of methylation over protonation in their quinine investigation.[161] The careful use of nitrogen protecting groups gave access to the isomeric form of singly-methylated quinine with a methyl group on N2 and no group on N1. The protonated equivalent of this isomer is not kinetically stable so has not been investigated. As predicted, unlike the *N1*-methylated derivatives, there was no detectable photoluminescence emission of the *N2*-methylated quinine **231**. The available lone pair of the quinuclidine N1 opens the low-energy charge transfer pathway and led solely to non-radiative decay so no emission bands were recorded.

Overall, this investigation demonstrates that *N*-methylation is a powerful strategy to elucidate the photoluminescence properties of organic materials. Investigating the behaviour of quinine analogues showed that methylation has a comparable effect to protonation, but offers several practical advantages including the ability to investigate molecules not accessible by protonation.

Analogous work has been conducted looking at the effect that *N*-methylation has on the photophysical properties of a series of analogues of rhodamine 123 [Figure 3.1.4.3].[152] This investigation found that each subsequent methylation (from 0 to 4) caused a systematic decrease of 500 cm^{-1} in the emission energy. Rhodamines are used in a wide range of applications including as biological probes, so it is valuable to

understand how synthetic modifications enable fine tuning of the emission signal.

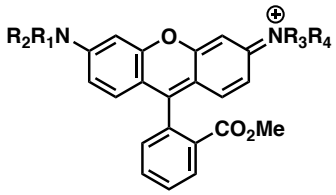

Rhodamine 123

$R_{1\text{-}4}$ = H, CH_3

Figure 3.1.4.3: Series of compounds based on Rhodamine 123

In summary, these reports show that the protonation of different nitrogen sites can have a big influence on the photophysical behaviour of nitrogen containing heterocycles. However, a major challenge of working with protonated species is they are difficult to isolate and characterise chemically. In some cases, this has been addressed by replacing *N*-protonation with *N*-methylation, however, studies looking at *N*-methylated compounds are limited. For example, the study of quinine focused on a substrate with a charge transfer pathway, but further research is needed to investigate the effects of *N*-methylation on systems with purely locally excited states. It is necessary to understand how *N*-methylation impacts the electronic state of the chromophore to develop more general structure-property relationships. Furthermore, quinine is a well studied substrate, but investigation of uncommon scaffolds is required to develop broader understanding of the effects of *N*-methylation, and how these compare to the effects of *N*-protonation. This research is necessary to investigate what causes these trends in photophysical behaviour, and facilitate the prediction of photophysical behaviour of new substrates in the future.

3.2 Aims

The principal aim of this investigation was to understand the effects of protonation on the conjugate system of the pyrazolo[3,4-c]pyridines by comparing the photophysical behaviour in neutral versus acidic conditions. As discussed in Section 3.1.4, there is ongoing work in the Etherington group investigating the effects of methylation, compared to protonation, of nitrogen heterocycles. Therefore, the second aim was to extend this existing research to see if these trends held true for the pyrazolo[3,4-c]pyridine scaffold. Analysing the photophysical behaviour of a series of methylated pyrazolo[3,4-c]pyridines would help to develop the understanding of the similarities between protonation and methylation. These experiments would also contribute to general structure-property relationships for the photophysical properties of nitrogen heterocycles.

3.3 Results and Discussion

The experiments discussed in the next section were conducted in collaboration with researchers at Northumbria University, Durham University, University of York, and Institut Ruder Bošković. The photoluminescence data was collected by Dr Chris Hogg (A series) and Ruth Pollard (B series), while the density functional theory (DFT) calculations were conducted by Dr Antonio Prlj. The pH titration analysis was carried out by Laura Duncan, and single X-ray crystal structures were solved by Dr Toby Blundell. I independently conducted the synthesis, purification, and characterisation of the two series of compounds, assisted in the collection of photoluminescence data for the B series, and carried out the below discussion.

Figure 3.3.0.1 shows the compounds that have been studied in this work with the corresponding labels. The singly methylated series of neutral compounds, **A1-4**, were synthesised according to the methods previously discussed in Section 2.2.6. [Note: compounds **A1-4**, were previously referred to as **208**, **207**, **206**, **205**, respectively] The synthesis of the doubly methylated salts, **B1-4**, will be described later in this section.

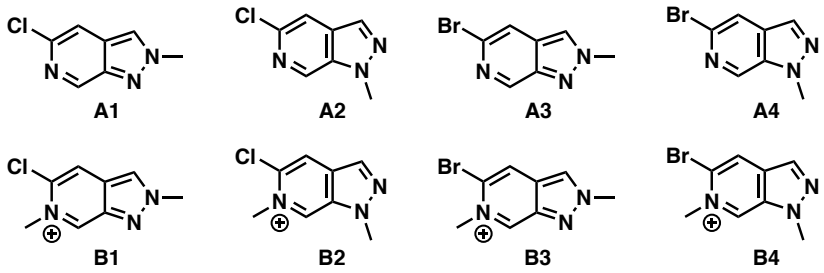

Figure 3.3.0.1: The neutral singly-methylated **A1-4** and doubly-methylated **B1-4** compounds studied in this chapter.

3.3.1 Photoluminescence of the A Series

To analyse the photophysical behaviour of the pyrazolo[3,4-c]pyridines, the absorption and photoluminescence of all four compounds in the A series was measured in aprotic MeCN and H_2SO_4 (0.1 M, pH $\approx$ 1). From Figure 3.3.1.1 it can clearly be seen that the absorption of **A1-4** in H_2SO_4 (0.1 M) (solid lines) is redshifted compared to the absorption in MeCN (dashed lines). The emission was also redshifted upon protonation by about 50 nm for all compounds. This result is in accordance with the literature and confirms observation from previous work in the Etherington group.[155,158–161] It was expected that upon protonation the absorption and photoluminescence of compounds **A1-4** would be redshifted compared to the neutral molecules because trapping the sp^2 lone pair decreases the energy of the electronic transition. Lower energy transitions correspond to longer wavelength emissions.

It is interesting to note that the emission profile of **A1** and **A3** were similar, as were **A2** and **A4**. This

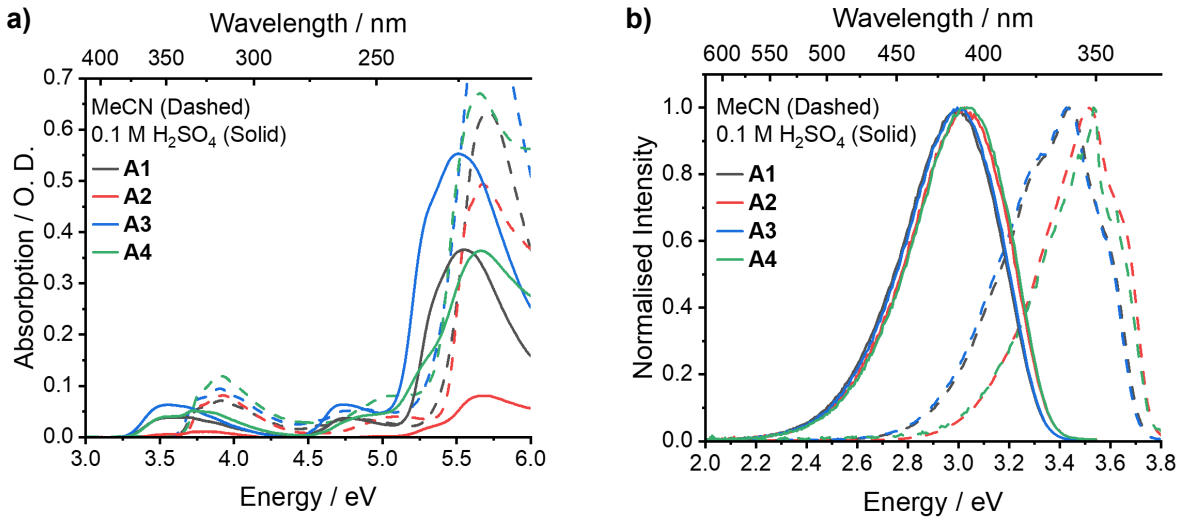

Figure 3.3.1.1: The **a)** absorption and **b)** photoluminescence of the A series compounds (20 μM) in both MeCN and H_2SO_4 (0.1 M).

indicates that the position of the methyl group, *N*-2 to *N*-1, has an influence on the peak emission energy. This was unsurprising as the choice in *N*-alkylation alters the conjugation pattern of the bicyclic system and therefore has a bigger impact on the energy level gaps of the molecular orbitals.

The effects of protonation on the efficiency of photoluminescence were also investigated. Table 3.1 shows the measured PLQY data for **A1-4** in MeCN and H_2SO_4 (0.1 M). As expected, there was a decrease in the fluorescence quantum yield for the bromine analogues **A3** and **A4** [Table 3.1, entry 3 & 4] compared to the chlorine analogues **A1** and **A2** [Table 3.1, entry 1 & 2]. This was due to the 'heavy atom effect', in which the presence of a heavy atom leads to decreased efficiency of fluorescence.[165] This happens because the heavy atom enhances spin-orbit coupling which increases the rate of intersystem crossing from singlet to triplet states. Therefore, a larger proportion of excited molecules decay via the triplet state and correspondingly the fluorescence decreases.

The PLQY data also shows a significant increase in quantum yield upon protonation. This trend matches that of quinine and other nitrogen heterocycles,[161] and is likely because protonation traps the nitrogen lone-pair and promotes the π to π^* transition. Although further mechanistic details are not fully understood.

In the pyrazolo[3,4-c]pyridine scaffold, there are two possible positions for protonation: *N*-6 on the pyridine ring, and *N*-1 or *N*-2 on the pyrazole ring that was not methylated. It was desirable to understand which nitrogen was protonated as a means to gain insight into the contributions of each nitrogen on the photoluminescence of the heterocycles. The challenge in defining the structure-property relationships for this scaffold was knowing which nitrogen becomes protonated first. DFT calculations

Table 3.1: PLQY data for A series compounds measured using relative methods by Dr Chris Hogg, University of York, and verified using absolute methods by Ruth Pollard, Northumbria University.

Entry	Compound	PLQY, MeCN[a]	PLQY, H_2SO_4 (0.1 M)[b,c]
1	**A1**	22%	87% (83%)
2	**A2**	13%	77% (70%)
3	**A3**	6%	36% (55%)
4	**A4**	< 1%	29% (29%)

[a] λ_{exc} = 315 nm, *conc* = 20 μM [b] λ_{exc} = 340 nm, *conc* = 20 μM
[c] = values in brackets are PLQY measured by absolute methods

were performed at the M06-2X/6-31+G(d,p) level with default SMD solvation (water) using Gaussian 16 software. Thermodynamic cycles were used to predict the pK_a values of each nitrogen on **A1** and **A2** which consistently found that *N*-6 was more basic by more than one pK_a unit.[166] However, the calculated values were too low to be reliable, especially considering the photoluminescence experiments showed the effects of protonation at around pH 1 [Figure 3.3.1.2].

Figure 3.3.1.2: Nitrogen pK_a values of **A1** and **A2** calculated by Dr Antonio Prlj, Institut Ruder Bošković.

Therefore, to understand the protonation of the A series compounds, the pK_a values were measured experimentally via titration. To do this, the photoluminescence intensity at the peak of emission (365 nm for **A1** and **A3** and 355 nm for **A2** and **A4**) was measured while the pH of the aqueous solution was varied by addition of aliquots of HCl solutions (0.025 M, 0.1 M, and 1 M) to shift the pH from around pH 5 to 0.5. The corresponding pH curves are displayed in Figure 3.3.1.3. Compound **A1** measured pK_a 2.5, compound **A2** measured pK_a 2.1, compound **A3** measured pK_a 2.1, and compound **A4** measured pK_a 1.1.

The pK_a data showed that the *N*-1 isomer was consistently more basic than the *N*-2 isomer for a given halogen. The corresponding pK_a value of *N*-methylpyrazole is 2.04,[167] which could indicate protonation occurred on the pyrazole ring. However, the pK_a data also showed that the bromine analogue was more basic than the chlorine analogue for a given *N*-methyl isomer, and the halogen is far from the pyrazole nitrogen atoms. *C*-2 substituents are known to impact the pK_a of an azinyl nitrogen, which could indicate protonation occurred on the pyridine ring. Yet in the case of pyridine, 2-bromopyridine (pK_a = 0.71) is more basic than 2-chloropyridine (pK_a = 0.49) because the greater electronegativity of the chlorine atom destabilises the protonated nitrogen.[168] Therefore, while these measured pK_a values confirmed that the pyrazolo[3,4-c]pyridines were protonated by H_2SO_4 (0.1 M), it was not conclusive which nitrogen was

protonated first. This challenge was addressed by analysing the doubly-methylated series **B1-4**.

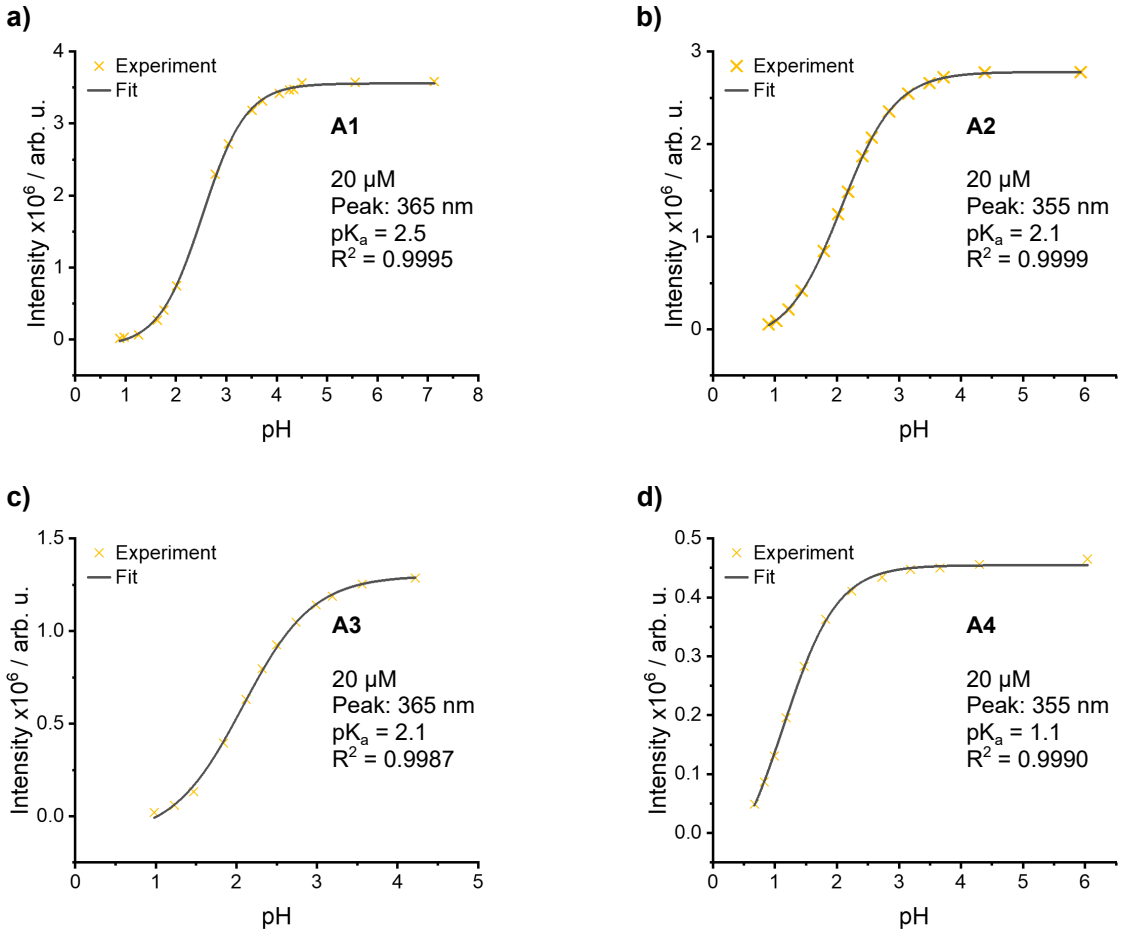

Figure 3.3.1.3: The pH curves for **A1**, **A2**, **A3**, and **A4** produced by Laura Duncan, Durham University.

3.3.2 Synthesis of the B series

The first methylation procedure used to generate the A series compounds involved alkylation by MeI. There was no evidence of multiple methylation events during these reactions, so it was clear that a stronger methylating agent would be required. Trimethyloxonium tetrafluoroborate [Me_3O][BF_4], known as a strong alkylating agent, was the obvious choice.[169] To explore this strategy, 5-chloro-2-methyl-pyrazolo[3,4-c]pyridine **A1** and [Me_3O][BF_4] (1.30 eq) were stirred in DCM at room temperature overnight and the methylated salt precipitated from the reaction mixture. The reaction mixture was cooled on ice before filtration under reduced pressure afforded the product as a white solid.

A peak in the LCMS at m/z = 182.16 indicated that only one methylation event had occurred, but there were two possible positions of *N*-methylation [Scheme 3.3.2.1]. The product was identified by observing a signal in the NOE NMR spectrum between N-C*H*$_3$ (4.39 ppm) and 7-*H* (10.24 ppm). Analysis of the ^{1}H-^{15}N HMBC also showed that methylation had occurred on the distal nitrogen.

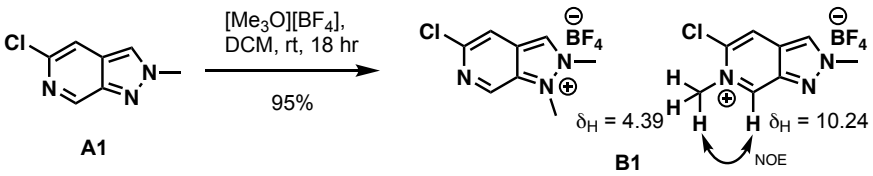

Scheme 3.3.2.1: Methylation of **A1** and structure determination of **B1**.

The same methodology was applied to 5-chloro-1-methyl-pyrazolo[3,4-c]pyridine **A2** and the desired product was collected as a white solid. In the case of **B2**, additional purification by recrystallisation from acetone was required to remove traces of the unmethylated substrate **A2**. Comparison of the ^{1}H NMR spectrum of **B1** and **B2** further supported the conclusion that methylation had occurred on *N*-6 because the two products were clearly different. Finally, following the recrystallisation from acetone, **B2** crystals of sufficient quality were collected and a single crystal X-ray structure confirmed the final product was methylated at *N*-6 [Figure 3.3.2.1]. For further structural comparison, recrystallisation was attempted for the other compounds in the A and B series. Unfortunately only crystals of **A3** were of sufficiently quality for reliable structure determination.

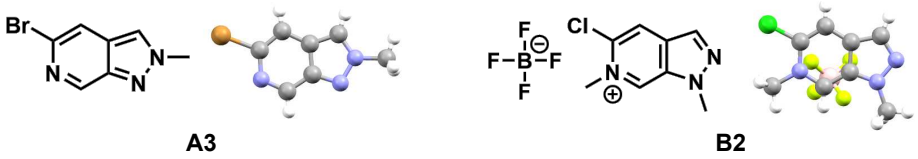

Figure 3.3.2.1: Single crystal X-ray structures of compounds **A3** and **B2**.

This synthetic methodology was applied to the bromine analogues affording **B3** and **B4** in 91% and 92% yield respectively. With the four desired methylated salts in hand, attention turned to the photophysical analysis.

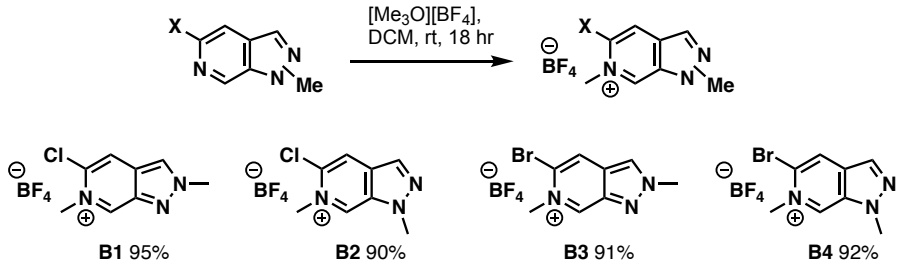

Figure 3.3.2.2: Methylation of **A1**, **A2**, **A3**, and **A4**.

3.3.3 Photoluminescence of the B Series

As discussed previously, *N*-methylation has begun to be explored as a method of analysing the effects of protonation on photoluminescence behaviour of nitrogen heterocycles. However, there are few examples of its use in the literature and its general application is not yet established. Therefore, it was first necessary to confirm that methylation had the same effect as protonation on the pyrazolo[3,4-c]pyridines. To do this, the absorption and photoluminescence of all four compounds **B1-4** were measured in aprotic MeCN and H_2SO_4 (0.1 M, pH $\approx$ 1). These spectra can be seen in Figure 3.3.3.1.

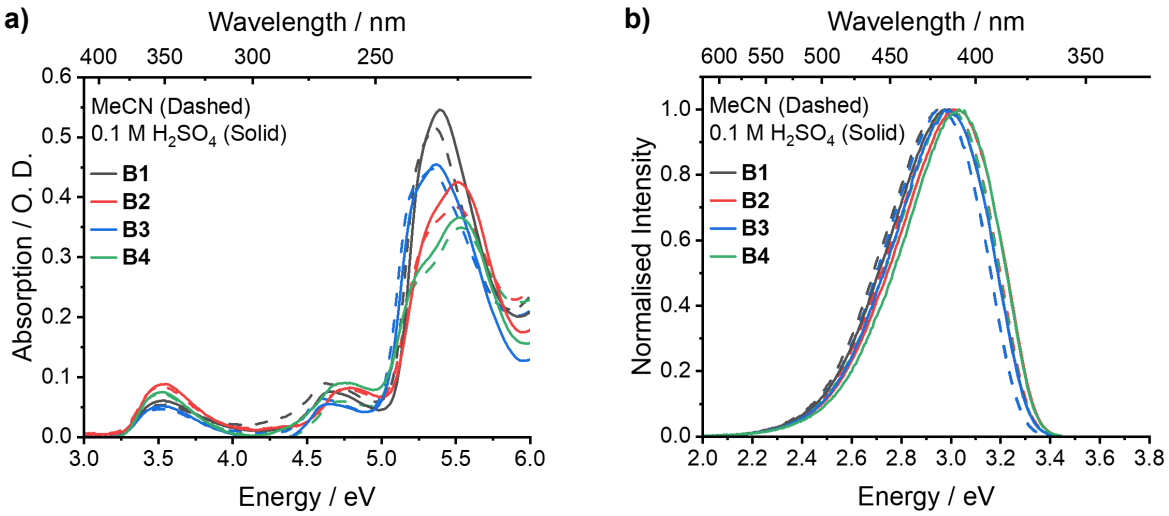

Figure 3.3.3.1: The **a)** absorption and **b)** photoluminescence of the B series compounds (20 μM) in both MeCN and H_2SO_4 (0.1 M).

As expected, there was no change in the absorption or emission between the **B1-4** in MeCN versus H_2SO_4 (0.1 M). Furthermore, the spectra of **B1-4** in MeCN were consistent with protonated **A1-4** in H_2SO_4 (0.1 M) [Figure 3.3.1.1]. This was strong evidence that protonation of **A1-4** occurred in the same manner as *N*-methylation (ie. on *N*-6). This also suggested that the second pyrazole nitrogen was not protonated, or at least that protonation of this nitrogen gave no further changes in the photophysical behaviour of the molecules.

The PLQY data was measured for the B series, showing minimal changes for **B1-4** between MeCN and H_2SO_4 (0.1 M) and the values were consistent with measurements of **A1-4** in H_2SO_4 (0.1 M) [Table 3.2]. The photoluminescence lifetimes of **A1-4** and **B1-4** were also measured. Figure 3.3.3.2 shows the lifetimes increase for all **A1-4** on moving from MeCN (solid) to H_2SO_4 (0.1 M) (dotted) which was consistent with moving to a new emission pathway. Meanwhile, no change in lifetime was observed between the two solvents for the B series, which is consistent with there being no change in the emission

pathway [Figure 3.3.3.3]. The lifetimes of **A1-4** in H_2SO_4 (0.1 M) were also very similar to that of **B1-4**, as displayed in Figure 3.3.3.4, which compares the two series in H_2SO_4 (0.1 M). These results extend the similarities observed between methylation and protonation of the nitrogen heterocycles.

Table 3.2: PLQY data for B series compounds measured using absolute methods by Ruth Pollard, Northumbria University.

Entry	Compound	PLQY, MeCN[a]	PLQY, H_2SO_4 (0.1 M)[b]
1	**B1**	73%	76%
2	**B2**	67%	61%
3	**B3**	19%	22%
4	**B4**	14%	12%

[a] λ_{exc} = 315 nm, *conc* = 20 μM [b] λ_{exc} = 340 nm, *conc* = 20 μM

It should be noted that there was a slight difference in the lifetimes of the bromine analogues **A3** and **B3**, but this was likely within error of the measurements [Figure 3.3.3.3]. This difference was not observed for **A4** to **B4** which implies it was not caused by the presence of the bromine. Further experiments to repeat these measurements would be needed to confirm the significance of these differences before further conclusions could be made.

It was also desirable to understand the effects of *N*-alkylation on the molecular orbitals to help explain the observed changes in emission energies. In this regard, the S_1 vertical emission transition energies of **A1**, **A2**, **B1**, and **B2** were calculated using DFT methods by Dr Antonio Prlj at Institut Ruder

Entry	Lifetime / ns	
	MeCN	H_2SO_4 (0.1 M)
A1	4.7	25
A2	2.2	18
A3	1.4	12
A4	0.8	6

conc = 20 μM

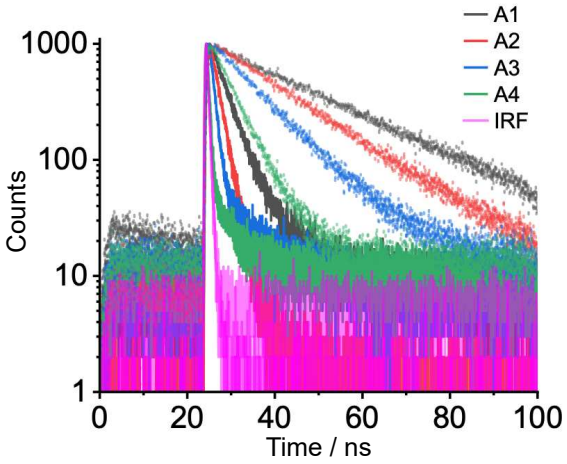

Figure 3.3.3.2: The time-correlated single photon counting measurements for the A series compounds in MeCN (solid) and H_2SO_4 (0.1 M) (dotted).

Entry	Lifetime / ns	
	MeCN	H_2SO_4 (0.1 M)
B1	27	27
B2	20	20
B3	6.8	7.4
B4	4.7	4.1

conc = 20 μM

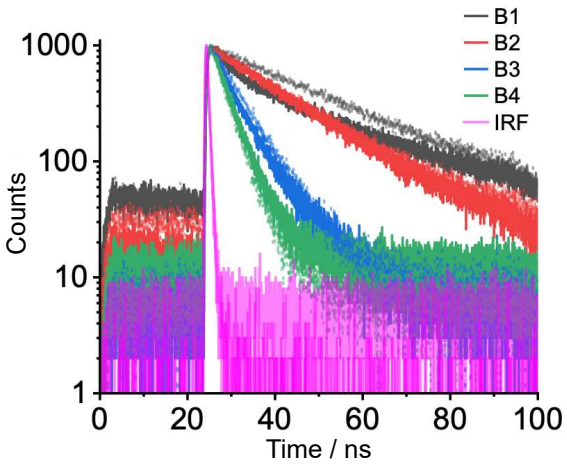

Figure 3.3.3.3: The time-correlated single photon counting measurements for the B series compounds in MeCN (solid) and H_2SO_4 (0.1 M) (dotted).

Entry	Lifetime / ns
	H_2SO_4 (0.1 M)
A1 (B1)	25 (27)
A2 (B2)	18 (20)
A3 (B3)	12 (7.4)
A4 (B4)	6 (4.1)

conc = 20 μM

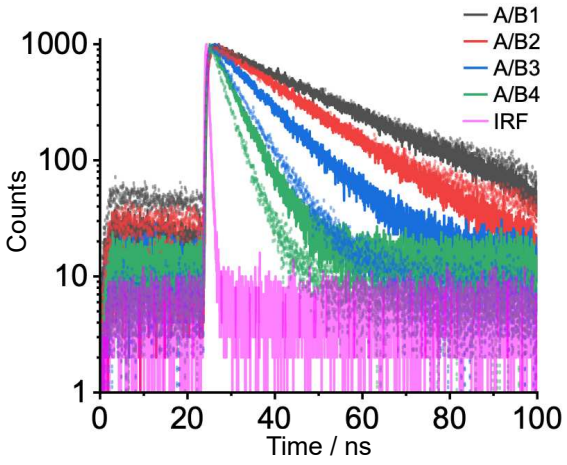

Figure 3.3.3.4: Comparison of the time-correlated single photon counting measurements for the A series (solid) and the B series (dotted) in H_2SO_4 (0.1 M).

Bošković [Table 3.3]. For both **A1** and **A2** the calculated emission energy decreased from about 3.65 for the neutral species to about 3.30 for the methyl salt. This agreed with the observed redshift upon methylation (or protonation). The differences between **A1** and **A2** were within error of the calculations and were too small to be interpreted further.

Table 3.3: S_1 vertical emission energies calculated by Dr Antonio Prlj, Institut Ruder Bošković.

Entry	Compound	S_1, gas	Oscillator Strength, f	S_1, MeCN
1	**A1**	3.37	0.035	3.64 (3.57*)
2	**B1**	3.22	0.068	3.35 (3.14*)
3	**A2**	3.77	0.101	3.66 (3.61*)
4	**B2**	3.05	0.081	3.28 (3.07*)

*including solvent equilibrium contributions

Further analysis of the molecular orbital involvement in the S_1 transition was undertaken by calculating the highest occupied natural transition orbital (HONTO) and the lowest unoccupied natural transition orbital (LUNTO) for **A1**, **B1**, **A2**, and **B2** [Figure 3.3.3.5]. The HONTO and the LUNTO are the natural transition orbitals for the molecule which offer a qualitative representation of the orbitals involved in the electronic transition.[170] This analysis identified a greater contribution from the *N*-1 methyl group in **A2**/**B2** compared to **A1**/**B1**. However, there were limited differences between the A series compounds and B series compounds, so little more could be interpreted about effects of *N*-methylation on the S_1 transition.

Finally, the effects of *N*-methylation on the proton shifts in the ^{1}H NMR spectra were considered. Comparing **A1** to **B1** saw a shift to higher frequency for all core protons by about 1 ppm: 7-*H* (9.01 to 10.14 ppm), 3-*H* (7.90 to 8.93 ppm), and 4-*H* (7.53 to 8.64 ppm). This was consistent with a decrease in electron density in the bicyclic system upon *N*-methylation. Meanwhile, comparing **A2** to **B2** saw a greater shift downfield for 7-*H* (8.70 to 10.11 ppm) and 4-*H* (7.61 to 8.71 ppm) but a smaller shift for 3-*H* (7.95 to 8.61 ppm). This demonstrated the greater aromaticity of the pyridine ring for the *N*-1 methylated isomer and explains why the photoluminescence of **A1** and **A3** was slightly redshifted compared to **A2** and **A4**.

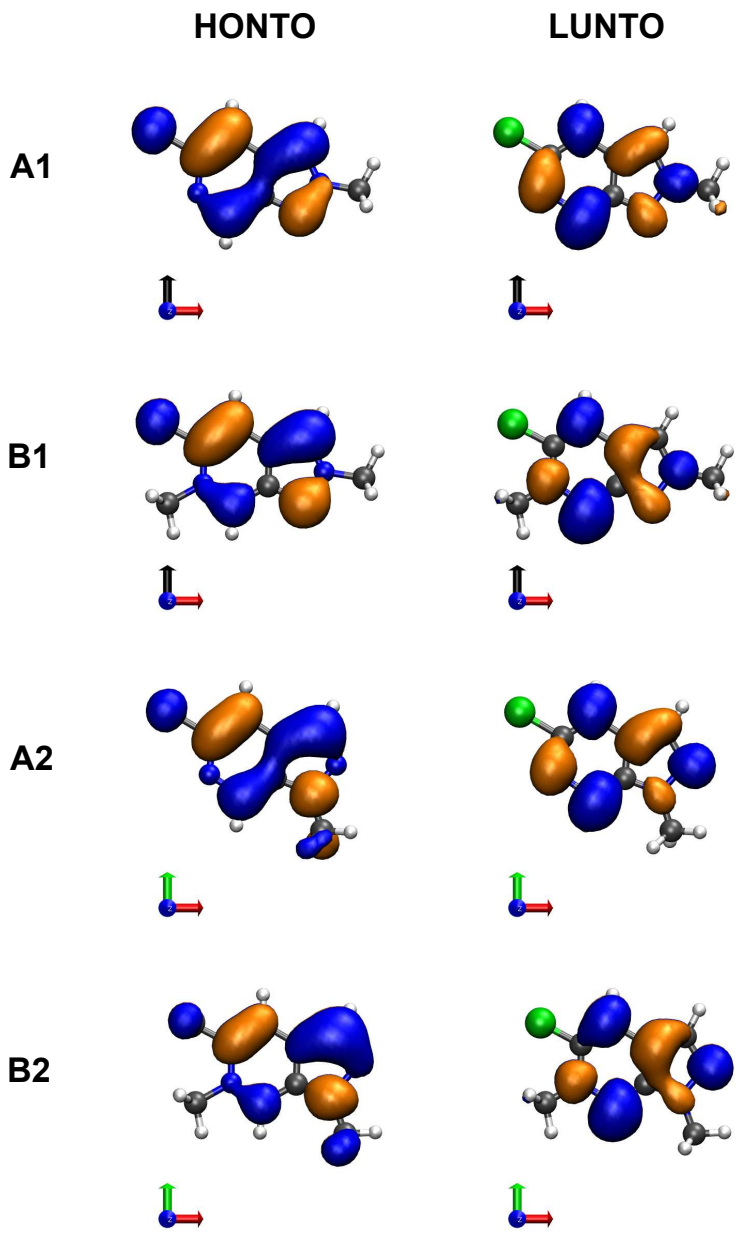

Figure 3.3.3.5: HONTO and LUNTO of **A1**, **B1**, **A2**, and **B2** calculated by Dr Antonio Prlj, Institut Ruder Bošković.

3.4 Conclusions and Future Directions

The photophysical behaviour was evaluated for two series based on the pyrazolo[3,4-c]pyrdine, the singly-methylated **A1-4** and the doubly-methylated salts **B1-4**. This analysis confirmed that methylation and protonation have a comparable effect on photoluminescence for pyridine nitrogen atoms. As more scaffolds are observed to follow this trend, it builds confidence in the broad applicability of this assumption. This will facilitate the analysis of more nitrogen heterocycles in the future. For example, structures that are insoluble or unstable in aqueous environments can be methylated in organic solution and analysed directly. Furthermore, as exemplified in the iso-methylated quinine **231**, this methodology can facilitate the analysis of structures not accessible by protonation.[161]

One limitation of this kind of photophysical analysis is that it is challenging to predict the behaviour of new molecular scaffolds. For example, even though there is strong evidence in the literature that protonation of an sp^2 nitrogen causes a redshift in emission, the extent of redshifting cannot be predicted. In the case of **A1** and **A2**, the DFT-calculated emission energy transitions were in line with a redshift in the photoluminescence but this was not quantifiable until the emission was measured experimentally. Photophysical analysis of more heterocycles is needed to build more extensive structure-property relationships to enable the prediction of behaviour in theoretical compounds.

Small organic fluorophores are attractive for applications as biological probes because small structural changes allow for the tuning of biological activity and could enable the modulation of photoluminescence behaviour. As discussed in Section 2.1.1, there are already examples of biologically active pyrazolo[3,4-c]pyridines reported in the literature. This scaffold would therefore be a promising starting point for developing photoluminescent biological probes in the future. In particular, the pH dependence of the photoluminescence demonstrated by the A series compounds indicates a potential application for pH sensing. Although the current pH range is not suitable for biological environments, future work could explore structural changes that modify the nitrogen pK_a while retaining the photoluminescence sensitivity.

Another way to expand the photophysical characterisation discussed herein, would be to explore the structure-property relationships of larger molecules containing the pyrazolo[3,4-c]pyridine core. For example, this heterocycle could replace the quinoline core to make a new series of quinine analogues, thus introducing a charge transfer pathway to the existing fluorophore. This would be an interesting research pathway with potential applications to explore TADF emitters. Quinoline has already been explored as an acceptor motif in TADF emitters,[171] and the quaternisation of sp^2 nitrogen atoms has been shown to activate TADF behaviour in other quinoline-based emitters.[172] The protonation/methylation of the pyrazolo[3,4-c]pyridine core was shown to impact its photophysical behaviour in a similar way to quinoline, making it a potential alternative acceptor motif for application in this class of molecules. Thus

far, the tuning of photophysical properties has only been explored for recognised *N*-heterocycle chromophores such as quinoline. Although much work would be needed to develop the compounds studied here into TADF emitters, understanding the fundamental behaviour of unknown heterocycles is a necessary first step to extend this research.

Chapter 4

Biological Characterisation of the Pyrazolo[3,4-c]pyridine Fragment Series

Chapter 2 outlined the generation of a versatile library of elaborated fragments focused on the pyrazolo[3,4-c]pyridine scaffold. To demonstrate the medicinal chemistry potential of this heterocyclic core, a series of fragment screenings were designed to test the biological activity and exemplify the concepts of vectorial functionalisation. Specifically this involved protein modelling for computational docking, ligand soaking for protein X-ray crystallography, and protein synthesis for thermal shift assays. The specific biological targets were chosen to complement research developing antileishmanials that is ongoing in the Pohl group at Durham University and the Trossini group at the Universidade de São Paulo. This chapter discusses the results and conclusions obtained from the different screening experiments, and the ideas for future improvements.

4.1 The Biological Target

4.1.1 Leishmaniasis

The World Health Organisation (WHO) defines neglected tropical diseases (NTDs) as a group of conditions that affect impoverished populations with devastating health, social, and economic consequences.[173] These diseases perpetuate a cycle of poor health, limit professional opportunities, and lead to stigma and social exclusion. NTDs affect some of the world's poorest communities and are associated with malnutrition, poor housing, poor sanitation, and limited access to clean water.

Leishmaniasis, one of the twenty NTDs, has an estimated 700,000 to 1 million new cases occurring annually.[174] It is a vector-borne parasitic disease endemic in nearly 100 countries in tropical and subtropical areas. Caused by at least 20 species of the genus *Leishmania,* Leishmaniasis is primarily zoonotic with mammalian hosts including humans and domestic and wild animals.[175] *Leishmania* is transmitted by the female phlebotomine sand flies. Already established in South-East Asia, Central and South America, and Africa, sand fly-transmitted infections are also an emerging problem in Europe as sand flies spread northward in connection with global warming.[176]

Current treatment options for Leishmaniasis are severely limited relying on Pentavalent antimonials (Sb^V), Miltefosine (MF), and Liposomal amphotericin B (LAmB) [Figure 4.1.1.1]. Pentavalent antimonials have been the main therapeutic option for several decades.[177] However, these compounds have low safety profiles and require daily injections for administration. Furthermore, while effective in most regions, there is increasing resistance to Sb^V in India.[178] The favoured alternative in this region is now a single dose of LAmB, yet this has high costs and requires refrigerated storage which limits its transportability. MF is increasingly becoming the preferred option in the new world as it is orally administered, making it easy to deliver to patients who cannot access a hospital.[177] However, treatment requires daily dosage for 28 days, and contraception for nearly 6 months, so costs are high and patients often fail to complete the course of treatment.

Another challenge in the treatment of Leishmaniasis is the many manifestations of the disease which depend on the species of parasite, the species of sand fly, the reservoir species, and the geographical location.[179] Different manifestations of the disease may require different courses of treatment as different parasites have shown sensitivity to different therapies. Currently, the treatment regimens are reliant on combinations of the same three drugs due to the limited options available. Consequently, there is desperate need to identify new drug targets in these parasites.

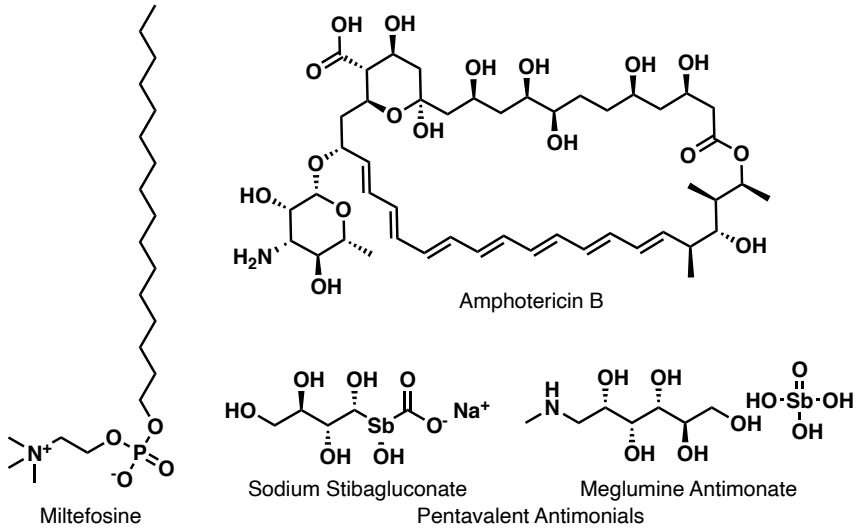

Figure 4.1.1.1: Current drug therapies for Leishmaniasis.

4.1.2 Sirtuins

The reversible acetylation of proteins has been associated with many cellular pathways such as metabolism, gene expression, DNA repair, cell proliferation, and apoptosis.[180] As such, the enzymes responsible for this activity are attractive therapeutic targets. Protein acetylation involves two families of enzymes; the acetyltransferases responsible for the acetyl group installation, and deacetylases that will remove this protein modification. Protein deacetylases are further divided into zinc-dependent (classes I, II, and IV) or NAD^+- dependent (class III) enzymes. The sirtuins belong to the second class as they show NAD^+-dependent deacetylase activity [Scheme 4.1.2.1].

Sirtuins are found across most organisms from archaebacteria to eukaryotes and the proteins maintain a high level of structural and functional similarity.[181] Bacteria typically express only one or two sirtuins while eukaryotes have more. Humans, like most mammals, have seven sirtuins (SIRT1-7) with SIRTs 1, 6 and 7 found in the nucleus, SIRT2 found in the cytoplasm, and SIRTs 3, 4 and 5 found in the mitochondria. Leishmania parasites express three sirtuins (SIR2RP1, SIR2RP2, and SIR2RP3).[182]

The cytosolic SIR2RP1 is the best characterised protein of the three sirtuins, shown to be essential for the survival of *L infantum* and *L major*.[183,184] More recently, the *de novo* crystal structure of the *L infantum* sirtuin *Li*SIR2RP1 in complex with an acetyl-lysine peptide substrate has also been solved at 1.99 Å.[185] The structure shows the main characteristics of all sirtuins; a large domain for the Rossman fold that binds the NAD^+ and a smaller zinc-binding domain. There are also disordered loops that connect the two main domains and aid with substrate binding and selectivity.[186]

The functional role of SIR2RP2 has been studied in *L donovani*.[182] It was found to be closer to the human homolog *h*SIRT4 and is localised to the parasite's mitochondria. In this case, *Ld*SIR2RP2 was not shown

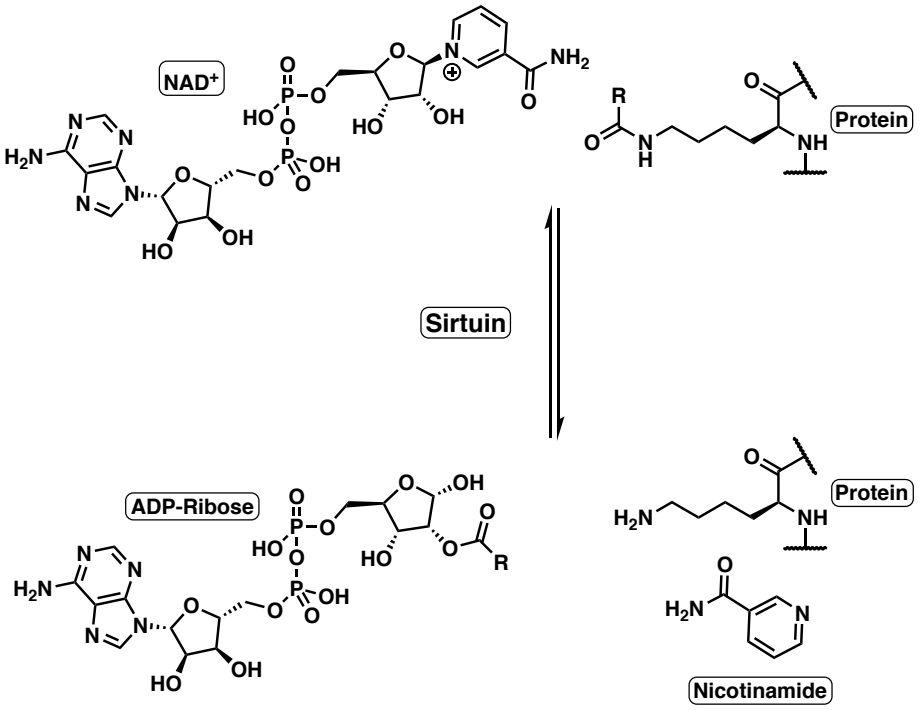

Scheme 4.1.2.1: General mechanism of the sirtuin enzyme activity.

to be essential for parasite survival, but its deletion did impact the growth kinetics and parasite infectivity. Furthermore, known sirtuin inhibitors were shown to have a greater impact on the growth of wild-type parasites compared to those with the *Ld*SIR2RP2 deletion, showing potential as a target for antileishmanials.

3D models of the SIR2RP3 enzyme of *L braziliensis* have also been generated through homology modelling and molecular dynamic simulations.[187] Molecular docking of the pan-sirtuin inhibitors nicotinamide and sirtinol [Figure 4.1.2.1], validated the protein models and highlighted important structural differences in the binding sites between the parasite protein and the nearest homologous human protein *h*SIRT5.

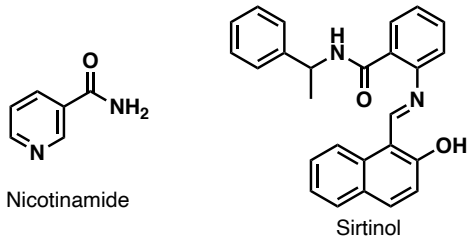

Figure 4.1.2.1: Two pan-sirtuin inhibitors, nicotinamide and sirtinol.

Sirtuins have recently been targeted as a way to inhibit *Trypanosoma cruzi*, another protozoan parasite that infects humans and causes Chagas disease.[188–190] *Trypanosoma* and *Leishmania* belong to the same family of *Trypanosomatidae* and therefore have many similarities. For example, looking specifically at the

sequences of the SIR2RP1 proteins, *Tc*SIR2 shares 58% identity with *Li*SIR2, and has several conserved motifs including the zinc-binding domain and the catalytic domain. *Tc*SIR2RP1 has been genetically validated as essential for the viability of the *T cruzi* parasites and validated as a therapeutic target for inhibition of *T cruzi*.[191] This is expected to apply to *L infantum* and *L major* as well, indicating the sirtuins as a good target for potential antileishmanials.

4.1.3 Cysteine Synthase

The ability of Leishmania parasites to survive the host's immune response relies on an ability to deal with excess reactive oxygen species. The main defence mechanism requires trypanothione, a low molecular weight thiol consisting of two molecules of glutathione linked by a spermidine bridge [Figure 4.1.3.1]. The thiol groups required for the synthesis of glutathione, and therefore trypanothione, come from the amino acid cysteine. *Leishmania* does not have a specific cysteine transporter so cannot rely on the uptake of extracellular cysteine. Cysteine biosynthesis is therefore an important process for the survival of the parasites.

Like other trypanosomatida, *L major* possesses two pathways for cysteine biosynthesis: (1) the *de novo* biosynthesis pathway comprising serine acetyltransferase (SAT) and cysteine synthase (CS) and (2) the reverse trans-sulfuration pathway comprising cystathionine β-synthase (CBS) and cystathionine γ-lyase (CGL) [Scheme 4.1.3.2].[192] These same two pathways were identified in *T cruzi* and Marciano *et al.* found that CS was expressed in greater levels in *T cruzi* amastagotes than epimastigotes, suggesting that the *de novo* pathway is more important during the mammalian infection stage.[193]

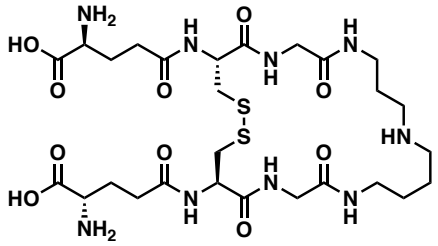

Figure 4.1.3.1: Structure of trypanothione.

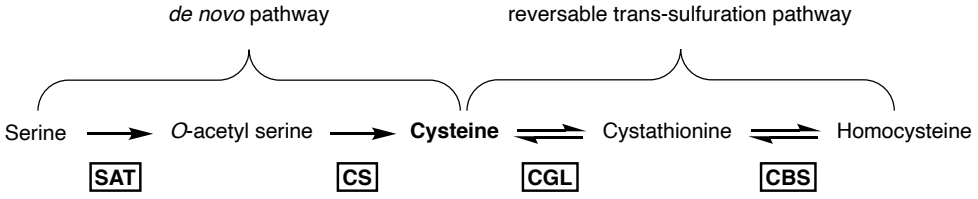

Scheme 4.1.3.1: The two pathways for cysteine biosynthesis in *Leishmania*.
SAT = serine acetyltransferase, CS = cysteine synthase, CGL = cystathionine γ-lyase, CBS = cystathionine β-synthase

Cysteine synthesis in *L infantum* has not been studied in as much detail, although comparison of the genes encoding relevant enzymes in *L major* suggested that *L infantum* also contains the same two pathways of cysteine biosynthesis. Recently the structure and function of *L infantum* CS (*Li*CS) was studied by Sowerby *et al.* to probe this enzyme for potential drug targets.[194] The crystal structure of *Li*CS revealed that the four lysine residues required for catalytic activity were conserved as was the sequence for binding the PLP cofactor. These observations imply the reaction mechanism is similar between *Li*CS and other *Trypanosoma* CS enzymes. The reaction sequence begins when the PLP cofactor forms a Schiff base with the lysine residue in the active site (**I**) which is then displaced by *O*-acetyl serine to form intermediate **II**. Deprotonation of the α-carbon promotes loss of an acetate ion forming α-aminoacrylate intermediate **III**. This intermediate undergoes nucleophilic attack by a sulfide ion and reprotonation of the α-carbon. Finally, the CS active site lysine reforms the bond to PLP, releasing cysteine, and reforming the active enzyme [Scheme 4.1.3.2].

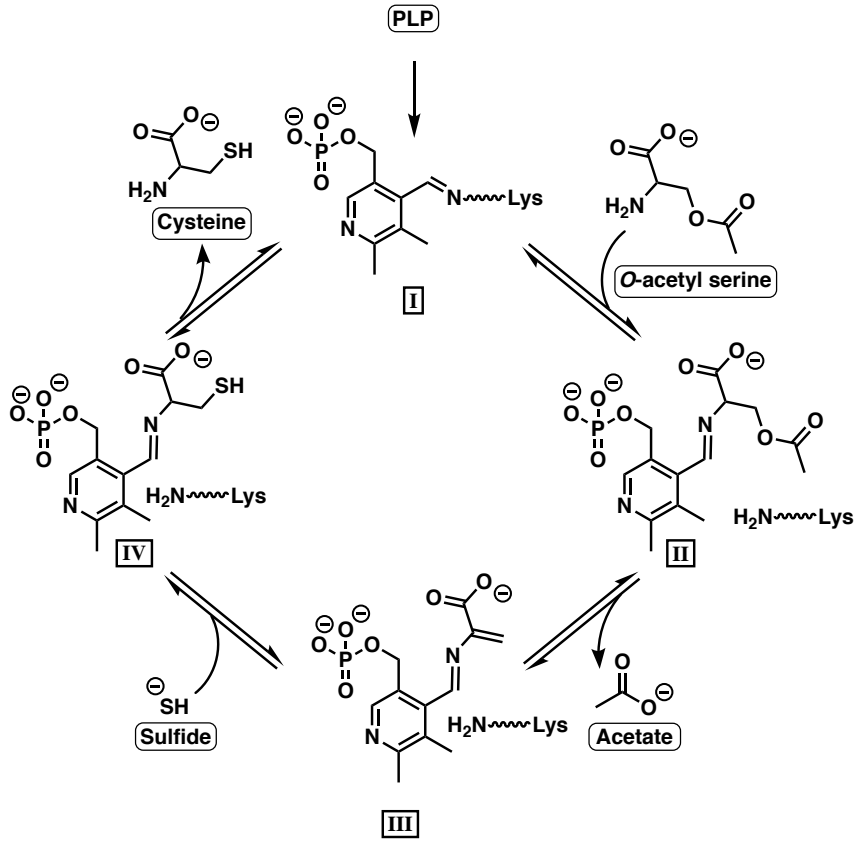

Scheme 4.1.3.2: The enzyme cycle of CS for the reaction of PLP with *O*-acetyl serine and a sulfide ion to produce cysteine.

The *de novo* cysteine biosynthesis pathway is found in plants (eg. *Arabidopsis thaliana*) and bacteria (eg. *Salmonella typhimurium*) but there is no equivalent in humans.[195,196] This pathway and the CS enzyme are, therefore, potential therapeutic targets for developing antileishmanials.

4.2 Biological Characterisation: Protein Modelling and Docking

A series of computational studies were conducted as a primary screening of the pyrazolo[3,4-c]pyridine scaffold. This was an attractive strategy because it avoided the need for protein production and the fragment samples would not be consumed. This focused on the *Leishmania* sirtuin proteins (SIR2), building on previous work in the Trossini group studying the sirtuin proteins of humans and trypanosomatids.[189,190,197]

4.2.1 SIR2 Protein Structures

The RCSB protein data bank (PDB) holds experimental structures for the open apo form and the closed ligand-bound form of the human *h*SIRT2 enzyme. Conversely, the only protein structure that exists for any of the *Leishmania* sirtuin enzymes is the apoenzyme of *L infantum*, *Li*SIR2RP1.[185]

The SIR2 gene family is conserved across organisms from archaebacteria to eukaryotes. Although the amino acid sequence shows significant variation, the protein structure is well conserved throughout with the Rossmann fold domain and the smaller zinc-binding domain always represented.[198]

Taking the human sirtuin as an example in Figure 4.2.1.1, there are distinct conformational differences between the apoenzyme with no ligands bound, and the holoenzyme binding the NAD^+ cofactor. Compared to the apo form of the enzyme, upon cofactor binding, the small zinc-binding domain twists towards the large Rossmann-fold domain effectively closing around the ligands into the active conformation. These conformational changes result in corresponding changes in the size and shape of the binding pockets. For example, Figure 4.2.1.2.a shows how the position of Phe-95 changes between the two forms of *h*SIRT2 and Figure 4.2.1.2.b highlights the important interaction between this residue and the NAD^+ cofactor in the *Lm*SIR2RP1 enzyme.

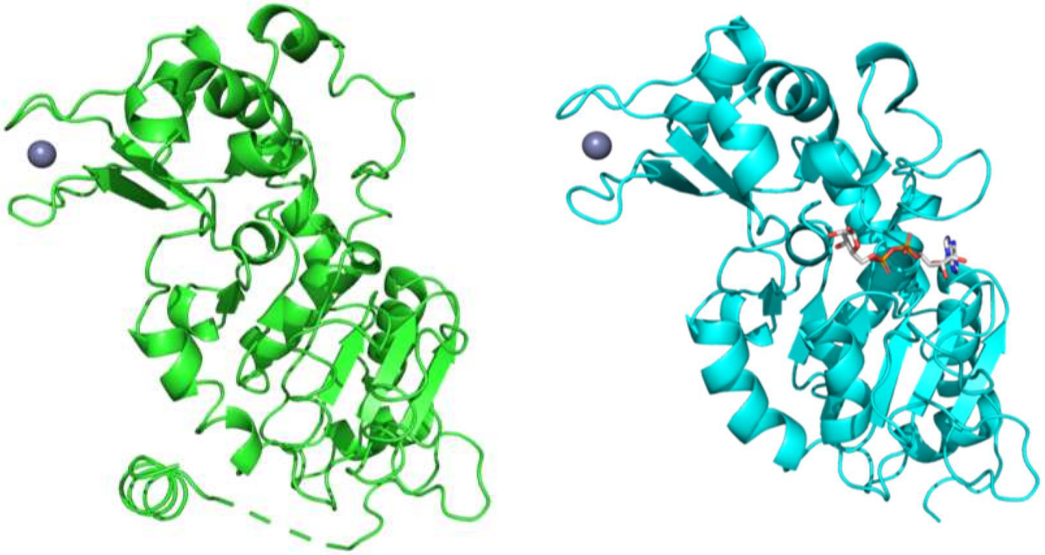

Figure 4.2.1.1: Comparison of the open apo-enzyme *h*SIRT2 (green)(PDB ID: 3ZGO),[199] and the closed holo-enzyme *h*SIRT2 (blue) binding the ADP-ribose ligand (grey) (PDB ID: 5D7O).[200]

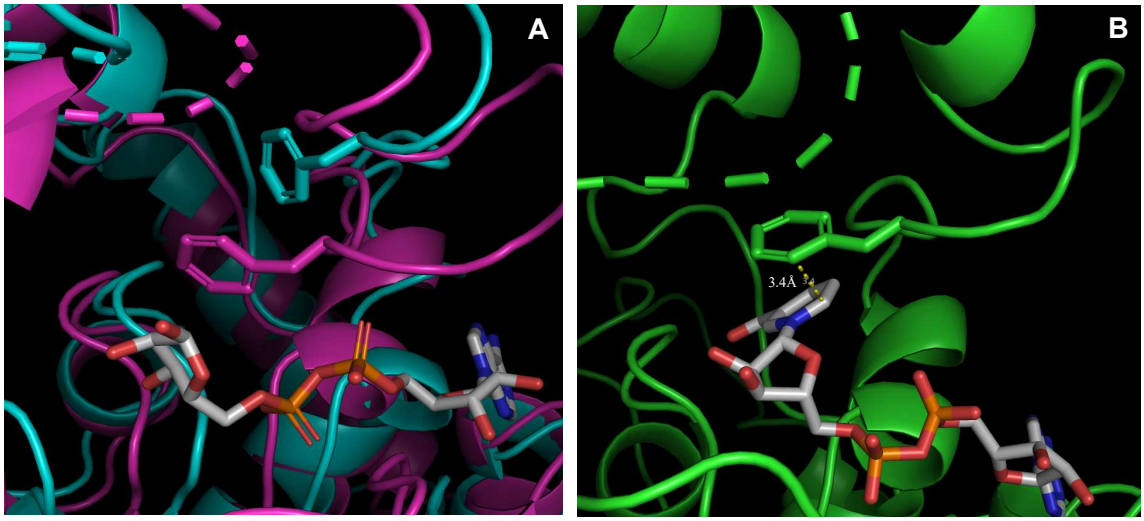

Figure 4.2.1.2: **A** compares the position of residue **F95** between the open apo- and closed holo-enzyme forms of the human sirtuin enzyme *h*SIRT2. The ribbon structure of the open apoenzyme is shown in blue (PDB ID: 3ZGO)[199] and the constructive form of the enzyme is shown in pink with the carbon atoms of the ADP-ribose ligand shown in grey (PDB ID: 5D7O).[200] **B** shows the protein structure model of *L major* SIR2RP1 (green) displaying the corresponding phenylalanine residue as sticks (**F50**) and the interatomic distance to the NAD^+ cofactor (grey) is shown by a yellow dashed line (distance calculated by PyMol).

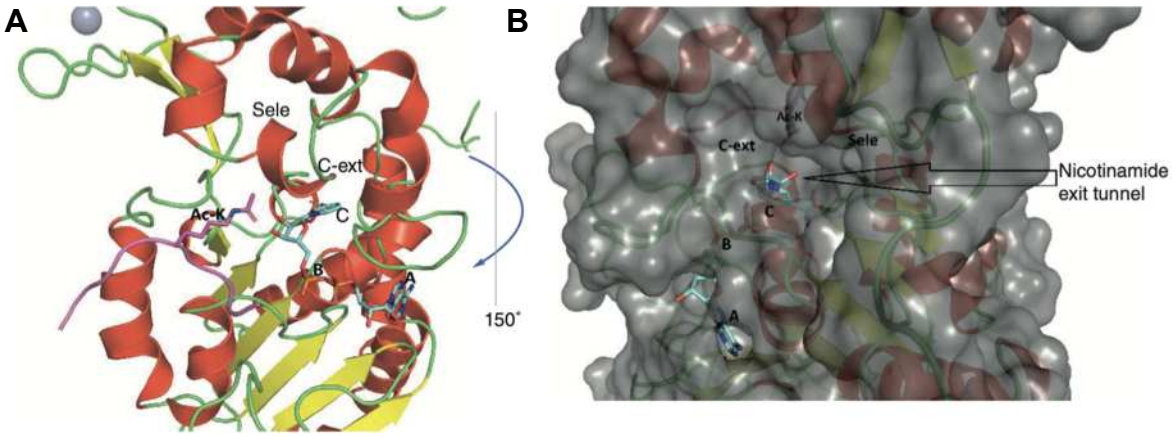

Figure 4.2.1.3: **A** and **B** show the key binding pockets of the *h*SIRT2 (PDB ID: 5D7O).[200] The α-helices are coloured red, β-strands yellow, and turns and loops are green. The *N*-acetylated-lysine containing peptide substrate (cellular tumour antigen p53 segment) (magenta) was superimposed from the SIR2Tm model (PDB ID: 2H4F),[201] and the NAD^+ cofactor (cyan) was superimposed from the *h*SIRT2 structure (PDB ID: 5DY4).[202] This figure was reproduced from André Berndt Penteado with permission from the author.[203]

Figure 4.2.1.3 shows the key binding pockets of the sirtuin enzymes. The B-pocket houses the nicotinamide portion of the NAD^+ cofactor so is well conserved across all NAD-binding proteins. This pocket was therefore an undesirable drug target as selectivity would be challenging. The C-pocket had more potential as it can be linked to the C-extended pocket or the substrate pocket by a suitably shaped ligand, offering increased specificity. The selectivity (sele) pocket, so named because it is involved in substrate selectivity, was also an attractive target for ligand binding as it can improve inhibitor selectivity as well.

The computational docking studies were carried out against the *L major* enzyme *Lm*SIR2RP1 (UniProt ID Q25337). As no crystal structure exists for this enzyme, it was first necessary to generate a protein model based on a close structure template. A BLAST search of the PDB returned the closest matching sequences as the *Li*SIRT2 (PDB ID: 5OL0, sequence identity 92.2%)[185] and the *h*SIRT2 (PDB ID: 5D7O, sequence identity 45.4%).[200,204] These sequences are compared in Figure 4.2.1.4 and Figure 4.2.1.5 shows the superposition of crystal structures of the *h*SIRT2 (PDB ID: 5D7O) and the *Li*SIR2RP1 (PDB ID: 5OL0) proteins. Due to the structural similarities, these crystal structures were used as the templates for homology modelling of the *L major* enzyme.

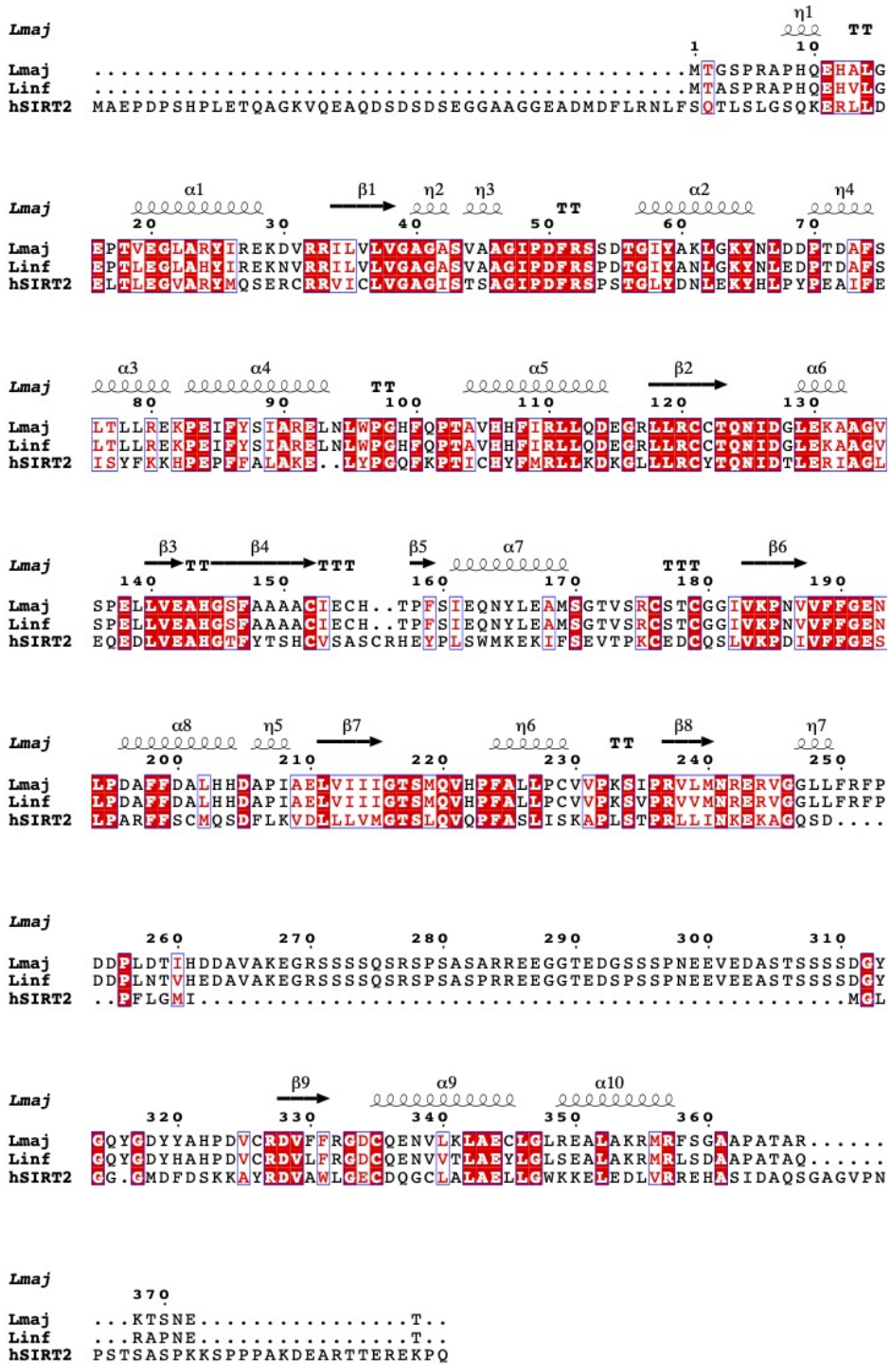

Figure 4.2.1.4: Protein sequence alignment of *L major*, *L infantum*, and *Homo Sapien* sirtuin proteins with secondary structure from the protein crystal structure of *L infantum* (PDB ID: 5OL0).[185] Sequence alignment achieved with Clustalw[205] and the image was generated using ESPript.[206]

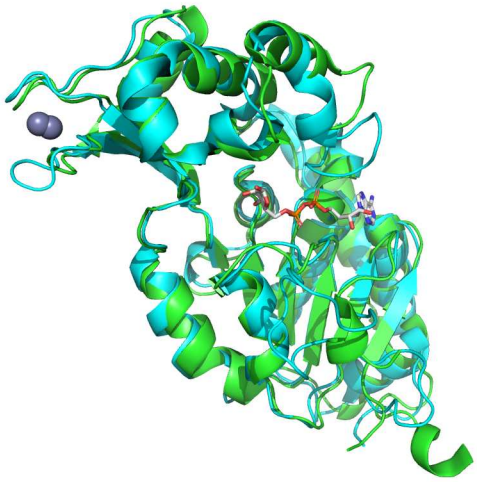

Figure 4.2.1.5: Comparison of *h*SIRT2 and *Li*SIR2RP1 crystal structures. The ribbon structure of *h*SIRT2 is shown in blue with the carbon atoms of the ADP-ribose ligand shown in grey (PDB ID: 5D7O) [200] and *Li*SIR2RP1 is shown as ribbon structure in green (PDB ID: 5OL0). [185]

4.2.1.1 Models from SwissModel

As well as the *L infantum* and human SIRT2 proteins, SwissModel also identified a model generated by AlphaFold (UniProt code Q8I6E4) as a potential template. The AlphaFold generated structure was not used as a template because it did not contain all the defining structural elements of the sirtuin enzyme which were expected to be conserved between organisms.

Models were generated based on both 5OL0 and 5D7O as templates and the quality was assessed by the SwissModel QMEANDisCo score [207] and ProCheck analysis. [208] The models generated by SwissModel generally had a good backbone structure, which returned higher global metrics (QMEANDisCo and overall Quality Factor). However, the residue metrics were less good, showing the positions of the side chains were not as well refined [Table 4.1, entry 1 & 2]. The position of the side chains was important for establishing fragment binding, so these models were not used in the docking studies and the software Modeller was used to generate alternative models. [209]

4.2.1.2 Models from Modeller

Models were again generated for the *L major* sequence based on using both crystal structures 5OL0 and 5D7O as templates. The challenge of using these crystal structures for modelling the *L major* protein was the disordered loop between residues N239 and D327 in the Rossmann-fold domain. In the *h*SIRT2 sequence this disordered loop is quite short, only 30 amino acids in lengths, whereas in the case of *L infantum*, this disordered loop is much longer. The protein crystals of *Li*SIR2RP1 could only be obtained with a significant deletion of 51 internal amino acids (P253-E303) and the loop is not represented in the crystal structure.

Therefore, this region of the *L major* model was poorly defined in both templates. The disordered loop is far from any of the major binding pockets, though, so the less well-defined structure should not impact results from the docking studies.

The first structures generated based on the 5D7O template contained a knot in the protein chain in the disordered loop, which is not a natural protein feature. Therefore, further model refinement was conducted focused on this region. As seen in Table 4.1 comparing entry 3 to 4 shows an improvement of the Quality Factor and the percentage of residues in the 'most favourable' regions of the Ramachandran plots once the loop was modelled separately. This same process was used for the models based on the 5OL0 template, with separate modelling of the disordered loop required to generate a feasible protein model [Table 4.1, entry 5].

Table 4.1: Comparison of the quality statistics for the models of the *L Major* protein sequence (UniProt code Q25337).

Entry	**Template**	**Sequence Identity**	**Method**	**Loop Modelled Separately**	**Quality Factor**	**Residues in Most Favourable Region**	**QMEAN DisCo**
1	5OL0	92.2%	SwissModel	No	80.25	86.5%	0.79
2	5D7O	45.4%	SwissModel	No	86.43	84.6%	0.69
3	5D7O	45.4%	Modeller	No	60.06	91.8%	0.62
4	5D7O	45.4%	Modeller	Yes	62.95	93.4%	0.60
5	5OL0	92.2%	Modeller	Yes	70.54	88.4%	0.75
6	5OL0	92.2%	MD	No	88.51	83.0%	0.71
7	5D7P	45.4%	Modeller	No	73.57	93.4%	0.63

4.2.1.3 Molecular Dynamics Model

To improve the modelled representation of the ligand binding sites, further structure refinement was conducted through molecular dynamics (MD). The MD computations were carried out by André Berndt Penteado, a PhD student in the Trossini group at the Universidade de São Paulo. The MD refined model showed an improved Quality Factor although the QMEANDisCo score was comparable to other models [Table 4.1, entry 6]. Furthermore, while the percentage of residues in the 'most favourable' region was slightly lower than for other models considered, there were zero residues in the 'unallowed' region. Redocking of the NAD^+ cofactor into this model also returned the crystal structure position with an RMSD value of 0.33 Å. Overall, these statistics mark it as a good quality model to be included in the docking studies.

4.2.1.4 The C-extended Pocket

As shown in Figure 4.2.1.3, one of the reported binding pockets of the *h*SIRT2 structure was the C-extended pocket. This was identified in an X-ray crystal structure of *h*SIRT2 with ligand EX243. EX243 is an indole-based inhibitor that predominantly occupied the C pocket but was also seen occupying the C-extended pocket [Figure 4.2.1.6] (PDB ID: 5D7P).[200] Crossdocking of the EX243 ligand into the generated models of *Lm*SIR2 identified that the existing structures did not have sufficient space to accommodate the ligand in the C-extended pocket [Figure 4.2.1.7.a and Figure 4.2.1.7.b]. This problem was due to a lack of flexibility in the protein structure during the docking simulations.

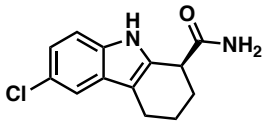

(*S*)-6-chloro-2,3,4,9-tetrahydro-1*H*-carbazole-1-carboxamide

EX243

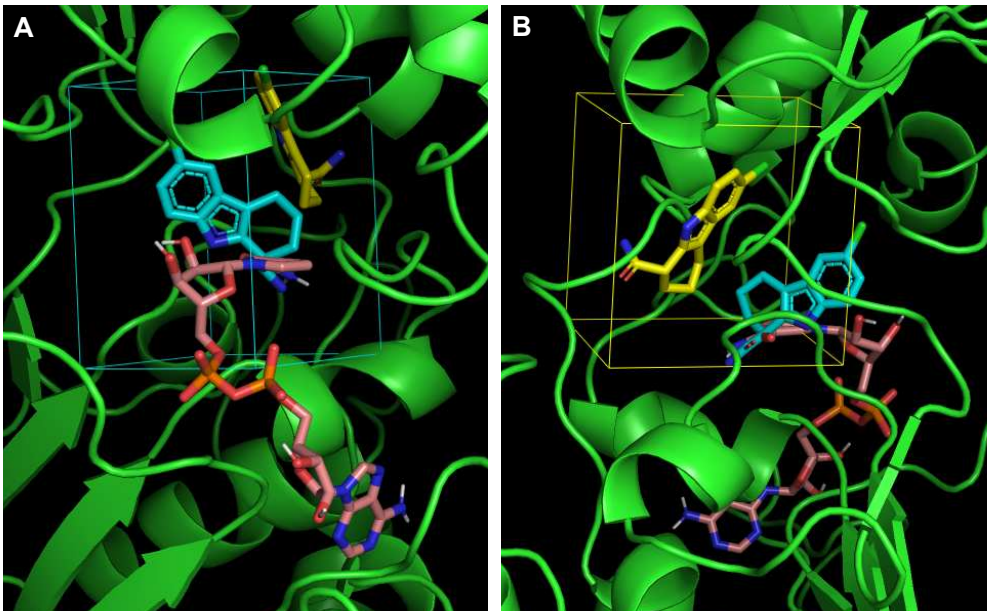

Figure 4.2.1.6: Protein chain of *L major* SIR2RP1 is shown in green ribbon and NAD^+ is shown in pink sticks. Two copies of the EX243 ligand are superimposed from the EX243-*h*SIRT2 crystal structure bound in the C-pocket (teal) and the C-extended pocket (yellow). In **A** the teal box is centred on the C-pocket and in **B** the yellow box is centred on the C-extended pocket.

To generate a more appropriately sized C-extended pocket in the protein, a new model was generated using the EX243-*h*SIRT2 complex (PDB ID: 5D7P)[200] as a template. In this case, the first model generated with the software Modeller had good quality statistics and a feasible shape for the disordered loop, so no further refinement was required. To confirm a good fit in the C-extended pocket, a cross-docking of the

EX243 ligand into the new *L major* model was carried out [Figure 4.2.1.7.c]. Figure 4.2.1.7.d shows the close match achieved between the calculated position in the new *L major* model and the observed position in the *h*SIRT2 crystals. This further confirmed the good quality of the protein model [Table 4.1, entry 7].

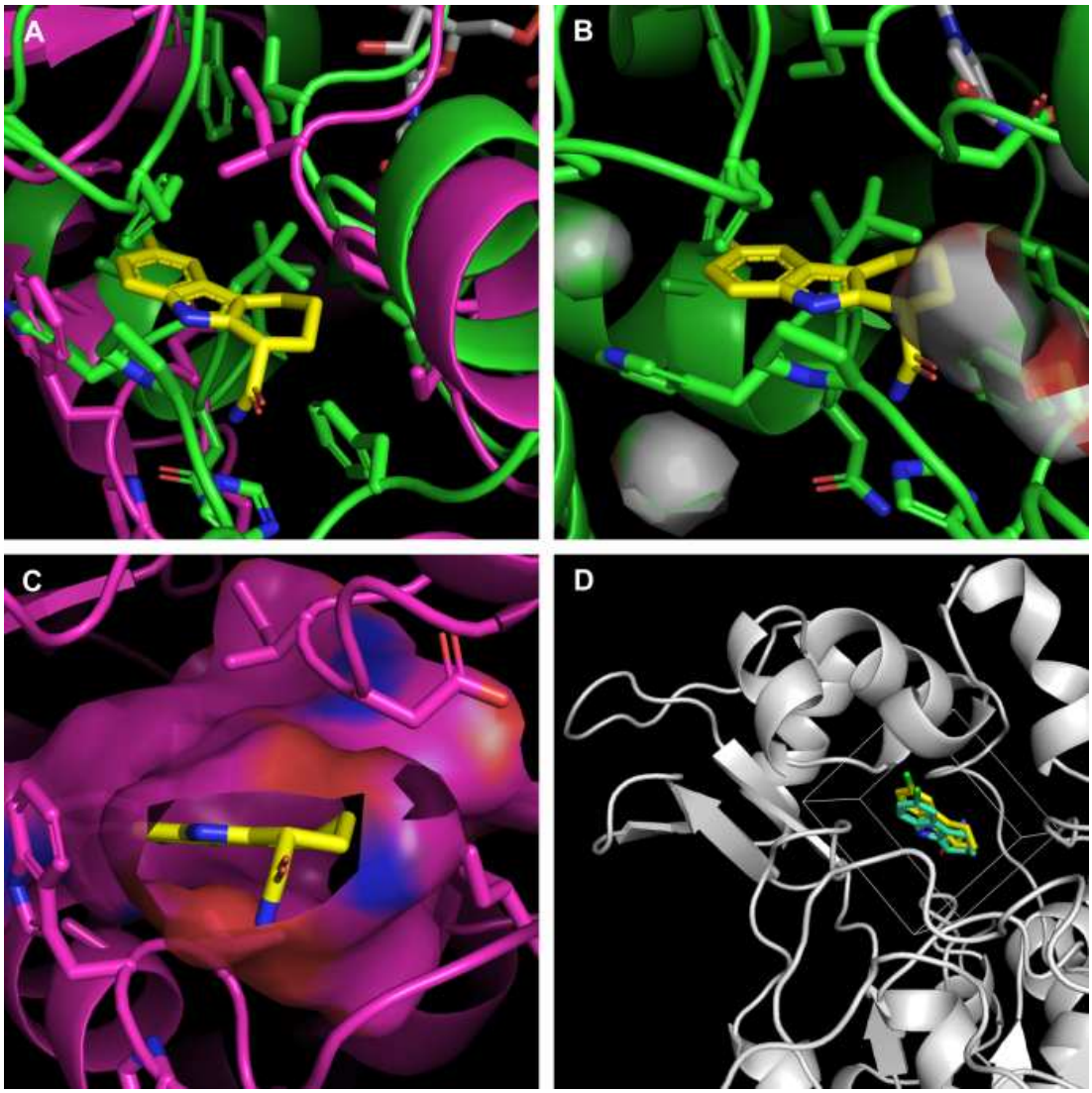

Figure 4.2.1.7: **A** compares the two models of *L major* based on the EX243-*h*SIRT2 complex (pink) and after MD refinement around NAD^+ (green). Side chains of residues within 5Å are shown to highlight the steric clashes likely with the EX243 ligand (yellow). **B** shows the cavity (grey surface) identified by PyMol between the residues within 5Å of the EX243 ligand, ie. no cavity at the location of the ligand. The *L major* model is in green. **C** shows the new *L major* model (pink) based on the EX243-*h*SIRT2 complex, the light pink surface shows the cavity identified by PyMol between the residues within 5Å of the EX243 ligand, there is now significant space for the ligand to complex. The EX243 ligand (yellow) is superimposed from the crystal structure of *h*SIRT2 (PDB ID: 5D7P).[200] **D** compares the results from the EX243 cross-docking with the ligand pose observed in the human crystals. The teal EX243 ligand was returned by the DockThor cross-docking and the yellow EX243 ligand was superimposed from the original *h*SIR2 crystal structure. The new *L major* model protein is shown in ribbon form in grey with the box used for docking outlined in white.

4.2.2 Fragment Library Docking

With the protein models in hand, attention turned to the computational docking. These studies were conducted with a small library of compounds based on the pyrazolo[3,4-c]pyridine scaffold incorporating different sized groups at the *C*-3, *C*-5, and *N*-1 positions [Figure 4.2.2.1]. Complimentary fragments based on different heteroaromatic rings, **L11-L13**, were included for comparison.

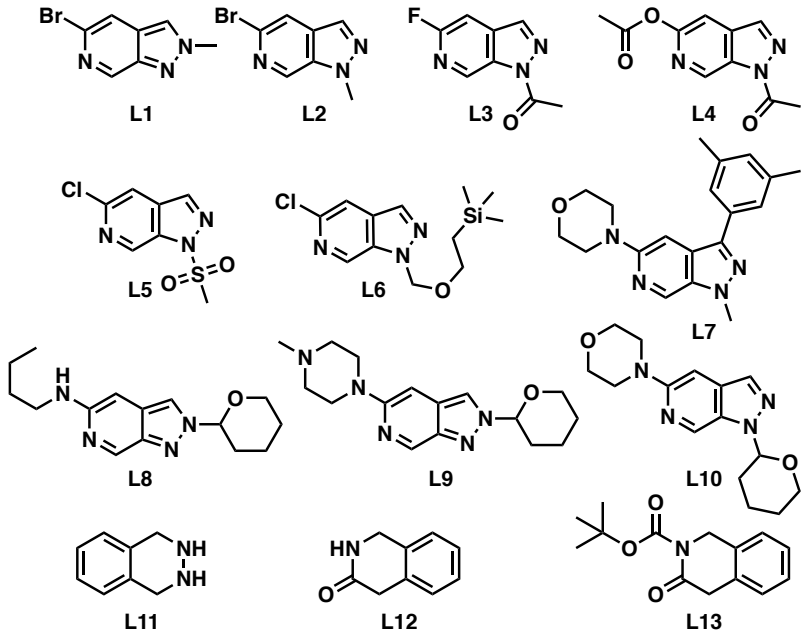

Figure 4.2.2.1: Library of fragments based on the pyrazolo[3,4-c]pyridine scaffold for use in virtual screening.

The virtual screening was carried out using the online programme DockThor with each round focused on a different binding pocket in turn. For each iteration, the DockThor programme calculated 10 binding poses for each ligand and identified the 3 best poses based on the calculated docking scores.[210] The ligands were also ranked based on the docking score of their single best binding pose. The docking scores are the predicted receptor-ligand binding affinities calculated by the DockTScore scoring function which is an empirical scoring function that was trained using the v2013 PDBBind core set.[210] Ligands binding in the range 10 to 100 μM would be expected to return binding scores in the range -8 to -5.[211]

4.2.2.1 Results and Discussion

The fragment library was screened against seven different pockets in the *Lm*SIR2RP1 protein; (1) the NAD^+ cofactor pocket, (2) the C-extended pocket of the 5D7O-templated model, (3) the C-extended pocket of the 5D7P-templated model, (4) the C-pocket focused where the EX243 ligand binds, (5) the selectivity pocket, (6) the substrate pocket with a big grid box, and (7) the substrate pocket with a small grid box.

The ligand ranking order for each pocket was usually very similar, with the larger ligands frequently being

higher ranked. Although, larger compounds were known to have more potential for binding interactions with the protein, it was expected that size would not be a differential factor across this fragment library. These results, however, indicated that the small size variation across the library was significant enough to consistently impact the docking scores.

Because the ranking order for each pocket was very similar, greater insight comes from comparing the docking scores and poses for specific ligands across the different pockets. For example, **L1**, **L3**, and **L7** are analysed in Table 4.2. This data set made it possible to more directly compare the suitability of the different binding pockets.

Table 4.2: Docking scores of ligands **L1**, **L3**, **L7** calculated by DockThor.

Entry	**Pocket**	***L1***	***L3***	***L7***	**Notes**
1	NAD^+	-7.306	-7.183	-10.370	
2	C-extended (5D7O)	-7.138	-6.392	-0.410	The pocket cavity was too small
3	C-extended (5D7P)	**-8.044**	-7.563	-10.048	
4	C-pocket (EX243)	-7.854	-7.704	-10.164	
5	Selectivity	-6.674	-6.222	-3.902	Very hydrophobic region
6	Substrate (big)	-7.849	-7.693	**-10.271**	Ligands adopted positions similar to those in NAD^+ pocket
7	Substrate (small)	-7.744	**-7.789**	-9.202	

The most obvious general trend was, as mentioned above, that the largest **L7** returns the highest docking scores. The very low score in the first screening of the C-extended pocket therefore stands out [Table 4.2, entry 2]. In this screen the smallest ligand **L1** was returned as the most strongly binding which indicated the pocket cavity was very small. The model based on the protein-ligand complex *h*SIR2-EX243 (PDB ID: 5D7P) had a much larger cavity for the C-extended pocket arising from the position of the EX243 ligand. When the screen was repeated with this model, the docking scores of all the ligands increased and the larger ligands were again ranked highly. This screen returned the highest score for **L1** compared to all other binding pockets. Figure 4.2.2.2 compares the pose of **L1** in the *L major* model to the EX243 ligand in 5D7P, highlighting the very similar positions. As the EX243 binding was dominated by hydrophobic interactions it was unsurprising that the most favourable position of **L1** lies on the same plane. This was a promising result that one of the small fragments could bind into this pocket and lock the enzyme in an unproductive conformation.

One challenge of constructing the docking simulation that focused on the substrate pocket was the proximity of the other binding pockets. When a large box was centred on the substrate pocket, the preferred positions returned for all the ligands were very similar to those returned when the grid box was centred on the NAD^+ cofactor binding site, Figure 4.2.2.3 illustrates this for **L7**. This result indicated that

the first box was too large covering too much of the protein. This was still an interesting result, however, because it showed the strength of binding within the NAD^+ pocket. A smaller box was used to constrain the ligands to the substrate cavity which then returned different poses. For example, the binding of **L1** was likely dominated by the hydrogen bond between the pyridine nitrogen and an arginine residue, identified as a polar contact in PyMol [Figure 4.2.2.4].

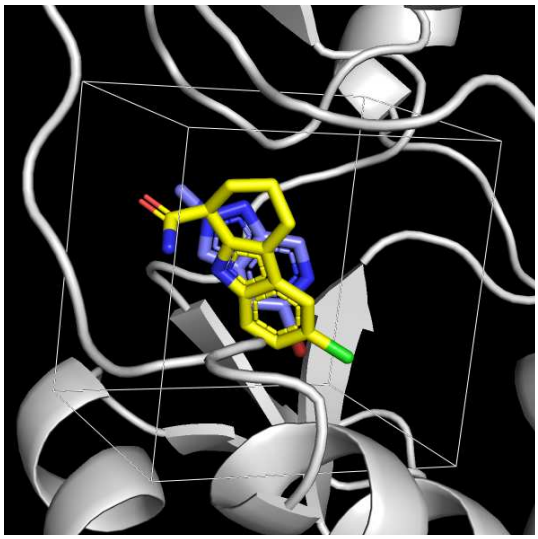

Figure 4.2.2.2: Comparison of the position of EX243 observed in the crystal structures with the best ranked pose of **L1** (blue) in the model of *L major* based on the *h*SIRT-EX243 model. The *L major* protein is shown in ribbon form in grey. The EX243 ligand (yellow) is superimposed from the crystal structure of *h*SIRT2 (PDB ID: 5D7P).[200] The white outline shows the box used in the docking study.

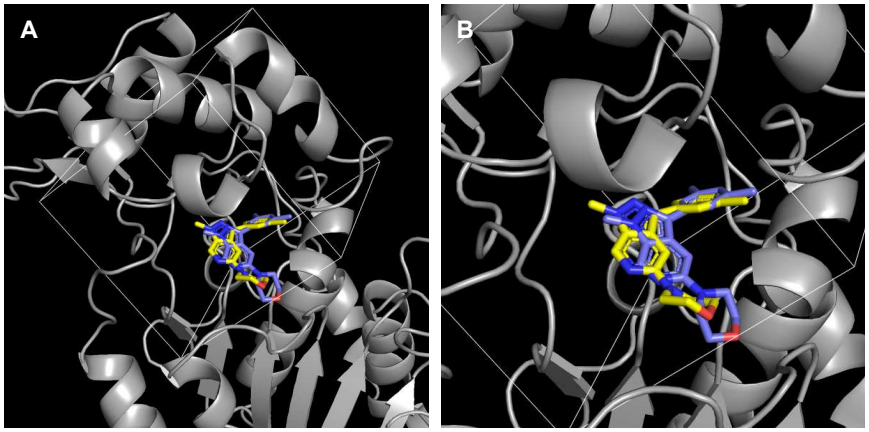

Figure 4.2.2.3: **A** shows the best ranked pose of **L7** returned when the box was centred on the substrate pocket (yellow) and centred on the NAD^+ pocket (blue). The *Lmajor* model from the MD refinement is show in ribbon form in grey. The large box used for docking in the substrate pocket is shown in white. **B** is a zoomed in view of figure **A**.

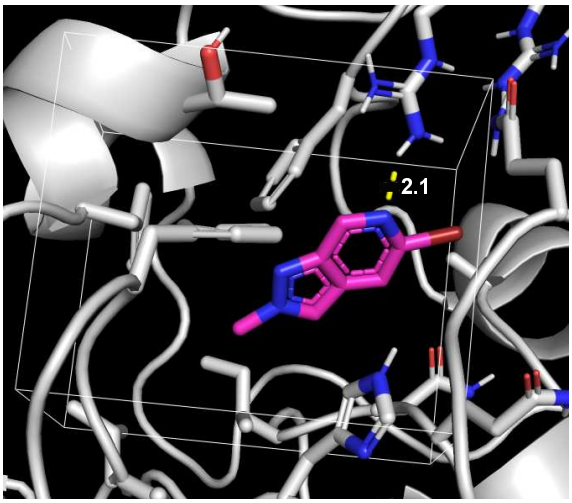

Figure 4.2.2.4: The best ranked pose of **L1** (pink) returned when the box was centred on the substrate pocket. The *L major* model from the MD refinement is show in ribbon form in grey. The smaller box used for docking in the substrate pocket is shown in white outline. The yellow dashed line is a hydrogen bond identified as a polar contact in PyMol with the distance 2.1 Å long.

4.2.3 Summary

Virtual screening of the focused fragment library highlighted that different fragments showed preference for different binding pockets which means there is a lot of potential to identify starting points for a competitive inhibitor. Furthermore, the proximity of the C-extended and Selectivity pockets opens up the possibility of extending the fragment beyond the NAD^+ pocket to improve potency and selectivity.

One challenge of this virtual screening was that there was often greater variation in docking score between the different ligands in one pocket than for the same ligand in different pockets. Therefore, it was hard to predict where a given fragment might bind. This promiscuity is a common criticism of virtual screening of fragments because their small size allows them to bind in many small clefts within a protein.

The example of the C-extended pocket demonstrated another limitation of virtual screening, highlighting the lack of flexibility in the protein models. This can be overcome by using different models to probe different areas of the protein structure but this does not guarantee that the fragment binding would be sufficiently potent to cause this structural change in the protein. The best way to confirm if the pyrazolo[3,4-c]pyridine scaffold had potential to bind to the *Leishmania* sirtuin proteins was to use another screening method to compare the results.

4.3 Biological Characterisation: X-ray Crystallography

The second screening approach was X-ray crystallography, an attractive strategy because it provides a wealth of structural information about the ligand-protein interactions. This could help identify differences in the binding positions of the fragments and give a deeper understanding to the preferences between different growth vectors. X-ray crystallography is also a suitable strategy for fragment screening because even low-molecular weight compounds with weak binding affinities can be identified.[212]

There are two strategies for generating crystals of the protein-ligand complexes required to probe the small molecule binding.[213] Firstly, co-crystallisation which introduces the small molecule to the protein in solution. The protein-ligand complex is then crystallised from this solution. Secondly, crystal soaking which exposes preformed protein crystals to a solution containing the small molecule. The small molecules then diffuse through solvent channels in the protein crystal and bind to the protein surface. After both strategies, the protein-ligand crystals are analysed by X-ray crystallography to determine if and where the small molecules are bound to the protein.

The main limitation of the co-crystallisation strategy is that protein crystallisation is very sensitive to changes in the protein solution. Even if crystallisation conditions have been established for the isolated protein, crystallisation of the protein-ligand complex may not be favourable. Further optimisation can be a lengthy process taking several days or weeks to establish new conditions.[214]

Crystal soaking is generally more common as, once the crystals are formed, greater numbers of compounds can be screened quickly. However, there are drawbacks to the soaking technique as well. Protein crystals contain up to 70% water, so diffusion of the small molecules is expected to be very fast, but it can take hours or days for a ligand to fully populate the binding pocket of the protein. Understanding the diffusion kinetics is important to ensure the success of a crystal soaking approach. There are also challenges in how well the preformed protein crystals can accommodate the small molecules. The protein structure may change in response to ligand binding which could disrupt the crystals and challenge later structure determination.

A case study of the two strategies compared the generation of protein-ligand complexes for the cAMP-dependent protein kinase from *Cricetulus griseus*.[213] The authors found that co-crystallisation lead to greater structural deviations than crystal soaking, especially for the larger, more flexible ligands. This indicates that the faster and simpler soaking strategy is well suited to investigating larger libraries of small rigid fragments, while co-crystallisation is better suited for testing larger ligands and lead compounds. Crystal soaking therefore appeared as the favourable technique to screen this fragment library.

The biggest limitation in X-ray crystallography is the challenge of generating protein crystals that are suitable for structure determination. Protein crystallisation relies on a “trial and error” sampling of

conditions varying the preparation of the protein and the method of crystallisation.[215] It requires bringing an extremely pure sample of protein to super saturation, without causing aggregation, then crystals grow either by vapor diffusion or by stimulation with a precipitant. Due to the time-consuming process and high attrition rate of protein crystallisation, fragment soaking was first trialled with crystals of *Li*CS that were generated by Dr Kate Sowerby, a structural biologist in the Pohl group at Durham University.[194]

4.3.1 Results and Discussion

The first soaking experiments used conditions previously optimised by Dr Kate Sowerby: soaking the crystals in fragment solutions at 100 mM in DMSO/water [Table 4.3, entry 1]. The *Li*CS protein can only withstand a maximum concentration of 10% DMSO in water, so stock DMSO solutions of the fragments were diluted stepwise with purified water to the required concentrations. Unfortunately, only a handful of fragments tolerated this solvent system and most precipitated below 50% DMSO. Even when the concentration of the fragments was decreased to 20 mM, most compounds could not tolerate the aqueous environments [Table 4.3, entry 2]. Due to the expected low binding affinity of the fragments, the concentration could not be reduced further as the protein binding pockets must be sufficiently occupied that fragments can be identified in the X-ray diffraction pattern.

An alternative strategy was based on previous experiments performed by Dr Kate Sowerby screening the commercial FragLites library against the *T cruzi* CS enzyme. This methodology added droplets of the fragment solutions at 500 mM in DMSO to a buffered aqueous solution containing protein crystals [Table 4.3, entry 3]. Despite the high concentration, a set of fragment solutions were prepared, and the 19 successful fragments are shown in Figure 4.3.1.1. However, when these solutions were introduced to the protein crystal droplets, precipitation of the compounds was observed on the surface of the droplets. This process is called 'salting' and indicated that the fragments were not completely soluble in the aqueous solution. As previously mentioned, high solubility was required to ensure reliable diffusion into the protein crystals so these conditions were also not suitable.

Table 4.3: Conditions trialled for preparing fragment solutions for crystal soaking

Entry	**Fragment Conc. / mM**	**Solvent System**	**Successful Fragments**
1	100	10% DMSO/Water	<5
2	20	10% DMSO/Water	<5
3	500	DMSO-*d*6	19 [Figure 4.3.1.1]

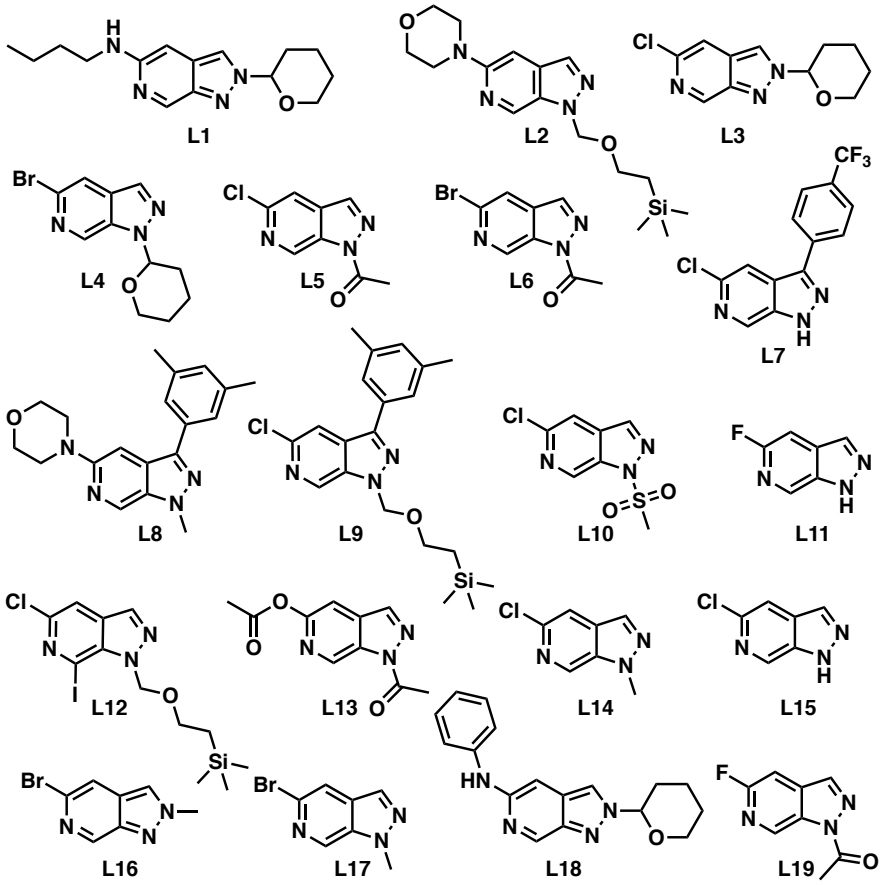

Figure 4.3.1.1: Library of fragments based on the pyrazolo[3,4-c]pyridine scaffold for screening by crystal soaking.

4.3.2 Summary

After these preliminary trials, it appeared that poor aqueous solubility was going to be an insurmountable obstacle to performing crystal soaking experiments with this set of fragments. The challenges of this methodology came predominantly from the high fragment concentrations required to ensure sufficient occupancy of the binding pockets. Therefore, attention turned to an alternative screening methodology that could be performed with lower fragment concentrations.

4.4 Biological Characterisation: Thermal Shift Assays

The thermal shift assay was a desirable alternative screening strategy due to its simple set-up and low sample requirements.[216] Thermal shift assays are common to fragment screening because the high throughput means large libraries can be screened easily. The main drawback of this technique is the limited information provided. The range of magnitudes of ΔT_m will depend on the specific protein, and sometimes small molecule ligands can actually destabilise the protein leading to negative ΔT_m values instead. This makes it hard to classify when a hit is real, but typically values of 0.5 – 2 °C are expected. Additionally, because each experiment provides only one measurement, there is limited information about the nature of the protein-ligand interactions.

Before any assays could be run to test the fragment binding, it was first necessary to express and purify the protein. *L infantum* SIR2RP1 was the target for these experiments because the existance of reported crystal structures indicated this protein would be the easiest to work with.

4.4.1 Protein Expression and Purification

The production of the *Li*SIR2RP1 protein was conducted first in a small batch to test the expression. Plasmids encoding the *Li*SIR2RP1 with His_6-tag (purchased from GenScript) were transformed into competent *E. coli* BL21 (DE3) cells by heat-shock and then verified by DNA sequencing. Transformants were grown in LB medium supplemented with Ampicillin (100 μg/mL) at 37 °C to $OD_{600} > 0.6$ and protein expression was induced overnight by isopropyl-thiogalactoside (1 mM). The cells were then disrupted by sonication and the soluble tagged protein was purified by affinity chromatography on an Akta Start Fast Protein Liquid Chromatography system with elution buffer A (50 mM TrisHCl (pH 7.5), 500 mM NaCl, 1 M imidazole, 2 mM β-mercaptoethanol). The presence of *Li*SIR2RP1 was confirmed by SDS-PAGE to be of good purity, and its identity was confirmed by protein mass spectrometry [Figure 4.4.1.1]. Expression and purification was then performed on a larger scale, with each 6 L batch producing around 10 mg of purified protein.

4.4.2 Results and Discussion

4.4.2.1 Protein Stability Tests

To generate meaningful results from the thermal shift assay, it was first necessary to establish the optimal conditions for the protein to produce well-fit reproducible denaturation curves. This increases confidence that any later changes in T_m were caused by the addition of the small molecules. To understand the behaviour of the *Li*SIR2RP1 protein, conditions were screened using the Durham Screening plates from Molecular Dimensions which tested a suite of buffers and pH environments, salts and additives designed

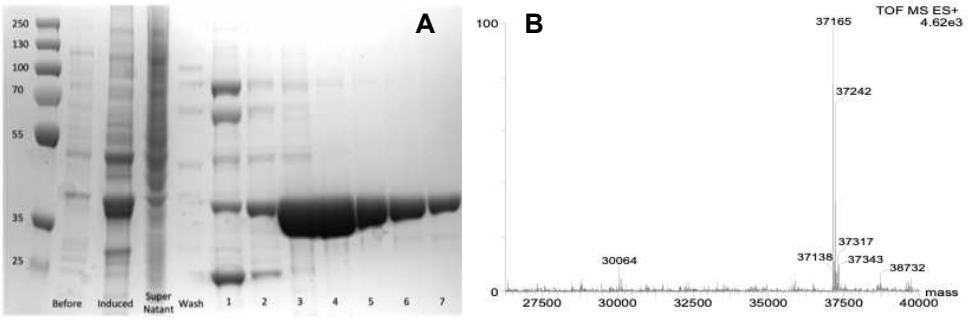

Figure 4.4.1.1: **A** shows SDS-PAGE gel of protein expression and purification. **B** shows MS (ESI) of purified protein calculated mass, M = 37170 Da

to (de)stabilise the protein.[217]

The first round of screening was conducted with *Li*SIR2RP1 in the standard Tris Buffer A (50 mM TrisHCl (pH 7.5), 500 mM NaCl). The fluorescence signal from each well was measured as the temperature increased from 24-96 °C at 1 °C per minute. Then the programme NAMI was used to plot the data and calculate the melting temperature. Figure 4.4.2.1.a and Figure 4.4.2.1.b shows the data output from the Durham pH screen and the Durham salt screen respectively. The data tables indicate a problem with the experiments. The large number of no signal (N/S) results suggested a low concentration of soluble protein leading to low fluorescence. Furthermore, when the individual melting curves were analysed it was clear that the few calculated T_m values were only an artifact imposed by the programme. An ideal temperature curve shows a steady background reading then a significant change in fluorescence level as the native protein moves to complete denaturation. This pattern was not seen for any of the wells, instead the gentle slopes indicate premature denaturation and/or aggregation of the protein. Figure 4.4.2.1.c-f demonstrates a representative sample of the melting curves generated in the Durham salt screen.

To address the premature denaturation, the protein was transferred into different buffer conditions. Dialysis into the HEPES buffer (20 mM HEPES (pH 7.5), 300 mM NaCl, 10% glycerol) caused significant precipitation of the protein. Although centrifugation and collection of the supernatant returned samples of good enough quality for another round of stability screens. Unfortunately, the results of both the pH and salt screens were again unable to return any meaningful melting curves. These results indicate that this protein construct cannot be stabilised in any of the screened conditions.

4.4.3 Summary

The screening kits combined tested more than 30 different salts at various concentrations, and 28 different buffer solutions across a pH range of 4 – 11. None of these conditions were suitable for stabilising the *Li*SIR2RP1 protein and without a reliable means of measuring T_m, it was not possible to conduct the fragment screening by thermal shift assay.

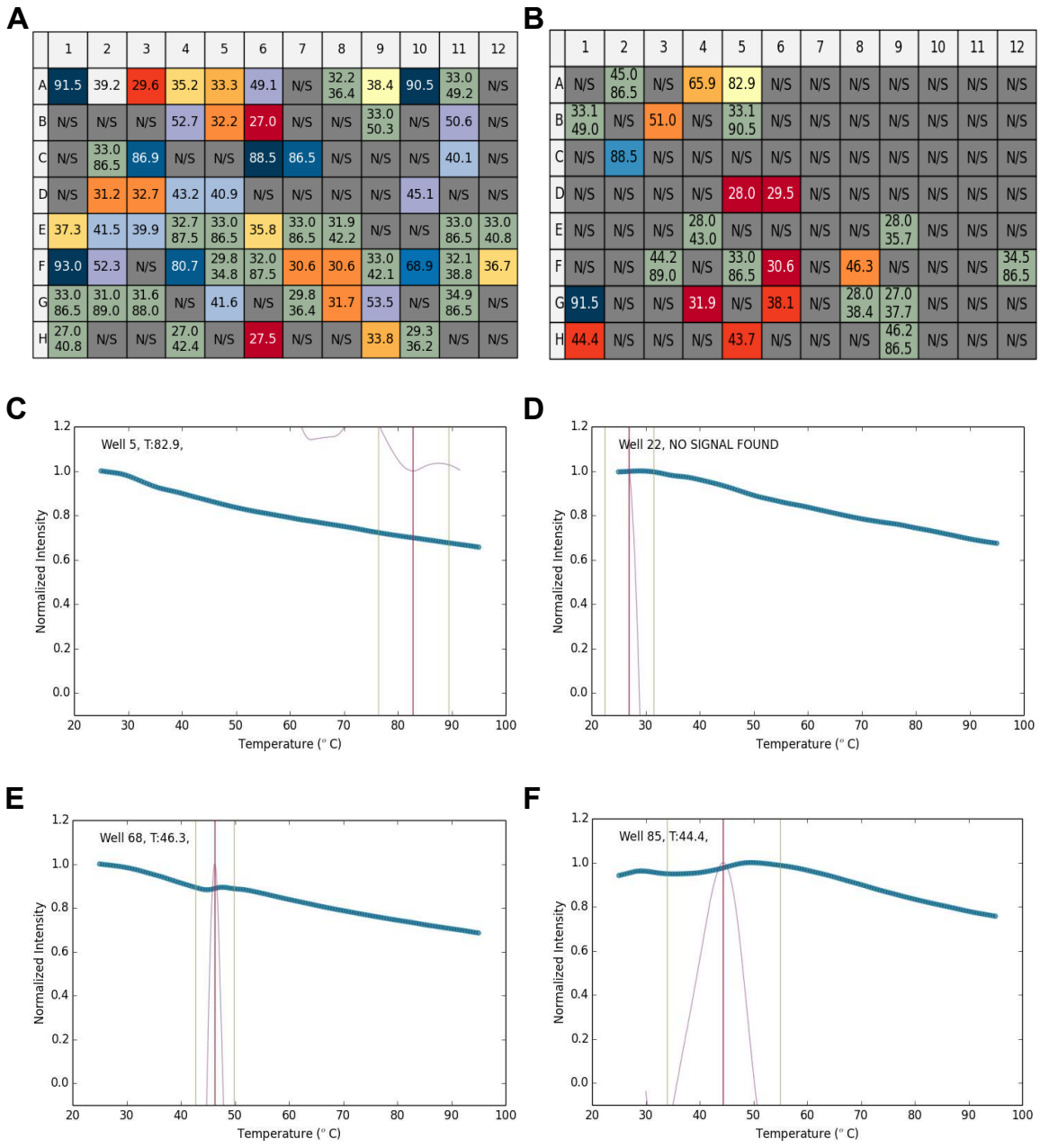

Figure 4.4.2.1: **A** and **B** show results from thermal shift assay testing the Durham salt screen and Durham pH screen. Wells with T_m within ±0.5 of the reference temperature appear white, wells bellow are graded from yellow to red, and wells above are graded from light blue to dark blue. Grey wells labelled 'N/S' had no discernible signal and wells that are coloured green indicate that two melting transitions were detected. **C-F** are exemplary melting curves for wells 5, 22, 68, and 85 respectively.

The *Li*SIR2RP1 used here was the complete protein sequence of 272 amino acids, yet the reported *Li*SIR2RP1 crystal structures were obtained only with recombinant *Li*SIR2RP1 possessing an extensive internal deletion of 51 internal amino acids.[185] This additional disordered region of the protein could be interfering with its stability in these conditions. One solution, therefore, would be to repeat the procedure with new plasmids that code instead for the deletion construct. However, due to time constraints, this was not pursued here.

4.5 Conclusions and Future Work

The objective of the work outlined in this chapter was to demonstrate the medicinal chemistry potential of the pyrazolo[3,4-c]pyridine core through a series of screening experiments to explore its biological activity. *L infantum* and *L major* were chosen as exemplary targets because the discovery of new antileishmanial drugs is of pressing need.

The preliminary screening was conducted with a computational docking strategy using the programme DockThor. A select library of fragments was screened against protein models for *Lm*SIR2RP1 generated through homology modelling from existing crystal structures of related proteins. The overall trend showed larger molecules generally ranking higher, yet different fragments showed preference for different pockets in the protein.

One advantage of virtual screening is the ability to quickly screen huge libraries of compounds. The fragment library chosen here was kept small so that each result could be individually interpreted, however this limited the information that could be gathered. Therefore, future work should look to screen a much larger library, or several selective libraries to better demonstrate trends in fragment binding. One such method would be to design multiple libraries with much tighter ranges of molecular weights, this would remove the obvious trend of larger ligands ranking more highly and so could highlight other molecular preferences instead. Another method would be to include compounds with the same moiety attached at different positions around the heterocyclic core. This would test how the fragment shapes compliment the protein structure and better exemplify the concept of growth vector elaboration.

It is possible to design many virtual libraries based on theoretical compounds containing the pyrazolo[3,4-c]pyridine core. However, the best way to confirm if the pyrazolo[3,4-c]pyridine scaffold had potential to bind to the *Leishmania* sirtuin proteins was to find a complimentary method to directly measure binding affinities.

The first physical screening method explored was ligand soaking for protein X-ray crystallography. However, preliminary tests with crystals of *Li*CS were unsuccessful due to the poor aqueous solubility of the small organic fragments. It was not possible to find a solvent system in which the protein crystals were stable that could also solubilise the fragments at a sufficient concentration to carry out the screening. This led to the exploration of other screening methods that could be performed with lower fragment concentrations.

Thermal shift assays were desirable as a simple method for screening with a relatively high throughput. For these experiments, the *L infantum* sirtuin protein was recombinantly produced and collected in high purity. Unfortunately, commercially available pH and salt screens were unable to identify conditions under which the protein was reliably stable. To proceed with these experiments, different methods of producing

the protein need to be explored. Changing the expression constructs, introducing internal deletions to the amino acid sequence, or co-expression with another stabilising protein are possible routes to improve the stability and function of the protein.

In the initial report describing the *Li*SIR2RP1 crystal structures, Ronin *et al.* also analysed the activity of the sirtuin enzymes using an assay to measure the deacetylation rate of an acetylated peptide substrate.[185] This analysis was applied to the full-length protein and the deletion constructs while either the NAD^+ concentration or peptide substrate concentration was varied. This report highlights biochemical assays as another potential method for assessing the effects that small molecules have on the protein.

Collaborators at the Universidade de São Paulo have previously developed a biochemical assay to screen compounds against the *T cruzi* sirtuin protein *Tc*SIR2RP1.[189] Work is currently ongoing to adapt this biochemical assay for use with the *Li*SIR2RP1 protein relevant to this investigation. This will enable the same experiments to be conducted with the pyrazolo[3,4-c]pyradine fragments in due course.

Nevertheless, there are still concerns about the aqueous solubility of the fragment library. The concentrations of ligand solutions for thermal shift assays and biochemical assays are lower than that required for crystal soaking (0.1 – 1 mM). However, the techniques are more sensitive to ligand aggregation and insolubilities. A large number of fragments based on the pyrazolo[3,4-c]pyridine scaffold were synthetically isolated, yet only a small number were amenable to forming an aqueous solution. This challenge of limited aqueous solubility would be a constant hurdle throughout any experiments to explore the biological activity of this scaffold.

Therefore, the most pressing concern, greater than the stability challenges of the *Li*SIR2RP1 protein, was the insolubility of the heterocycles. A library of fragments with good aqueous solubility would open up additional methods of screening and improve the overall biological characterisation. The next challenge, and the focus of the following chapter, was to synthesise a new fragment library based on a nitrogen heterocyclic core with structural characteristics to enhance aqueous solubility.

Chapter 5

The Next Generation of *N*-heterocycles

The low solubility of the pyrazolo[3,4-c]pyridine compounds made it practically challenging to conduct a complete fragment screening. An additional concern was the negative implications that the poor aqueous solubility has for the compounds' potential as a drug candidate. Solubility impacts the absorption, distribution, and clearance properties of drug molecules in the body. In the hopes of finding a new scaffold with better prospects as a drug candidate, it was necessary to design new nitrogen-containing bicyclic cores with structural characteristics to enhance their solubility.

The following chapter details the work undertaken to design and optimise the synthesis of these new scaffolds. First, a literature review of factors affecting compound solubility highlighted the potential of semi-saturated scaffolds and inspiration from the "Rings of the Future" then led to the design of the azabenzolactams. Exploration of methods for their vectorial functionalisation then led to an in-depth investigation into methodology development for the electrochemical oxidation of cyclic amines to the corresponding *N,O*-acetals. Also described is the decoration of these compounds by reaction with organozinc reagents. The scope of which was expanded through the use of boronic acids and esters. Finally, with a look to the future, potential methods for the elaboration along other growth vectors are discussed.

5.1 Compound Solubility

5.1.1 Sp^3 Fraction and Aromatic Ring Count

Good aqueous solubility is an essential physical property of a potential drug compound as it affects a compound's uptake and distribution around the body. Demonstrating its importance, there are many available methods that enable a prediction of a compound's solubility from various calculated or measured properties. Different models rely on group contribution methods,[91,218,219] or quantitative methods from calculated properties such as molecular topography[220,221] and 3D descriptors[222–224], or are based on quantum mechanics calculations.[225,226]

A standard approach, appreciated for its simplicity, is the General Solubility Equation (GSE, equation 5.1) which requires only two easily measurable parameters – melting point and $\log P$.[227] This equation shows that aqueous solubility is inversely proportional to the lipophilicity of the compound. However, as this relationship is based on properties measured for the whole compound, it does nothing to explain which parts of a compound's structure are contributing to the lipophilicity/solubility.

$$\log S_{\mathrm{w}} = 0.5 - 0.01(MP - 25) - \log P \tag{5.1}$$

General solubility equation (GSE) where S_w = aqueous solubility, MP = melting point in °C and P = octanol-water partition coefficient

Lipophilicity generally increases as compounds get larger, but certain groups have greater contributions to lipophilicity than others. One in-depth investigation looked at the effects of the aromatic ring count (ARC) of a compound, analysing several important metrics associated with success in drug development including aqueous solubility and lipophilicity.[228] Here 'aromatic rings' included all-carbon aromatic rings and heteroaromatics with each ring in a fused system being counted separately. In this system of counting, the pyrazolo[3,4-c]pyridine **77** would have an ARC of 2.

This analysis of compounds in the GSK database showed a clear correlation between increasing ARC and decreasing solubility, as even two aromatic rings caused many compounds to suffer from low solubility (< 50 μg/mL) [Figure 5.1.1.1]. Values of $c\log P$ and $\log D$ (D = octanol-water distribution coefficient measured at pH 7.4) also increase with ring count, in accordance with GSE 5.1. More surprising is the analysis here shows that ARC affects aqueous solubility, even within a narrow range of $c\log P$ value [Figure 5.1.1.2]. Comparing compounds with $2 < c\log P < 3$, 80% of those with no aromatic rings have solubility > 100 μg mL^{-1}, compared to 55% of compounds with ARC = 1, and only 40% of compounds with ARC = 2. This trend continues with increasing ARC leading to greater percentages of low solubility compounds for a given $c\log P$.

Trends between ARC and other parameters were also considered including serum albumin binding,

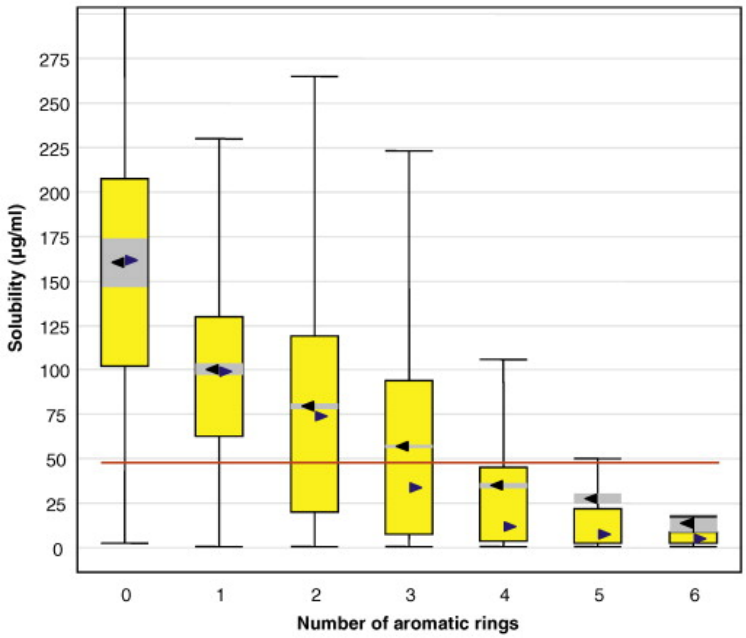

Aromatic ring count	0	1	2	3	4	5	6
Mean solubility	161	100	79	57	36	28	14
Median solubility	161	99	74	34	12	8	5
Q1	102	63	20	8	4	3	3
Q3	207	130	119	94	45	22	9
Number of compounds	184	1,379	8,711	13,204	6,127	1,725	195

Drug Discovery Today

Figure 5.1.1.1: Box plot and table of compound solubility and aromatic ring count. The orange line in the graph indicates the 50 μg/mL solubility level. Copied with permission from T. Ritchie and S. Macdonald, *Drug Discovery Today*, 2009, **14**, 1011–1020.[228]

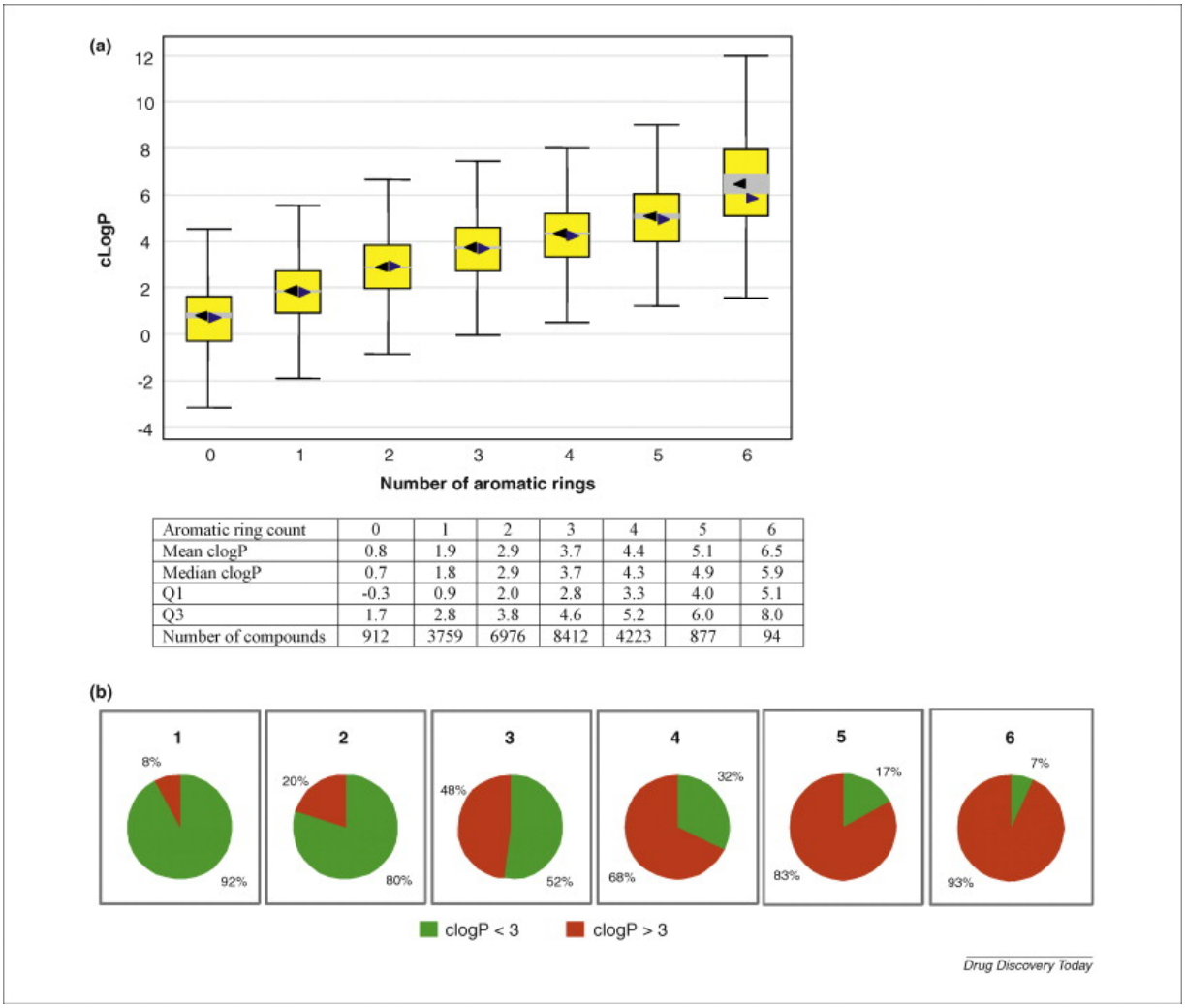

Aromatic ring count	0	1	2	3	4	5	6
Mean clogP	0.8	1.9	2.9	3.7	4.4	5.1	6.5
Median clogP	0.7	1.8	2.9	3.7	4.3	4.9	5.9
Q1	-0.3	0.9	2.0	2.8	3.3	4.0	5.1
Q3	1.7	2.8	3.8	4.6	5.2	6.0	8.0
Number of compounds	912	3759	6976	8412	4223	877	94

Figure 5.1.1.2: Box plot, table and pie charts of aromatic ring count and $c\log P$ (Daylight). Pie charts show the ratio of lipophilicity for compounds with differing numbers of aromatic rings (one to six, left to right). Green segments represent the percentage of compound with $c\log P < 3$, and red segments represent the percentage of compounds with $c\log P > 3$. Abbreviations: Q1, quartile 1; Q3, quartile 3. Copied with permission from T. Ritchie and S. Macdonald, *Drug Discovery Today*, 2009, **14**, 1011–1020.[228]

cytochrome P450 inhibition, and hERG inhibition. Although not directly related to solubility/lipophilicity these are important considerations in a drug development programme and will determine a candidate's chances of success. This likely explains why, when looking at 280 compounds in the GSK pipeline, the mean ARC value declines from 3.3 in compounds at pre-clinical candidate selection to 2.3 in compounds in proof-of-concept trials in humans. This is compared to an average ARC of 1.6 in approved oral drugs. Overall, it was concluded that the fewer aromatic rings found in an oral drug candidate, then the more successful that candidate is likely to be.

One limitation of this investigation was that no account was made for compound size. Compounds with more aromatic rings are likely to have greater molecular weights, and so these trends could simply reflect the drawbacks of larger molecules. It is shown elsewhere that *molecular obesity* - the addition of excess molecular weight and lipophilicity to compounds in the pursuit of increased potency, but at the loss of other essential ADME properties - has been detrimental in many drug discovery campaigns.[229]

Lovering *et al.* addressed this by considering instead the sp^3 fraction (Fsp^3) which gives a direct measure of saturation; the smaller the number, the more aromatic the compound (Equation 5.2).[230] The Fsp^3 was considered for all compounds in the GVK Biosciences database from 1980 to 2009.

$$Fsp^3 = \text{number } sp^3 \text{ carbons / total carbon count} \tag{5.2}$$

The equation used to calculate the sp^3 fraction (Fsp^3) of a given molecule.

This analysis demonstrated that more saturated compounds (higher Fsp^3) had higher aqueous solubility ($\log S_{\text{w}}$). Compounds in the database were grouped by their reported aqueous solubility; those with $\log S_{\text{w}} = -6$ (poor solubility) had an average Fsp^3 of 0.31 compared to those with $\log S_{\text{w}} = 2$ (good solubility) which had an average Fsp^3 of 0.67. As predicted by the GSE, a similar trend was observed for melting point with the more saturated compounds having lower recorded melting points. Molecules with a melting point $< 50\,°\text{C}$ had an average Fsp^3 of 0.31, while molecules with a melting point $> 300\,°\text{C}$ had a lower average Fsp^3 of 0.11.

As in the GSK study above, these characteristics could also be correlated with clinical progression. The average Fsp^3 was found to increase from 0.36 for molecules in the discovery stage up to 0.47 for approved drugs. This analysis corroborates the argument that greater sp^3 count and lower aromaticity improves the solubility of organic compounds and leads to improved chance of clinical progression.

Taken in isolation, these studies would imply that, in terms of aromatic rings, fewer is always better. Yet aromatic and heteroaromatic structures are prevalent in small molecule drugs and continue to feature heavily in screening collections. This is because replacing the aromatic rings with aliphatic chains of the same heavy atom-count has many consequences beyond changes in lipophilicity and solubility. The effects of increasing the rotatable bond count and molecular flexibility is discussed in the next section.

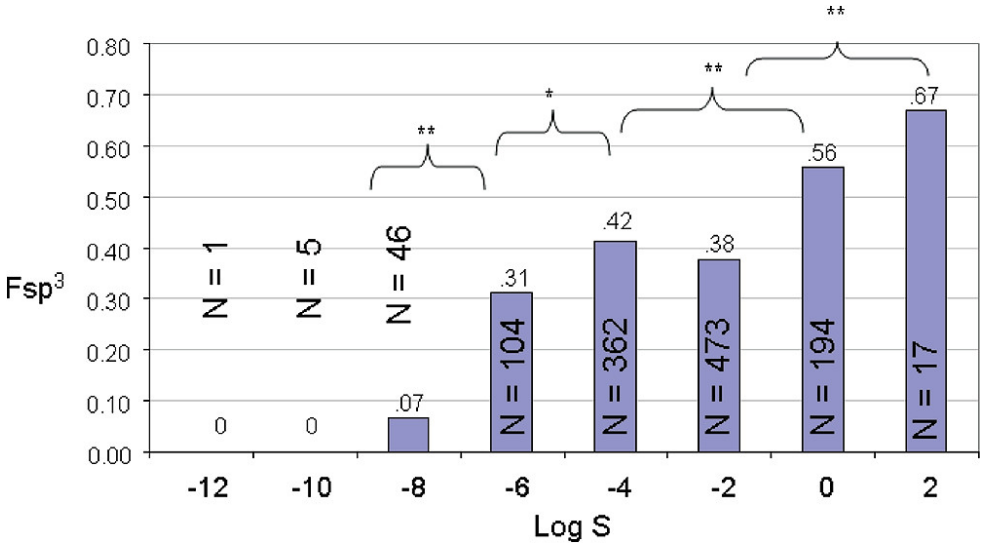

Figure 5.1.1.3: Mean Fsp3 for compounds in different stages of development. **P value <0.001. Reprinted with permission from F. Lovering, J. Bikker and C. Humblet, *Journal of Medicinal Chemistry*, 2009, **52**, 6752–6756.[230]

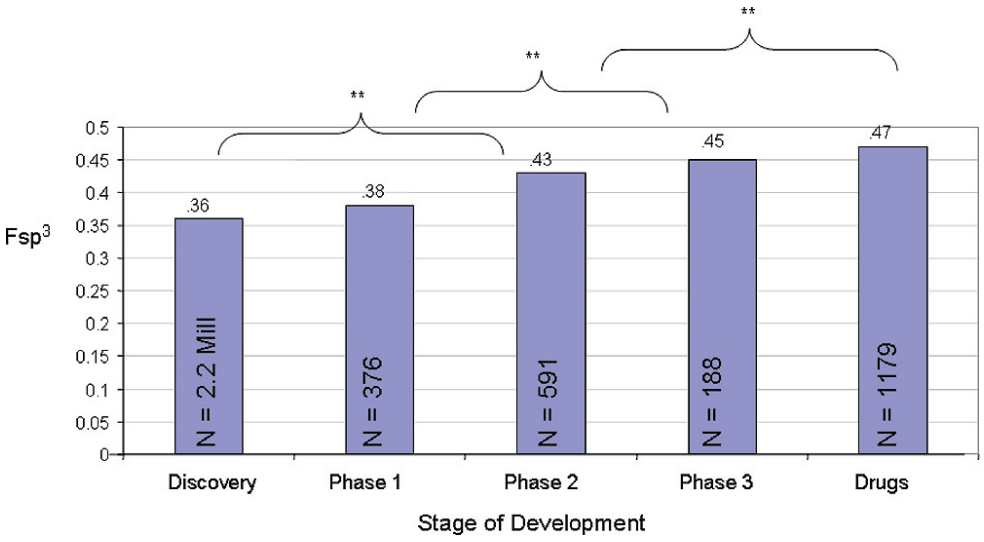

Figure 5.1.1.4: Mean Fsp3 for compounds in different stages of development. **P value <0.001. Reprinted with permission from F. Lovering, J. Bikker and C. Humblet, *Journal of Medicinal Chemistry*, 2009, **52**, 6752–6756.[230]

5.1.2 Rotatable Bonds and Molecular Flexibility

Aliphatic chains have a very flexible backbone with many rotatable bonds, and therefore many available conformations in solution. Upon protein binding, the compound must adopt the single productive conformation, meaning significant loss of entropy. This leads to high energy barriers to protein binding. The rigid structure of cyclic structures is likely to increase their affinity relative to unsaturated linear molecules, because a reduced entropy term increases the total ligand-receptor binding energy.[228] Ligand affinity is especially important in fragment library screenings where biological activity of fragments is generally low due to their small size. Therefore, it is necessary to balance ligand binding energy with physicochemical properties during the optimisation of a drug compound.

The correlation between reduced molecular flexibility, often measured by the number of rotatable bonds, and increased oral bioavailability was first discussed by Veber *et al.*[231] The rat oral bioavailability was compared to the rotatable bond count (NRot) for a set of over 1,000 drug compounds. For the group of compounds with NRot ≤ 7, about 65% passed the threshold of good oral bioavailability (good = 20% or greater). This dropped to less than 25% of the compounds with NRot ≥ 10. The compounds were then split at molecular weight 500 Da, and the analysis was repeated. The same trend was observed for both the light ($<$ 500 Da) and heavy ($>$ 500 Da) compounds, with fewer rotatable bonds correlating with greater rat oral bioavailability. Although this comparison was limited because there were not many light compounds with NRot ≥ 10 and not many heavy compounds with NRot ≤ 7.

Similar studies comparing the physicochemical properties of compounds from development to market also confirmed the trend that compounds with smaller NRot have better oral bioavailability.[232,233] The now widely used benchmark is NRot ≤ 10 and this kind of molecular flexibility descriptor is commonly included alongside Lipinski's Rule of 5 for good bioavailability.[234–237]

In Veber's definition, a rotatable bond is defined as any single bond, not in a ring, bound to a non-terminal heavy atom. Amide C-N bonds are generally excluded from the count due to their high rotational energy barrier. Saturated rings fall outside of this definition, and do not contribute to the rotatable bond count. Compared to aromatic rings, they do contribute to the overall molecular flexibility, just to a lesser extent than linear chains.[237] The incorporation of saturated ring systems has been identified as a method of improving the solubility of drug candidates[238] with additional advantages including lowering the toxicity of drug metabolites and increasing the potential for structural diversity through stereoisomerism.[239,240]

Solubility-driven optimisation through incorporation of saturated ring structures has been demonstrated as a viable strategy to produce promising drug candidates. It was utilised in the pursuit of phosphodiesterase-4D inhibitors by a series of 1,7-napthyridine compounds [Scheme 5.1.2.1].[241] Increasing the sp^3 fraction by replacing the benzene ring in **232** with a cyclohexane linker, gave increased solubility from 2.3 mg/L (6.25 mM) to 920 mg/L (2.6 mM) at pH 6.8. While there was a marked drop in potency, the $>$350-fold

increase in solubility and overall improvement of pharmacokinetic properties produced compounds with good *in vivo* efficacy. Compound **233** measured a bioavailability of F = 52 ± 9%, compared to 8 ± 3% for **232**, and EC_{50} = 1.2 mg/kg. This shows the importance of balancing potency and physical properties. After this targeted improvement of solubility, compound **233** was progressed as a clinical candidate.

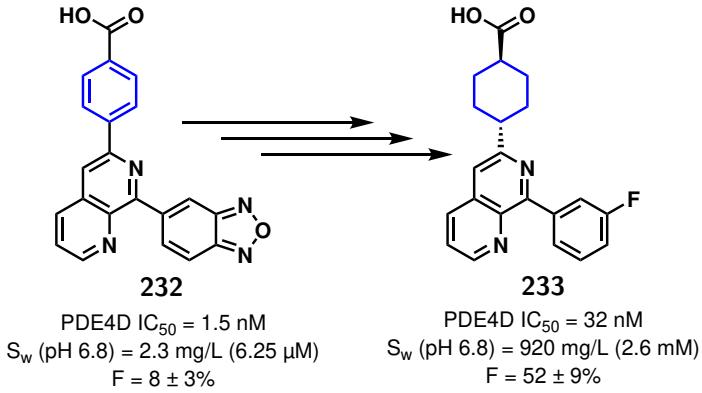

Scheme 5.1.2.1: Solubility-driven optimisation of phosphodiesterase-4D inhibitors.

Aqueous solubility was also an important factor in the reported development of non-nucleoside reverse transcriptase inhibitors as a treatment for HIV. This programme started from the approved drug Etavirine, which suffered from low oral bioavailability and poor solubility. In this case, structural modifications involved replacing the cyanobenzene with a piperidine linker to increase the sp^3 fraction in this portion of the molecule [Scheme 5.1.2.2].[242] Further optimisation, including the addition of polar groups, led to **234** with an overall 10-fold improvement in aqueous solubility and retention of HIV inhibition.[243]

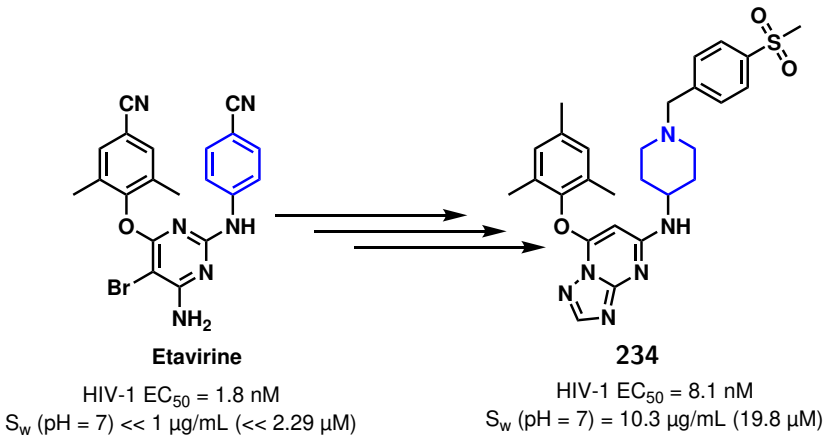

Scheme 5.1.2.2: Solubility-driven optimisation of etavirine.

Overall, there is strong evidence to support the ideas that having too many aromatic rings is detrimental and that having too many rotatable bonds is also detrimental to a compound's drug potential. The above examples demonstrate the benefits of incorporating more saturated ring systems into a drug molecule to

balance flexibility/rigidity and solubility/potency.

5.1.3 Semi-saturated Bicyclic Rings

As discussed previously, nitrogen heterocycles are a privileged class of structures in biologically active molecules so should remain prominent in the exploration of drug-like space. Compared to the aromatic heterocycles like the "Rings of the Future" scaffolds, semi-saturated fused rings offer an improvement in many physical properties due to their increased sp^3 fraction, as demonstrated in the comparison of isoquinoline and tetrahydroisoquinoline [Table 5.1]. Semi-saturated fused rings also have advantages over entirely saturated aliphatic heterocycles, for example the reduced number of available conformations simplifies structure elucidation while the retained chromophore eases purification. The aromatic portion of the scaffold also remains amenable to the many well-established methods of C-H activation, useful for diversification.

Table 5.1: Physcial properties of isoquinoline and tetrahydroisoquinoline.[245]

	Isoquinline	**Tetrahydroisoquinoline**
Solubility (mg/mL)	5.66	Miscible
pK_{BHX}[244]	1.94	2.04
pK_a	5.4 (at 25 °C)	9.3 (at 37 °C)
$\log P$	2.09	1.71
mp (°C)	25	-30

A widely reported approach for the introduction of semi-saturated ring structures employs partial reduction of an aromatic system. This was demonstrated by Bradbury *et al.* in the formation of triazolopyridazines as a series of androgen receptor down regulators [Scheme 5.1.3.1].[246] Compound **235** was suffering from poor solubility (S_w (pH 7.4) = 5.4 mM) and high hydrophobicity ($\log D = 3.2$). Partial saturation of the triazolopyridazine ring was carried out by Pd-catalysed hydrogenation. This returned significant improvement in solubility (S_w (pH 7.4) = 577 mM) and reduction in hydrophobicity ($\log D = 2.5$) leading to a higher free plasma fraction and reduced human clearance. Overall, this modification resulted in compound **236** being chosen as a clinical candidate to progress to Phase I trials.

Another approach to generate semi-saturated heterocycles was exemplified in the synthesis of a series of triazolopiperazines **237** [Scheme 5.1.3.2].[247] This time, formation of the semi-saturated scaffold involved a one-pot amide coupling and hydrazine cyclisation to form a decorated triazole intermediate **238**, followed by a Tsunoda cyclisation to form the piperazine ring. The authors present examples substituted at several positions around the ring with a range of aryl, alkyl, and spirocyclic substituents. This variation was always introduced prior to formation of the bicyclic system and no late-stage functionalisation was attempted.

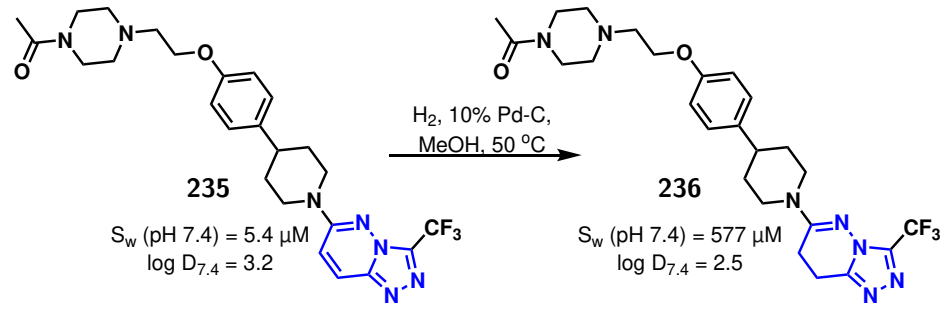

Scheme 5.1.3.1: Partial saturation of a triazolopyridazine for improved solubility of androgen receptor down regulators.

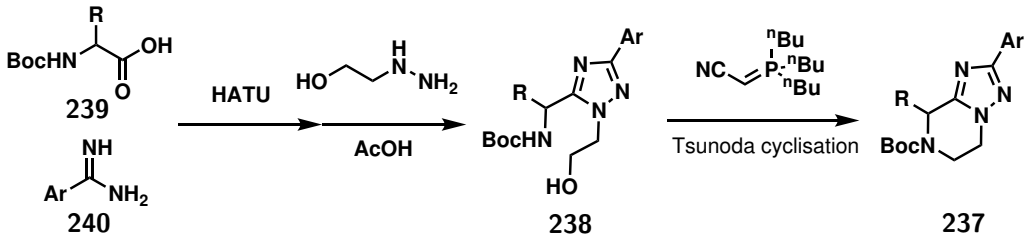

Scheme 5.1.3.2: Tsunoda cyclisation for the formation of a triazole containing semi-saturated bicycle.

5.1.4 Summary

The poor aqueous solubility of the pyrazolo[3,4-c]pyridines raised many concerns over the compounds' potential as drug candidates, because solubility impacts the absorption, distributions, and clearance properties of drug molecules in the body. A review of the literature highlighted that the best way to address these concerns was by decreasing the aromatic ring count and increasing the overall sp^3 fraction of the scaffolds. Increasing saturation helps lower the $c\log P$ which, in accordance with GSE [Equation 5.1], corresponds to increased aqueous solubility.

The challenge, however, is that too many rotatable bonds and excessive molecular flexibility can limit a compound's biological activity. This arises due to the large entropy term upon protein binding. It is therefore necessary to balance ligand binding energy with compound physicochemical properties throughout the design and optimisation of new drug compounds.

One way to address this challenge is by the use of semi-saturated bicyclic scaffolds. The cyclic structure maintains conformational rigidity, while the increased saturation improves solubility. The aromatic portion can be functionalised by a broad range of C-H activation strategies, while the sp^3 centres introduce more 3-dimensionality and open new possibilities for vectorial functionalisation. Two approaches arise for the synthesis of this type of scaffold; the partial saturation of an existing aromatic system, and the *de novo* cyclisation reactions. The next section explores the formation of semi-saturated scaffolds, and both methods of synthesis are explored.

5.2 2nd Generation "Rings of the Future"

As discussed in Section 1.3, the aim of this project was to develop novel fragment libraries to explore new areas of chemical space to enhance future drug discovery programmes. This is paramount in the move to more aqueous soluble cores. Inspiration for the first heterocyclic core came from the 2009 publication that introduced the "Rings of the Future" and this publication was again selected to develop the second series because of the unique heterocycles it presented.[34]

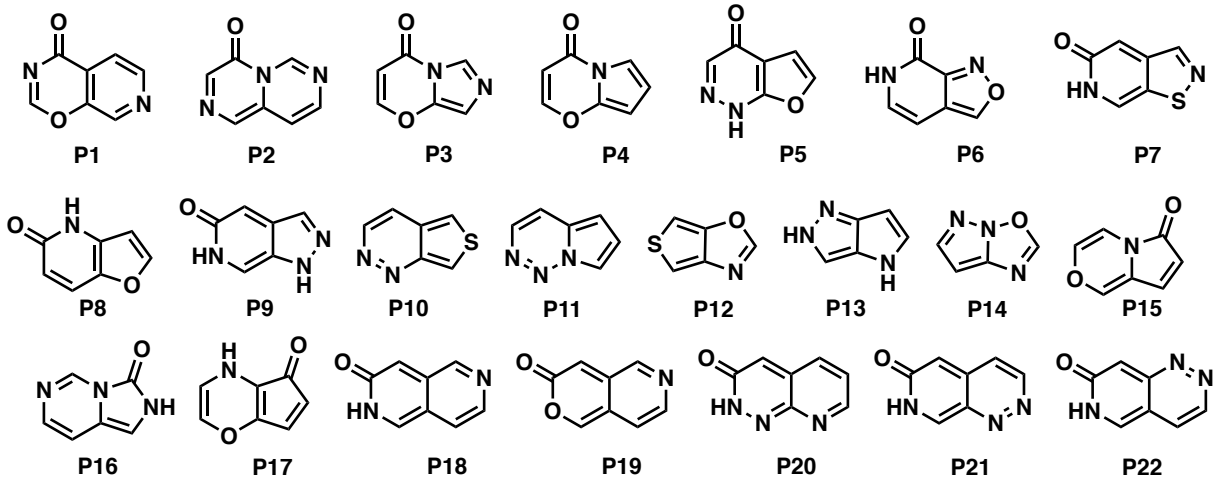

Figure 5.2.0.1: The 22 heterocyclic scaffolds published as the "Rings of the Future".[34]

Of the 22 heterocyclic scaffolds [repeated in Figure 5.2.0.1], there is much similarity across **P18** to **P22** with these molecules containing a pyridine-like ring and an amide functionality. Maintaining these features, while increasing the sp^3 fraction, led to the design of the azabenzolactam series [Figure 5.2.0.2]. These heterocyclic scaffolds were chosen to balance the enhanced solubility and polarity of the lactam rings with the rigidity of the small bicyclic system.

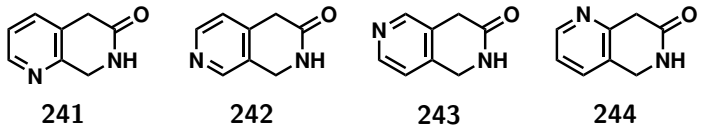

Figure 5.2.0.2: The azabenzolactam scaffolds.

These scaffolds were also attractive targets because, while both the pyridine and lactam structures are prevalent in drug compounds, there is limited precedence for the fused systems. Compounds **242**, **243**, and **244** have been reported in industrial patents for small molecule inhibitors targetting ferroportin to treat iron imbalance, although the bicyclic scaffold was oxidised and the carbonyl was replaced in the final compounds, so they no longer contain the azabenzolactam scaffold [Figure 5.2.0.3].[248] Similarly, compound **243** appeared as an intermediate in a reported synthesis of **P18**, but the lactam ring was

oxidised to give a fully aromatic product [Scheme 5.2.0.1].[72] Compound **242** also appears as a substructure of the fibroblast growth factor receptor inhibitor patented by Incyte Corporations, this time retaining the lactam ring [Scheme 5.2.0.2].[249] The most elusive scaffold from this series was compound **241**. This is listed as commercially available from Apollo Scientific UK, but at £1,100 per gram it is clear that a synthetic route from cheaper starting materials was desperately needed.[250] Therefore, the next aim of synthetic work was to develop efficient routes to the heterocyclic cores containing these ring structures.

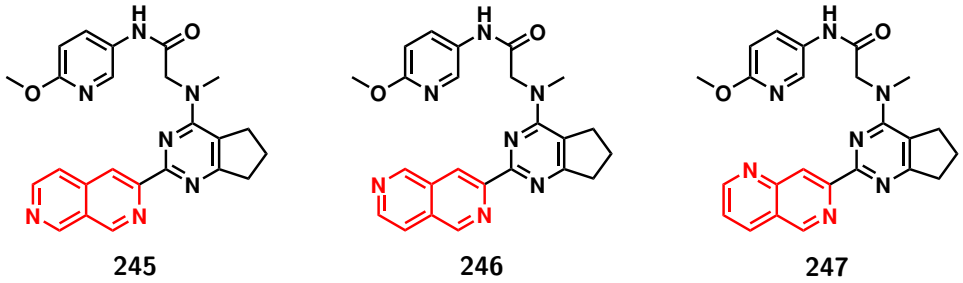

Figure 5.2.0.3: Patented ferroportin inhibitors based on azabenzolactams **242**, **243**, and **244**.[248]

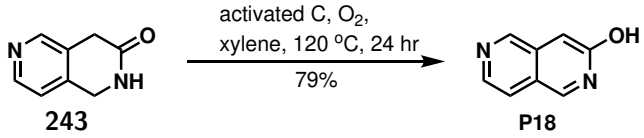

Scheme 5.2.0.1: Azabenzolactam **243** appears as an intermediate in this reported synthesis of **P18**.[72]

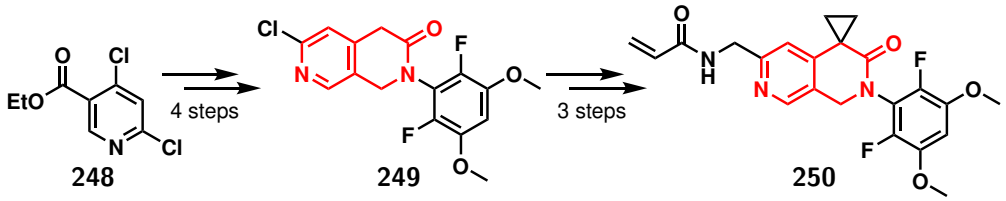

Scheme 5.2.0.2: Azabenzolactam **242** is a substructure of patented fibroblast growth factor receptor inhibitors.[249]

5.2.1 Generating Semi-saturated Scaffolds

There are two possible approaches to generating a semi-saturated scaffold: (1) the partial saturation of the corresponding fully aromatic bicyclic system, and (2) the *de novo* synthesis of the semi-saturated scaffold from non-cyclic starting materials. To begin exploring the synthesis of semi-saturated scaffolds, both of these approaches were first trialled for a simplified benzolactam target, 1,4-dihydroisoquinolin-3-one **251**.

5.2.1.1 By Partial Saturation

As in the reported synthesis of the triazolopyridazines discussed in Section 5.1.3, the partial saturation of aromatic systems is possible by catalytic hydrogenation. Stirring a solution of isoquinolin-3-ol **252** in the presence of palladium on carbon (Pd/C) under a hydrogen atmosphere gave rise to the desired benzolactam **251** [Scheme 5.2.1.1].

After 18 hours, NMR spectroscopy and LCMS confirmed no starting material remained and the product was collected in quantitative yields. However, attempts at subsequent transformations were very low yielding. Therefore, despite performing a Celite filtration of the reaction mixture, there were concerns that metal contaminants were persistent in the final product. Subsequently, further purification by flash column chromatography afforded the final product in 70% yield.

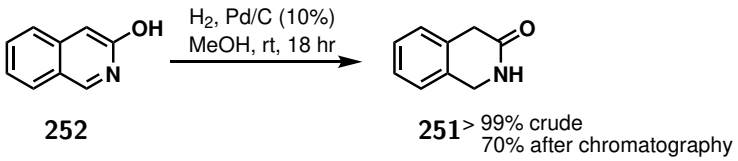

Scheme 5.2.1.1: Synthesis of the benzolactam scaffold by the partial saturation of isoquinolin-3-ol **252**.

5.2.1.2 *De Novo* Synthesis

It was also desirable to identify an efficient route to benzolactam **251** that did not require a fully aromatic starting material. One possible route reported in the literature started from 2-indanone **253**.[251,252] This reaction proceeds by a Schmidt reaction which introduces a nitrogen next to a ketone to form an amide unit.[253] In this reaction, the ketone carbonyl group undergoes nucleophilic addition of the azide, then one of the alkyl groups migrates to the nitrogen atom with loss of nitrogen gas. Attack by water and tautomerisation finally gives the desired amide. Scheme 5.2.1.2 outlines the mechanism of the Schmidt reaction for a general ketone.

There are two possible mechanistic pathways; one that follows a Baeyer-Villiger type rearrangement, and one that follows a Beckmann type rearrangement.[254] The preferred pathway depends on the type of acid present in the reaction. The powerful dehydrating properties of concentrated sulfuric acid are believed to favour the Beckmann type rearrangement as it promotes dehydration to imine formation. In contrast, aqueous acids like concentrated hydrochloric acid are believed to favour the Baeyer-Villiger type rearrangement. In the case of an asymmetric ketone, especially aryl-alkyl ketones, the type of acid used can influence which group preferentially migrates. This behaviour was explored by Crosby *et al.* in the synthesis of 6,7-bicyclic lactams [Scheme 5.2.1.3].[254]

In the synthesis of **251** the choice of acid was less important because the symmetric ketone removes the selectivity question. Therefore, NaN_3 was added portion-wise (10 parts over 5 min) to a cooled solution

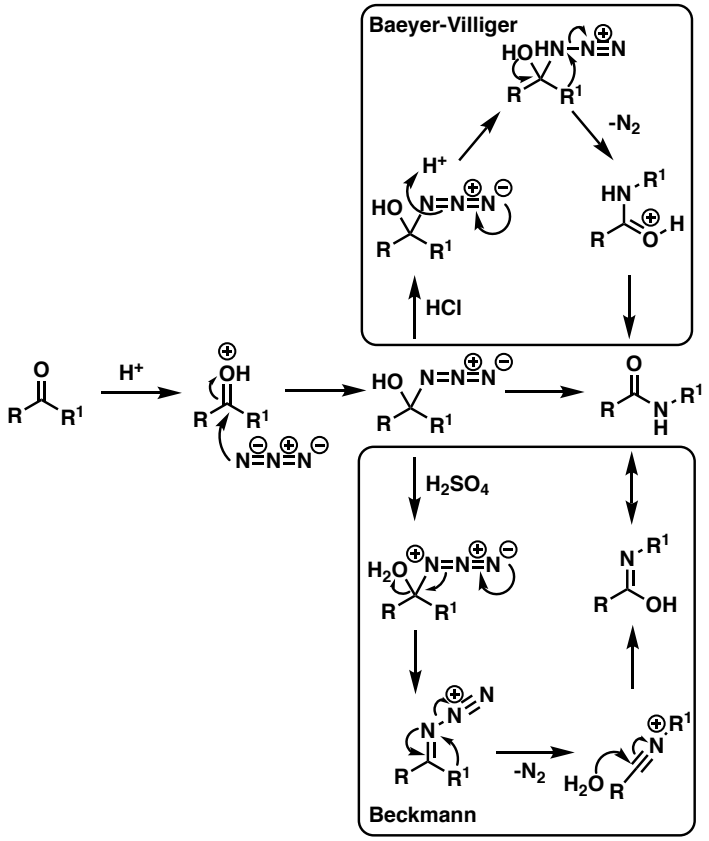

Scheme 5.2.1.2: The Schmidt reaction mechanism by Baeyer-Villiger or Beckmann rearrangements

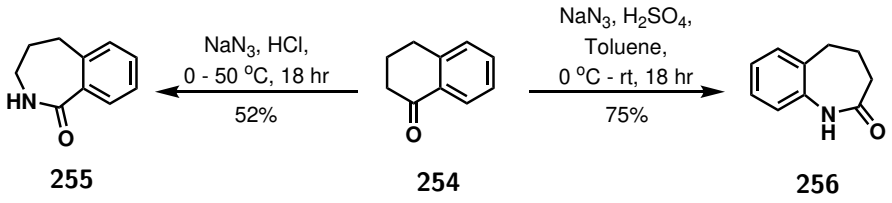

Scheme 5.2.1.3: Influence of the acid on the outcome of the Schmidt reaction.

of 2-indanone **253** (1.00 eq) in concentrated HCl. The reaction was stirred overnight then quenched by slowly pouring over ice. K_2CO_3 was added to the aqueous phase until pH 9 and the product was extracted then purified by flash column chromatography. This afforded the benzolactam in 58% yield identified in the LCMS by a peak at m/z = 148.11 [Scheme 5.2.1.4].

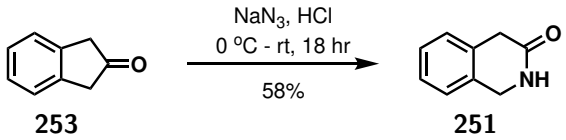

Scheme 5.2.1.4: Synthesis of the benzolactam scaffold by the Schmidt reaction of NaN_3 and indanone **253**

Purification of benzolactam **251** was challenged by sticking/streaking on the column caused by the strong interactions between the basic nitrogen group and the acidic silica gel. Reaction yields were limited by significant losses during purification and scale-up was limited by solvent requirements. This is a well known challenge of purifying amides that can often be overcome by moving to a reverse phase solvent system. However, in this case reverse phase purification did not afford the product in sufficient purity to be useable in subsequent reactions. To address these issues, it was desirable to find a route directly to an *N*-protected lactam.

One such route, reported by Cheng *et al.* utilised a Baeyer-Villiger oxidation to introduce an ester functionality followed by condensation with *p*-toluenesulfonamide to generate the tosyl-protected benzolactam. As well as aiding purification, this method was also desirable because introducing the protecting group and the amide functionality in the same step should give higher yields overall.

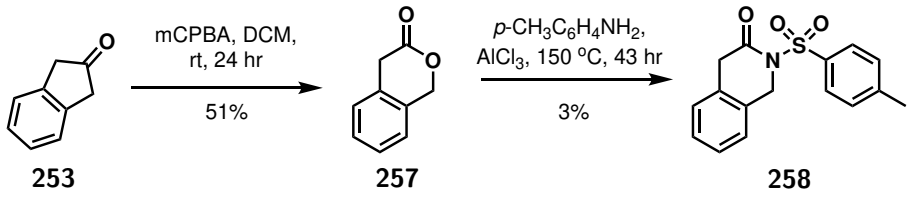

Scheme 5.2.1.5: Synthesis of the benzolactam scaffold by the Baeyer-Villiger oxidation of indanone **253**.

Treatment of 2-indanone **253** with mCPBA in DCM saw the Baeyer-Villiger oxidation produce reasonable amounts of the ester intermediate **257**. However, the displacement to the amide was not efficient with very little product collected even after 43 hours. In the literature report, the reacting amines were anilines or benzylamines which are more nucleophilic than the sulfonamide used here. This reduced nucleophilicity likely explains the reduced reactivity in this case. The reactivity of other amine nucleophiles or other Lewis acid conditions were not explored here.

5.2.1.3 Summary

Multiple methods were trialled to synthesise benzolactam **251** as a simplified example to explore the different approaches of forming a semi-saturated scaffold. For the case of benzolactam **251**, the yields were higher and more reliable for the partial hydrogenation method. However, this route relies on there being an easily synthesisable or commercially available aromatic starting molecule. This does not exist for the azabenzolactams series. Therefore, finding an efficient *de novo* synthesis is a more attractive route for the pursuit of novel heterocyclic scaffolds as greater diversity can be introduced to the core.

5.2.2 Synthesis of the Azabenzolactams

The synthetic work to develop and optimise the synthesis of the azabenzolactams scaffolds was performed by two project students, Joseph C Foster (JCF) and Mingyu Lou (MYL), under my supervision.

5.2.2.1 Retrosynthetic Analysis

Retrosynthetic analysis was employed to deconstruct the first target heterocycle **241** as shown in Figure 5.2.2.1. The first disconnection was between the C-N bond of the amide group in **I**, resulting in the primary amine and carboxylic acid shown in **II**. This benzyl amine can in turn be generated from the reduction of a nitrile group, so a functional group interconversion gave nitrile **III**. The next disconnection was the C-C bond between the pyridine and the carbonyl group in **III**. The best control for this reaction was expected to be from a 1,3-dicarbonyl **V** as the nucleophile, which necessitates an additional decarboxylation step prior to the reductive cyclisation. A halo-cyanopyridine **IV** was expected to be the best electrophile due to the ease of performing S_NAr reactions of pyridines. This was also an affordable, commercial starting material with multiple analogues available, so the synthetic endeavours started here. Scheme 5.2.2.1 shows the proposed forward synthesis.

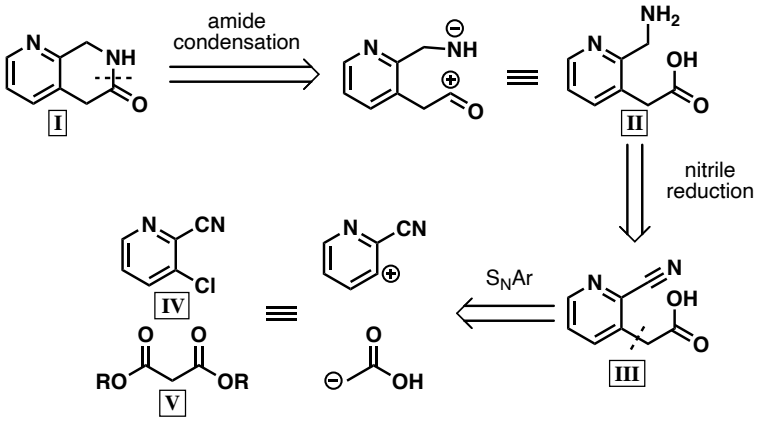

Figure 5.2.2.1: Retrosynthetic analysis of the azabenzolactams

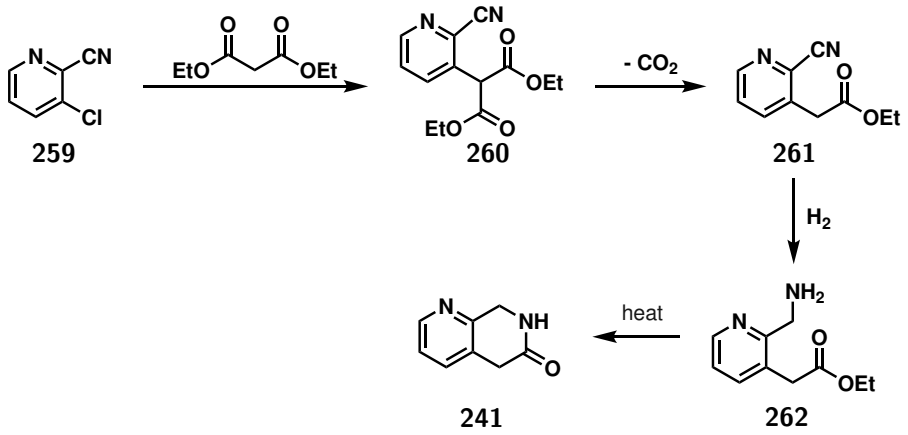

Scheme 5.2.2.1: Proposed synthetic route to the azabenzolactams

5.2.2.2 S_NAr for the Formation of Diethyl(cyanopyridinyl)malonates

The first step in the formation of the azabenzolactams was the nucleophilic attack of a dicarbonyl to displace the halogen. There was literature precedent for the reaction between chloropyridine and diethyl malonate at reflux in THF, but preliminary trials by JCF saw no product generation under these conditions.[72] Exchanging the solvent for 1,4-dioxane allowed for the reaction temperature to be increased to try to promote reaction, but there was still no product detected [Table 5.2, entry 2 & 3]. Moving the reaction to DMSO and increasing the temperature further finally generated the desired product, as evidenced by the new signals in the crude ^{1}H NMR spectrum at 5.14 ppm (1H), 4.32-4.18 ppm (4H), and 1.28 ppm (6H) representing the now substituted diethyl malonate [Table 5.2, entry 4]. However, the yield was not sufficient to progress with the synthesis and further optimisation was necessary.

Table 5.2: Exploring conditions for the S_NAr reaction of 3-chloro-2-cyanopyridine.

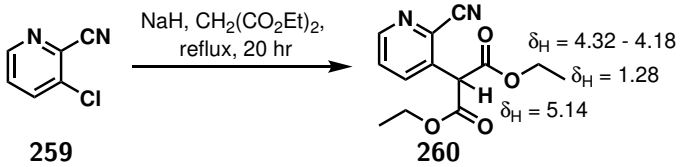

259 260

Entry	Solvent	Temperature	Time	Yield[a]
1	THF	66 °C	20 hr	0%
2	1,4-dioxane	101 °C	20 hr	0%
3	1,4-diozane	175 °C (MW)	8 hr	0%
4	DMSO	189 °C	20 hr	20%

As higher temperatures were not enough to encourage sufficient reaction, the influence of the halogen was next investigated. The rate-determining step of the S_NAr reaction is loss of aromaticity and formation of the Meisenheimer intermediate. Exchanging the chlorine with fluorine was therefore expected to decrease the energy barrier to reaction because its greater electron withdrawing ability stabilises the Meisenheimer intermediate. Reaction of fluoropyridine **263** was first trialled in THF which saw yields of 20-30%, a significant improvement over the chlorine analogue. Moving to 1,4-dioxane and increasing the reaction temperature again afforded **260** in 48-63% yields [Scheme 5.2.2.2].

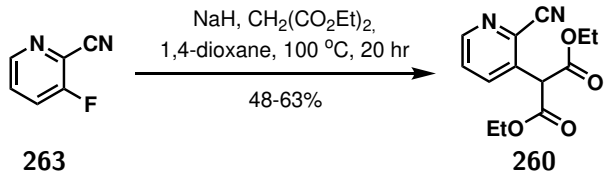

263 260

Scheme 5.2.2.2: S_NAr reaction of 3-fluoro-2-cyanopyridine to form diethyl(cyanopyridinyl)malonate **260**.

5.2.2.3 Krapcho Decarboxylation

The Krapcho decarboxylation is a reaction that eliminates an ester group when a β-electron withdrawing group, such as in the diethyl malonate, is present. This method was preferred over the standard sequence of saponification, decarboxylation, and re-esterification, because in one step it removed one ester unit without effecting the other. This reaction is believed to proceed by one of two mechanisms depending on the steric nature of the α-carbon [Scheme 5.2.2.3].[255] For an α,α-disubstituted ester **I** with a small alkyl group, the anion of the salt attacks the alkyl group in an S_N2 fashion yielding intermediate **II**. Decarboxylation gives intermediate **III** and protonation by water takes this to the final product **IV**. For less sterically demanding α-monosubstituted esters **V** or when the alkyl group is bulky, the anion of the salt attacks the carbonyl group instead to form tetrahedral intermediate **VI**. This breaks down into the carbanionic intermediate **VII**, which is then protonated to give the final product **VIII**. The other product **IX** is then hydrolysed to give CO_2 and an alcohol. Although only monosubstituted, the diethyl α-pyridinyl malonate substrate was expected to proceed by the S_N2 mechanism due to the steric demands of the *ortho*-substituted pyridine and the small ethyl ester.

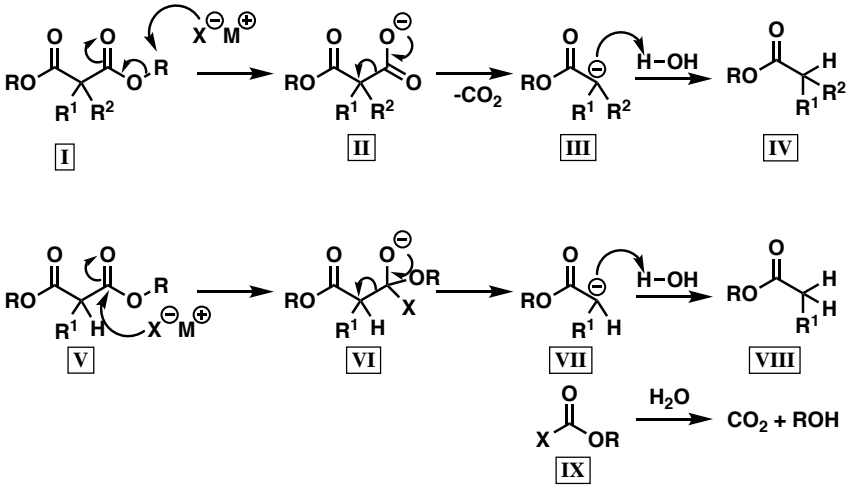

Scheme 5.2.2.3: Mechanism for the Krapcho decarboxylation

Conditions for the Krapcho decarboxylation were taken from the literature [Scheme 5.2.2.4]: LiCl was added to a solution of diethyl 2-(2-cyanopyridin-3-yl)malonate in DMSO/H_2O and heated to 100 °C overnight.[256] Preliminary tests saw **261** produced in yields of 51%, but complete removal of the DMSO solvent proved challenging. This was addressed by developing a multi-step extraction procedure as a form of liquid-liquid partition chromatography. This new method resulted in an increased yield of 77%.

5.2.2.4 Reductive Cyclisation for Lactam Formation

The reductive cyclisation of an aromatic nitrile onto an ester was demonstrated by Nicolaou *et al.* in the synthesis of analogues of platensimycin, an antibiotic that was first isolated from *Streptomyces platensis* by

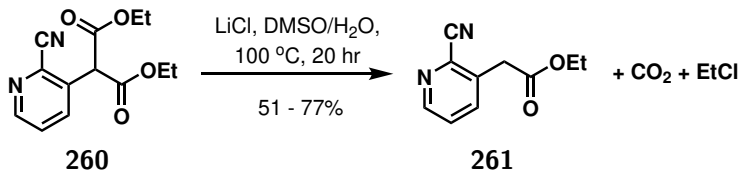

Scheme 5.2.2.4: The Krapcho decarboxylation of diethyl 2-(2-cyanopyridin-3-yl)malonate **260**.

scientists at Merck in 2006.[257,258] Catalytic hydrogenation of the nitrile gave the corresponding primary amine, which then spontaneously cyclised to form the lactam with 39% overall yield [Scheme 5.2.2.5].

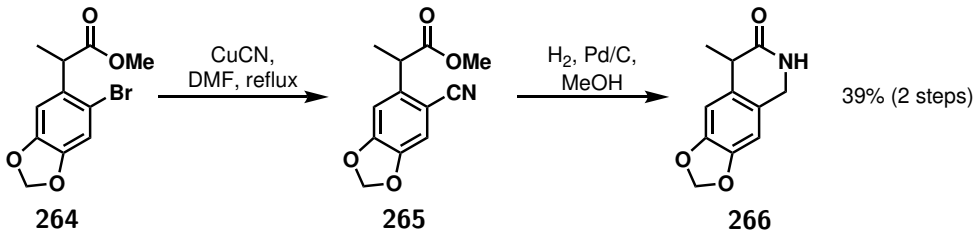

Scheme 5.2.2.5: Literature example of the reductive cyclisation of an aromatic nitrile onto an ester to form a benzolactam system.[257]

Nicolaou *et al.* used methanol as the solvent, while collaborators at USP performed a similar reaction using an EtOH:AcOH solvent system instead. For the ethyl 2-(2-cyanopyridin-3-yl)acetate **261**, the best conversion was achieved in 100% ethanol with the cyclised product collected in 41% yield [Scheme 5.2.2.6]. The yield from the intramolecular reaction was somewhat limited by the occurrence of intermolecular reactions. Nevertheless, the final product had been isolated and the complete synthesis is detailed in Scheme 5.2.2.7.

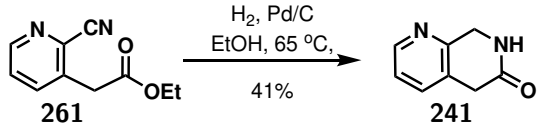

Scheme 5.2.2.6: Pd-catalysed reductive cyclisation of an aromatic nitrile onto an ester to form azabenzolactam **241**.

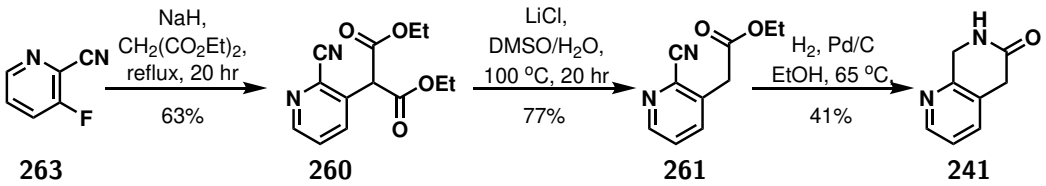

Scheme 5.2.2.7: Complete synthesis of 7,8-dihydro-1,7-naphthyridin-6(*5H*)-one **241**.

5.2.2.5 Other Analogues

With a complete synthetic route established, these conditions could be applied to the other halo-cyanopyridine analogues to generate all four desired azabenzolactams. Table 5.3 outlines the yields for each step.

Table 5.3: Synthesis of four analogues of the azabenzolactam scaffold.

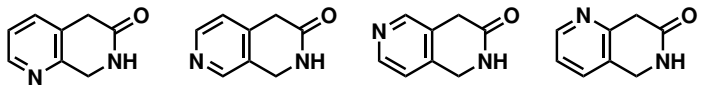

241 **242** **243** **244**

Entry	Target	S_NAr Yield	Krapcho Yield	Cyclisation Yield
1	**241**	63%	77%	41%
2	**242**	59%	52%	31%
3	**243**	50%	46%	47%
4	**244**	38%	46%	41%

There was limited variation in yield of the S_NAr reaction between *meta*- and *para*-substitution [Table 5.3, entry 1 to 3] which was likely due to the proximity of the electron-withdrawing *ortho*-cyano group dominating reactivity. The lower yield for the S_NAr reaction of 2-fluoronicotinonitrile **267** was surprising, as this substitution reaction was expected to be fast at *C*-2 [Table 5.3, entry 4]. This result was attributed to the low solubility of the substrate limiting the rate of reaction. Also the low yields of the reduction/cyclisation reaction across the series could likely be attributed to a slow rate of ring closure due to the absence of an acid-base catalyst in the reaction mixture.

The next objective was to explore methods of vectorial functionalisation. However, this would require significant quantities of each scaffold, making the low yields for this three-step synthesis undesirable. Therefore, first MYL undertook steps to further optimise the synthesis of the azabenzolactam scaffolds to establish a route that was more suitable for large scale synthesis.

5.2.2.6 Scale-up and Further Optimisation

To address the challenges with the large scale synthesis, MYL looked to further optimise each synthetic transformation in turn. While performing the S_NAr reaction on a five-gram-scale in THF, the substrate showed poor solubility and slow conversion. GCMS analysis of the crude reaction mixture showed significant amounts of the diethyl malonate remaining, suggesting the base had been consumed before the reaction was complete. Returning to 1,4-dioxane improved the solubility of the substrate while increasing the equivalents of NaH from 2.0 to 2.5 saw a further increase in yield. The product could now be isolated in 69% yield, almost double that achieved by JCF on a small scale [Table 5.3, entry 4].

The Krapcho decarboxylation was found to perform well on a larger scale. Increasing the temperature from 100 °C to 140 °C proved advantageous, increasing the rate of conversion and helping dispel the generated gases. Additional improvements were made by performing the Krapcho decarboxylation without first isolating the diethyl 2-(3-cyanopyridin-2-yl)malonate **268**. This streamlined procedure returned compound **269** in 61% yield over two steps, comparable to that of the total yield of the two separate steps [Scheme 5.2.2.8].

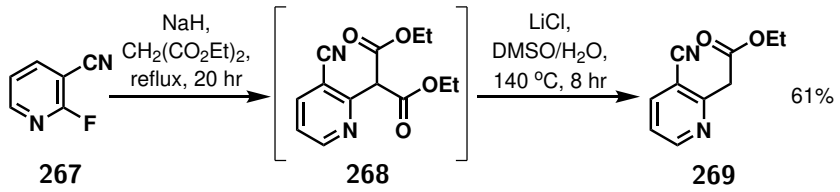

Scheme 5.2.2.8: One-pot S_NAr and Krapcho decarboxylation procedure.

Attention finally turned to the scale up of the reductive cyclisation step. In the small-scale reaction, treatment of **269** with H_2 in the presence of catalytic Pd/C afforded the cyclised product in 41% yield. On a larger scale, the conversion was significantly diminished and the product was challenging to isolate from any unreacted intermediate, returning isolated yields of less than 30%. There were few options for additional optimisation of this methodology due to the limited number of variables in the reaction. Therefore, alternative methods were explored for the hydrogenation and ring closing reactions.

Compared to hydrogen gas, sodium borohydride is a milder reducing agent and much safer to handle on large scale. It has also been employed in the reduction of a benzylic nitrile group to a primary amine in the formation of nonpeptide oxytocin receptor agonists [Scheme 5.2.2.9].[259] The presence of a cobalt chloride additive in this reaction had the added benefit of being a Lewis acid to promote the subsequent intramolecular cyclisation. Pleasingly, treatment of **269** with $NaBH_4$ and $CoCl_2$ in MeOH afforded the cyclised product and the scaled-up reaction afforded **244** in an isolated yield of 67% [Scheme 5.2.2.10]. This new methodology had the additional benefits of being safer to carry out without the need for large amounts of hydrogen gas and proceeding in less than 2 hours compared to the multi-day reactions of the previous methodology.

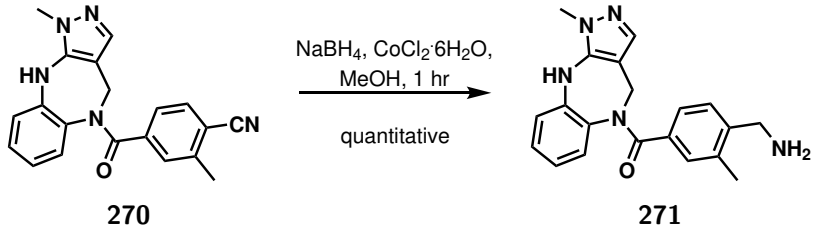

Scheme 5.2.2.9: Reduction of a benzylic nitrile group to a primary amine in the formation of nopeptid oxytocin receptor agonists.[259]

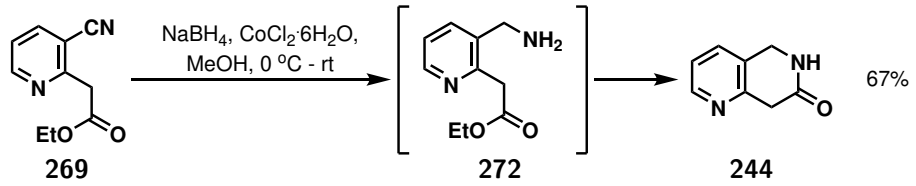

Scheme 5.2.2.10: Reduction and cyclisation of **269** for the formation of the bicyclic scaffold **244**.

It was expected that the reduction reaction would not be affected by an additional ester unit in the starting material (**268** vs **269**), making it possible to complete the hydrolysis reaction and the reduction reaction in a single step. To test this, the product of the S_NAr reaction **268** was treated directly with $NaBH_4$ and $CoCl_2$ which afforded the bicyclic scaffold in 67% yield. Thus, further route optimisation was achieved by combining the reduction and cyclisation, with the removal of the ester group, and the bicyclic scaffold could be generated in two steps [Scheme 5.2.2.11].

Scheme 5.2.2.11: Streamlined synthesis of 5,8-dihydro-1,6-naphthyridin-7(6H)-one **244**.

5.2.2.7 Summary

The azabenzolactams were chosen as a new scaffold of interest after concerns of low aqueous solubility of the pyrazolo[3,4-c]pyridine fragments. Still inspired by the "Rings of the Future", the semi-saturated scaffolds offered an increased sp^3-fraction. JCF first optimised conditions for the small-scale synthesis of the four azabenzolactam analogues by a three-step synthesis involving nucleophilic substituion, Krapcho decarboxylation, and reductive cyclisation. However, the application of these conditions on a larger scale highlighted additional challenges of this synthetic route. Further optimisation was then undertaken by MYL to develop a more efficient two-step synthesis of **244** by moving to a $NaBH_4$ reduction that facilitated the cyclisation *in situ*. These conditions were suitable for large-scale preparation, so with the new scaffolds in hand, attention turned to their vectorial functionalisation.

5.3 Vectorial Functionalisation Strategies

As discussed previously, an important part of any fragment-based drug development pipeline is the synthetic elaboration of hit fragments into larger, more potent lead molecules. Vectorial functionalisation, the ability to selectively introduce new functional groups at specific positions on a fragment core, plays a crucial role in hit-to-lead progression. With a robust and scalable synthesis of the azabenzolactams now in hand, the next goal was to develop methods of late-stage funtionalisation to access growth-vectors around the heterocyclic scaffold. These efforts could include *N*-methylation, Aldol condensation, and Minisci reactions, but the first position explored was the carbon adjacent to the amide nitrogen. Inaccessible by organic bases, pursuit of this position would require a method of aliphatic C-H activation. This led to an in-depth investigation into the electrochemical oxidation and subsequent arylation of cyclic amines.

5.3.1 Electrochemical Oxidation Overview

5.3.1.1 Basics of Electrochemical Reactions

Electrochemical synthesis describes the reactions of organic compounds promoted by a flow of electric current. It is different from standard chemical reactions because reacting species transfer electrons via an external electrical circuit rather than directly between ions or molecules.[260] This transfer of electrons that occurs at each electrode is described by a half-reaction, and the two half reactions together make up the whole electrochemical system. Each half-reaction has a thermodynamically determined redox potential which describes the tendency of a chemical species to undergo a single electron transfer. Due to inefficiencies specific to each cell design and operational conditions, the applied potential required to promote a reaction must be higher than the reaction's redox potential. This potential difference is described as the overpotential, which is the driving force of the reaction.

Generally considered as clean and environmentally benign, electrosynthesis is an attractive methodology with many advantages compared to conventional organic synthesis.[261] These advantages include improved reaction economy, reduced environmental impact, milder reaction conditions, and access to new reaction pathways that cannot necessarily be accessed by other synthetic methods.[261]

In an electrochemical reaction, the electrons can take the place of oxidants or reductants and so facilitate many transformations under metal-free conditions removing the requirements for toxic catalysts.[262] Furthermore, the current or voltage can be adjusted to alter the oxidation or reduction capacity of the electrochemical system as desired. Electrons can also take the place of nucleophiles or leaving groups which reduces waste and improves reaction economy.[263]

Another advantage is that electrochemical reactions are usually carried out under milder conditions than

traditional methods which may rely on elevated temperature or pressure.[264] The milder conditions often make for greater functional group tolerance, improving reaction scope or reducing the requirements for protecting groups.[262] This is particularly advantageous for medicinal chemistry as a means of late-stage functionalisation of drug-like molecules or as a way to improve the overall efficiency of a reaction sequence.

The series of discoveries that led to what is now known as electrosynthesis started in 1800 when Italian physicist Volta invented the first battery capable of maintaining a constant current, a prerequisite for any electrochemical reaction.[265] The next significant advancement came in 1833 when Faraday discovered the law of electromagnetism and then showed that hydrocarbons were formed by the electrolysis of an aqueous solution of potassium acetate.[266] Then in 1849, Kolbe reported the electrochemical oxidation of isovaleric acid forming isobutyl radicals and CO_2, a process now known as Kolbe Electrolysis [Scheme 5.3.1.1].[267] Due to these discoveries, Faraday and Kolbe are widely regarded as pioneers of organic electrochemistry.

Scheme 5.3.1.1: Kolbe Electrolysis.

Since the 1800s, electrosynthesis has been applied to many diverse transformations helped by new developments in processes and equipment. The simplest reaction setup has a single vessel with a reaction mixture connected to the power source through two electrodes; the working electrode initiates the single electron transfer for the reaction and the counter electrode completes the circuit. In some cases, the reaction proceeds via high energy intermediates which can be quenched prematurely by the counter electrode, preventing reaction. This can be overcome by using a *divided cell* in which the anodic and cathodic half cells are separated by a porous diaphragm or an ion-selective membrane [Figure 5.3.1.1, right]. An early example of the divided cell was described for the demineralisation of sugar syrup in 1890.[268] Another solution specific to cathodic reductions, is to use a sacrificial anode made from a readily oxidizable metal (eg. Zn, Fe, or Mg) as the oxidative dissolution of the anode occurs preferentially to the oxidation of any reaction intermediates.[269]

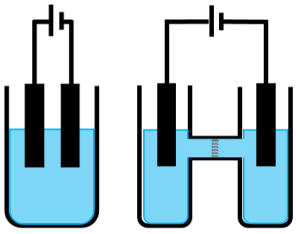

Figure 5.3.1.1: Schematic representation of an undivided (left) and a divided (right) electrochemical cell.

The high overpotentials required to initiate the single electron transfer may not be tolerated by certain functional groups in the substrate. In this case, *indirect electrolysis* by electronic mediators may be used to

bypass the high energy electron-transfer mechanisms and enable reactions to proceed at lower operational electrode potentials.[270] Common electronic mediators include triaryl amines, nitroxyl radicals, transition metal complexes, and ionic halides. For example, the mediator 4-acetamido-2,2,6,6-tetramethyl-piperidinedin-1-oxyl (ACT) was used to facilitate the oxidation of primary alcohols and aldehydes to their respective acids [Scheme 5.3.1.2].[271] The reactions were conducted at room temperature in an aqueous medium and the carbonate/bicarbonate buffer served as both the base and electrolyte for the reaction.

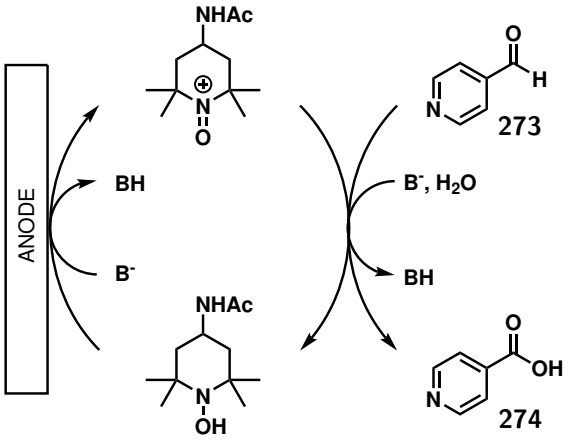

Scheme 5.3.1.2: The ACT-mediated oxidation of aldehyde **273** to carboxylic acid **274**.

Sometimes the reaction-limiting sensitivity is not in the electrolysis substrate at all, but in the other reagents present. For example, nucleophiles in an electrochemical system may be sensitive to competitive oxidation. This challenge was addressed with the invention of *cation pools* where carbocations are generated by electrochemical oxidation and accumulated in the absence of nucleophiles.[272] The carbocations then react with the nucleophiles in a separate step. The lifetime and stability of the generated cations often limits the versatility of this method and necessitates a more complex setup as the electrochemistry must be performed at cryogenic temperatures in a divided cell. These challenges may be overcome by the *cation flow* method where the cations are generated in a microflow electrochemical system and combined with nucleophiles in sequence.[272]

Electrochemical flow methodology has been applied elsewhere to improve the scope of reactions, for example in the one-step cathodic coupling of activated olefins with benzyl bromide derivatives reported by He *et al.*,[273] and it offers a route to scale-up electrochemical processes to kilogram amounts.[274] The innate scalability of electrosynthesis makes it an attractive methodology for industrial processes such as the electrochemical fluorination of hydrocarbons (Simons process)[275] and the synthesis of adiponitrile (Monsanto process) [Scheme 5.3.1.4].[276]

Electrochemistry has been used in a huge breadth of synthetic transformations, from electrogenerated acids[277] to electrogenerated bases,[278] from anodic oxidations to cathodic reductions, and to paired

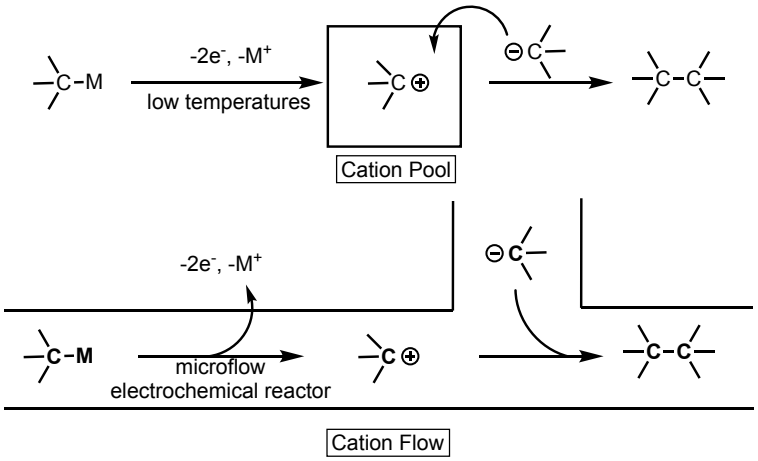

Scheme 5.3.1.3: Schematic representation of Cation Pool (top) and Cation Flow (bottom) electrochemical technologies.

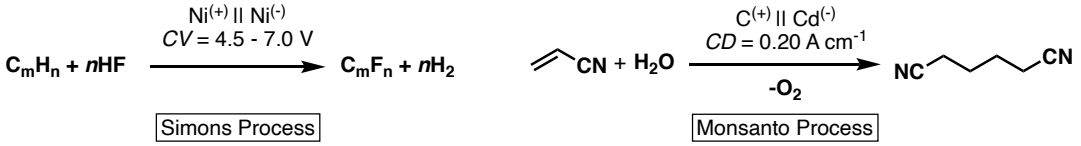

Scheme 5.3.1.4: The Simons process for electrochemical fluorination of hydrocarbons and the Monsanto process for the synthesis of adiponitrile.

electrolysis where two productive redox processes occur in the same vessel.[279] Space precludes a complete review of all methods of electrochemical synthesis, so the next section focuses on the transformation most relevant to the work undertaken in Section 5.4 for the functionalisation of cyclic amines.

5.3.1.2 Shono-type Oxidation

One of the most versatile electrochemical transformations is anodic oxidation to a cationic species that is then trapped by a nucleophile. When the reaction is carried out in an alcohol solvent, the reactive intermediate is trapped directly forming a stable C-O bond. For example, the anodic oxidation of amines initially generates an iminium cation which, when trapped by an alcohol, generates the α-alkoxy product as an isolable *N,O*-acetal [Scheme 5.3.1.5]. Although the anodic oxidation of amides was first reported by Ross *et al.* in 1966,[280] Shono and Matsumura really pioneered this line of research, exploring the anodic oxidation of *N,N*-dialkylcarbamates, sulfonamides, and amidophosphates, and demonstrating the utility of

the *N,O*-acetal intermediates.[281–286]

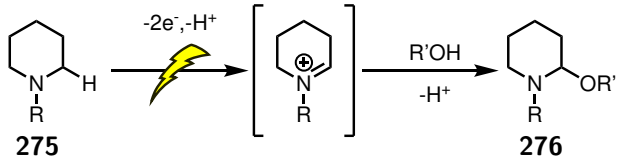

Scheme 5.3.1.5: General scheme of the Shono-oxidation.

The Shono oxidation has since become the standard electrochemical method for α-C-H oxidation of tertiary amides and protected amines, yet the mechanism remains under discussion. The oxidation is initiated by the single electron transfer from the nitrogen lone pair forming an *N*-cation radical (**II**), and ends at an iminium ion (**IV**) which is trapped by the nucleophilic solvent, often alcohol or water.[287] This is often described as proceeding via deprotonation to a *C*-centred radical (**III**), before a second single electron transfer forms the iminium ion [Scheme 5.3.1.6, pathway A]. However, the electrochemical oxidation of cyclopropane-substituted pyrrolidines, explored by Novaes *et al.*, gives evidence to support a more concerted proton-coupled electron transfer [Scheme 5.3.1.6, pathway B]. Ring-opening of cyclopropanes is rapid due to the released ring strain, yet as no radical-initiated ring opening of **III** to **VI** was observed, a concerted mechanism was more likely.[288] These observations were further supported by DFT calculations which found the second electron transfer to proceed at a more negative electropotential than the first, making it essentially barrierless. This explains the preferential generation of the iminium intermediate and formation of the *N,O*-acetals.

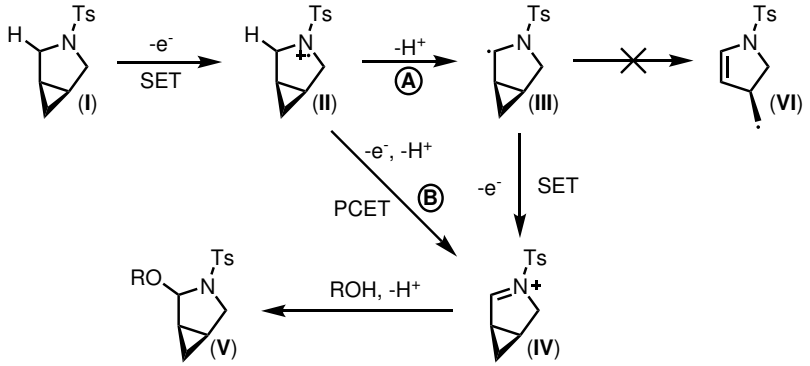

Scheme 5.3.1.6: Proposed mechanism for the anodic oxidation of cyclic amines.
SET=single electron transfer, PCET=proton-coupled electron transfer

Once isolated, the *N,O*-acetals obtained in Shono oxidations are ready for further reaction. Activation by Lewis acids such as $BF_3.OEt_2$ and $AlCl_3$ regenerates the iminium ions. These may then be treated with a range of nucleophile types. For example, triphenylphosphonium salts displaced the electrochemically introduced methoxy group of *N*-acyl-α-amino acids **277** to transform them into α-amidoalkylating agents **278** with the formation of a new C-P bond [Scheme 5.3.1.7.a].[289] Commonly employed carbon

nucleophiles include silyl enol ethers, as in the formation of cyclohexanone **279** [Scheme 5.3.1.7.b], as well as cyanotrimethylsilane and allyltrimethylsilane, as in the formation of allylpyrrolidine **280** [Scheme 5.3.1.7.c].[282,290,291] Nitrogen nucleophiles have also demonstrated utility, for example in the preparation of nazlinine **281**.[292] Here Kabeshov *et al*. combined the Shono oxidation of pyrolidine and other cyclic amines with a Pictet-Spengler cyclisation to yield a small library of indole alkaloids [Scheme 5.3.1.7.d].

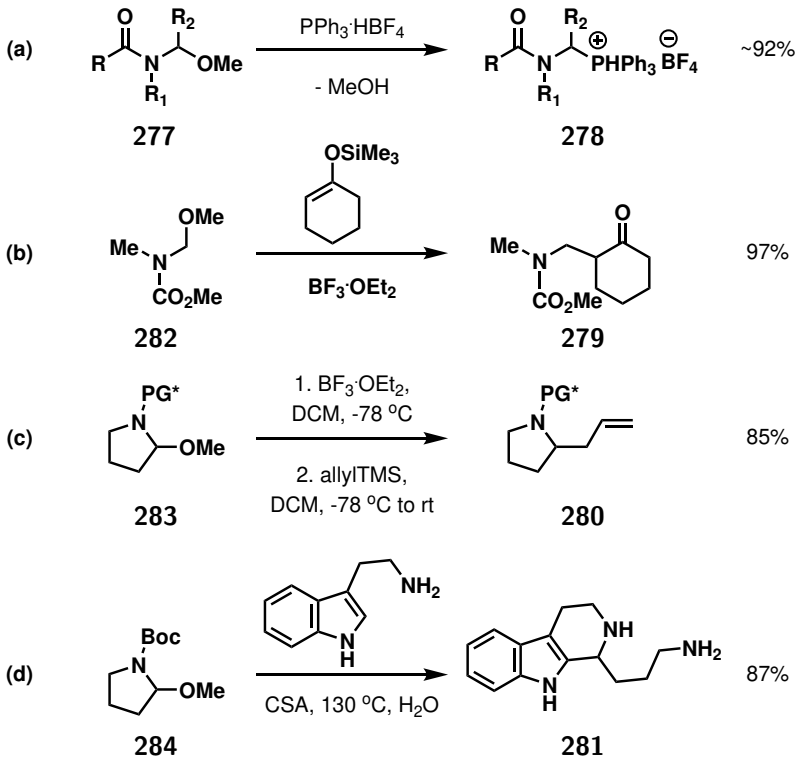

Scheme 5.3.1.7: Example applications for *N,O*-acetal products of the Shono oxidation.

More recent works have explored other electrochemical methods of α-functionalisation of cyclic amines. Gong and Huang developed a methodology for introducing a C-N bond in the α-addition of anilines **285** to *N*-methyl pyrrolidone (NMP) **286** [Scheme 5.3.1.8.a].[293] This methodology required a precise reaction set up to achieve the required selectivity because under standard conditions aniline is more easily oxidizable than NMP. This challenge was overcome by using a Pt-wire anode and a low concentration of aniline. The small surface area of the Pt-wire compared to a Pt-foil anode increased the current density, which increased the cell's overpotential. Meanwhile the high concentration of NMP close to the surface of the electrode promoted its oxidation over aniline. The conditions tolerated a range of commercial anilines generating 20 pyrrolidone and *N*-methyl pyrrolidone products. One drawback of this method is the large excess of NMP that is required (>20 equivalents), which limits the diversity that can be introduced to the amide coupling partner.

There are also increasingly reported examples of oxidations of amines promoted by electronic mediators. TEMPO is a popular reagent due to its stability in aqueous and non-aqueous media. The presence of mediators lowers the required overpotential which lowers the energy requirements, reduces the cost and environmental impact of the electosynthesis, and offers a route to more sensitive substrates. Moreover, TEMPO-mediated reactions experience higher turnover frequencies than non-mediated reactions leading to more efficient reaction progression.

A TEMPO mediator was used in the recently reported electrochemical direct aryl-coupling of pyrrolidines with benzene-1,4-dicarbonitrile [Scheme 5.3.1.8.b].[294] This reaction proceeded via a paired electrolysis, where the anodic Shono oxidation of pyrrolidine **287** was matched by the cathodic reduction of the benzonitrile **288**. Paired electrolysis is often limited by the stability of the anodic and cathodic intermediates so this reaction benefitted from the milder conditions afforded by the electronic mediator and the reaction yields almost doubled upon addition of TEMPO.

TEMPO-mediated electrochemical Shono oxidation was also utilised in the Cu-catalysed cross-coupling of tetrahydroisoquinolines **289** with terminal alkynes **290** [Scheme 5.3.1.8.c].[295] The redox mediator here was necessary to decrease the required overpotential and protect the sensitive nucleophiles and metal ligands present in the reaction mixture.

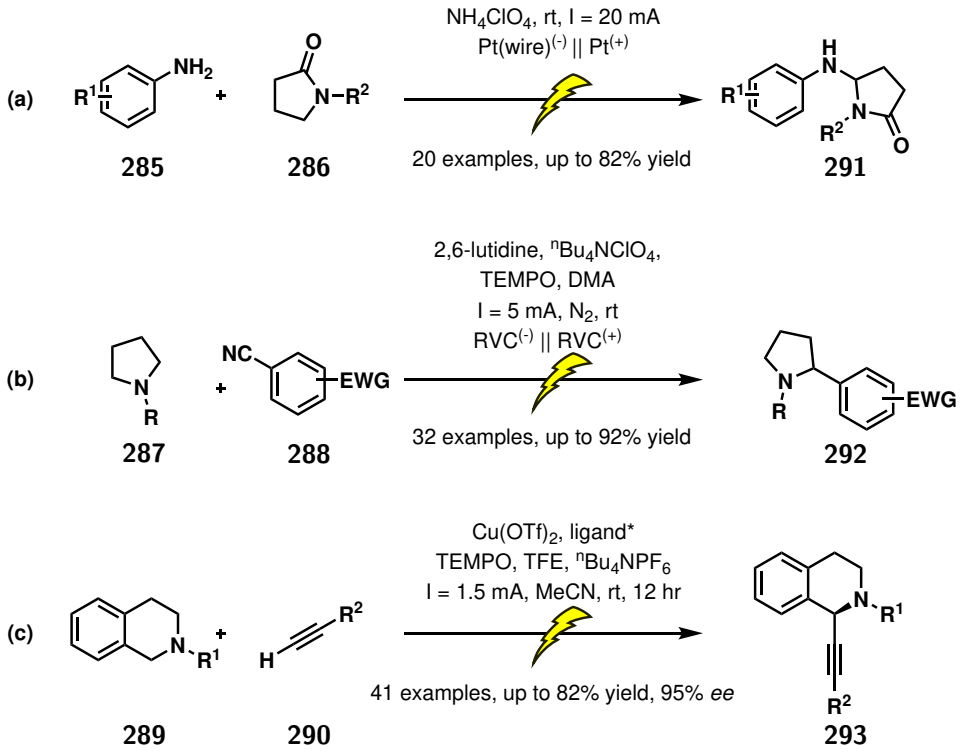

Scheme 5.3.1.8: Recent advances in applications of the Shono oxidation to synthetic chemistry.

In all of the examples thus far, the amine substrate has been relatively simple, either symmetrical or with

only one position readily oxidisable. Additional substituents on the α-carbon introduces new selectivity challenges. The original work of Shono and Matsumura predominantly focused on carbamates or acylated amines which were known to react on the less substituted α-carbon. Libendi *et al.* have further investigated this trend and found that the *N*-protecting group affected the stability of the iminium ion and controlled where the oxidation occurred. Carbonyl- and sulfonyl-based protecting groups always favoured the less substituted side (kinetic product) and only the use of cyano-protection afforded oxidation on the more substituted side (thermodynamic product).[291] This was a valuable addition to the anodic oxidation of cyclic amines and opened the possibility of 2,2-disubstitution by consecutive rounds of anodic oxidation to generate quaternary carbon centres [Scheme 5.3.1.9].

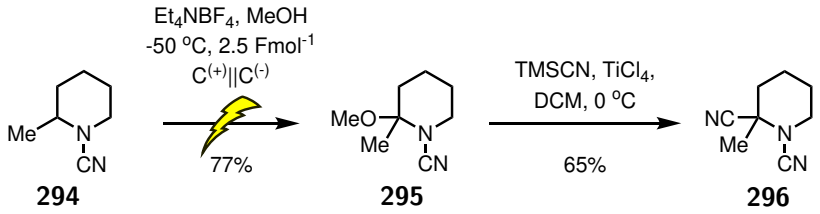

Scheme 5.3.1.9: Electrochemical oxidation route to generating quaternary carbon centres.

The question of selectivity means that Shono oxidations have generally been used only for the formation of structurally simple compounds or at early stages in complex syntheses. In particular the standard methodology does not tolerate substrates with free amines and sp^2-nitrogen atoms due to their propensity to undergo oxidation. This limits the applications of the Shono oxidation, and would exclude the azabenzolactams.

To address this gap, Lin described a modified-Shono oxidation to broaden the scope to include nitrogen containing substrates.[288] They introduced a trifluoroacetic acid additive to temporarily protect the sensitive nitrogen groups by way of an *in situ* protonation [Scheme 5.3.1.10]. This addition increased selectivity but suppressed the overall reactivity. This in turn was overcome by replacing the standard methanol solvent with trifluoroethanol (TFE). TFE has a higher redox potential than methanol so is less easily oxidised and is more stable to the anodic oxidation conditions. This improved the Faraday efficiency of the reaction and facilitated the use of greater overpotentials, enabling the activation of more obstinate substrates. The use of a fluorinated alcohol also provided a better leaving group in the *N,O*-acetal to aid the subsequent nucleophilic substitution reactions.

This represents an attractive methodology for the activation of aliphatic C-H bonds in nitrogen containing heterocycles with potential applications in late-stage functionalisation.

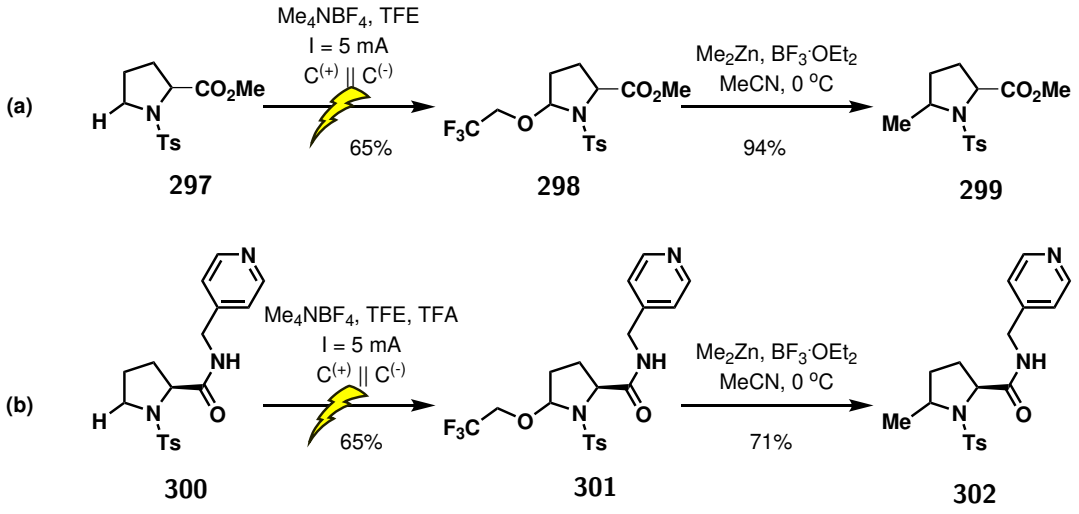

Scheme 5.3.1.10: Modified-Shono oxidation of cyclic amines for α-methylation.

5.3.1.3 Summary

Electrochemical synthesis is a powerful and versatile technique that compliments conventional organic synthesis. In particular, the Shono oxidation appears as an attractive method for the α-functionalisation of amine and amide substrates.

One limitation of the Shono oxidation was the poor tolerance to other nitrogen atoms present in the substrate. These introduced challenges of selectivity and off-target oxidations. This was addressed by Novaes *et al.* with modified conditions using TFE and TFA to access substrates containing basic amines and pyridine-like nitrogens.[288]

In this work, the *N,O*-acetals were subsequently reacted with the transition metal-based nucleophile dimethyl zinc to furnish a range of methylated products. The organozinc reagents, therefore, represent an unexplored opportunity for introducing further diversity into the amine substrates. The value of the *N,O*-acetals isolated from a Shono oxidation is the range of nucleophiles that can be introduced by the formation of new C-P, C-C, and C-N bonds. However, there are fewer examples of new sp^2-sp^3 bonds being introduced as aryl nucleophiles are less common. Aryl zinc nucleophiles are therefore a potential strategy to address this matter.

5.3.2 Boron-to-Zinc Transmetalation

Organozinc reagents are sources of carbon nucleophiles commonly used in the arylation of aldehydes.[296,297] First pioneered by Fu,[298] the arylation of aldehydes to prepare chiral diarylmethanols has received much attention as this is a valuable motif for many pharmacologically and biologically important compounds [Scheme 5.3.2.1].

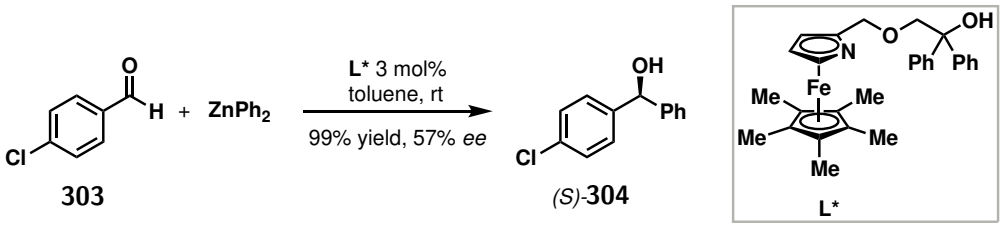

Scheme 5.3.2.1: First example of the arylation of aldehydes to generate a chiral diarylalcohol.[298]

Early methods used the reactive diphenylzinc as the nucleophile, yet selectivity was challenged by the competitive rate of the uncatalysed background reaction.[299] This was overcome by mixing diethylzinc and diphenylzinc, in a ratio of 2:1, to form ethylphenylzinc *in situ*.[299] Under these conditions, selectivity improved leading to higher enantiomeric excess (*ee*) and catalytic loading could be reduced from 10 mol % to 2.5 mol %. For example, the reaction of 4-chlorobenzaldehyde **303** afforded the desired alcohol **304** in 86% yield with 93% *ee* [Scheme 5.3.2.2].

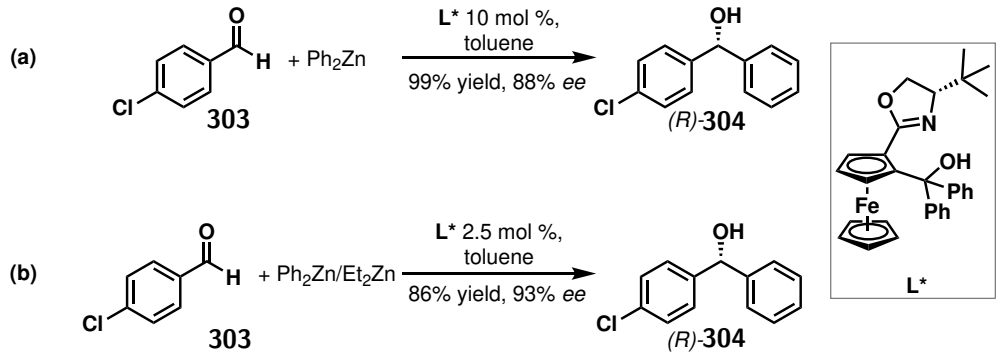

Scheme 5.3.2.2: Addition of a phenyl group to 4-chlorobenzaldehye **303**.[299]

A lot of research has focused on developing new catalysts to control the stereoselective addition of a phenyl ring, including planar chiral ferrocenyl oxazolines,[299] 2,2'-dihydroxy-1,1'-biphenyl derivatives,[300] and β-amino alcohols[301] [Scheme 5.3.2.3]. Yet all of these methods faced the same limitation. The scope of the transferable aryl group was limited to a phenyl ring because diphenylzinc was the only widely available commercial diaryl zinc reagent.

This limitation was addressed by a 2002 report from Bolm which significantly changed the field.[302] This

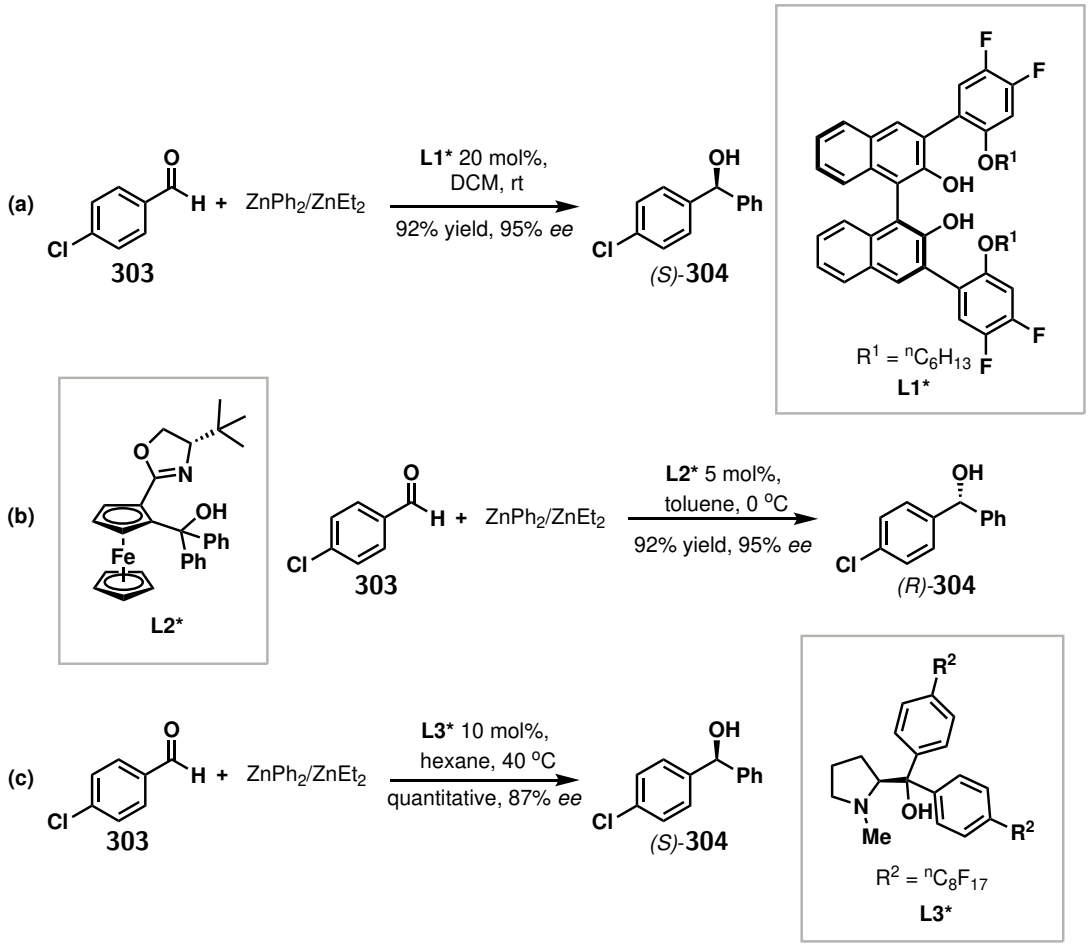

Scheme 5.3.2.3: Examples of ligands developed for the stereoselective addition of diphenylzinc to aromatic aldehydes.

approach used aryl boronic acids as the source of the transferable aryl group, preforming the aryl zinc species in a boron-to-zinc exchange reaction with diethylzinc before the addition of the aldehyde. Arylboronic acids offer a cheaper and less toxic alternative to the expensive diphenyl zinc and expand the scope to include substituted aryl groups. By this approach, both enantiomers of a given product can be prepared selectively with the same chiral ligand just by appropriate choice of reaction partners [Scheme 5.3.2.4].

In contrast to the much studied asymmetric addition to aldehydes, methods for the preparation of chiral amines by addition of organometallic reagents to C=N bonds were comparatively lacking. Tomioka *et al.* described a method using $Cu(OTf)_2$ and amidophosphine ligands for enantioselective addition of dialkylzinc to *N*-sulfonyl imines,[87] while Hoveyda and Snapper *et al.* reported a Zr-catalysed method employing a peptide ligand.[303] However, both of these methods required additional metal complexes and specially tailored ligands which are costly to prepare.

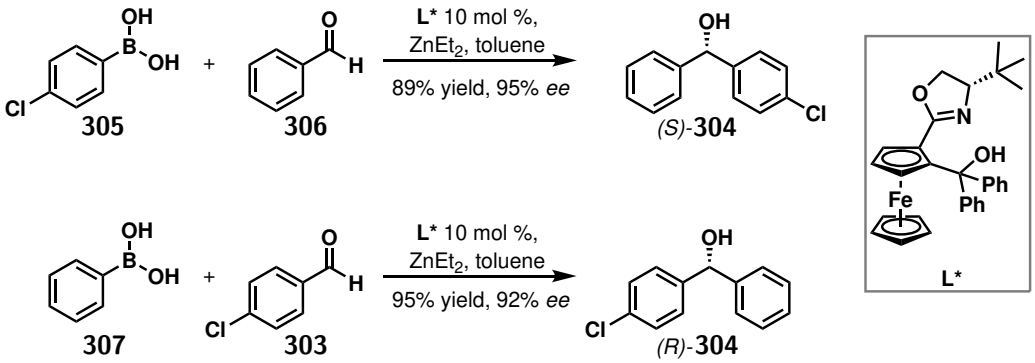

Scheme 5.3.2.4: Stereoselective addition of aromatic groups to aldehydes in the formation of chiral diarylmethanols.

Dahmen and Braise then reported a catalytic method for dialkylzinc addition to imines which required no additional metal (except the organozinc species) and made use of chiral β-amino alcohol ligands.[304] This was an attractive strategy as it could make use of the wealth of existing β-amino alcohol ligands that had been developed for the dialkylzinc additions to aldehydes. In this methodology, reactive *N*-acyl imines were generated from *N*-(formyl)-α-(*p*-tolylsulfonyl)benzylamines **308** by deprotonation and elimination of the sulfinate unit [Scheme 5.3.2.5]. In this report the methodology was also extended to the addition of phenyl groups by using a diphenyl/diethylzinc mixture as had been demonstrated for aldehydes previously. The combination of a [2,2]paracyclophane-based ligand and a diphenyl/diethylzinc mixture generated chiral diarylamines in excellent yields and enantioselectivity [Scheme 5.3.2.5].

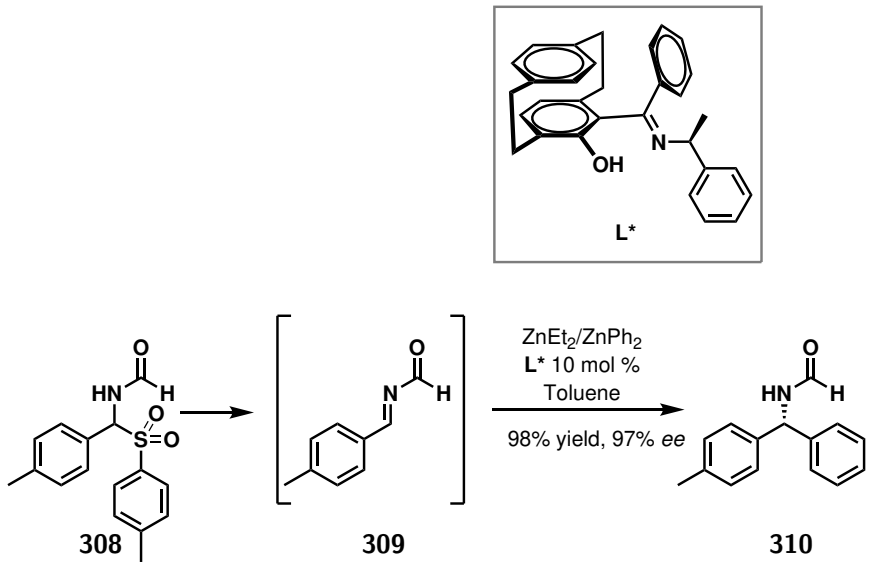

Scheme 5.3.2.5: Catalytic methods for the stereoselective addition of diphenylzinc to *N*-formyl imine **308**.

This methodology faced the same pitfall that the scope of the transferable aryl group was limited by the availability of diaryl zinc reagents. Following the precedent of the reactions with aldehydes, this limitation

was again addressed through the use of boronic acids.

The Ellman group found that the use of inorganic base K_3PO_4 played an important role in optimising the Rh-catalysed addition of aryl boronic acids to diverse aliphatic *N*-tosyl imines [Scheme 5.3.2.6.a].[305] Meanwhile Ma *et al.* developed a chiral C_2-symmetric cationic Pd^{2+} complex with *N*-heterocyclic carbene ligands for the enantioselective arylation of *N*-tosyl imines with aryl boronic acids [Scheme 5.3.2.6.b].[306] These conditions tolerated a range of aromatic imines and aryl boronic acids but relied on expensive metal catalysts.

Ni is often used as a low-cost replacement for Pd and more recent examples have also reported its application to this transformation.[307] The first Ni(II)-catalysed reactions employed a *tropos* phosphine-oxazoline biphenyl ligand returning a range of chiral amine products in yields up to 99% and enantioselectivities up to 99% [Scheme 5.3.2.6.c].[308] This methodology was also applied to the reaction of ketimines to generate α-tertiary amines [Scheme 5.3.2.6.d]. Ketimines substituted with small methyl and ethyl ester groups retained high selectivity, but other alkyl and aryl groups were not tolerated.

These reactions of ketimines are the only example of more complicated substrates and overall the current reaction scope is limited. Furthermore, all of these reactions were based on the reactivity of neutral imines, often formed from the corresponding aldehyde or through a multi-step synthesis from the primary amine.[305] There are no examples of tertiary amines reacting in this way which would involve a charged iminium intermediate.

Many of these approaches are also limited by the use of expensive and toxic heavy metals. While attempts have been made to address this by developing Ni catalysts, other strategies are still desirable. In particular, Zn is an attractive alternative as a first row transition metal with a low toxicity. Although the reaction with $ZnEt_2$/$ZnPh_2$ was demonstrated for the addition of a phenyl ring, other Zn-based nucleophiles are still lacking. Unlike the numerous reports of aldehyde arylation, the boron-to-zinc transfer remains underutilized in the realm of amine functionalisation.

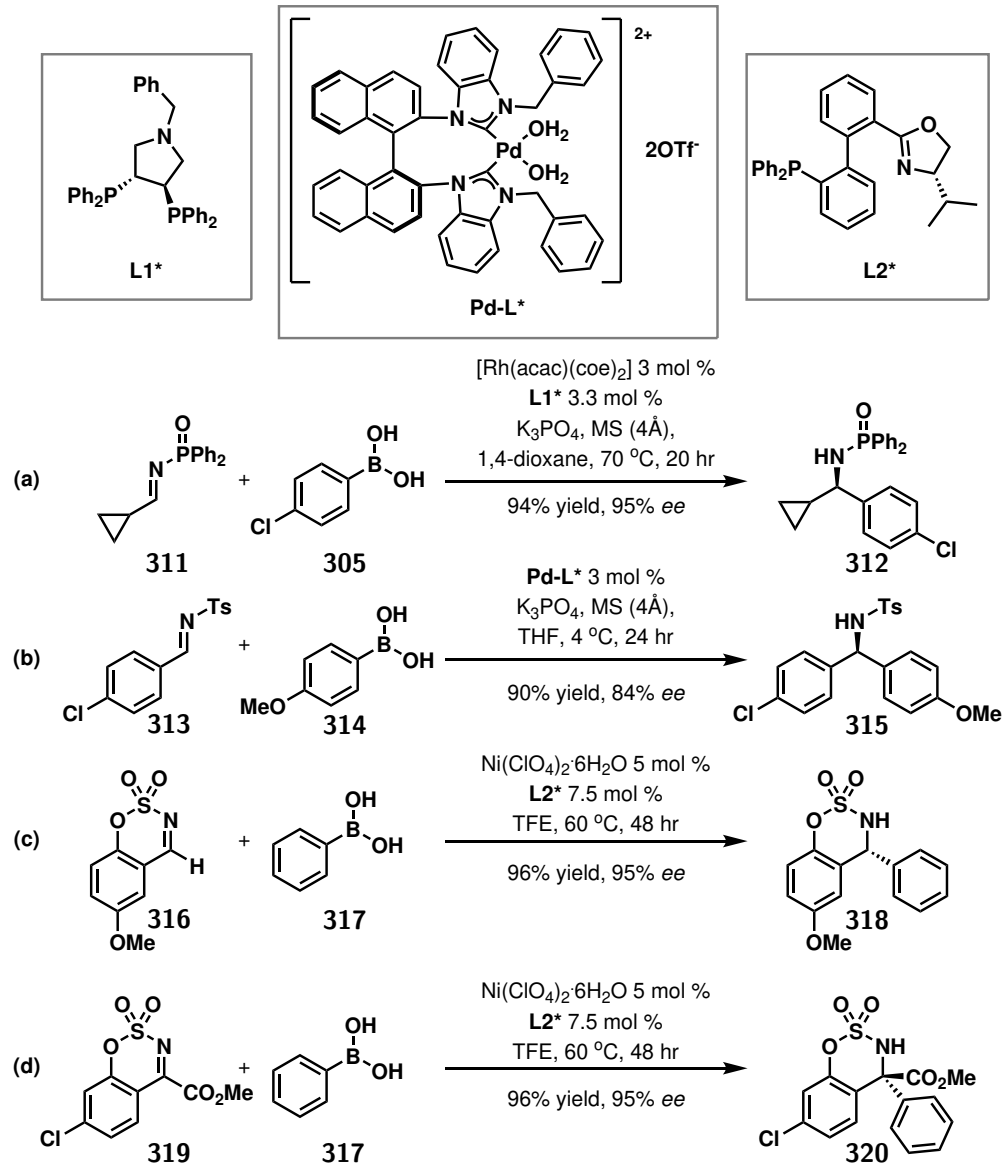

Scheme 5.3.2.6: Catalytic methods for the stereoselective addition of boronic acids to various imines.

5.4 Results and Discussion

5.4.1 α-arylation of Cyclic Amines

As discussed in Section 5.3.1.2, the Shono oxidation represents an attractive strategy for the activation of C-H bonds in aliphatic amines. The generated *N,O*-acetals may be subjected to a range of subsequent reactions including the substitution by organozinc reagents reported by Novaes *et al.*.[288] However, this methodology was limited by the small range of organozinc reagents that are commercially available. The aim of this chapter was to address these existing limitations by combining the electrochemical oxidation with the boron-to-zinc transmetalation described above. The proposed methodology is outlined in Scheme 5.4.1.1 and the synthetic efforts are described in the following sections.

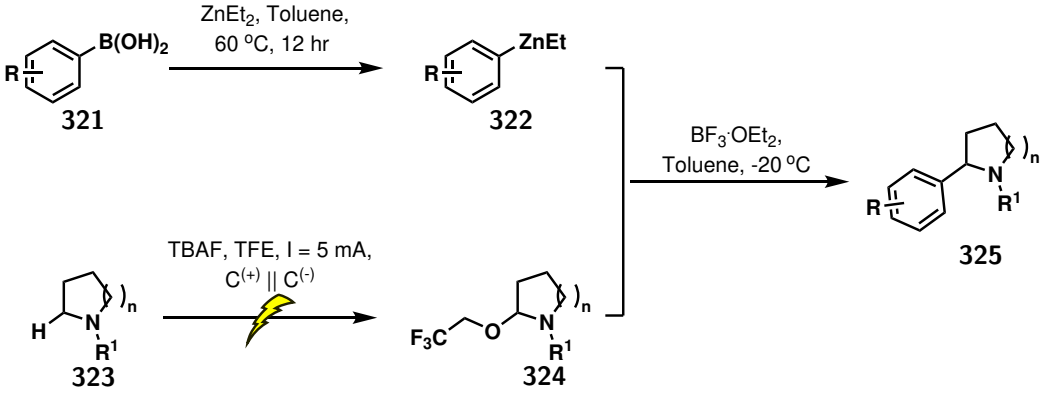

Scheme 5.4.1.1: Proposed methodology combining the Shono oxidation and boron-to-zinc transmetalation to furnish a library of arylated cyclic amines.

5.4.1.1 *N*-tosylation of Cyclic Amines

The electrochemical oxidation and arylation methodology was explored for a range of *N*-protected cyclic amines. The (4-methylphenyl)sulfonyl (tosyl) group was chosen because the generated *N,O*-acetals were stable and easy to handle due to the electron withdrawing nature of the sulfonamide. Sulfonamide compounds, also called sulfa drugs, have been reported for a broad range of therapeutic applications, so this strategy was also relevant to future medicinal chemistry applications.[309] Finally, as discussed by Shono[285] and Okumura,[310] the *N*-tosyl group can be removed by electrochemical reduction under mild conditions, although this chemistry was not explored here.

The *N*-tosylation of pyrrolidine **326** was conducted following the standard procedure reported by Kokotos *et al.*.[311] Pyrrolidine (1.00 eq) was treated with triethylamine (1.50 eq) followed by the addition of a solution of 4-toluenesulfonyl chloride (TsCl) (1.50 eq). After purification by chromatography, the desired product 1-((4'-methylphenyl)sulfonyl)pyrrolidine **327** was collected as a white solid in 91% yield [Scheme 5.4.1.2].

While successful in generating the desired product in good yield, a drawback of this approach was that flash column chromatography was required to isolate the product from the excess TsCl in the reaction mixture.

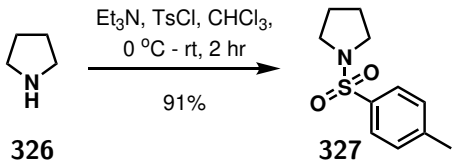

Scheme 5.4.1.2: Installation of the *N*-tosyl protecting group.

This problem was overcome by adapting the literature procedure to reduce the amount of TsCl to be the limiting reagent. For the preparation of *N*-tosyl piperidine **328**, piperidine **329** (1.50 eq) was treated with triethylamine (2.00 eq), followed by the addition of a solution of TsCl (1.00 eq). After all the TsCl had reacted, monitored by TLC, the reaction was quenched with H_2O then washed with HCl to remove the excess base. *N*-tosylpiperidine **328** was collected as a white solid in 93% yield without further purification and its purity was confirmed by the recorded melting point of 99-100 °C which agrees with the data in the literature.[312] This new procedure maintained high yields and removed the requirement for additional purification so was adopted for the remaining cyclic amine substrates. Figure 5.4.1.1 illustrates the *N*-tosyl amines that were prepared by this methodology, affording the desired products in good yields from 75-97%.

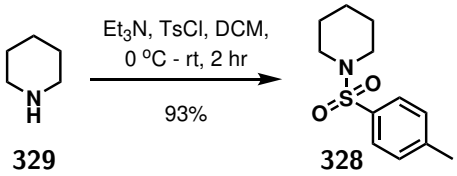

Scheme 5.4.1.3: Installation of the *N*-tosyl protecting group.

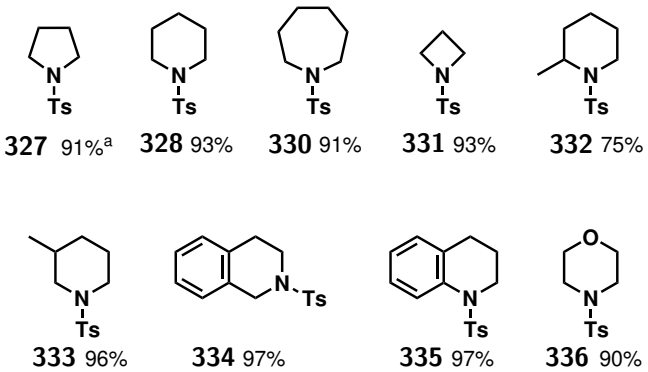

Figure 5.4.1.1: *N*-tosyl cyclic amines. [a] = prepared by the method in Scheme 5.4.1.2

5.4.1.2 Oxidation of *N*-tosyl Piperidine

Piperidine was chosen as a model substrate because the 6-membered ring closely resembles the target azabenzolactams. This was an important consideration as ring size and orbital geometry play a role in the stability of the intermediate radicals due to overlap and stabilisation from the nitrogen lone pair. The first objective was then to establish the reproducibility of the conditions for the modified-Shono oxidation reported by Novaes *et al*.[288]

The electrochemical cell (IKA ElectraSyn 2.0) was set up with two graphite electrodes, magnetic stirrer bar, *N*-tosyl piperidine **328** (0.30 mmol), TFE (4 mL), and tetrabutylammonium fluoride (TBAF) as the supporting electrolyte, then a constant current of I = 5 mA was applied. The overall oxidation reaction requires 2 electrons, however after 2 F mol^{-1} had passed there was only about 40% conversion to the product, identified by a peak at m/z = 238.22 in the LCMS corresponding to $[M\text{-}C_2F_3O]^+$. Increasing this to 3 F mol^{-1} returned product **337** in around 80% conversion as evidenced by the characteristic anomeric proton at 5.39 ppm in the ^{1}H NMR spectrum.

Initial attempts to purify the product identified an instability to chloroform leading to elimination of the trifluoroethyl side chain. Adjusting the chromatography solvent system to petroleum ether 40-60:DCM and exchanging the NMR solvent for acetone-*d6* afforded compound **337** in an isolated yield of 81% [Table 5.4].

Table 5.4: Conditions explored for the electrochemical oxidation of *N*-tosyl piperidine.

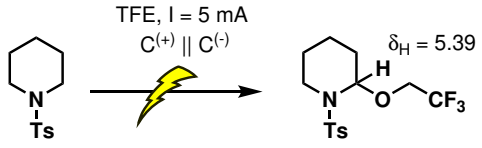

328 **337**

Entry	Electrolyte	Solvent	Charge	Yield
1	TBAF	TFE	2 F mol^{-1}	40%[a]
2	TBAF	TFE	3 F mol^{-1}	81%
3	Bu_4NBF_4	TFE	3 F mol^{-1}	46%
4	TBAF	MeCN (1.2 eq TFE)	3 F mol^{-1}	No reaction

[a] = conversion estimated from LCMS

To verify these as the optimal conditions, tetrabutylammonia tetrafluoroborate was also trialled as an electrolyte but this had a significant reduction on reaction efficiency. To test the solvent requirements, conditions were also explored for near-stoichiometric amounts of TFE (1.2 eq with MeCN as bulk solvent), but no product was isolated [Table 5.4, entry 4]. The requirements for an alcohol solvent were likely due to the instability of the iminium ion having a short lifetime at room temperature so a high concentration of alcohol was required to trap it quickly. It has also been discussed in the literature that

the alcohol helps facilitate the proton transfer to form the iminium in the first place.[288] Therefore, the standard electrochemical reactions were performed in TFE with TBAF as the supporting electrolyte.

When the electrochemical oxidation was performed on a larger scale, corrosion of the anode was observed and the reaction efficiency was reduced. This was overcome by alternating the polarity of the electrochemical cell on a 2-minute cycle. Hence the optimised conditions employed TBAF as supporting electrolyte, TFE as the reaction solvent, two graphite electrodes and the reaction run at a constant current of I = 5 mA, alternating every 2 minutes, until 3 F mol^{-1} had passed. Once all the substrate was consumed, the contents of the reaction vessel was washed into a clean flask with DCM and concentrated under reduced pressure. The desired *N,O*-acetal was then isolated by flash column chromatography. With this route to the *N,O*-acetal established, attention could turn to the second step and reactions with organozinc reagents.

5.4.1.3 α-Phenylation of *N*-tosyl Piperidine

The reactivity of the *N,O*-acetal was first demonstrated by simple trapping with $ZnEt_2$ which afforded the 2-ethyl piperidine **338** in 92% yield [Scheme 5.4.1.4]. This confirmed the lability to organozinc nucleophiles in the presence of a Lewis acid. While $ZnPh_2$ was available for the introduction of a simple aryl group, the power of the proposed transformation was in the ability to introduce a range of substituents. Therefore, conditions were explored to introduce the phenyl group starting from $PhB(OH)_2$ instead.

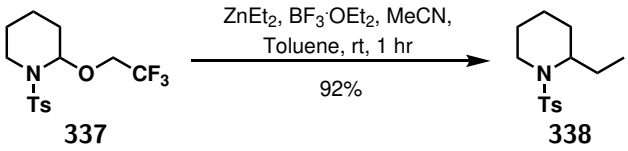

Scheme 5.4.1.4: Reaction of the *N,O*-acetal **337** with $ZnEt_2$.

Based on the seminal work of Bolm, a mixed aryl-alkyl zinc reagent could be generated by heating $PhB(OH)_2$ and $ZnEt_2$ in toluene for 12 hours.[302] Whilst these conditions successfully generated the desired α-phenylated amine **339** in 62% yield, a considerable amount of the ethyl product **338** was also isolated. It is not understood why this side reaction appears to be much faster in the reactions with iminium intermediates than has been reported in comparable reactions with benzaldehydes. Nevertheless, new conditions were explored to address this problem and improve selectivity for the phenyl product.

In these optimisation reactions, the ratio of the phenyl product **339** to the ethyl product **338** was monitored by ^{1}H NMR spectroscopy, comparing the integral of the α-proton at 5.27 ppm and 3.86 ppm respectively, using 1,3,5-trimethoxybenzene as an internal standard at 6.11 ppm. The results are shown in Table 5.5.

The 1:3 B:Zn ratio used in the initial reaction was well established in the literature.[313] This was believed

Table 5.5: Optimising the boron:zinc ratio for the formation of *N*-tosyl-2-phenyl-piperidine.

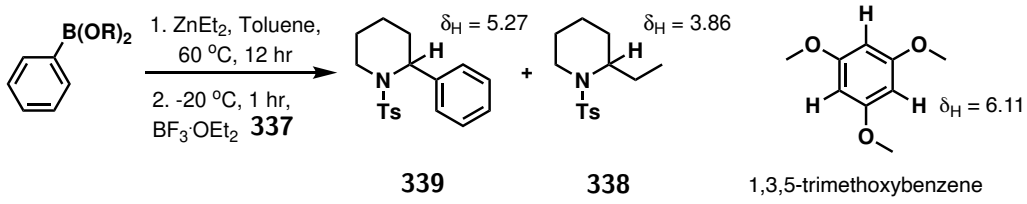

Entry	$ArB(OR)_2$	B:Zn	ZnX_2	temp.	339:338 ratio[a]	Isolated Yield
1	$PhB(OH)_2$ (2.4eq)	1:3	$ZnEt_2$ (7.2eq),	-20 °C	79:21	62%
2	PhB(pin) (2.4eq)	1:3	$ZnEt_2$ (7.2eq)	-20 °C	86:14	51%
3	PhB(pin) (2.4eq)	1:1	$ZnEt_2$ (2.4eq)	-20 °C	81:19	78%
4	PhB(pin) (4.8eq)	2:1	$ZnEt_2$ (2.4eq)	-20 °C	93:7	-
5	PhB(pin) (7.2eq)	3:1	$ZnEt_2$ (2.4eq)	-20 °C	98:2	-
6	PhB(pin) (2.4eq)	1:0.5	$ZnEt_2$ (1.2eq)	-20 °C	64:36	-
7	PhB(pin) (2.4eq)	0:1	None	-20 °C	No reaction	
8	PhB(pin) (2.4eq)	1:1	$ZnCl_2$ (2.4eq)	-20 °C	No reaction	
9	$TSMCH_2MgCl$	-	ZnPhCl	-20 °C	60:40[b]	-

[a] Product ratio determined by ^{1}H NMR [b] Side product substituted with -CH_2TMS not -Et

necessary for reactions with boronic acids due to coordination of the free oxygen to the zinc metal. Swapping to the boronic acid pinacol ester allowed for a reduction in the amount of $ZnEt_2$ required with no loss of efficiency [Table 5.5, entry 1 to 3]. Increasing the B:Zn ratio further saw an additional increase in the ratio of phenyl product **339** to ethyl product **338**. However, even with a generous excess of the boronic acid pinacol ester, it was not possible to entirely eliminate the ethyl product **338** and a trace could still be seen by analysis of the ^{1}H NMR spectrum [Table 5.5, entry 5]. Removing $ZnEt_2$ entirely from the reaction mixture, or replacing it with $ZnCl_2$, were both unsuccessful and no desired product was detected in either case [Table 5.5, entry 7 & 8].

Another class of organozinc reagents, reported by Berger *et al.*, was $Zn(CH_2TMS)R$, where R = alkyl or aryl group and TMS = trimethylsilyl group.[314] The authors employed -CH_2TMS as a "nontransferable ligand" to improve the efficiency of the addition of the desired R group. This strategy was demonstrated for the enantioselective addition of pentane to benzaldehyde, where using just 1.8 equivalents of the mixed zinc species **340** afforded the desired product **341** in 92% yield [Scheme 5.4.1.5]. The high efficiency of the reported transfer made this an attractive potential strategy.

To test this approach, the required zinc reagent was prepared according to the methodology reported by Berger *et al.*[314] $ZnCl_2$ (1 M in THF) was added to a solution of PhLi (1.9 M in Bu_2O) at -78 °C to generate ZnPhCl. This solution was then treated with $TMSCH_2MgCl$ (1 M in Et_2O) to generate the desired

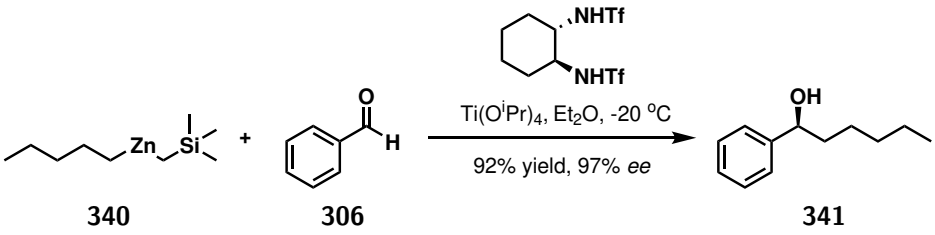

Scheme 5.4.1.5: Literature example of the alternative organozinc reagent $Zn(CH_2TMS)R$.[314]

$ZnPh(CH_2TMS)$ **342** which was transferred into dry toluene for reaction with *N,O*-acetal **337** [Scheme 5.4.1.6.a]. Despite the reported efficiency of the reaction with benzaldehyde, the efficiency of the formation of phenyl product **339** was not improved for the piperidine substrate [Table 5.5, entry 9]. Furthermore, the need for additional steps to generate the zinc reagent made this route less favourable.

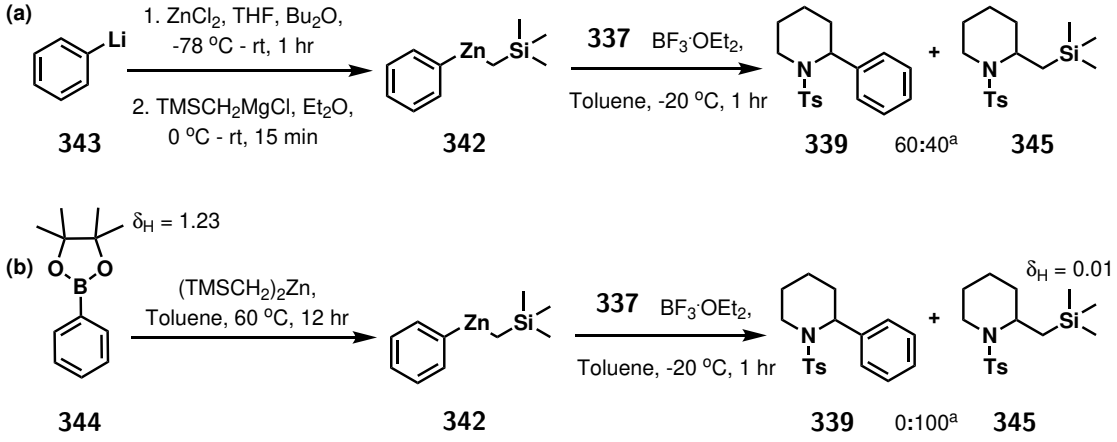

Scheme 5.4.1.6: Exploring conditions for the formation of *N*-tosyl-2-phenyl-piperidine using $ZnPh(CH_2TMS)$.
[a] = product ratio calculated from ^1H NMR spectra

In an attempt to reduce the synthetic steps, conditions were also explored for generating $ZnPh(CH_2TMS)$ **342** by replacing $ZnEt_2$ with $Zn(CH_2TMS)_2$ in the reaction with PhBpin [Scheme 5.4.1.6.b]. However, there was no evidence for the phenyl product **339** in the crude ^1H NMR spectrum. Instead the 2-CH_2TMS product **345** was identified by a strong peak at 0.01 ppm, corresponding to the silylmethyl groups, and significant amounts of phenyl boronic acid pinacol ester **344** were identified by the characteristic methyl singlet at 1.23 ppm. This indicated that the transmetallation step was unsuccessful and that this route was not viable.

A 1:1 ratio of ArBpin and $ZnEt_2$ was, therefore, chosen as the best balance of conversion and reaction economy. With these standard conditions established, attention then turned to optimise the reaction conditions for the substitution step.

The first element investigated was the Lewis acid. While previous reports relied on four equivalents of boron

trifluoride etherate ($BF_3{\cdot}OEt_2$),[288] there was no loss in conversion upon reducing this to stoichiometric amounts [Table 5.6, entry 1 & 2]. In the absence of the Lewis acid, no reaction was seen even with extended reaction times and elevated temperatures [Table 5.6, entry 5 & 6]. This was consistent with previously reported observations and confirms that a Lewis acid was required to activate the *N,O*-acetal to reaction.[313,315]

Table 5.6: Optimising conditions for the formation of *N*-tosyl-2-phenyl-piperidine by variation in the Lewis acid.

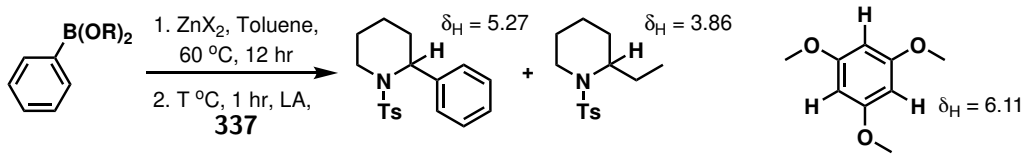

Entry	Lewis acid	ZnX_2	T	Yield 339[a]	Yield 338[a]	Ratio
1[b]	$BF_3{\cdot}OEt_2$ (4 eq)	$ZnEt_2$	-20 °C	51%[c]	11%[c]	82:18
2	$BF_3{\cdot}OEt_2$ (1 eq)	$ZnEt_2$	-20 °C	70%	16%	81:19
3	$BF_3{\cdot}OEt_2$	$ZnEt_2$	-20 °C to 0 °C	27%	4%	87:13
4	$BF_3{\cdot}OEt_2$	$ZnEt_2$	-78 to -20 °C	45%	28%	61:39
5	No $BF_3.OEt_2$	$ZnEt_2$	-20 °C	No reaction		
6	No $BF_3.OEt_2$	$ZnEt_2$	-20 to 25 °C	No reaction		
7	$ZnCl_2$	$ZnEt_2$	-20 °C	3%	trace	-
8	no additional LA	1:1 $ZnCl_2$:$ZnEt_2$	-20 °C	No reaction		
9	$BF_3{\cdot}OEt_2$	1:1 $ZnCl_2$:$ZnEt_2$	-20 °C	11%	24%	32:68
10	$AlCl_3$	$ZnEt_2$	-20 °C	0%	0%	*
11	$Ti(O^iPr)_4$	$ZnEt_2$	-20 °C	0%	0%	*
12	$Ti(O^iPr)_4$	$ZnEt_2$	-78 to -20 °C	0%	0%	*
13	$TiCl_4$	$ZnEt_2$	-20 °C	14%	13%	51:49
14	$TiCl_4$	$ZnEt_2$	-78 to -20 °C	34%	27%	56:44
15	TMSOTf	$ZnEt_2$	-78 to -20 °C	3%	11%	24:76
16	TMSOTf	$ZnEt_2$	-20 to 25 °C	9%	3%	75:25

[a] Product ratio determined by ^1H NMR
[b] Reaction performed with $PhB(OH)_2$ instead of PhB(pin)
[c] Isolated yield
* Significant starting material remaining

Subsequently, a range of other Lewis acids was tested with product formation again monitored by ^1H NMR spectroscopy. $ZnCl_2$ was trialled in various combinations with $ZnEt_2$ and $BF_3{\cdot}OEt_2$ but was found unsuitable for the aryl transfer and inefficient as a Lewis acid with only limited product generation [Table 5.6, entry 7 to 9]. Other options, $AlCl_3$ and $Ti(O^iPr)_4$, also left much of the acetal unreacted [Table 5.6, entry 10 to 12]. $TiCl_4$ did lead to more efficient substitution, but even at lower temperatures

this was at the cost of selectivity between ethyl and aryl transfer [Table 5.6, entry 13 & 14]. TMSOTf was also disappointing, with the desired phenyl product generated in low yield with poor selectivity [Table 5.6, entry 15 & 16]. Therefore, 1 equivalent of $BF_3{\cdot}OEt_2$ was adopted as the standard conditions for the remainder of the study [Scheme 5.4.1.7].

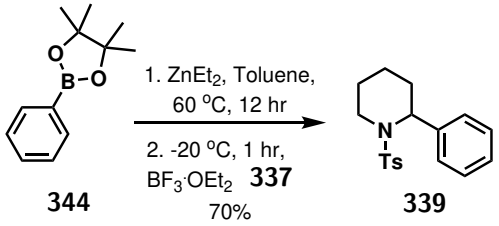

Scheme 5.4.1.7: Arylation of piperidine to generate **339** under standard conditions.

The effects of the nitrogen protecting group were also explored. An electron withdrawing group on the nitrogen was essential to stabilise the radical intermediate so an amide was chosen as an alternative to the sulfonamide group. This was introduced by treating piperidine **329** with triethylamine followed by 4-methylbenzoyl chloride. The reaction was quenched with H_2O, then washed with HCl, before purification by flash column chromatography afforded the desired product **346** as a white solid in 84% yield [Scheme 5.4.1.8].

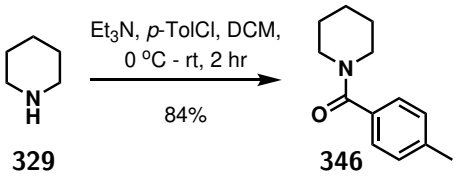

Scheme 5.4.1.8: Installation of the 4-methylbenzoyl (*p*-Tol) protecting group.

Treatment of this substrate with the standard electrochemical conditions gave *N,O*-acetal **347** in good yields of 70% [Scheme 5.4.1.9]. The substitution reaction of this substrate was also successful albeit requiring elevated temperatures and prolonged reaction times to provide comparable yields [Scheme 5.4.1.10]. This was likely due to an increased stability of the acetal and a higher barrier to forming the iminium ion caused by greater coordination of the nitrogen lone pair into the amide-carbonyl bond. This coordination was evident in the ^{1}H NMR spectrum by the existence of rotamers causing a broadening of the peaks corresponding to the protons on the piperidine ring compared to the sharp peaks for the aromatic protons (7.28 and 7.34 ppm).

5.4.1.4 Variation in the Aryl Boronic Acid

With a set of robust conditions for the efficient generation of *N*-tosyl-2-phenyl-piperidine **339**, attention turned to expanding the scope of this reaction sequence through variation of the aryl coupling partner. The

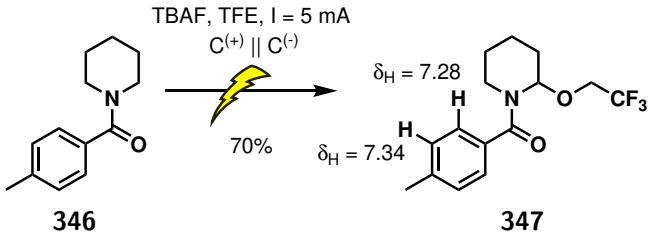

Scheme 5.4.1.9: Electrochemical oxidation of piperidine **346** under standard conditions.

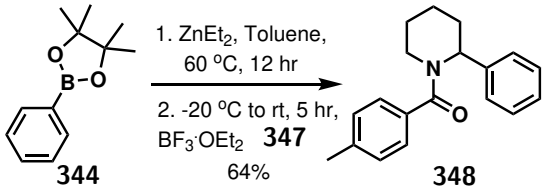

Scheme 5.4.1.10: Arylation of piperidine **347** under standard conditions.

same conditions that were established for the introduction of a phenyl group were explored for a range of boronic acids and pinacol esters [Figure 5.4.1.2]. Good overall yields could be realised with arenes possessing electron donating substituents, generating piperidines substituted with a 4-methylphenyl **349** and 4-methoxyphenyl **350** group in good yields. Similarly, an allyl substituent could be introduced with comparable efficiency generating *N*-tosyl-2-allyl-piperidine **351** in 72% yield.

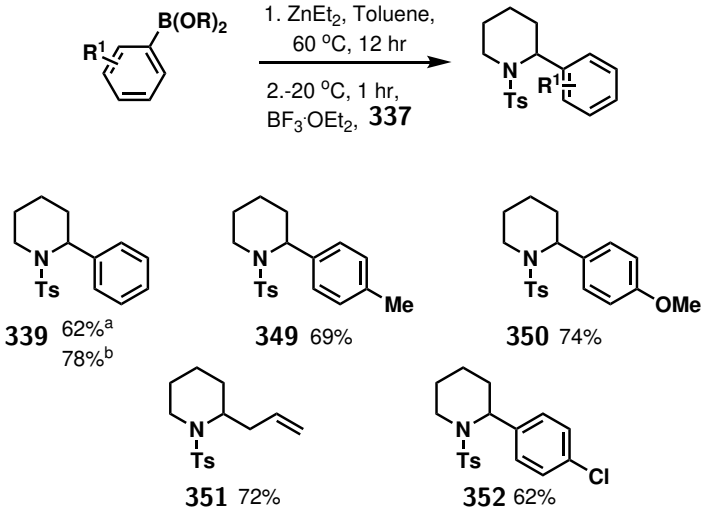

Figure 5.4.1.2: Scope of the arylation reaction of **337** with a range of boronic acids and esters.

[a] Reaction with $PhB(OH)_2$ [b] Reaction with PhB(pin)

In contrast, the electron deficient 4-chlorophenyl boronic acid led to poorer conversion, requiring twice as long until all the *N,O*-acetal was consumed, and affording the substituted piperidine **352** in 62% yield. The yield-limiting factor in this case was the competing reaction of ethyl transfer. Strongly electron withdrawing

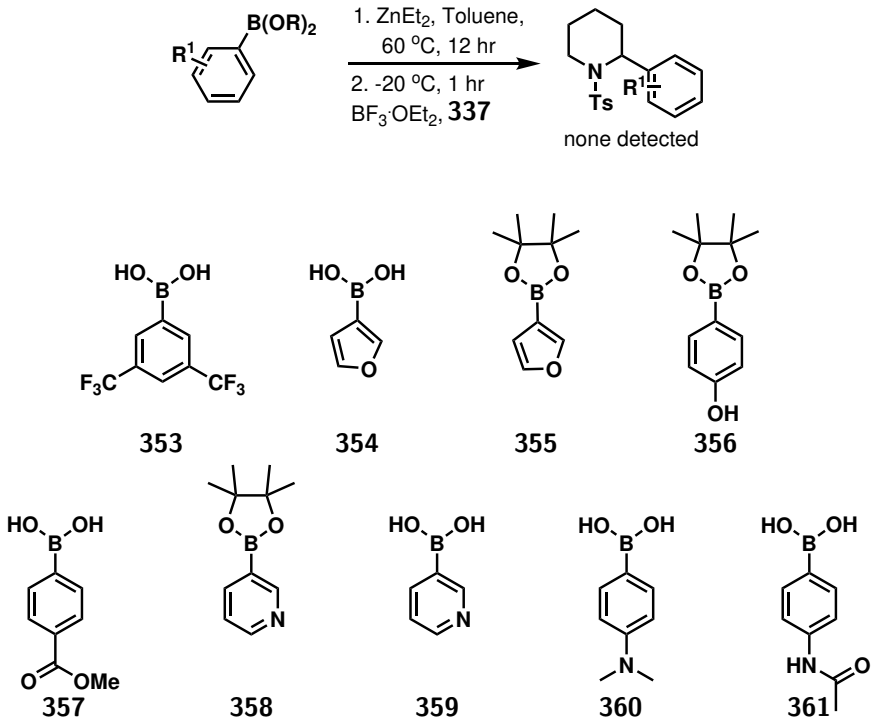

Figure 5.4.1.3: Limitations of the arylation reaction of **337** with various boronic acids and esters.

groups further deactivated the aryl transfer as evidenced by the reaction with bis-trifluoromethyl boronic acid **353** leading to mostly ethyl transfer with only a trace of the desired product seen by a peak at m/z = 452.22 in the LCMS corresponding to $[M + H]^+$ [Figure 5.4.1.3].

The poor reactivity of electron poor boronic acids was consistent with reports in the literature. In a study of the reaction kinetics of the boron-to-zinc transmetalation for the arylation of aldehydes, Jimeno *et al.* found that, while the transmetalation process should not vary with the electronic nature of the aryl boronate, there is a marked effect on the kinetics of the arylation step.[313] The effect was exemplified by comparing the two routes to forming compound **362** or **363** [Scheme 5.4.1.11]. Faster reaction times were observed when the electron-donating groups were on the aryl group being transferred and the electron-withdrawing groups were on the aldehyde substrate. This trend likely explains why reactions of very electron-poor aryl boronic acids are absent from the literature.

The attempted reactions with furan-based boronate esters led to rapid decomposition of the furan reagent upon addition of the Lewis acid. Chan *et al.* reported the formation of both enantiomers of furan-2-yl(phenyl)methanol **366** starting from either the furanyl or the phenyl boronic acid in the presence of a binaphthyl-amino alcohol ligand [Scheme 5.4.1.12].[316] This report shows that boron-to-zinc transmetallation of furan is possible and that furanylzinc is a suitable nucleophile. Therefore, the incompatibilities observed here could instead be accounted for by the oxygen competing for coordination to the Lewis acid preventing the desired reaction.

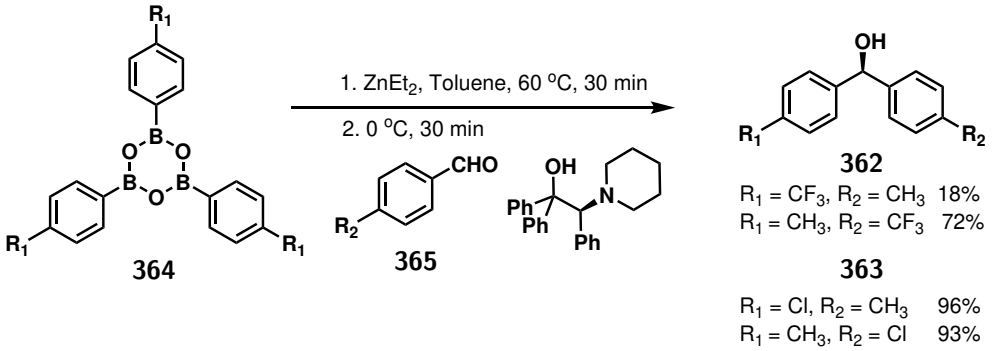

Scheme 5.4.1.11: Effects of electron withdrawing/donating groups on the rate of aryl transfer.

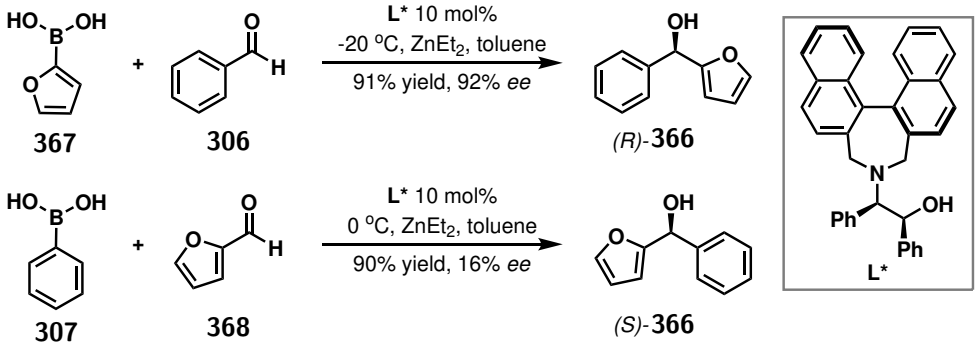

Scheme 5.4.1.12: Literature example of successful boron-to-zinc transmetallation and arylation reactions with furan-containing reagents.[316]

Other unsuccessful reactions include those with hydroxyphenyl, methyl benzoate, pyridine, and aniline boronate reagents [Figure 5.4.1.3]. These reactions predominantly led to the formation of elimination product **369** as evidenced by the two alkenyl signals in the ^{1}H NMR spectra at 6.65 ppm (6-*H*) and 4.99 ppm (5-*H*). This observation indicates that neither an aryl or ethyl zinc reagent was available for reaction with the forming iminium ion suggesting the zinc metal was deactivated by coordination to the lone pairs of the heteroatom.

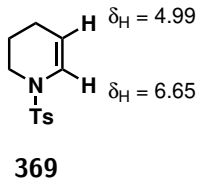

369

Figure 5.4.1.4: The elimination product 1-((4'-methylphenyl)sulfonyl)-1,2,3,4-tetrahydropyridine **369**.

5.4.1.5 Variation in the Cyclic Amine

After establishing the extent of variation that could be introduced through the aryl boron reagents, efforts turned to explore the variation that was possible in the cyclic amine substrate. Building on the standard conditions optimised for the piperidine substrate, cyclic amines with different sized rings were explored [Figure 5.4.1.5]. Pleasingly, electrochemical oxidation of *N*-tosyl azepane **330** was equally viable affording *N,O*-acetal **370** in 67% yield. Good yields were also possible for the pyrrolidine substrate **327** generating *N,O*-acetal **371** after a simple modification of the electrolyte to Me_4NBF_4 [Table 5.7, entry 1 & 2].

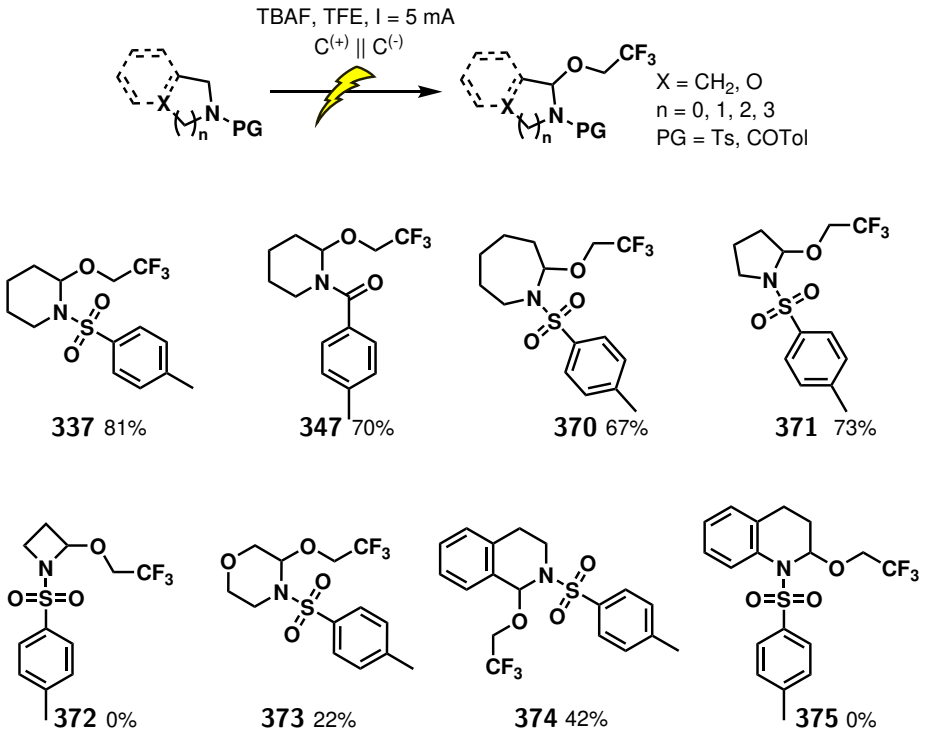

Figure 5.4.1.5: *N,O*-acetals generated from a range of cyclic amines.

Electrochemical oxidation of azetidine **331** was observed by the appearance of a peak at m/z = 228.18 in the LCMS which corresponds to the $[M\text{-}C_2HF_3]^+$ ion. However, this reaction was not efficient and the *N,O*-acetal **372** was not stable enough to be isolated. Instead the linear products **376** and **377** were isolated, albeit in low yields [Figure 5.4.1.6]. This is consistent with reports in the literature that the anodic oxidation of *N*-formyl azetidine **378** goes via a cyclic *N,O*-acetal intermediate **379** to afford *N*-(3,3-dimethoxypropyl) formamide **380** in 83% yield [Scheme 5.4.1.13].[317,318] This likely occurs by an acid-catalysed ring opening which is promoted by releasing the strain in the 4-membered ring. It is interesting to note that electrochemical reactions of 4-membered lactams have been reported for the formation of 4-acetoxy-2-azetidinone **381** [Scheme 5.4.1.14], indicating that the presence of a carbonyl in the ring is required to stabilise the iminium intermediate in these rections.[319]

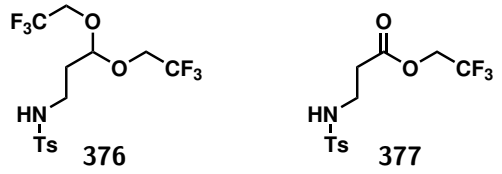

Figure 5.4.1.6: Ring opening products isolated from the anodic oxidation of azetidine **331**.

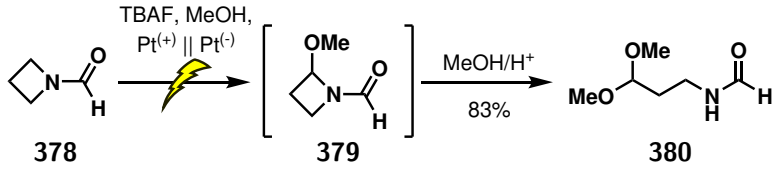

Scheme 5.4.1.13: Literature example of acid-catalysed ring opening of *N*-formyl azetidine upon anodic oxidation.[318]

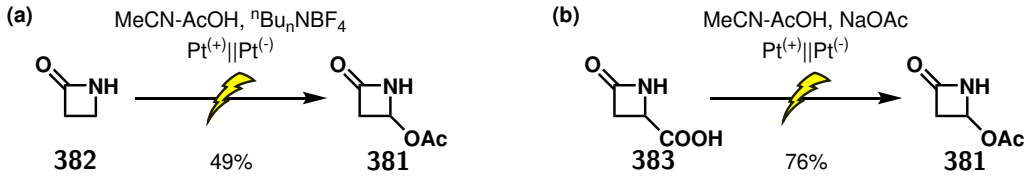

Scheme 5.4.1.14: Literature example of electrochemical reactions to form 4-acetoxy-2-azetidinone **381** by **a)** an anodic oxidation and **b)** a Kolbe-type electrolysis.[319]

The electrochemical oxidation of more complex cyclic amines was also explored. *N*-tosyl morpholine **336** reacted selectively α to the nitrogen atom to afford *N,O*-acetal **373** and, consistent with this, pyran did not undergo the initial oxidation step under the standard conditions. All attempts to oxidise benzo-fused

Table 5.7: Variation in electrolyte for the electrochemical oxidation of more challenging substrates.

Entry	Substrate	Electrolyte	Duration	Product	Yield
1	**327**	TBAF	3 F mol^{-1}, I = 5 mA	**371**	35%
2	**327**	Me_4NBF_4	3 F mol^{-1}, I = 5 mA	**371**	73%
3	**331**	TBAF	3 F mol^{-1}, I = 5 mA	**372**	0%[a]
4	**331**	Me_4NBF_4	5 F mol^{-1}, I = 10 mA	**372**	0%[a]
5	**331**	TBAF	3 F mol^{-1}, I = 15 mA	**372**	0%[a]
6	**335**	Me_4NBF_4	3 F mol^{-1}, I = 5 mA	**375**	No reaction[b]
7	**335**	TBAF	3 F mol^{-1}, I = 5 mA	**375**	No reaction[b]
8	**334**	Bu_4NBF_4	3.5 hr, I = 10 mA	**374**	50% by NMR
9	**334**	TBAF	3 F mol^{-1}, I = 5 mA	**374**	90% by NMR (42%)[c]

[a] Isolated ring opening products **376** and **377** [b] SM recollected [c] Isolated yield in brackets

derivatives proved to be challenging. The *N,O*-acetal from tetrahydroisoquinoline **374** could be isolated in low yield whereas tetrahydroquinoline **335** did not afford any observable *N,O*-acetal **375** upon electrochemical oxidation. This parallels reported observations in the literature.[288] Attempts to improve efficiency of the electrochemical oxidation of these two substrates by varying the electrolyte were also unsuccessful [Table 5.7, entry 6 to 9]. Nevertheless, sufficient amounts of tetrahydroisoquinoline *N,O*-acetal **374** had been isolated [Figure 5.4.1.5], so the substitution reactions for this and the other *N,O*-acetals could be explored.

Following the standard boron-to-zinc transmetalation procedure, the substitution reactions of the varied *N,O*-acetals afforded a range of arylated cyclic amines in generally good yields [Figure 5.4.1.7]. Of particular interest is the reaction of morpholine **373** which, despite lower yields in the oxidation step, was the most efficient substrate in the arylation step. Similarly, generating tetrahydroisolquinoline **374** was low yielding in the oxidation step, but showed comparable reactivity in the substitution step. This pattern indicates that a lower stability of the *N,O*-acetals hindered its initial generation but promoted its subsequent reaction with the organozinc reagents.

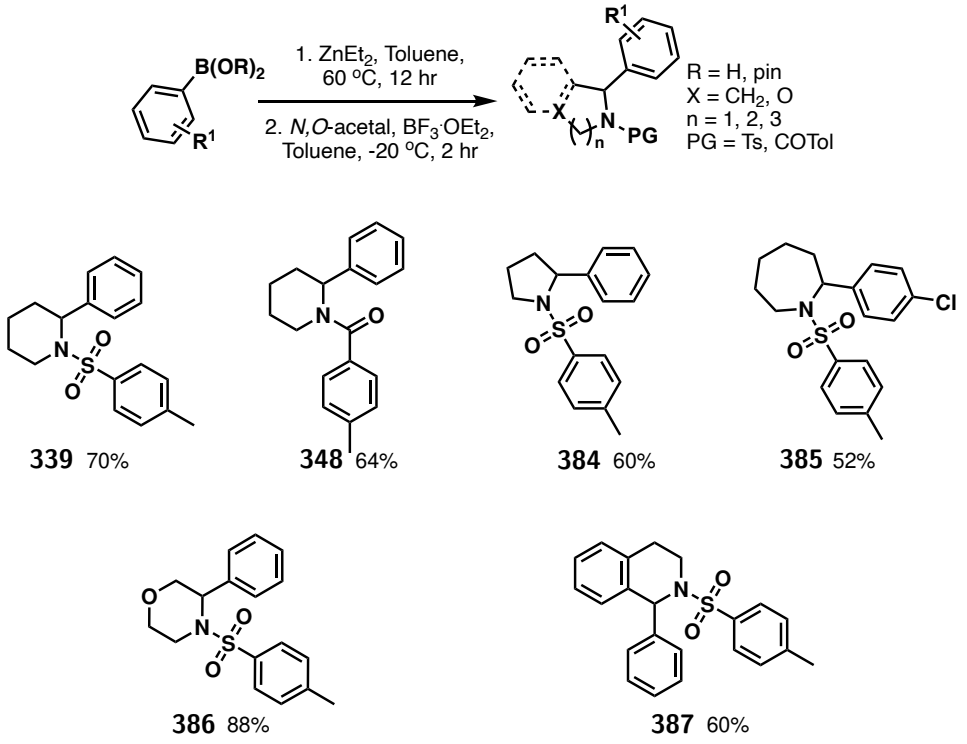

Figure 5.4.1.7: The α-arylated products generated from a range of cyclic amines.

5.4.1.6 Substituted Piperidine Rings

The final aspect to be explored was the effects of additional substituents in the piperidine ring. Oxidation of 2-methyl piperidine **332** under standard conditions occurred exclusively on the less hindered 6-position

to afford the *N,O*-acetal **388**, evidenced by the anomeric proton at 5.45 ppm [Scheme 5.4.1.15]. This was in agreement with previous work reported by Libendi *et al.* who found that the *N*-protecting group affected the regiochemistry of the oxidation with carbonyl- and sulfonyl-based protecting groups always favouring the less substituted side and only the use of cyano-protection favouring oxidation on the more substituted side.[291] This trend occurs because the carbonyl- and sulfonyl-based protecting groups stabilise the less substituted iminium **389** so it is comparably stable to the more substituted iminium **390**. Reaction then occurs at the less sterically hindered position [Figure 5.4.1.8].

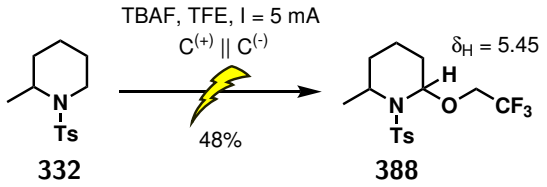

Scheme 5.4.1.15: Electrochemical oxidation of 2-methylpiperidine **332**.

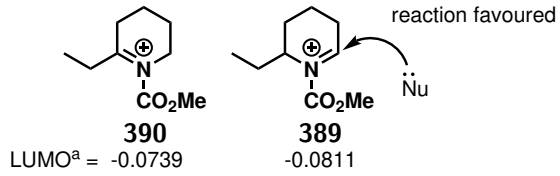

Figure 5.4.1.8: Analysis of iminium stability reported by Libendi *et al.*[291]

[a] = reported values for the LUMO calculated using DFT/6-31G* method of Gaussian 03 software

Treatment of the isolated *N,O*-acetal **388** with $ZnEt_2$ afforded the 2-ethyl-6-methyl piperidine **391** in high yields [Scheme 5.4.1.16]. The regiochemistry was confirmed by observing two peaks for a C*H* group α to the nitrogen corresponding to 2-*H* (3.90 ppm) and 6-*H* (4.11 ppm). Only one set of signals was observed in the ^{1}H NMR spectrum, implying the formation of a single diastereomer. The absence of any cross peaks in the NOE NMR spectrum suggests this could be the trans product, however further investigation is necessary to confirm the final product conformation.

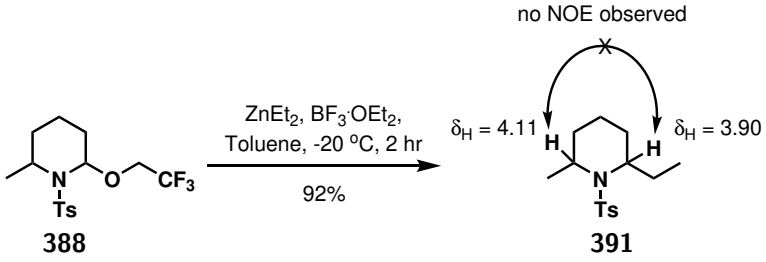

Scheme 5.4.1.16: Ethylation of 2-methylpiperidine **388**.

Following this success, the *N,O*-acetal **388** was treated with the standard arylation conditions with 4-chlorophenyl boronic acid **305** [Scheme 5.4.1.17]. The arylated product was collected as a mixture with

a ratio of 1:1.3 and a total yield of 21%. Only one peak was observed in the LCMS, corresponding to the $[M(^{35}Cl) + H]^+$ ion at m/z = 364.28, yet two sets of peaks were observed in the NMR spectra, indicating these were diastereomers of **392**. The presence of two peaks for an α-C-*H* group confirms that both products have the aryl group on *C*-6. Comparison of the $J_{H\text{-}H}$ coupling values for the 2-*H* proton between the products (major isomer: doublet, J = 5.6 Hz; and minor isomer: double-doublet, J = 7.0, 4.3 Hz) indicated that the major isomer has the aryl group in a more axial position while the minor isomer has the aryl group more equatorial. Due to the complex coupling of the other C-H signals, further analysis was not possible and the cis/trans configuration could not be identified. This reaction was less efficient than the ethylation, taking 4 hours until all the starting material was consumed and generating significant amounts of the elimination product **393** (36% yield) and the ethyl product **391** (26% yield).

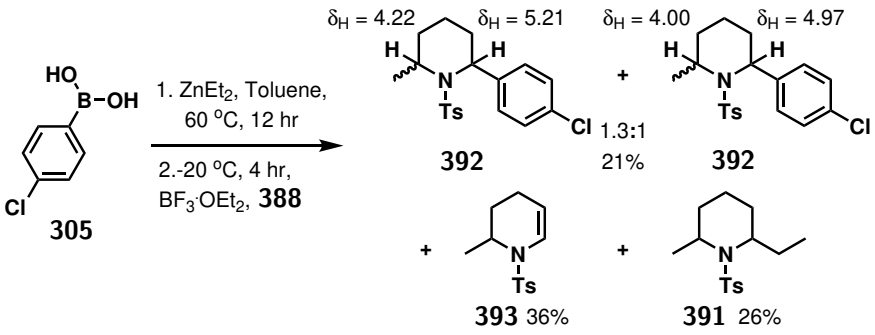

Scheme 5.4.1.17: Arylation of 2-methylpiperidine **388**.

Reactions of the 3-methyl piperidine substrate returned an even more complicated mixture of products. The electrochemical oxidation generated four isomers which could not be separated by chromatography. The crude ^{1}H NMR spectrum contained four signals corresponding to the anomeric proton; two triplets corresponding to diastereomers of 5-methyl-2-trifluoroethoxypiperidine **394**, and two doublets corresponding to diastereomers of 3-methyl-2-trifluoroethoxypiperidine **395** [Scheme 5.4.1.18]. It was clear from the product ratio (6:53:32:9) that although oxidation had not been completely selective, there was still a preference for reaction at the less hindered position. For all four *N,O*-acetals, the signal for the anomeric proton showed $J_{H\text{-}H}$ coupling values in the range 2-5 Hz. This indicates that the proton was in the equatorial position as any axial-axial coupling would have given rise to a larger coupling constant ($J > 8$ Hz).[320] This observation is consistent with the anomeric effect, which describes the preference of electronegative atoms to favour the axial position when adjacent to a heteroatom in the ring, though it gives no indication of the configuration of the methyl group.

To test the relative reactions of the different *N,O*-acetal isomers **394** and **395**, this mixture was treated with $ZnEt_2$. The total conversion of this reaction was 87% with the generated product as a mixture of four isomers, the expected structures are shown in Scheme 5.4.1.19. Unfortunately, individual isomers could not be isolated and structural assignment was challenged by the many overlapping CH_2 peaks in the

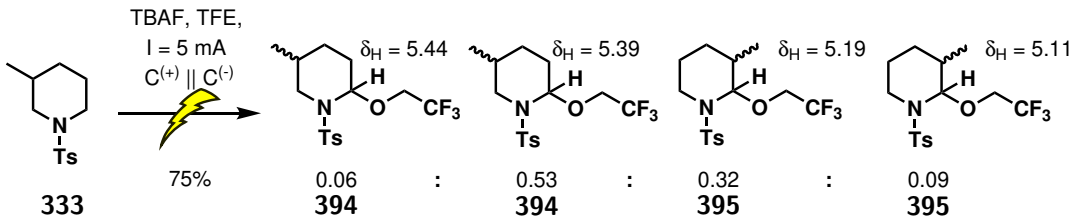

Scheme 5.4.1.18: Electrochemical oxidation of 3-methylpiperidine **333**. Product ratios determined by ^{1}H NMR spectroscopy.

^{1}H NMR spectrum meaning the major isomer could not be identified. Only trace amounts of an elimination product was observed, highlighting the efficiency of the ethyl transfer compared to the arylation of 2-methylpiperidine **388** above. This was identified as the 5,6-elimination product **396** by the two alkenyl signals in the ^{1}H NMR spectra at 6.65 ppm (6-*H*) and 4.95 (5-*H*), while none of the 2,3-elimination product **397** was observed [Figure 5.4.1.9]. This likely reflects the greater amount of 5-methyl-2-trifluoroethoxypiperidine **394** in the starting material.

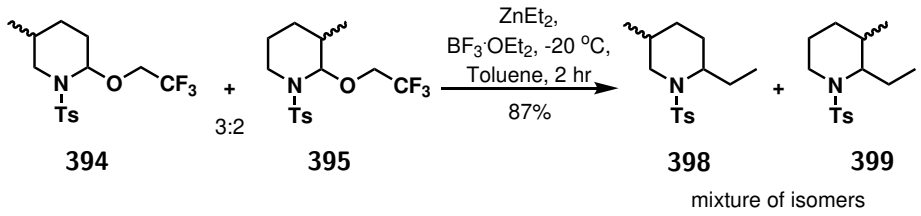

Scheme 5.4.1.19: Ethylation of 3-methylpiperidine **394** and **395**.

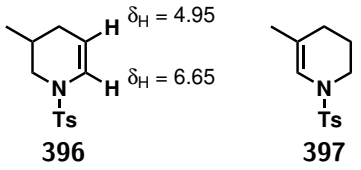

Figure 5.4.1.9: Elimination products from the reaction of 3-methylpiperidine **400**.

5.5 Conclusions and Future Work

A new two-step methodology was identified as an attractive approach for the α-functionalisation of the cyclic amines. This combined a modified Shono oxidation with trapping with TFE followed by a substitution reaction by an aryl zinc, generated *in situ* from the corresponding aryl boronic acid, in the presence of a Lewis acid. The scope of this methodology was explored with variation in both the aryl zinc reagent and the amine substrate.

While substitution was possible for electron rich and mildly electron poor aryl boronic acids, giving the desired products in good overall yields of 52-88%, more work is needed to extend this methodology to incorporate electron poor aryl groups and other basic functionalities. In the case of aniline and pyridine containing boronic acids, the limitation was the boron-to-zinc transmetalation. It is, therefore, necessary to explore other routes to generate the aryl zinc reagent. For example, C-H activation by TMPMgCl·LiCl generates an organomagnesium species that can be transmetalated to zinc by stirring with $ZnCl_2$ [Scheme 5.5.0.1.a]. As discussed in Section 2.2.3.2, this methodology is tolerant to nitrogen heterocycles and the nitrogen lone pair helps direct the metal to control selectivity. Another possible strategy was briefly explored in Table 5.5, generating ZnPhCl from the corresponding phenyl lithium and $ZnCl_2$. This was an undesirable route to phenyl piperidine **339** due to the additional steps. However, this route could be an attractive strategy to access specific aryl groups that are not amenable to the standard boron-to-zinc transmetalation due to the range of aryl lithium reagents available [Scheme 5.5.0.1.b].[321]

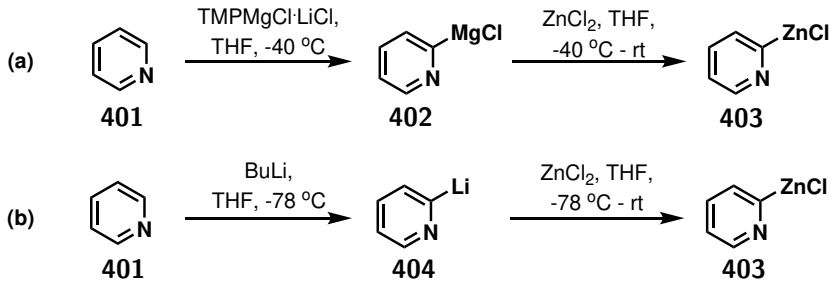

Scheme 5.5.0.1: Alternative routes to 2-pyridyl zinc chloride **403**

Variation in the amine substrate was broadly tolerated, furnishing 8 different *N,O*-acetals. However, challenges in selectivity arose for substituted piperidine rings with activation of 2-methyl and 3-methyl piperidine giving intractable product mixtures. The isomer mixtures recovered from reaction of these unsymmetrical cyclic amines highlights the need for a regio- and diastereoselective method. As discussed previously, the asymmetric arylation of aldehydes is generally catalysed by chiral β-amino alcohol ligands which coordinate to the zinc metal. Unfortunately, these were not compatible with the requirements for a Lewis acid as they interact with each other instead. An alternative strategy to control the reaction would be with a chiral protecting group on the nitrogen. The proximity of the nitrogen to the reaction centre

means a large protecting group may exert enough control over the approaching nucleophile to afford a selective reaction.

Chiral auxiliaries in the form of sulfur- and phosphorous-based protecting groups have been reported by Royer and colleagues for the Shono oxidation of cyclic amines, affording methoxylated products in diastereomeric ratios (*dr*) up to 70/30.[322,323] In most cases, these chiral auxiliaries also controlled the addition of allyltrimethylsilane to the methoxy compounds [Scheme 5.5.0.2].[290] The ability of the chiral protecting group to control other substitution reactions have not yet been explored making it a compelling strategy to apply to this two-step functionalisation. The use of chiral auxiliaries could be a promising route to arylate cyclic amines in a diastereoselective manner.

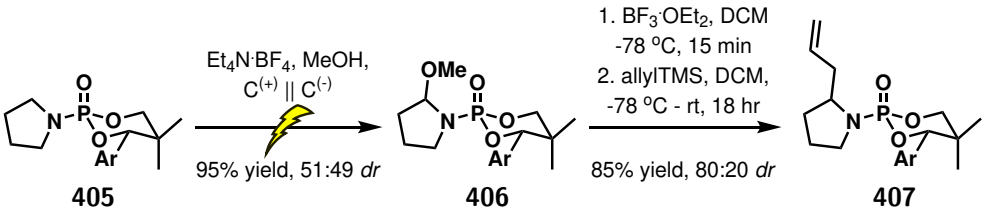

Scheme 5.5.0.2: Asymmetric allylation of piperidine using a chiral phosphorous protecting.[290]

To extend the methodology described in this chapter, further work is needed to optimise the conditions for more complicated amines to improve the efficiency of the oxidation of substrates such as tetrahydroisoquinoline. To extend the substrate scope to include the azabenzolactams, this would likely require the use of TFA to transiently protect the basic nitrogen functionalities against oxidation, as described by Novaes *et al.* [Scheme 5.5.0.3].[288] This methodology would then offer a route to the *N,O*-acetals that could be treated with a range of aryl zinc reagents to afford the desired α-arylated azabenzolactams.

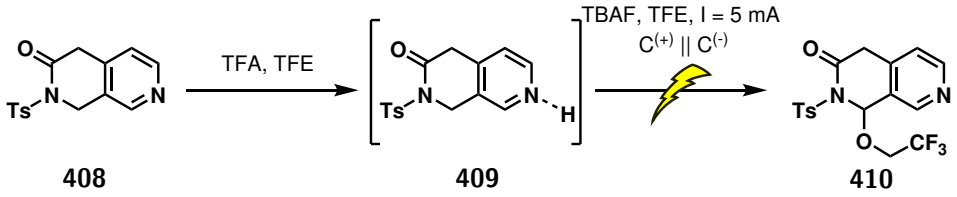

Scheme 5.5.0.3: Suggested electrochemical oxidation of the azalactam scaffold using a transient acid protection.

Chapter 6

Conclusions

Nitrogen heterocycles offer many advantages to the development of biologically active molecules and, as such, are common motifs in pharmaceutical compounds. However, the range of heterocycles represented in commercial drug compounds is still limited. Novel molecular scaffolds are an attractive strategy to increase the structural diversity and generate novel intellectual property. Yet, a major challenge of working with heterocycles is that synthetic methods of accessing decorated heterocycles often involve complex *de novo* syntheses. Optimising new synthetic routes can be laborious and costly, while the range of tolerated functionalities may be limited by the conditions of heterocyclic formation. These synthetic challenges can limit the diversity of compounds that can be generated for further testing.

To address these challenges, this project set out with two synthetic objectives. Firstly, to develop strategies to synthesise fragment cores based on under-represented nitrogen heterocycles. Secondly, to develop methods for the functionalisation of these nitrogen heterocycles to generate diverse fragment libraries. It was also desirable to demonstrate their value to future drug discovery programmes by exploring the biological activity of the fragments against exemplary protein targets.

The first part of this work focused on the 5-halo-*1H*-pyrazolo[3,4-*c*]pyridine scaffolds [Figure 6.0.0.1]. An efficient and robust synthesis was established and strategies were demonstrated for the selective elaboration along multiple reaction vectors. Firstly, different nitrogen protection strategies were explored for *N*-1 and *N*-2 on the pyrazole ring which facilitated subsequent functionalisation reactions. A tandem C-H borylation and Suzuki-Miyaura cross-coupling strategy was then explored to introduce electron-rich and electron-poor aryl groups at the *C*-3 position and a range of 5-amino analogues were generated by Buchwald-Hartwig amination. The *C*-7 vector was accessed by a *turbo*-Grignard metalation strategy which enabled reaction with a range of electrophiles or transmetalation to zinc followed by Negishi cross-coupling with diverse aryl halides. More elaborated analogues were also generated through short multi-vector sequences to generate an elaborated library of compounds.

Figure 6.0.0.1: 5-halopyrazolo[3,4-c]pyridine scaffolds **77**, and **185**

The biological characterisation of this library, both by crystal soaking and thermal shift assays, were challenged by the limited aqueous solubility of the heterocycles. A potential method to address this challenge would be to explore methods of elaboration focused on introducing aliphatic or polar groups.

The Suzuki-Miyaura and Negishi cross-coupling employed here exploited sp^2-sp^2 bond formation. This extended the planarity of the molecules and rapidly increased the aromatic ring count of the fragments, which was detrimental to the compound's aqueous solubility. Buchwald-Hartwig amination is one example of Pd-catalysed cross-coupling that can be used to introduce aliphatic groups, but strategies for sp^2-sp^3 Suzuki-Miyaura cross-coupling should also be explored. The choice of electrophile to react with the *turbo*-Grignard intermediate is another possible avenue to introduce more polarity as the reaction of aldehydes generates 2° alcohols. The work here only explored aromatic aldehydes so this could also be extended to more aliphatic examples.

The other strategy to address the low aqueous solubility of the pyrazolo[3,4-c]pyridine fragments would be increasing the sp^3-fraction of the heterocyclic scaffold itself. As discussed, this has been demonstrated to be possible by the partial reduction of the aromatic heterocycle by Pd-catalysis. A similar methodology could be explored for the partial reduction of the pyrazolo[3,4-c]pyridine ring, increasing the sp^3-fraction of compounds in the existing fragment library.

The chemistry of semi-saturated scaffolds was also pursued in the later part of this work, leading to the design of the azabenzolactams [Figure 6.0.0.2]. A three-step synthesis was first established starting from the corresponding halo-cyanopyridine which afforded the four azabenzolactam analogues. This procedure was later optimised to a more efficient two-step synthesis for scaffold **244**, although the application of these conditions to the other azabenzolactam analogues is still outstanding.

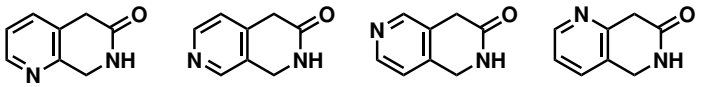

Figure 6.0.0.2: Azabenzolactam scaffolds **241**, **242**, **243**, and **244**

Early efforts for the vectorial functionalisation of the azabenzolactams identified a two-step methodology for the α-functionalisation of the cyclic amines. This combined a modified Shono oxidation in TFE with a substitution reaction by phenyl zinc in the presence of a Lewis acid. Variation in amine ring size, protecting group, morpholines, and benzo-fused systems were all tolerated. The scope of this methodology was also

expanded to introduce variation in the α-substituent by first performing a boron-to-zinc transmetalation of commercial aryl boronic acids, to generate a range of aryl zinc reagents. This methodology was suitable for electron-rich aryl boronic acids, although limitations were uncovered in the reaction of electron-poor and hetero aryl boronic acids. To overcome these limitations, alternative methods of generating the aryl zinc reagent should be explored, for example from the corresponding aryl lithium or magnesium in place of the boronic acid.

As discussed, another way to extend this methodology would be exploring the stereoselectivity of the substitution reaction, for example by employing a chiral protecting group on the nitrogen. Future work should also explore the optimisation of the established conditions for more complicated amines to facilitate the efficient oxidation of the azabenzolactams. This methodology would then offer a route to the *N,O*-acetals that could be treated with a range of arylzinc reagents to afford the desired α-arylated azabenzolactams.

As with the pyrazolo[3,4-c]pyridines, it would be desirable to establish methods for the functionalisation of all the major growth vectors on the azabenzolactam scaffolds. These efforts could include *N*-methylation, Aldol condensation, and Minisci reactions. Although much synthetic work is still required to establish a second fragment library based on these scaffolds.

Bibliography

[1] M. Congreve, R. Carr, C. Murray and H. Jhoti, *Drug Discovery Today*, 2003, **8**, 876–877.

[2] C. Lipinski, F. Lombardo, B. Dominy and P. Feeney, *Advanced Drug Delivery Reviews*, 1997, **23**, 3–25.

[3] S. Bembenek, B. Tounge and C. Reynolds, *Drug Discovery Today*, 2009, **14**, 278–283.

[4] E. Mashalidis, P. Sledź, S. Lang and C. Abell, *Nature protocols*, 2013, **8**, 2309–24.

[5] J. Revillo Imbernon, C. Jacquemard, G. Bret, G. Marcou and E. Kellenberger, *RSC Medicinal Chemistry*, 2022, **13**, 300–310.

[6] Otava Chemicals, *General Fragments Library*, 2022, `www.otavachemicals.com/products/fragment-libraries/general-fragment-library`, Accessed: 08/04/2022.

[7] Life Chemicals, *3D-shaped Fragment Library*, 2024, `www.lifechemicals.com/fragment-libraries/3d-shaped-fragment-library`, Accessed: 08/04/2024.

[8] D. Sydow, P. Schmiel, J. Mortier and A. Volkamer, *Journal of Chemical Information and Modeling*, 2020, **60**, 6081–6094.

[9] P. Kirsch, V. Jakob, K. Oberhausen, S. Stein, I. Cucarro, T. Schulz and M. Empting, *Journal of Medicinal Chemistry*, 2019, **62**, 3924–3939.

[10] C. Markert, G. Thoma, H. Srinivas, B. Bollbuck, R. Lüönd, W. Miltz, R. Wälchli, R. Wolf, J. Hinrichs, C. Bergsdorf, K. Azzaoui, C. Penno, K. Klein, N. Wack, P. Jäger, F. Hasler, C. Beerli, P. Loetscher, J. Dawson, G. Wieczorek, S. Numao, A. Littlewood-Evans and T. Röhn, *Journal of Medicinal Chemistry*, 2021, **64**, 1889–1903.

[11] W. Jencks, *Proceedings of the National Academy of Science USA*, 1981, **78**, 4046–50.

[12] A. Frank, M. Feldkamp, J. Kennedy, A. Waterson, N. Pelz, J. Patrone, B. Vangamudi, D. Camper, O. Rossanese, W. Chazin and S. Fesik, *Journal of Medicinal Chemistry*, 2013, **56**, 9242–9250.

[13] Y. Heakal, M. Kester and S. Savage, *Ann Pharmacother*, 2011, **45**, 1399–405.

[14] J. Tsai, J. Lee, W. Wang, J. Zhang, H. Cho, S. Mamo, R. Bremer, S. Gillette, J. Kong, N. Haass, K. Sproesser, L. Li, K. Smalley, D. Fong, Y.-L. Zhu, A. Marimuthu, H. Nguyen, B. Lam, J. Liu, I. Cheung, J. Rice, Y. Suzuki, C. Luu, C. Settachatgul, R. Shellooe, J. Cantwell, S.-H. Kim, J. Schlessinger, K. Zhang, B. West, B. Powell, G. Habets, C. Zhang, P. Ibrahim, P. Hirth, D. Artis, M. Herlyn and G. Bollag, *Proceedings of the National Academy of Sciences*, 2008, **105**, 3041–3046.

[15] M. Addie, P. Ballard, D. Buttar, C. Crafter, G. Currie, B. Davies, J. Debreczeni, H. Dry, P. Dudley, R. Greenwood, P. Johnson, J. Kettle, C. Lane, G. Lamont, A. Leach, R. Luke, J. Morris, D. Ogilvie, K. Page, M. Pass, S. Pearson and L. Ruston, *Journal of Medicinal Chemistry*, 2013, **56**, 2059–2073.

[16] U. Food and Drug Administration, *FDA approves capivasertib with fulvestrant*, 2024, `www.fda.gov/drugs/resources-information-approved-drugs/fda-approves-capivasertib-fulvestrant-breast-cancer`, Accessed: 24/09/2024.

[17] G. Chessari, R. Grainger, R. Holvey, R. Ludlow, P. Mortenson and D. Rees, *Chemical Science*, 2021, **12**, 11976–11985.

[18] J.-L. Reymond, R. van Deursen, L. Blum and L. Ruddigkeit, *Medicinal Chemistry Communications*, 2010, **1**, 30–38.

[19] L. Ruddigkeit, R. van Deursen, L. Blum and J.-L. Reymond, *Journal of Chemical Information and Modeling*, 2012, **52**, 2864–2875.

[20] J. Medina-Franco, A. Chávez-Hernández, E. López-López and F. Saldívar-González, *Molecular Informatics*, 2022, **41**, 2200116.

[21] A. Mirza, R. Desai and J. Reynisson, *European Journal of Medicinal Chemistry*, 2009, **44**, 5006–5011.

[22] M. Lajiness, M. Vieth and J. Erickson, *Current Opinion in Drug Discovery & Development*, 2004, **7**, 470–477.

[23] P. Polishchuk, T. Madzhidov and A. Varnek, *Journal of Computer-Aided Molecular Design*, 2013, **27**, 675–679.

[24] R. Bohacek, C. McMartin and W. Guida, *Medicinal Research Reviews*, 1996, **16**, 3–50.

[25] A.-D. Gorse, *Current Topics in Medicinal Chemistry*, 2006, **6**, 3–18.

[26] CAS, *Cas Registry*, 2023, Accessed: 23/09/2023.

[27] A. Gironda-Martínez, E. J. Donckele, F. Samain and D. Neri, *ACS Pharmacology & Translational Science*, 2021, **4**, 1265–1279.

[28] P.-P. Yang, Y.-J. Li, Y. Cao, L. Zhang, J.-Q. Wang, Z. Lai, K. Zhang, D. Shorty, W. Xiao, H. Cao, L. Wang, H. Wang, R. Liu and K. S. Lam, *Nature Communications*, 2021, **12**, 4494.

[29] S. Kaur, L. McGuire, D. Tang, G. Dollinger and V. Huebner, *Journal of Protein Chemistry*, 1997, **16**, 505–511.

[30] M. Lin and M. J. Shapiro, *The Journal of Organic Chemistry*, 1996, **61**, 7617–7619.

[31] Enamine, *REAL database*, 2024, `www.enamine.net/compound-collections/real-compounds/real-database`, Accessed: 15/10/2024.

[32] eMolecules, *Chemical Space | eXplore | Computational Chemistry*, 2024, `www.emolecules.com/explore`, Accessed: 09/11/2024.

[33] A. Neumann, L. Marrison and R. Klein, *ACS Medicinal Chemistry Letters*, 2023, **14**, 466–472.

[34] W. Pitt, D. Parry, B. Perry and C. Groom, *Journal of Medicinal Chemistry*, 2009, **52**, 2952–63.

[35] M. Haritha and C. H. Suresh, *Journal of Computational Chemistry*, 2023, **44**, 1550–1559.

[36] W. Abdou, A. Sediek and M. Khidre, *Monatshefte für Chemie - Chemical Monthly*, 2008, **139**, 617.

[37] J. Barton, D. Lapham and D. Rowe, *Journal of the Chemical Society, Perkin Transactions 1*, 1985, 131–133.

[38] K. Gehanne, J.-C. Lancelot, S. Lemaitre, H. El-Kashef and S. Rault, *Heterocycles*, 2008, **75**, 3015.

[39] S. Zinchenko, R. Efimenko, S. Suikov, K. Kobrakov and S. Bogza, *Chemistry of Heterocyclic Compounds*, 2009, **45**, 365–369.

[40] M. Raggatt, T. Simpson and S. Wrigley, *Chemical Communications*, 1999, 1039–1040.

[41] D. Sivakumar, C. Lahiri and D. Chakravortty, *Medicinal Chemistry Research*, 2013, **22**, 1804–1811.

[42] Z. Xia, K. Wang, J. Zheng, Z. Ma, Z. Jiang, X. Wang and X. Lv, *Organic & Biomolecular Chemistry*, 2012, **10**, 1602–1611.

[43] T. Bannister, C. Lasmezas, Z. Minghai and A. Albertson, *Compounds and Use Thereof for Treatment of Neurodegenerative, Degenerative and Metabolic Disorders*, 2024, Patent: US2024262831A.

[44] G. Cirrincione, A. Almerico, P. Barraja, P. Diana, A. Lauria, A. Passannanti, C. Musiu, A. Pani, P. Murtas, C. Minnei, M. Marongiu and P. La Colla, *Journal of Medicinal Chemistry*, 1999, **42**, 2561–2568.

[45] J. Crum and C. Fuchsman, *Journal of Heterocyclic Chemistry*, 1966, **3**, 252–256.

[46] F. Slowinski, O. Ben Ayad, O. Ziyaret, C. Botuha, L. Le Falher, K. Aouane and S. Thorimbert, *Organic Letters*, 2013, **15**, 3494–3497.

[47] L. Le Falher, A. Mumtaz, A. Nina Diogo, S. Thorimbert and C. Botuha, *European Journal of Organic Chemistry*, 2017, **2017**, 827–832.

[48] T. Sparey, P. Abeywickrema, S. Almond, N. Brandon, N. Byrne, A. Campbell, P. Hutson, M. Jacobson, B. Jones, S. Munshi, D. Pascarella, A. Pike, G. Prasad, N. Sachs, M. Sakatis, V. Sardana, S. Venkatraman and M. Young, *Bioorganic & Medicinal Chemistry Letters*, 2008, **18**, 3386–3391.

[49] C. McBride, Z. Cheruvallath, M. Komandla, M. Tang, P. Farrell, J. Lawson, D. Vanderpool, Y. Wu, D. Dougan, A. Plonowski, C. Holub and C. Larson, *Bioorganic & Medicinal Chemistry Letters*, 2016, **26**, 2779–2783.

[50] Z. Hou, S. Oishi, Y. Suzuki, T. Kure, I. Nakanishi, A. Hirasawa, G. Tsujimoto, H. Ohno and N. Fujii, *Organic & Biomolecular Chemistry*, 2013, **11**, 3288–3296.

[51] M. Nayak, H. Batchu and S. Batra, *Tetrahedron Letters*, 2012, **53**, 4206–4208.

[52] W. Mederski, M. Osswald, D. Dorsch, M. Christadler, C.-J. Schmitges and C. Wilm, *Bioorganic & Medicinal Chemistry Letters*, 1999, **9**, 619–622.

[53] D. Ramesh, C. Chandrashekhar and V. Vaidya, *Indian Journal of Chemistry*, 2008, **47**, 753–758.

[54] L. Fu, X. Huang, D. Wang, P. Zhao and K. Ding, *Synthesis*, 2011, **2011**, 1547–1554.

[55] P. Brown, J. Russell, R. Thomson and A. Wylie, *Journal of the Chemical Society C: Organic*, 1968, 842–848.

[56] M. Devi, B. Nameirakpam, T. Devi, S. Mayanglambam, K. Singh, S. Sougrakpam, S. Shadia, M. Tongbram, S. Singh, D. Sahoo and Y. Rajashekar, *International Journal of Tropical Insect Science*, 2020, **40**, 549–559.

[57] T. Fegel, C. Boot, C. Broeckling, J. Baron and E. Hall, *Journal of Geophysical Research: Biogeosciences*, 2019, **124**, 1988–2004.

[58] A. Kelemen, B. Szabo, P. Kovacs and G. Keserű, *Tetrahedron Letters*, 2016, **57**, 64–66.

[59] E. Csimbók, D. Takács, J. Balog, O. Egyed, N. May-Nagy and G. Keserű, *Tetrahedron Letters*, 2016, **57**, 4401–4404.

[60] T. Selby and B. Smith, *Heterobicyclic Alkylthio-Bridged Isoxazolines*, 2010, Patent: 20100099561.

[61] Y. Kondo and T. Otake, *Electrochromic Material and Method for Producing Same*, 2011, Patent: WO 2011111683.

[62] T. Kenta, H. Hideyuki and K. Yasuyuki, *Conjugated Polymer Compound and Organic Semiconductor Device Containing the Same*, 2011, Patent: 2011032426.

[63] H. Sugiura and K. Nomura, *Organic Semiconductor Device, as well as Compound, Composition, and Coating Film for Same*, 2015, Patent: WO 2015029910.

[64] M. Nishizeki, N. Yasukawa, H. Ito and K. Hiroshi, *Organic Electroluminescent Element, Display Device and Illuminating Device*, 2016, Patent: JP 2016219490.

[65] K. Hayashi, T. Watanabe, K. Toyama, J. Kamon, M. Minami, M. Uni and M. Nasu, *Tricyclic Hetercyclic Compounds and JAK Inhibitors*, 2015, Patent: US2014200344.

[66] X. Hao, *Cinnolines as Inhibitors of HPK1*, 2024, Patent: WO2021004535A1.

[67] S. Chen, J. Yan, Z. Wang and Z. Ding, *Polycyclic Compound and Application Thereof*, 2024, Patent: US20240216357A1.

[68] W. Huting, Y. Xu, S. Lei, D. Haolin, L. Lei, S. Guanglong, M. Qinghua, W. Jianhao and W. Jingjing, *SOS1 Inhibitors*, 2024, Patent: CN117800922A.

[69] J. Lindström, L. Persson, J. Viklund, E. Kesicki, E. Hickey, M. Dahlgren and A. Gerasyuto, *Aminopyridine Derivatives as Phosphatidylinositol Phosphate Kinase Inhibitors*, 2024, Patent: WO2019126731A1.

[70] S. Hoelder, J. Blagg, S. Solanki, H. Woodward, S. Naud, V. Bavetsias, P. Sheldrake, P. Innocenti, K.-M. Cheung and B. Atrash, *Inhibitor Compounds*, 2012, Patent: US9890157B2.

[71] J. Li, J. Gao, G. Li, W. Xiong and Q. Zhang, *The Journal of Organic Chemistry*, 2013, **78**, 12760–12768.

[72] P. da Silva Júnior, L. Rezende, J. Gimenes, V. Maltarollo, J. Dale, G. Trossini, F. da Silva Emery and A. Ganesan, *RSC Advances*, 2016, **6**, 22777–22780.

[73] D. Chapman and J. Hurst, *Journal of the Chemical Society, Perkin Transactions 1*, 1980, **Part 5**, 2398–2404.

[74] M. Moir, J. Danon, T. Reekie and M. Kassiou, *Expert Opinion on Drug Discovery*, 2019, **14**, 1137–1149.

[75] S. Antonysamy, G. Hirst, F. Park, P. Sprengeler, F. Stappenbeck, R. Steensma, M. Wilson and M. Wong, *Bioorganic & Medicinal Chemistry Letters*, 2009, **19**, 279–282.

[76] D. J. Maly, I. C. Choong and J. A. Ellman, *Proceedings of the National Academy of Sciences*, 2000, **97**, 2419–2424.

[77] A. Goldman and K. Goldberg, *Activation and Functionalization of C—H Bonds*, American Chemical Society, 2004, vol. 885, pp. 1–43.

[78] T. Cernak, K. Dykstra, S. Tyagarajan, P. Vachal and S. Krska, *Chemical Society Reviews*, 2016, **45**, 546–576.

[79] S.-J. Lou, Q. Chen, Y.-F. Wang, D.-Q. Xu, X.-H. Du, J.-Q. He, Y.-J. Mao and Z.-Y. Xu, *ACS Catalysis*, 2015, **5**, 2846–2849.

[80] B. Liu, H.-Z. Jiang and B.-F. Shi, *The Journal of Organic Chemistry*, 2014, **79**, 1521–1526.

[81] L. Ackermann, E. Diers and A. Manvar, *Organic Letters*, 2012, **14**, 1154–1157.

[82] L. Niu, H. Yang, R. Wang and H. Fu, *Organic Letters*, 2012, **14**, 2618–2621.

[83] J. Yao, R. Feng, Z. Wu, Z. Liu and Y. Zhang, *Advanced Synthesis & Catalysis*, 2013, **355**, 1517–1522.

[84] F. Kakiuchi, K. Igi, M. Matsumoto, T. Hayamizu, N. Chatani and S. Murai, *Chemistry Letters*, 2002, **31**, 396–397.

[85] J. Li, S. De Sarkar and L. Ackermann, *C-H Bond Activation and Catalytic Functionalization I*, Springer International Publishing, Cham, 2016, pp. 217–257.

[86] Y. Fujiwara, I. Moritani, S. Danno and R. Asano, *Journal of the American Chemical Society*, 1969, **91**, 7166–7169.

[87] H. Fujihara, K. Nagai and K. Tomioka, *Journal of the American Chemical Society*, 2000, **122**, 12055–12056.

[88] H. Tajuddin, P. Harrisson, B. Bitterlich, J. C. Collings, N. Sim, A. S. Batsanov, M. S. Cheung, S. Kawamorita, A. C. Maxwell, L. Shukla, J. Morris, Z. Lin, T. B. Marder and P. G. Steel, *Chemical Science*, 2012, **3**, 3505–3515.

[89] Q. Li and H. Zhang, *Chemistry – A European Journal*, 2015, **21**, 16379–16382.

[90] C.-Y. Jia, J.-Y. Li, G.-F. Hao and G.-F. Yang, *Drug Discovery Today*, 2020, **25**, 248–258.

[91] Daylight, *ClogP Manual*, 2024, `daylight.com/dayhtml/doc/clogp/index.html`, Accessed: 07/10/2024.

[92] V. Giannouli, N. Lougiakis, I. Kostakis, N. Pouli, P. Marakos, A.-L. Skaltsounis, S. Nam, R. Jove, D. Horne, R. Tenta, H. Pratsinis and D. Kletsas, *Bioorganic & Medicinal Chemistry Letters*, 2016, **26**, 5229–5233.

[93] N. Lougiakis, P. Marakos, N. Poul and J. Balzarini, *Chemical and Pharmaceutical Bulletin*, 2008, **56**, 775–780.

[94] V. Kourafalos, P. Marakos, N. Pouli and L. Townsend, *Synlett*, 2002, **2002**, 1479–1482.

[95] V. Kourafalos, P. Marakos, N. Pouli and L. Townsend, *The Journal of Organic Chemistry*, 2003, **68**, 6466–6469.

[96] C. M. Park, V. B. Jadhav, J.-H. Song, S. Lee, H. Y. Won, S. U. Choi and Y. H. Son, *Bulletin of the Korean Chemical Society*, 2017, **38**, 595–602.

[97] G.-D. Zhu, V. Gandhi, J. Gong, S. Thomas, K. Woods, X. Song, T. Li, R. Diebold, Y. Luo, X. Liu, R. Guan, V. Klinghofer, E. Johnson, J. Bouska, A. Olson, K. Marsh, V. Stoll, M. Mamo, J. Polakowski, T. Campbell, R. Martin, G. Gintant, T. Penning, Q. Li, S. Rosenberg and V. Giranda, *Journal of Medicinal Chemistry*, 2007, **50**, 2990–3003.

[98] M. Sklepari, N. Lougiakis, A. Papastathopoulos, N. Pouli, P. Marakos, V. Myrianthopoulos, T. Robert, S. Bach, E. Mikros and S. Ruchaud, *Chemical & Pharmaceutical Bulletin*, 2017, **65**, 66–81.

[99] D. Matsuda, Y. Kobashi, A. Mikami, M. Kawamura, F. Shiozawa, K. Kawabe, M. Hamada, K. Oda, S. Nishimoto, K. Kimura, M. Miyoshi, N. Takayama, H. Kakinuma and N. Ohtake, *Bioorganic & Medicinal Chemistry Letters*, 2016, **26**, 3441–3446.

[100] A.-M. Fantel, V. Myrianthopoulos, A. Georgoulis, N. Lougiakis, I. Zantza, G. Lamprinidis, F. Augsburger, P. Marakos, C. Vorgias, C. Szabo, N. Pouli, A. Papapetropoulos and E. Mikros, *Molecules*, 2020, **25**, 3739.

[101] D. Atukuri, *Chemical Biology & Drug Design*, 2022, **100**, 376–388.

[102] V.-A. Bakalakou, B. Mavroidi, A. Kalampaliki, B. Josselin, S. Bach, A.-L. Skaltsounis, P. Marakos, N. Pouli, M. Pelecanou, V. Myrianthopoulos, S. Ruchaud and I. Kostakis, *European Journal of Medicinal Chemistry Reports*, 2024, **12**, 100193.

[103] A. Angeli, V. Kartsev, A. Petrou, B. Lichitsky, A. Komogortsev, M. Pinteala, A. Geronikaki and C. Supuran, *Pharmaceuticals*, 2022, **15**, 316.

[104] P. Marakos, N. Pouli, D. Wise and L. Townsend, *Synlett*, 1997, **5**, 561–562.

[105] O. Tsikouris, T. Bartl, J. Toušek, N. Lougiakis, T. Tite, P. Marakos, N. Pouli, E. Mikros and R. Marek, *Magnetic Resonance in Chemistry*, 2008, **46**, 643–649.

[106] S. Heller and S. Natarajan, *Organic Letters*, 2007, **9**, 4947–4950.

[107] S. Verma and L. LaFrance, *Tetrahedron Letters*, 2009, **50**, 383–385.

[108] I. Baxendale, *Personal Communication*, 2021.

[109] D. Brown and J. Boström, *Journal of Medicinal Chemistry*, 2016, **59**, 4443–4458.

[110] A. Lennox and G. Lloyd-Jones, *Chemical Society Reviews*, 2014, **43**, 412–443.

[111] L. Britton, J. Docherty, A. Dominey and S. Thomas, *Molecules*, 2020, **25**, 905.

[112] M. Grundy, K. Yuan, G. Nichol and M. Ingleson, *Chemical Science*, 2021, **12**, 8190–8198.

[113] J. Fernández-Salas, S. Manzini, L. Piola, A. Slawin and S. Nolan, *Chemical Communications*, 2014, **50**, 6782–6784.

[114] J. Wright, P. Scott and P. Steel, *Angewandte Chemie International Edition*, 2021, **60**, 2796–2821.

[115] C. Haldar, M. Hoque, J. Chaturvedi, M. Hassan and B. Chattopadhyay, *Chemical Communications*, 2021, **57**, 13059–13074.

[116] T. Ishiyama, K. Ishida and N. Miyaura, *Tetrahedron*, 2001, **57**, 9813–9816.

[117] J. Takagi, K. Sato, J. Hartwig, T. Ishiyama and N. Miyaura, *Tetrahedron Letters*, 2002, **43**, 5649–5651.

[118] S. Sadler, H. Tajuddin, I. Mkhalid, A. Batsanov, D. Albesa-Jove, M. Cheung, A. Maxwell, L. Shukla, B. Roberts, D. Blakemore, Z. Lin, T. Marder and P. Steel, *Organic & Biomolecular Chemistry*, 2014, **12**, 7318–7327.

[119] P. Cox, A. Leach, A. Campbell and G. Lloyd-Jones, *Journal of the American Chemical Society*, 2016, **138**, 9145–9157.

[120] H. Kuivila, J. Reuwer and J. Mangravite, *Journal of the American Chemical Society*, 1964, **86**, 2666–2670.

[121] S. Sadler, A. Hones, B. Roberts, D. Blakemore, T. Marder and P. Steel, *The Journal of Organic Chemistry*, 2015, **80**, 5308–5314.

[122] P. da Silva Júnior, S. de Melo, M. de Paula, R. Vessecchi, T. Opatz, J. Day, A. Ganesan and F. da Silva Emery, *Organic & Biomolecular Chemistry*, 2022, **20**, 7483–7490.

[123] B. Prasad, R. Adepu, S. Sandra, D. Rambabu, G. Krishna, C. Reddy, G. Deora, P. Misra and M. Pal, *Chemical Communications*, 2012, **48**, 10434–10436.

[124] S. Searles and S. Nukina, *Chemical Reviews*, 1959, **59**, 1077–1103.

[125] D. Slade, N. Pelz, W. Bodnar, J. Lampe and P. Watson, *The Journal of Organic Chemistry*, 2009, **74**, 6331–6334.

[126] G. Jaffari and A. Nunn, *Journal of the Chemical Society, Perkin Transactions 1*, 1973, 2371–2374.

[127] M. Cheung, A. Boloor and J. Stafford, *The Journal of Organic Chemistry*, 2003, **68**, 4093–4095.

[128] J. Deng, D. Paone, A. Ginnetti, H. Kurihara, S. Dreher, S. Weissman, S. Stauffer and C. Burgey, *Organic Letters*, 2009, **11**, 345–347.

[129] M. Skipsey, K. Knight, M. Brazier-Hicks, D. Dixon, P. Steel and R. Edwards, *Journal of Biological Chemistry*, 2011, **286**, 32268–32276.

[130] T. dos Santos, H. Orenha, V. Murie, R. Vessecchi and G. Clososki, *Organic Letters*, 2021, **23**, 7396–7400.

[131] Z. Dong, G. Clososki, S. Wunderlich, A. Unsinn, J. Li and P. Knochel, *Chemistry – A European Journal*, 2009, **15**, 457–468.

[132] M. Balkenhohl, B. Salgues, T. Hirai, K. Karaghiosoff and P. Knochel, *Organic Letters*, 2018, **20**, 3114–3118.

[133] K. Anderson and S. Buchwald, *Angewandte Chemie International Edition*, 2005, **44**, 6173–6177.

[134] E. Kolychev, A. Andrey, P. Dzhevakov, A. Bush, V. Shuntikov, V. Khrustalev and M. Nechaev, *Dalton transactions*, 2013, **42**, 6859–6866.

[135] C.-J. Li, *Chemical Reviews*, 2005, **105**, 3095–3166.

[136] M. M. Heravi, Z. Kheilkordi, V. Zadsirjan, M. Heydari and M. Malmir, *Journal of Organometallic Chemistry*, 2018, **861**, 17–104.

[137] B. T. Ingoglia, C. C. Wagen and S. L. Buchwald, *Tetrahedron*, 2019, **75**, 4199–4211.

[138] R. Dorel, C. P. Grugel and A. M. Haydl, *Angewandte Chemie International Edition*, 2019, **58**, 17118–17129.

[139] H. Cao, Q. Cheng and A. Studer, *Science*, 2022, **378**, 779–785.

[140] D. Stephens and O. Larionov, *Tetrahedron*, 2015, **71**, 8683–8716.

[141] P. Guo, J. Joo, S. Rakshit and D. Sames, *Journal of the American Chemical Society*, 2011, **133**, 16338–16341.

[142] M. Ye, G.-L. Gao and J.-Q. Yu, *Journal of the American Chemical Society*, 2011, **133**, 6964–6967.

[143] T. S. Teets, *Photoluminescence*, American Chemical Society, Washington, DC, USA, 2021.

[144] B. Valeur and M. N. Berberan-Santos, *Journal of Chemical Education*, 2011, **88**, 731–738.

[145] P. Bunker and P. Jensen, *Molecular Symmetry and Spectroscopy*, NRC research press, 2006, vol. 46853.

[146] M. E. D. García and R. Badía-Laíño, *Encyclopedia of Analytical Science*, Academic Press, Oxford, 3rd edn, 2019, pp. 327–340.

[147] D. Phillips, R. Drake, D. O'Connor and R. Christensen, *Instrumentation Science & Technology*, 1985, **14**, 267–292.

[148] M. Levitus, *Methods and Applications in Fluorescence*, 2020, **8**, 033001.

[149] W. H. Melhuish, *The Journal of Physical Chemistry*, 1961, **65**, 229–235.

[150] N. T. Kalyani and S. J. Dhoble, *Renewable and Sustainable Energy Reviews*, 2012, **16**, 2696–2723.

[151] R. Pode, *Renewable and Sustainable Energy Reviews*, 2020, **133**, 110043.

[152] J. C. K. Kung, A. Forman and R. A. Jockusch, *Physical Chemistry Chemical Physics*, 2019, **21**, 10261–10271.

[153] P. P. Ghoroghchian, M. J. Therien and D. A. Hammer, *WIREs Nanomedicine and Nanobiotechnology*, 2009, **1**, 156–167.

[154] K. Kikuchi, *Chemistry Society Review*, 2010, **39**, 2048–2053.

[155] N. R. Paisley, S. V. Halldorson, M. V. Tran, R. Gupta, S. Kamal, W. R. Algar and Z. M. Hudson, *Angewandte Chemie International Edition*, 2021, **60**, 18630–18638.

[156] J.-H. Lee, I.-H. Lee, Y.-J. Choe, S. Kang, H. Y. Kim, W.-P. Gai, J.-S. Hahn and S. R. Paik, *Biochemical Journal*, 2009, **418**, 311–323.

[157] N. R. Paisley, C. M. Tonge and Z. M. Hudson, *Frontiers in Chemistry*, 2020, **8**, 1–14.

[158] P. Krumholz, *Journal of the American Chemical Society*, 1951, **73**, 3487–3492.

[159] K. Nakamoto, *The Journal of Physical Chemistry*, 1960, **64**, 1420–1425.

[160] J. O. Watson, R. M. Pollard, M. T. Sims, M. K. Etherington and J. P. Knowles, *The Journal of Physical Chemistry B*, 2024, **128**, 11208–11215.

[161] A. T. Turley, A. Danos, A. Prlj, A. P. Monkman, B. F. E. Curchod, P. R. McGonigal and M. K. Etherington, *Chemical Science*, 2020, **11**, 6990–6995.

[162] D. Pant, G. Joshi and H. Tripathi, *Pramana*, 1986, **27**, 161–170.

[163] Y. Suzuki, M. Yagi and A. Kikuchi, *Photochemical & Photobiological Sciences*, 2023, **22**, 2851–2859.

[164] W. Qin, A. Vozza and A. M. Brouwer, *The Journal of Physical Chemistry C*, 2009, **113**, 11790–11795.

[165] N. Ibrayev, E. Seliverstova, R. Valiev, A. Aymagambetova and D. Sundholm, *Physical Chemistry Chemical Physics*, 2024, **26**, 25986–25993.

[166] R. Casasnovas, J. Ortega-Castro, J. Frau, J. Donoso and F. Muñoz, *International Journal of Quantum Chemistry*, 2014, **114**, 1350–1363.

[167] J. Zheng, *IUPAC Dissociation Constants: v1.0*, 2022, `https://doi.org/10.5281/zenodo.7236453`, Accessed: 21/10/2022.

[168] R. Linnell, *The Journal of Organic Chemistry*, 1960, **25**, 290–290.

[169] T. Curphey, *Organic Syntheses*, 1988, **6**, 1019.

[170] R. L. Martin, *The Journal of Chemical Physics*, 2003, **118**, 4775–4777.

[171] I. Bhattacharjee, N. Acharya and D. Ray, *Chemical Communications*, 2019, **55**, 1899–1902.

[172] A. Klimash, A. Prlj, D. S. Yufit, A. Mallick, B. F. E. Curchod, P. R. McGonigal, P. J. Skabara and M. K. Etherington, *Journal of Materials Chemistry C*, 2022, **10**, 9484–9491.

[173] World Health Organisation, *Neglected Tropical Diseases*, 2024, `https://www.who.int/news-room/questions-and-answers/item/neglected-tropical-diseases`, Accessed: 16/10/2024.

[174] World Health Organisation, *Leishmaniasis - Factsheet*, 2024, `www.who.int/news-room/fact-sheets/detail/leishmaniasis`, Accessed: 27/10/2024.

[175] S. Burza, S. Croft and M. Boelaert, *Lancet*, 2018, **392**, 951–970.

[176] European Centre for Disease Prevention and Control, *Phlebotomine Sand Flies - Factsheet*, 2017, `www.ecdc.europa.eu/en/disease-vectors/facts/phlebotomine-sand-flies`, Accessed: 10/11/2024.

[177] S. Sundar, J. Singh, V. Singh, N. Agrawal and R. Kumar, *Expert Opinion on Orphan Drugs*, 2024, **12**, 19–32.

[178] S. Hendrickx, P. Guerin, G. Caljon, S. Croft and L. Maes, *Parasitology*, 2018, **145**, 453–463.

[179] B. Alemayehu and M. Alemayehu, *Health Science Journal*, 2017, **11**, 519–525.

[180] R. Silva, G. Bassi, N. Câmara and N. Moretti, *Molecular Immunology*, 2023, **160**, 150–160.

[181] W. Zheng, *European Journal of Medicinal Chemistry*, 2013, **59**, 132–140.

[182] N. Mittal, R. Muthuswami and R. Madhubala, *PLOS Neglected Tropical Diseases*, 2017, **11**, e0005590.

[183] B. Vergnes, D. Sereno, N. Madjidian-Sereno, J. Lemesre and A. Ouaissi, *Gene*, 2002, **296**, 139–50.

[184] B. Vergnes, D. Sereno, J. Tavares, A. Cordeiro-da Silva, L. Vanhille, N. Madjidian-Sereno, D. Depoix, A. Monte-Alegre and A. Ouaissi, *Gene*, 2005, **363**, 85–96.

[185] C. Ronin, D. Costa, J. Tavares, J. Faria, F. Ciesielski, P. Ciapetti, T. Smith, J. MacDougall, A. Cordeiro-da Silva and I. Pemberton, *PLOS ONE*, 2018, **13**, e0193602.

[186] R. Kadam, V. Kiran and N. Roy, *Bioorganic & Medicinal Chemistry Letters*, 2006, **16**, 6013–6018.

[187] L. Sacconnay, D. Smirlis, E. Queiroz, J. Wolfender, M. Soares, P.-A. Carrupt and A. Nurisso, *Molecular BioSystems*, 2013, **9**, 2223–2230.

[188] T. Matutino Bastos, M. Botelho Pereira Soares, C. Haddad Franco, L. Alcântara, L. Antonini, M. Sabatino, N. Mautone, L. Holanda Freitas-Junior, C. Moraes, R. Ragno, D. Rotili, S. Schenkman, A. Mai and N. Silvio Moretti, *International Journal of Molecular Science*, 2020, **21**, 3659.

[189] G. Ferreira, T. Kronenberger, V. Maltarollo, A. Poso, F. de Moura Gatti, V. Almeida, S. Marana, C. Lopes, D. Tezuka, S. de Albuquerque, F. da Silva Emery and G. Trossini, *Pharmaceuticals*, 2023, **16**, 428–442.

[190] R. Gomes, E. Fornari, A. Rocha, G. Tripodi, F. Emery and G. Trossini, *Future Medicinal Chemistry*, 2021, **13**, 1397–1409.

[191] L. Gaspar, R. P. Coron, P. KongThoo Lin, D. M. Costa, B. Perez-Cabezas, J. Tavares, M. Roura-Ferrer, I. Ramos, C. Ronin, L. L. Major, F. Ciesielski, I. K. Pemberton, J. MacDougall, P. Ciapetti, T. K. Smith and A. Cordeiro-da Silva, *PLOS Neglected Tropical Diseases*, 2018, **12**, e0006180.

[192] R. Williams, G. Westrop and G. Coombs, *Biochemical Journal*, 2009, **420**, 451–462.

[193] D. Marciano, M. Santana and C. Nowicki, *Molecular and Biochemical Parasitology*, 2012, **185**, 114–120.

[194] K. Sowerby, S. Freitag-Pohl, A. Murillo, A. Silber and E. Pohl, *Acta Crystallographica Section D*, 2023, **79**, 518–530.

[195] E. R. Bonner, R. E. Cahoon, S. M. Knapke and J. M. Jez, *Journal of Biological Chemistry*, 2005, **280**, 38803–38813.

[196] P. Burkhard, G. Jagannatha Rao, E. Hohenester, K. D. Schnackerz, P. F. Cook and J. N. Jansonius, *Journal of Molecular Biology*, 1998, **283**, 121–133.

[197] A. Penteado, H. Hassanie, R. Gomes, F. da Silva Emery and G. Trossini, *Future Medicinal Chemistry*, 2023, **15**, 1–21.

[198] I. Hanukoglu, *Biochemistry and Molecular Biology Education*, 2015, **43**, 206–209.

[199] S. Moniot, M. Schutkowski and C. Steegborn, *Journal of Structural Biology*, 2013, **182**, 136–143.

[200] T. Rumpf, S. Gerhardt, O. Einsle and M. Jung, *Acta Crystallographica Section F Structural Biology Communications*, 2015, **71**, 1498–1510.

[201] K. Hoff, J. Avalos, K. Sens and C. Wolberger, *Structure*, 2006, **14**, 1231–1240.

[202] M. Schiedel, T. Rumpf, B. Karaman, A. Lehotzky, J. Oláh, S. Gerhardt, J. Ovádi, W. Sippl, O. Einsle and M. Jung, *Journal of Medicinal Chemistry*, 2016, **59**, 1599–1612.

[203] A. Berndt Penteado, *Personal Communication*, 2023.

[204] S. Altschul, T. Madden, A. Schäffer, J. Zhang, Z. Zhang, W. Miller and D. Lipman, *Nucleic Acids Research*, 1997, **25**, 3389–3402.

[205] F. Madeira, N. Madhusoodanan, J. Lee, A. Eusebi, A. Niewielska, A. R. N. Tivey, R. Lopez and S. Butcher, *Nucleic Acids Research*, 2024, **52**, W521–W525.

[206] X. Robert and P. Gouet, *Nucleic Acids Research*, 2014, **42**, W320–W324.

[207] G. Studer, C. Rempfer, A. Waterhouse, R. Gumienny, J. Haas and T. Schwede, *Bioinformatics*, 2019, **36**, 1765–1771.

[208] R. Laskowski, M. MacArthur, D. Moss and J. Thornton, *Journal of Applied Crystallography*, 1993, **26**, 283–291.

[209] G. Janson and A. Paiardini, *Bioinformatics*, 2021, **37**, 1471–1472.

[210] I. Guedes, A. Barreto, D. Marinho, E. Krempser, M. Kuenemann, O. Sperandio, L. Dardenne and M. Miteva, *Scientific Reports*, 2021, **11**, 3198.

[211] I. A. Guedes, M. M. Pereira da Silva, M. Galheigo, E. Krempser, C. S. de Magalhães, H. J. Correa Barbosa and L. E. Dardenne, *Computation Resources for Molecular Biology*, 2024, **436**, 168548.

[212] L. Maveyraud and L. Mourey, *Molecules*, 2020, **25**, 1030.

[213] B. Wienen-Schmidt, M. Oebbeke, K. Ngo, A. Heine and G. Klebe, *Chem*, 2021, **16**, 292–300.

[214] I. Müller, *Acta Crystallographica Section D*, 2017, **73**, 79–92.

[215] M. Dessau and Y. Modis, *JoVE*, 2011, e2285.

[216] M. K. Grøftehauge, N. R. Hajizadeh, M. J. Swann and E. Pohl, *Acta Crystallographica Section D*, 2015, **71**, 36–44.

[217] M. Dimensions, *Online Store*, 2024, `moleculardimensions.com/en`, Accessed: 10/11/2024.

[218] R. Kühne, R. Ebert, F. Kleint, G. Schmidt and G. Schüürmann, *Chemosphere*, 1995, **30**, 2061–2077.

[219] G. Klopman, S. Wang and D. Balthasar, *Journal of Chemical Information and Computer Sciences*, 1992, **32**, 474–482.

[220] I. Tetko, V. Tanchuk, T. Kasheva and A. Villa, *Journal of Chemical Information and Computer Sciences*, 2001, **41**, 1488–1493.

[221] J. Huuskonen, *Journal of Chemical Information and Computer Sciences*, 2000, **40**, 773–777.

[222] A. Yan and J. Gasteiger, *Journal of Chemical Information and Computer Sciences*, 2003, **43**, 429–434.

[223] H. Sun, P. Shah, K. Nguyen, K. Yu, E. Kerns, M. Kabir, Y. Wang and X. Xu, *Bioorganic & Medicinal Chemistry*, 2019, **27**, 3110–3114.

[224] Y. Ma, Z. Gao, P. Shi, M. Chen, S. Wu, C. Yang, J. Wang, J. Cheng and J. Gong, *Frontiers of Chemical Science and Engineering*, 2022, **16**, 523–535.

[225] X.-L. Zeng, H.-J. Wang and Y. Wang, *Chemosphere*, 2012, **86**, 619–625.

[226] D. Yaffe, Y. Cohen, G. Espinosa, A. Arenas and F. Giralt, *Journal of Chemical Information and Computer Sciences*, 2001, **41**, 1177–1207.

[227] N. Jain and S. Yalkowsky, *Journal of Pharmaceutical Sciences*, 2001, **90**, 234–252.

[228] T. Ritchie and S. Macdonald, *Drug Discovery Today*, 2009, **14**, 1011–1020.

[229] M. Hann, *Medicinal Chemistry Communications*, 2011, **2**, 349–355.

[230] F. Lovering, J. Bikker and C. Humblet, *Journal of Medicinal Chemistry*, 2009, **52**, 6752–6756.

[231] D. Veber, S. Johnson, H.-Y. Cheng, B. Smith, K. Ward and K. Kopple, *Journal of Medicinal Chemistry*, 2002, **45**, 2615–2623.

[232] J. Blake, *BioTechniques*, 2003, **34**, S16–S20.

[233] M. Wenlock, R. Austin, P. Barton, A. Davis and P. Leeson, *Journal of Medicinal Chemistry*, 2003, **46**, 1250–1256.

[234] C. Bergström, R. Holm, S. Jørgensen, S. Andersson, P. Artursson, S. Beato, A. Borde, K. Box, M. Brewster, J. Dressman, K.-I. Feng, G. Halbert, E. Kostewicz, M. McAllister, U. Muenster, J. Thinnes, R. Taylor and A. Mullertz, *European Journal of Pharmaceutical Sciences*, 2014, **57**, 173–199.

[235] B. Aungst, *Journal of Pharmaceutical Sciences*, 2017, **106**, 921–929.

[236] M. Varma, R. Obach, C. Rotter, H. Miller, G. Chang, S. Steyn, A. El-Kattan and M. Troutman, *Journal of Medicinal Chemistry*, 2010, **53**, 1098–1108.

[237] G. Caron, V. Digiesi, S. Solaro and G. Ermondi, *Drug Discovery Today*, 2020, **25**, 621–627.

[238] N. Ahmad, *Bioorganic & Medicinal Chemistry Letters*, 2016, **26**, 2975–2979.

[239] C. Marson, *Advances in Heterocyclic Chemistry*, Academic Press, 2017, vol. 121, pp. 13–33.

[240] J. St. Jean, DJ and C. Fotsch, *Journal of Medicinal Chemistry*, 2012, **55**, 6002–6020.

[241] N. Press, R. Taylor, J. Fullerton, P. Tranter, C. McCarthy, T. Keller, N. Arnold, D. Beer, L. Brown, R. Cheung, J. Christie, A. Denholm, S. Haberthuer, J. Hatto, M. Keenan, M. Mercer, H. Oakman, H. Sahri, A. Tuffnell, M. Tweed, J. Tyler, T. Wagner, J. Fozard and A. Trifilieff, *Journal of Medicinal Chemistry*, 2012, **55**, 7472–7479.

[242] X. Chen, P. Zhan, C. Pannecouque, J. Balzarini, E. De Clercq and X. Liu, *European Journal of Medicinal Chemistry*, 2012, **51**, 60–66.

[243] B. Huang, C. Li, W. Chen, T. Liu, M. Yu, L. Fu, Y. Sun, H. Liu, E. De Clercq, C. Pannecouque, J. Balzarini, P. Zhan and X. Liu, *European Journal of Medicinal Chemistry*, 2015, **92**, 754–765.

[244] C. Laurence, K. Brameld, J. Graton, J.-Y. Le Questel and E. Renault, *Journal of Medicinal Chemistry*, 2009, **52**, 4073–4086.

[245] M. Walker, *Bioorganic & Medicinal Chemistry Letters*, 2017, **27**, 5100–5108.

[246] R. Bradbury, D. Acton, N. Broadbent, A. Brooks, G. Carr, G. Hatter, B. Hayter, K. Hill, N. Howe, R. Jones, D. Jude, S. Lamont, S. Loddick, H. McFarland, Z. Parveen, A. Rabow, G. Sharma-Singh, N. Stratton, A. Thomason, D. Trueman, G. Walker, S. Wells, J. Wilson and J. Wood, *Bioorganic and Medicinal Chemistry Letters*, 2013, **23**, 1945–1948.

[247] O. Lorthioir, R. Greenwood, A. Lister and M. Tucker, *Tetrahedron Letters*, 2020, **61**, 152600.

[248] X. Qing, C. Alt, L. Zhe, N. Shahul, P. M. Rademacher and C. W. Yee, *Methods of Use for Pyrimidines as Ferroportin Inhibitors*, 2021, Patent: WO 2021/222483 A1.

[249] L. Liang, W. Liangxing, Q. Ding-Quan and Y. Wenqing, *Bicyclic Heterocycles as FGFR4 Inhibitors*, 2016, Patent: US20161507876A.

[250] Apollo Scientific, *Chemical Products Online Store*, 2024, `store.apolloscientific.co.uk/product/78-dihydro-17-naphthyridin-65h-one`, Accessed: 20/11/2024.

[251] S.-L. Shi, X.-F. Wei, Y. Shimizu and M. Kanai, *Journal of the American Chemical Society*, 2012, **134**, 17019–17022.

[252] G. Chen, J. Cao, Q. Wang and J. Zhu, *Organic Letters*, 2020, **22**, 322–325.

[253] H. Wolff, *Organic Reactions*, John Wiley and Sons, Inc., 2011, pp. 307–336.

[254] I. Crosby, J. Shin and B. Capuano, *Australian Journal of Chemistry*, 2010, **63**, 211–226.

[255] P. Poon, A. Banerjee and M. Laya, *Journal of Chemical Research*, 2011, **35**, 67–73.

[256] J. Chen, Z. Xu, T. Wang, J. Lyssikatos and C. Ndubaku, *Synlett*, 2014, **25**, 89–92.

[257] K. Nicolaou, A. Stepan, T. Lister, A. Li, A. Montero, G. Tria, C. Turner, Y. Tang, J. Wang, R. Denton and D. Edmonds, *Journal of the American Chemical Society*, 2008, **130**, 13110–13119.

[258] J. Wang, S. Soisson, K. Young, W. Shoop, S. Kodali, A. Galgoci, R. Painter, G. Parthasarathy, Y. Tang, R. Cummings, S. Ha, K. Dorso, M. Motyl, H. Jayasuriya, J. Ondeyka, K. Herath, C. Zhang, L. Hernandez, J. Allocco, A. Basilio, J. Tormo, O. Genilloud, F. Vicente, F. Pelaez, L. Colwell, S. Lee, B. Michael, T. Felcetto, C. Gill, L. Silver, J. Hermes, K. Bartizal, J. Barrett, D. Schmatz, J. Becker, D. Cully and S. Singh, *Nature*, 2006, **441**, 358–361.

[259] M.-C. Frantz, J. Rodrigo, L. Boudier, T. Durroux, B. Mouillac and M. Hibert, *Journal of Medicinal Chemistry*, 2010, **53**, 1546–1562.

[260] A. Bard and L. Faulkner, *Electrochemical Methods: Fundamentals and Applications*, Wiley, 2000.

[261] B. Frontana-Uribe, R. Little, J. Ibanez, A. Palma and R. Vasquez-Medrano, *Green Chemistry*, 2010, **12**, 2099–2119.

[262] A. O'Brien, A. Maruyama, Y. Inokuma, M. Fujita, P. Baran and D. Blackmond, *Angewandte Chemie International Edition*, 2014, **53**, 11868–11871.

[263] S. Tang, L. Zeng and A. Lei, *Journal of the American Chemical Society*, 2018, **140**, 13128–13135.

[264] E. Horn, B. Rosen and P. Baran, *ACS Central Science*, 2016, **2**, 302–308.

[265] W. Nicholson, *Journal of Natural Philosophy, Chemistry and the Arts*, 1800, **4**, 179–191.

[266] M. Faraday, *Experiment Researches in Electricity*, Cambridge University Press, New York, USA, 1855.

[267] H. Kolbe, *Journal für praktische Chemie*, 1847, **41**, 137–139.

[268] E. Maigrot and J. Sabates, *Apparat zur Lauterung von Zuckersaften mittels Elektrizitat*, 1890, German Patent: 50443.

[269] O. Sock, M. Troupel and J. Perichon, *Tetrahedron Letters*, 1985, **26**, 1509–1512.

[270] E. Steckhan, *Angewandte Chemie International Edition in English*, 1986, **25**, 683–701.

[271] M. Rafiee, Z. Konz, M. Graaf, H. Koolman and S. Stahl, *ACS Catalysis*, 2018, **8**, 6738–6744.

[272] J.-i. Yoshida and S. Suga, *Chemistry – A European Journal*, 2002, **8**, 2650–2658.

[273] P. He, P. Watts, F. Marken and S. Haswell, *Angewandte Chemie International Edition*, 2006, **45**, 4146–4149.

[274] D. Cantillo, *Current Opinion in Electrochemistry*, 2024, **44**, 101459.

[275] J. Simons, *Journal of The Electrochemical Society*, 1949, **95**, 47.

[276] D. Danly, *Journal of The Electrochemical Society*, 1984, **131**, 435C.

[277] N. Kise, *Encyclopedia of Applied Electrochemistry*, Springer New York, New York, NY, 2014, pp. 702–706.

[278] S. Kashimura and K. Matsumoto, *Encyclopedia of Applied Electrochemistry*, Springer New York, New York, NY, 2014, pp. 706–713.

[279] M. Yan, Y. Kawamata and P. Baran, *Chemical Reviews*, 2017, **117**, 13230–13319.

[280] S. Ross, M. Finkelstein and R. Petersen, *Journal of the American Chemical Society*, 1966, **88**, 4657–4660.

[281] T. Shono, H. Hamaguchi and Y. Matsumura, *Journal of the American Chemical Society*, 1975, **97**, 4264–4268.

[282] T. Shono, Y. Matsumura and K. Tsubata, *Journal of the American Chemical Society*, 1981, **103**, 1172–1176.

[283] T. Shono, Y. Matsumura and K. Tsubata, *Tetrahedron Letters*, 1981, **22**, 3249–3252.

[284] T. Shono, Y. Matsumura and T. Kanazawa, *Tetrahedron Letters*, 1983, **24**, 1259–1262.

[285] T. Shono, Y. Matsumura, K. Tsubata, K. Uchida, T. Kanazawa and K. Tsuda, *The Journal of Organic Chemistry*, 1984, **49**, 3711–3716.

[286] T. Shono, Y. Matsumura, K. Uchida, K. Tsubata and A. Makino, *The Journal of Organic Chemistry*, 1984, **49**, 300–304.

[287] T. Shono, *Tetrahedron*, 1984, **40**, 811–850.

[288] L. Novaes, J. Ho, K. Mao, K. Liu, M. Tanwar, M. Neurock, E. Villemure, J. Terrett and S. Lin, *Journal of the American Chemical Society*, 2022, **144**, 1187–1197.

[289] R. Mazurkiewicz, J. Adamek, A. Październiorniok-Holewa, K. Zielińska, W. Simka, A. Gajos and K. Szymura, *The Journal of Organic Chemistry*, 2012, **77**, 1952–1960.

[290] E. Sierecki, G. Errasti, T. Martens and J. Royer, *Tetrahedron*, 2010, **66**, 10002–10007.

[291] S. Libendi, Y. Demizu, Y. Matsumura and O. Onomura, *Tetrahedron*, 2008, **64**, 3935–3942.

[292] M. Kabeshov, B. Musio, P. Murray, D. Browne and S. Ley, *Organic Letters*, 2014, **16**, 4618–4621.

[293] M. Gong and J.-M. Huang, *Chemistry – A European Journal*, 2016, **22**, 14293–14296.

[294] Y. Ma, X. Yao, L. Zhang, P. Ni, R. Cheng and J. Ye, *Angewandte Chemie International Edition*, 2019, **58**, 16548–16552.

[295] P.-S. Gao, X.-J. Weng, Z.-H. Wang, C. Zheng, B. Sun, Z.-H. Chen, S.-L. You and T.-S. Mei, *Angewandte Chemie International Edition*, 2020, **59**, 15254–15259.

[296] M. Paixão, A. Braga and D. Lüdtke, *Journal of the Brazilian Chemical Society*, 2008, **19**, 813–830.

[297] F. Schmidt, R. Stemmler, J. Rudolph and C. Bolm, *Chemical Society Reviews*, 2006, **35**, 454–470.

[298] P. Dosa, J. Ruble and G. Fu, *The Journal of Organic Chemistry*, 1997, **62**, 444–445.

[299] C. Bolm, N. Hermanns, J. Hildebrand and K. Muñiz, *Angewandte Chemie International Edition*, 2000, **39**, 3465–3467.

[300] W.-S. Huang and L. Pu, *Tetrahedron Letters*, 2000, **41**, 145–149.

[301] J. Park, H. Lee, C. Bolm and B. Kim, *Chemistry – A European Journal*, 2005, **11**, 945–950.

[302] C. Bolm and J. Rudolph, *Journal of the American Chemical Society*, 2002, **124**, 14850–14851.

[303] J. Porter, J. Traverse, A. Hoveyda and M. Snapper, *Journal of the American Chemical Society*, 2001, **123**, 10409–10410.

[304] N. Hermanns, S. Dahmen, C. Bolm and S. Bräse, *Angewandte Chemie International Edition*, 2002, **41**, 3692–3694.

[305] M. Trincado and J. Ellman, *Angewandte Chemie International Edition*, 2008, **47**, 5623–5626.

[306] G.-N. Ma, T. Zhang and M. Shi, *Organic Letters*, 2009, **11**, 875–878.

[307] I. Egorov, S. Santra, D. Kopchuk, I. Kovalev, G. Zyryanov, A. Majee, B. Ranu, V. Rusinov and O. Chupakhin, *Advanced Synthesis & Catalysis*, 2020, **362**, 4293–4324.

[308] M. Quan, L. Tang, J. Shen, G. Yang and W. Zhang, *Chemical Communications*, 2017, **53**, 609–612.

[309] C. Zhao, K. Rakesh, L. Ravidar, W.-Y. Fang and H.-L. Qin, *European Journal of Medicinal Chemistry*, 2019, **162**, 679–734.

[310] T. Iwasaki, K. Matsumoto, M. Matsuoka, T. Takahashi and K. Okumura, *Bulletin of the Chemical Society of Japan*, 1973, **46**, 852–855.

[311] C. G. Kokotos and V. K. Aggarwal, *Chemical Communications*, 2006, 2156–2158.

[312] T. Pavlovska, I. Weisheitelová, C. Pramthaisong, M. Sikorski, U. Jahn and R. Cibulka, *Advanced Synthesis & Catalysis*, 2023, **365**, 4662–4671.

[313] C. Jimeno, S. Sayalero, T. Fjermestad, G. Colet, F. Maseras and M. A. Pericàs, *Angewandte Chemie International Edition*, 2008, **47**, 1098–1101.

[314] S. Berger, F. Langer, C. Lutz, P. Knochel, T. A. Mobley and C. K. Reddy, *Angewandte Chemie International Edition in English*, 1997, **36**, 1496–1498.

[315] E. Le Gall, S. Sengmany, C. Hauréna, E. Léonel and T. Martens, *Journal of Organometallic Chemistry*, 2013, **736**, 27–35.

[316] G. Lu, F. Y. Kwong, J.-W. Ruan, Y.-M. Li and A. S. C. Chan, *Chemistry – A European Journal*, 2006, **12**, 4115–4120.

[317] J. Y. Becker, *ChemElectroChem*, 2024, **11**, e202400023.

[318] Z. Blum, M. Malmberg and K. Nyberg, *Chemischer Informationsdienst*, 1982, **13**, 078.

[319] M. Mori, K. Kagechika, K. Tohjima and M. Shibasaki, *Tetrahedron Letters*, 1988, **29**, 1409–1412.

[320] A. Huitric, J. Carr, W. Trager and B. Nist, *Tetrahedron*, 1963, **19**, 2145–2151.

[321] M. Schlosser and F. Mongin, *Chemistry Society Review*, 2007, **36**, 1161–1172.

[322] S. Turcaud, T. Martens, E. Sierecki, J. Pérard-Viret and J. Royer, *Tetrahedron Letters*, 2005, **46**, 5131–5134.

[323] E. Sierecki, S. Turcaud, T. Martens and J. Royer, *Synthesis*, 2006, 3199 – 3208.

Chapter 7

Experimental

7.1 Materials and Methods

All solvents and reagents were purchased from commercial suppliers and used without further purification unless otherwise stated. Microwave reactions were carried out in a Persona Chemistry Emrys Optimizer Automated Multi-User Microwave Synthesizer. Electrochemical reactions were carried out in an IKA ElectraSyn 2.0. Final compound purification by flash column chromatography was performed on a CombiFlash® System from Teledyne Isco equipped with an UV-light detector using prepacked silica RediSep Rf cartridges with the stated solvent gradient. Crude mixtures to be purified were dry loaded onto silica (normal phase) or Celite® 545 (reverse phase) prior to running the column. NMR spectra were recorded on the following instruments: Bruker Neo 700 MHz spectrometer with operating frequencies of 700 MHz for ^{1}H and 175 MHz for ^{13}C; Varian VNMRS-600 with operating frequencies of 600 MHz for ^{1}H and 150 MHz for ^{13}C NMR; and Varian VNMRS-400 with operating frequencies of 400 MHz for ^{1}H and 376 MHz for ^{19}F NMR. Spectra were referenced to $CDCl_3$ (δ_H 7.26 ppm, δ_C 77.16 ppm), CD_3OD (δ_H 4.87 ppm, δ_C 49.00 ppm), or DMSO (δ_H 2.50 ppm, δ_C 39.52 ppm). Chemical shifts are reported in parts per million (ppm), coupling constants (J) in hertz (Hz) and multiplicity as singlet (s), doublet (d), triplet (t), quartet (q), pentet (p), sextet (s), multiplet (m) or a combination thereof. All J values are $J_{H\text{-}H}$ unless otherwise stated. All ^{1}H NMR and ^{13}C NMR spectral assignments were made with the aid of ^{1}H^{1}H COSY, ^{1}H^{1}H NOESY, ^{1}H^{13}C HSQC and ^{1}H^{13}C HMBC NMR experiments. Infra-red spectra were recorded on a Perkin Elmer Paragon 1000 FT-IR spectrometer or a Perkin Elmer RX FT-IR spectrometer with Golden Gate Diamond ATR apparatus. IR assignments are in wavenumbers (cm^{-1}).

Melting points (mp) were recorded on Thermo Scientific Electrothermal IA9100 Digital Melting Point apparatus. Reaction monitoring by thin layer chromatography was performed using Merck F254 silica gel 60 aluminium sheets pre-coated with silica gel. High resolution mass spectrometry (HRMS) and liquid chromatography mass spectrometry (LC-MS) were recorded on a Waters TQD mass spectrometer ESI-LC water (0.1 % formic acid): MeCN/MeOH, flow rate 0.6 mL min^{-1} with a UPLC BEH C18 1.7 μm (2.1 mm x 50 mm) column. Gas chromatography mass spectrometry (GCMS) was carried out on a Shimadzu QP2010- Ultra with a temperature gradient 50 °C – 300 °C and a hold time of 5 mins, using a Rxi-17Sil MS (0.15 μm x 10 m x 0.15 mm) column.

7.2 Chapter 2

7.2.1 Substrate Synthesis

1'-{5-Chloro-*1H*-pyrazolo[3,4-c]pyridin-1-yl}ethan-1'-one 116

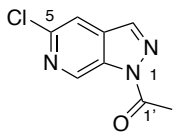

Ac_2O (33 mL, 0.35 mol, 10.0 eq) was added to a solution of 6-chloro-4-methylpyridin-3-amine **113** (5.00 g, 35 mmol, 1.00 eq) in DCE (140 mL) and stirred at room temperature for 90 minutes under a nitrogen atmosphere. $NaNO_2$ (9.68 g, 0.14 mol, 4.00 eq) was added and the reaction mixture stirred at room temperature for 3 hours, then heated overnight at 90 °C. The reaction mixture was concentrated under reduced pressure then diluted with sat. $NaHCO_3$ (150 mL). The product was extracted into EtOAc (5 x 100 mL) then washed with H_2O (4 x 100 mL) and brine (2 x 100 mL), dried over $MgSO_4$, filtered, and concentrated under reduced pressure to give 1'-{5-chloro-*1H*-pyrazolo[3,4-c]pyridin-1-yl}ethan-1'-one as a white solid (6.57 g, 34 mmol, 96%) with mp 138-139 °C. No further purification was necessary.

δ_H (400 MHz, $CDCl_3$) 9.56 (1H, s, 7-*H*), 8.15 (1H, s, 3-*H*), 7.69 (1H, s, 4-*H*), 2.81 (3H, s, C(O)C*H*$_3$); δ_C (101 MHz, $CDCl_3$) 170.3 (*C*=O), 144.7 (*C*-5), 138.0 (*C*-7), 137.8 (*C*-3), 134.7 (*C*-7a), 133.8 (*C*-3a), 114.8 (*C*-4), 22.6 (C(O)*C*H_3); V_{max} (ATR) 1729 (C=O), 1390, 1353, 634 cm^{-1}; LC-MS (ESI) [M (^{35}Cl) + H]$^+$ 196.069, [M (^{37}Cl)+ H]$^+$ 198.007, [M (^{35}Cl) + H – $COCH_3$] 154.035, [M (^{37}Cl) + H – $COCH_3$] 156.011; HRMS (ESI) found [M + H]$^+$ 196.0290, $C_8H_7N_3O^{35}Cl$ requires *M* 196.0278. The analytical data were consistent with the literature.[1]

5-Chloro-*1H*-pyrazolo[3,4-c]pyridine 77

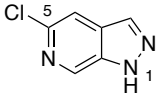

NaOMe (0.150 g, 2.8 mmol, 0.25 eq) was added to a solution of 1'-{5-chloro-*1H*-pyrazolo[3,4-c]pyridin-1-yl}ethan-1'-one **116** (2.00 g, 10 mmol, 1.00 eq) in anhydrous MeOH (0.2 M, 50 mL) and stirred at room temperature for 15 minutes. The reaction was quenched by addition of HCl:MeOH 1:100 (8 mL) until acidic pH and concentrated under reduced pressure. The crude product was taken up in H_2O then adjusted to pH 10 by addition of aqueous NaOH then extracted with EtOAc. The combined organic layers were washed with brine, dried over $MgSO_4$, filtered, and concentrated to afford 5-chloro-*1H*-pyrazolo[3,4-c]pyridine as a white solid (1.49 g, 10 mmol, 95%) with mp 225-226 °C.

δ_H (400 MHz, MeOD) 8.80 (1H, s, 7-*H*), 8.15 (1H, d, J = 1.2 Hz, 3-*H*), 7.82 (1H, d, J = 1.2 Hz, 4-*H*); δ_C (101 MHz, MeOD) 141.0 (*C*-5), 137.6 (*C*-7a), 135.1 (*C*-7), 134.2 (*C*-3), 131.2 (*C*-3a), 115.6 (*C*-4); V_{max} (ATR) 2995, 909, 736, 652 cm^{-1}; LC-MS (ESI) [M (^{35}Cl) + H]$^+$ 154.113, [M (^{37}Cl)+ H]$^+$ 156.128; HRMS (ESI) found [M + H]$^+$ 154.0167, $C_6H_5N_3{}^{35}Cl$ requires *M* 154.0172.

[1] D. Chapman and J. Hurst, *Journal of the Chemical Society, Perkin Transactions 1*, 1980, **5**, 2398-2404.

1'-{5-Bromo-*1H*-pyrazolo[3,4-c]pyridin-1-yl}ethan-1'-one 187

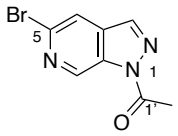

Ac_2O (2.5 mL, 27 mmol, 10.0 eq) was added to a solution of 6-bromo-4-methylpyridin-3-amine **186** (0.500 g, 2.7 mmol) in DCE (10 mL) and stirred at room temperature for 45 minutes under a nitrogen atmosphere. $NaNO_2$ (0.738 g, 11 mmol, 4.00 eq) was added and the reaction mixture stirred at room temperature for 3 hours, then heated overnight at 90 °C. The reaction mixture was concentrated under reduced pressure then diluted with $NaHCO_3$ (40 mL). The product was extracted into EtOAc (4 x 25 mL) then washed with H_2O (2 x 25 mL) and brine (2 x 25 mL), dried over $MgSO_4$, filtered, and concentrated under reduced pressure to give 1'-{5-bromo-*1H*-pyrazolo[3,4-c]pyridin-1-yl}ethan-1'-one as a yellow solid (0.553 g, 2.3 mmol, 86%) mp 129-149 °C. No further purification was necessary.

δ_H (600 MHz, $CDCl_3$) 9.54 (1H, t, J = 1.0 Hz, 7-*H*), 8.13 (1H, d, J = 1.0 Hz, 3-*H*), 7.85 (1H, d, J = 1.0 Hz, 4-*H*), 2.79 (3H, s, C(O)CH_3); δ_C (151 MHz, $CDCl_3$) 170.2 (*C*=O), 138.5 (*C*-7), 137.5 (*C*-3), 135.0 (*C*-7a), 134.1 (*C*-5), 133.8 (*C*-3a), 118.7 (*C*-4), 22.5 (*C*H_3); V_{max} (ATR) 1711 (C=O), 1383, 1349, 889, 740 cm^{-1}; LC-MS (ESI) [M (^{79}Br) + H]$^+$ 240.079, [M (^{81}Br)+ H]$^+$ 242.093; HRMS (ESI) found [M + H]$^+$ 239.9796, $C_8H_7{}^{79}BrN_3O$ requires *M* 239.9772.

5-Bromo-*1H*-pyrazolo[3,4-c]pyridine 185

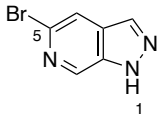

NaOMe (0.027 g, 0.50 mmol, 0.25 eq) was added to a solution of 1-{5-bromo-*1H*-pyrazolo[3,4-c]pyridin-1-yl}ethan-1-one **187** (0.480 g, 2.0 mmol, 1.00 eq) in dry MeOH (8 mL)and stirred at room temperature for 30 minutes. The reaction was quenched by addition of HCl in MeOH (1:100) (5 mL), then concentrated under reduced pressure. The crude product was taken up in H_2O (25 mL) and adjusted to pH 10 by addition of aqueous NaOH. The product was extracted into EtOAc (3 x 25 mL) then washed with brine (25 mL), dried over MgSO4, filtered, and concentrated under reduced pressure. 5-bromo-*1H*-pyrazolo[3,4-c]pyridine (0.372 g, 1.9 mmol, 94%) was collected as a pale yellow solid with mp 238-239 °C without further purification.

δ_H (600 MHz, MeOD) 8.78 (1H, s, 7-*H*), 8.13 (1H, s, 3-*H*), 7.97 (1H, s 4-*H*); δ_C (151 MHz, MeOD) 136.5 (*C*-5), 134.2 (*C*-7), 132.6 (*C*-3), 130.0 (*C*-7a), 128.6 (*C*-3a), 118.2 (*C*-4); V_{max} (ATR) 1462, 952, 873, 785, 753 cm^{-1}; LC-MS (ESI) [M (^{79}Br) + H]198.083, [M (^{81}Br)+ H]$^+$ 200.059; HRMS (ESI) found [M + H]$^+$ 197.9680, $C_6H_5{}^{79}BrN_3$ require *M* 197.9667.

7.2.2 Protecting Groups and Alkylations

5-Chloro-1-methanesulfonyl-*1H*-pyrazolo[3,4-c]pyridine 130

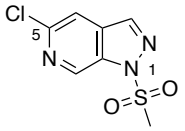

A solution of 5-chloro-*1H*-pyrazolo[3,4-c]pyridine **77** (0.500 g, 5.3 mmol, 1.00 eq) in anhydrous THF (10 mL) was added slowly to a suspension of NaH (0.195 g, 8.1 mmol, 2.50 eq) in anhydrous THF (16 mL) at 0 °C under a nitrogen atmosphere. MsCl was added over 5 minutes then the reaction allowed to return to room temperature and stirred for 2 hours. The reaction was quenched with H_2O:propan-2-ol 1:1 (20 mL) then concentrated under reduced pressure. The reaction mixture was diluted with H_2O (20 mL) and extracted into DCM (4 x 20 mL). The combined organic layers were washed with brine (20 mL), dried over $MgSO_4$, filtered, and concentrated under reduced pressure to afford 5-chloro-1-methanesulfonyl-*1H*-pyrazolo[3,4-c]pyridine as a yellow solid (0.695 g, 3.0 mmol, 92%) with mp 157-158 °C.

δ_H (600 MHz, $CDCl_3$) 9.26 (1H, t, J = 1.0 Hz, 7-*H*), 8.31 (1H, d, J = 1.0 Hz, 3-*H*), 7.73 (1H, d, J = 1.0 Hz, 4-*H*), 3.39 (3H, s, S*CH*$_3$); δ_C (151 MHz, $CDCl_3$) 144.6 (*C*-5), 139.0 (*C*-3), 135.9 (*C*-7), 135.8 (*C*-7a), 132.8 (*C*-3a), 114.9 (*C*-4), 41.5 (S*C*H$_3$); V_{max} (ATR) 1364, 557, 515 cm^{-1}; LC-MS (ESI) [M (^{35}Cl) + H]$^+$ 232.097, [M (^{37}Cl)+ H]$^+$ 234.150; HRMS (ESI) found [M + H]$^+$ 231.9941, $C_7H_7N_3SO_2{}^{35}Cl$ requires *M* 231.9948.

Compounds 133 and 132

DHP (0.36 mL, 3.9 mmol, 3.00 eq) then *p*TsOH (0.025 g, 0.13 mmol, 0.10 eq) in DCM (5 mL) were added slowly to a solution of 5-chloro-*1H*-pyrazolo[3,4-c]pyridine **77** (0.200 g, 1.3 mmol, 1.00 eq) in DCM (3 mL) over ice. The reaction mixture was stirred for 5 minutes then allowed to return to room temperature and stirred for 3 hours. The reaction mixture was diluted with DCM (25 mL) then washed with sat. $NaHCO_3$ (3 x 20 mL), dried over $MgSO_4$, filtered, and concentrated under reduced pressure. Purification by silica gel flash column chromatography (EtOAc:Pet Ether 40-60 0-50%) afforded 5-chloro-2-(tetrahydropyran-2'-yl)-*2H*-pyrazolo[3,4-c]pyridine **133** (0.206 g, 0.87 mmol, 66%) as a yellow oil and 5-chloro-1-(tetrahydropyran-2'-yl)-*1H*-pyrazolo[3,4-c]pyridine **132** as a white solid (0.0434 g, 0.18 mmol, 14%) with mp 89-93 °C. . $R_{f,\mathbf{133}}$ = 0.76 and $R_{f,\mathbf{132}}$ = 0.57 in EtOAc:Hexanes 1:1.

5-Chloro-1-(tetrahydropyran-2'-yl)-*1H*-pyrazolo[3,4-c]pyridine 133

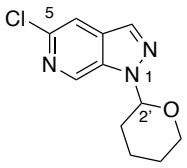

δ_H (600 MHz, $CDCl_3$) 8.91 (1H, t, J = 1.0 Hz, 7-*H*), 7.99 (1H, d, J = 0.8 Hz, 3-*H*), 7.62 (1H, d, J = 1.1 Hz, 4-*H*), 5.79 (1H, dd, J = 8.7, 2.7 Hz, 2'-*H*), 3.97 (1H, dtd, J = 11.7, 4.0, 1.5 Hz, 6'-*H*), 3.76 (1H, ddd, J = 11.7, 9.3, 3.4 Hz, 6'-*H*), 2.49 – 2.41 (1H, m, 3'-*H*), 2.16 – 2.08 (1H, m, 3'-*H*), 2.16 – 2.08 (1H, m, 4'-*H*), 1.81 – 1.74 (1H, m, 4'-*H*), 1.76 – 1.69 (1H, m, 5'-*H*), 1.72 – 1.67 (1H, m, 5'-*H*); δ_C (151 MHz, $CDCl_3$) 141.3 (*C*-5), 135.5 (*C*-7a), 134.4 (*C*-7), 132.4 (*C*-3), 131.6 (*C*-3a), 114.4 (*C*-4), 86.6 (*C*-2'), 67.3 (*C*-6'), 29.6 (*C*-3'), 25.0 (*C*-5'), 22.0 (*C*-4'); V_{max} (ATR) 1466, 1418, 1063, 871 cm^{-1}; LC-MS (ESI) [M (^{35}Cl) + H]$^+$ 238.178, [M (^{37}Cl)+ H]$^+$ 240.193, [M (^{35}Cl) + H – C_5H_9O] 154.073, [M (^{37}Cl) + H – C_5H_9O] 156.087; HRMS (ESI) found [M + H]$^+$ 238.0759, $C_{11}H_{13}{}^{35}ClN_3O$ requires *M* 238.0747.

5-Chloro-2-(tetrahydropyran-2'-yl)-*2H*-pyrazolo[3,4-c]pyridine 132

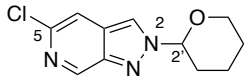

δ_H (600 MHz, $CDCl_3$) 9.07 (1H, t, J = 1.1 Hz, 7-*H*), 8.19 (1H, d, J = 1.1 Hz, 3-*H*), 7.57 (1H, d, J = 1.1 Hz, 4-*H*), 5.73 (1H, dd, J = 9.1, 2.9 Hz, 2'-*H*), 4.12 (1H, dtd, J = 11.7, 3.8, 1.6 Hz, 6'-*H*), 3.80 (1H, ddd, J = 11.7, 9.9, 3.3 Hz, 6'-*H*), 2.31 – 2.26 (1H, m, 3'-*H*), 2.14 (1H, dddd, J = 13.2, 11.0, 9.1, 4.2 Hz, 3'-*H*), 2.07 – 2.02 (1H, m, 4'-*H*), 1.82 – 1.72 (1H, m, 4'-*H*/5'-*H*), 1.82 – 1.72 (1H, m, 4'-*H*/5'-*H*), 1.72 – 1.70 (1H, m, 5'-*H*); δ_C (151 MHz, $CDCl_3$) 144.7 (*C*-7), 144.3 (*C*-5), 140.7(*C*-7a), 125.9 (*C*-3a), 120.6 (*C*-3), 113.2 (*C*-4), 89.7 (*C*-2'), 68.0 (*C*-6'), 31.6 (*C*-3'), 24.9 (*C*-5'), 21.8 (*C*-4'); V_{max} (ATR) 1475, 1053 (C-O), 724 cm^{-1}; LC-MS (ESI) [M (^{35}Cl) + H]$^+$ 238.221, [M (^{37}Cl)+ H]$^+$ 240.273, [M (^{35}Cl) + H – C_5H_9O] 154.113, [M (^{37}Cl) + H – C_5H_9O] 156.116; HRMS (ESI) found [M + H]$^+$ 238.0736, $C_{11}H_{13}{}^{35}ClN_3O$ requires *M* 238.0747.

5-Bromo-1-(tetrahydropyran-2'-yl)-*1H*-pyrazolo[3,4-c]pyridine 190

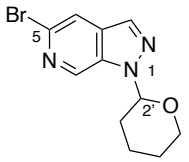

DHP (0.28 mL, 3.0 mmol, 3.00 eq) then pTsOH·H_2O (0.019 g, 0.10 mmol, 0.10 eq) were added slowly to a solution of 5-bromo-*1H*-pyrazolo[3,4-c]pyridine **185** (0.200 g, 1.0 mmol, 1.00 eq) in DCM (7 mL) over ice. After 5 minutes the reaction mixture was allowed to return to room temperature, then stirred for 22 hours. The reaction was diluted with DCM (20 mL) then washed with sat. $NaHCO_3$ (3 x 25 mL) and brine (20 mL), dried over $MgSO_4$, filtered, and concentrated under reduced pressure to a yellow oil. Purification by silica gel flash column chromatography (EtOAc:Pet Ether 40-60 0-25%) afforded 5-bromo-1-(tetrahydropyran-2'-yl)-*1H*-pyrazolo[3,4-c]pyridine as a white solid (0.233 g, 0.83 mmol, 82%) with mp 125-127 °C.

δ_H (600 MHz, $CDCl_3$) 8.91 (1H, t, J = 1.0 Hz, 7-*H*), 8.00 (1H, d, J = 1.0 Hz, 3-*H*), 7.80 (1H, d, J = 1.0 Hz, 4-*H*), 5.80 (1H, dd, J = 9.2, 2.9 Hz, 2'-*H*), 3.97 (1H, ddt, J = 9.2, 5.4, 2.5 Hz, 6'-*H*), 3.82-3.73 (1H, m, 6'-*H*), 2.54 – 2.40 (1H, m, 3'-*H*), 2.20 – 2.08 (1H, m, 3'-*H*), 2.20 – 2.08 (1H, m, 5'-*H*), 1.85 – 1.46 (2H, m, 4'-*H*), 1.85 – 1.46 (1H, m, 5'-*H*); δ_C (151 MHz, $CDCl_3$) 135.8 (*C*-5), 134.9 (*C*-7), 132.2 (*C*-3), 131.8 (*C*-7a), 130.6 (*C*-3a), 118.4 (*C*-4), 86.6 (*C*-2'), 67.3 (*C*-6'), 29.6 (*C*-3'), 25.0 (*C*-4'), 22.0 (*C*-5'); V_{max} (ATR) 1465, 1047, 911, 733 cm^{-1}; LC-MS (ESI) [M (^{79}Br) + H]$^+$ 282.150, [M (^{81}Br)+ H]$^+$ 283.963, [M (^{79}Br) + H – C_5H_9O] 198.121, [M (^{81}Br) + H – C_5H_9O] 200.097; HRMS (ESI) found [M + H]$^+$ 282.0249, $C_{11}H_{13}{}^{79}BrN_3O$ requires *M* 282.0242.

5-Bromo-2-(tetrahydropyran-2'-yl)-*2H*-pyrazolo[3,4-c]pyridine 191

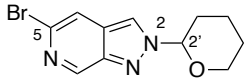

DHP (0.55 mL, 6.1 mmol, 3.00 eq) then pTsOH·H_2O (0.038 g, 0.20 mmol, 0.10 eq) were added slowly to a solution of 5-bromo-*1H*-pyrazolo[3,4-c]pyridine **185** (0.400 g, 2.0 mmol, 1.00 eq) in DCM (15 mL) over ice. After 5 minutes the reaction mixture was allowed to return to room temperature, then stirred for 2 hours. The reaction was diluted with DCM (20 mL) then washed with sat. $NaHCO_3$ (3 x 25 mL) and brine (20 mL), dried over $MgSO_4$, filtered, and concentrated under reduced pressure to a yellow oil. Purification by silica gel flash column chromatography (EtOAc:Pet Ether 40-60 0-40%) afforded 5-bromo-2-(tetrahydropyran-2'-yl)-*2H*-pyrazolo[3,4-c]pyridine as a white solid (0.426 g, 1.5 mmol, 75%) with mp

58-60 °C. 5-bromo-1-(tetrahydropyran-2'-yl)-*1H*-pyrazolo[3,4-c]pyridine (0.035 g, 0.13 mmol, 6.2%) was also collected. $R_{f,\mathbf{190}}$ = 0.61 and $R_{f,\mathbf{191}}$ = 0.37 in EtOAc:Hexanes 1:2.

δ_H (600 MHz, $CDCl_3$) 9.05 (1H, t, *J* = 1.0 Hz, 7-*H*), 8.19 (1H, d, *J* = 1.0 Hz, 3-*H*), 7.76 (1H, d, *J* = 1.0 Hz, 4-*H*), 5.73 (1H, dd, *J* = 9.2, 2.9 Hz, 2'-*H*), 4.12 (1H, ddt, *J* = 9.2, 5.4, 2.5 Hz, 6'-*H*), 3.80 (1H, ddd, *J* = 11.7, 9.9, 3.3 Hz, 6'-*H*), 2.31 – 2.25 (1H, m, 3'-*H*), 2.18 – 2.08 (1H, m, 3'-*H*), 2.07 – 2.01 (1H, m, 5'-*H*), 1.83 – 1.66 (2H, m, 4'-*H*), 1.83 – 1.66 (1H, m, 5'-*H*); δ_C (151 MHz, $CDCl_3$) 144.9 (*C*-7), 144.4 (*C*-5), 130.0 (*C*-7a), 126.3 (*C*-3a), 120.4 (*C*-3), 117.3 (*C*-4), 89.7 (*C*-2'), 68.0 (*C*-6'), 31.6 (*C*-3'), 24.9 (*C*-4'), 21.8 (*C*-5'); V_{max} (ATR) 1471, 1147, 1092, 1044, 918 cm^{-1}; LC-MS (ESI) [M (^{79}Br) + H]$^+$ 282.112, [M (^{81}Br)+ H]$^+$ 283.898, [M (^{79}Br) + H – C_5H_9O] 198.083, [M (^{81}Br) + H – C_5H_9O] 200.097; HRMS (ESI) found [M + H]$^+$ 282.0250, $C_{11}H_{13}{}^{79}BrN_3O$ requires *M* 282.0242.

SEM Protection Route 1

A solution of the starting *1H*-pyrazolo[3,4-c]pyridine (1.00 eq) in anhydrous THF was added slowly to a suspension of NaH (1.50 eq) in anhydrous THF at 0 °C under a nitrogen atmosphere. The mixture was stirred at 0 °C for 30 minutes then SEM-Cl (1.50 eq) was added dropwise. The reaction mixture was allowed to return to room temperature then stirred until no starting material remained. The reaction was quenched by addition of H_2O:propan-2-ol 1:1 then concentrated under reduced pressure. The crude product was diluted with H_2O, extracted with DCM, washed with brine, dried over $MgSO_4$, filtered, and concentrated. Purification by silica gel flash column chromatography with the stated solvent system afforded the two product isomers.

SEM Protection Route 2

Dicyclohexylmethylamine (1.20 eq) then SEM-Cl (1.20 eq) were added to a solution of the starting *1H*-pyrazolo[3,4-c]pyridine (1.00 eq) in anhydrous THF nitrogen and the reaction mixture was stirred at room temperature overnight. The reaction was quenched by addition of NaOH solution then concentrated under reduced pressure to remove the THF. The crude product was extracted with EtOAc, washed with brine, dried over $MgSO_4$, filtered, and concentrated. The purification by silica gel flash column chromatography with the stated solvent system afforded the two product isomers.

Compounds 136 and 137

SEM protection route 1 was applied to 5-chloro-*1H*-pyrazolo[3,4-c]pyridine **77** (0.200 g, 1.3 mmol, 1.00 eq) then purification by silica gel flash column chromatography (EtOAc:Hexanes 0-25%) afforded 5-chloro-1-{[2'-(trimethylsilyl)ethoxy]methyl}-*1H*-pyrazolo[3,4-c]pyridine **136** (0.167 g, 0.59 mmol, 45%) as a colourless oil and 5-chloro-2-{[2'-(trimethylsilyl)ethoxy]methyl}-*2H*-pyrazolo[3,4-c]pyridine **137** (0.108 g, 0.38 mmol, 29%) as a yellow solid with mp 66.8-67.2 °C. $R_{f,\mathbf{136}}$ = 0.49, $R_{f,\mathbf{137}}$ = 0.32 in EtOAc:Hexanes 1:4.

SEM protection route 2 was applied to 5-chloro-*1H*-pyrazolo[3,4-c]pyridine **77** (0.330 g, 2.1 mmol, 1.00 eq) then purification by silica gel flash column chromatography (EtOAc:Hexanes 0-25%) afforded 5-chloro-1-{[2'-(trimethylsilyl)ethoxy]methyl}-*1H*-pyrazolo[3,4-c]pyridine **136** (0.127 g, 0.45 mmol, 21%) as a colourless oil and 5-chloro-2-{[2'-(trimethylsilyl)ethoxy]methyl}-*2H*-pyrazolo[3,4-c]pyridine **137** (0.270 g, 0.95 mmol, 44%) as a yellow solid with mp 66.8-67.2 °C. $R_{f,\mathbf{136}}$ = 0.49, $R_{f,\mathbf{137}}$ = 0.32 in EtOAc:Hexanes 1:4.

5-Chloro-1-{[2'-(trimethylsilyl)ethoxy]methyl}-*1H*-pyrazolo[3,4-c]pyridine 136

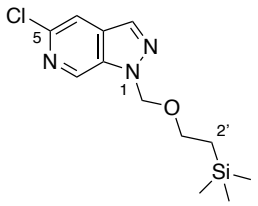

δ_H (400 MHz, $CDCl_3$) 8.92 (1H, t, *J* = 1.0 Hz, 7-*H*), 8.04 (1H d, *J* = 1.0 Hz, 3-*H*), 7.70 (1H, d, *J* = 1.0 Hz, 4-*H*), 5.82 (2H, s, NCH_2O), 3.60 – 3.51 (2H, m, OCH_2C), 0.96 – 0.86 (2H, m, CH_2Si), -0.05 (9H, s, $Si(CH_3)_3$); δ_C (101 MHz, $CDCl_3$) 141.7 (*C*-5), 135.7 (*C*-7), 133.7 (*C*-7a), 132.8 (*C*-3), 131.8 (*C*-3a), 114.6 (*C*-4), 78.7 (NCH_2O), 67.2 (OCH_2CH_2), 17.8 ($CH_2Si(CH_3)_3$), -1.4 ($Si(CH_3)_3$); V_{max} (ATR) 1469, 1079, 1061, 834, 801, 785 cm^{-1}; LC-MS (ESI) [M (^{35}Cl) + H]$^+$ 284.245, [M (^{37}Cl)+ H]$^+$ 286.260; HRMS (ESI) found [M + H]$^+$ 284.0992, $C_{12}H_{19}N_3OSi^{35}Cl$ requires *M* 284.0986.

5-Chloro-2-{[2'-(trimethylsilyl)ethoxy]methyl}-*2H*-pyrazolo[3,4-c]pyridine 137

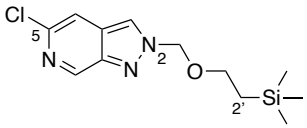

δ_H (400 MHz, $CDCl_3$) 9.10 (1H, t, *J* = 1.1 Hz, 7-*H*), 8.14 (1H, d, *J* = 1.1 Hz, 3-*H*), 7.60 (1H, d, *J* = 1.1 Hz, 4-*H*), 5.77 (2H, s, NCH_2O), 3.68 – 3.59 (2H, m, OCH_2CH_2), 1.00 – 0.90 (2H, m, CH_2Si), -0.03 (9H, s, $Si(CH_3)_3$); δ_C (101 MHz, $CDCl_3$) 145.7 (*C*-5), 145.3 (*C*-7), 141.0 (*C*-7a), 127.8 (*C*-3a), 125.4 (*C*-3), 115.1 (*C*-4), 83.6 (NCH_2O), 68.9 (OCH_2CH_2), 18.6 (CH_2Si), -1.5 ($Si(CH_3)_3$); V_{max} (ATR) 1249, 1088, 1054, 854, 832 cm^{-1}; LC-MS (ESI) [M (^{35}Cl) + H]$^+$ 284.245, [M (^{37}Cl)+ H]$^+$ 286.260; HRMS (ESI) found [M + H]$^+$ 284.0989, $C_{12}H_{19}N_3OSi^{35}Cl$ requires *M* 284.0986.

Compounds 188 and 189

SEM protection route 1 was applied to 5-bromo-*1H*-pyrazolo[3,4-c]pyridine **185** (1.00 g, 5.1 mmol, 1.00 eq). Purification by silica gel flash column chromatography (EtOAc:Pet Ether 40-60 0-50%) afforded 5-bromo-1-{[2-(trimethylsilyl)ethoxy]methyl}-*1H*-pyrazolo[3,4-c]pyridine **188** (0.785 g, 2.4 mmol, 47%) as a colourless oil and 5-bromo-2-{[2'-(trimethylsilyl)ethoxy]methyl}-*2H*-pyrazolo[3,4-c]pyridine **189** (0.435 g, 1.3 mmol, 26%) as a yellow solid with mp 61-62 °C. $R_{f,\mathbf{188}}$ = 0.78, $R_{f,\mathbf{189}}$ = 0.43 in EtOAc:Pet Ether 40-60 1:4.

SEM protection route 2 was applied to 5-bromo-*1H*-pyrazolo[3,4-c]pyridine **185** (0.200 g, 1.0 mmol, 1.00 eq) then purification by silica gel flash column chromatography (EtOAc:Pet Ether 40-60 0-50%) afforded 5-bromo-1-{[2-(trimethylsilyl)ethoxy]methyl}-*1H*-pyrazolo[3,4-c]pyridine **188** (0.060 g, 0.18 mmol, 18%) as a colourless oil and 5-bromo-2-{[2'-(trimethylsilyl)ethoxy]methyl}-*2H*-pyrazolo[3,4-c]pyridine **189** (0.105 g, 0.32 mmol, 32%) as a yellow solid with mp 61-62 °C. $R_{f,\mathbf{188}}$ = 0.78, $R_{f,\mathbf{189}}$ = 0.43 in EtOAc:Pet Ether 40-60 1:4.

5-Bromo-1-{[2-(trimethylsilyl)ethoxy]methyl}-*1H*-pyrazolo[3,4-c]pyridine 188

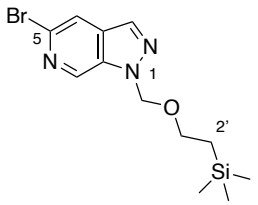

δ_H (600 MHz, $CDCl_3$) 8.89 (1H, t, J = 1.0 Hz, 7-*H*), 8.01 (1H, d, J = 1.0 Hz, 3-*H*), 7.84 (1H, d, J = 1.0 Hz, 4-*H*), 5.79 (2H, s, NCH_2O), 3.56 – 3.50 (2H, m, OCH_2CH$_2$), 0.91 – 0.85 (2H, m, OCH$_2$CH_2Si), -0.07 (9H, s, Si(CH_3)$_3$); δ_C (151 MHz, $CDCl_3$) 135.9 (*C*-5), 134.0 (*C*-7), 132.5 (*C*-3), 131.9 (*C*-7a), 131.9 (*C*-3a), 118.4 (*C*-4), 78.6 (N*C*H$_2$O), 67.0 (O*C*H$_2$CH$_2$), 17.7 (CH$_2$*C*H$_2$Si), -1.5 (Si(*C*H$_3$)$_3$); V_{max} (ATR) 1467, 1088, 865, 839, 779 cm^{-1}; LC-MS (ESI) [M(^{79}Br) +H]$^+$ 328.211, [M(^{81}Br)+H]$^+$ 329.959; HRMS (ESI) found [M + H]$^+$ 328.0478, $C_{12}H_{19}{}^{79}BrN_3OSi$ requires *M* 328.0481.

5-Bromo-2-{[2'-(trimethylsilyl)ethoxy]methyl}-*2H*-pyrazolo[3,4-c]pyridine 189

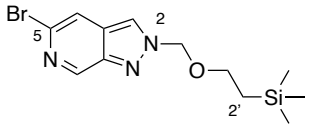

δ_H (600 MHz, $CDCl_3$) 9.08 (1H, t, J = 1.1 Hz, 7-*H*), 8.13 (1H, d, J = 1.1 Hz, 3-*H*), 7.78 (1H, d, J = 1.1 Hz, 4-*H*), 5.77 (2H, s, NCH_2O), 3.66 – 3.61 (2H, m, OCH_2CH$_2$), 0.98 – 0.91 (2H, m, OCH$_2$CH_2Si), -0.03 (9H, s, Si(CH_3)$_3$); δ_C (151 MHz, $CDCl_3$) 144.9 (*C*-7), 144.5 (*C*-5), 130.2 (*C*-7a), 126.8 (*C*-3a), 121.6 (*C*-3), 117.1 (*C*-4), 82.6 (N*C*H$_2$O), 68.2 (O*C*H$_2$CH$_2$), 17.8 (CH$_2$*C*H$_2$Si), -1.5 (Si(*C*H$_3$)$_3$); V_{max} (ATR) 1105, 1041, 914, 840, 735 cm^{-1}; LC-MS (ESI) [M(^{79}Br) +H]$^+$ 328.211, [M(^{81}Br) + H]$^+$ 329.997; HRMS (ESI) found [M + H]$^+$ 328.0485, $C_{12}H_{19}{}^{79}BrN_3OSi$ requires *M* 328.0481.

Compounds 207 and 208

A cooled solution of 5-chloro-*1H*-pyrazolo[3,4-c]pyridine **77** (0.100 g, 0.65 mmol, 1.00 eq) and NaH (0.031 g, 0.78 mmol, 1.20 eq) in THF (3 mL) was stirred for 30 minutes on ice under a nitrogen atmosphere. MeI (0.06 mL, 0.98 mmol, 1.50 eq) was added and the reaction mixture was allowed to return to room temperature. After 45 minutes the reaction was quenched with H_2O:propan-2-ol 1:1 (10 mL) then concentrated under reduced pressure. The product was extracted with DCM (3 x 15 mL) and the combined organic layers were washed with brine (20 mL), dried over $MgSO_4$, filtered, and concentrated under reduced pressure to form a yellow solid. Purification by silica gel flash column chromatography (EtOAc:Pet Ether 40-60 0-60%) afforded 5-chloro-1-methyl-*1H*-pyrazolo[3,4-c]pyridine **207** (0.033 g, 0.20 mmol, 31%) as a white solid with mp 102-104 °C, and 5-chloro-2-methyl-*2H*-pyrazolo[3,4-c]pyridine **208** as a white solid (0.046 g, 0.28 mmol, 42%) with mp 134-146°C. $R_{f,\,\mathbf{207}}$ = 0.50 and $R_{f,\mathbf{208}}$ = 0.18 in EtOAc:Pet Ether 40-60 1:2.

5-Chloro-1-methyl-*1H*-pyrazolo[3,4-c]pyridine 207

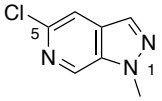

δ_H (600 MHz, $CDCl_3$) 8.70 (1H, d, J = 1.0 Hz, 7-*H*), 7.95 (1H, d, J = 1.0 Hz, 3-*H*), 7.61 (1H, t, J = 1.0 Hz, 4-*H*), 4.16 (3H, s, NCH_3); δ_C (151 MHz, $CDCl_3$) 140.7 (*C*-5), 136.0 (*C*-7a), 132.7 (*C*-7), 131.6 (*C*-3), 130.6 (*C*-3a), 114.2 (*C*-4), 36.3 (*C*H$_3$); V_{max} (ATR) 1545, 1539, 1346, 713 cm^{-1}; LC-MS (ESI) [M(^{35}Cl) +

H]$^+$ 168.059, [M(^{37}Cl) + H]$^+$ 170.073; HRMS (ESI) found [M + H]$^+$ 168.0338, $C_7H_8{}^{35}ClN_3$ requires *M* 168.0323. The analytical data were consistent with the literature.[2]

5-Chloro-2-methyl-*2H*-pyrazolo[3,4-c]pyridine 208

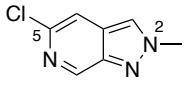

δ_H (600 MHz, $CDCl_3$) 9.01 (1H, t, *J* = 1.0 Hz, 7-*H*), 7.90 (1H, d, *J* = 1.0 Hz 3-*H*), 7.53 (1H, d, *J* = 1.0 Hz, 4-*H*), 4.27 (3H, s, NC*H*$_3$); δ_C (151 MHz, $CDCl_3$) 144.7 (*C*-5), 143.6 (*C*-7), 140.5 (*C*-7a), 126.6 (*C*-3a), 122.9 (*C*-3), 112.6 (*C*-4), 41.1 (N*C*H$_3$); V_{max} (ATR) 1545, 1539, 1346, 713 cm^{-1}; LC-MS (ESI) [M(^{35}Cl) + H]$^+$ 168.059, [M(^{37}Cl)+ H]$^+$ 170.111; HRMS (ESI) found [M + H]$^+$ 168.0334, $C_7H_8{}^{35}ClN_3$ requires *M* 168.0323. The analytical data were consistent with the literature.[2]

Compounds 205 and 206

A cooled solution of 5-bromo-*1H*-pyrazolo[3,4-c]pyridine **185** (0.500 g, 2.5 mmol, 1.00 eq) and NaH (0.121 g, 3.0 mmol, 1.20 eq) in THF (13 mL) was stirred for 30 minutes on ice under a nitrogen atmosphere. MeI (0.24 mL, 3.8 mmol, 1.50 eq) was added and the reaction mixture was allowed to return to room temperature. After 45 minutes the reaction was quenched with H_2O:propan-2-ol 1:1 (30 mL) then concentrated under reduced pressure. The product was extracted with DCM (4 x 25 mL) and the combined organic layers were washed with brine (20 mL), dried over $MgSO_4$, filtered, and concentrated under reduced pressure to form a yellow solid. Purification by silica gel flash column chromatography (EtOAc:Pet Ether 40-60 0-75%) gave 5-bromo-1-methyl-*1H*-pyrazolo[3,4-c]pyridine **205** (0.191 g, 0.90 mmol, 36%) as a white solid with mp 109-110 °C, and 5-bromo-2-methyl-*2H*-pyrazolo[3,4-c]pyridine **206** (0.268 g, 1.3 mmol, 50%) as a white solid with mp 175-178 °C. $R_{f,\mathbf{205}}$ = 0.17 and $R_{f,\mathbf{206}}$ = 0.58 in EtOAc:Pet Ether 40-60 1:1.

5-Bromo-1-methyl-*1H*-pyrazolo[3,4-c]pyridine 205

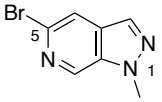

δ_H (700 MHz, $CDCl_3$) 8.65 (1H, d, *J* = 1.0 Hz, 7-*H*), 7.91 (1H, d, *J* = 1.0 Hz, 3-*H*), 7.74 (1H, t, *J* = 1.0 Hz, 4-*H*), 4.11 (3H, s, NC*H*$_3$); δ_C (176 MHz, $CDCl_3$) 136.3 (*C*-5), 133.2 (*C*-7), 131.5 (*C*-3), 130.8 (*C*-7a), 130.0 (*C*-3a), 118.2 (*C*-4), 36.4 (*C*H$_3$); V_{max} (ATR) 1473, 1050, 765, 640, 428 cm^{-1}; LC-MS (ESI) [M(^{79}Br) + H]$^+$ 212.031, [M(^{81}Br) + H]$^+$ 214.045; HRMS (ESI) found [M + H]$^+$ 211.9835, $C_7H_7{}^{79}BrN_3$ requires *M* 211.9823.

5-Bromo-2-methyl-*2H*-pyrazolo[3,4-c]pyridine 206

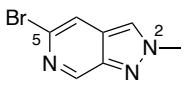

δ_H (700 MHz, $CDCl_3$) 8.93 (1H, s, 7-*H*), 7.85 (1H, s, 3-*H*), 7.64 (1H, s, 4-*H*), 4.22 (3H, s, NC*H*$_3$); δ_C (176 MHz, $CDCl_3$) 144.8 (*C*-5), 143.9 (*C*-7), 129.9 (*C*-7a), 127.0 (*C*-3a), 122.8 (*C*-3), 116.7 (*C*-4), 41.2 (N*C*H$_3$); V_{max} (ATR) 1154, 1043, 902, 489, 441 cm^{-1}; LC-MS (ESI) [M(^{79}Br) + H]$^+$ 212.039, [M(^{81}Br) +

[2] A. Papastathopoulos *et al*, *European Journal of Medicinal Chemistry*, 2021, **218**, 113387

H]$^+$ 214.025; HRMS (ESI) found [M + H]$^+$ 211.9837, $C_7H_7{}^{79}BrN_3$ requires *M* 211.9823.

Compounds 209 and 210

A cooled solution of 5-chloro-*1H*-pyrazolo[3,4-c]pyridine **77** (0.200 g, 1.3 mmol, 1.00 eq) and NaH (0.047 g, 1.6 mmol, 1.20 eq) in THF (6.5 mL) was stirred for 30 minutes on ice under a nitrogen atmosphere. 1-iodopropane (0.19 mL, 2.0 mmol, 1.50 eq) was added and the reaction mixture was allowed to return to room temperature. After stirring overnight, the reaction was quenched with NH_4Cl (25 mL) then volatiles were removed under reduced pressure. The product was extracted with EtOAc (3 x 30 mL), and the combined organic layers washed with brine (30 mL), dried over $MgSO_4$, filtered, then concentrated under reduced pressure to give the crude product as an orange solid. The final products were purified by silica gel flash column chromatography (EtOAc:Hexanes 0-35%) affording compound **209** as a white solid (0.068g, 0.35 mmol, 27%) with mp 53-55 °C and compound **210** as a yellow solid (0.089g, 0.46 mmol, 35%) mp 56-60 °C. $R_{f,\mathbf{209}}$ = 0.48 and $R_{f,\mathbf{210}}$ = 0.31 in EtOAc:Hexanes 1:3.

5-Chloro-1-propyl-*1H*-pyrazolo[3,4-c]pyridine 209

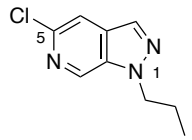

δ_H (400 MHz, $CDCl_3$) 8.73 (1H, s, 7-*H*), 7.99 (1H, s, 3-*H*), 7.63 (1H, s, 4-*H*), 4.42 (2H, t, *J* = 7.3 Hz, NCH_2CH$_2$), 1.98 (2H, s, *J* = 7.3 Hz, CH_2CH$_3$), 0.92 (3H, t, *J* = 7.3 Hz, CH$_2$CH_3); δ_C (101 MHz, $CDCl_3$) 140.6 (*C*-5), 135.7 (*C*-7a), 132.8 (*C*-7), 131.6 (*C*-3), 130.5 (*C*-3a), 114.3 (*C*-4), 51.5 (N*C*H$_2$CH$_2$), 23.4 (*C*H$_2$CH$_3$), 11.3 (CH$_2$*C*H$_3$); V_{max} (ATR) 1470, 1066, 907, 730 cm^{-1}; LC-MS (ESI) [M(^{35}Cl) + H]$^+$ 196.145, [M(^{37}Cl) + H]$^+$ 198.121; HRMS found [M + H]$^+$ 196.0643, $C_9H_{11}N_3{}^{35}Cl$ requires *M* 196.0642.

5-Chloro-2-propyl-*2H*-pyrazolo[3,4-c]pyridine 210

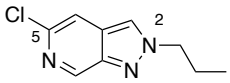

δ_H (400 MHz, $CDCl_3$) 9.03 (1H, t, *J* = 1.1 Hz 7-*H*), 7.92 (1H, d, *J* = 1.1 Hz, 3-*H*), 7.54 (1H, d, *J* = 1.1 Hz, 4-*H*), 4.43 (2H, t, *J* = 7.3 Hz, NCH_2CH$_2$), 2.06 (2H, s, *J* = 7.3 Hz, CH_2CH$_3$), 0.95 (3H, t, *J* = 7.3 Hz, CH$_2$CH_3); δ_C (101 MHz, $CDCl_3$) 144.6 (*C*-5), 143.8 (*C*-7), 140.3 (*C*-7a), 126.3 (*C*-3a), 122.1 (*C*-3), 112.7 (*C*-4), 56.2 (N*C*H$_2$CH$_2$), 23.9 (*C*H$_2$CH$_3$), 11.1 (CH$_2$*C*H$_3$); V_{max} (ATR) 1476, 1152, 1056, 726 cm^{-1}; LC-MS (ESI) [M(^{35}Cl) + H]$^+$ 196.145, [M(^{37}Cl) + H]$^+$ 198.121; HRMS found [M + H]$^+$ 196.0644, $C_9H_{11}N_3{}^{35}Cl$ requires *M* 196.0642.

7.2.3 Borylation Suzuki-Miyaura Cross-coupling

General Procedure A for tandem Borylation and Suzuki-Miyaura cross-coupling.

[Ir(COD)OMe]$_2$ (0.025 eq), B_2pin_2 (1.10 eq), and dtbpy (0.05 eq) were sealed in an oven-dried microwave reaction vial and degassed with N_2/vacuum cycling. A solution of the SEM-protected pyrazolo[3,4-c]pyridine in anhydrous MTBE (0.4 M) was added under nitrogen. The reaction mixture was heated in a microwave reactor at 100 °C until GCMS analysis showed complete borylation had occurred, then concentrated under reduced pressure to afford the crude boronate ester. To the crude boronate ester was added Cs_2CO_3 (2.00 eq), Pd(dppf)Cl_2 (0.025 eq), the aryl halide (1.10 eq) and anhydrous DMAc (1 M) under nitrogen. The reaction mixture was heated in a microwave reactor at 120 °C until GCMS analysis showed no boronate ester remained. The reaction mixture was filtered

through Celite® and the residue washed with EtOAc. The combined filtrates were concentrated under reduced pressure, and the residue was dissolved in H_2O then extracted with EtOAc. The combined organic layers were washed with brine, dried over $MgSO_4$, filtered, and concentrated. The product was purified by silica gel flash column chromatography using the stated solvent system.

General Procedure B for tandem Borylation and Suzuki-Miyaura cross-coupling with CuCl.

$[Ir(COD)OMe]_2$ (0.025 eq), B_2pin_2 (1.10 eq), and dtbpy (0.05 eq) were sealed in an oven-dried microwave reaction vial and degassed with N_2/vacuum cycling. A solution of the SEM-protected pyrazolo[3,4-c]pyridine in anhydrous MTBE (0.4 M) was added under nitrogen. The reaction mixture was heated in a microwave reactor at 100 °C until GCMS analysis showed complete borylation had occurred, then concentrated under reduced pressure to afford the crude boronate ester. To the crude boronate ester was added Cs_2CO_3 (1.00 eq), $Pd(OAc)_2$ (0.025 eq), 1,1'-Bis(diphenylphosphino) ferrocene (dppf) (0.050 eq), CuCl (1.00 eq), the aryl halide (1.10 eq) and anhydrous DMAc (1 M) under nitrogen. The reaction mixture was heated in a microwave reactor at 120 °C until GCMS analysis showed no boronate ester remained. The reaction mixture was filtered through Celite® and the residue washed with EtOAc. The combined filtrates were concentrated under reduced pressure, and the residue was dissolved in H_2O then extracted with EtOAc. The combined organic layers were washed with brine, dried over $MgSO_4$, filtered, and concentrated. The product was purified by silica gel flash column chromatography using the stated solvent system.

5-Chloro-3-[4'-(trifluoromethyl)phenyl]-1-{[2"-(trimethylsilyl)ethoxy]methyl}-*1H*-pyrazolo[3,4-c]pyridine 140

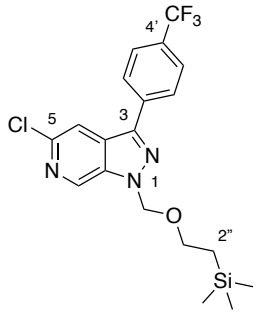

General procedure A was applied to 5-chloro-1-{[2'-(trimethylsilyl)ethoxy]methyl}-*1H*-pyrazolo[3,4-c]pyridine **136** (0.150 g, 0.53 mmol, 1.00 eq) with 4-bromobenzotrifluoride (0.08 mL, 0.58 mmol, 1.10 eq). After purification by silica gel flash column chromatography (EtOAc:Hexanes 0-15%), 5-chloro-3-[4'-(trifluoromethyl)phenyl]-1-{[2"-(trimethylsilyl)ethoxy]methyl}-*1H*-pyrazolo[3,4-c]pyridine was isolated as a white solid (0.127 g, 0.30 mmol, 56%) with mp 87-90 °C.

δ_H (700 MHz, $CDCl_3$) 8.98 (1H, d, J = 1.2 Hz, 7-*H*), 8.08 (2H, d, J = 8.1 Hz, 2', 6'-*H*), 7.96 (1H, d, J = 1.2 Hz, 4-*H*), 7.82 (2H, d, J = 8.1 Hz, 3', 5'-*H*), 5.89 (2H, s, NCH_2O), 3.67 – 3.62 (2H, m, OCH_2CH$_2$), 0.98 – 0.93 (2H, m, CH_2Si), -0.03 (9H, s, Si(CH_3)$_3$); δ_C (176 MHz, $CDCl_3$) 142.8 (*C*-3), 142.5 (*C*-5), 137.3 (*C*-7a), 135.5 (m, *C*-1'), 134.3 (*C*-7), 130.9 (q, J_{CF} = 32.5 Hz, *C*-4'), 129.4 (*C*-3a), 127.5 (*C*-2', 6'), 126.2 (q, J_{CF} = 3.8 Hz, *C*-3', 5'), 124.2 (q, J_{CF} = 272.8 Hz, *C*F$_3$), 114.6 (*C*-4), 79.1 (NCH$_2$O), 67.4 (OCH$_2$CH$_2$), 17.9 (*C*H$_2$Si), -1.3 (Si(*C*H$_3$)$_3$); δ_F (376 MHz, $CDCl_3$) -62.66; V_{max} (ATR) 1324, 1164, 1066, 860, 825 cm^{-1}; LC-MS (ESI) [M (^{35}Cl) + H]$^+$ 428.282 [M (^{37}Cl)+ H]$^+$ 430.296; HRMS (ESI) found [M + H]$^+$ 428.1165, *M* $C_{19}H_{22}N_3OSi^{35}ClF_3$ requires 428.1173.

Methyl 4'-(5-chloro-1-{[2"-(trimethylsilyl)ethoxy]methyl}-*1H*-pyrazolo[3,4-c]pyridin-3-yl)benzoate 144

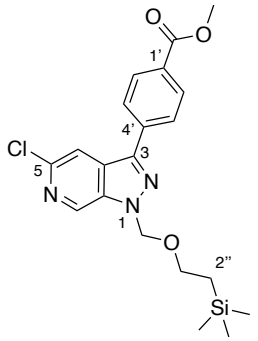

General procedure A was applied to 5-chloro-1-{[2'-(trimethylsilyl)ethoxy]methyl}-*1H*-pyrazolo[3,4-c]pyridine **136** (0.050 g, 0.009 mmol, 1.00 eq) with methyl 4-iodobenzoate (0.069 g, 0.26 mmol, 1.50 eq). After purification by silica gel flash column chromatography (EtOAc:Hexanes 0-15%) methyl 4'-(5-chloro-1-{[2"-(trimethylsilyl)ethoxy]methyl}-*1H*-pyrazolo[3,4-c]pyridin-3-yl)benzoate was isolated as an off-white solid (0.035 g, 0.083 mmol, 47%) with mp 98-103 °C.

δ_H (600 MHz, $CDCl_3$) 8.92 (1H, d, J = 1.1 Hz, 7-*H*), 8.20 – 8.15 (2H, m, 3', 5'-*H*), 8.02 – 7.97 (2H, m, 2', 6'-*H*), 7.93 (1H, d, J = 1.1 Hz, 4-*H*), 5.84 (2H, s, NCH_2O), 3.95 (3H, s, OCH_3), 3.65 – 3.58 (2H, m, OCH_2CH$_2$), 0.94 – 0.87 (2H, m, CH_2Si), -0.07 (9H, s, Si(CH_3)$_3$); δ_C (151 MHz, $CDCl_3$) 166.6 (*C*=O), 142.7 (*C*-3), 142.5 (*C*-5), 137.1 (*C*-7a), 136.1 (*C*-1'), 134.1 (*C*-7), 130.3 (*C*-2', 6'), 130.2 (*C*-4'), 129.3 (*C*-3a), 126.9 (*C*-3', 5'), 114.6 (*C*-4), 78.9 (NCH$_2$O), 67.2 (OCH$_2$CH$_2$), 52.3 (OCH$_3$), 17.7 (*C*H$_2$Si), -1.5 (Si(*C*H$_3$)$_3$); V_{max} (ATR) 1714 (C=O), 1089, 833, 818, 701 cm^{-1}; LC-MS (ESI) [M (^{35}Cl) + H]$^+$ 418.287, [M (^{37}Cl)+ H]$^+$ 420.301; HRMS (ESI) found [M + H]$^+$ 418.1347, $C_{20}H_{25}N_3O_3Si^{35}Cl$ requires *M* 418.1332.

5-Chloro-3-(4'-nitrophenyl)-1-{[2"-(trimethylsilyl)ethoxy]methyl}-*1H*-pyrazolo[3,4-c]pyridine 145

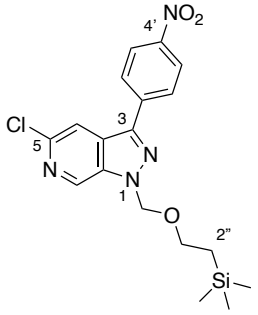

General procedure A was applied to 5-chloro-1-{[2'-(trimethylsilyl)ethoxy]methyl}-*1H*-pyrazolo[3,4-c]pyridine **136** (0.150g, 0.53 mmol, 1.00 eq) with 1-iodo-4-nitrobenzene (0.145 g, 0.58 mmol, 1.10 eq). After purification by silica gel flash column chromatography (EtOAc:Hexanes 0-20%), 5-chloro-3-(4'-nitrophenyl)-1-{[2"-(trimethylsilyl)ethoxy]methyl}-*1H*-pyrazolo[3,4-c]pyridine was isolated as a white solid (0.129 g, 0.32 mmol, 60%) with mp 111-113 °C.

δ_H (600 MHz, $CDCl_3$) 8.96 (1H, d, J = 1.2 Hz, 7-*H*), 8.41 – 8.35 (2H, m, 3',5'-*H*), 8.15 – 8.09 (2H, m, 2',6'-*H*), 7.94 (1H, d, J = 1.2 Hz, 4-*H*), 5.86 (2H, s, NCH_2O), 3.64 – 3.59 (2H, m, OCH_2CH$_2$), 0.95 – 0.88 (2H, m, CH$_2$CH_2Si), -0.06 (9H, s, Si(CH_3)$_3$); δ_C (151 MHz, $CDCl_3$) 147.7 (*C*-4'), 143.0 (*C*-5), 141.4 (*C*-3), 138.1 (*C*-1'), 137.1 (*C*-7a), 134.4 (*C*-7), 129.2 (*C*-3a), 127.6 (*C*-3', 5'), 124.4 (*C*-2', 6'), 114.3 (*C*-4), 79.1 (NCH$_2$O), 67.4 (OCH$_2$CH$_2$), 17.7 (CH$_2$CH$_2$Si), -1.5 (Si(*C*H$_3$)$_3$); V_{max} (ATR) 1516 (N=O asymmetric), 1349 (N=O symmetric), 1074, 857, 834, 821 cm^{-1}; LC-MS (ESI) [M (^{35}Cl) + H]$^+$ 405.282, [M (^{37}Cl) + H]$^+$ 407.297; HRMS (ESI) found [M + H]$^+$ 405.1153, $C_{18}H_{22}N_4O_3Si^{35}Cl$ requires *M* 405.1150.

5-Chloro-3-(3',5'-dimethylphenyl)-1-{[2"-(trimethylsilyl)ethoxy]methyl}-*1H*-pyrazolo[3,4-c]pyridine 146

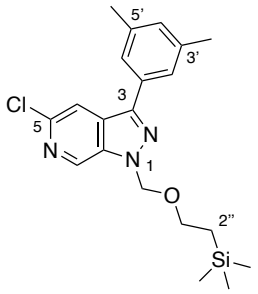

General procedure A was applied to 5-chloro-1-{[2'-(trimethylsilyl)ethoxy]methyl}-*1H*-pyrazolo[3,4-c]pyridine **136** (0.200 g, 0.71 mmol, 1.00 eq) with 1-iodo-3,5-dimethylbenzene (0.11 mL, 0.78 mmol, 1.10 eq). After purification by silica gel flash column chromatography (EtOAc:Hexanes 0-20%), 5-chloro-3-(3',5'-dimethylphenyl)-1-{[2"-(trimethylsilyl)ethoxy]methyl}-*1H*-pyrazolo[3,4-c] pyridine was isolated as a colourless oil (0.127 g, 0.33 mmol, 47%).

δ_H (600 MHz, $CDCl_3$) 8.90 (1H, d, J = 1.1 Hz, 7-*H*), 7.92 (1H, d, J = 1.1 Hz, 4-*H*), 7.52 – 7.49 (2H, m, 2',6'-*H*), 7.12 – 7.09 (1H, m, 4'-*H*), 5.83 (2H, s, NCH_2O), 3.64 – 3.58 (2H, m, OCH_2CH$_2$), 2.43 (6H, q, J = 0.7 Hz, Ar-CH_3), 0.94 – 0.89 (2H, m, CH$_2$CH_2Si), -0.06 (9H, s, Si(CH_3)$_3$); δ_C (151 MHz, $CDCl_3$) 144.3 (*C*-3), 141.9 (*C*-5), 138.8 (*C*-3',5'), 137.0 (*C*-7a), 133.7 (*C*-7), 131.5 (*C*-1'), 130.7 (*C*-4'), 129.5 (*C*-3a), 125.0 (*C*-2',6'), 115.0 (*C*-4), 78.7 (NCH$_2$O), 67.0 (OCH$_2$CH$_2$), 21.4 (Ar-*C*H$_3$), 17.7 (CH$_2$*C*H$_2$Si), -1.47 (Si(*C*H$_3$)$_3$); V_{max} (ATR) 1089, 863, 839 cm^{-1}; LC-MS (ESI) [M (^{35}Cl) + H]$^+$ 388.371, [M (^{37}Cl) + H]$^+$ 390.385; HRMS (ESI) found [M + H]$^+$ 388.1616, $C_{20}H_{27}{}^{35}ClN_3OSi$ requires *M* 388.1612.

5-Chloro-3-[4'-(trifluoromethyl)phenyl]-2-{[2"-(trimethylsilyl)ethoxy]methyl}-*2H*-pyrazolo[3,4-c]pyridine 141

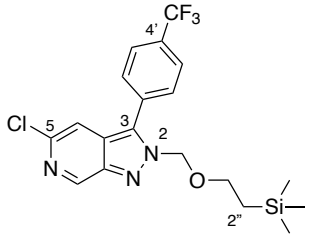

General procedure B was applied to 5-chloro-2-{[2'-(trimethylsilyl)ethoxy]methyl}-*2H*-pyrazolo[3,4-c]pyridine **137** (0.100 g, 0.35 mmol, 1.00 eq) with 1-bromo-4-(trifluoromethyl)benzene (0.087 g, 0.39 mmol, 1.10 eq). Purification by silica gel flash column chromatography (EtOAc:Hexanes 0-20%) afforded 5-chloro-3-[4'-(trifluoromethyl)phenyl]-2-{[2"-(trimethylsilyl)ethoxy]methyl}-*2H*-pyrazolo[3,4-c]pyridine as a yellow solid (0.072 g, 0.17 mmol, 48%) with mp 104-105 °C.

δ_H (600 MHz, $CDCl_3$) 9.15 (1H, d, J = 1.3 Hz, 7-*H*), 7.89 (2H, d, J = 8.3 Hz, 2',6'-*H*), 7.85 (2H, d, J = 8.3 Hz, 3',5'-*H*), 7.59 (1H, d, J = 1.3 Hz, 4-*H*), 5.74 (2H, s, NCH_2O), 3.89 – 3.82 (2H, m, OCH_2CH$_2$), 1.00 – 0.93 (2H, m, CH$_2$CH_2Si), -0.01 (9H, s, Si(CH_3)$_3$); δ_C (151 MHz, $CDCl_3$) 145.0 (*C*-7), 143.8 (*C*-5), 141.7 (*C*-7a), 134.9 (*C*-3), 131.6 (d, J_{CF} = 1.4 Hz, *C*-1'), 131.4 (q, $J_{C\text{-}F}$ = 33.0 Hz, *C*-4'), 129.9 (*C*-2',6'), 126.3 (q, $J_{C\text{-}F}$ = 3.7 Hz, *C*-3',5'), 125.6 (*C*-3a), 123.7 (q, $J_{C\text{-}F}$ = 272.4 Hz, *C*F$_3$), 112.7 (*C*-4), 80.1 (NCH$_2$O), 68.4 (OCH$_2$CH$_2$), 17.9 (CH$_2$*C*H$_2$Si), -1.5 (Si(*C*H$_3$)$_3$); δ_F (376 MHz, $CDCl_3$) -62.84; V_{max} (ATR) 1323, 911, 732 cm^{-1}; LC-MS (ESI) [M (^{35}Cl) + H]$^+$ 428.236, [M (^{37}Cl)+ H]$^+$ 430.251; HRMS (ESI) found [M + H]$^+$ 428.1177, $C_{19}H_{22}N_3OSiF_3{}^{35}Cl$ requires *M* 428.1173.

Methyl 4'-(5-chloro-2-{[2"-(trimethylsilyl)ethoxy]methyl}-*2H*-pyrazolo[3,4-c]pyridin-3-yl)benzoate 147

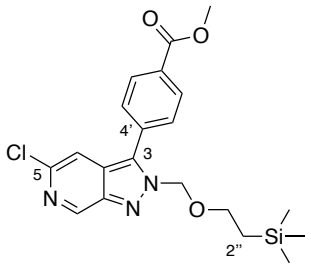

General procedure B was applied to 5-chloro-2-{[2'-(trimethylsilyl)ethoxy]methyl}-*2H*-pyrazolo[3,4-c]pyridine **137** (0.150 g, 0.53 mmol, 1.00 eq) with methyl 4-iodobenzoate (0.152 g, 0.58 mmol, 1.10 eq). Purification by reverse phase flash column chromatography (MeOH:H_2O 0-100%) afforded methyl 4'-(5-chloro-2-{[2"-(trimethylsilyl)ethoxy]methyl}-*2H*-pyrazolo[3,4-c] pyridin-3-yl)benzoate as a yellow solid (0.088 g, 0.21 mmol, 40%) with mp 99 – 103 °C.

δ_H (600 MHz, $CDCl_3$) 9.11 (1H, d, *J* = 1.3 Hz, 7-*H*), 8.23 (2H, d, *J* = 8.1 Hz, 2',6'-*H*), 7.81 (2H, d, *J* = 8.2 Hz, 3',5'-*H*), 7.61 – 7.56 (1H, d, *J* = 1.3 Hz, 4-*H*), 5.73 (2H, s, NCH_2O), 3.97 (3H, s, OCH_3), 3.90 – 3.83 (2H, m, OCH_2CH_2), 0.99 – 0.94 (2H, m, CH_2CH_2Si), -0.01 (9H, s, Si(CH_3)$_3$); δ_C (151 MHz, $CDCl_3$) 166.3 (*C*(=O)OCH$_3$), 144.9 (*C*-7), 143.8 (*C*-7a), 141.5 (*C*-5), 135.5 (*C*-3), 132.3 (*C*-4'), 130.8 (*C*-1'), 130.5 (*C*-2',6'), 129.4 (*C*-3',5'), 125.6 (*C*-3a), 112.9 (*C*-4), 80.1 (NCH$_2$O), 68.3 (OCH$_2$CH$_2$), 52.4 (OCH$_3$), 17.9 (CH$_2$CH$_2$Si), -1.4 (Si(CH$_3$)$_3$); V_{max} (ATR) 1727 (C=O), 1279, 837, 741 cm^{-1}; LC-MS (ESI) [M (^{35}Cl) + H]$^+$ 418.318, [M (^{37}Cl) + H]$^+$ 420.332; HRMS found [M + H]$^+$ 418.1361, $C_{20}H_{25}{}^{35}ClN_3O_3Si$ requires *M* 418.1354.

5-Chloro-3-(4'-nitrophenyl)-2-{[2"-(trimethylsilyl)ethoxy]methyl}-*2H*-pyrazolo[3,4-c]pyridine 148

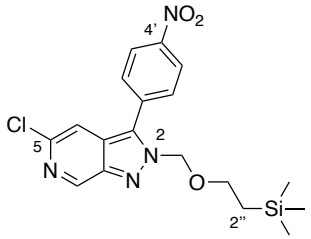

General procedure B was applied to 5-chloro-2-{[2'-(trimethylsilyl)ethoxy]methyl}-*2H*-pyrazolo[3,4-c]pyridine **137** (0.150g, 0.53 mmol, 1.00 eq) with 1-iodo-4-nitrobenzene (0.145 g, 0.58 mmol, 1.10 eq). Purification by reverse phase flash column chromatography (MeOH:H_2O 0-100%) afforded 5-chloro-3-(4'-nitrophenyl)-2-{[2"-(trimethylsilyl)ethoxy]methyl}-*2H*-pyrazolo[3,4-c]pyridine as a yellow oil (0.066 g, 0.16 mmol, 31%).

δ_H NMR (600 MHz, $CDCl_3$) 9.16 (1H, d, *J* = 1.3 Hz, 7-*H*), 8.46 – 8.43 (2H, m, 3',5'-*H*), 7.99 – 7.96 (2H, m, 2',6'-*H*), 7.60 (1H, d, *J* = 1.3 Hz, 4-*H*), 5.76 (2H, s, NCH_2O), 3.92 – 3.87 (2H, m, OCH_2CH$_2$), 1.02 – 0.97 (2H, m, CH$_2$CH_2Si), 0.01 (9H, s, Si(CH_3)$_3$); δ_C NMR (151 MHz, $CDCl_3$) 148.0 (*C*-4'), 145.2 (*C*-7), 143.8 (*C*-7a), 142.3 (*C*-5), 134.3 (*C*-1'), 134.0 (*C*-3), 130.3 (*C*-2',6'), 125.8 (*C*-3a), 124.6 (*C*-3',5'), 112.5 (*C*-4), 80.4 (NCH$_2$O), 68.6 (OCH$_2$CH$_2$), 18.0 (OCH$_2$CH$_2$Si), -1.4 (Si(CH$_3$)$_3$); V_{max} (ATR) 1523 (N-O, asymmetric), 1349 (N-O, symmetric), 858, 838, 734, 698 cm^{-1}; [M(^{35}Cl) + H]$^+$ 405.320, [M(^{37}Cl) + H]$^+$ 407.297; HRMS found [M + H]$^+$ 405.1146, $C_{18}H_{22}{}^{35}ClN_4O_3Si$ requires *M* 405.1150.

5-Chloro-3-(3',5'-dimethylphenyl)-2-{[2"-(trimethylsilyl)ethoxy]methyl}-*2H*-pyrazolo[3,4-c]pyridine 142

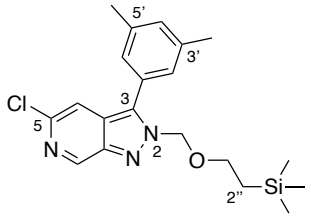

General procedure B was applied to 5-chloro-2-{[2'-(trimethylsilyl)ethoxy]methyl}-*2H*-pyrazolo[3,4-c]pyridine **137** (0.100g, 0.35 mmol, 1.00 eq) with 1-iodo-3,5-dimethylbenzene (0.06 mL, 0.39 mmol, 1.10 eq). Purification by silica gel flash column chromatography (EtOAc:Pet Ether 40-60 0-20%) afforded 5-chloro-3-(3',5'-dimethylphenyl)-2-{[2"-(trimethylsilyl)ethoxy]methyl}-*2H*-pyrazolo[3,4-c]pyridine as a yellow oil (0.065 g, 0.17 mmol, 48%).

δ_H (600 MHz, $CDCl_3$) 9.11 (1H, d, J = 1.2 Hz, 7-*H*), 7.57 (1H, d, J = 1.2 Hz, 4-*H*), 7.30 – 7.27 (2H, m, 2',6'-*H*), 7.17 – 7.14 (1H, m, 4'-*H*), 5.72 (2H, s, NCH_2O), 3.86 – 3.80 (2H, m, OCH_2CH_2), 2.43 (6H, q, J = 0.7 Hz, Ar-CH_3), 0.98 – 0.93 (2H, m, CH_2CH_2Si), -0.01 (9H, s, $Si(CH_3)_3$); δ_C (151 MHz, $CDCl_3$) 144.6 (*C*-7), 143.9 (*C*-5), 140.6 (*C*-7a), 139.0 (*C*-3',5'), 137.2 (*C*-3), 131.3 (*C*-4'), 127.8 (*C*-1'), 127.3 (*C*-2',6'), 125.4 (*C*-3a), 113.5 (*C*-4), 79.8 (NCH_2O), 68.1 (OCH_2CH_2), 21.4 (Ar-CH_3), 17.9 (CH_2CH_2Si), -1.4 ($Si(CH_3)_3$); V_{max} (ATR) 1465, 1106, 1085, 1061, 858, 838 cm^{-1}; LC-MS (ESI) [M (^{35}Cl) + H]$^+$ 388.333, [M (^{37}Cl) + H]$^+$ 390.347; HRMS (ESI) found [M + H]$^+$ 388.1598, $C_{20}H_{27}{}^{35}ClN_3OSi$ requires *M* 388.1612.

7.2.4 Metal-base Chemistry

2,2,6,6-Tetramethylpiperidine magnesium chloride lithium chloride (TMPMgCl·LiCl)

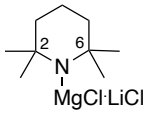

An oven dried RBF wrapped in foil to exclude light was charged with *turbo*-Grignard (isopropyl magnesium chloride lithium chloride complex, 1.3 M in THF) under a nitrogen atmosphere in an ice + salt bath. Freshly distilled 2,2,6,6-tetramethylpiperidine (TMPH) (1.05 eq) was added dropwise and the reaction stirred for 48 hours generating a dark grey solution. The concentration of the metal-base was calculated via titration against benzoic acid in THF conducted under a nitrogen atmosphere in an ice bath. The prepared TMPMgCl·LiCl solution was stored at -18 °C under a dry nitrogen atmosphere.

General Procedure C for deproto-metalation by TMPMgCl·LiCl and trapping with an electrophile.

An oven dried RBF was charged with a solution of the stated substrate (1.00 eq) in dry THF (0.5 M) and cooled to -40 °C under a nitrogen atmosphere. TMPMgCl·LiCl in THF (2.00 eq) was added dropwise and the reaction was stirred for 30 minutes at -40 °C. The corresponding electrophile was added at -40 °C, then the reaction was stirred at room temperature for the time stated. The reaction was quenched with sat. $NaHSO_3$ and the crude product extracted with EtOAc, then the combined organic layers were washed with brine, dried over $MgSO_4$, filtered, and concentrated under reduced pressure. The product was purified by silica gel flash column chromatography using the stated solvent system.

General Procedure D for deproto-metalation by TMPMgCl·LiCl and transmetalation to Zn for Negishi cross-coupling.

An oven-dried reaction vessel was charged with a solution of the substrate (1.00 eq) in dry THF (0.5 M), the atmosphere was exchange to nitrogen, and the solution cooled to -40 °C. TMPMgCl·LiCl in THF (2.00

eq) was added dropwise and the reaction was stirred for 30 minutes at -40 °C. A solution of $ZnCl_2$ (1.00 eq) in THF (1 M) was added and the reaction stirred for 30 minutes at -40 °C. In a separate oven-dried reaction vessel, a solution of the corresponding (hetero)aryl halide (1.50 eq) and $Pd(PPh_3)_4$ (0.05 eq) in THF (0.5 M) were stirred at room temperature for 30 minutes. This solution was added to the main reaction mixture at -40 °C, then the reaction was stirred at room temperature overnight. The reaction was quenched with sat. NH_4Cl and the crude product extracted with EtOAc, then the combined organic layers were washed with brine, dried over $MgSO_4$, filtered, and concentrated under reduced pressure. The product was purified by silica gel flash column chromatography using the stated solvent system.

5-Chloro-7-iodo-1-{[2'-(trimethylsilyl)ethoxy]methyl}-*1H*-pyrazolo[3,4-c]pyridine 158

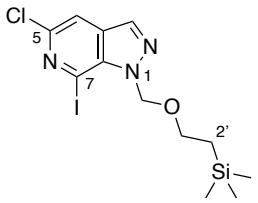

General procedure C was applied to 5-chloro-1-{[2'-(trimethylsilyl)ethoxy] methyl}-*1H*-pyrazolo[3,4-c]pyridine **136** (0.100g, 0.35 mmol, 1.00 eq) with electrophile I_2 (0.134 g, 0.53 mmol, 1.50 eq) for 1 hour. Purification by reverse phase flash column chromatography (MeOH:H_2O 0-100%) afforded 5-chloro-7-iodo-1-{[2'-(trimethylsilyl)ethoxy]methyl}-*1H*-pyrazolo[3,4-c]pyridine as a yellow oil (0.080g, 0.20 mmol, 55%).

δ_H (700 MHz, $CDCl_3$) 8.06 (1H, s, 3-*H*), 7.66 (1H, s, 4-*H*), 6.14 (2H, s, NCH_2O), 3.66 – 3.61 (2H, m, OCH_2CH$_2$), 0.99 – 0.93 (2H, m, CH$_2$CH_2Si), 0.00 (9H, s, Si(CH_3)$_3$); δ_C (176 MHz, $CDCl_3$) 140.1 (*C*-5), 138.3 (*C*-7a), 132.5 (*C*-3), 131.9 (*C*-3a), 114.1 (*C*-4), 96.3 (*C*-7), 77.7 (NCH_2O), 66.7 (OCH_2CH$_2$), 17.9 (CH$_2$CH_2Si), -1.3 (Si(CH_3)$_3$); V_{max} (ATR) 1082, 914, 798, 739 cm^{-1}; LC-MS (ESI) [M (^{35}Cl) + H]$^+$ 410.147, [M (^{37}Cl) + H]$^+$ 412.161; HRMS found [M + H]$^+$ 409.9954, $C_{12}H_{18}{}^{35}ClIN_3OSi$ requires *M* 409.9952.

5-Chloro-7-(phenylsulfanyl)-1-{[2'-(trimethylsilyl)ethoxy]methyl}-*1H*-pyrazolo[3,4-c]pyridine 159

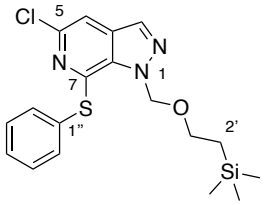

General procedure C was applied to 5-chloro-1-{[2'-(trimethylsilyl)ethoxy]methyl}-*1H*-pyrazolo[3,4-c]pyridine **136** (0.150g, 0.53 mmol, 1.00 eq) with electrophile S_2Ph_2 (0.173 g, 0.79 mmol, 1.50 eq) for 18 hours. Purification by reverse phase flash column chromatography (MeCN:H_2O 0-100%) afforded 5-chloro-7-(phenylsulfanyl)-1-{[2'-(trimethylsilyl)ethoxy]methyl}-*1H*-pyrazolo[3,4-c]pyridine as a yellow oil (0.104 g, 0.27 mmol, 50%).

δ_H (700 MHz, $CDCl_3$) 7.98 (1H, s, 3-*H*), 7.58 (2H, dd, J = 7.5, 2.1 Hz, 2",6"-*H*), 7.43 – 7.40 (2H, m, 3",5"-*H*), 7.43 – 7.40 (1H, m, 4"-*H*), 7.39 (1H, s, 4-*H*), 6.09 (2H, s, NCH_2O), 3.64 – 3.59 (2H, m, OCH_2CH$_2$), 0.95 – 0.90 (2H, m, OCH$_2$CH_2Si), -0.04 (9H, s, Si(CH_3)$_3$); δ_C (176 MHz, $CDCl_3$) 143.1 (*C*-7), 140.9 (*C*-5), 134.4 (*C*-2",6"), 134.3 (*C*-7a), 133.1 (*C*-3), 132.3 (*C*-3a), 129.4 (*C*-1"), 129.3 (*C*-3",5"), 129.1 (*C*-4"), 111.6 (*C*-4), 79.9 (NCH_2O), 66.7 (OCH_2CH$_2$Si), 17.9 (OCH$_2$CH_2Si), -1.3 (Si(CH_3)$_3$); V_{max} (ATR) 1078, 856, 833, 796, 689 cm^{-1}; LC-MS (ESI) [M (^{35}Cl) + H]$^+$ 392.209, [M (^{37}Cl) + H]$^+$ 394.223; HRMS found [M + H]$^+$ 392.1020, $C_{18}H_{23}{}^{35}ClN_3OSSi$ requires *M* 392.1020.

(5-Chloro-1-{[2'-(trimethylsilyl)ethoxy]methyl}-*1H*-pyrazolo[3,4-c]pyridin-7-yl)(4"-chlorophenyl)methanol 160

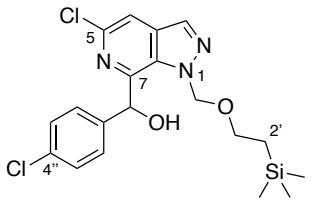

General procedure C was applied to 5-chloro-1-{[2'-(trimethylsilyl)ethoxy]methyl}-*1H*-pyrazolo[3,4-c]pyridine **136** (0.100 g, 0.35 mmol, 1.00 eq) with electrophile 4-chlorobenzaldehyde (0.111 g, 0.79 mmol, 2.25 eq) for 4 hours. Purification by reverse phase flash column chromatography (MeCN:H_2O 0-100%) afforded (5-chloro-1-{[2'-(trimethylsilyl)ethoxy]methyl}-*1H*-pyrazolo[3,4-c] pyridin-7-yl)(4"-chlorophenyl)methanol as a yellow solid (0.072 g, 0.17 mmol, 48%) with mp 82-84 °C.

δ_H (600 MHz, $CDCl_3$) 8.00 (1H, s, 3-*H*), 7.66 (1H, s, 4-*H*), 7.28 (2H, d, J = 8.4 Hz, 3",5"-*H*), 7.18 (2H, d, J = 8.4 Hz, 2",6"-*H*), 6.43 (1H, s, C(OH)*H*), 5.47 – 5.38 (2H, m, NCH_2O), 3.49 – 3.36 (2H, m, OCH_2CH_2), 0.93 – 0.75 (2H, m, CH_2CH_2Si), -0.07 (9H, s, Si(CH_3)$_3$); δ_C (151 MHz, $CDCl_3$) 145.7 (*C*-7), 140.9 (*C*-4"), 139.9 (*C*-5), 134.3 (*C*-1"), 133.7 (*C*-3a), 132.7 (*C*-3), 132.6 (*C*-7a), 129.2 (*C*-3",5"), 129.1 (*C*-2",6"), 114.3 (*C*-4), 79.8 (NCH_2O), 71.7 (*C*(OH)H), 66.5 (OCH_2CH_2), 17.6 (OCH_2CH_2Si), -1.6 (Si(CH_3)$_3$); V_{max} (ATR) 3410 (br, O-H), 2961, 1075, 833 cm^{-1}; LC-MS (ESI) [M (^{35}Cl) + H]$^+$ 424.208, [M (^{37}Cl) + H]$^+$ 426.222; HRMS found [M + H]$^+$ 424.1013, $C_{19}H_{24}{}^{35}Cl_2N_3O_2Si$ requires *M* 424.1015.

(5-Chloro-1-{[2'-(trimethylsilyl)ethoxy]methyl}-*1H*-pyrazolo[3,4-c]pyridin-7-yl)(phenyl)methanol 161

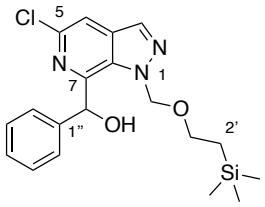

General procedure C was applied to 5-chloro-1-{[2'-(trimethylsilyl)ethoxy]methyl}-*1H*-pyrazolo[3,4-c]pyridine **136** (0.100 g, 0.35 mmol, 1.00 eq) with electrophile benzaldehyde (0.05 mL, 0.53 mmol, 1.50 eq) for 4 hours. Purification by reverse phase flash column chromatography (MeCN:H_2O 0-100%) afforded (5-chloro-1-{[2'-(trimethylsilyl)ethoxy]methyl}-*1H*-pyrazolo[3,4-c]pyridin-7-yl) (phenyl)methanol as a yellow solid (0.090 g, 0.23 mmol, 66%) with mp 63-68 °C.

δ_H (600 MHz, $CDCl_3$) 8.00 (1H, s, 3-*H*), 7.66 (1H, s, 4-*H*), 7.34 – 7.30 (2H, m, 3",5"-*H*), 7.30 – 7.28 (1H, m, 4"-*H*), 7.26 – 7.23 (2H, m, 2",6"-*H*), 6.47 (1H, s, C(OH)*H*), 5.46 – 5.37 (2H, m, NCH_2O), 5.29 (1H, br s, O-*H*),3.51-3.38 (2H, m, OCH_2CH_2), 0.96 – 0.78 (2H, m, CH_2CH_2Si), -0.05 (9H, s, Si(CH_3)$_3$); δ_C (151 MHz, $CDCl_3$) 146.3 (*C*-7), 142.4 (*C*-1"), 139.8 (*C*-5), 133.6 (*C*-3a), 132.7 (*C*-7a), 132.7 (*C*-3), 129.1 (*C*-3",5"), 128.5 (*C*-4"), 127.7 (*C*-2",6"), 114.0 (*C*-4), 79.8 (NCH_2O), 72.4 (*C*(OH)H), 66.5 (OCH_2CH_2), 17.6 (CH_2CH_2Si), -1.5 (Si(CH_3)$_3$); V_{max} (ATR) 3337 (br, O-H), 2958, 1085, 1070, 1063 cm^{-1}; LC-MS (ESI) [M (^{35}Cl) + H]$^+$ 390.271, [M (^{37}Cl) + H]$^+$ 392.285; HRMS found [M + H]$^+$ 390.1403, $C_{19}H_{25}{}^{35}ClN_3O_2Si$ requires *M* 390.1405.

5-Chloro-1-{[2'-(trimethylsilyl)ethoxy]methyl}-*1H*-pyrazolo[3,4-c]pyridine-7-carbaldehyde 162

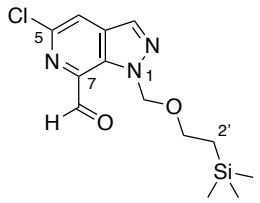

General procedure C was applied to 5-chloro-1-{[2'-(trimethylsilyl)ethoxy]methyl}-*1H*-pyrazolo[3,4-c]pyridine **136** (0.200 g, 0.70 mmol, 1.00 eq) with neat DMF (0.08 mL, 1.05 mmol, 1.50 eq) for 5 hours. Purification by silica gel flash column chromatography (EtOAc:Hexanes 5-25%) afforded 5-chloro-1-{[2-(trimethylsilyl)ethoxy]methyl}-*1H*-pyrazolo[3,4-c]pyridine-7-carbaldehyde as a cream solid (0.107 g, 0.34 mmol, 49%) with mp 60-62 °C.

δ_H (600 MHz, $CDCl_3$) 10.16 (1H, s, C(=O)*H*), 8.18 (1H, s, 3-*H*), 7.94 (1H, s, 4-*H*), 6.25 (2H, s, NCH_2O), 3.47 – 3.41 (2H, m, OCH_2CH_2), 0.84 – 0.77 (2H, m, CH_2CH_2Si), -0.11 (9H, s, Si(CH_3)$_3$); δ_C NMR (151 MHz, $CDCl_3$) 191.2 (*C*=O), 140.5 (*C*-5), 138.0 (*C*-7), 135.7 (*C*-3a), 133.6 (*C*-3), 132.2 (*C*-7a), 120.0 (*C*-4), 81.7 (NCH_2O), 66.5 (OCH_2CH_2), 17.7 (CH_2CH_2Si), -1.6 (Si(CH_3)$_3$); V_{max} (ATR) 1717 (C=O), 1085, 1056, 838, 796 cm^{-1}; LC-MS (ESI) [M (^{35}Cl) + H]$^+$ 312.211, [M (^{37}Cl) + H]$^+$ 314.187; HRMS found [M + H]$^+$ 312.0938, $C_{13}H_{19}{}^{35}ClN_3O_2Si$ requires *M* 312.0935.

5-Chloro-7-(4'-methoxyphenyl)-1-{[2"-(trimethylsilyl)ethoxy]methyl}-*1H*-pyrazolo[3,4-c]pyridine 163

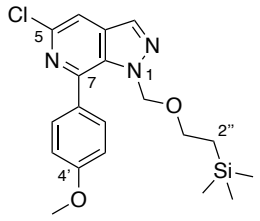

General procedure D was applied to 5-chloro-1-{[2'-(trimethylsilyl)ethoxy]methyl}-*1H*-pyrazolo[3,4-c]pyridine **136** (0.100 g, 0.35 mmol, 1.00 eq) with 1-iodo-4-methoxybenzene (0.124 g, 0.53 mmol, 1.50 eq). Purification by reverse phase flash column chromatography (MeCN:H_2O 0-100%) afforded 5-chloro-7-(4'-methoxyphenyl)-1-{[2"-(trimethylsilyl)ethoxy]methyl}-*1H*-pyrazolo[3,4-c] pyridine as a yellow oil (0.108 g, 0.28 mmol, 79%).

δ_H (600 MHz, $CDCl_3$) 8.10 (1H, s, 3-*H*), 7.68 – 7.62 (2H, m, 2',6'-*H*), 7.61 (1H, s, 4-*H*), 7.05 – 7.00 (2H, m, 3',5'-*H*), 5.45 (2H, s, NCH_2O), 3.88 (3H, s, OCH_3), 3.39 – 3.33 (2H, m, OCH_2CH_2), 0.80 – 0.73 (2H, m, CH_2CH_2Si), -0.08 (9H, s, Si(CH_3)$_3$); δ_C (151 MHz, $CDCl_3$) 160.7 (*C*-4'), 145.4 (*C*-7), 140.7 (*C*-5), 134.2 (*C*-7a), 133.4 (*C*-3), 133.2 (*C*-3a), 130.7 (*C*-2',6'), 129.5 (*C*-1'), 113.9 (*C*-3',5'), 112.7 (*C*-4), 78.2 (NCH_2O), 66.5 (OCH_2CH_2), 55.4 (O(CH_3)), 17.7 (CH_2CH_2Si), -1.5 (Si(CH_3)$_3$); V_{max} (ATR) 1253 (Ar-O), 1078 (O-Me), 838, 800 cm^{-1}; LC-MS (ESI) [M (^{35}Cl) + H]$^+$ 390.271, [M (^{37}Cl) + H]$^+$ 392.285; HRMS found [M + H]$^+$ 390.1416, $C_{19}H_{25}{}^{35}ClN_3O_2Si$ requires M 390.1405.

4-(5'-Chloro-1'-((2"-(trimethylsilyl)ethoxy)methyl)-*1H*-pyrazolo[3,4-c]pyridin-7'-yl)benzonitrile 164

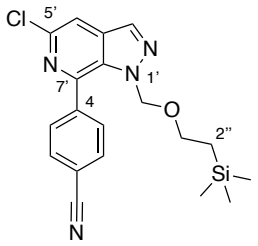

General procedure D was applied to 5-chloro-1-{[2'-(trimethylsilyl)ethoxy]methyl}-*1H*-pyrazolo[3,4-c]pyridine **136** (0.100 g, 0.35 mmol, 1.00 eq) with 4-iodobenzonitrile (0.121 g, 0.55 mmol, 1.50 eq). Purification by reverse phase column chromatography (MeCN:H_2O 50-100%) afforded 4-(5'-chloro-1'-((2"-(trimethylsilyl)ethoxy)methyl)-*1H*-pyrazolo[3,4-c]pyridin-7'-yl)benzonitrile as a cream solid (0.113 g, 0.29 mmol, 83%) with mp 90-94 °C.

δ_H (600 MHz, $CDCl_3$) 8.13 (1H, s, 3'-*H*), 7.85 (2H, d, *J* = 7.9 Hz, 2,6-*H*), 7.81 (2H, d, *J* = 7.9 Hz, 3,5-*H*), 7.71 (1H, s, 4'-*H*), 5.38 (2H, s, NCH_2O), 3.40 (2H, m, OCH_2CH$_2$), 0.77 (2H, m, CH$_2$CH_2Si), -0.07 (9H, s, Si(CH_3)$_3$); δ_C (151 MHz, $CDCl_3$) 143.0 (*C*-7'), 141.4 (*C*-4), 140.9 (*C*-5'), 133.7 (*C*-3'a), 133.6 (*C*-7'a), 133.4 (*C*-3'), 132.1 (*C*-2,6), 130.2 (*C*-3,5), 118.3 (*C*≡N), 114.3 (*C*-4'), 113.4 (*C*-1), 78.4 (NCH_2O), 66.8 (OCH_2CH$_2$), 17.7 (CH$_2$CH_2Si), -1.5 (Si(CH_3)$_3$); V_{max} (ATR) 2230 (C≡N), 1070, 856, 837, 815 cm^{-1}; LC-MS (ESI) [M (^{35}Cl) + H]$^+$ 385.330, [M (^{37}Cl) + H]$^+$ 387.307; HRMS found [M + H]$^+$ 385.1250, $C_{19}H_{22}{}^{35}ClN_4OSi$ requires *M* 385.1251.

5-Chloro-7-(pyridin-2'-yl)-1-((2"-(trimethylsilyl)ethoxy)methyl)-*1H*-pyrazolo[3,4-c]pyridine 165

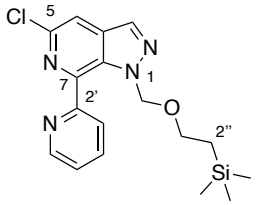

General procedure D was applied to 5-chloro-1-{[2'-(trimethylsilyl)ethoxy]methyl}-*1H*-pyrazolo[3,4-c]pyridine **136** (0.100 g, 0.35 mmol, 1.00 eq) with 2-iodopyridine (0.06 mL, 0.55 mmol, 1.50 eq). Purification by reverse phase flash column chromatography (MeCN:H_2O 0-80%) afforded 5-chloro-7-(pyridin-2'-yl)-1-((2"-(trimethylsilyl) ethoxy)methyl)-*1H*-pyrazolo[3,4-c]pyridine as a yellow oil (0.091 g, 0.25 mmol, 71%).

δ_H (700 MHz, $CDCl_3$) 8.74 (1H, ddd, *J* = 4.8, 1.8, 0.9 Hz, 6'-*H*), 8.11 (1H, s, 3-*H*), 8.08 (1H, dt, *J* = 7.8, 0.9 Hz, 3'-*H*), 7.91 (1H, td, *J* = 7.8, 1.8 Hz, 4'-*H*), 7.72 (1H, s, 4-*H*), 7.42 (1H, ddd, *J* = 7.8, 4.8, 0.9 Hz, 5'-*H*), 6.02 (2H, s, NCH_2O), 3.14 – 3.05 (2H, m, OCH_2CH$_2$), 0.59 – 0.49 (2H, m, CH$_2$CH_2Si), -0.22 (9H, s, Si(CH_3)$_3$); δ_C (176 MHz, $CDCl_3$) 156.0 (*C*-2'), 148.3 (*C*-6'), 143.7 (*C*-7), 140.3 (*C*-5), 137.4 (*C*-4'), 134.7 (*C*-3a), 133.5 (*C*-7a), 133.1 (*C*-3), 125.2 (*C*-3'), 124.1 (*C*-5'), 114.7 (*C*-4), 80.9 (NCH_2O), 66.0 (OCH_2CH$_2$), 17.6 (CH$_2$CH_2Si), -1.5 (Si(CH_3)$_3$); V_{max} (ATR) 1078, 863, 837, 796 cm^{-1}; LC-MS (ESI) [M (^{35}Cl) + H]$^+$ 361.274, [M (^{37}Cl) + H]$^+$ 362.288; HRMS found [M + H]$^+$ 361.1253, $C_{17}H_{22}{}^{35}ClN_4OSi$ requires *M* 361.1251.

5-Chloro-3-iodo-2-{[2'-(trimethylsilyl)ethoxy]methyl}-*2H*-pyrazolo[3,4-c]pyridine 166

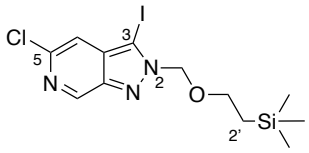

TMPMgCl·LiCl in THF (0.9 M) (0.19 mL, 0.017 mmol 1.20 eq.) was added dropwise to a cooled solution of 5-chloro-2-{[2'-(trimethylsilyl)ethoxy]methyl}-*2H*-pyrazolo[3,4-c]pyridine **137** (0.040g, 0.14 mmol, 1.00 eq) and the reaction was stirred for 1 hour at -78 °C under a nitrogen atmosphere. A solution of I_2 in THF (0.5 M) (0.11 mL, 0.21 mmol, 1.50 eq) was added, then the reaction was stirred at room temperature for 1 hour. The reaction was quenched with sat. NH_4Cl (10 mL) and the crude product extracted with EtOAc (3 x 10 mL), then the combined organic layers were washed with brine (10 mL), dried over $MgSO_4$, filtered, and concentrated under reduced pressure. Purification by silica gel flash column chromatography (EtOAc:Pet Ether 40-60 0-20%) afforded 5-chloro-3-iodo-2-{[2'-(trimethylsilyl)ethoxy]methyl}-*2H*-pyrazolo[3,4-c]pyridine as a white solid (0.0063 g, 0.015 mmol, 11%) with mp 101-103 °C.

δ_H (600 MHz, $CDCl_3$) 8.85 (1H, d, J = 1.1 Hz, 7-*H*), 7.45 (1H, d, J = 1.1 Hz, 4-*H*), 5.78 (2H, s, NCH_2O), 3.59 – 3.53 (2H, m, OCH_2CH$_2$), 0.92 – 0.85 (2H, m, CH$_2$CH_2Si), -0.05 (9H, s, Si(CH_3)$_3$); δ_C (151 MHz, $CDCl_3$) 142.3 (*C*-5), 136.4 (*C*-3), 136.2 (*C*-7a), 133.9 (*C*-7), 114.9 (*C*-4), 90.3 (*C*-3a), 79.0 (NCH$_2$O), 67.3 (OCH$_2$CH$_2$), 17.7 (CH$_2$CH$_2$Si), -1.5 (Si(CH$_3$)$_3$); V_{max} (ATR) 1463, 1085, 816, 736 cm^{-1}; LC-MS (ESI) [M (^{35}Cl) + H]$^+$ 410.147, [M (^{37}Cl) + H]$^+$ 412.161; HRMS found [M + H]$^+$ 409.9952, $C_{12}H_{18}{}^{35}ClIN_3OSi$ requires *M* 409.9952.

7.2.5 Buchwald-Hartwig Amination

General Procedure E for Buchwald-Hartwig Amination.

Pd_2dba_3 (0.05 eq), *rac*-BINAP (0.12 eq), NaO^{t}Bu (3.00 eq), and the stated protected pyrazolo[3,4-c]pyridine (1.00 eq) were sealed under a nitrogen atmosphere. The stated amine (1.10 eq) was added under nitrogen, followed by dry THF (0.1 M). The deep red solution was stirred overnight at 55 °C until LCMS analysis confirmed complete conversion of the starting substrate. The reaction was cooled to room temperature, diluted with EtOAc and filtered through Celite®, washing the cake with additional EtOAc. This solution was concentrated under reduced pressure. The product was purified by silica gel flash column chromatography using the stated solvent system.

4-[2'-(Oxan-2"-yl)-*2H*-pyrazolo[3,4-c]pyridin-5'-yl]morpholine 184

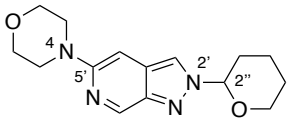

General procedure E was applied to 5-bromo-2-(oxan-2'-yl)-*2H*-pyrazolo[3,4-c]pyridine **191** (0.080 g, 0.28 mmol, 1.00 eq) with morpholine (0.03 mL, 0.31 mmol, 1.10 eq). Purification by silica gel flash column chromatography (EtOAc:Pet Ether 40-60 0-100%) afforded 4-[2'-(oxan-2"-yl)-*2H*-pyrazolo[3,4-c]pyridin-5'-yl] morpholine as a dark green oil (0.051 g, 0.18 mmol, 62%).

δ_H (600 MHz, $CDCl_3$) 9.05 (1H, t, J = 1.2 Hz, 7'-*H*), 7.99 (1H, d, J = 1.2 Hz, 3'-*H*), 6.58 (1H, d, J = 1.2 Hz, 4'-*H*), 5.66 (1H, dd, J = 8.2, 4.1 Hz, 2"-*H*), 4.13 – 4.07 (1H, m, 6"-*H*), 3.91 – 3.87 (4H, m, 2,6-H_2), 3.79 – 3.75 (1H, m, 6"-*H*), 3.40 – 3.35 (4H, m, 3,5-H_2), 2.23 – 2.16 (2H, m, 3"-*H*), 2.07 – 2.01 (1H, m, 4"-*H*), 1.79 – 1.63 (1H, m, 4"-*H*), 1.79 – 1.63 (2H, m, 5"-*H*); δ_C (151 MHz, $CDCl_3$) 154.1 (*C*-5'), 143.3 (*C*-7'), 142.7 (*C*-7'a), 126.1 (*C*-3'a), 119.3 (*C*-3'), 91.8 (*C*-4'), 89.2 (*C*- 2"), 67.8 (*C*-6"), 66.9 (*C*-2,6), 48.1

(*C*-3,5), 31.2 (*C*-3"), 24.9 (*C*-5"), 21.9 (*C*-4"); V_{max} (ATR) 1495, 1200, 998, 729 cm^{-1}; LC-MS (ESI) $[M + H]^+$ 289.294; HRMS (ESI) found $[M + H]^+$ 289.1670, $C_{15}H_{21}N_4O_2$ requires *M* 289.1665.

_N_-butyl-2-(oxan-2'-yl)-_2H_-pyrazolo[3,4-c]pyridin-5-amine 192

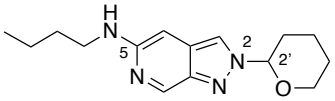

General procedure E was applied to 5-bromo-2-(oxan-2'-yl)-*2H*-pyrazolo[3,4-c]pyridine **191** (0.080 g, 0.28 mmol, 1.00 eq) with *N*-butylamine (0.03 mL, 0.31 mmol, 1.10 eq). Purification by silica gel flash column chromatography (EtOAc:Pet Ether 40-60 0-80%) afforded *N*-butyl-2-(oxan-2'-yl) -*2H*-pyrazolo[3,4-c]pyridine-5-amine as a brown solid (0.049 g, 0.18 mmol, 63%) with mp 105-109 °C.

δ_H (600 MHz, $CDCl_3$) 8.91 (1H, dd, J = 1.4, 0.9 Hz, 7-*H*), 7.89 (1H, d, J = 0.9 Hz, 3-*H*), 6.25 (1H, d, J = 1.4 Hz, 4-*H*), 5.65 – 5.62 (1H, m, 2'-*H*), 4.13 – 4.06 (1H, m, 6'-*H*), 3.78 – 3.74 (1H, m, 6'-*H*), 3.13 (2H, t, J = 7.1 Hz, $NHCH_2CH_2$), 2.24 – 2.17 (2H, m, 3'-*H*), 2.08 – 2.02 (1H, m, 4'-*H*), 1.78 – 1.68 (1H, m, 4'-*H*), 1.78 – 1.68 (1H, m, 5'-*H*), 1.68 – 1.65 (2H, m, $NHCH_2CH_2CH_2$), 1.68 – 1.65 (1H, m, 5'-*H*), 1.53 – 1.42 (2H, m, $CH_2CH_2CH_3$), 0.96 (3H, t, J = 7.4 Hz, $CH_2CH_2CH_3$); δ_C (151 MHz, $CDCl_3$) 152.5 (*C*-5), 143.7 (*C*-7), 142.4 (*C*-7a), 126.7 (*C*-3a), 118.2 (*C*-3), 89.1 (*C*-2'), 86.3 (*C*-4), 67.8 (*C*-6'), 43.4 ($NHCH_2CH_2$), 31.3 ($NHCH_2CH_2$), 31.1 (*C*-3'), 24.9 (*C*-5'), 21.9 (*C*-4'), 20.4 ($CH_2CH_2CH_3$), 13.9 ($CH_2CH_2CH_3$); V_{max} (ATR) 1635, 1507, 1089, 1048 cm^{-1}; LC-MS (ESI) $[M + H]^+$ 275.309; HRMS (ESI) found $[M + H]^+$ 275.1874, $C_{15}H_{22}N_4O$ requires *M* 275.1872.

1-Methyl-4-[2'-(oxan-2"-yl)-_2H_-pyrazolo[3,4-c]pyridin-5'-yl]piperazine 194

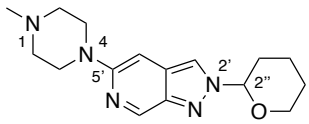

General procedure E was applied to 5-bromo-2-(oxan-2'-yl)-*2H*-pyrazolo[3,4-c]pyridine **191** (0.080 g, 0.28 mmol, 1.00 eq) with *N*-methylpiperazine (0.04 mL, 0.31 mmol, 1.10 eq). Purification by silica gel flash column chromatography (EtOAc:Pet Ether 40-60 0-100%, MeOH:EtOAc 0-30%) afforded 1-methyl-4-[2'-(oxan-2"-yl)-*2H*-pyrazolo[3,4-c]pyridin-5'-yl]piperazine as a green oil (0.064 g, 0.21 mmol, 75%).

δ_H (600 MHz, $CDCl_3$) 9.04 (1H, t, J = 1.3 Hz, 7'-*H*), 7.97 (1H, t, J = 1.3 Hz, 3'-*H*), 6.59 (1H, d, J = 1.3 Hz, 4'-*H*), 5.68 – 5.62 (1H, m, 2"-*H*), 4.12 – 4.06 (1H, m, 6"-*H*), 3.80 – 3.73 (1H, m, 6"-*H*), 3.47 – 3.41 (4H, m, 3,5-H_2), 2.66 – 2.60 (4H, m, 2,6-H_2), 2.37 (3H, d, J = 2.3 Hz, NCH_3), 2.21 – 2.17 (2H, m, 3"-*H*), 2.07 – 2.00 (1H, m, 5"-*H*), 1.80 – 1.68 (1H, m, 4"-*H*), 1.80 – 1.68 (1H, m, 5"-*H*), 1.68 – 1.62 (1H, m, 4"-*H*); δ_C (151 MHz, $CDCl_3$) 154.2 (*C*-5'), 143.3 (*C*-7'), 142.5 (*C*-7'a), 126.2 (*C*-3'a), 119.2 (*C*-3'), 91.9 (*C*-4'), 89.2 (*C*-2"), 67.8 (*C*-6"), 54.9 (*C*-2,6), 47.6 (*C*-3,5), 46.0 (NCH_3), 31.2 (*C*-3"), 24.9 (*C*-4"), 21.9 (*C*-5"); V_{max} (ATR) 1632, 1496, 1215, 1203 cm^{-1}; LC-MS (ESI) $[M + H]^+$ 302.368; HRMS (ESI) found $[M + H]^+$ 302.1983, $C_{16}H_{24}N_5O$ requires *M* 302.1981.

2-(Oxan-2'-yl)-_N_-phenyl-_2H_-pyrazolo[3,4-c]pyridin-5-amine 195

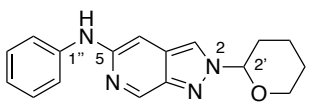

General procedure E was applied to 5-bromo-2-(oxan-2'-yl)-*2H*-pyrazolo[3,4-c]pyridine **191** (0.080 g, 0.28 mmol, 1.00 eq) with aniline (0.03 mL, 0.31 mmol, 1.10 eq). Purification by silica gel flash column chromatography (EtOAc:Pet Ether 40-60 0-60%) afforded 2-(oxan-2'-yl)-*N*-phenyl-*2H*-pyrazolo[3,4-c] pyridin-5-amine as a green solid (0.063 g, 0.21 mmol, 75%) with mp 130-133 °C.

δ_H (600 MHz, $CDCl_3$) 9.02 (1H, t, J = 1.2 Hz, 7-*H*), 7.97 (1H, d, J = 1.2 Hz, 3-*H*), 7.34 – 7.28 (2H, m, 3",5"-*H*), 7.24 – 7.21 (2H, m, 2",6"-*H*), 7.08 (1H, d, J = 1.2 Hz, 4-*H*), 7.01 – 6.95 (1H, m, 4"-*H*), 6.62 (1H, s, N-*H*), 5.67 (1H, dd, J = 8.7, 3.4 Hz, 2'-*H*), 4.12 – 4.08 (1H, m, 6'-*H*), 3.78 – 3.75 (1H, m, 6'-*H*), 2.24 – 2.14 (2H, m, 3'-*H*), 2.07 – 2.01 (1H, m, 5'-*H*), 1.79 – 1.64 (2H, m, 4'-*H*), 1.79 – 1.64 (1H, m, 5'-*H*); δ_C (151 MHz, $CDCl_3$) 147.8 (*C*-5), 143.7 (*C*-7), 142.9 (*C*-7a), 142.0 (*C*-1"), 129.5 (*C*-3",5"), 126.4 (*C*-3a), 121.9 (*C*-4"), 119.3 (*C*-3), 119.1 (*C*-2",6"), 92.4 (*C*-4), 89.4 (*C*-2'), 68.0 (*C*-6'), 31.4 (*C*-3'), 25.0 (*C*-4'), 22.0 (*C*-5'); V_{max} (ATR) 1633, 1603, 1493, 1089, 1047 cm^{-1}; LC-MS (ESI) $[M + H]^+$ 295.299; HRMS (ESI) found $[M + H]^+$ 295.1578, $C_{17}H_{19}N_4O$ requires *M* 295.1559.

4-[1'-(Oxan-2"-yl)-*1H*-pyrazolo[3,4-c]pyridin-5'-yl]morpholine 196

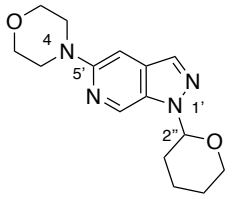

General procedure E was applied to 5-bromo-1-(oxan-2-yl)-1H-pyrazolo[3,4-c]pyridine **190** (0.080 g, 0.28 mmol, 1.00 eq) with morpholine (0.03 mL, 0.31 mmol, 1.10 eq). Purification by silica gel flash column chromatography (EtOAc:Pet Ether 40-60 0-60%) followed by HPLC separation afforded 4-[1'-(oxan-2"-yl)-*1H*-pyrazolo[3,4-c]pyridin-5'-yl]morpholine as a pink solid (0.036 g, 0.12 mmol, 43%) with mp 122-123 °C.

δ_H (400 MHz, $CDCl_3$) 8.84 (1H, t, J = 1.0 Hz, 7'-*H*), 7.89 (1H, d, J = 1.0 Hz, 3'-*H*), 6.79 (1H, d, J = 1.0 Hz, 4'-*H*), 5.74 (1H, dd, J = 9.0, 2.5 Hz, 2"-*H*), 4.00 – 3.97 (1H, m, 6"-*H*), 3.90 (4H, t, J = 4.4 Hz, 2,6-H_2), 3.79 – 3.73 (1H, m, 6"-*H*), 3.42 (4H, td, J = 4.4, 1.7 Hz, 3,5-H_2), 2.56 – 2.41 (1H, m, 3"-*H*), 2.16 – 2.11 (1H, m, 3"-*H*), 2.11 – 2.06 (1H, m, 4"-*H*), 1.85 – 1.62 (1H, m, 4"-*H*), 1.85 – 1.62 (2H, m, 5"-*H*); δ_C (101 MHz, $CDCl_3$) 155.1 (*C*-5'), 132.8 (*C*-7'), 132.6 (*C*-7'a), 132.4 (*C*-3'), 132.1 (*C*-3'a), 95.1 (*C*-2"), 86.3 (*C*-4'), 67.4 (*C*-6"), 67.0 (*C*-2,6), 48.0 (*C*-3,5), 29.6 (*C*-3"), 25.2 (*C*-4"), 22.3 (*C*-5"); V_{max} (ATR) 1485, 1453, 1228, 1124, 1045, 970, 919 cm^{-1}; LC-MS (ESI) $[M + H]^+$ 289.294; HRMS (ESI) found $[M + H]^+$ 289.1664, $C_{15}H_{21}N_4O_2$ requires *M* 289.1664.

4-(1'-{[2"-(Trimethylsilyl)ethoxy]methyl}-*1H*-pyrazolo[3,4-c]pyridin-5'-yl)morpholine 193

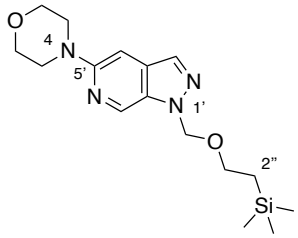

General procedure E was applied to 5-bromo-1-{[2'-(trimethylsilyl)ethoxy]methyl}-*1H*-pyrazolo[3,4-c]pyridine **188** (0.300 g, 0.91 mmol, 1.00 eq) with morpholine (0.09 mL, 1.0 mmol, 1.10 eq). Purification by silica gel flash column chromatography (EtOAc:Pet Ether 40-60 0-30%) afforded 4-(1'-{[2"-(trimethylsilyl)ethoxy]methyl}-*1H*-pyrazolo[3,4-c]pyridin-5'-yl)morpholine as a pale green solid (0.297 g, 0.89 mmol, 97%) with mp 86-88 °C.

δ_H (600 MHz, $CDCl_3$) 8.79 (1H, t, J = 1.1 Hz, 7'-*H*), 7.88 (1H, d, J = 1.1 Hz, 3'-*H*), 6.81 (1H, d, J = 1.1 Hz, 4'-*H*), 5.73 (2H, s, NCH_2O), 3.92 – 3.88 (4H, m, 2,6-H_2), 3.55 – 3.49 (2H, m, OCH_2CH_2), 3.46 – 3.42 (4H, m, 3,5-H_2), 0.90 – 0.84 (2H, m, CH_2CH_2Si), -0.07 (9H, s, $Si(CH_3)_3$); δ_C (151 MHz, $CDCl_3$) 155.1 (*C*-5'), 132.7 (*C*-3'a), 132.5 (*C*-3'), 132.1 (*C*-7'a), 131.9 (*C*-7'), 94.9 (*C*-4'), 78.3 (NCH_2O), 66.9 (*C*-2,6), 66.6 (OCH_2CH_2), 47.8 (*C*-3,5), 17.74 (CH_2CH_2Si), -1.5 ($Si(CH_3)_3$); V_{max} (ATR) 1483, 1081, 907,

840, 735 cm^{-1}; LC-MS (ESI) $[M + H]^+$ 335.393; HRMS (ESI) found $[M + H]^+$ 335.1931, $C_{16}H_{27}N_4O_2Si$ requires *M* 335.1903.

4-(2'-{[2"-(Trimethylsilyl)ethoxy]methyl}-*2H*-pyrazolo[3,4-c]pyridin-5'-yl)morpholine 197

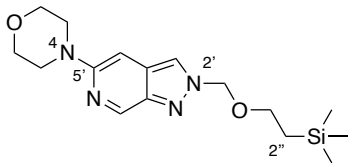

General procedure E was applied to 5-bromo-2-{[2'-(trimethylsilyl)ethoxy]methyl}-*2H*-pyrazolo[3,4-c]pyridine **189** (0.200 g, 0.61 mmol, 1.00 eq) with morpholine (0.06 mL, 0.67 mmol, 1.10 eq). Purification by silica gel flash column chromatography (EtOAc:Pet Ether 40-60 0-60%) afforded 4-(2'-{[2"-(trimethylsilyl)ethoxy]methyl}-*2H*-pyrazolo[3,4-c]pyridin-5'-yl)morpholine as a green oil (0.123 g, 0.37 mmol, 60%).

δ_H (600 MHz, $CDCl_3$) 9.07 (1H, d, J = 1.1 Hz, 7'-*H*), 7.94 (1H, d, J = 1.1 Hz, 3'-*H*), 6.60 (1H, s, 4'-*H*), 5.70 (2H, s, NCH_2O), 3.92 – 3.88 (4H, m, 2,6-H_2), 3.64 – 3.58 (2H, m, OCH_2CH_2), 3.42 – 3.38 (4H, m, 3,5-H_2), 0.96 – 0.90 (2H, m, CH_2CH_2Si), -0.04 (9H, s, $Si(CH_3)_3$); δ_C (151 MHz, $CDCl_3$) 154.2 (*C*-5'), 143.4 (*C*-7'), 142.9 (*C*-7'a), 126.9 (*C*-3'a), 120.7 (*C*-3'), 91.6 (*C*-4'), 82.2 (NCH_2O), 67.9 (OCH_2CH_2), 66.9 (*C*-2,6), 48.0 (*C*-3,5), 17.8 CH_2CH_2Si), -1.5 ($Si(CH_3)_3$); V_{max} (ATR) 1498, 1119, 1104, 914, 735 cm^{-1}; LC-MS (ESI) $[M + H]^+$ 335.355; HRMS (ESI) found $[M + H]^+$ 335.1911, $C_{16}H_{27}N_4O_2Si$ requires *M* 335.1903.

7.2.6 Multi-vector Sequences

5-Chloro-1-methyl-3-[4'-(trifluoromethyl)phenyl]-*1H*-pyrazolo[3,4-c]pyridine 211

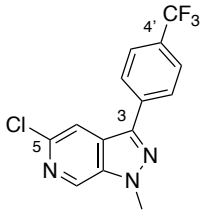

Route 1 Trimethoxonium tetrafluoroborate (0.036 g, 0.23 mmol, 2.00 eq) and 5-chloro-3-[4'-(trifluoromethyl)phenyl]-1-{[2"-(trimethylsilyl)ethoxy]methyl}-*1H*-pyrazolo[3,4-c]pyridine **140** (0.050 g, 0.12 mmol, 1.0 eq) were sealed under a nitrogen atmosphere. Anhydrous EtOAc (1.5 mL) was added and the reaction stirred at room temperature for 8 hours. The reaction mixture was concentrated under reduced pressure to afford a white solid. The crude salt was taken up in anhydrous DCM (1.0 mL) then TFA (2.0 mL) was added dropwise under a nitrogen atmosphere, and the reaction stirred at room temperature for 3 days. The reaction was diluted with DCM (10 mL) then washed with sat. $NaHCO_3$ (3 x 15 mL) and brine (20 mL), then dried over $MgSO_4$, filtered, and concentrated under reduced pressure. Purification by silica gel flash column chromatography (MeOH:DCM 0-30%) afforded 5-chloro-1-methyl-3- [4'-(trifluoromethyl)phenyl]-*1H*-pyrazolo[3,4-c]pyridine as a red semi-solid (0.024 g, 0.075 mmol, 66%).

Route 2 Trimethoxonium tetrafluoroborate (0.026 g, 0.18 mmol, 1.50 eq) and 5-chloro-3-[4'-(trifluoromethyl)phenyl]-2-{[2"-(trimethylsilyl)ethoxy]methyl}-*2H*-pyrazolo[3,4-c]pyridine **141** (0.050 g, 0.12 mmol, 1.00 eq) were sealed under a nitrogen atmosphere. Anhydrous EtOAc (3.0 mL) was added and the reaction stirred at room temperature overnight. The reaction mixture was concentrated under reduced pressure then washed with minimal H_2O. Purification by silica gel flash column chromatography (MeOH:DCM 0-30%) afforded 5-chloro-1-methyl-3-[4'-(trifluoromethyl)phenyl]-*1H*-pyrazolo[3,4-c]pyridine as a red semi-solid (0.018 g, 0.059 mmol, 50%).

δ_H (600 MHz, DMSO) 9.85 (1H, s, 7-*H*), 8.77 (1H, s, 4-*H*), 8.34 (2H, d, J = 8.1 Hz, 2',6'-*H*), 7.83 (2H, d, J = 8.1 Hz, 3',5'-*H*), 4.35 (3H, s, NCH_3); δ_C (151 MHz, DMSO) 142.1 (*C*-3)*, 138.3 (*C*-5)*, 137.9 (*C*-7), 135.2 (*C*-1'), 132.24 (*C*-7a), 128.6 (q, $J_{C\text{-}F}$ = 31.8 Hz, *C*-4'), 127.3 (*C*-2',6'), 126.9 (*C*-3a)*, 126.0 (q, $J_{C\text{-}F}$ = 3.9 Hz, *C*-3',5'), 126.3 (q, $J_{C\text{-}F}$ = 272.1 Hz, *C*F_3), 118.8 (*C*-4), 47.3 (N*C*H_3); δ_F (376 MHz, DMSO) -62.91; V_{max} (ATR) 1329, 1071, 1018, 847 cm^{-1}; LC-MS (ESI): [M (^{35}Cl) + H]$^+$ 312.217, [M (^{37}Cl)+ H]$^+$ 314.269; HRMS (ESI) found [M + H]$^+$ 312.0504, $C_{14}H_{10}N_3{}^{35}ClF_3$ requires *M* 312.0515.
*resolved in ^{13}C NMR at 90 °C.

5-Chloro-1-methyl-3-(4'-nitrophenyl)-*1H*-pyrazolo[3,4-c]pyridine 214

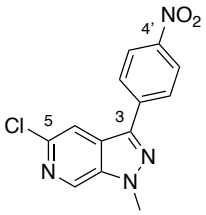

Trimethoxonium tetrafluoroborate (0.027 g, 0.19 mmol, 1.50 eq) and 5-chloro-3-[4'-nitrophenyl]-1-{[2"-(trimethylsilyl)ethoxy]methyl}-*1H*-pyrazolo[3,4-c]pyridine **145** (0.050 g, 0.12 mmol, 1.00 eq) were sealed under nitrogen. Anhydrous EtOAc (3.0 mL) was added and the reaction stirred at room temperature for 6 hours, a pale precipitate was generated. TFA (2.0 mL) was added dropwise and the reaction stirred at room temperature overnight. The reaction mixture was

diluted with EtOAc (2.0 mL) then concentrated under reduced pressure. EtOAc (3 x 10 mL) was used as an azeotroping agent to remove the TFA by concentrating the product under reduced pressure 3 times to afford a white solid, the trifluoroacetate salt. Stirring with NH_3 in MeOH (1.0 mL) then washing with minimal H_2O afforded 5-chloro-1-methyl-3-(4'-nitrophenyl)-*1H*-pyrazolo[3,4-c]pyridine as a bright yellow solid (0.034 g, 0.12 mmol, 95%) which is thermally unstable above 170 °C.

δ_H (400 MHz, DMSO) 9.73 (1H, s, 7-*H*), 8.65 (1H, s, 4-*H*), 8.42 (2H, d, J = 9.0 Hz, 3',5'-*H*), 8.29 (2H, d, J = 9.0 Hz, 2',6'-*H*), 4.30 (3H, s, NCH_3); δ_H (600 MHz, DMSO + TFA) 10.10 (1H, s, 7-*H*), 9.15 (1H, s, 4-*H*), 8.40 (2H, d, J = 8.9 Hz, 3',5'-*H*), 8.37 (2H, d, J = 8.9 Hz, 2',6'-*H*), 4.46 (3H, s, NCH_3); δ_C (151 MHz, DMSO + TFA) 147.6 (*C*-4'), 142.2 (*C*-3), 137.7 (*C*-7), 137.7 (*C*-5), 136.4 (*C*-1'), 134.2 (*C*-7a), 128.2 (*C*-3',5'), 127.2 (*C*-3a), 124,4 (*C*-2',6'), 119.7 (*C*-4), 47.9 (N*C*H_3); V_{max} (ATR) 1592 (N=O, asymmetric), 1503, 1329 (N=O, symmetric), 856 cm^{-1}; LC-MS (ESI): [M (^{35}Cl) + H]$^+$ 289.104, [M (^{37}Cl)+ H]$^+$ 291.157; HRMS (ESI) found [M + H]$^+$ 289.0509, $C_{13}H_{10}N_4O_2{}^{35}Cl$ requires *M* 289.0492.

5-Chloro-7-iodo-3-(4'-(trifluoromethyl)phenyl)-1-((2"-(trimethylsilyl)ethoxy)methyl)-*1H*-pyrazolo[3,4-c]pyridine 216

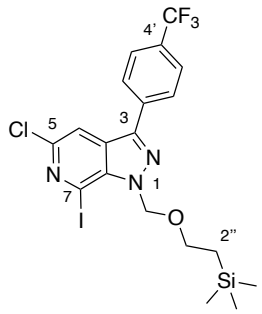

General procedure C was applied to 5-chloro-3-[4-(trifluoromethyl)phenyl]-1-{[2-(trimethylsilyl)ethoxy]methyl}-*1H*-pyrazolo[3,4-c]pyridine **140** (0.140 g, 0.33 mmol, 1.00 eq) with electrophile I_2 (0.125 g, 0.49 mmol, 1.50 eq) for 1 hour. Purification by reverse phase flash column chromatography (MeOH:H_2O 50-100%) afforded 5-chloro-7-iodo-3-(4-(trifluoromethyl)phenyl)-1-((2-(trimethylsilyl)ethoxy)methyl) –*1H*–pyrazolo[3,4-c]pyridine as a yellow oil (0.119 g, 0.22 mmol, 66%) with mp 138-140 °C.

δ_H (700 MHz, $CDCl_3$) 7.98 (2H, d, J = 8.1 Hz, 2',6'-*H*), 7.83 (1H, s, 4-*H*), 7.79 (2H, d, J = 8.1 Hz, 3',5'-*H*), 6.16 (2H, s, NCH_2O), 3.70 – 3.65 (2H, m, OCH_2CH$_2$), 0.94 (2H, m, CH$_2$CH_2Si), -0.04 (9H, s, Si(CH_3)$_3$); δ_C (176 MHz, $CDCl_3$) 142.2 (*C*-3), 141.0 (*C*-5), 139.6 (*C*-7a), 134.8 (q, $J_{C\text{-}F}$ = 1.4 Hz, *C*-1'), 131.2 (q, $J_{C\text{-}F}$ = 32.7 Hz, *C*-4'), 129.5 (*C*-3a), 127.8 (*C*-2',6'), 126.3 (q, J = 3.8 Hz, *C*-3',5'), 124.1 (q, J = 272.2 Hz, *C*F$_3$), 114.0 (*C*-4), 97.1 (*C*-7), 77.9 (N*C*H$_2$O), 66.8 (O*C*H$_2$CH$_2$), 17.9 (CH$_2$*C*H$_2$Si), -1.3 (Si(*C*H$_3$)$_3$); δ_F (376 MHz, $CDCl_3$) -62.72; V_{max} (ATR) 1327, 1078, 840, 826 cm^{-1}; LC-MS (ESI) [M (^{35}Cl) + H]$^+$ 554.14, [M (^{37}Cl) + H]$^+$ 556.16, [M (^{35}Cl) + H – I] 428.27, [M (^{37}Cl) + H – I] 430.21; HRMS found [M + H]$^+$ 554.0149, $C_{19}H_{21}{}^{35}ClF_3IN_3OSi$ requires *M* 554.0139.

4-{1'-Methyl-*1H*-pyrazolo[3,4-c]pyridin-5'-yl}morpholine 218

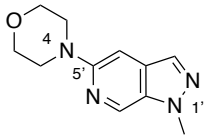

General procedure E was applied to 5-bromo-1-methyl-*1H*-pyrazolo[3,4-c]pyridine **205** (0.150 g, 0.71 mmol, 1.00 eq) with morpholine (0.07 mL, 0.78 mmol, 1.10 eq). Purification by silica gel flash column chromatography (EtOAc:Pet Ether 40-60 0-70%) afforded 4-{1'-methyl-*1H*-pyrazolo[3,4-c]pyridin-5'-yl}morpholine as a yellow solid (0.297 g, 0.89 mmol, 97%).

δ_H (600 MHz, $CDCl_3$) 8.63 (1H, t, J = 1.0 Hz, 7'-*H*), 7.83 (1H, d, J = 1.0 Hz, 3'-*H*), 6.77 (1H, d, J = 1.0

Hz, 4'-*H*), 4.10 (3H, s, N-CH_3), 3.91 – 3.86 (4H, m, 2,6-H_2), 3.42 – 3.38 (4H, m, 3,5-H_2); δ_C (151 MHz, $CDCl_3$) 154.7 (*C*-5'), 133.4 (*C*-7'a), 131.3 (*C*-7'), 131.1 (*C*-3'), 130.9 (*C*-3'a), 94.9 (*C*-4'), 66.9 (*C*-2,6), 48.0 (*C*-3,5), 36.0 (N-*C*H_3); V_{max} (ATR) 1492, 1225, 1116, 967 cm^{-1}; LC-MS (ESI) $[M + H]^+$ 219.214; HRMS (ESI) found $[M + H]^+$ 219.1254, $C_{11}H_{15}N_4O$ requires *M* 219.1246.

4-[3'-(3",5"-Dimethylphenyl)-1'-methyl-*1H*-pyrazolo[3,4-c]pyridin-5'-yl]morpholine 217

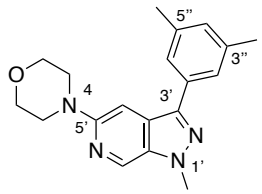

General procedure A was applied to 4-{1'-methyl-*1H*-pyrazolo[3,4-c]pyridin-5'-yl}morpholine **218** (0.130 g, 0.60 mmol, 1.00 eq) with 1-iodo-3,5-dimethylbenzene (0.09 mL, 0.66 mmol, 1.10 eq). Purification by silica gel flash column chromatography (EtOAc:Pet Ether 40-60 0-80%) afforded 4-[3'-(3",5"-dimethylphenyl)-1'-methyl-*1H*-pyrazolo[3,4-c]pyridin-5'-yl]morpholine as a yellow solid (0.106 g, 0.33 mmol, 55%) with mp 118-120 °C.

δ_H (700 MHz, $CDCl_3$) 8.70 (1H, d, J = 1.3 Hz, 7'-*H*), 7.55 (2H, m, 2",6"-*H*), 7.11 – 7.09 (1H, m, 4"-*H*), 7.08 (1H, d, J = 1.3 Hz, 4'-*H*), 4.20 (3H, s, NCH_3), 3.99 – 3.95 (4H, m, 2,6-H_2), 3.52 – 3.48 (4H, m, 3,5-H_2), 2.47 (6H, q, J = 0.8 Hz, Ar-CH_3); δ_C (176 MHz, $CDCl_3$) 155.1 (*C*-5'), 142.7 (*C*-3'), 138.5 (*C*-3",5"), 134.8 (*C*-7'a), 133.0 (*C*-1"), 131.6 (*C*-7'), 129.7 (*C*-4"), 128.5 (*C*-3'a), 124.8 (*C*-2",6"), 95.3 (*C*-4'), 66.9 (*C*-2,6), 48.1 (*C*-3,5), 36.1 (N*C*H_3), 21.5 (Ar-*C*H_3); V_{max} (ATR) 1617, 1488, 1451, 1231, 1122, 963 cm^{-1}; LC-MS (ESI) $[M + H]^+$ 323.346; HRMS (ESI) found $[M + H]^+$ 323.1876, $C_{19}H_{23}N_4O$ requires *M* 323.1872.

7.3 Chapter 3

General Procedure F for the methylation of pyrazolo[3,4-c]pyridines.

The stated *N*-methyl-pyrazolo[3,4-c]pyridine (1.00 eq) and $[Me_3O][BF_4]$ (1.30 eq) were stirred in DCM at room temperature overnight. The reaction was cooled on ice for 10 minutes then filtered under reduced pressure. The collected solid was washed with cold solvent to afford the pure product as a white solid.

5-Chloro-2,6-dimethyl-2*H*-pyrazolo[3,4-c]pyridin-6-ium tetrafluoroboranuide B1

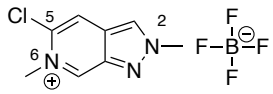

General procedure F was applied to 5-chloro-2-methyl-*2H*-pyrazolo[3,4-c]pyridine **208** (**A1**) (0.100 g, 0.58 mmol, 1.00 eq) and 5-chloro-2,6-dimethyl-*2H*-pyrazolo[3,4-c]pyridin-6-ium tetrafluoroboranuide was collected as a white solid (0.153 g, 0.57 mmol, 95%) with mp 218 – 220 °C.

δ_H (600 MHz, $(CD_3)_2CO$) 10.14 (1H, s, 7-*H*), 8.93 (1H, s, 3-*H*), 8.64 (1H, s, 4-*H*), 4.66 (3H, s, 6-CH_3), 4.56 (3H, s, 2-CH_3); δ_C (151 MHz, $(CD_3)_2CO$) 145.2 (*C*-7), 141.9 (*C*-7a), 131.6 (*C*-5), 128.2 (*C*-3a), 127.9 (*C*-3), 120.4 (*C*-4), 47.9 (6-*C*H_3), 42.1 (2-*C*H_3); V_{max}(ATR) 1030 (strong, N-CH_3), 1005 (strong, N-CH_3) cm^{-1}; LC-MS (ESI) [M (^{35}Cl)]$^+$ 182.121, [M(^{37}Cl)]$^+$ 184.173; HRMS (ESI) found [M]$^+$ 182.0485, $C_8H_9N_3{}^{35}Cl$ requires *M* 182.0485.

5-Chloro-1,6-dimethyl-1*H*-pyrazolo[3,4-c]pyridin-6-ium tetrafluoroboranuide B2

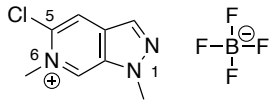

General procedure F was applied to 5-chloro-1-methyl-1*H*-pyrazolo[3,4-c]pyridine **207** (**A2**) (0.250 g, 1.49 mmol, 1.00 eq). Following additional purification by recrystallisation from acetone, 5-chloro-1,6-dimethyl-*1H*-pyrazolo[3,4-c]pyridin-6-ium tetrafluoroboranuide was collected as a white solid (0.363 g, 1.35 mmol, 90%) with mp 226 – 231 °C.

δ_H (700 MHz, $(CD_3)_2CO$) 10.11 (1H, s, 7-*H*), 8.71 (1H, s, 4-*H*), 8.61 (1H, s, 3-*H*), 4.70 (3H, s, 6-CH_3), 4.43 (3H, s, 1-CH_3); δ_C (176 MHz, $(CD_3)_2CO$) 136.1 (*C*-5), 136.1 (*C*-7), 134.7 (*C*-7a), 133.6 (*C*-3), 131.7 (*C*-3a), 120.2 (*C*-4), 48.2 (6-*C*H_3), 37.0 (1-*C*H_3); V_{max}(ATR) 1056 (strong, N-CH_3), 1041 (strong, N-CH_3) cm^{-1}; LC-MS (ESI) [M (^{35}Cl)]$^+$ 182.159, [M(^{37}Cl)]$^+$ 184.173; HRMS (ESI) found [M]$^+$ 182.0488, $C_8H_9N_3{}^{35}Cl$ requires *M* 182.0485.

5-Bromo-2,6-dimethyl-2*H*-pyrazolo[3,4-c]pyridin-6-ium tetrafluoroboranuide B3

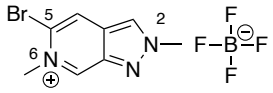

General procedure F was applied to 5-bromo-2-methyl-2*H*-pyrazolo[3,4-c]pyridine **206** (**A3**) (0.330 g, 1.56 mmol, 1.00 eq) and 5-bromo-2,6-dimethyl-*2H*-pyrazolo[3,4-c]pyridin-6-ium tetrafluoroboranuide was collected as a white solid (0.448 g, 1.43 mmol, 92%) with mp 218 – 221 °C.

δ_H (700 MHz, $(CD_3)_2CO$) 10.21 (1H, s, 7-*H*), 8.93 (1H, s, 3-*H*), 8.83 (1H, s, 4-*H*), 4.71 (3H, s, 6-CH_3), 4.59 (3H, s, 2-CH_3); δ_C (176 MHz, $(CD_3)_2CO$) 145.5 (*C*-7), 142.4 (*C*-7a), 128.4 (*C*-5), 127.6 (*C*-3), 124.7 (*C*-4), 120.5 (*C*-3a), 50.8 (6-*C*H_3), 42.0 (2-*C*H_3); V_{max}(ATR) 1025 (strong, N-CH_3), 1000 (strong, N-CH_3) cm^{-1}; LC-MS (ESI) [M (^{79}Br)]$^+$ 226.093, [M(^{81}Br)]$^+$ 228.107; HRMS (ESI) found [M]$^+$ 225.9983, $C_8H_9N_3{}^{79}Br$ requires *M* 225.9980.

5-Bromo-1,6-dimethyl-1*H*-pyrazolo[3,4-c]pyridin-6-ium tetrafluoroboranuide B4

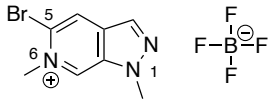

General procedure F was applied to 5-bromo-1-methyl-1*H*-pyrazolo[3,4-c]pyridine **205** (**A4**) (0.290 g, 1.37 mmol, 1.00 eq) and 5-bromo-1,6-dimethyl-*1H*-pyrazolo[3,4-c]pyridin-6-ium tetrafluoroboranuide was collected as a white solid (0.389 g, 1.24 mmol, 91%) which is thermally unstable above 240 °C.

δ_H (700 MHz, $(CD_3)_2CO$) 10.17 (1H, s, 7-*H*), 8.86 (1H, s, 4-*H*), 8.58 (1H, s, 3-*H*), 4.74 (3H, s, 6-CH_3), 4.42 (3H, s, 1-CH_3); δ_C (176 MHz, $(CD_3)_2CO$) 136.5 (*C*-7), 135.2 (*C*-7a), 133.3 (*C*-3), 131.6 (*C*-3a), 124.3 (*C*-4), 122.8 (*C*-5), 51.1 (6-*C*H_3), 37.0 (1-*C*H_3); V_{max}(ATR) 1026 (strong, N-CH_3), 1002 (strong, N-CH_3) cm^{-1}; LC-MS (ESI) $[M(^{79}Br)]^+$ 226.055, $[M(^{81}Br)]^+$ 227.955; HRMS (ESI) found $[M]^+$ 225.9978, $C_8H_9N_3{}^{79}Br$ requires *M* 225.9980.

7.3.1 Photophysical Characterisation

The absorption spectra, the photoluminescence spectra, and the spectra for PLQY calculations were measured on a Cary 5000 UV-Vis-NIR or a Shimadzu SolidSpec-3700i spectrophotometer and a Jobin Yvon HORIBA Fluorolog 3 or HORIBA Fluorolog-QM. The spectra that were measure to produce the pK_a plots were measured on a Cary 5000 UV-Vis-NIR and Jobin Yvon HORIBA Fluorolog 3. The pH of the samples were measured with a Jenway 924 005 pH electrode following initial calibration of the pH probe using commercially available buffer solutions at pH 4 and 9.21. A sigmoidal curve of absorbance vs pH was fitted using a non-linear least squares iterative analysis by Boltzmann using Origin 2021b software.

Absolute measurements of the PLQYs of the A series and B series compounds were taken using an integrating sphere in conjuction with a HORIBA Fluorolog-QM. The PLQYs were calculated using the in-built function of the software.

The PLQYs of the A series compounds were also measured using the relative method according to the standard literature procedure of Williams *et al.*.[3] For this, the integrated fluorescence intensity was recorded for each compound and compared to the known standard of quinine sulfate in aqueous H_2SO_4 (0.1 M) with a literature quantum yield of 54%.[4]

The fluorescence lifetimes of the A series and B series were determined using time-correlated single photon counting using a HORIBA CeltaFlex system in conjunction with a λ = 310 nm DeltaDiode (DeltaDiode-310). The principles and methods of time-correlated single photon counting are described by Phillips *et al.*.[5] The decay data was fitted with a single exponential according to Equation 7.1,

$$y(t) = A_1 e^{\frac{-t}{t_1}} + y_0 \tag{7.1}$$

where A_1 is the initial amplitude, y_0 is the baseline fluorescence count, and t_1 is the recorded lifetime of the excited state species in ns. A single exponential fit was used for these molecules as only one emissive excited state species is expected and it is good practice to use the minimum number of exponentials for the expected number of excited states.

The recorded values for the absolute measured PLQYs and the fluorescence lifetimes were calculated from single experiments conducted by Ruth Pollard, Northumbria University. Experiments to repeat these measurements will be completed in due course.

[3] A.T.R. Williams, S.A. Winfield and J.N. Miller, *Analyst*, 1983, **108**, 1067.
[4] W. H. Melhuish, *Journal of Physical Chemistry*, 1961, **65**, 229–235.
[5] D. Phillips, R.C. Drake, D.V. O'Connor and R.L. Christensen, *Instrumentation Science & Technology*, 1985, **14**, 267-292.

7.3.2 X-ray Crystallography Data

X-ray crystal structure determination was performed by Dr Toby Blundell, Durham University.

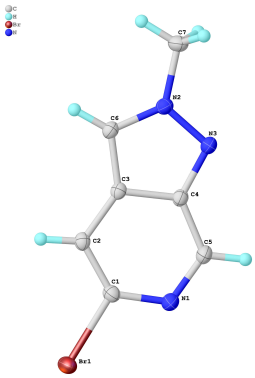

Single crystals of $C_7H_6BrN_3$ (FW 212.06) and were obtained via recrystallisation from AcOH. A suitable crystal was selected and analysed on a Bruker D8Venture diffractometer (IμS microfocus sources, focusing mirrors, CMOS Photo100 detector) using MoKα (λ = 0.71073 Å) radiation, equipped with Crysostream (Oxford Cryosystems) open-flow nitrogen cryostats. The temperature was maintained at 120 K during data collection. Using Olex2 the structure was solved with the ShelXS structure solution program using Intrinsic Phasing and refined with the ShelXL refinement package using Least Squares minimisation.

Crystallographic Data: elongated plates, colourless, 0.605 x 0.272 x 0.193 mm^3; orthorhombic, Pbca; a = 10.4302(4) Å, b = 11.0190(4) Å, c = 13.1647(5) Å; α = 90°, β = 90°, γ = 90°; V = 1513.02(10) Å^3; Z = 8; ρ_{calc} = 1.862 g cm^3; μ(MoKα) = 5.363 mm^{-1}; 73762 reflections collected (6.19 < 2Θ < 69.99) with 3327 independent reflections (R_{int} = 0.0645, R_{sigma} = 0.0248) and the final R_1 = 0.0475, wR_2 = 0.0592 (all data).

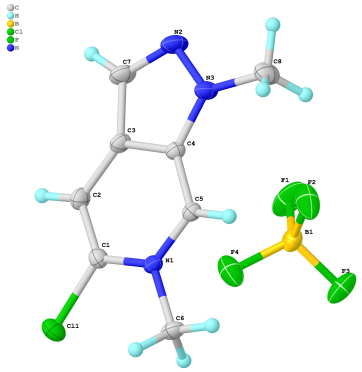

Single crystals of $C_8H_9BClF_4N_3$ (FW 269.44) and were obtained via recrystallisation from AcOH. A suitable crystal was selected and analysed on a Bruker D8Venture diffractometer (IμS microfocus sources, focusing mirrors, CMOS Photo100 detector) using MoKα (λ = 0.71073 Å) radiation, equipped with Crysostream (Oxford Cryosystems) open-flow nitrogen cryostats. The temperature was maintained at 120 K during data collection. Using Olex2 the structure was solved with the ShelXS structure solution program using Intrinsic Phasing and refined with the ShelXL refinement package using Least Squares minimisation.

Crystallographic Data: plates, colourless, 0.292 x 0.272 x 0.240 mm^3; monoclinic, $P2_{1/n}$; a = 10.7790(4) Å, b = 7.1399(3) Å, c = 14.5176(2) Å; α = 90°, β = 92.006(2)°, γ = 90°; V = 1116.60(8) Å^3; Z = 4; ρ_{calc} = 1.603 g cm^3; μ(MoKα) = 0.375 mm^{-1}; 56859 reflections collected (4.63 < 2Θ < 72.602) with 5284 independent reflections (R_{int} = 0.0509, R_{sigma} = 0.0306) and the final R_1 = 0.0629, wR_2 = 0.1125 (all data).

7.4 Chapter 4

7.4.1 Materials and Methods

Biological grade reagents, buffers and media were commercially sourced. Media and buffers were made up using purified water from a MilliQ® water purification system according to manufacturer's instructions. *E. coli* cultures were grown in LB media which was sterilised by autoclave prior to supplementing with 100 μg mL^{-1} ampicillin. SDS-PAGE gels were run alongside PageRuler Plus Prestained Protein Ladder, 10 to 250 kDa (Thermo Fisher Scientific) as a reference.

Buffers

Table 7.1: Tris Buffer A

Component	Quantity	Final concentration
TrisHCl	7.9 g	50 mM
NaCl	29.2 g	500 mM
Imidazole	2.0 g	30 mM
β-mercaptoethanol (1 M)	2 mL	2 mM

made to final volume 1 L with MilliQ® water, pH to 7.5

Table 7.2: Tris Buffer B

Component	Quantity	Final concentration
TrisHCl	7.9 g	50 mM
NaCl	29.2 g	500 mM
Imidazole	68.1 g	1 M
β-mercaptoethanol (1 M)	2 mL	2 mM

made to final volume 1 L with MilliQ® water, pH to 7.5

Table 7.3: HEPES Buffer

Component	Quantity	Final concentration
HEPES	4.7 g	20 mM
NaCl	17.5 g	300 mM
Glycerol	100 mL	1 M

made to final volume 1 L with MilliQ® water, pH to 7.5

7.4.2 Protein Expression and Purification

The genes for expressing the *Li*SIR2RP1 protein (UniProt: A0A6L0XH39) with a His_6-tag were codon optimised for expression in *E. coli* and purchased from GenScript.

The recombinant plasmids were transformed into competent *E. coli* BL21 (DE3) cells by heat-shock transformation at 42 °C for 45 seconds. The cells were then transferred to fresh plates of LB medium supplemented with 100 μg mL^{-1} ampicillin and incubated at 37 °C overnight.

To verify the identity of the expressed protein, a single culture of the transformed cells were transferred to fresh LB medium supplemented with 100 μg mL^{-1} ampicillin and incubated at 37 °C until $OD_{600} > 0.6$. The bacteria cultures were then induced with 0.1% Isopropyl β-D-1-thiogalactopyranoside (IPTG) and incubated at 25 °C overnight. Samples for gene expression were prepared with the GeneJET Plasmid Miniprep kit (Thermo Fisher Scientific). The generated forward and reverse DNA sequences were translated into amino acid sequences using ExPasy and compared to the desired sequence for the *Li*SIR2RP1 protein (UniProt: A0A6L0XH39) giving 100% match.

To collect the expressed protein, the cells were harvested by centrifugation (4,000 rpm for 25 min at 4 °C). The harvested cells were then suspended in the lysis buffer (Tris Buffer A) and lysed by sonication (10 sec on, 20 sec off for 5 minutes at 45% intensity). The cell lysates were centrifuged (21,000 rpm for 30 min at 4 °C) and the resulting supernatant was passed through a 0.45 μM Syringe Filter (Thermo Fisher Scientific). The protein was purified by affinity chromatography on an Akta Start Fast Protein Liquid Chromatography system using a HisTrap HP nickel ion-affinity chromatography column which was pre-equilibrated with the loading buffer (Tris Buffer A). Increasing concentration of the elution buffer (Tris Buffer B) (0-100%) was used to elute the protein over 5 column-volumes. Protein fractions were analysed for homogeneity on SDS-PAGE and concentrated to $1\ \mathrm{mg\,mL^{-1}}$. Time-of-flight mass spectrometry (ESI) found mass 37165 Da, and the calculated protein mass minus the first methionine 37301 Da – 131 Da = 37170 Da, thus confirming the protein was of the expected molecular weight.

With the protein identity confirmed, samples of these transformed *E. coli* BL21 cells were transferred to solution of glycerol:H_2O 50:50 and frozen at -80 °C for future protein expression following the same procedure on a larger scale.

7.4.3 Docking Experiments

The virtual screening experiments were performed using the online DockThor programme.[6] The protein structure of *Lm*SIR2RP1 was uploaded, sometimes including the NAD+ cofactor, along with the compound library to be screened. A cubic box of 20 Å was centred on the protein pocket of interest to define the searchable space and the virtual screening was performed using the standard configuration of the DockThor platform. For each virtual screening, the DockThor programme calculated 10 binding poses for each ligand and identified the 3 best poses based on the calculated docking scores. The ligands were also ranked based on the docking score of the single best binding pose. The search box was redefined to focus on each protein binding pocket in turn.

Table 7.4: Docking Experiments

Pocket	Search box centre (x,y,z)	DockThor ID
NAD+	(-1.89, -2.58, -8.33)	Dock@Dock.CBRADWSDJA
C-extended (small)	(7.68, 2.78, -3.95)	Dock@Dock.CBRAFQQ55Z
C-extended (5D7P)	(9.48, 5.11, -3.87)	Dock@Dock.CBRBJP7HL2
C-pocket (EX243)	(7.68, 2.78, -3.95)	Dock@Dock.CBRAFQLNFB
Selectivity	(15.30, 1.80, -3.71)	Dock@Dock.CBRAS5ZXEH
Substrate (big)	(9.24, 0.30, -5.74)	Dock@Dock.CBRAQJ2ACU
Substrate (small)	(9.24, 0.30, -5.74)	Dock@Dock.CBRAS5OYUV

7.4.4 Thermal Shift Assay

To perform the protein stability screening, thermal shift assays were performed in a 96-well plate format using the Durham salt and Durham pH screening kits (Molecular Dimensions). Each well contained $0.5\ \mathrm{mg\,mL^{-1}}$ *Li*SIR2RP1 protein, 10 μL buffer, 10 X SYPRO Orange dye, and 10 μL of the corresponding screening solution. The plates were sealed using StarSeal Advanced Polyolefin Film (Starlab) and centrifuged (1,000 rpm, 2 min at 4 °C). TSA analysis was achieved using 7500 Fast Real-Time PCR System with fluorescence data collected between 24-96 °C at a temperature gradient of 1 °C per min with $\lambda_{\mathrm{excitation}}$ = 455-485 nm and $\lambda_{\mathrm{emission}}$ = 567-596 nm. Thermal shift data was analysed using NAMI software.[7]

[6] I.A. Guedes, A.M.S. Barreto, D. Marinho, E. Krempser, M.A. Kuenemann, O. Sperandio, L.E. Dardenne and M.A. Miteva, *Scientific Reports*, 2021, **11**, 3198

[7] M.K. Grøftehauge, N.R. Hajizadeh, M.J. Swann, and E. Pohl, *Acta Cryst.*, 2015, **D71**, 36-44

7.5 Chapter 5

7.5.1 Benzolactams

1,4-Dihydroisoquinolin-3-one 251

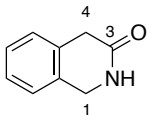

Route 1 An oven-dried RBF was charged with isoquinolin-3-ol (1.00 g, 6.9 mmol, 1.00 eq) and Pd/C (10%) (0.733 g, 6.9 mmol, 1.00 eq) under a nitrogen atmosphere. Dry MeOH (45 mL) was added and one balloon of H_2 was bubbled through the solution then changed for a fresh balloon and the reaction was stirred under a H_2 atmosphere overnight. The reaction mixture was filtered through Celite® and the residue washed with MeOH. Purification by reverse phase flash column chromatography (MeCN:H_2O 0-20%) afforded 1,4-dihydroisoquinolin-3-one as a yellow solid (0.710 g, 4.8 mmol, 70%) with mp 148-150 °C.

Route 2 NaN_3 was added portion-wise (10 parts over 5 min) to a solution of 2-indanone **253** (0.661 g, 5.0 mmol, 1.00 eq) in conc HCl (15 mL) on ice then the reaction was stirred overnight. The reaction was quenched by pouring the reaction mixture over ice (30 g) then K_2CO_3 was added until pH 9. The reaction was extracted with DCM (4 x 30 mL) then the combined organic layers were washed with brine, dried over $MgSO_4$, filtered, and concentrated under reduced pressure. Purification by silica gel flash column chromatography (EtOAc:Hexanes 0-100%) afforded 1,4-dihydroisoquinolin-3-one as a pale solid (0.429 g, 2.9 mmol, 58%) with mp 148-150 °C.

δ_H (400 MHz, $CDCl_3$) 7.55 – 7.45 (1H, br s, N-*H*), 7.28 – 7.22 (1H, m, 6-*H*), 7.28 – 7.22 (1H, m, 7-*H*), 7.20 – 7.15 (1H, m, 8-*H*), 7.20 – 7.15 (1H, m, 5-*H*), 4.52 (2H, s, 1-H_2), 3.60 (2H, s, 4-H_2); δ_C (101 MHz, $CDCl_3$) 171.9 (*C*=O), 131.7 (*C*-8a), 130.9 (*C*-4a), 127.8 (*C*-8), 127.6 (*C*-7), 126.8 (*C*-6), 125.4 (*C*-5), 45.42 (*C*-1), 36.5 (*C*-4); LC-MS (ESI) $[M + H]^+$ 148.11; HRMS found $[M + H]^+$ 148.0682, $C_9H_{10}NO$ requires *M* 148.0757. The analytical data were consistent with the literature.[8]

1,4-Dihydro-*3H*-isochromen-3-one 257

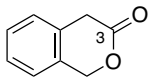

m-Chloroperoxybenzoic acid (0.979 g, 5.7 mmol, 1.5 eq) was added to a solution of 2-indanone (0.500 g, 3.8 mmol, 1.00 eq) in DCM (15 mL) on ice under a nitrogen atmosphere. The reaction mixture was allowed to return to room temperature, then stirred for 24 hours. The reaction was quenched by addition of sat. $NaHCO_3$ (30 mL), then extracted with DCM (3 x 35 mL). The combined organic layers were washed with brine, dried over $MgSO_4$, filtered, and concentrated under reduced pressure. Purification by silica gel flash column chromatography (EtOAc:Pet Ether 40-60 0-20%) afforded 1,4-dihydro-*3H*-isochromen-3-one as a white solid (0.287 g, 1.9 mmol, 51%) with mp 80-82 °C.

δ_H (400 MHz, $CDCl_3$) 7.41 – 7.30 (1H, m, 6-*H*), 7.41 – 7.30 (1H, m, 7-*H*), 7.30 – 7.21 (1H, m, 8-*H*), 7.30 – 7.21 (1H, m, 5-*H*), 5.34 (2H, s, 1-H_2), 3.74 (2H, s, 4-H_2); δ_C (101 MHz, $CDCl_3$) 170.7 (*C*=O), 131.6 (*C*-8a), 131.0 (*C*-4a), 128.9 (*C*-8), 127.4 (*C*-7), 127.1 (*C*-6), 124.7 (*C*-5), 70.1 (*C*-1), 36.2 (*C*-4); LC-MS (ESI) $[M + H]^+$ 149.09; HRMS found $[M + H]^+$ 149.0593, $C_9H_9O_2$ requires *M* 149.0603. The analytical data were consistent with the literature.[9]

[8] S.N. Smith, S.J. Connon, *European Journal of Organic Chemistry*, 2021, **2021**, 5540.
[9] C.-Y. Cheng, H.-B., Tsai, and M.-S. Lin, *Journal of Heterocyclic Chemistry*, 1995, **32**, 73-77.

2-(4'-Methylphenyl)sulfonyl-1,4-dihydroisoquinolin-3(*2H*)-one 258

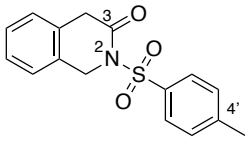

$AlCl_3$ (0.045 g, 0.34 mmol, 0.20 eq), 1,4-dihydro-*3H*-isochromen-3-one **257** (0.250 g, 1.69 mmol, 1.00 eq), and *p*-toluenesulfonamide (0.433 g, 2.5 mmol, 1.50 eq) were heated at 120 °C for 43 hours under a nitrogen atmosphere. The reaction mixture was left to cool to room temperature and the resulting solid was dissolved in EtOAc (25 mL) then washed with HCl (1 M) (30 mL). The aqueous layer was extracted with EtOAc (2 x 25 mL) and the combined organic layers were dried over $MgSO_4$ then filtered and concentrated under reduced pressure. Purification by silica gel flash column chromatography (EtOAc:Pet Ether 40-60 0-60%) afforded 2-(4'-methylphenyl)sulfonyl-1,4-dihydroisoquinolin-3(*2H*)-one as a white solid (0.016 g, 0.051 mmol, 3%) with mp 195-196 °C.

δ_H (700 MHz, $CDCl_3$) 7.89 (2H, d, J = 8.3 Hz, 2',6'-*H*), 7.35 – 7.31 (1H, m, 8-*H*), 7.31 – 7.29 (1H, m, 6-*H*) 7.31 - 7.29 (1H, m, 7-*H*), 7.28 (2H, d, J = 8.3 Hz, 3',5'-*H*), 7.16 – 7.13 (1H, m, 5-*H*), 5.08 (2H, s, 1-*H*), 3.62 (2H, s, 4-*H*), 2.40 (3H, s, Ar'-CH_3); δ_C (176 MHz, $CDCl_3$) 168.9 (*C*=O), 145.0 (*C*-4'), 135.8 (*C*-1'), 131.5 (*C*-4a), 131.4 (*C*-8a), 129.4 (*C*-3',5'), 128.6 (*C*-2',6'), 128.5 (*C*-7), 127.4 (*C*-6), 127.2 (*C*-8), 125.8 (*C*-5), 48.8 (*C*-1), 40.5 (*C*-4), 21.7 (Ar'-*C*H_3); LC-MS (ESI) $[M + H]^+$ 302.22; HRMS found $[M + H]^+$ 302.0862, $C_{16}H_{16}NO_3S$ requires *M* 302.0851. The analytical data were consistent with the literature.[10]

7.5.2 Amine Protecting Groups

General Procedure G for *N*-tosyl protection.

Triethylamine (2.00 eq) was added to a solution of the cyclic amine (1.50 eq) in DCM (0.8 M) under a nitrogen atmosphere stirring on ice. After 10 minutes, a solution of TsCl (1.00 eq) in DCM (0.5 M) was added slowly and the reaction was allowed to return to room temperature. After 2 hours, the reaction was quenched with H_2O then extracted with DCM three times. The combined organic layers were washed with HCl (1 M) twice, and brine, then dried over $MgSO_4$. The solution was filtered and concentrated under reduced pressure to afford the product as a white solid.

1-((4'-Methylphenyl)sulfonyl)piperidine 328

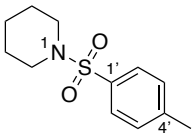

General procedure G was applied to piperidine (1.2 mL, 12 mmol, 1.50 eq) to afford 1-((4'-methylphenyl)sulfonyl)piperidine as a white solid (1.75 g, 7.3 mmol, 93%) with mp 99-100 °C.

δ_H (600 MHz, $CDCl_3$) 7.63 (2H, d, J = 8.2, 2',6'-*H*), 7.30 (2H, d, J = 8.2, 3',5'-*H*), 2.99 – 2.93 (4H, m, 2,6-H_2), 2.42 (3H, s, 4'-CH_3), 1.62 (4H, m, 3,5-H_2), 1.43 – 1.36 (2H, m, 4-H_2); δ_C (151 MHz, $CDCl_3$) 143.3 (*C*-4'), 133.3 (*C*-1'), 129.5 (*C*-3',5'), 127.7 (*C*-2',6'), 46.9 (*C*-2,6), 25.1 (*C*-3,5), 23.5 (*C*-4), 21.5 (Ar'-*C*H_3); LC-MS (ESI) $[M + H]^+$ 240.231; HRMS found $[M + H]^+$ 240.1061, $C_{12}H_{18}NO_2S$ requires *M* 240.1058. The analytical data were consistent with the literature.[11]

[10] L. Wu, J. Chen, P. Lu, Y. Wang, *Tetrahedron*, 2021, **84**, 132019.

[11] Giang Luu, T., Kim, H.-K., *Adv. Synth. Catal.* **2023**, 365, 1671.
T. Pavlovska, I. Weisheitelová, C. Pramthaisong, M. Sikorski, U. Jahn, R. Cibulka, *Adv. Synth. Catal*, 2023, **365**, 4662.

(4-Methylphenyl)(piperidin-1'-yl)methanone 346

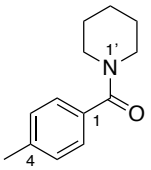

Triethylamine (1.8 mL, 13 mmol, 2.00 eq) was added to a solution of piperidine (0.96 mL, 10 mmol, 1.50 eq) in DCM (25 mL) under a nitrogen atmosphere stirring on ice. After stirring for 10 minutes, 4-methylbenzoyl chloride (0.94 mL, 6.5 mmol, 1.00 eq) was added and the reaction mixture was allowed to return to room temperature. After 2 hours the reaction was quenched with H_2O (30 mL). The aqueous layer was extracted with DCM (3 x 20 mL). The combined organic layers were washed with HCl (1M, 15 mL), H_2O (15 mL), and brine (25 mL), then dried over $MgSO_4$, filtered, and concentrated under reduced pressure. Purification by silica gel flash column chromatography (EtOAc:Pet Ether 40-60 0-40%) afforded (4-methylphenyl)(piperidin-1'-yl)methanone as a white solid (1.11 g, 5.4 mmol, 84%) with mp 53-55 °C.

δ_H (400 MHz, $CDCl_3$) 7.28 (2H, d, J = 8.1 Hz, 2,6-*H*), 7.18 (2H, d, J = 7.8 Hz, 3,5-*H*), 3.68 (2H, br s, 2'/6'-H_2), 3.35 (2H, br s, 2'/6'-H_2), 2.36 (3H, s, Ar-CH_3), 1.65 (2H, br s, 4'-H_2), 1.61 (2H, br s, 3'/5'-H_2), 1.52 (2H, br s, 3'/5'-H_2); δ_C (101 MHz, $CDCl_3$) 170.5 (*C*=O), 139.4 (*C*-4), 133.6 (*C*-1), 129.0 (*C*-3,5), 126.9 (*C*-2,6), 48.9 (*C*-2'/6'), 43.3 (*C*-2'/6'), 26.4 (*C*-3'/5'), 25.8 (*C*-3'/5'), 24.7 (*C*-4'), 21.4 (Ar-*C*H_3). LC-MS (ESI) $[M + H]^+$ 204.202; HRMS found $[M + H]^+$ 204.1388, $C_{13}H_{18}NO$ requires *M* 204.1388. The analytical data were consistent with the literature.[12]

1-((4'-Methylphenyl)sulfonyl)pyrrolidine 327

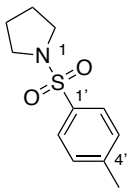

Triethylamine (2.9 mL, 21 mmol, 1.50 eq) was added to a solution of pyrrolidine (1.2 mL, 14 mmol, 1.00 eq) in chloroform (5 mL) under a nitrogen atmosphere stirring on ice. After 10 minutes, a solution of TsCl (4.0 g, 21 mmol, 1.50 eq) in chloroform (5 mL) was added slowly over 10 minutes. After 1 hour, the reaction was allowed to return to room temperature. After 2 hours the reaction was quenched with aqueous $NaHCO_3$ (5%, 25 mL). The reaction mixture was extracted with EtOAc (50 mL). The organic layer was washed with aqueous citric acid (5%, 2 × 40 mL), H_2O (25 mL), aqueous $NaHCO_3$ (5%, 2 × 25 mL) and brine (20 mL). The organic layer was dried over $MgSO_4$ concentrated under reduced pressure. Purification by silica gel flash column chromatography (EtOAc:Pet Ether 40-60 0-25%) afforded 1-((4'-methylphenyl)sulfonyl)pyrrolidine as a white solid (2.88 g, 13 mmol, 91%) with mp 122.3-123.0 °C.

δ_H (400 MHz, $CDCl_3$) 7.71 (2H, d, J = 8.3 Hz, 2',6'-*H*), 7.32 (2H, d, J = 8.0 Hz, 3',5'-*H*), 3.28 – 3.16 (4H, m, 2,5-H_2), 2.43 (3H, s, Ar-CH_3), 1.81 – 1.68 (4H, m, 3,4-H_2); δ_C (101 MHz, $CDCl_3$) 143.3 (*C*-4'), 134.0 (*C*-1'), 129.6 (*C*-3',5'), 127.6 (*C*-2',6'), 47.9 (*C*-2,5), 25.2 (*C*-3,4), 21.5 (Ar-*C*H_3); LC-MS (ESI) $[M + H]^+$ 226.169; HRMS found $[M + H]^+$ 226.0902, $C_{11}H_{16}NO_2S$ requires *M* 226.0902. The analytical data were consistent with the literature.[13]

[12] A.M. Veatch, S. Liu, E.J. Alexanian, *Angew. Chem. Int. Ed.*, **2022**, 61, e202210772; *Angew. Chem.*, 2022, **134**, e202210772.
[13] C.G. Kokotos, V.K. Aggarwal, *Chem. Commun.*, 2006, **20**, 2156-2158

1-((4'-Methylphenyl)sulfonyl)azepane 330

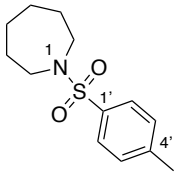

General procedure G was applied to azepane (0.89 mL, 7.9 mmol, 1.50 eq) to afford 1-((4'-methylphenyl)sulfonyl)azepane as a white solid (1.21 g, 4.8 mmol, 91%) with mp 76-77 °C.

δ_H (700 MHz, $CDCl_3$) 7.67 (2H, d, J = 8.4 Hz, 2',6'-*H*), 7.29 (2H, d, J = 8.4 Hz, 3',5'-*H*), 3.25 (4H, t, J = 5.9 Hz, 2,7-H_2), 2.42 (3H, s, Ar'-CH_3), 1.73 – 1.69 (4H, m, 3,6-H_2), 1.59 – 1.57 (4H, m, 4,5-H_2); δ_C (176 MHz, $CDCl_3$) 142.8 (*C*-4'), 136.6 (*C*-1'), 129.6 (*C*-3',5'), 127.0 (*C*-2',6'), 48.2 (*C*-2,7), 29.2 (*C*-3,6), 26.9 (*C*-4,5), 21.5 (Ar'-*C*H_3); LC-MS (ESI) $[M + H]^+$ 254.216; HRMS found $[M + H]^+$ 254.1222, $C_{13}H_{20}NO_2S$ requires *M* 254.1215.[14]

1-((4'-Methylphenyl)sulfonyl)azetidine 331

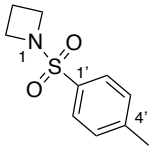

General procedure G was applied to azetidine (0.53 mL, 7.9 mmol, 1.50 eq) to afford 1-((4'-methylphenyl)sulfonyl)azetidine as a white solid (1.03 g, 4.9 mmol, 93%) with mp 122-123 °C.

δ_H (700 MHz, $CDCl_3$) 7.75 (2H, d, J = 8.2 Hz, 2',6'-*H*), 7.40 (2H, d, J = 8.2 Hz, 3',5'-*H*), 3.79 (4H, t, J = 7.4 Hz, 2,4-H_2), 2.48 (3H, s, Ar'-CH_3), 2.08 (2H, p, J = 7.4 Hz, 3-H_2); δ_C (176 MHz, $CDCl_3$)143.9 (*C*-4'), 131.6 (*C*-1'), 129.7 (*C*-2',6'), 128.4 (*C*-3',5'), 50.9 (*C*-2,4), 21.6 (Ar'-*C*H_3), 15.3 (*C*-3); LC-MS (ESI) $[M + H]^+$ 212.145; HRMS found $[M + H]^+$ 212.0754, $C_{10}H_{14}NO_2S$ requires *M* 212.0745. The analytical data were consistent with the literature.[15]

2-Methyl-1-((4'-methylphenyl)sulfonyl)piperidine 332

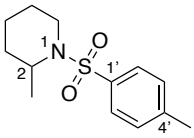

General procedure G was applied to 2-methylpiperidine (1.4 mL, 12 mmol, 1.50 eq) to afford 2-methyl-1-((4'-methylphenyl)sulfonyl)piperidine as a white solid (1.49 g, 5.9 mmol, 75%) with mp 54.3-55.2 °C.

δ_H (700 MHz, $CDCl_3$) 7.72 (2H, d, J = 7.8 Hz, 2',6'-*H*), 7.29 (2H, d, J = 7.8 Hz, 3',5'-*H*), 4.28 – 4.22 (1H, m, 2-*H*), 3.74 – 3.69 (1H, m, 6-*H*), 2.99 (1H, td, J = 13.0, 2.7 Hz, 6-*H*), 2.43 (3H, s, Ar'-CH_3), 1.66 – 1.61 (1H, m, 3-*H*), 1.61 – 1.55 (1H, m, 5-*H*), 1.56 – 1.50 (2H, m, 4-*H*), 1.47 – 1.42 (1H, m, 3-*H*), 1.42 – 1.34 (1H, m, 5-*H*), 1.08 (3H, d, J = 6.8 Hz, 2-CH_3); δ_C (176 MHz, $CDCl_3$) 142.8 (*C*-4'), 138.4 (*C*-1'), 129.6 (*C*-3',5'), 127.0 (*C*-2',6'), 48.6 (*C*-2), 40.3 (*C*-6), 30.4 (*C*-3), 25.2 (*C*-5), 21.5 (Ar'-*C*H_3), 18.2 (*C*-4), 15.3 (2-*C*H_3); LC-MS (ESI) $[M + H]^+$ 254.145; HRMS found $[M + H]^+$ 254.1210, $C_{13}H_{20}NO_2S$ requires *M* 254.1215. The analytical data were consistent with the literature.[16]

[14]A.O. Terent'ev, O.M. Mulina, D.A. Pirgach, M.A. Syroeshkin, A.P. Glinushkin, G.I. Nikishin, *Mendeleev Communications*, 2016, **26**(6), 538-539

[15]W.R. Vaughan, R.S. Klonowski, R.S. McElhinney, and B.B. Millward, *J. Org. Chem.*, 1961, **26**(1), 138–144

[16]L.F.T. Novaes, J.S.K. Ho, K. Mao, K. Liu, M. Tanwar, M. Neurock, E. Villemure, J.A. Terrett, and S. Lin, *J. Am. Chem. Soc.*, 2022,

3-Methyl-1-((4'-methylphenyl)sulfonyl)piperidine 333

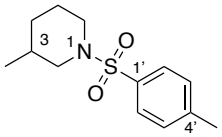

General procedure G was applied to 3-methylpiperidine (1.4 mL, 12 mmol, 1.50 eq) to afford 3-methyl-1-((4'-methylphenyl)sulfonyl)piperidine as a white solid (1.92 g, 7.6 mmol, 96%) with mp 108-109 °C.

δ_H (600 MHz, $CDCl_3$) 7.63 (2H, d, J = 8.2 Hz, 2',6'-*H*), 7.31 (2H, d, J = 8.2 Hz, 3',5'-*H*), 3.67 – 3.62 (1H, m, 6-*H*), 3.62 – 3.58 (1H, m, 2-*H*), 2.43 (3H, s, Ar'-CH_3), 2.20 (1H, td, J = 11.5, 2.7 Hz, 6-*H*), 1.87 (1H, t, J = 10.7 Hz, 2-*H*), 1.77 – 1.72 (1H, m, 3-*H*), 1.72 – 1.66 (1H, m, 4-*H*), 1.72 – 1.66 (1H, m, 5-*H*), 1.66 – 1.56 (1H, m, 5-*H*), 0.86 (3H, d, J = 6.6 Hz, 3-CH_3), 0.85 – 0.77 (1H, m, 4-*H*); δ_C (151 MHz, $CDCl_3$) 143.2 (*C*-4'), 133.3 (*C*-1'), 129.5 (*C*-3',5'), 127.7 (*C*-2',6'), 53.2 (*C*-2), 46.4 (*C*-6), 32.1 (*C*-4), 30.7 (*C*-3), 24.7 (*C*-5), 21.5 (Ar'-*C*H_3), 19.0 (3-*C*H_3); V_{max} (ATR) 1334, 1151, 753, 652, 580, 552 cm^{-1}; LC-MS (ESI) $[M + H]^+$ 254.178; HRMS found $[M + H]^+$ 254.1215, $C_{13}H_{20}NO_2S$ requires M 254.1215.

2-((4'-Methylphenyl)sulfonyl)-1,2,3,4-tetrahydroisoquinoline 334

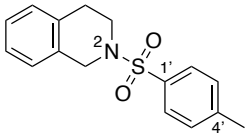

General procedure G was applied to 1,2,3,4-tetrahydroisoquiniline (1.0 mL, 7.9 mmol, 1.50 eq) to afford 2-((4'-methylphenyl)sulfonyl)-1,2,3,4-tetrahydroisoquinoline as a white solid (1.47 g, 5.1 mmol, 97%) with mp 141-143 °C.

δ_H (600 MHz, $CDCl_3$) 7.71 (2H, d, J = 8.2 Hz, 2',6'-*H*), 7.31 (2H, d, J = 8.2 Hz, 3',5'-*H*), 7.14 – 7.12 (1H, m, 6-*H*), 7.16 – 7.09 (1H, m, 7-*H*), 7.07 – 7.05 (1H, m, 5-*H*), 7.02 – 7.00 (1H, m, 8-*H*), 4.24 (2H, s, 1-H_2), 3.34 (2H, t, J = 5.9 Hz, 3-H_2), 2.92 (2H, t, J = 5.9 Hz, 4-H_2), 2.41 (3H, s, Ar'-CH_3); δ_C (151 MHz, $CDCl_3$) 143.6 (*C*-4'), 133.3 (*C*-1'), 133.1 (*C*-4a), 131.6 (*C*-8a), 129.7 (*C*-3',5'), 128.8 (*C*-5), 127.7 (*C*-2',6'), 126.7 (*C*-7), 126.3 (*C*-8), 126.3 (*C*-6), 47.5 (*C*-1), 43.7 (*C*-3), 28.9 (*C*-4), 21.5 (Ar'-*C*H_3); LC-MS (ESI) $[M + H]^+$ 288.192; HRMS found $[M + H]^+$ 288.1066, $C_{16}H_{18}NO_2S$ requires M 288.1058. The analytical data were consistent with the literature.[17]

1-((4'-Methylphenyl)sulfonyl)-1,2,3,4-tetrahydroquinoline 335

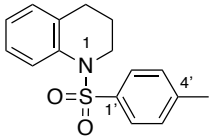

General procedure G was applied to 1,2,3,4-tetrahydroquiniline (0.59 mL, 4.7 mmol, 1.50 eq) to afford 1-((4'-methylphenyl)sulfonyl)-1,2,3,4-tetrahydroquinoline as a white solid (0.88 g, 3.0 mmol, 97%) with mp 95-96 °C.

δ_H (600 MHz, $CDCl_3$) 7.81 – 7.76 (1H, m, 8-*H*), 7.48 – 7.45 (2H, m, 2',6'-*H*), 7.19 – 7.17 (2H, m, 3',5'-*H*), 7.17 – 7.16 (1H, m, 7-*H*), 7.06 (1H, td, J = 7.4, 1.2 Hz, 6-*H*), 7.01 – 6.98 (1H, m, 5-*H*), 3.81 – 3.78 (2H, m, 2-H_2), 2.43 (2H, t, J = 6.7 Hz, 4-H_2), 2.37 (3H, s, Ar'-CH_3), 1.66 – 1.60 (2H, m, 3-H_2); δ_C (151 MHz, $CDCl_3$) 143.6 (*C*-4'), 136.9 (*C*-8a), 136.8 (*C*-1'), 130.8 (*C*-4a), 129.6 (*C*-3',5'), 129.2 (*C*-5), 127.1 (*C*-2',6'),

144, 1187-1197

[17]R. Sword, S. O'Sullivan, J.A. Murphy, *Australian Journal of Chemistry*, 2013, **66**, 314-322

126.5 (*C*-7), 125.0 (*C*-8), 125.0 (*C*-6), 46.6 (*C*-2), 26.7 (*C*-4), 21.6 (Ar'-*C*H_3), 21.6 (*C*-3); LC-MS (ESI) $[M + H]^+$ 288.192; HRMS found $[M + H]^+$ 287.0976, $C_{16}H_{17}NO_2S$ requires *M* 287.0980. The analytical data were consistent with the literature.[18]

4-((4'-Methylphenyl)sulfonyl)morpholine 336

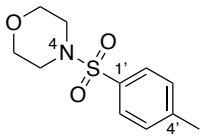

General procedure G was applied to morpholine (1.0 mL, 12 mmol, 1.50 eq) to give 4-((4'-methylphenyl)sulfonyl)morpholine as a white solid (1.7 g, 7.1 mmol, 90%) with mp 147-149 °C.

δ_H (700 MHz, $CDCl_3$) 7.64 (2H, d, *J* = 8.2 Hz, 2',6'-*H*), 7.34 (2H, d, *J* = 8.2 Hz, 3',5'-*H*), 3.74 (4H, dd, *J* = 4.8, 4.6 Hz, 2,6-H_2), 2.98 (4H, dd, *J* = 4.8, 4.6 Hz, 3,5-H_2), 2.45 (3H, s, Ar'-CH_3); δ_C (176 MHz, $CDCl_3$) 144.0 (*C*-4'), 132.1 (*C*-1'), 129.8 (*C*-3',5'), 127.9 (*C*-2',6'), 66.1 (*C*-2,6), 46.0 (*C*-3,5), 21.6 (Ar'-*C*H_3); LC-MS (ESI) $[M + H]^+$ 242.017; HRMS found $[M + H]^+$ 242.0849, $C_{11}H_{16}NO_3S$ requires *M* 242.0851. The analytical data were consistent with the literature.[19]

[18]H. Yamamoto, G. Pandey, Y. Asai, M. Nakano, A. Kinoshita, K. Namba, H. Imagawa, and M. Nishizawa, *Organic Letters*, 2007, **9**(20), 4029-4032

[19]M. Koohgard, and M. Hosseini-Sarvari, *Catal. Sci. Technol.*, 2020, **10**, 6825-6839

7.5.3 Electrochemical Oxidation

General Procedure H for electrochemical oxidation.

The cyclic substrate (1.0 mmol) and $Bu_4NF{\cdot}3H_2O$ (0.40 mmol) were sealed in an ElectraSyn reaction vial with graphite electrodes. 2,2,2-trifluoroethanol (4 mL) was added and the reaction run at a constant current of I = 5 mA, alternating every 2 minutes, until the required charge had passed through the system. The contents of the reaction vessel was washed into a clean flask with DCM then concentrated under reduced pressure. The *N,O*-acetal was isolated by flash column chromatography using the stated solvent system.

1-((4'-Methylphenyl)sulfonyl)-2-(2",2",2"-trifluoroethoxy)piperidine 337

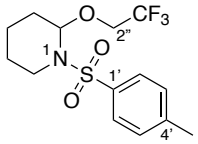

General procedure H was applied to 1-((4'-methylphenyl)sulfonyl)piperidine **328** (0.239 g, 1.0 mmol, 1.00 eq) and purification by silica gel flash column chromatography (Pet Ether 40-60:DCM 0-70%) afforded 1-((4'-methylphenyl)sulfonyl)-2-(2",2",2"-trifluoroethoxy)piperidine as a white solid (0.274 g, 0.81 mmol, 81%) with mp 46-48 °C.

δ_H (600 MHz, $(CD_3)_2CO$) 7.76 (2H, d, *J* = 8.1 Hz, 3', 5'-*H*), 7.42 (2H, d, *J* = 8.1 Hz, 2', 6'-*H*), 5.39 (1H, t, *J* = 2.9 Hz, 2-*H*), 4.01 (2H, q, $J_{H\text{-}F}$ = 9.0 Hz, OCH_2CF_3), 3.62 – 3.58 (1H, m, 6-*H*), 3.07 (1H, td, *J* = 13.3, 2.9 Hz, 6-*H*), 2.42 (3H, s, Ar'-CH_3), 1.92 – 1.88 (1H, m, 3-*H*), 1.65 (1H, qt, *J* = 13.2, 3.6 Hz, 4-*H*), 1.55 – 1.51 (1H, m, 5-*H*), 1.49 – 1.44 (1H, m, 4-*H*), 1.44 – 1.38 (1H, m, 3-*H*), 1.23 – 1.12 (1H, m, 5-*H*); δ_C (151 MHz, $(CD_3)_2CO$) 143.6 (*C*-4'), 138.0 (*C*-1'), 130.0 (*C*-3', 5'), 127.0 (*C*-2', 6'), 124.38 (q, $J_{C\text{-}F}$ = 277.4 Hz, OCH_2CF_3), 83.4 (C-2), 63.9 (q, $J_{C\text{-}F}$ = 34.2 Hz, OCH_2CF_3), 40.5 (*C*-6), 29.0 (*C*-3), 23.6 (*C*-5), 20.5 (Ar'-CH_3), 17.4 (*C*-4); δ_F (376 MHz, $(CD_3)_2CO$) -74.76 (t, $J_{F\text{-}H}$ = 9.0 Hz); LC-MS (ESI) $[M\text{-}C_2H_2F_3]^+$ 256.192, $[M\text{-}C_2H_2F_3O]^+$ 238.216; HRMS found $[M\text{-}C_2H_2F_3O]^+$ 238.0900, $C_{12}H_{16}NO_2S$ requires *M* 238.0902. The analytical data were consistent with the literature.[20]

(4-Methylphenyl)(2'-(2",2",2"-trifluoroethoxy)piperidin-1'-yl)methanone 347

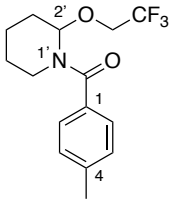

General procedure H was applied to (4-methylphenyl)(piperidin-1-yl)methanone **346** (0.203 g, 1.0 mmol, 1.00 eq) and purification by silica gel flash column chromatography (Pet Ether 40-60:EtOAc 0-25%) afforded (4-methylphenyl)(2'-(2",2",2"-trifluoroethoxy)piperidin-1'-yl)methanone as a colourless oil (0.211 g, 0.70 mmol, 70%).

δ_H (500 MHz, DMSO-*d6*)* 7.31 (2H, d, *J* = 8.2 Hz, 2,6-*H*), 7.26 (2H, d, *J* = 8.2 Hz, 3,5-*H*), 5.60 (1H, br s, 2'-*H*), 4.07 – 3.88 (2H, m, OCH_2CF_3), 3.75 (1H, br s, 6'-*H*), 3.13 – 3.00 (1H, m, 6'-*H*), 2.36 (3H, s, Ar-CH_3), 1.95 – 1.85 (1H, m, 3'-*H*), 1.78 – 1.67 (1H, m, 3'-*H*), 1.78 – 1.67 (1H, m, 4'-*H*), 1.67 – 1.58 (1H, m, 4'-*H*), 1.67 – 1.58 (1H, m, 5'-*H*), 1.55 – 1.43 (1H, m, 5'-*H*); δ_C (126 MHz, DMSO-*d6*)* 171.3 (*C*=O), 140.0 (*C*-4), 133.4 (*C*-1), 129.4 (*C*-3,5), 127.3 (*C*-2, 6), 124.7 (q, $J_{C\text{-}F}$ = 278.7 Hz, CH_2CF_3), 82.0 (*C*-2'), 64.5 (q, $J_{C\text{-}F}$ = 34.6 Hz, OCH_2CF_3), 40.7 (*C*-6'), 29.7 (*C*-3'), 25.0 (*C*-5'), 21.2 (Ar-CH_3), 18.5 (*C*-4'); δ_F

[20] L.F.T. Novaes, J.S.K. Ho, K. Mao, K. Liu, M. Tanwar, M. Neurock, E. Villemure, J.A. Terrett, and S. Lin, *J. Am. Chem. Soc.*, 2022, **144**, 1187-1197

(376 MHz, DMSO-*d6*) -72.88 (t, $J_{F\text{-}H}$ = 9.3 Hz); V_{max} (ATR) 1634 (C=O), 1415, 1272, 1147, 973 cm^{-1}; LC-MS (ESI) $[M + H]^+$ 302.254; HRMS found $[M + H]^+$ 302.1365, $C_{15}H_{19}F_3NO_2$ requires *M* 302.1368. * VT NMR at T = 80 °C

1-((4'-Methylphenyl)sulfonyl)-2-(2",2",2"-trifluoroethoxy)azepane 370

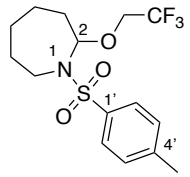

General procedure H was applied to 1-((4'-methylphenyl)sulfonyl)azepane **330** (0.253 g, 1.0 mmol, 1.00 eq) and purification by silica gel flash column chromatography (Pet Ether 40-60:DCM 0-50%) afforded 1-((4'-methylphenyl)sulfonyl)-2-(2",2",2"-trifluoroethoxy)azepane as a colourless oil (0.237 g, 0.67 mmol, 67%).

δ_H (600 MHz, $(CD_3)_2CO$) 7.81 (2H, d, *J* = 8.2 Hz, 2',6'-*H*), 7.43 (2H, d, *J* = 8.2 Hz, 3',5'-*H*), 5.45 (1H, ddd, *J* = 7.6, 6.2, 1.0 Hz, 2-*H*), 3.99 (2H, q, $J_{H\text{-}F}$ = 9.1 Hz, OCH_2CF_3), 3.57 (1H, dddd, *J* = 15.3, 5.5, 2.6, 1.2 Hz, 7-*H*), 3.25 (1H, ddd, *J* = 15.3, 11.5, 2.0 Hz, 7-*H*), 2.42 (3H, s, Ar'-CH_3), 2.23 – 2.17 (1H, m, 3-*H*), 1.73 – 1.67 (1H, m, 3-*H*), 1.60 – 1.52 (1H, m, 4-*H*), 1.56 – 1.50 (1H, m, 5-*H*), 1.53 – 1.48 (1H, m, 6-*H*), 1.49 – 1.42 (1H, m, 6-*H*), 1.40 – 1.32 (1H, m, 5-*H*), 1.12 – 1.04 (1H, m, 4-*H*); δ_C (151 MHz, $(CD_3)_2CO$) 143.6 (*C*-4'), 138.4 (*C*-1'), 129.7 (*C*-2',6'), 127.3 (*C*-3',5'), 124.4 (q, $J_{C\text{-}F}$ = 277.4 Hz, CH_2CF_3), 87.7 (*C*-2), 64.4 (q, $J_{C\text{-}F}$ = 34.1 Hz, OCH_2CF_3), 42.6 (*C*-7), 34.2 (*C*-3), 29.5 (*C*-5), 27.1 (*C*-6), 21.4 (*C*-4), 20.5 (Ar'-CH_3); δ_F (376 MHz, $(CD_3)_2CO$) -74.90 (t, $J_{F\text{-}H}$ = 9.1 Hz); V_{max} (ATR) 1154, 1086, 1027, 925, 737 cm^{-1}; LC-MS (ESI) $[M\text{-}OCH_2CF_3]^+$ 252.202; HRMS found $[M + H]^+$ 352.1179, $C_{15}H_{21}F_3NO_3S$ requires *M* 352.1194.

1-((4'-Methylphenyl)sulfonyl)-2-(2",2",2"-trifluoroethoxy)pyrrolidine 371

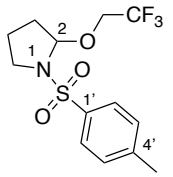

General procedure H with an Me_4NBF_4 electrolyte was applied to 1-((4'-methylphenyl)sulfonyl) pyrrolidine **327** (0.225 g, 1.0 mmol, 1.00 eq) and purification by reverse phase flash column chromatography (MeCN:H_2O 0-60%) afforded 1-((4'-methylphenyl)sulfonyl)-2-(2",2",2"-trifluoroethoxy) pyrrolidine as a white solid (0.235 g, 0.73 mmol, 73%) with mp 76-78 °C.

δ_H (600 MHz, $(CD_3)_2CO$) 7.78 (2H, d, *J* = 8.0 Hz, 2',6'-*H*), 7.44 (2H, d, *J* = 8.0 Hz, 3',5'-*H*), 5.39 (1H, d, *J* = 5.9 Hz, 2-*H*), 4.28 – 4.12 (2H, m, OCH_2CF_3), 3.45 (1H, ddd, *J* = 10.1, 8.2, 2.3 Hz, 5-*H*), 3.13 (1H, td, *J* = 10.1, 7.3 Hz, 5-*H*), 2.44 (3H, s, Ar-CH_3), 2.05 – 1.94 (1H, m, 4-*H*), 1.90 (1H, ddd, *J* = 13.1, 5.9, 1.8 Hz, 3-*H*), 1.85 – 1.76 (1H, m, 4-*H*), 1.47 – 1.38 (1H, m, 3-*H*); δ_C (151 MHz, $(CD_3)_2CO$) 144.0 (*C*-4'), 135.4 (*C*-1'), 129.8 (*C*-3',5'), 127.4 (*C*-2',6'), 124.5 (q, $J_{C\text{-}F}$ = 277.3 Hz, CH_2CF_3), 91.3 (*C*-2), 64.2 (q, $J_{C\text{-}F}$ = 34.0 Hz, OCH_2CF_3), 47.7 (*C*-5), 32.6 (*C*-3), 22.7 (*C*-4), 20.5 (Ar-CH_3); δ_F (376 MHz, $(CD_3)_2CO$) -74.81 (t, $J_{F\text{-}H}$ = 9.1 Hz); LC-MS (ESI) $[M\text{-}C_2F_3]^+$ 242.169; HRMS found $[M\text{-}C_2F_3]^+$ 242.0859, $C_{11}H_{16}NO_3S$ requires *M* 242.0851. The analytical data were consistent with the literature.[21]

[21] L.F.T. Novaes, J.S.K. Ho, K. Mao, K. Liu, M. Tanwar, M. Neurock, E. Villemure, J.A. Terrett, and S. Lin, *J. Am. Chem. Soc.*, 2022, **144**, 1187-1197

4-((4'-Methylphenyl)sulfonyl)-3-(2",2",2"-trifluoroethoxy)morpholine 373

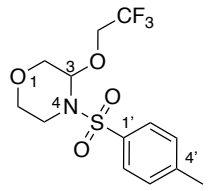

General procedure H was applied to 4-((4'-methylphenyl)sulfonyl)morpholine **336** (0.241 g, 1.0 mmol, 1.00 eq) and purification by reverse phase flash column chromatography (H_2O:MeCN 0-50%) afforded 4-((4'-methylphenyl)sulfonyl)-3-(2",2",2"-trifluoroethoxy)morpholine as a colourless oil (0.076 g, 0.22 mmol, 22%).

δ_H (600 MHz, $(CD_3)_2CO$) 7.82 – 7.77 (2H, m, 2',6'-*H*), 7.47 – 7.43 (2H, m, 3',5'-*H*), 5.23 (1H, s, 3-*H*), 4.14 – 4.05 (2H, m, CH_2CF_3), 3.96 (1H, d, J = 12.5 Hz, 2-*H*), 3.80 – 3.73 (1H, m, 6-*H*), 3.51 – 3.43 (1H, m, 5-*H*), 3.39 (1H, dd, J = 12.5, 2.1 Hz, 2-*H*), 3.31 (1H, td, J = 12.1, 3.2 Hz, 5-*H*), 3.24 (1H, td, J = 11.2, 2.5 Hz, 6-*H*), 2.44 (3H, s, Ar'-CH_3); δ_C (151 MHz, $(CD_3)_2CO$) 144.8 (*C*-4'), 138.1 (*C*-1'), 130.6 (*C*-3',5'), 128.1 (*C*-2',6'), 125.0 (q, $J_{C\text{-}F}$ = 277.5 Hz, CH_2CF_3), 82.5 (*C*-3), 68.5 (*C*-2), 65.8 (*C*-6), 65.0 (q, $J_{C\text{-}F}$ = 34.4 Hz, OCH_2CF_3), 41.3 (*C*-5), 21.3 (Ar'-CH_3); δ_F (376 MHz, $(CD_3)_2CO$) -74.70 (t, $J_{F\text{-}H}$ = 9.0 Hz); V_{max} (ATR) 1276, 1161, 1090, 934, 548 cm^{-1}; LC-MS (ESI) $[M\text{-}C_2H_2F_3O]^+$ 240.040; HRMS found $[M + H]^+$ 340.0844, $C_{13}H_{17}F_3NO_4S$ requires *M* 340.0830.

2-((4'-Methylphenyl)sulfonyl)-1-(2",2",2"-trifluoroethoxy)-1,2,3,4-tetrahydroisoquinoline 374

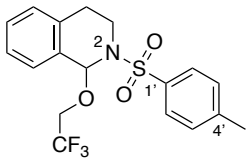

General procedure H was applied to 2-((4'-methylphenyl)sulfonyl)-1,2,3,4-tetrahydroisoquinoline **334** (0.287 g, 1.0 mmol, 1.00 eq) and purification by reverse phase flash column chromatography (H_2O:MeCN 0-50%) afforded 2-((4'-methylphenyl)sulfonyl)-1-(2",2",2"-trifluoroethoxy) -1,2,3,4-tetrahydroisoquinoline as a colourless oil (0.161 g, 0.42 mmol, 42%).

δ_H (600 MHz, $(CD_3)_2CO$) 7.73 – 7.68 (2H, m, 2',6'-*H*), 7.44 – 7.40 (1H, m, 8-*H*), 7.33 – 7.29 (2H, m, 3',5'-*H*), 7.26 – 7.22 (1H, m, 6-*H*), 7.26 – 7.22 (1H, m, 7-*H*), 7.08 – 7.03 (1H, m, 5-*H*), 6.25 (1H, s, 1-*H*), 4.32 – 4.18 (2H, m, CH_2CF_3), 3.84 (1H, dddd, J = 13.8, 6.0, 3.3, 1.0 Hz, 3-H_{eq}), 3.57 (1H, ddd, J = 13.8, 11.4, 4.5 Hz, 3-H_{ax}), 2.67 (1H, ddd, J = 16.6, 4.5, 3.3 Hz, 4-H_{eq}), 2.50 (1H, ddd, J = 16.6, 11.4, 6.0 Hz, 4-H_{ax}), 2.35 (3H, s, Ar'-CH_3); δ_C (151 MHz, $(CD_3)_2CO$) 143.9 (*C*-4'), 137.8 (*C*-1'), 134.1 (*C*-4a), 132.1 (*C*-8a), 129.7 (*C*-3',5'), 128.9 (*C*-7), 128.8 (*C*-8), 128.5 (*C*-5), 126.9 (*C*-2',6'), 126.4 (*C*-6), 124.48 (q, $J_{C\text{-}F}$ = 277.0 Hz, CH_2CF_3), 83.9 (*C*-1), 64.2 (q, $J_{C\text{-}F}$ = 34.1 Hz, OCH_2CF_3), 38.8 (*C*-3), 26.1 (*C*-4), 20.4 (Ar'-CH_3); δ_F (376 MHz, $(CD_3)_2CO$) -74.51 (t, $J_{F\text{-}H}$ = 9.1 Hz); V_{max} (ATR) 336, 1275, 1153, 762, 665, 585, 548 cm^{-1}; LC-MS (ESI) $[M\text{-}C_2H_2F_3O]^+$ 286.064; HRMS found $[M\text{-}C_2H_2F_3O]^+$ 286.0898, $C_{16}H_{16}NO_2S$ requires *M* 286.0902.

2-Methyl-1-((4'-methylphenyl)sulfonyl)-6-(2",2",2"-trifluoroethoxy)piperidine 388

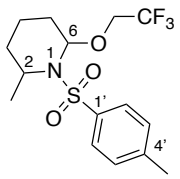

General procedure H was applied to 2-methyl-1-((4'-methylphenyl)sulfonyl)piperidine **332** (0.253 g, 1.0 mmol, 1.00 eq) and purification by silica gel flash column chromatography (Pet Ether 40-60:DCM 0-50%) afforded 2-methyl-1-((4'-methylphenyl)sulfonyl)-6-(2",2",2"-trifluoroethoxy)piperidine as a colourless oil (0.169 g, 0.48 mmol, 48%).

δ_H (700 MHz, $(CD_3)_2CO$) 7.78 (2H, d, J = 8.3 Hz, 2',6'-*H*), 7.45 (2H, d, J = 8.3 Hz, 3',5'-*H*), 5.47 (1H, dd, J = 4.1, 1.9 Hz, 6-*H*), 4.15 – 4.07 (2H, m, OCH_2CF$_3$), 4.03 – 3.96 (1H, m, 2-*H*), 2.45 (3H, s, Ar'-CH_3), 1.96 – 1.91 (1H, m, 5-*H*), 1.88 (1H, tt, J = 13.6, 3.5 Hz, 4-*H*), 1.50 – 1.43 (1H, m, 3-*H*), 1.43 – 1.35 (1H, m, 5-*H*), 1.37 (3H, d, J = 7.0 Hz, 2-CH_3), 1.36 – 1.30 (1H, m, 4-*H*), 1.26 – 1.19 (1H, m, 3-*H*); δ_C (176 MHz, $(CD_3)_2CO$) 143.5 (*C*-4'), 138.1 (*C*-1'), 129.8 (*C*-2',6'), 126.7 (*C*-3',5'), 124.6 (q, $J_{C\text{-}F}$ = 277.3 Hz, OCH$_2$*C*F$_3$), 83.7 (*C*-6), 63.9 (q, $J_{C\text{-}F}$ = 34.0 Hz, O*C*H$_2$CF$_3$), 48.3 (*C*-2), 29.7 (*C*-5), 28.5 (*C*-3), 20.5 (Ar'-*C*H$_3$), 20.0 (2-*C*H$_3$), 12.5 (*C*-4); δ_F (376 MHz, $(CD_3)_2CO$) -69.39 (t, $J_{F\text{-}H}$ = 9.2 Hz); V_{max} (ATR) 2946, 1146, 1101, 677 cm^{-1}; LC-MS (ESI) [M-$C_2H_2F_3O$]$^+$ 252.392; HRMS found [M-$C_2H_2F_3O$]$^+$ 252.1068, $C_{13}H_{18}NO_2S$ requires *M* 252.1058.

5-Methyl-1-((4'-methylphenyl)sulfonyl)-2-(2",2",2"-trifluoroethoxy)piperidine 394 and 3-methyl-1-((4'-methylphenyl)sulfonyl)-2-(2",2",2"-trifluoroethoxy)piperidine 395

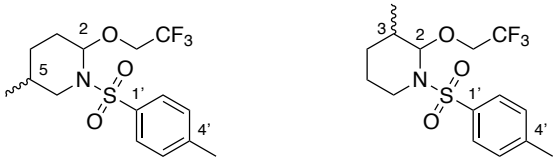

General procedure H was applied to 3-methyl-1-((4'-methylphenyl)sulfonyl)piperidine **333** (0.253 g, 1.0 mmol, 1.00 eq) and purification by silica gel flash column chromatography (Pet Ether 40-60:DCM 0-50%) afforded a mixture of diastereomers of 5-methyl-1-((4'-methylphenyl)sulfonyl)-2-(2",2",2"-trifluoroethoxy)piperidine and 3-methyl-1-((4'-methylphenyl)sulfonyl)-2-(2",2",2"-trifluoroethoxy) piperidine as a colourless oil (0.262 g, 0.75 mmol, 75%).

δ_H (400 MHz, $(CD_3)_2CO$) 7.82 – 7.76 (4H, m, Ar-*H*), 7.48 – 7.42 (4H, m, Ar-*H*), 5.46 (0.1H, t, J = 2.8 Hz, NC*H*(OR)CH$_2$), 5.40 (1H, t, J = 2.5 Hz, NC*H*(OR)CH$_2$), 5.21 (0.6H, d, J = 3.1 Hz, NC*H*(OR)CHR'), 5.13 (0.2H, d, J = 1.9 Hz, NC*H*(OR)CHR'), 4.10 – 3.95 (4H, m, OCH_2CF$_3$), 3.66 – 3.53 (2H, m, 6-*H*), 3.17 – 3.02 (1H, m, 6-*H*), 2.82 (1.5H, s, Ar'-CH_3), 2.77 – 2.67 (1H, m, CH_2), 2.45 (6H, s, Ar'-CH_3), 1.99 – 1.88 (2H, m, CH_2, 1.59 – 1.11 (9H, m, CH_2), 0.97 (2H, d, J = 6.6 Hz, 3-CH_3), 0.88 (0.5H, d, J = 7.2 Hz, 3-CH_3), 0.82 (3H, d, J = 6.4 Hz, 3-CH_3), 0.72 (0.5H, d, J = 7.1 Hz, 3-CH_3); δ_C (101 MHz, $(CD_3)_2CO$) 143.6 (Ar-*C*), 138.0 (Ar-*C*), 129.9 (Ar-*C*), 129.8 (Ar-*C*), 129.6 (Ar-*C*), 127.4 (Ar-*C*), 127.0 (Ar-*C*), 126.8 (Ar-*C*), 86.8 (N*C*H(OR)CH$_2$), 82.8 (N*C*H(OR)CH$_2$), 64.1 (N*C*H$_2$CH$_2$), 63.7 (N*C*H$_2$CH$_2$), 46.9 (*C*H$_2$), 39.8 (*C*H$_2$), 35.3(*C*H$_2$), 26.1 (*C*H$_2$), 25.8 (*C*H$_2$), 24.0 (*C*H$_2$), 20.5 (Ar'-*C*H$_3$), 18.2 (Ar'-*C*H$_3$), 16.9 (*C*H$_2$); δ_F (376 MHz, $(CD_3)_2CO$) -74.73 (t, $J_{F\text{-}H}$ = 9.1 Hz), -74.77 (t, $J_{F\text{-}H}$ = 9.1 Hz), -74.86 (t, $J_{F\text{-}H}$ = 9.1 Hz), -74.88 (t, $J_{F\text{-}H}$ = 9.0 Hz).

A small amount of one diastereomer of 3-methyl-1-((4'-methylphenyl)sulfonyl)-2-(2",2",2"-trifluoroethoxy)piperidine was isolated as a colourless oil (0.040 g, 0.11 mmol, 11%).

δ_H (700 MHz, $(CD_3)_2CO$) 7.80 (2H, d, J = 8.2 Hz, 2',6'-*H*), 7.45 (2H, d, J = 8.2 Hz, 3',5'-*H*), 5.21 (1H, d, J = 3.1 Hz, 2-*H*), 4.09 – 4.01 (2H, m, OCH_2CF$_3$), 3.64 – 3.58 (1H, m, 6-*H*), 3.11 (1H, td, J = 13.5, 2.9 Hz, 6-*H*), 2.45 (3H, s, Ar'-CH_3), 1.57 – 1.53 (1H, m, 5-*H*) 1.53 – 1.50 (1H, m, 3-*H*), 1.47 (1H, qd, J = 12.7, 3.5 Hz, 4-*H*), 1.43 – 1.38 (1H, m, 4-*H*), 1.18 (1H, qt, J = 13.1, 4.5 Hz, 5-*H*), 0.97 (3H, d, J = 6.6 Hz, 3-CH_3); δ_C (176 MHz, $(CD_3)_2CO$) 143.6 (*C*-4'), 138.4 (*C*-1'), 129.9 (*C*-3',5'), 126.8 (*C*-2',6'), 127.1 – 121.9 (q, $J_{C\text{-}F}$ = 278.1 Hz, OCH$_2$*C*F$_3$), 86.8 (*C*-2), 64.1 (q, $J_{C\text{-}F}$ = 34.1 Hz, O*C*H$_2$CF$_3$), 39.8 (*C*-6), 35.3 (*C*-3), 25.8 (*C*-4), 24.0 (*C*-5), 20.5 (Ar'-*C*H$_3$), 16.9 (3-*C*H$_3$); δ_F (376 MHz, $(CD_3)_2CO$) -74.73 (t, J = 9.0 Hz); V_{max} (ATR) 2940, 1277, 1150, 935, 660,581 cm-1; LC-MS (ESI) [M + H]$^+$ 352.343; HRMS found [M + H]$^+$ 352.1190, $C_{15}H_{21}F_3NO_3S$ requires *M* 352.1194.

7.5.4 Arylation Products

General Procedure I for the reaction of aryl boronic acids with *N,O*-acetals.

A solution of Et_2Zn (1.5 M in toluene) (7.20 eq) was added to the stated boronic acid (2.40 eq) in an oven-dried reaction vessel under nitrogen and the resulting mixture was heated at 60 °C overnight. Once this solution was cooled to -20 °C, the *N,O*-acetal (1.00 eq) in toluene (1.0 mL) was added under nitrogen. After 5 minutes, $BF_3{\cdot}OEt_2$ (1.00 eq) was added dropwise, and the reaction stirred at -20 °C for up to 3 hours. The reaction was quenched with aqueous sat. NH_4Cl, extracted with DCM, dried over $MgSO_4$, and concentrated under reduced pressure. The product was isolated by flash column chromatography with the stated solvent system.

General Procedure J for the reaction of arylboronic pinacol esters with *N,O*-acetals.

A solution of Et_2Zn (1.5 M in toluene) (2.40 eq) was added to the stated arylboronic pinacol ester (2.40 eq) in an oven-dried reaction vessel under nitrogen and the resulting mixture was heated at 60 °C overnight. Once this solution was cooled to -20 °C, the *N,O*-acetal (1.00 eq) in toluene (1.0 mL) was added under nitrogen. After 5 minutes, $BF_3{\cdot}OEt_2$ (1.00 eq) was added dropwise, and the reaction stirred at -20 °C for up to 3 hours. The reaction was quenched with aqueous sat. NH_4Cl, extracted with DCM, dried over $MgSO_4$, and concentrated under reduced pressure. The product was isolated by flash column chromatography with the stated solvent system.

2-(Phenyl)-1-((4'-methylphenyl)sulfonyl)piperidine 339

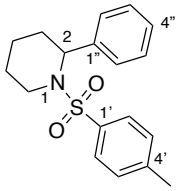

General procedure J was applied to 1-((4'-methylphenyl)sulfonyl)-2-(2",2",2"-trifluoroethoxy)piperidine **337** (0.100 g, 0.30 mmol, 1.00 eq) with phenylboronic acid pinacol ester (0.145 g, 0.71 mmol, 2.40 eq). Purification by reverse phase flash column chromatography (H_2O:MeCN 50-70%) afforded 2-(phenyl)-1-((4'-methylphenyl)sulfonyl)piperidine as a white solid (0.073 g, 0.23 mmol, 78%) with mp 130-132 °C.

δ_H (600 MHz, $CDCl_3$) 7.77 – 7.72 (2H, m, 2',6'-*H*), 7.35 – 7.30 (2H, m, 2",6"-*H*), 7.35 – 7.30 (2H, m, 3",5"-*H*), 7.29 – 7.27 (2H, m, 3',5'-*H*), 7.24 – 7.20 (1H, m, 4"-*H*), 5.28 – 5.23 (1H, m, 2-*H*), 3.86 – 3.79 (1H, m, 6-*H*), 3.00 (1H, ddd, J = 14.3, 12.9, 3.0 Hz, 6-*H*), 2.43 (3H, s, Ar'-CH_3), 2.24 – 2.17 (1H, m, 3-*H*), 1.69 – 1.60 (1H, m, 3-*H*), 1.51 – 1.46 (1H, m, 4-*H*), 1.45 – 1.34 (1H, m, 4-*H*), 1.41 – 1.37 (1H, m, 5-*H*), 1.28 (1H, qt, J = 12.9, 4.2 Hz, 5-*H*); δ_C (151 MHz, $CDCl_3$) 142.9 (*C*-4'), 138.9 (*C*-1"), 138.7 (*C*-1'), 129.7 (*C*-3',5'), 128.6 (*C*-3",5"), 127.0 (*C*-2',6'), 127.0 (*C*-2",6"), 126.8 (*C*-4"), 55.2 (*C*-2), 41.8 (*C*-6), 27.2 (*C*-3), 24.3 (*C*-5), 21.5 (Ar'-*C*H_3), 18.9 (*C*-4); V_{max} (ATR) 1151, 945, 723, 663, 563 cm^{-1}; LC-MS (ESI) $[M + H]^+$ 316.239; HRMS found $[M + H]^+$ 316.1375, $C_{18}H_{22}NO_2S$ requires *M* 316.1371.

Alternative method to produce 2-(phenyl)-1-((4'-methylphenyl)sulfonyl)piperidine 339

$ZnCl_2$ (0.74 mL, 0.74 mmol, 2.50 eq) in THF (1 M) was added slowly to a solution of PhLi (0.39 mL, 0.74 mmol, 2.50 eq) in Bu_2O (1.9 M) at -78 °C. This mixture was allowed to return to room temperature then stirred for 1 hour to generate a solution of ZnPhCl. This solution was then cooled to 0 °C and treated with $Si(CH_3)_3CH_2MgCl$ (1 M in Et_2O) (0.74 mL, 0.74 mmol, 2.50 eq). After 10 minutes, the reaction mixture was allowed to return to room temperature then stirred for 15 minutes to generate the desired $ZnPh(CH_2Si(CH_3)_3)$ **342**. Volatiles were removed under reduced pressure then the atmosphere was exchanged to nitrogen and the solid residue was taken up in dry toluene and cooled to -20 °C. A solution of 1-((4'-methylphenyl)sulfonyl)-2-(2",2",2"-trifluoroethoxy)piperidine **337** (0.100 g, 0.30 mmol, 1.00 eq) in toluene (1.0 mL) was added, followed by $BF_3{\cdot}OEt_2$ (0.04 mL, 0.30 mmol, 1.00 eq) and the reaction was stirred at -20 °C for 1 hour. The reaction was quenched and the product extracted following the usual procedure described in general procedure I. The product ratio of 2-(phenyl)-1-

((4'-methylphenyl)sulfonyl)piperidine to 1-((4'-methylphenyl)sulfonyl)-2-((trimethylsilyl)methyl) piperidine was 60:40, determined by ^{1}H NMR spectroscopy.

2-(4'-Methylphenyl)-1-((4"-methylphenyl)sulfonyl)piperidine 349

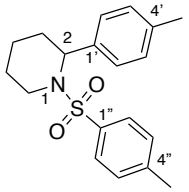

General procedure I was applied to 1-((4'-methylphenyl)sulfonyl)-2-(2",2",2"-trifluoroethoxy)piperidine **337** (0.100 g, 0.30 mmol, 1.00 eq) with (4-methylphenyl)boronic acid (0.097 g, 0.71 mmol, 2.40 eq). Purification by reverse phase flash column chromatography (H_2O:MeCN 50-70%) afforded 2-(4'-methylphenyl)-1-((4"-methylphenyl)sulfonyl)piperidine as a white solid (0.067 g, 0.21 mmol, 69%) with mp 87-89 °C.

δ_H (600 MHz, $CDCl_3$) 7.75 (2H, d, J = 8.3 Hz, 2",6"-*H*), 7.29 (2H, d, J = 8.3 Hz, 3",5"-*H*), 7.22 (2H, d, J = 7.9 Hz, 2',6'-*H*), 7.13 (2H, d, J = 7.9 Hz, 3',5'-*H*), 5.22 (1H, d, J = 4.9 Hz, 2-*H*), 3.84 – 3.80 (1H, m, 6-*H*), 3.00 (1H, ddd, J = 14.2, 12.7, 3.1 Hz, 6-*H*), 2.43 (3H, s, Ar"-CH_3), 2.33 (3H, s, Ar'-CH_3), 2.21 – 2.16 (1H, m, 3-*H*), 1.67 – 1.61 (1H, m, 3-*H*), 1.52 – 1.47 (1H, m, 4-*H*), 1.47 – 1.39 (1H, m, 4-*H*), 1.39 – 1.35 (1H, m, 5-*H*), 1.29 (1H, qt, J = 12.9, 4.4 Hz, 5-*H*); δ_C (151 MHz, $CDCl_3$) 142.9 (*C*-4"), 138.8 (*C*-1"), 136.4 (*C*-4'), 135.8 (*C*-1'), 129.6 (*C*-3",5"), 129.3 (*C*-3',5'), 127.0 (*C*-2",6"), 126.9 (*C*-2',6'), 55.1 (*C*-2), 41.8 (*C*-6), 27.2 (*C*-3), 24.3 (*C*-5), 21.5 (Ar"-*C*H_3), 20.9 (Ar'-*C*H_3), 18.9 (*C*-4); V_{max} (ATR) 1155, 903, 723, 656 cm^{-1}; LC-MS (ESI) [M + H]$^+$ 330.225; HRMS found [M + H]$^+$ 330.1512, $C_{19}H_{24}NO_2S$ requires *M* 330.1528.

2-(4'-Methoxyphenyl)-1-((4"-methylphenyl)sulfonyl)piperidine 350

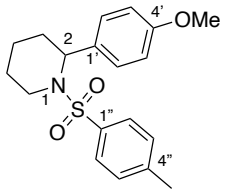

General procedure I was applied to 1-((4'-methylphenyl)sulfonyl)-2-(2",2",2"-trifluoroethoxy)piperidine **337** (0.100 g, 0.30 mmol, 1.00 eq) with (4-methoxyphenyl)boronic acid (0.108 g, 0.71 mmol, 2.40 eq). Purification by reverse phase flash column chromatography (H_2O:MeCN 0-100%) afforded 2-(4'-methoxyphenyl)-1-((4"-methylphenyl)sulfonyl)piperidine as a pale solid (0.076 g, 0.22 mmol, 74%) with mp 110-111 °C.

δ_H (600 MHz, $CDCl_3$) 7.76 – 7.71 (2H, m, 2",6"-*H*), 7.28 (2H, m, 3",5"-*H*), 7.26 – 7.21 (2H, m, 2',6'-*H*), 6.86 – 6.82 (2H, m, 3',5'-*H*), 5.21 – 5.17 (1H, m, 2-*H*), 3.83 – 3.77 (1H, m, 6-*H*), 3.78 (3H, s, OCH_3), 2.98 (1H, m, 6-*H*), 2.42 (3H, s, 4"-CH_3), 2.14 (1H, m, 3-*H*), 1.61 (1H, m, 3-*H*), 1.46 (1H, m, 4-*H*), 1.43 – 1.34 (1H, m, 4-*H*), 1.43 – 1.34 (1H, m, 5-*H*), 1.27 (1H, m, 5-*H*); δ_C (151 MHz, $CDCl_3$) 158.4 (*C*-4'), 142.9 (*C*-4"), 138.7 (*C*-1"), 130.7 (*C*-1'), 129.7 (*C*-3",5"), 128.2 (*C*-2',6'), 127.0 (*C*-2",6"), 113.9 (*C*-3',5'), 55.3 (OCH_3), 54.8 (*C*-2), 41.7 (*C*-6), 27.2 (*C*-3), 24.3 (*C*-5), 21.5 (4"-*C*H_3), 18.9 (*C*-4); V_{max} (ATR) 1320, 1148, 1102, 949, 734, 538 cm^{-1}; LC-MS (ESI) [M + H]$^+$ 346.263; HRMS found [M + H]$^+$ 346.1483, $C_{19}H_{24}NO_3S$ requires *M* 346.1477.

1-((4'-Methylphenyl)sulfonyl)-2-(prop-2"-en-1"-yl)piperidine 351

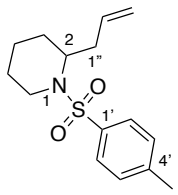

General procedure J was applied to 1-((4'-methylphenyl)sulfonyl)-2-(2",2",2"-trifluoroethoxy)piperidine **337** (0.200 g, 0.59 mmol, 1.00 eq) with allylboronic pinacol ester (0.239 g, 1.4 mmol, 2.40 eq). Purification by reverse phase flash column chromatography (MeCN:H_2O 50-70%) afforded 1-((4'-methylphenyl)sulfonyl)-2-(prop-2"-en-1"-yl)piperidine as a yellow oil (0.120 g, 0.43 mmol, 72%).

δ_H (700 MHz, $CDCl_3$) 7.73 (2H, d, J = 7.8 Hz, 2',6'-*H*), 7.29 (2H, d, J = 7.8 Hz, 3',5'-*H*), 5.73 – 5.70 (1H, m, $CH_2CH{=}CH_2$), 5.07 – 5.02 (2H, m, $CH_2CH{=}CH_2$), 4.12 (1H, q, J = 6.7 Hz, 2-*H*), 3.78 (1H, dd, J = 13.8, 4.2 Hz, 6-*H*), 2.99 (1H, td, J = 13.8, 2.6 Hz, 6-*H*), 2.44 (3H, s, Ar-CH_3), 2.37 – 2.27 (2H, m, $CH_2CH{=}CH_2$), 1.60 – 1.56 (1H, m, 3-*H*), 1.54 – 1.50 (2H, m, 4-*H*), 1.54 – 1.50 (1H, m, 5-*H*), 1.47 – 1.41 (1H, m, 3-*H*), 1.35 – 1.25 (1H, m, 5-*H*); δ_C (176 MHz, $CDCl_3$) 142.8 (C-4'), 138.8 (*C*-1'), 135.0 ($CH_2CH{=}CH_2$), 129.6 (*C*-3',5') 127.0 (*C*-2',6'), 117.2 ($CH_2CH{=}CH_2$), 52.4 (*C*-2), 34.0 ($CH_2CH{=}CH_2$), 26.6 (*C*-3), 21.5 (Ar-CH_3), 18.2 (*C*-4); V_{max} (ATR) 1333, 1149 (C=C), 923, 549 cm^{-1}; LC-MS (ESI) $[M + H]^+$ 280.211; HRMS found $[M + H]^+$ 280.1362, $C_{15}H_{22}NO_2S$ requires *M* 280.1371.

2-(4'-Chlorophenyl)-1-((4"-methylphenyl)sulfonyl)piperidine 352

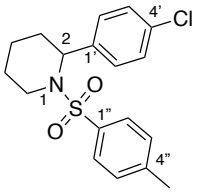

General procedure I was applied to 1-((4'-methylphenyl)sulfonyl)-2-(2",2",2"-trifluoroethoxy)piperidine **337** (0.100 g, 0.30 mmol, 1.00 eq) with (4-chlorophenyl)boronic acid (0.111 g, 0.71 mmol, 2.40 eq). Purification by reverse phase flash column chromatography (H_2O:MeCN 0-100%) afforded 2-(4'-chlorophenyl)-1-((4"-methylphenyl)sulfonyl)piperidine as a white solid (0.064 g, 0.18 mmol, 62%) with mp 93-95 °C.

δ_H (700 MHz, $CDCl_3$) 7.77 (2H, d, J = 7.4 Hz, 2",6"-*H*), 7.32 (2H, d, J = 7.4 Hz, 3",5"-*H*), 7.31 (2H, d, J = 7.0 Hz, 3',5'-*H*), 7.30 (2H, d, J = 7.0 Hz, 2',6'-*H*), 5.23 (1H, d, J = 4.3 Hz, 2-*H*), 3.85 (1H, d, J = 14.8 Hz, 6-*H*), 3.02 – 2.94 (1H, m, 6-*H*), 2.46 (3H, s, Ar"-CH_3), 2.21 – 2.14 (1H, m, 3-*H*), 1.69 – 1.63 (1H, m, 3-*H*), 1.54 – 1.50 (1H, m, 4-*H*), 1.45 – 1.40 (1H, m, 5-*H*), 1.40 – 1.35 (1H, m, 4-*H*), 1.33 – 1.27 (1H, m, 5-*H*); δ_C (176 MHz, $CDCl_3$) 143.1 (*C*-4"), 138.5 (*C*-1"), 137.6 (*C*-4'), 132.8 (*C*-1'), 129.8 (C-3",5"), 128.7 (*C*-3',5'), 128.5 (*C*-2',6'), 127.0 (*C*-2",6"), 54.9 (*C*-2) 41.9 (*C*-6), 27.3 (*C*-3), 24.2 (*C*-5), 21.6 (Ar-CH_3), 18.9 (*C*-4); V_{max} (ATR) 1153, 938, 712, 544 cm^{-1}; LC-MS (ESI) $[M(^{35}Cl)+H]^+$ 350.253, LC-MS (ESI) $[M(^{37}Cl)+H]^+$ 352.229; HRMS found $[M + H]^+$ 350.0987, $C_{18}H_{21}{}^{35}ClNO_2S$ requires *M* 350.0982.

(4-Methylphenyl)(2'-phenylpiperidin-1'-yl)methanone 348

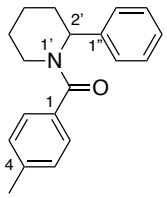

General procedure J was applied to (4-methylphenyl)(2'-(2",2",2"-trifluoroethoxy) piperidin-1'-yl)methanone **347** (0.100 g, 0.33 mmol, 1.00 eq) with phenylboronic pinacol ester (0.163 g, 0.80 mmol, 2.40 eq). Modified to react at room temperature after the addition of $BF_3.OEt_2$. Purification by silica gel flash column chromatography (EtOAc:Pet Ether 40-60 0-30%) afforded (4-methylphenyl) (2'-phenylpiperidin-1'-yl)methanone as a white solid (0.059 g, 0.21 mmol, 64%) with mp 110-111 °C.

δ_H (500 MHz, DMSO-*d6*)* 7.42 – 7.37 (2H, m, 2",6"-*H*), 7.33 – 7.29 (2H, m, 3",5"-*H*), 7.33 – 7.29 (2H, m, 2,6-*H*), 7.28 – 7.25 (1H, m, 4"-*H*), 7.25 – 7.22 (2H, m, 3,5-*H*), 5.49 (1H, br s, 2'-*H*), 3.90 (1H, br s, 6'-*H*), 2.89 – 2.81 (1H, m, 6'-*H*), 2.41 – 2.35 (1H, m, 3'-*H*), 2.33 (3H, s, Ar-CH_3), 1.94 – 1.86 (1H, m, 3'-*H*), 1.64 (1H, dt, J = 12.5, 3.7 Hz, 4'-*H*), 1.58 – 1.48 (2H, m, 5'-*H*), 1.45 – 1.39 (1H, m, 4-*H*); δ_C (126 MHz, DMSO-*d6*)* 170.8 (*C*=O), 139.9 (*C*-1), 139.3 (*C*-4), 134.3 (*C*-1"), 129.4 (*C*-3,5), 129.1 (*C*-2,6), 126.9 (*C*-4"), 126.8 (*C*-3",5"), 126.8 (*C*-2",6"), 53.8 (*C*-2'), 41.9 (*C*-6'), 28.2 (*C*-3'), 25.7 (*C*-5'), 21.2 (Ar-*C*H_3), 19.8 (*C*-4'); V_{max} (ATR) 1620 (C=O), 1414, 835, 751 cm^{-1}; LC-MS (ESI) $[M + H]^+$ 280.287; HRMS found $[M + H]^+$ 280.1714, $C_{19}H_{22}NO$ requires *M* 280.1701.
* VT NMR conducted at 80 °C

1-((4'-Methylphenyl)sulfonyl)-2-phenylpyrrolidine 384

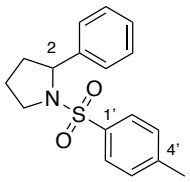

General procedure I was applied to 1-((4'-methylphenyl)sulfonyl)-2-(2",2",2"-trifluoroethoxy)pyrrolidine **371** (0.090 g, 0.28 mmol, 1.00 eq) with phenylboronic acid (0.081 g, 0.67 mmol, 2.40 eq). Purification by reverse phase flash column chromatography (H_2O:MeCN 0-60%) afforded 1-((4'-methylphenyl)sulfonyl) -2-phenylpyrrolidine as a white solid (0.050 g, 0.17 mmol, 60%) with mp 100-104 °C.

δ_H (700 MHz, $CDCl_3$) 7.69 – 7.65 (2H, m, 2',6'-*H*), 7.31 – 7.30 (2H, m, 2",6"-*H*), 7.30 – 7.29 (2H, m, 3",5"-*H*), 7.29 – 7.27 (2H, m, 3',5'-*H*), 7.24 – 7.21 (1H, m, 4"-*H*), 4.79 (1H, dd, J = 8.2, 3.8 Hz, 2-*H*), 3.65 – 3.58 (1H, m, 5-*H*), 3.47 – 3.39 (1H, m, 5-*H*), 2.43 (3H, s, Ar'-CH_3), 2.03 – 1.95 (1H, m, 3-*H*), 1.90 – 1.78 (1H, m, 3-*H*), 1.90 – 1.78 (1H, m, 4-*H*), 1.70 – 1.62 (1H, m, 4-*H*); δ_C (176 MHz, $CDCl_3$) 143.4 (*C*-4'), 143.2 (*C*-1"), 135.3 (*C*-1'), 129.7 (*C*-3',5'), 128.4 (*C*-3",5"), 127.6 (*C*-2',6'), 127.1 (*C*-4"), 126.3 (*C*-2",6"), 63.4 (*C*-2), 49.5 (*C*-5), 35.9 (*C*-3), 24.1 (*C*-4), 21.7 (Ar'-*C*H_3); V_{max} (ATR) 1332, 1156, 665, 586, 547 cm^{-1}; LC-MS (ESI) $[M + H]^+$ 302.216; HRMS found $[M + H]^+$ 302.1213, $C_{17}H_{19}NO_2S$ requires *M* 302.1215.

2-(4'-Chlorophenyl)-1-((4"-methylphenyl)sulfonyl)azepane 385

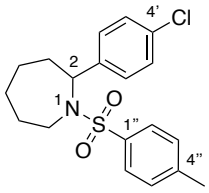

General procedure I was applied to 1-((4'-methylphenyl)sulfonyl)-2-(2",2",2"-trifluoroethoxy)azepane **370** (0.100 g, 0.30 mmol, 1.00 eq) with (4-chlorophenyl)boronic acid (0.101 g, 0.68 mmol, 2.40 eq). Purification by reverse phase flash column chromatography (H_2O:MeCN 0-65%) afforded 2-(4'-chlorophenyl)-1- ((4"-methylphenyl)sulfonyl)azepane as a white solid (0.054 g, 0.15 mmol, 52%) with mp 114-117 °C.

δ_H (700 MHz, $CDCl_3$) 7.34 (2H, d, J = 8.1 Hz, 2",6"-*H*), 7.09 (2H, d, J = 8.5 Hz, 3',5'-*H*), 7.05 (2H, d, J = 8.1 Hz, 3",5"-*H*), 6.94 (2H, d, J = 8.5 Hz, 2',6'-*H*), 4.99 (1H, dd, J = 11.7, 6.0 Hz, 2-*H*), 3.90 (1H, dt, J = 15.2, 3.6 Hz, 7-*H*), 3.25 – 3.13 (1H, m, 7-*H*), 2.34 (3H, s, Ar"-CH_3), 2.25 – 2.14 (1H, m, 3-*H*), 1.89 – 1.81 (1H, m, 4-*H*), 1.84 – 1.78 (1H, m, 5-*H*), 1.78 – 1.72 (2H, m, 6-*H*), 1.66 – 1.59 (1H, m, 3-*H*), 1.53 – 1.44 (1H, m, 4-*H*), 1.29 – 1.19 (1H, m, 5-*H*); δ_C (176 MHz, $CDCl_3$)142.7 (*C*-4"), 141.3 (*C*-1'), 138.0 (*C*-1"), 132.5 (*C*-4'), 129.1 (*C*-3",5"), 128.3 (*C*-3',5'), 127.5 (*C*-2',6'), 127.0 (*C*-2",6"), 61.0 (*C*-2), 45.3 (*C*-7), 37.5 (*C*-3), 30.7 (*C*-6), 29.4 (*C*-5), 25.7 (*C*-4), 21.4 (Ar"-*C*H_3); V_{max} (ATR) 1332, 1147, 1088, 811, 657, 577, 538, 522 cm^{-1}; LC-MS (ESI) $[M(^{35}Cl)+H]^+$ 364.200, LC-MS (ESI) $[M(^{37}Cl)+H]^+$ 366.215; HRMS found $[M + H]^+$ 364.1137, $C_{19}H_{23}{}^{35}ClNO_2S$ requires *M* 364.1138.

4-((4'-Methylphenyl)sulfonyl)-3-phenylmorpholine 386

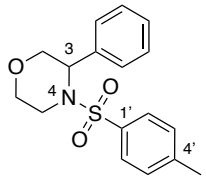

General procedure J was applied to 4-((4'-methylphenyl)sulfonyl)-3-(2",2",2"-trifluoroethoxy)morpholine **373** (0.056 g, 0.17 mmol, 1.00 eq) with phenylboronic pinacol ester (0.081 g, 0.40 mmol, 2.40 eq). Purification by reverse phase flash column chromatography (H_2O:MeCN 0-100%) afforded 4-((4'-methylphenyl)sulfonyl)-3-phenylmorpholine as a white solid (0.046 g, 0.15 mmol, 88%) with mp 131-132 °C.

δ_H (700 MHz, $CDCl_3$) 7.60 (2H, d, J = 8.3 Hz, 2',6'-*H*), 7.48 – 7.46 (2H, m, 2",6"-*H*), 7.32 – 7.27 (3H, m, 3",4",5"-*H*), 7.25 (2H, d, J = 8.3 Hz, 3',5'-*H*), 4.79 (1H, dd, J = 2.4, 3.7 Hz, 3-H_{eq}), 4.16 (1H, dd, J = 12.0, 2.4 Hz, 2-H_{eq}), 3.81 (1H, ddd, J = 11.5, 3.3, 2.4 Hz, 6-H_{eq}), 3.74 (1H, dd, J = 12.0, 3.7 Hz, 2-H_{ax}), 3.56 (1H, ddd, J = 11.5, 10.9, 2.5 Hz, 6-H_{ax}), 3.50 (1H, J = 13.9, 2.5, 2.4, 5-H_{eq}), 3.37 (1H, ddd, J = 13.9, 10.9, 3.3 Hz, 5-H_{ax}), 2.43 (3H, s, Ar'-CH_3); δ_C (176 MHz, $CDCl_3$) 143.4 (*C*-4'), 137.7 (*C*-1"), 136.9 (*C*-1'), 129.6 (*C*-3',5'), 128.4 (*C*-3",5"), 128.3 (*C*-2",6"), 127.7 (*C*-4"), 127.3 (*C*-2',6'), 69.4 (*C*-2), 66.2 (*C*-6), 56.1 (*C*-3), 42.1 (*C*-5), 21.5 (Ar'-*C*H_3); V_{max} (ATR) 1153, 1113, 944, 555 cm^{-1}; LC-MS (ESI) $[M + H]^+$ 318.444; HRMS found $[M + H]^+$ 318.1173, $C_{17}H_{20}NO_3S$ requires *M* 318.1164.

2-((4'-Methylphenyl)sulfonyl)-1-phenyl-1,2,3,4-tetrahydroisoquinoline 387

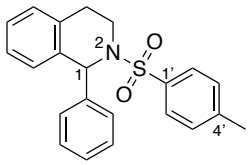

General procedure J was applied to 2-((4'-methylphenyl)sulfonyl)-1-(2",2",2"-trifluoroethoxy)-1,2,3,4-tetrahydroisoquinoline **374** (0.125 g, 0.32 mmol, 1.00 eq) with phenylboronic pinacol ester (0.159 g, 0.78 mmol, 2.40 eq). Modified to react at room temperature after the addition of $BF_3.OEt_2$. Purification by reverse phase flash column chromatography (H_2O:MeCN 0-50%) afforded 2-((4'-methylphenyl) sulfonyl)-1-phenyl-1,2,3,4-tetrahydroisoquinoline as a white solid (0.071 g, 0.20 mmol, 60%) with mp 160-163 °C.

δ_H (600 MHz, $CDCl_3$) 7.54 (2H, d, J = 8.2 Hz, 2',6'-*H*), 7.28 – 7.20 (1H, m, 4"-*H*), 7.28 – 7.20 (2H, m, 3",5"-*H*), 7.20 – 7.17 (2H, m, 2",6"-*H*), 7.15 – 7.10 (1H, m, 7-*H*), 7.15 – 7.10 (1H, m, 6-*H*), 7.08 (2H, d, J = 8.2 Hz, 3',5'-*H*), 7.01 – 6.96 (1H, m, 8-*H*), 7.01 – 6.96 (1H, m, 5-*H*), 6.23 (1H, s, 1-*H*), 3.76 (1H, dddd, J = 14.1, 6.6, 2.7, 1.1 Hz, 3-*H*), 3.31 (1H, ddd, J = 14.1, 11.2, 5.1 Hz, 3-*H*), 2.67 (1H, ddd, J = 16.7, 11.2, 6.6 Hz, 4-*H*), 2.57 (1H, ddd, J = 16.7, 5.1, 2.7 Hz, 4-*H*), 2.32 (3H, s, Ar'-CH_3); δ_C (151 MHz, $CDCl_3$) 143.0 (*C*-4'), 141.5 (*C*-1"), 137.7 (*C*-1'), 134.0 (*C*-8a), 133.8 (*C*-4a), 129.3 (*C*-3',5'), 128.9 (*C*-5), 128.7 (*C*-2",6"), 128.4 (*C*-8), 128.2 (*C*-3",5"), 127.6 (*C*-4"), 127.1 (*C*-7), 127.0 (*C*-2',6'), 126.1 (*C*-6), 59.2 (*C*-1), 39.1 (*C*-3), 26.7 (*C*-4), 21.4 (Ar'-*C*H_3); V_{max} (ATR) 1333, 1157, 666, 577, 547 cm^{-1}; LC-MS (ESI) $[M + H]^+$ 280.211; HRMS found $[M + H]^+$ 364.1372, $C_{22}H_{22}NO_2S$ requires M 364.1371.

2-(4'-Chlorophenyl)-6-methyl-1-((4"-methylphenyl)sulfonyl)piperidine 392

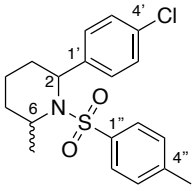

General procedure I was applied to 2-methyl-1-((4'-methylphenyl)sulfonyl)-6-(2",2",2"-trifluoroethoxy)piperidine **388** (0.100 g, 0.29 mmol, 1.00 eq) with (4-chlorophenyl)boronic acid (0.107 g, 0.68 mmol, 2.40 eq). Purification by reverse phase flash column chromatography (H_2O:MeCN 0-60%) afforded 2-(4'-chlorophenyl)-6-methyl-1-((4"-methylphenyl)sulfonyl)piperidine as a colourless oil (0.022 g, 0.06 mmol, 21%). The product was identified as two diastereomers by NMR analysis.

major isomer:

δ_H (600 MHz, $CDCl_3$) 7.77 (2H, d, J = 8.2 Hz, 2",6"-*H*), 7.50 (2H, d, J = 7.8 Hz, 2',6'-*H*), 7.32 (2H, d, J = 8.2 Hz, 3",5"-*H*), 7.30 (2H, d, J = 7.8 Hz, 3',5'-*H*), 5.22 (1H, d, J = 5.6 Hz, 2-*H*), 4.26 – 4.19 (1H, m, 6-*H*), 2.44 (3H, s, Ar"-CH_3), 2.30 – 2.24 (1H, m, 3-*H*), 1.76 – 1.59 (1H, m, 4-*H*), 1.44 – 1.32 (1H, m, 3-*H*), 1.44 – 1.32 (1H, m, 4-*H*), 1.32 – 1.22 (2H, m, 5-*H*), 0.83 (3H, d, J = 7.1 Hz, 6-CH_3); δ_C (151 MHz, $CDCl_3$) 143.0 (*C*-4"), 140.0 (*C*-1'), 138.5 (*C*-1"), 132.7 (*C*-4'), 129.8 (*C*-3",5") 128.7 (*C*-2',6'), 128.3 (*C*-3',5'), 126.8 (*C*-2",6"), 52.4 (*C*-2), 49.1 (*C*-6), 28.8 (*C*-5), 24.9 (*C*-3), 21.5 (Ar"-*C*H_3), 21.4 (6-*C*H_3), 14.1 (*C*-4).

minor isomer:

δ_H (600 MHz, $CDCl_3$) 7.40 (2H, d, J = 8.1 Hz, 2",6"-*H*), 7.13 (2H, d, J = 8.1 Hz, 3",5"-*H*), 7.09 (2H, d, J = 8.6 Hz, 2',6'-*H*), 7.06 (2H, d, J = 8.6 Hz, 3',5'-*H*), 4.97 (1H, dd, J = 7.0, 4.3 Hz, 2-*H*), 4.04 – 3.97 (1H, m, 6-*H*), 2.39 (3H, s, Ar"-CH_3), 2.11 – 2.04 (1H, m, 3-*H*, 1.94 – 1.86 (1H, m, 3-*H*), 1.75 – 1.68 (1H,

m, 4-*H*), 1.71 – 1.60 (2H, m, 5-*H*), 1.65 – 1.56 (1H, m, 4-*H*), 1.40 (3H, d, J = 7.0 Hz, 6-CH_3); δ_C (151 MHz, $CDCl_3$) 142.4 (*C*-4"), 140.6 (*C*-1"), 137.9 (*C*-1'), 132.8 (*C*-4'), 129.7 (*C*-2',6'), 129.1 (*C*-3",5"), 127.9 (*C*-3',5'), 126.9 (*C*-2",6"), 57.2 (*C*-2), 51.7 (*C*-6), 31.8 (*C*-5), 30.3 (*C*-3), 21.4 (Ar"-*C*H_3), 19.2 (*C*-4), 18.7 (6-*C*H_3).

V_{max} (ATR) 1493, 1329, 1164, 544 cm^{-1}; LC-MS (ESI) $[M + H]^+$ 364.276; HRMS found $[M + H]^+$ 364.1138, $C_{19}H_{23}{}^{35}ClNO_2S$ requires *M* 364.1138.

1-((4'-Methylphenyl)sulfonyl)-2-((trimethylsilyl)methyl)piperidine 345

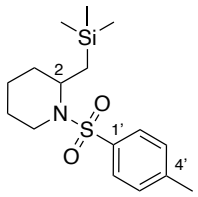

A preprepared solution of $Zn(CH_2Si(CH_3)_3)_2$ (1.4 mL, 0.71 mmol, 2.40 eq) in toluene (0.5 M) was added to a solution of 1-((4'-methylphenyl)sulfonyl)-2-(2",2",2"-trifluoroethoxy)piperidine **337** (0.100 g, 0.30 mmol, 1.00 eq) in toluene (0.3 M) under nitrogen at 0 °C. After 5 minutes, $BF_3{\cdot}OEt_2$ (1.00 eq) was added and the reaction stirred at 0 °C for 2 hours. The reaction was quenched with sat. NH_4Cl (20 mL), then extracted with DCM (3 x 25 mL) and washed with brine (20 mL). Purification by silica gel flash column chromatography (Pet Ether 40-60:EtOAc 0-10%) afforded 1-((4'-methylphenyl)sulfonyl) -2-((trimethylsilyl)methyl)piperidine as a white solid (0.077 g, 0.24 mmol, 79%) with mp 103-104 °C.

δ_H (600 MHz, $CDCl_3$) 7.69 (2H, d, J = 8.2 Hz, 2',6'-*H*), 7.27 (2H, d, J = 8.2 Hz, 3',5'-*H*), 4.29 – 4.23 (1H, m, 2-*H*), 3.72 – 3.65 (1H, m, 6-*H*), 3.00 (1H, td, J = 13.3, 2.7 Hz, 6-*H*), 2.41 (3H, s, Ar'-CH_3), 1.57 – 1.52 (1H, m, 3-*H*), 1.57 – 1.52 (1H, m, 4-*H*), 1.52 – 1.47 (1H, m, 5-*H*), 1.50 – 1.44 (1H, m, 4-*H*), 1.42 – 1.35 (1H, m, 3-*H*), 1.35 – 1.23 (1H, m, 5-*H*), 1.05 (1H, dd, J = 14.5, 10.7 Hz, CH_2Si$(CH_3)_3$), 0.62 (1H, dd, J = 14.5, 4.4 Hz, CH_2Si$(CH_3)_3$), 0.01 (9H, s, Si(CH_3)$_3$); δ_C (151 MHz, $CDCl_3$) 142.9 (*C*-2'), 138.9 (*C*-1'), 129.7 (*C*-3',5'), 127.2 (*C*-2',6'), 50.7 (*C*-2), 40.1 (*C*-6), 30.0 (*C*-3), 25.0 (*C*-5), 21.6 (Ar'-*C*H_3), 18.1 (*C*-4), 17.8 (*C*H_2Si$(CH_3)_3$), -0.97 (Si(*C*H_3)$_3$); V_{max} (ATR) 2945, 1152, 906, 729 cm^{-1}; LC-MS (ESI) $[M + H]^+$ 326.652; HRMS found $[M + H]^+$ 326.1607, $C_{16}H_{28}NO_2SSi$ requires *M* 326.1610.

7.5.5 Ethyl Products

General Procedure K for the reaction of diethyl zinc with *N,O*-acetals.

A solution of Et_2Zn (1.5 M in toluene) (3.00 eq) was added to a cooled solution of the *N,O*-acetal (1.00 eq) in MeCN (0.1 M) at -20 °C under nitrogen. After 5 minutes, $BF_3{\cdot}OEt_2$ (1.00 eq) was added dropwise, and the reaction stirred at -20 °C for up to 3 hours. The reaction was quenched with sat. NH_4Cl, extracted with DCM, dried over $MgSO_4$, and concentrated under reduced pressure. The product was isolated by flash column chromatography with the stated solvent system.

2-Ethyl-1-((4'-methylphenyl)sulfonyl)piperidine 338

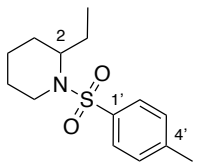

General procedure K was applied to 1-(4'-methylphenyl)sulfonyl)-2-(2",2",2"-trifluoroethoxy)piperidine **337** (0.050 g, 0.15 mmol, 1.00 eq). Purification by reverse phase flash column chromatography (H_2O:MeCN 40-80%) afforded 2-ethyl-1-((4'-methylphenyl)sulfonyl)piperidine as a colourless oil (0.036 g, 0.14 mmol, 92%).

δ_H (700 MHz, $CDCl_3$) 7.65 (2H, d, J = 8.0 Hz, 2',6'-*H*), 7.20 (2H, d, J = 8.0 Hz, 3',5'-*H*), 3.86 (1H, q, J = 7.0 Hz, 2-*H*), 3.68 (1H, J = 14.0, 4.2, 6-*H*), 2.90 (1H, d, J = 14.0, 2.8 Hz, 6-*H*), 2.35 (3H, s, Ar'-CH_3), 1.59 – 1.53 (1H, m, CH_2CH$_3$), 1.46 – 1.38 (1H, m, 3-*H*), 1.43 (1H, s, CH_2CH$_3$), 1.42 – 1.39 (2H, m, 4-*H*), 1.40 – 1.35 (1H, m, 5-*H*), 1.36 – 1.30 (1H, m, 3-*H*), 1.18 – 1.11 (1H, m, 5-*H*), 0.80 (3H, t, J = 7.4 Hz, CH$_2$CH_3); δ_C (176 MHz, $CDCl_3$) 142.7 (*C*-4'), 139.1 (*C*-1'), 129.6 (*C*-3',5'), 127.0 (*C*-2',6'), 54.5 (*C*-2), 40.6 (*C*-6), 27.0 (*C*-3), 24.5 (*C*-5), 22.4 (*C*H$_2$CH$_3$), 21.5 (Ar'-*C*H$_3$), 18.4 (*C*-4), 11.0 (CH$_2$*C*H$_3$); LC-MS (ESI) [M + H]$^+$ 268.240; HRMS found [M + H]$^+$ 268.1374, $C_{14}H_{22}NO_2S$ requires *M* 268.1371. The analytical data were consistent with the literature.[22]

2-Ethyl-1-((4'-methylphenyl)sulfonyl)pyrrolidine 411

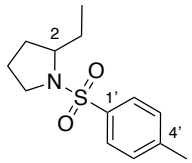

Collected as a side product from the reaction of 1-(4'-methylphenyl)sulfonyl)-2-(2",2",2"-trifluoroethoxy) pyrrolidine **371** (0.090 g, 0.28 mmol, 1.00 eq) with phenylboronic acid (0.081 g, 0.67 mmol, 2.40 eq). Purification by reverse phase flash column chromatography (H_2O:MeCN 40-80%) afforded 2-ethyl-1-((4'-methylphenyl)sulfonyl)pyrrolidine as a white solid (0.007 g, 0.026 mmol, 9%) with mp 69-71 °C.

δ_H (700 MHz, $CDCl_3$) 7.72 (2H, d, J = 8.2 Hz, 3',5'-*H*), 7.30 (1H, d, J = 8.2 Hz, 2',6'-*H*), 3.57 – 3.49 (1H, m, 2-*H*), 3.39 – 3.35 (1H, m, 5-*H*), 3.21 – 3.17 (1H, m, 5-*H*), 2.42 (3H, s, Ar'-CH_3), 1.90 – 1.81 (1H, m, CH_2CH$_3$), 1.78 – 1.74 (1H, m, 4-*H*), 1.59 – 1.55 (2H, m, 3-*H*), 1.53 – 1.44 (1H, m, CH_2CH$_3$), 1.53 – 1.44 (1H, m, 4-*H*) , 0.91 (3H, t, J = 7.4 Hz, CH$_2$CH_3); δ_C (176 MHz, $CDCl_3$) 143.3 (*C*-4'), 135.2 (*C*-1'), 129.7 (*C*-3',5'), 127.6 (*C*-2',6'), 62.0 (*C*-2), 49.1 (*C*-5), 30.3 (*C*-3), 29.3 (*C*H$_2$CH$_3$), 24.3 (*C*-4), 21.7 (Ar'-*C*H$_3$), 10.5 (CH$_2$*C*H$_3$); V_{max} (ATR) 1334, 1154, 586, 549 cm^{-1}; LC-MS (ESI) [M + H]$^+$ 254.216; HRMS found [M + H]$^+$ 254.1224, $C_{13}H_{20}NO_2S$ requires *M* 254.1215.

2-Ethyl-6-methyl-1-((4'-methylphenyl)sulfonyl)piperidine 391

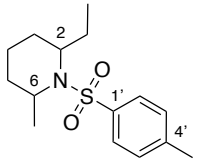

General procedure K was applied to 2-methyl-1-((4'-methylphenyl)sulfonyl)-6-(2",2",2"-trifluoroethoxy) piperidine **388** (0.100 g, 0.29 mmol, 1.00 eq). Purification by reverse phase flash column chromatography (H_2O:MeCN 40-80%) afforded 2-ethyl-6-methyl-1-((4'-methylphenyl)sulfonyl)piperidine as a white solid (0.074 g, 0.26 mmol, 92%) with mp 77-82 °C.

δ_H (600 MHz, $CDCl_3$) 7.73 – 7.67 (2H, m, 2',6'-*H*), 7.30 – 7.22 (2H, m, 3',5'-*H*), 4.15 – 4.07 (1H, m, 6-*H*), 3.90 (1H, q, J = 7.0 Hz, 2-*H*), 2.41 (3H, s, Ar'-CH_3), 1.82 – 1.72 (1H, m, CH_2CH$_3$), 1.67 – 1.60 (1H, m, 4-*H*), 1.59 – 1.58 (1H, m, CH_2CH$_3$), 1.55 – 1.50 (1H, m, 3-*H*), 1.41 – 1.32 (1H, m, 5-*H*), 1.30 (3H, d, J = 7.1 Hz, 6-CH_3), 1.30 – 1.25 (1H, m, 4-*H*), 1.29 – 1.21 (1H, m, 3-*H*), 1.28 – 1.20 (1H, m, 5-*H*), 0.97 (3H, t, J = 7.4 Hz, CH$_2$CH_3); δ_C (151 MHz, $CDCl_3$) 142.5 (*C*-4'), 139.1 (*C*-1'), 129.5 (*C*-3',5'), 126.7 (*C*-2',6'), 54.2 (*C*-2), 48.0 (*C*-6), 29.3 (*C*-5), 28.3 (*C*H$_2$CH$_3$), 26.9 (*C*-3), 21.8 (6-*C*H$_3$), 21.5 (Ar'-*C*H$_3$), 13.7 (*C*-4), 11.9 (CH$_2$*C*H$_3$); V_{max} (ATR) 1330, 1165, 659, 603 cm^{-1}; LC-MS (ESI) [M + H]$^+$ 282.378; HRMS found [M + H]$^+$ 282.1530, $C_{15}H_{24}NO_2S$ requires *M* 282.1528.

[22]R.C.F. Jones, I. Turner, K.J. Howard, *Tetrahedron Letters*, 1993, **34**(39), 6329-6332

2-Ethyl-1-((4'-methylphenyl)sulfonyl)azepane 412

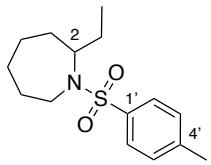

Collected as a side product from the reaction of 1-(4'-methylphenyl)sulfonyl)-2-(2",2",2"-trifluoroethoxy) azepane **370** (0.070 g, 0.20 mmol, 1.00 eq) with 4-chlorophenylboronic acid (0.075 g, 0.48 mmol, 2.40 eq). Purification by reverse phase flash column chromatography (H_2O:MeCN 30-70%) afforded 2-ethyl-1-((4'-methylphenyl)sulfonyl)azepane as a colourless oil (0.014 g, 0.050 mmol, 25%).

δ_H (600 MHz, $CDCl_3$) 7.71 (2H, d, J = 8.3 Hz, 2',6'-*H*), 7.25 (2H, d, J = 8.3 Hz, 3',5'-*H*), 3.82 – 3.78 (1H, m, 2-*H*), 3.75 (1H, dt, J = 15.1, 3.7 Hz, 7-*H*), 2.89 (1H, ddd, J = 15.1, 11.4, 2.5 Hz, 7-*H*), 2.40 (3H, s, Ar'-CH_3), 2.09 – 2.01 (1H, m, 3-*H*), 1.75 – 1.65 (1H, m, 5-*H*), 1.64 – 1.58 (1H, m, 4-*H*), 1.64 – 1.58 (1H, m, 6-*H*), 1.57 – 1.51 (1H, m, 6-*H*), 1.50 – 1.41 (1H, m, CH_2CH$_3$), 1.40 – 1.30 (1H, m, CH_2CH$_3$), 1.25 – 1.19 (1H, m, 3-*H*) 1.24 – 1.19 (1H, m, 4-*H*), 1.23 – 1.18 (1H, m, 5-*H*), 0.75 (3H, t, J = 7.5 Hz, CH$_2$CH_3); δ_C (151 MHz, $CDCl_3$) 142.6 (*C*-4'), 139.3 (*C*-1'), 129.4 (*C*-3',5'), 127.1 (*C*-2',6'), 58.3 (*C*-2), 43.3 (*C*-7), 33.9 (*C*-3), 29.4 (*C*-5), 29.1 (*C*-6), 27.6 (*C*H$_2$CH$_3$), 24.1 (*C*-4), 21.5 (Ar'-*C*H$_3$), 10.5 (CH$_2$*C*H$_3$); V_{max} (ATR) 1330, 1150, 573, 550 cm^{-1}; LC-MS (ESI) [M + H]$^+$ 282.226; HRMS found [M + H]$^+$ 282.1534, $C_{15}H_{24}NO_2S$ requires *M* 282.158.

1-Ethyl-2-((4'-methylphenyl)sulfonyl)-1,2,3,4-tetrahydroisoquinoline 413

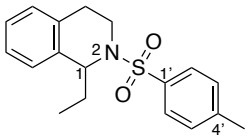

Collected as a side product from the reaction of 2-((4'-methylphenyl)sulfonyl)-1-(2",2",2"-trifluoroethoxy)-1,2,3,4-tetrahydroisoquinoline **374** (0.125 g, 0.32 mmol, 1.00 eq) with phenylboronic acid pinacol ester (0.159 g, 0.78 mmol, 2.40 eq). Purification by reverse phase flash column chromatography (H_2O:MeCN 0-50%) afforded 1-ethyl-2-((4'-methylphenyl)sulfonyl)-1,2,3,4-tetrahydroisoquinoline as a pale yellow solid (0.024 g, 0.077 mmol, 24%) with mp 77-78 °C.

δ_H (600 MHz, $CDCl_3$) 7.61 – 7.56 (2H, m, 2',6'-*H*), 7.14 – 7.11 (1H, m, 7-*H*), 7.11 – 7.08 (2H, m, 3',5'-*H*), 7.08 – 7.05 (1H, m, 6-*H*), 7.05 – 7.02 (1H, m, 8-*H*), 6.87 (1H, d, J = 7.5 Hz, 5-*H*), 4.87 (1H, dd, J = 8.4, 6.4 Hz, 1-*H*), 3.85 – 3.78 (1H, m, 3-*H*), 3.45 (1H, ddd, J = 14.1, 9.2, 6.4 Hz, 3-*H*), 2.55 – 2.46 (2H, m, 4-*H*), 2.31 (3H, s, Ar'-CH_3), 1.86 – 1.75 (2H, m, CH_2CH$_3$), 1.02 (3H, t, J = 7.4 Hz, CH$_2$CH_3); δ_C (151 MHz, $CDCl_3$) 142.9 (*C*-4'), 137.9 (*C*-1'), 136.8 (*C*-8a), 132.7 (*C*-4a), 129.3 (*C*-3',5'), 128.8 (*C*-5), 127.0 (*C*-2',6'), 127.0 (*C*-8), 126.5 (*C*-6), 126.0 (*C*-7), 58.1 (*C*-1), 38.8 (*C*-3), 30.7 (*C*H$_2$CH$_3$), 26.3 (*C*-4), 21.4 (Ar'-*C*H$_3$), 11.2 (CH$_2$*C*H$_3$); V_{max} (ATR) 1334, 1162, 661, 549 cm^{-1}; LC-MS (ESI) [M + H]$^+$ 316.163; HRMS found [M + H]$^+$ 316.1381, $C_{18}H_{22}NO_2S$ requires *M* 316.1371.

2-Ethyl-5-methyl-1-((4'-methylphenyl)sulfonyl)piperidine 398 and **2-ethyl-3-methyl-1-((4'-methylphenyl)sulfonyl)piperidine 399**

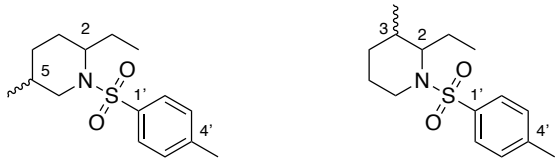

General procedure K was applied to a mixture of 5-methyl-1-((4'-methylphenyl)sulfonyl)

-2-(2",2",2"-trifluoroethoxy)piperidine **394** and 3-methyl-1-((4'-methylphenyl)sulfonyl)-2-(2",2",2"-trifluoroethoxy)piperidine **395** (0.100 g, 0.29 mmol, 1.00 eq). Purification by silica gel flash column chromatography (Pet Ether 40-60:DCM 30-70%) afforded a mixture of diastereomers of 2-ethyl-3-methyl-1-((4'-methylphenyl)sulfonyl)piperidine and 2-ethyl-5-methyl-1-((4'-methylphenyl) sulfonyl)piperidine as a colourless oil (0.070 g, 0.25 mmol, 87%).

δ_H (700 MHz, $CDCl_3$) 7.76 – 7.68 (8H, m, Ar'-*H*), 7.30 – 7.25 (8H, m Ar'-*H*), 3.94 – 3.89 (4H, m, NC*H*(R)CH_2), 3.87 – 3.83 (3H, m, NC*H*(R)CH_2), 3.84 – 3.82 (2H, m, NC*H*(R)CH_2), 3.77 – 3.72 (1H, m, NC$H_2$$CH_2$), 3.72 – 3.67 (4H, m, NC$H_2$$CH_2$), 3.67 – 3.61 (2H, m, NC*H*(R)CH_2), 3.64 – 3.62 (2H, m, NC$H_2$$CH_2$), 3.38 – 3.34 (1H, m, NC$H_2$$CH_2$), 3.18 (1H, dd, J = 13.1, 3.4 Hz, NC*H*(R)CH_2), 2.91 – 2.86 (2H, m, NC$H_2$$CH_2$), 2.89 – 2.84 (2H, m, NC$H_2$$CH_2$), 2.55 (4H, dd, J = 13.9, 11.8 Hz, NC$H_2$$CH_2$), 2.44 (1H, s, Ar'-C$H_3$), 2.43 (7H, s, Ar'-C$H_3$), 2.42 (4H, s, Ar'-C$H_3$), 1.88 – 1.10 (32H, m, C$H_2$$CH_2$), 1.00 (2H, d, J = 7.0 Hz, 3-CH_3), 0.90 – 0.84 (12H, m, CH_2R), 0.83 – 0.77 (9H, m, CH_2R); δ_C (176 MHz, $CDCl_3$) 142.8 (Ar'-*C*), 142.7 (Ar'-*C*), 142.7 (Ar'-*C*), 142.7 (Ar'-*C*), 139.5 (Ar'-*C*), 139.1 (Ar'-*C*), 139.0 (Ar'-*C*), 138.8 (Ar'-*C*), 129.7 (Ar'-*C*), 129.6 (Ar'-*C*), 129.5 (Ar'-*C*), 129.5 (Ar'-*C*), 127.1 (Ar'-*C*), 127.1 (Ar'-*C*), 127.1 (Ar'-*C*), 127.0 (Ar'-*C*), 60.5 (N*C*H(R)CH_2), 59.5 (N*C*H(R)CH_2), 55.1 (N*C*H(R)CH_2), 53.9 (N*C*H(R)CH_2), 47.2(N$CH_2$$CH_2$), 46.1 (N$CH_2$$CH_2$), 39.8(N$CH_2$$CH_2$), 40.6 (N$CH_2$$CH_2$), 33.6 (*C*H($CH_3$)), 30.2 (*C*H($CH_3$)), 29.3 (*C*H($CH_3$)), 27.5 (*C*H($CH_3$)), 27.4 ($CH_2$*C*$H_2$), 27.2 ($CH_2$*C*$H_2$), 27.1 ($CH_2$*C*$H_2$), 24.8 ($CH_2$*C*$H_2$), 24.5 ($CH_2$*C*$H_2$), 22.4 ($CH_2$*C*$H_2$), 21.6 (Ar'-*C*$H_3$), 21.6 (Ar'-*C*$H_3$), 21.6 (Ar'-*C*$H_3$), 21.6 (Ar'-*C*$H_3$), 19.7 ($CH_2$*C*$H_2$), 19.2 ($CH_2$*C*$H_3$), 19.0 ($CH_2$*C*$H_3$), 18.4 ($CH_2$*C*$H_3$), 17.0 ($CH_2$*C*$H_3$), 16.6 ($CH_2$*C*$H_2$), 11.5 (R-*C*$H_3$), 11.2 (R-*C*$H_3$), 11.1 (R-*C*$H_3$), 11.0 (R-*C*$H_3$); LC-MS (ESI) $[M + H]^+$ 282.226; HRMS found $[M + H]^+$ 282.1537, $C_{15}H_{24}NO_2S$ requires *M* 282.1528.

7.5.6 Elimination Products

1-((4'-Methylphenyl)sulfonyl)-1,2,3,4-tetrahydropyridine 369

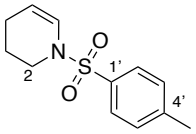

Collected as a side product from the reaction of 1-((4'-methylphenyl)sulfonyl)-2-(2",2",2"-trifluoroethoxy)-piperidine **337** (0.150 g, 0.45 mmol, 1.00 eq) with (4-(dimethylamino)phenyl)boronic acid (0.176 g, 1.1 mmol, 2.40 eq). Purification by reverse phase flash column chromatography (H_2O:MeCN 0-60%) afforded 1-((4'-methylphenyl)sulfonyl)-1,2,3,4-tetrahydropyridine as a white solid (0.060 g, 0.26 mmol, 57%) with mp 54-55 °C.

δ_H (400 MHz, $CDCl_3$) 7.72 – 7.64 (2H, m, 2',6'-*H*), 7.36 – 7.26 (2H, m, 3',5'-*H*), 6.65 (1H, dt, J = 8.2, 2.0 Hz, 6-*H*), 4.99 (1H, dt, J = 8.2, 3.9 Hz, 5-*H*), 3.42 – 3.35 (2H, m, 2-*H*), 2.44 (3H, s, Ar'-CH_3), 1.94 – 1.90 (2H, m, 3-*H*), 1.72 – 1.62 (2H, m, 4-*H*); δ_C (101 MHz, $CDCl_3$) 143.7 (*C*-4'), 135.3 (*C*-1'), 129.8 (*C*-3',5'), 127.2 (*C*-2',6'), 125.2 (*C*-6), 108.4 (*C*-5), 44.0 (*C*-2), 21.7 (*C*-3), 21.1 (*C*-4), 21.1 (Ar'-*C*H_3); LC-MS (ESI) $[M + H]^+$ 238.354; HRMS found $[M + H]^+$ 238.0905, $C_{12}H_{16}NO_2S$ requires *M* 238.0902. The analytical data were consistent with the literature.[23]

2-Methyl-1-((4'-methylphenyl)sulfonyl)-1,2,3,4-tetrahydropyridine 393

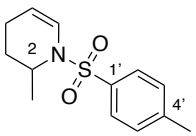

[23] G. Zanella, M. Petrović, D. Scarpi, E.G. Occhiato, E. Gómez-Bengoa, *Beilstein J. Org. Chem.*, 2020, **16**, 3059–3068

Collected as a side product from the reaction of 2-methyl-1-((4-methylphenyl)sulfonyl)-6-(2,2,2-trifluoroethoxy)piperidine **388** (0.100 g, 0.29 mmol, 1.00 eq) with (4-chlorophenyl)boronic acid (0.107 g, 0.68 mmol, 2.40 eq). Purification by reverse phase flash column chromatography (H_2O:MeCN 0-60%) afforded 2-methyl-1-((4'-methylphenyl)sulfonyl)-1,2,3,4-tetrahydropyridine as a colourless oil (0.026 g, 0.10 mmol, 36%).

δ_H (600 MHz, $CDCl_3$) 7.67 (2H, d, J = 7.9 Hz, 2',6'-*H*), 7.28 (2H, d, J = 7.9 Hz, 3',5'-*H*), 6.64 – 6.59 (1H, m, 6-*H*), 5.01 – 4.96 (1H, m, 5-*H*), 4.12 – 4.07 (1H, m, 2-*H*), 2.41 (3H, s, Ar'-CH_3), 2.04 – 1.94 (1H, m, 4-*H*), 1.87 – 1.79 (1H, m, 4-*H*), 1.47 – 1.40 (1H, m, 3-*H*), 1.16 (3H, d, J = 6.7 Hz, 2-CH_3), 1.13 – 1.04 (1H, m, 3-*H*); δ_C (151 MHz, $CDCl_3$) 143.2 (*C*-4'), 136.4 (*C*-1'), 129.6 (*C*-3',5'), 126.8 (*C*-2',6'), 123.3 (*C*-6), 107.6 (*C*-5), 48.5 (*C*-2), 25.2 (*C*-3), 21.5 (Ar'-*C*H_3), 18.2 (2-*C*H_3), 16.9 (*C*-4); V_{max} (ATR) 1340, 1168, 683, 549 cm^{-1}; LC-MS (ESI) $[M + H]^+$ 252.050; HRMS found $[M + H]^+$ 252.1064, $C_{13}H_{18}NO_2S$ requires M 252.1058.

3-Methyl-1-((4'-methylphenyl)sulfonyl)-1,2,3,4-tetrahydropyridine 396

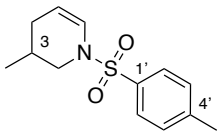

Collected as a side product from the reaction of 3-methyl-1-((4-methylphenyl)sulfonyl)-2-(2,2,2-trifluoroethoxy)piperidine **395** (0.100 g, 0.29 mmol, 1.00 eq) with Et_2Zn (1.5 M in toluene) (0.57 mL, 0.85 mmol, 3.00 eq). Purification by reverse phase flash column chromatography (H_2O:MeCN 0-60%) afforded 3-methyl-1-((4'-methylphenyl)sulfonyl)-1,2,3,4-tetrahydropyridine as a colourless oil (0.0021 g, 8.3 mmol, 2.9%).

δ_H (700 MHz, $CDCl_3$) 7.69 – 7.67 (2H, m, 2',6'-*H*), 7.34 – 7.31 (2H, m, 3',5'-*H*), 6.67 – 6.63 (1H, m, 6-*H*), 4.95 (1H, ddd, J = 8.1, 5.0, 2.7 Hz, 5-*H*), 3.65 – 3.59 (1H, m, 2-*H*), 2.66 (1H, dd, J = 11.7, 10.0 Hz, 2-*H*), 2.45 (3H, s, Ar-CH_3), 2.06 – 1.97 (1H, m, 4-*H*), 1.83 – 1.74 (1H, m, 3-*H*), 1.60 – 1.53 (1H, m, 4-*H*), 0.93 (3H, d, J = 6.7 Hz, 3-CH_3); δ_C (176 MHz, $CDCl_3$) 143.5 (*C*-4'), 135.2 (*C*-1'), 129.7 (*C*-3',5'), 127.0 (*C*-2',6'), 124.6 (*C*-6), 107.3 (*C*-5), 49.8 (*C*-2), 29.4 (*C*-4), 26.5 (*C*-3), 21.6 (Ar'-*C*H_3), 18.7 (3-*C*H_3); V_{max} (ATR) 2925, 1342, 1165, 682, 548 cm^{-1}; LC-MS (ESI) $[M + H]^+$ 252.012; HRMS found $[M + H]^+$ 252.1063, $C_{13}H_{18}NO_2S$ requires M 252.1058.

Appendix A

NMR Spectra

^{1}H NMR (400 MHz, $CDCl_3$) and ^{13}C NMR (101 MHz, $CDCl_3$) of compound **116**

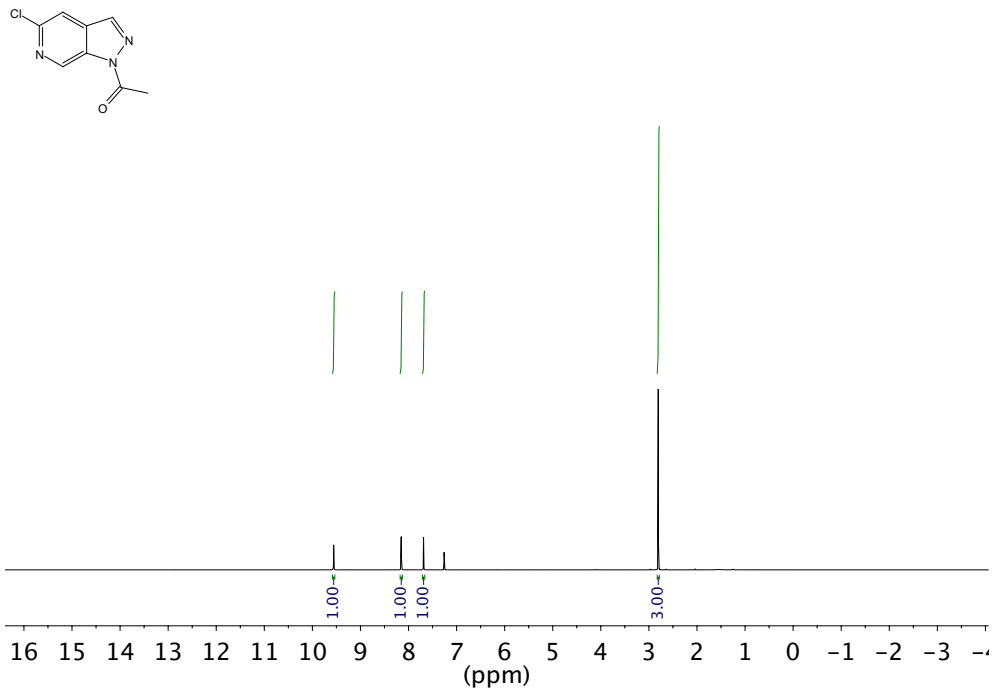

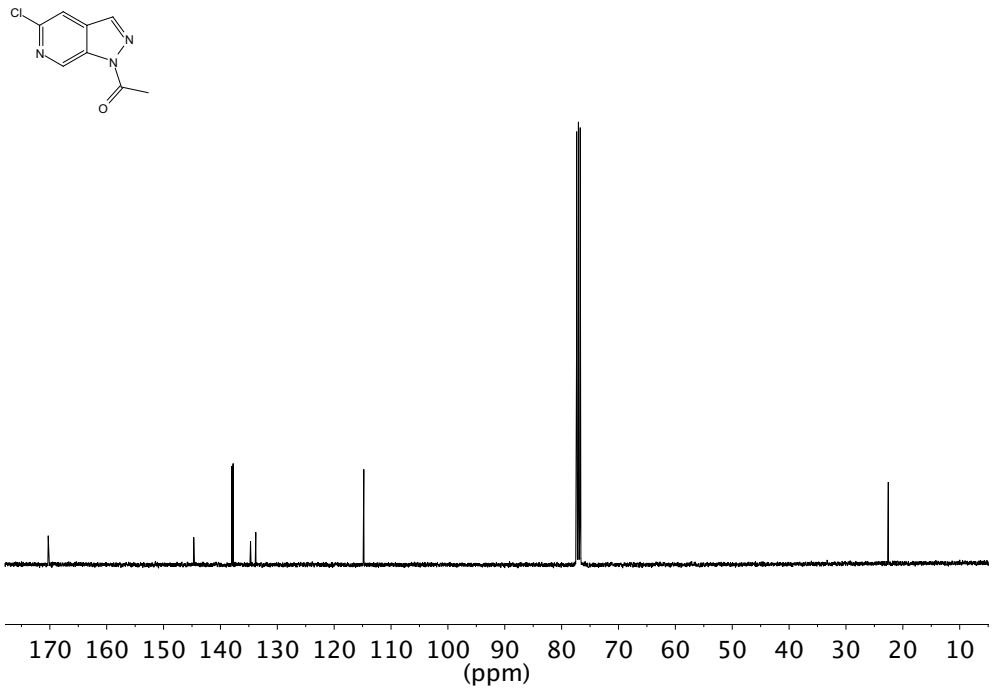

^{1}H NMR (400 MHz, MeOD) and ^{13}C NMR (101 MHz, MeOD) of compound **77**

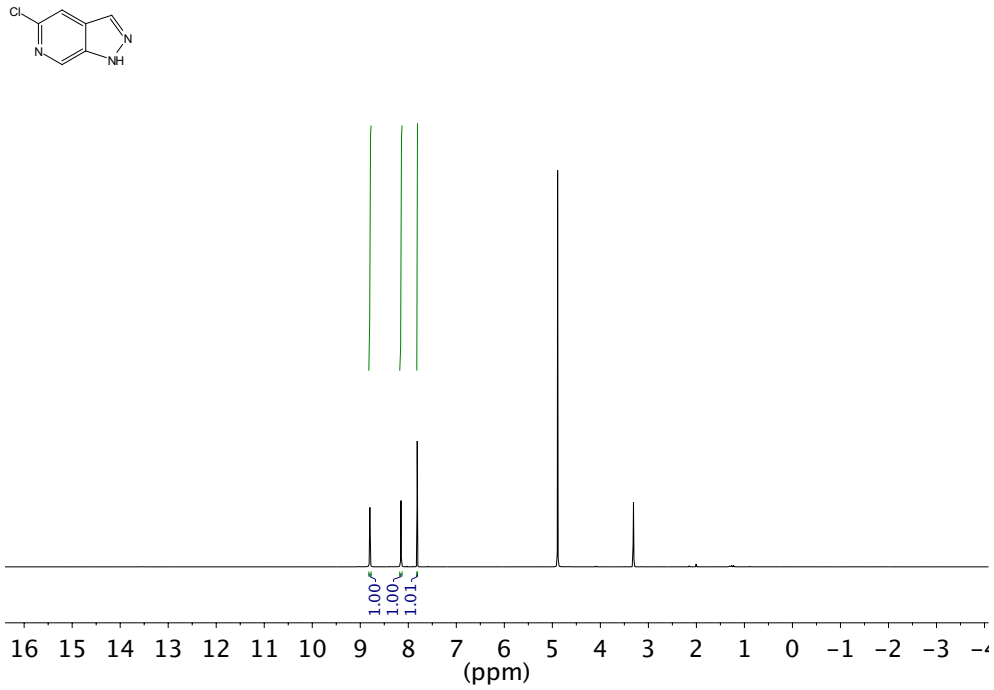

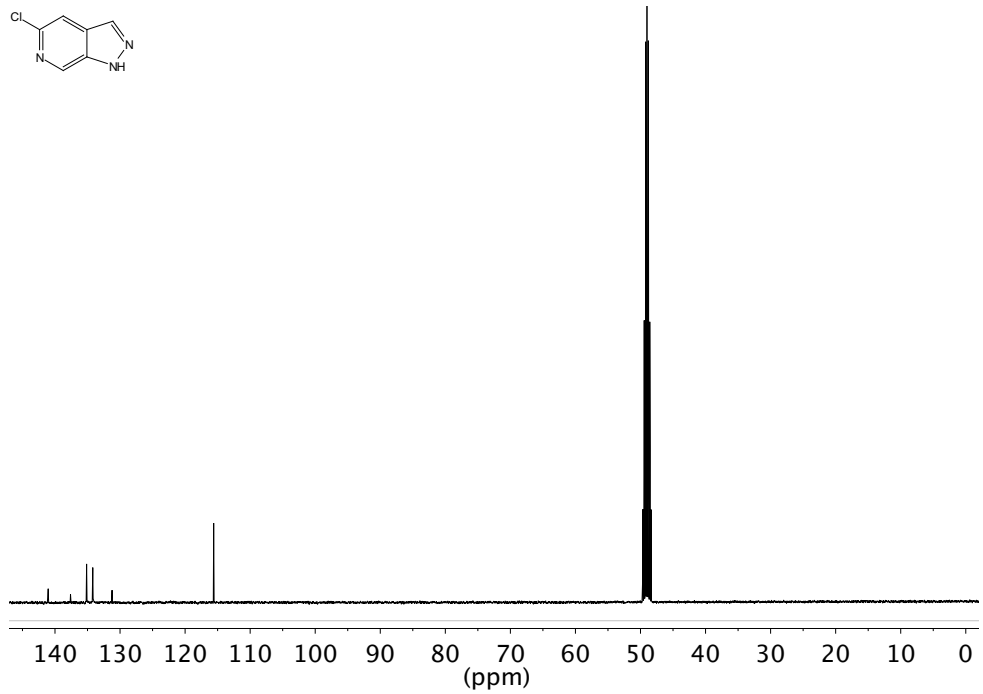

^{1}H NMR (600 MHz, $CDCl_3$) and ^{13}C NMR (151 MHz, $CDCl_3$) of compound **187**

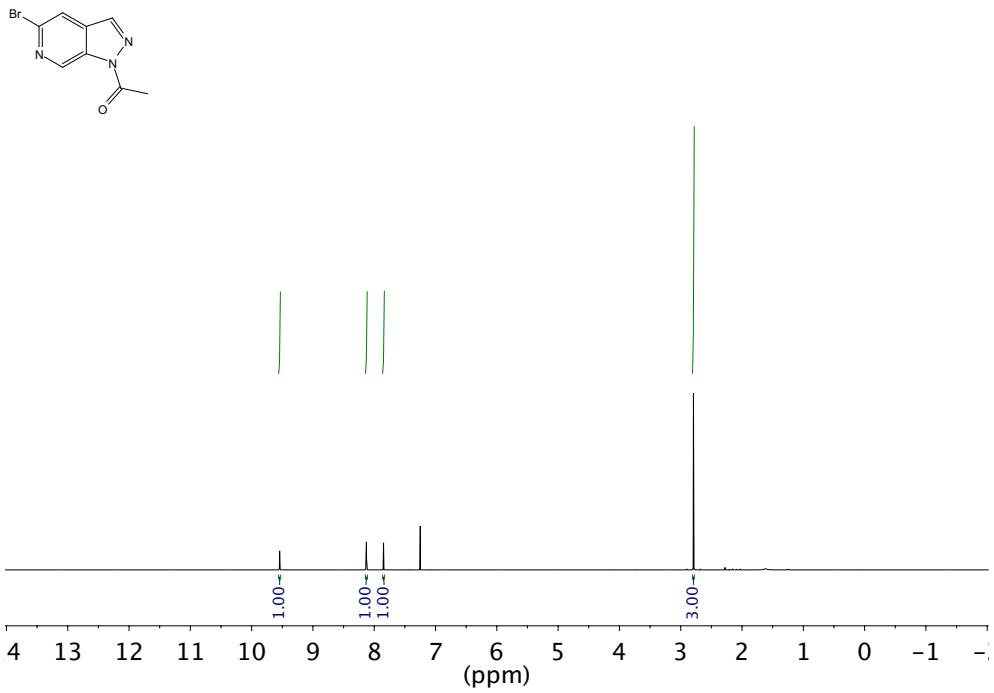

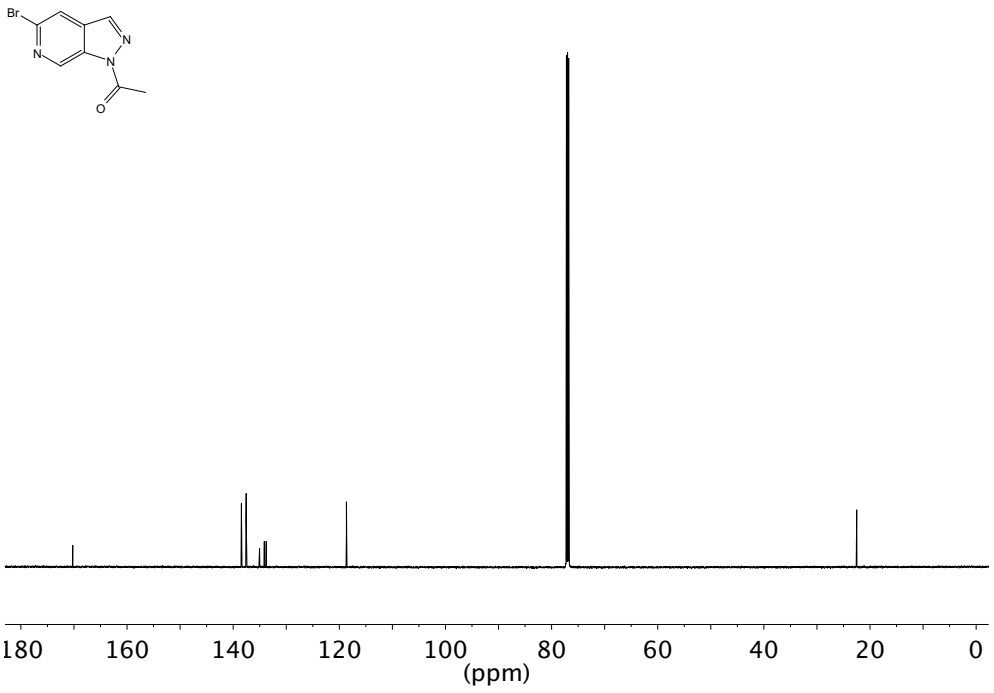

^{1}H NMR (600 MHz, MeOD) and ^{13}C NMR (151 MHz, MeOD) of compound **185**

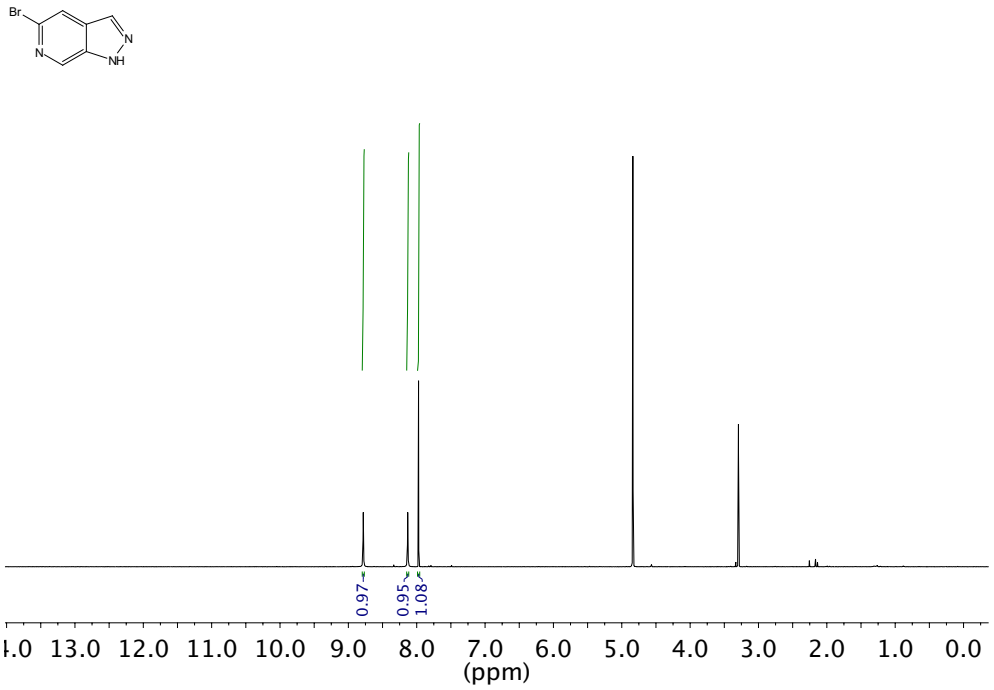

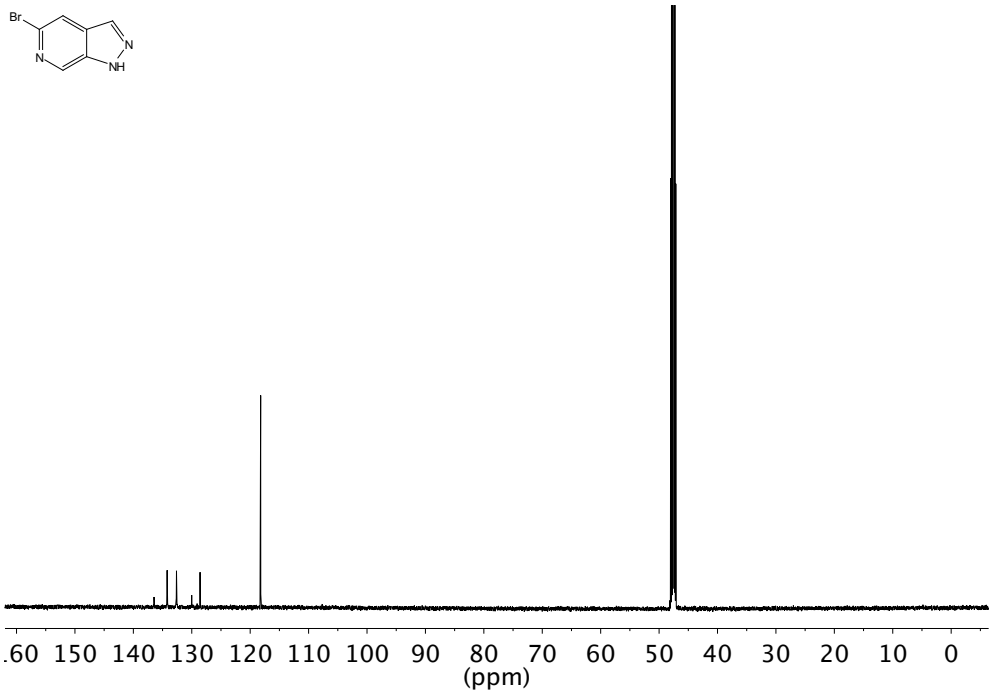

^{1}H NMR (600 MHz, $CDCl_3$) and ^{13}C NMR (151 MHz, $CDCl_3$) of compound **130**

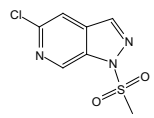

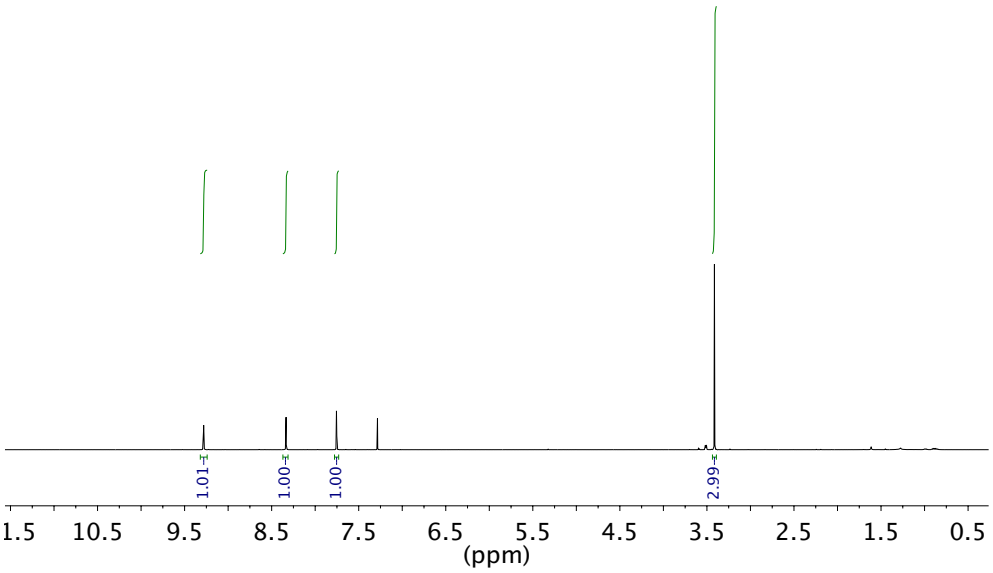

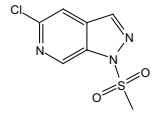

^{1}H NMR (600 MHz, $CDCl_3$) and ^{13}C NMR (151 MHz, $CDCl_3$) of compound **133**

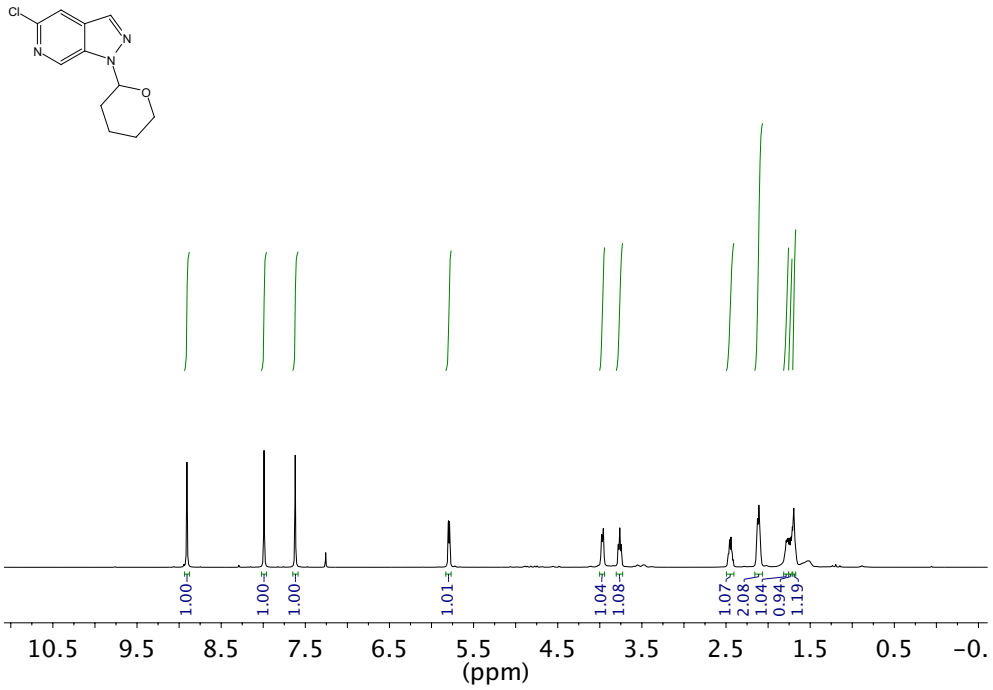

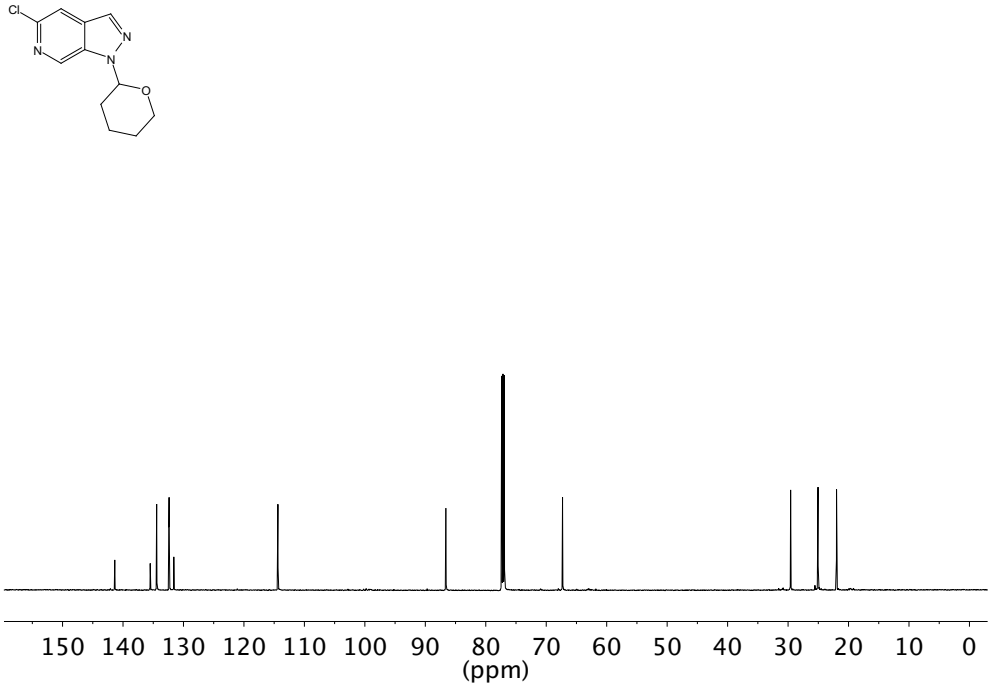

^{1}H NMR (600 MHz, $CDCl_3$) and ^{13}C NMR (151 MHz, $CDCl_3$) of compound **132**

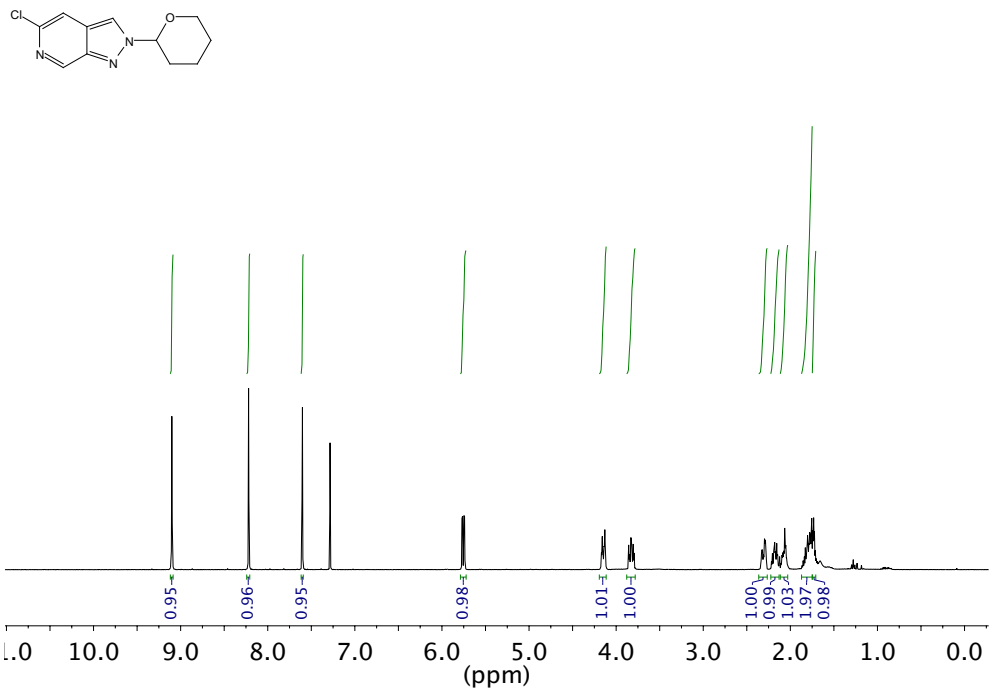

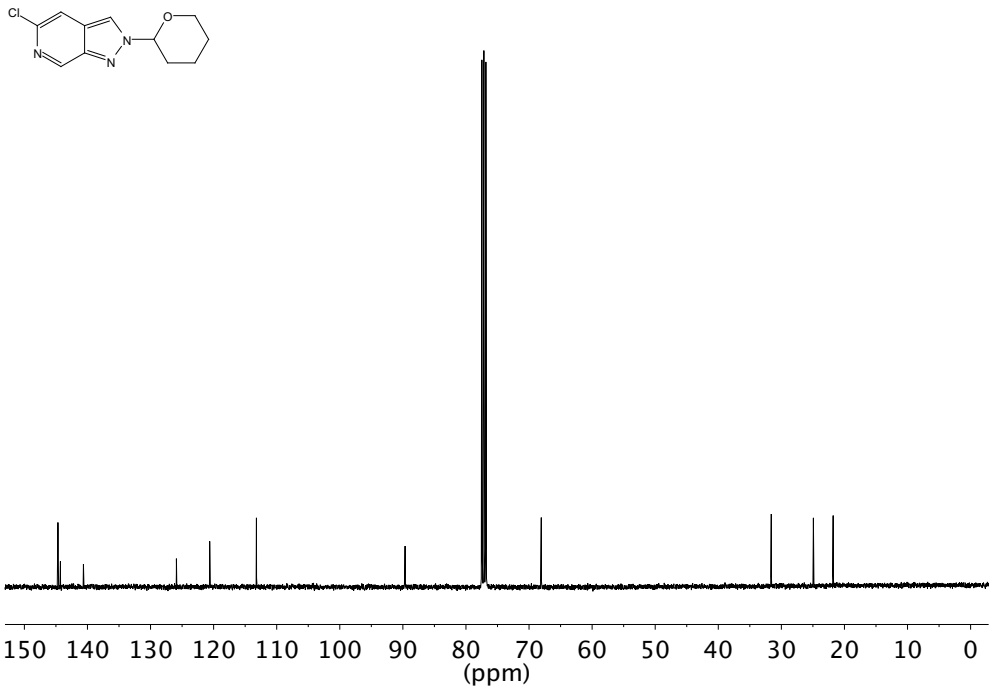

^{1}H NMR (600 MHz, $CDCl_3$) and ^{13}C NMR (151 MHz, $CDCl_3$) of compound **190**

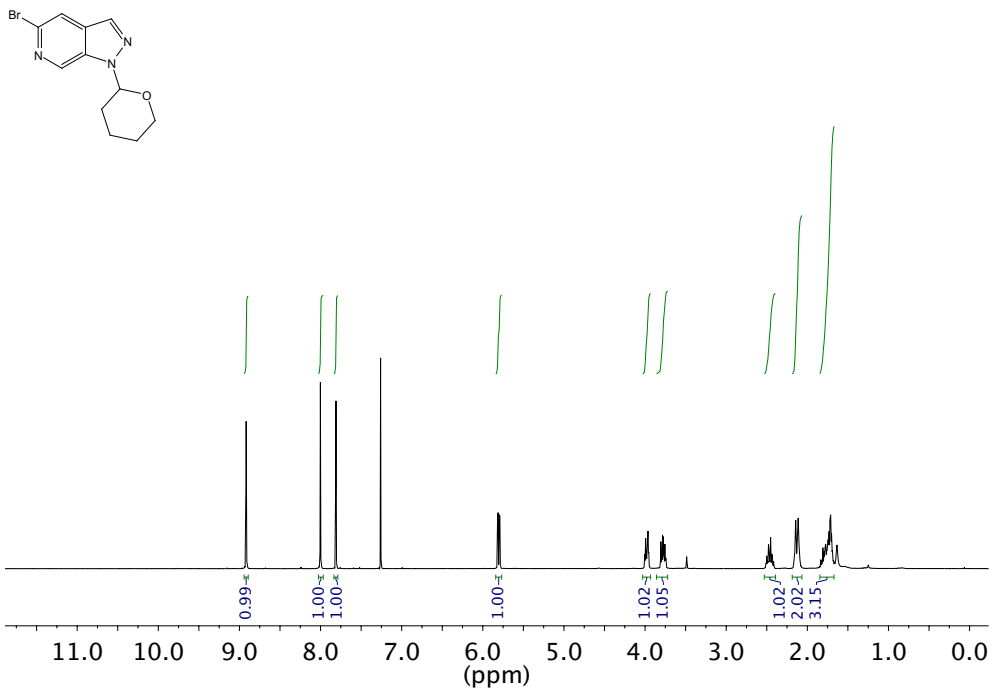

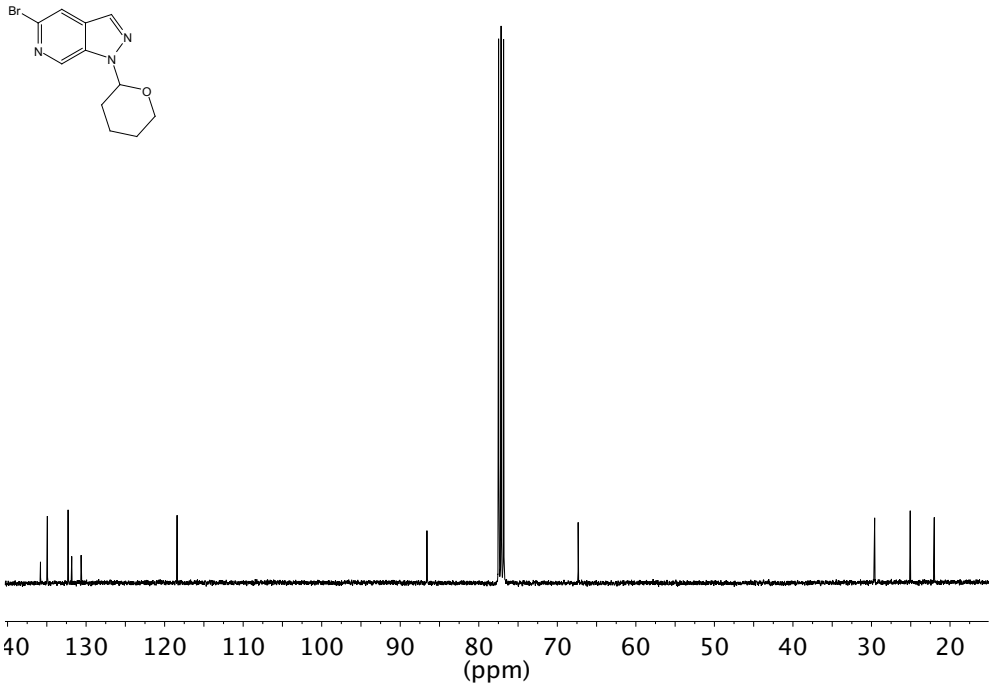

^{1}H NMR (600 MHz, $CDCl_3$) and ^{13}C NMR (151 MHz, $CDCl_3$) of compound **191**

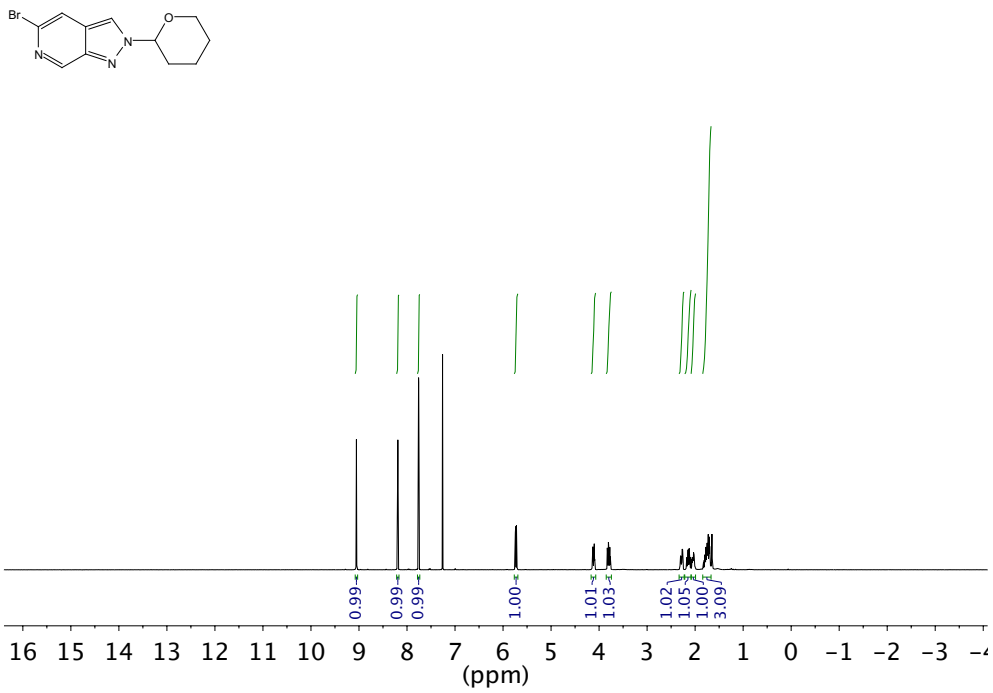

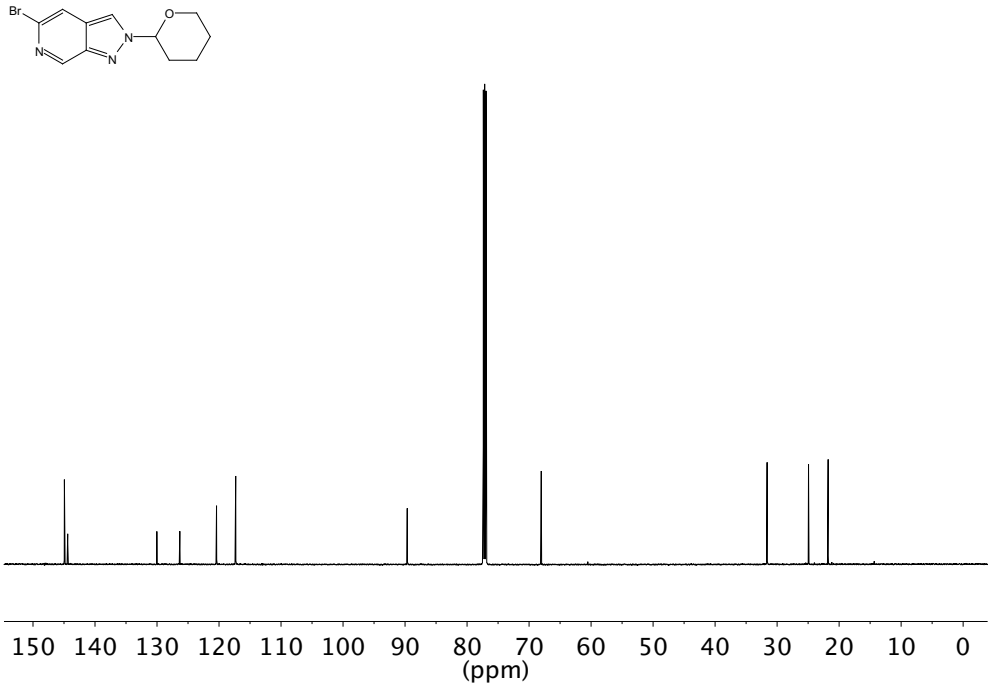

^{1}H NMR (400 MHz, $CDCl_3$) and ^{13}C NMR (101 MHz, $CDCl_3$) of compound **136**

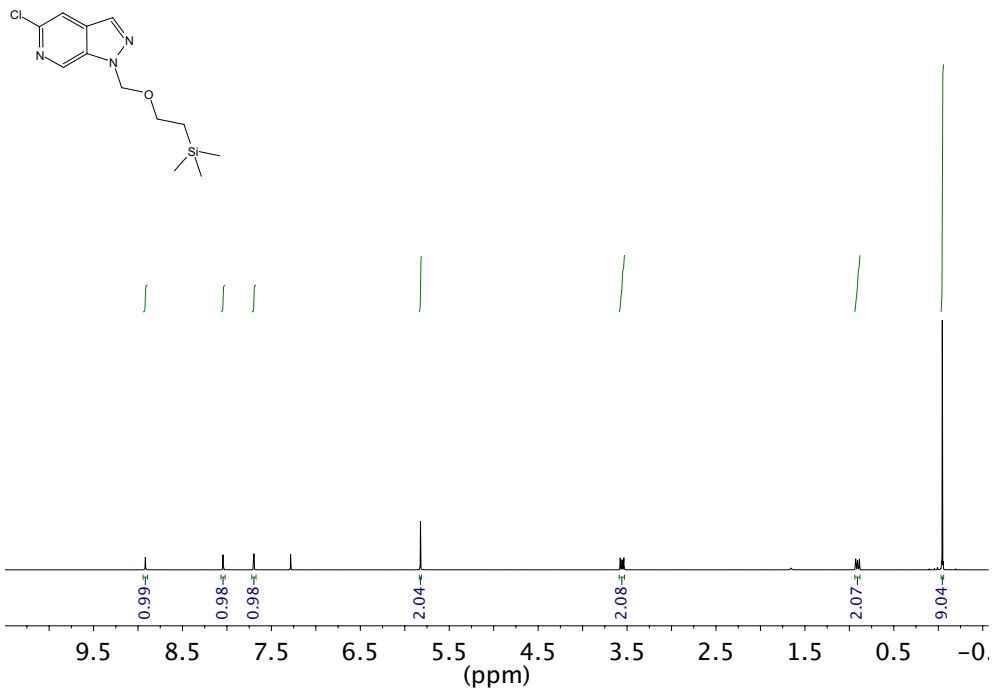

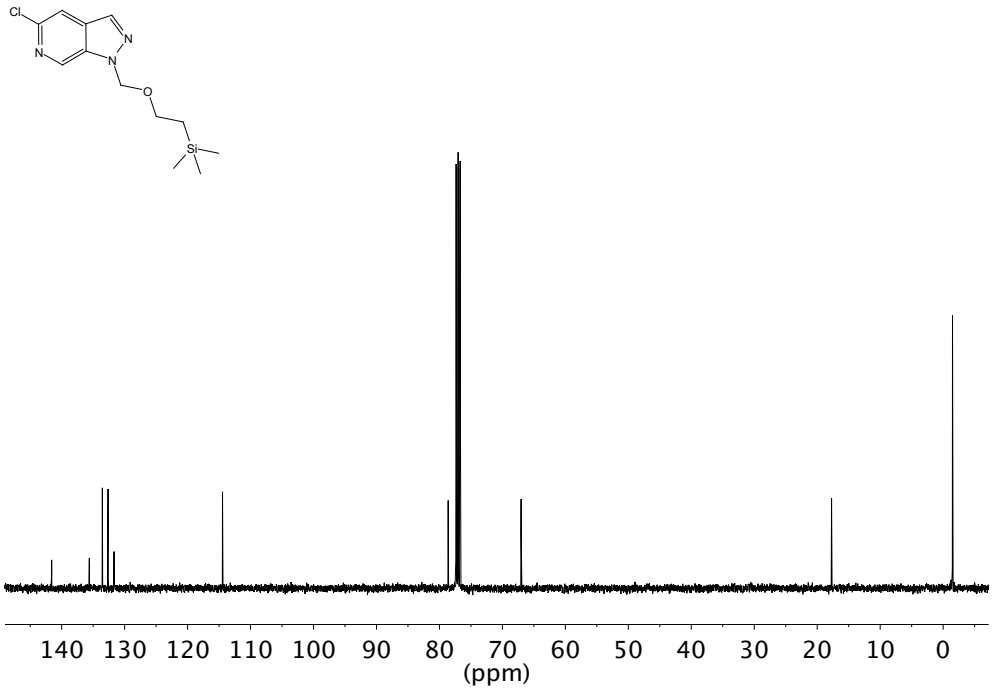

^{1}H NMR (600 MHz, $CDCl_3$) and ^{13}C NMR (151 MHz, $CDCl_3$) of compound **137**

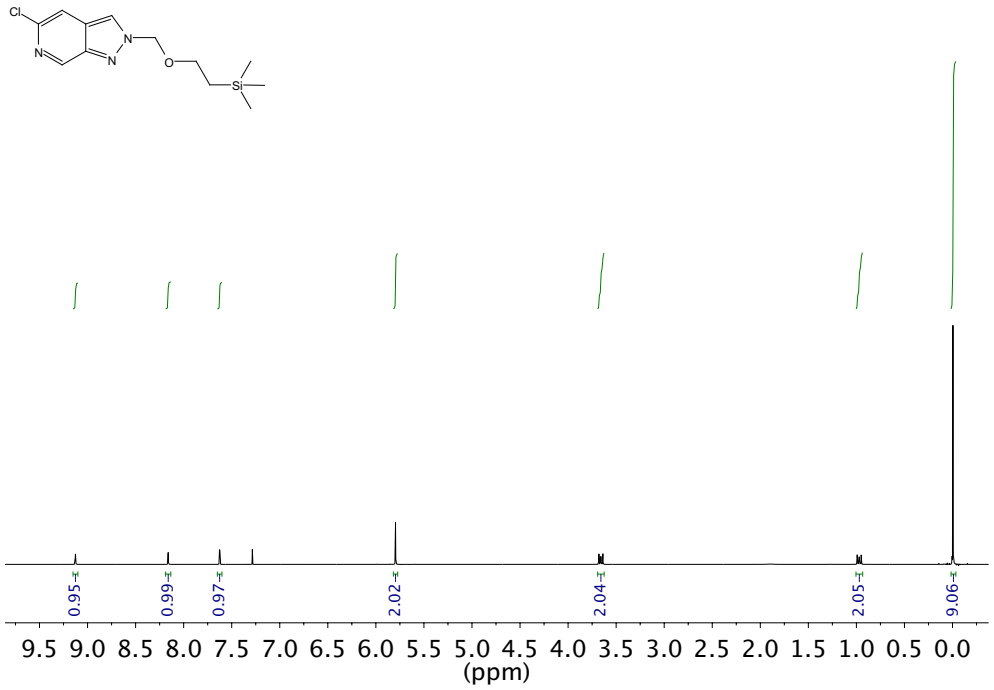

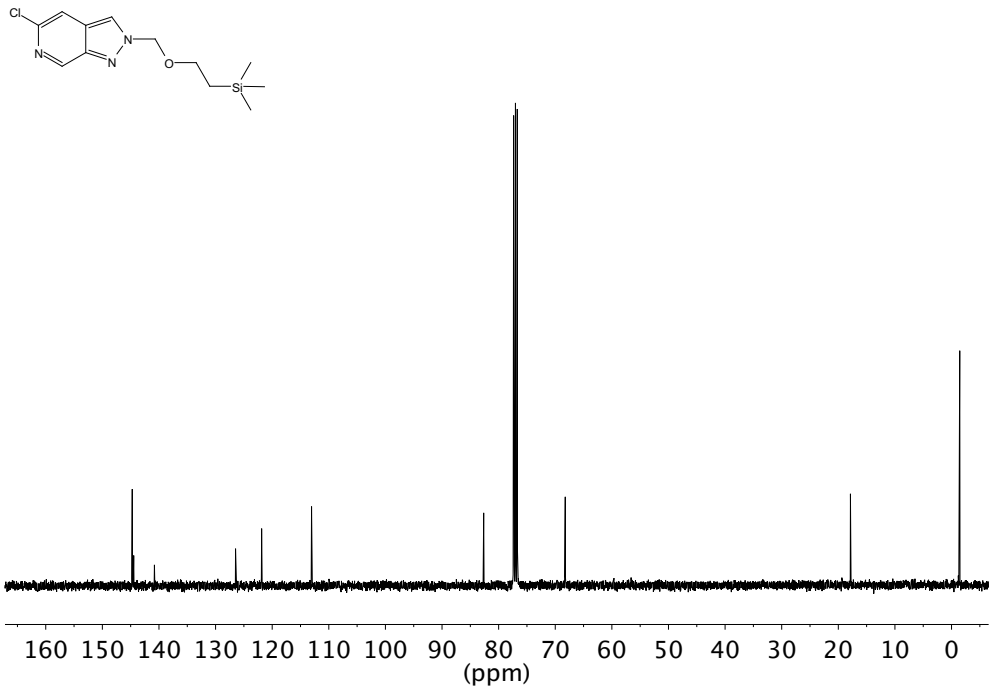

^{1}H NMR (600 MHz, $CDCl_3$) and ^{13}C NMR (151 MHz, $CDCl_3$) of compound **188**

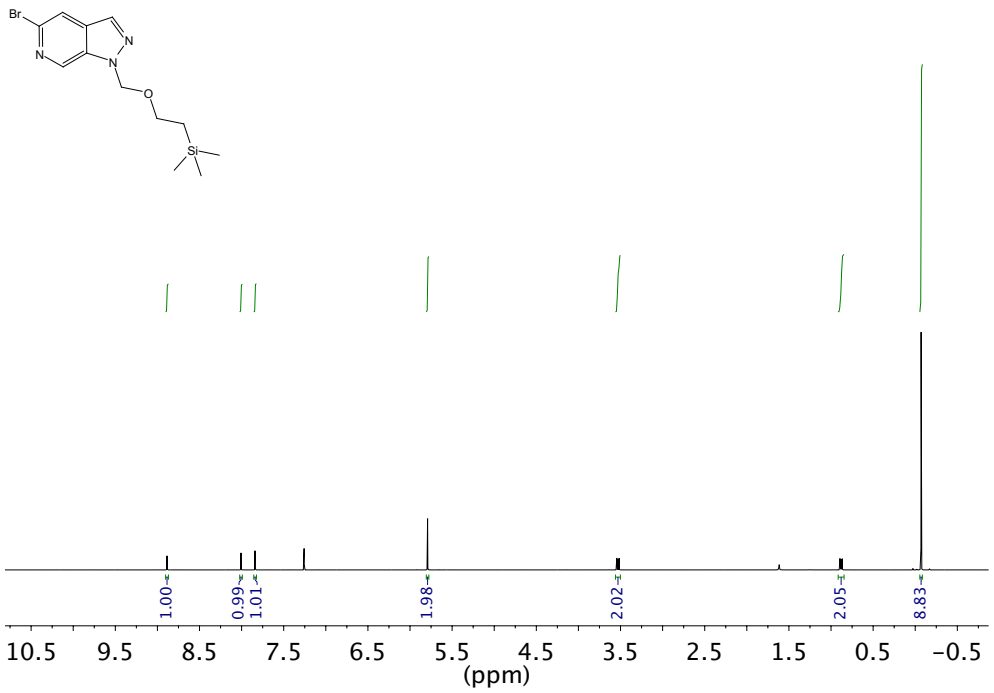

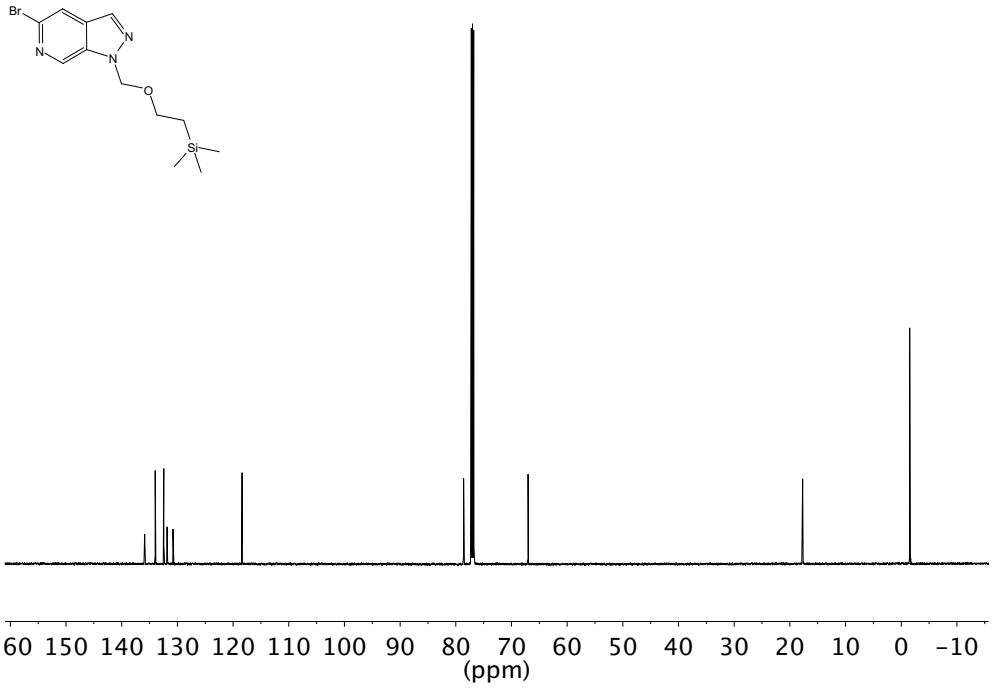

^{1}H NMR (600 MHz, $CDCl_3$) and ^{13}C NMR (151 MHz, $CDCl_3$) of compound **189**

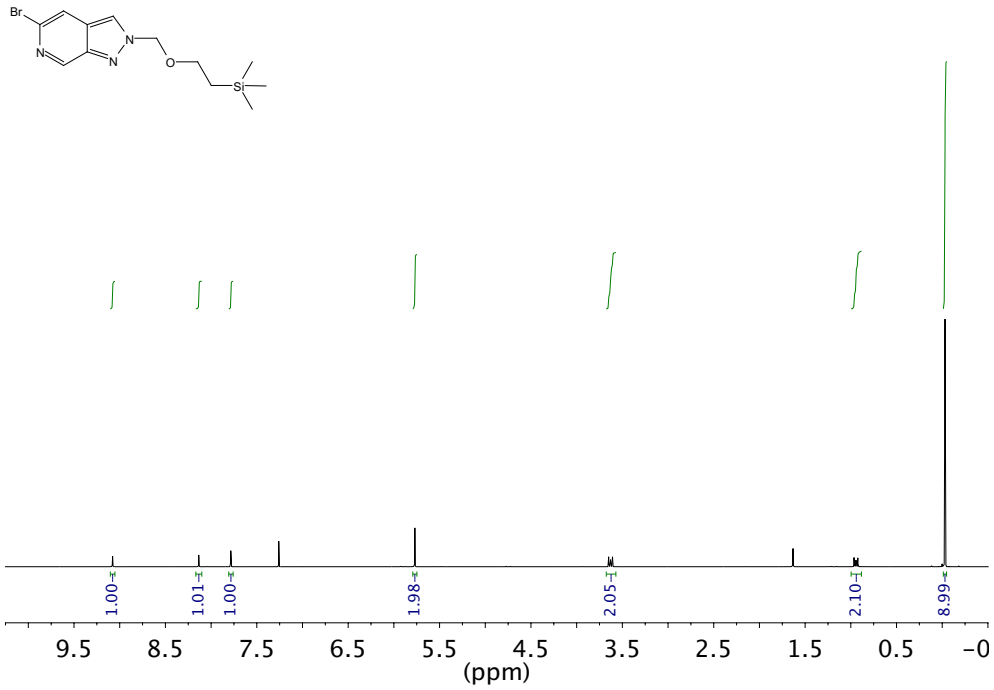

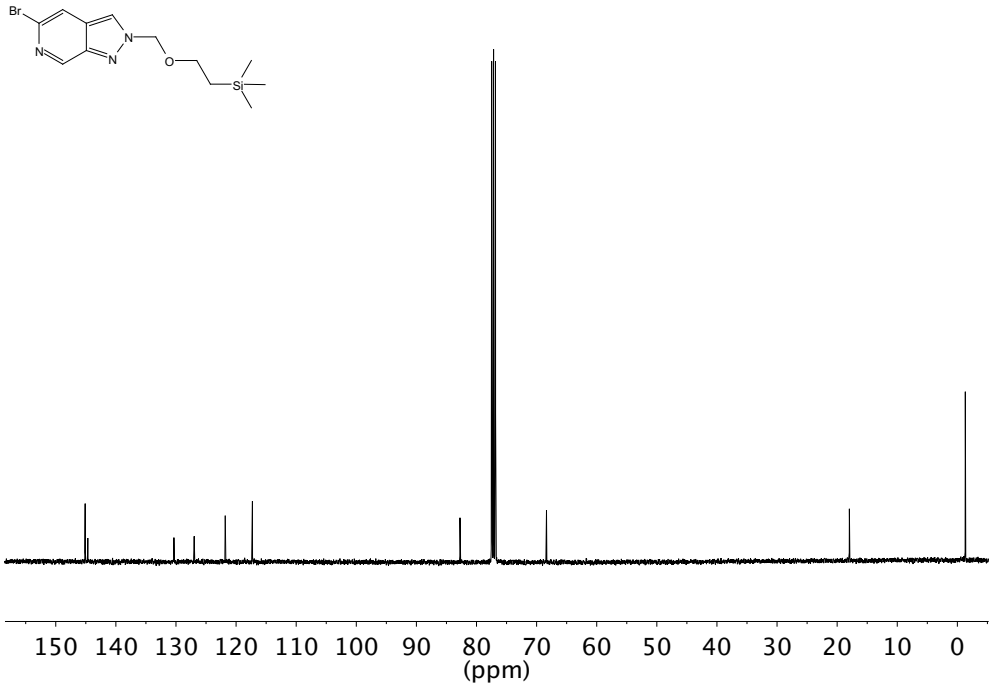

^{1}H NMR (600 MHz, $CDCl_3$) and ^{13}C NMR (151 MHz, $CDCl_3$) of compound **207**

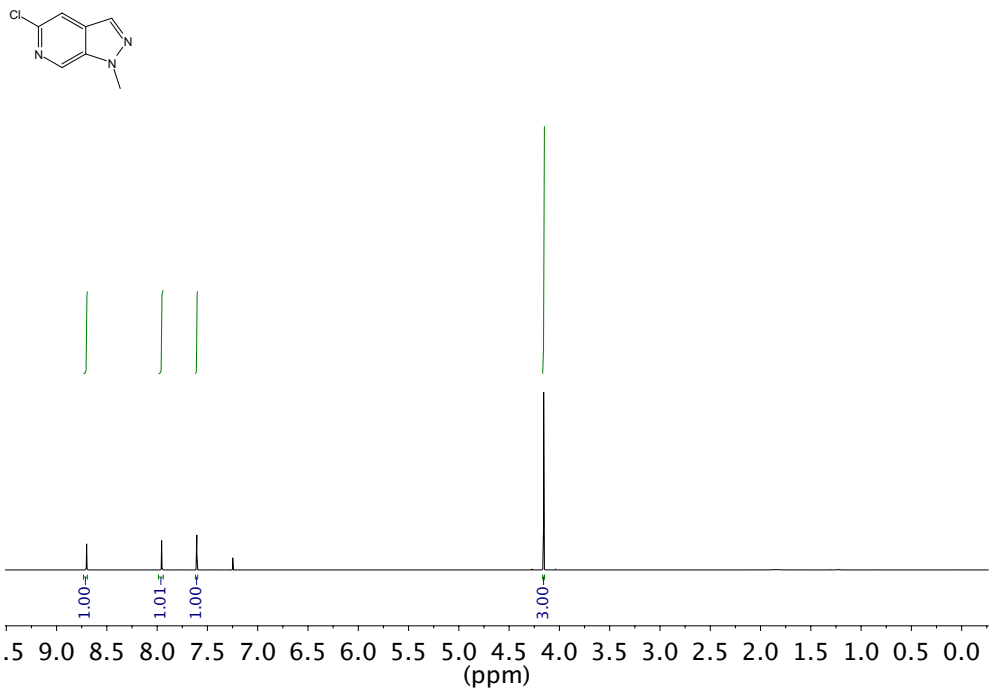

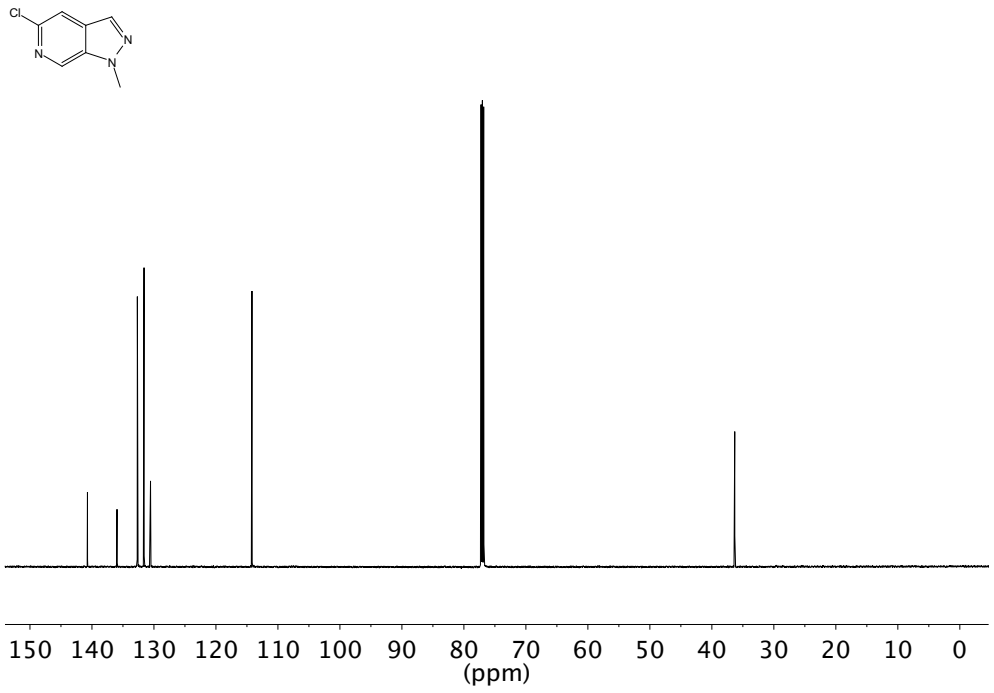

^{1}H NMR (600 MHz, $CDCl_3$) and ^{13}C NMR (151 MHz, $CDCl_3$) of compound **208**

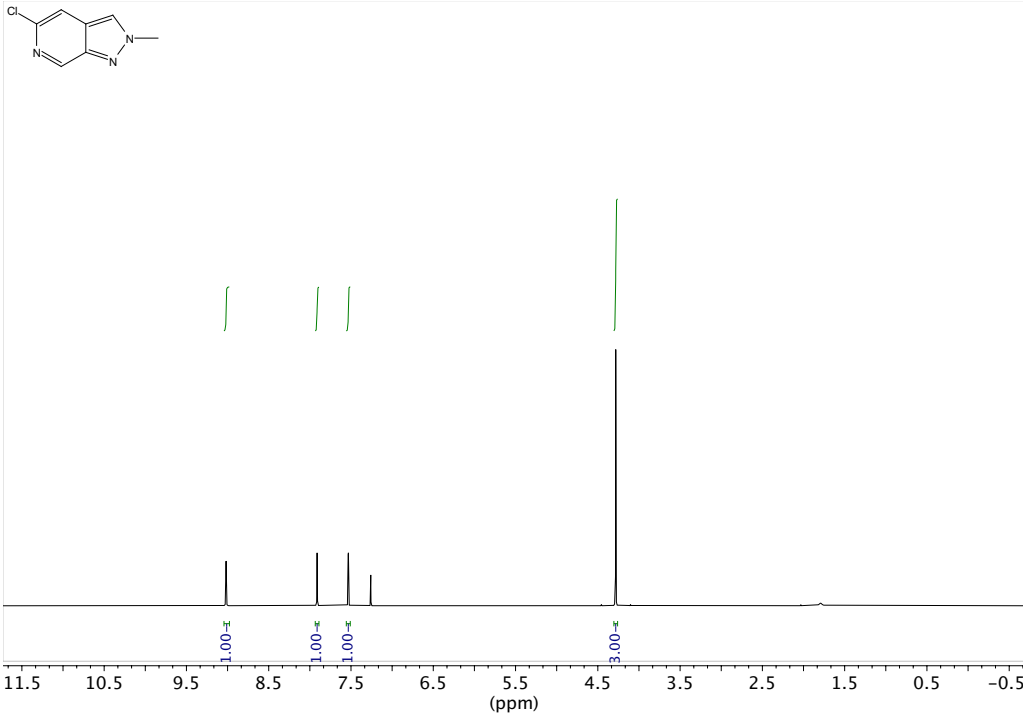

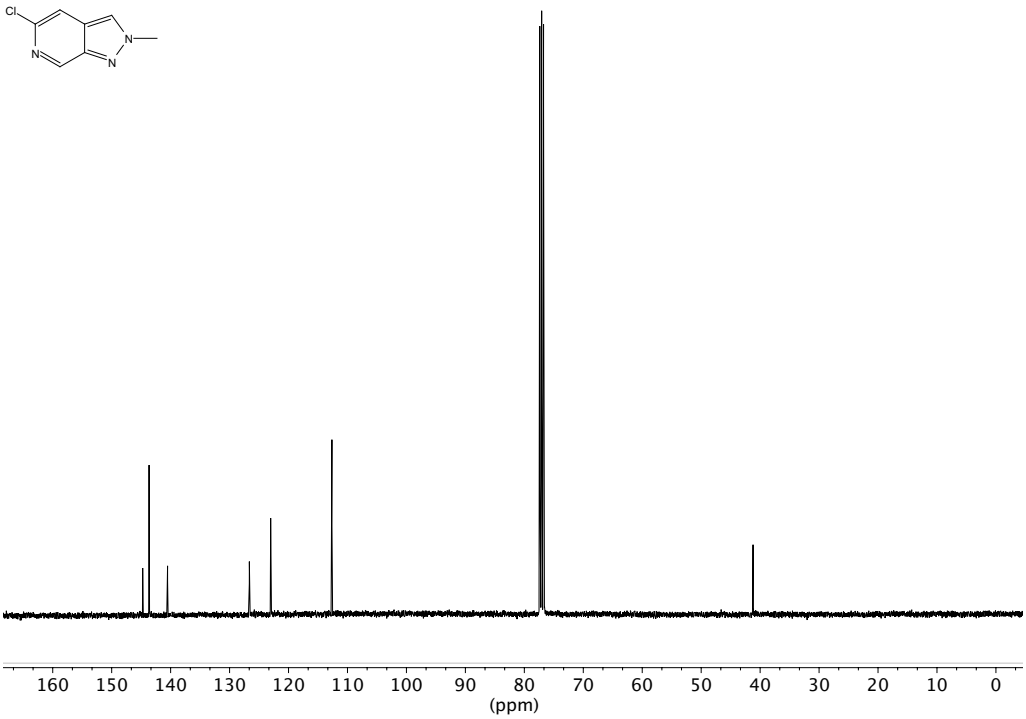

^{1}H NMR (600 MHz, $CDCl_3$) and ^{13}C NMR (151 MHz, $CDCl_3$) of compound **205**

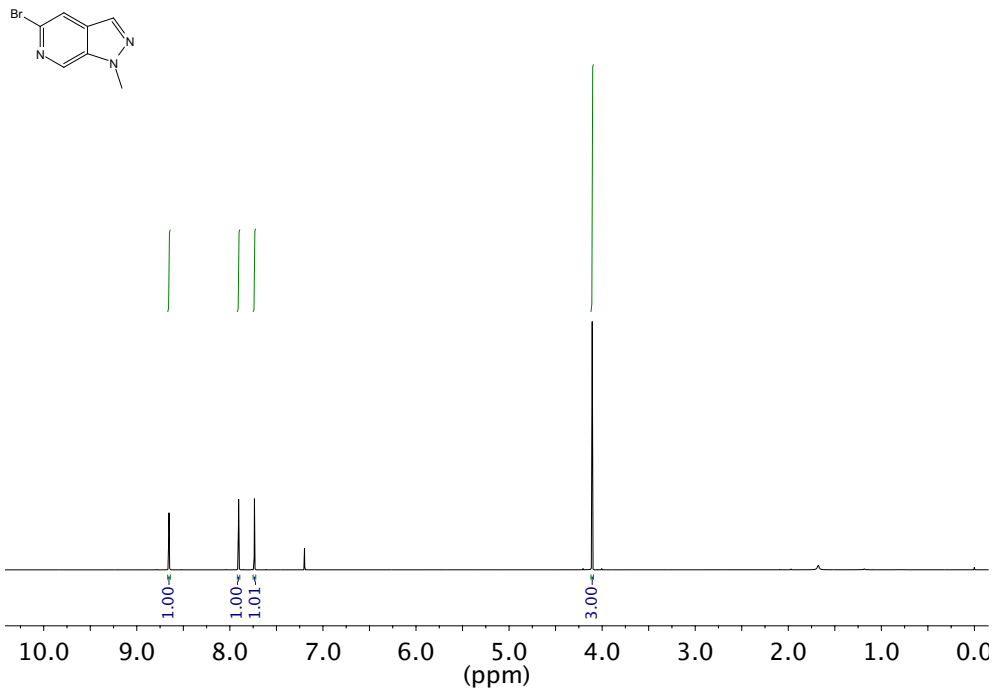

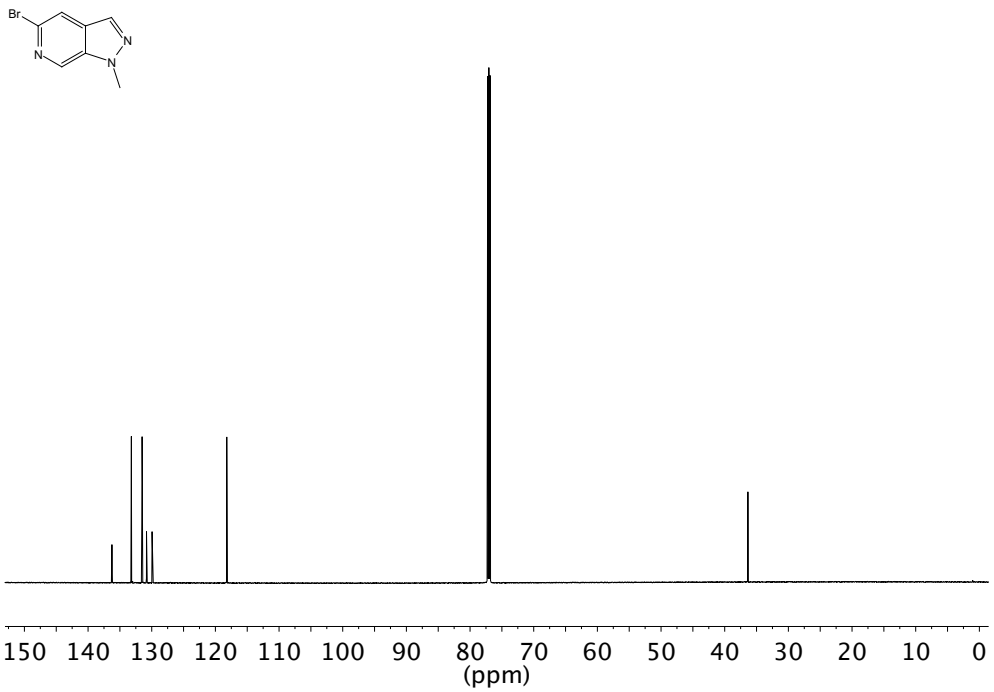

^{1}H NMR (600 MHz, $CDCl_3$) and ^{13}C NMR (151 MHz, $CDCl_3$) of compound **206**

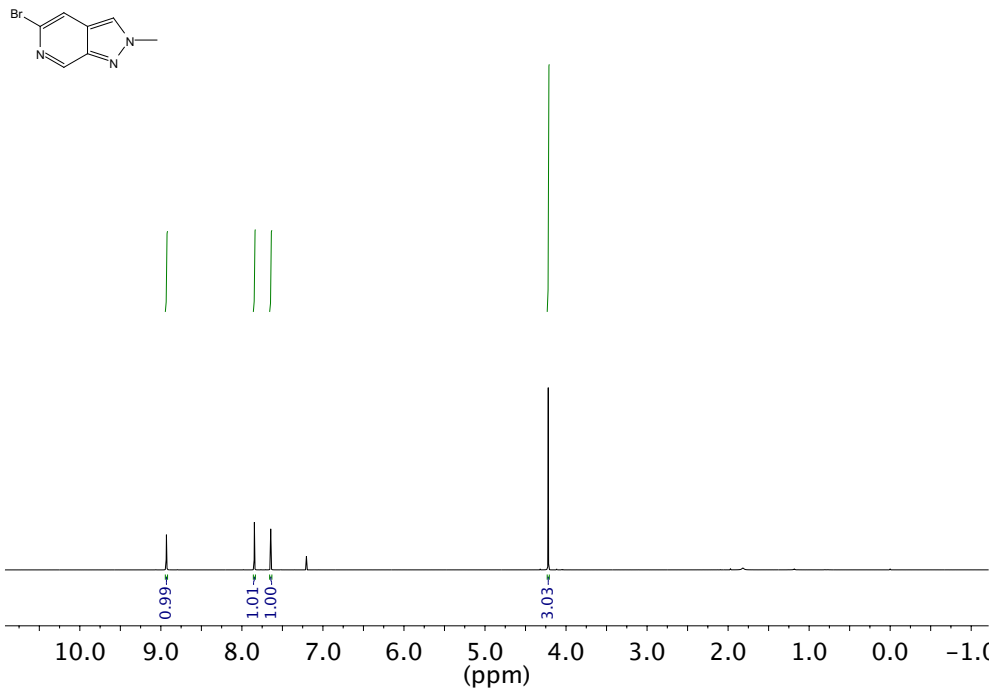

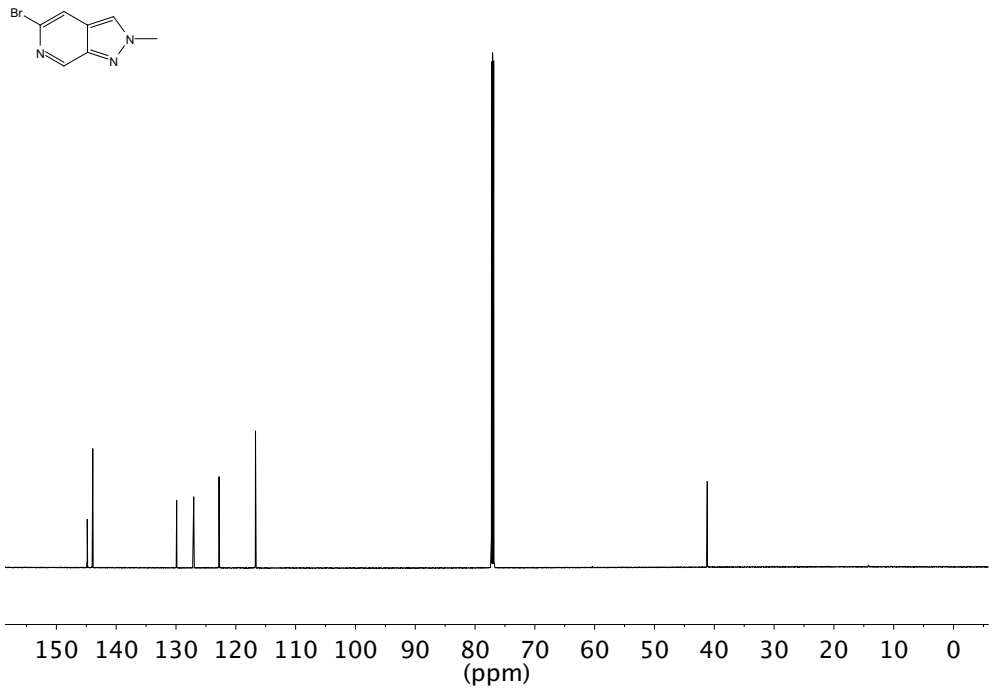

^{1}H NMR (600 MHz, $CDCl_3$) and ^{13}C NMR (151 MHz, $CDCl_3$) of compound **209**

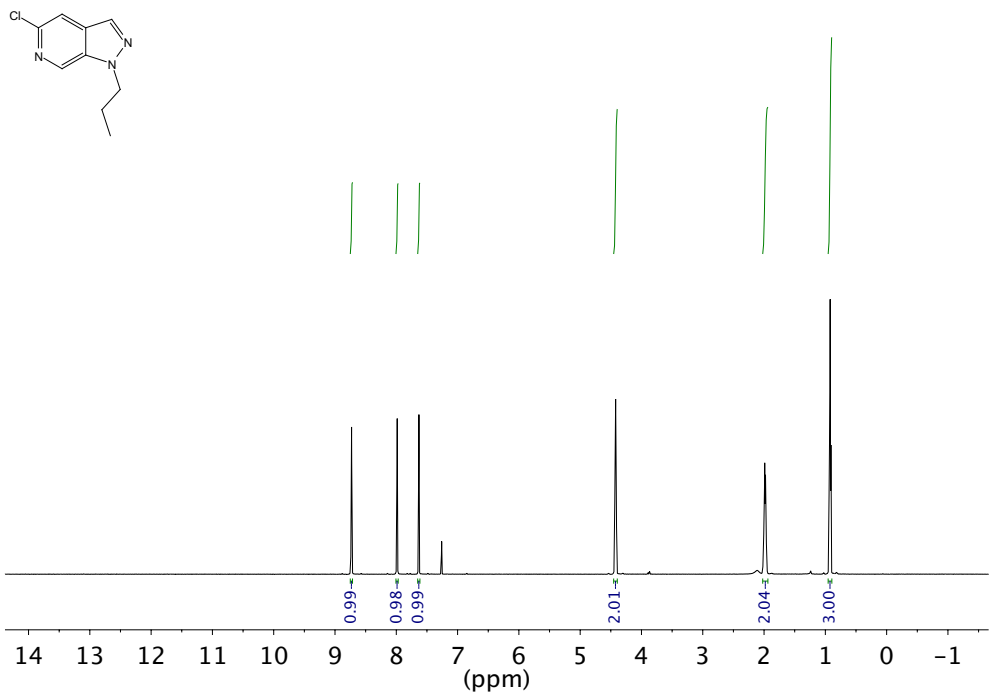

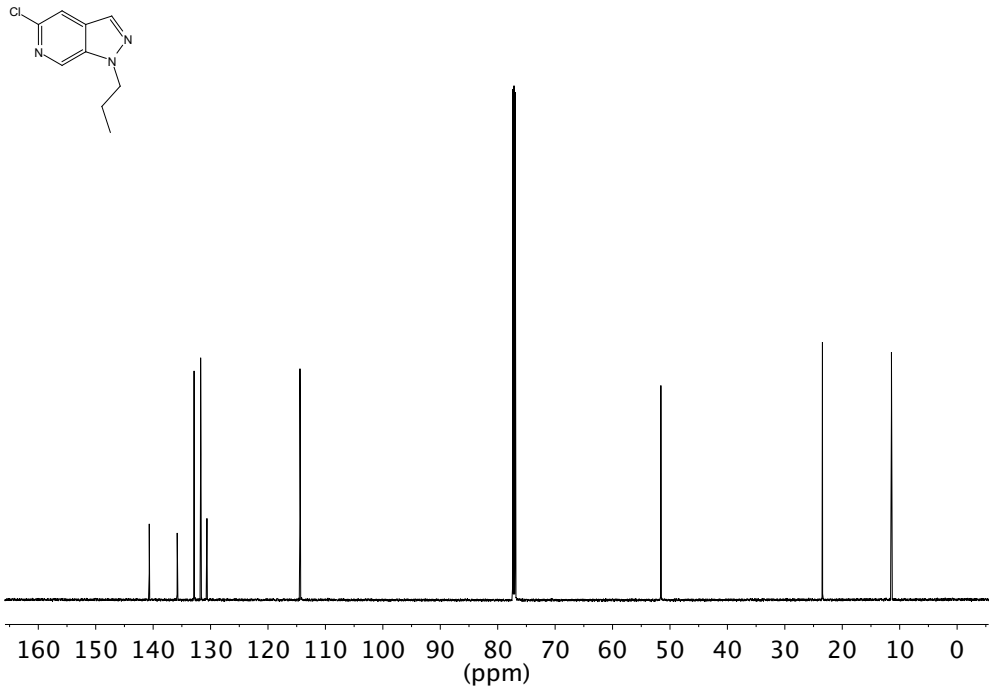

^{1}H NMR (600 MHz, $CDCl_3$) and ^{13}C NMR (151 MHz, $CDCl_3$) of compound **210**

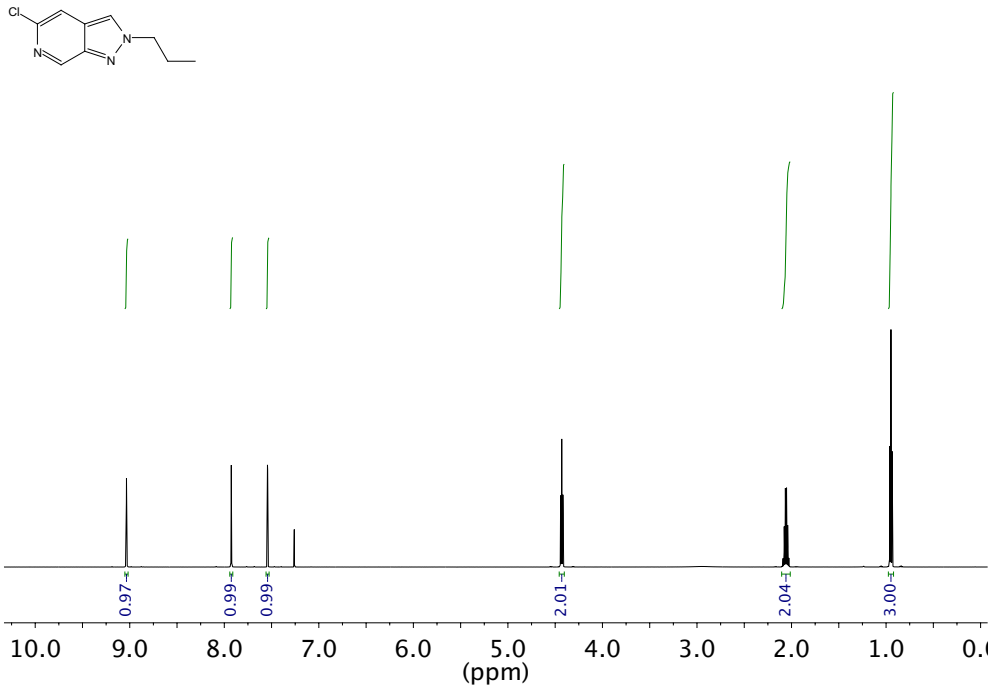

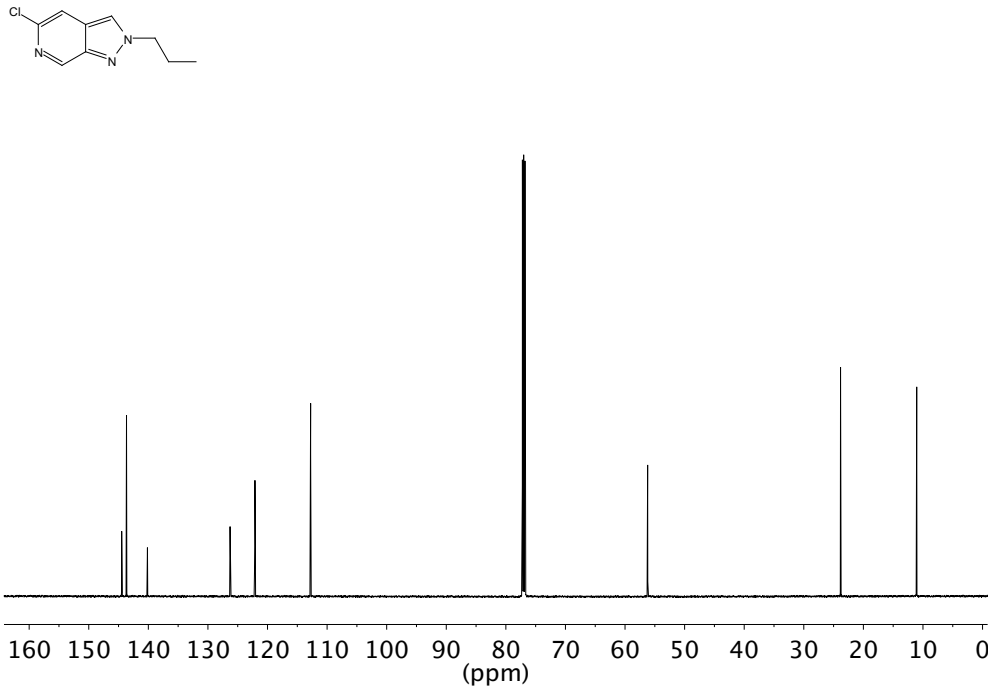

^{1}H NMR (600 MHz, $CDCl_3$) and ^{13}C NMR (151 MHz, $CDCl_3$) of compound **140**

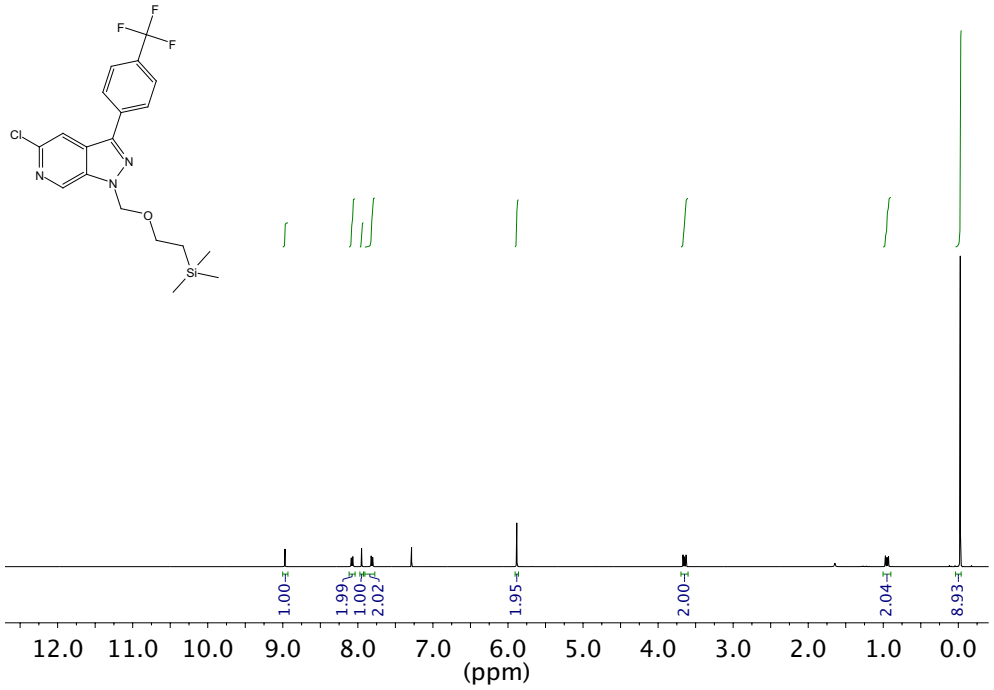

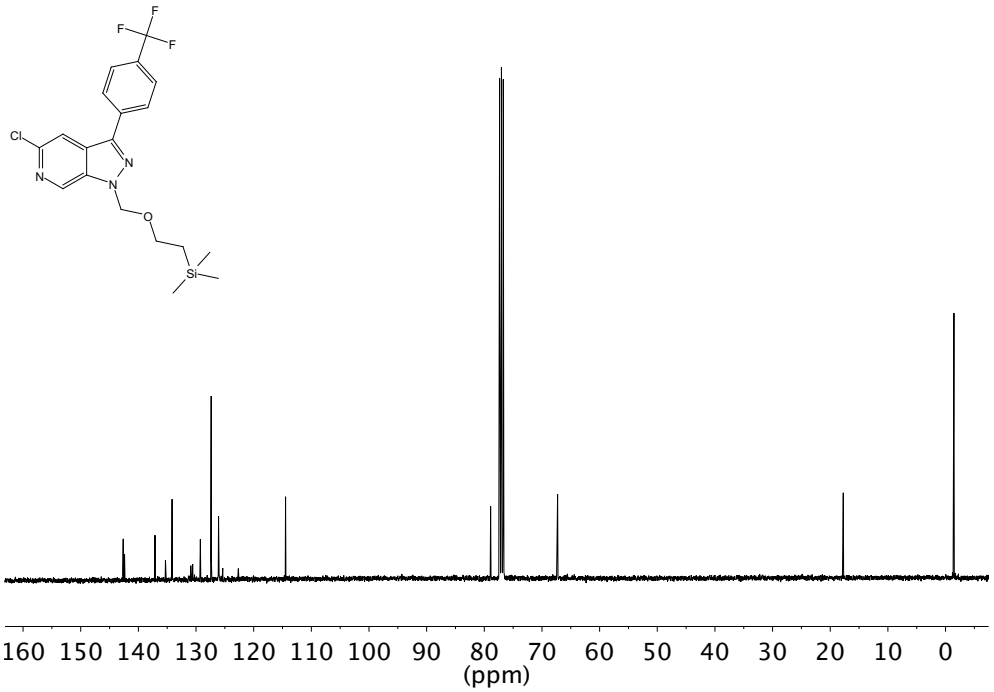

^{19}F NMR (376 MHz, $CDCl_3$) of compound **140**

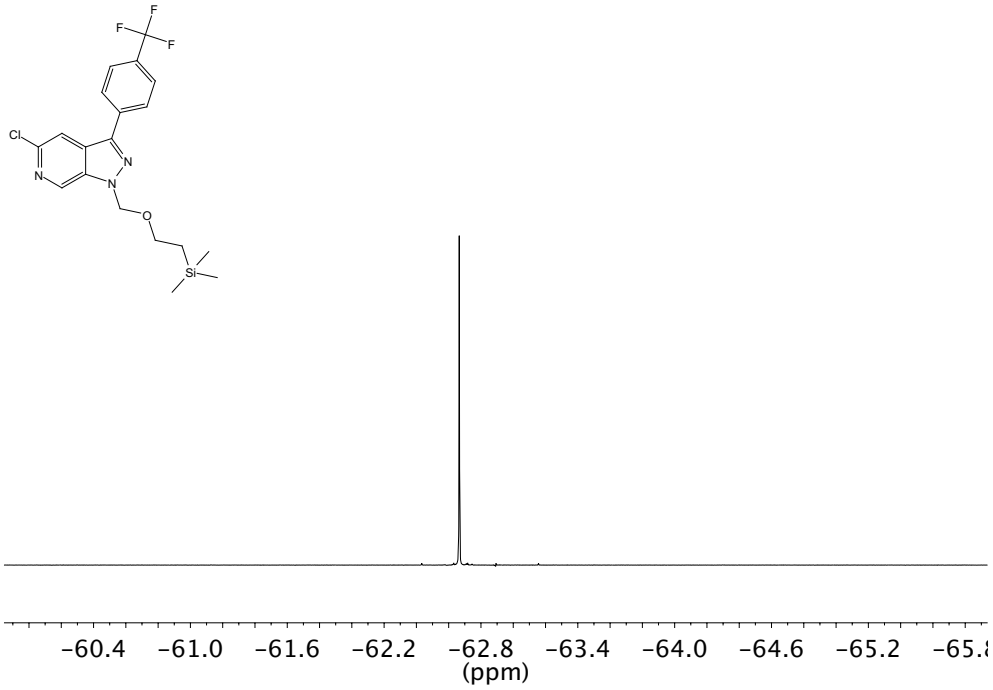

^{1}H NMR (600 MHz, $CDCl_3$) and ^{13}C NMR (151 MHz, $CDCl_3$) of compound **144**

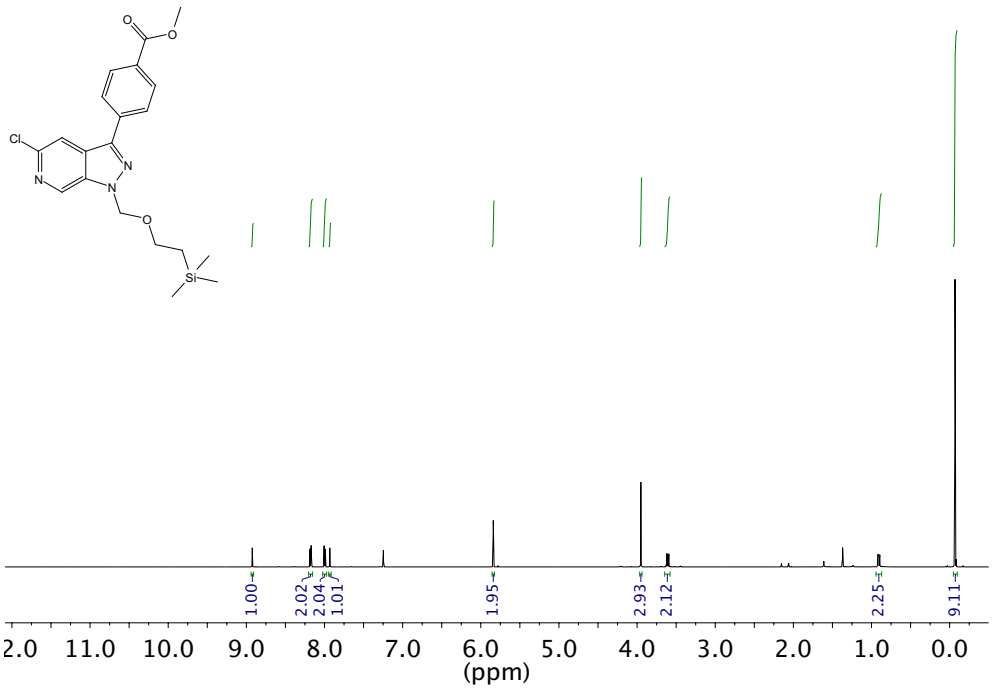

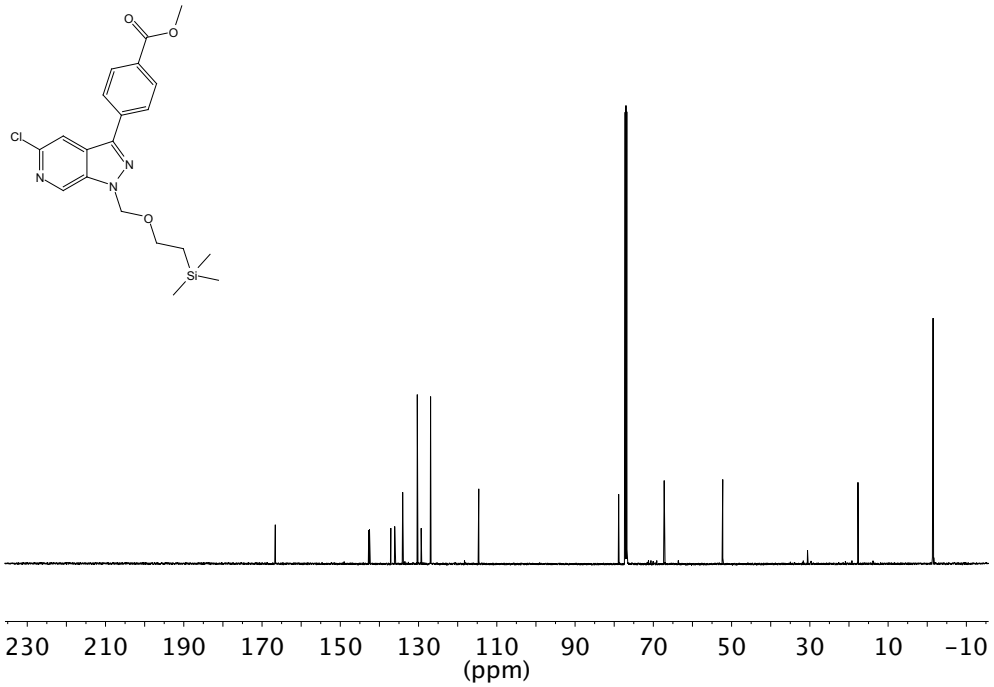

^{1}H NMR (600 MHz, $CDCl_3$) and ^{13}C NMR (151 MHz, $CDCl_3$) of compound **145**

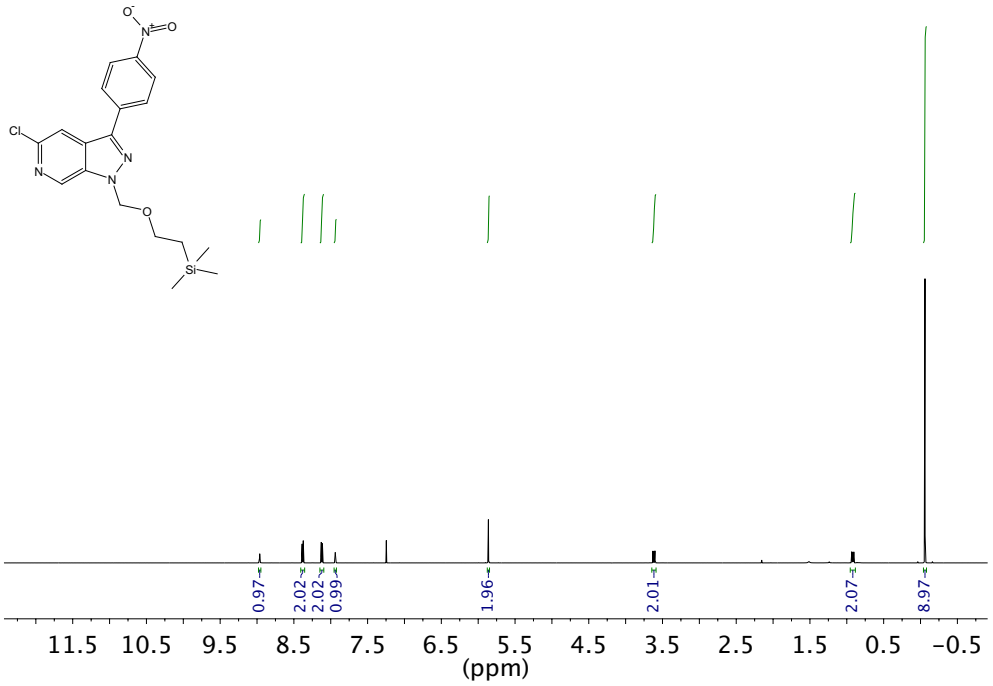

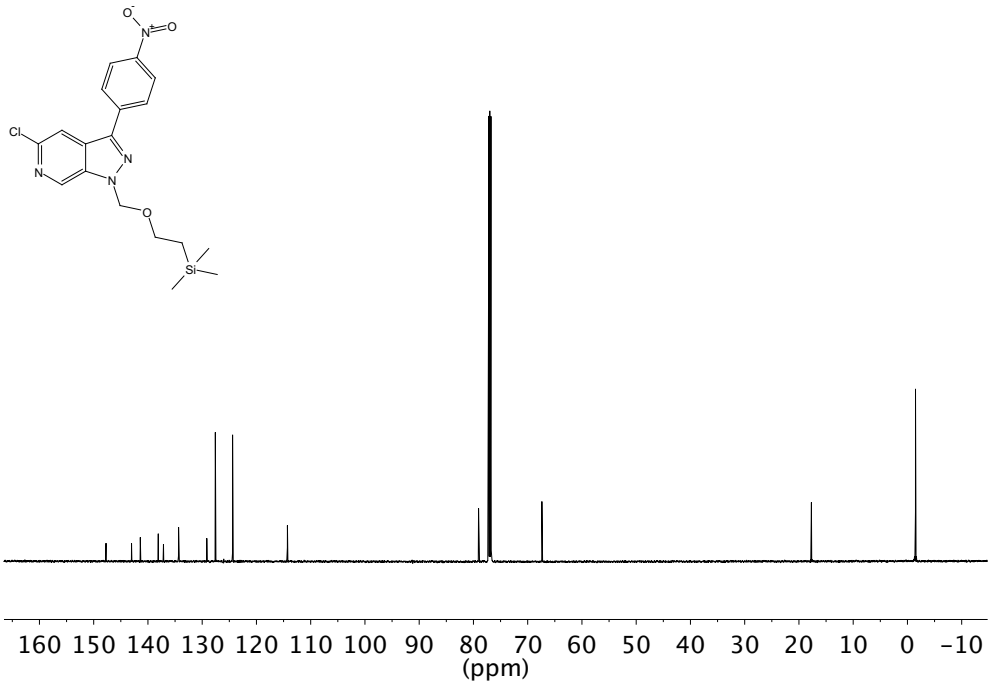

^{1}H NMR (600 MHz, $CDCl_3$) and ^{13}C NMR (151 MHz, $CDCl_3$) of compound **146**

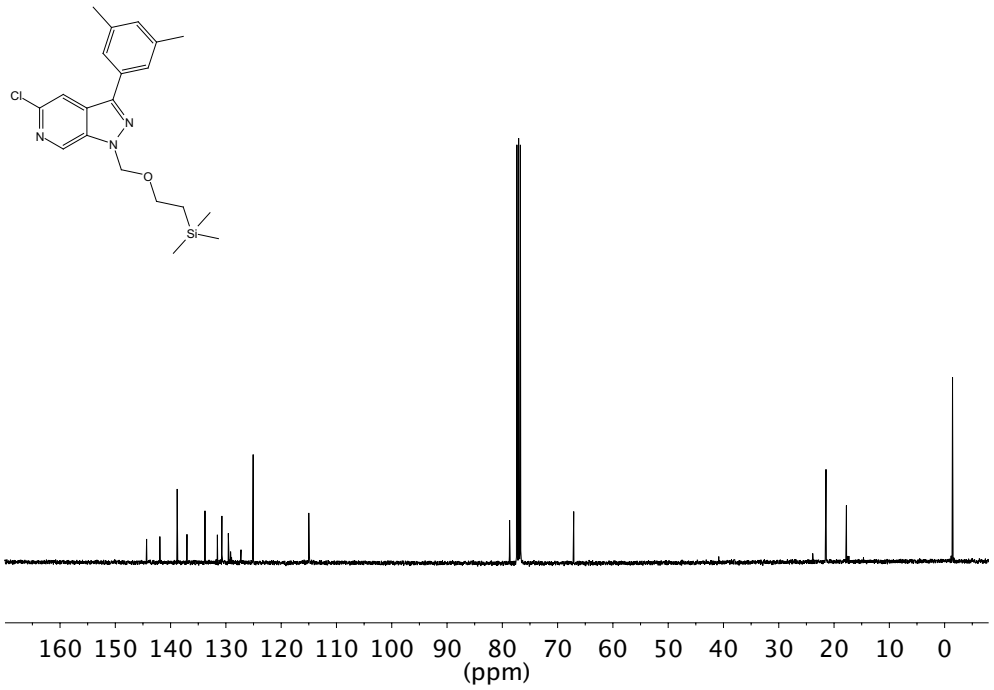

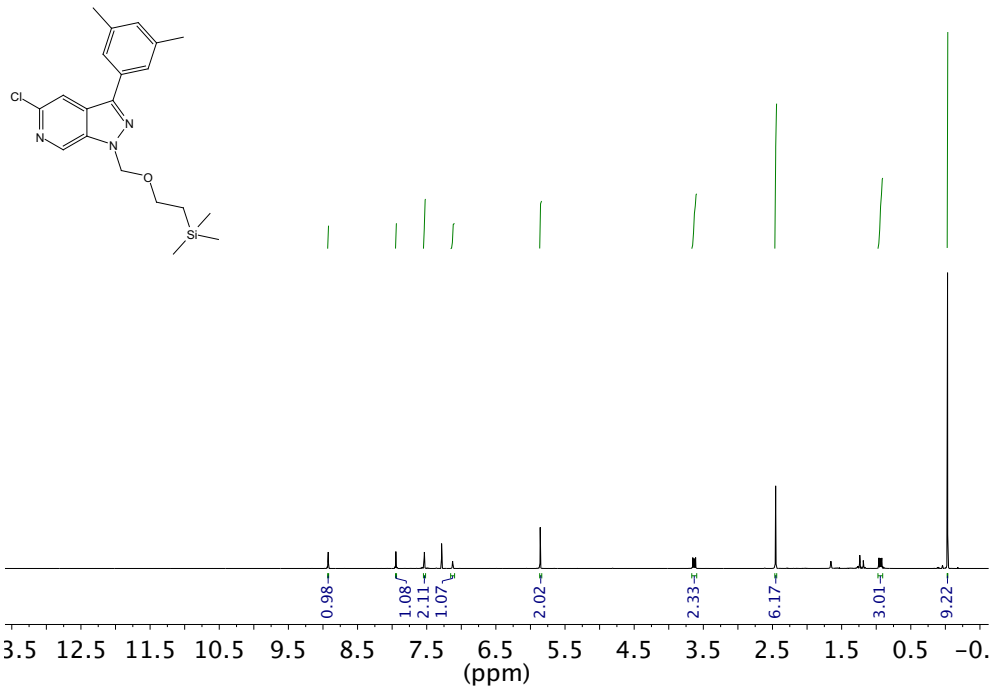

^{1}H NMR (600 MHz, $CDCl_3$) and ^{13}C NMR (151 MHz, $CDCl_3$) of compound **141**

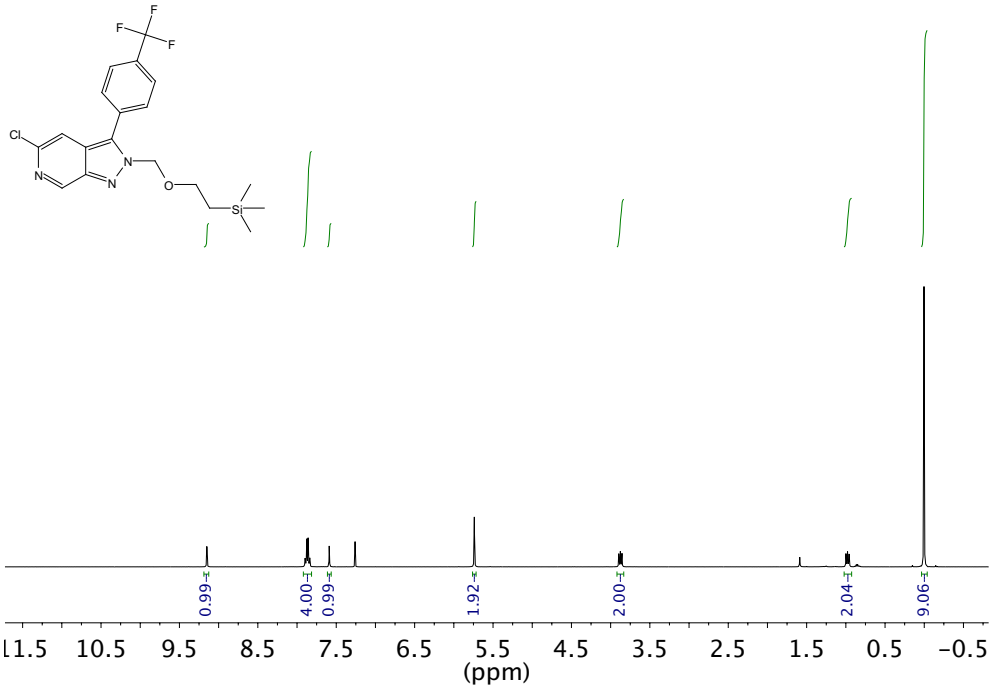

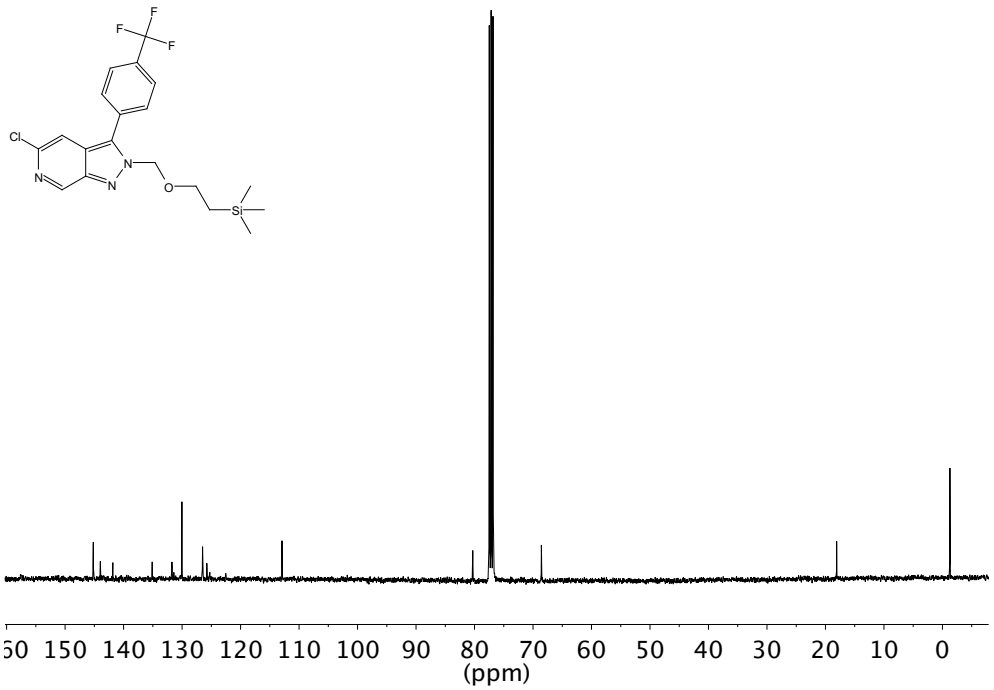

^{19}F NMR (376 MHz, $CDCl_3$) of compound **141**

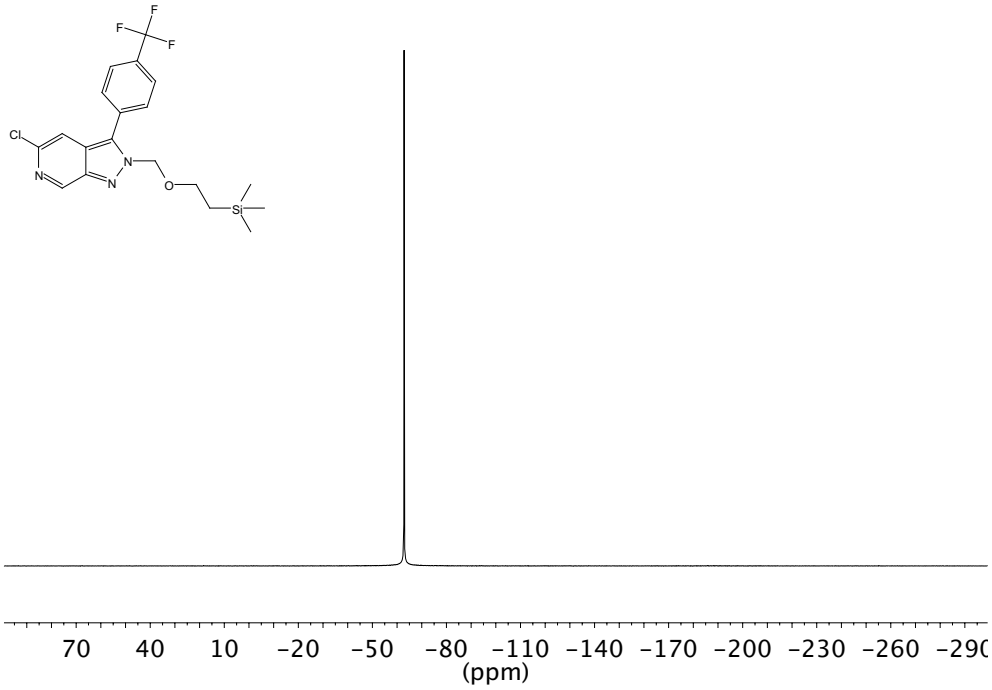

^{1}H NMR (600 MHz, $CDCl_3$) and ^{13}C NMR (151 MHz, $CDCl_3$) of compound **147**

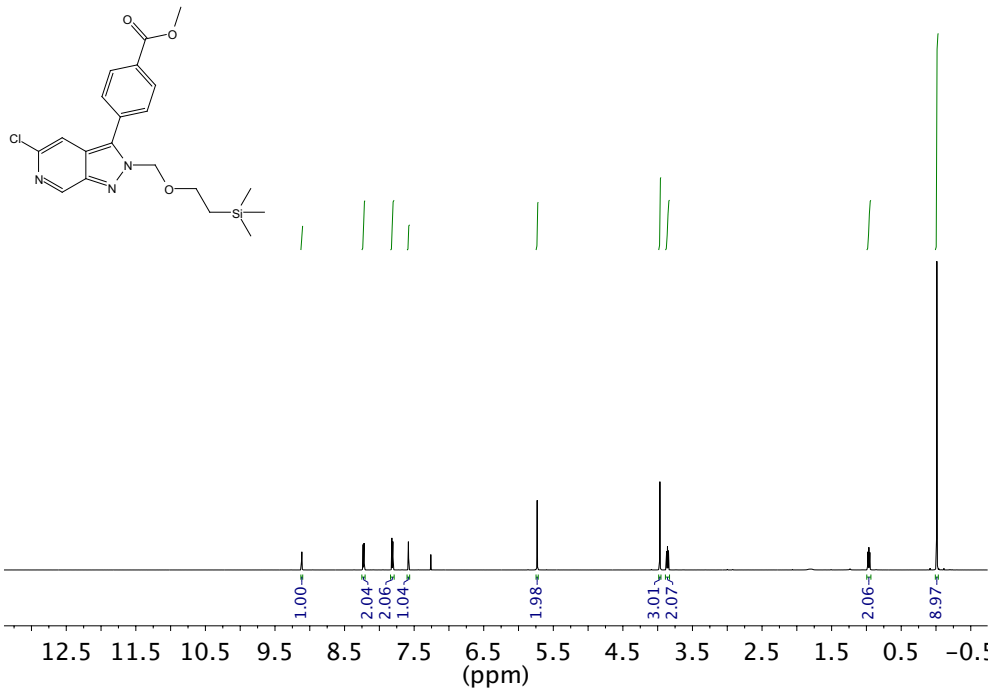

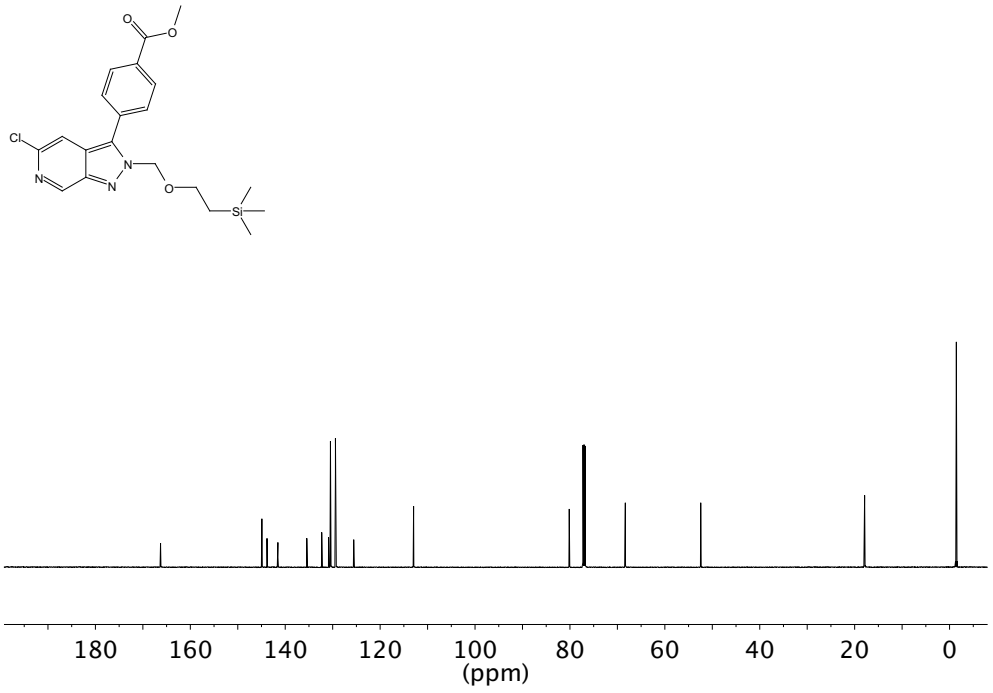

^{1}H NMR (600 MHz, $CDCl_3$) and ^{13}C NMR (151 MHz, $CDCl_3$) of compound **148**

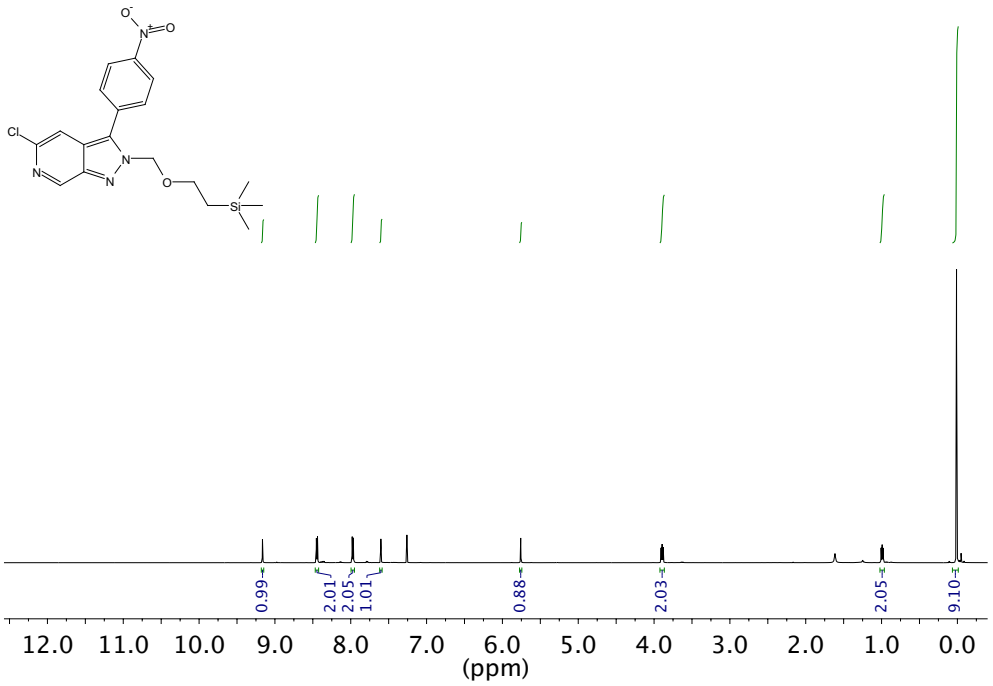

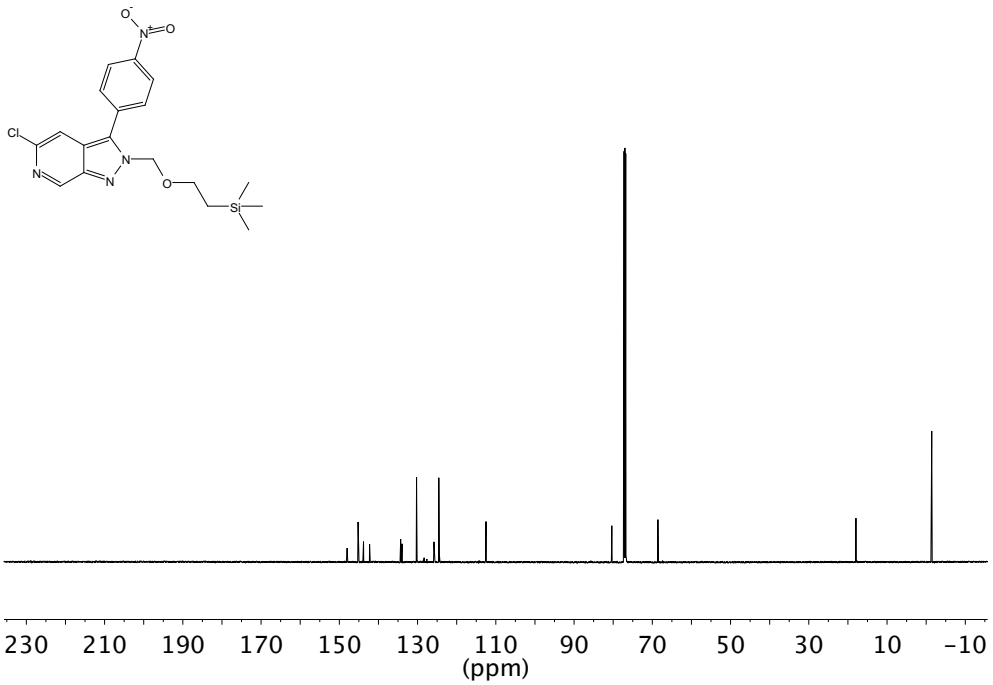

^{1}H NMR (600 MHz, $CDCl_3$) and ^{13}C NMR (151 MHz, $CDCl_3$) of compound **142**

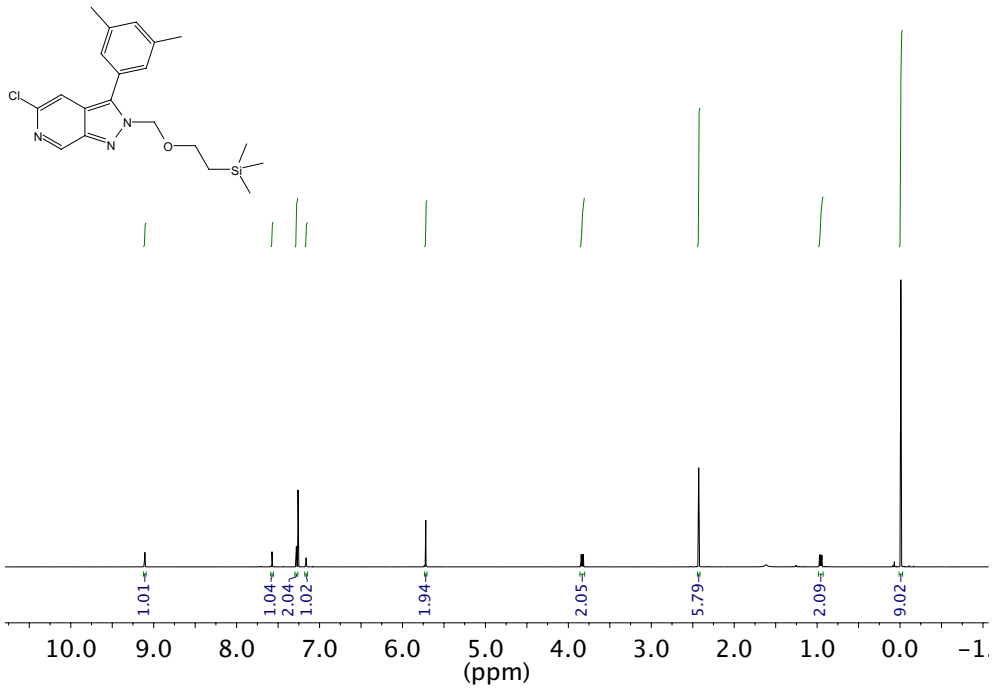

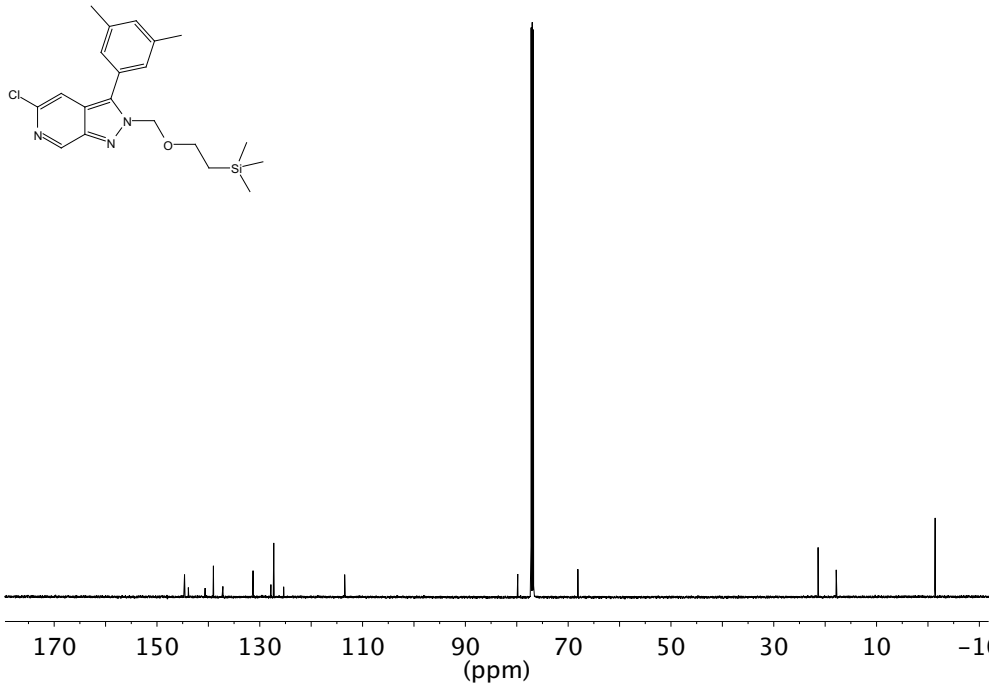

^{1}H NMR (700 MHz, $CDCl_3$) and ^{13}C NMR (176 MHz, $CDCl_3$) of compound **158**

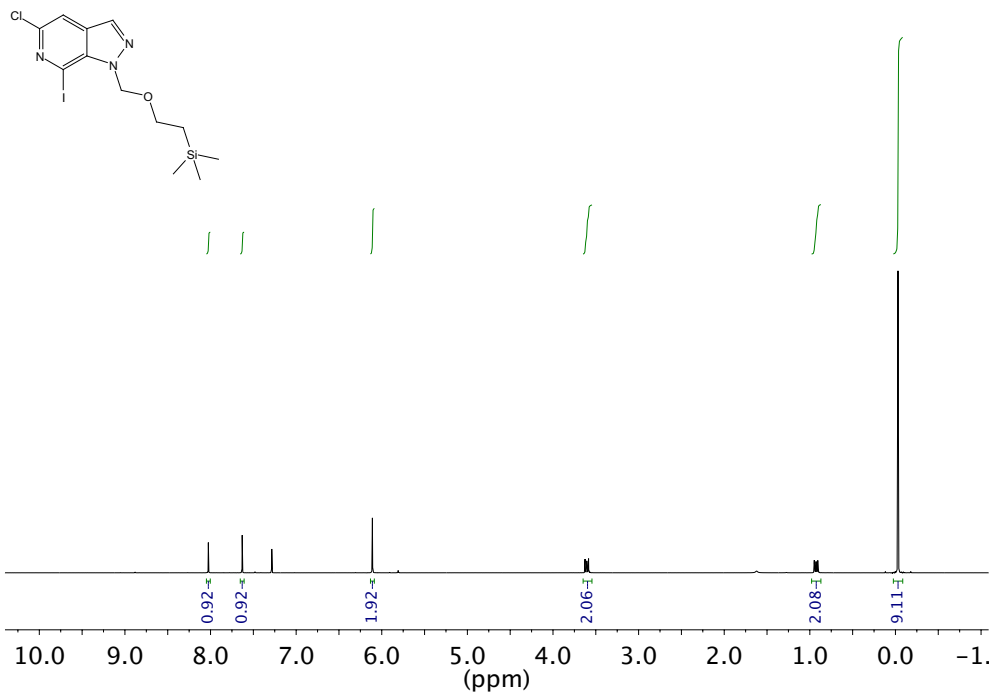

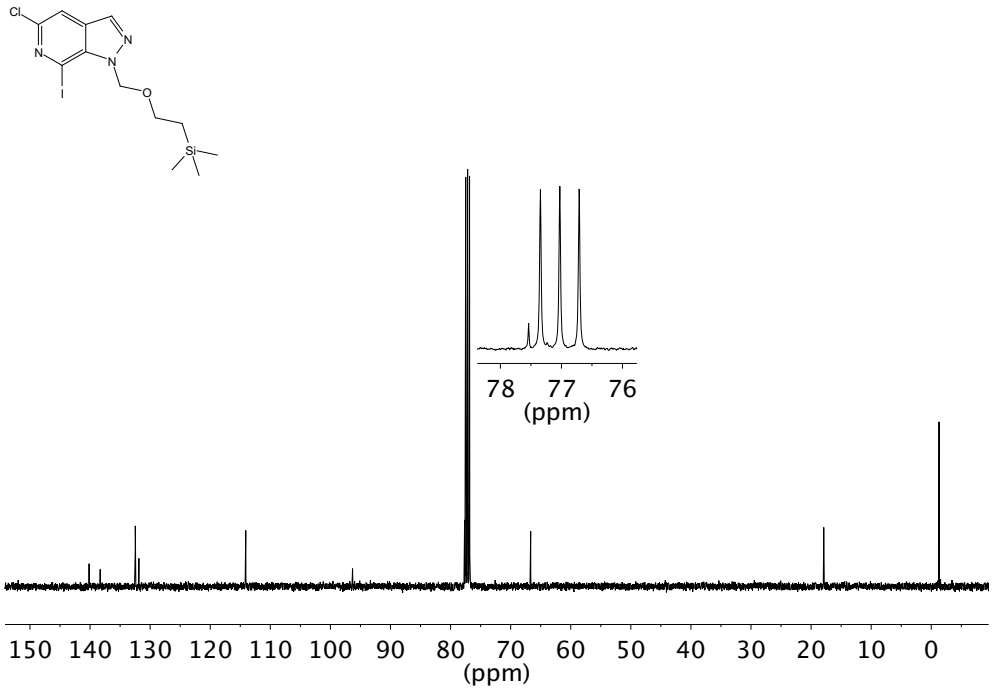

^{1}H NMR (700 MHz, $CDCl_3$) and ^{13}C NMR (176 MHz, $CDCl_3$) of compound **159**

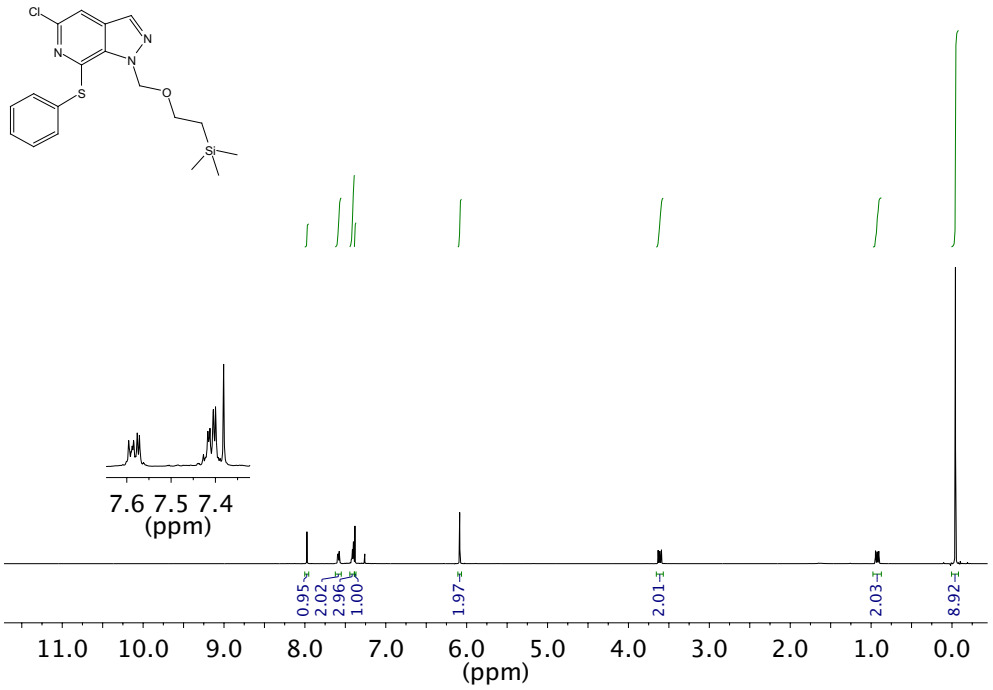

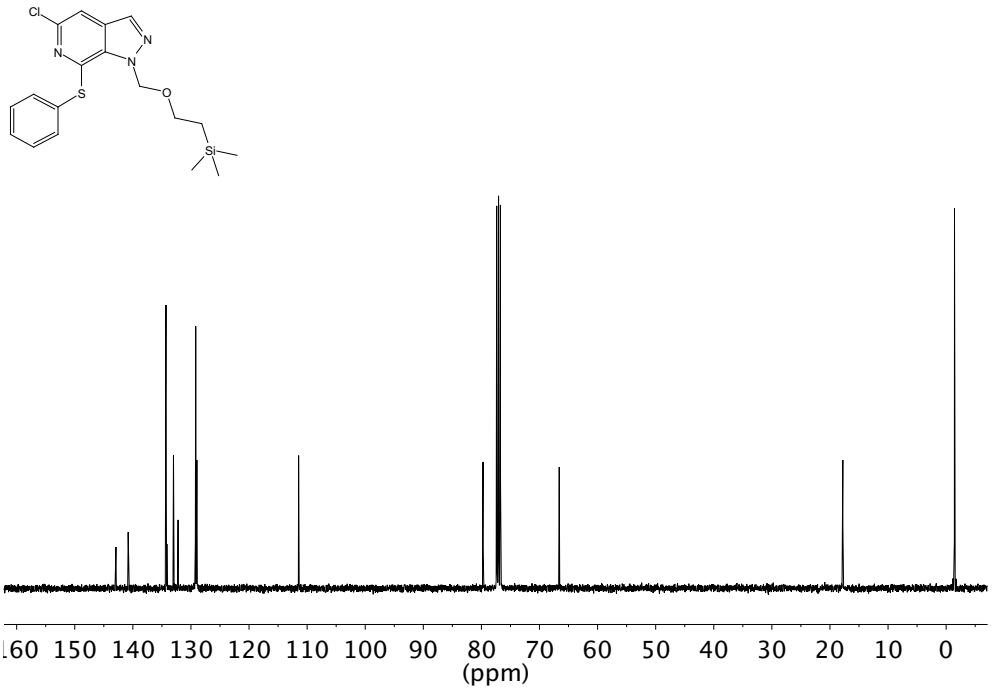

^{1}H NMR (600 MHz, $CDCl_3$) and ^{13}C NMR (151 MHz, $CDCl_3$) of compound **160**

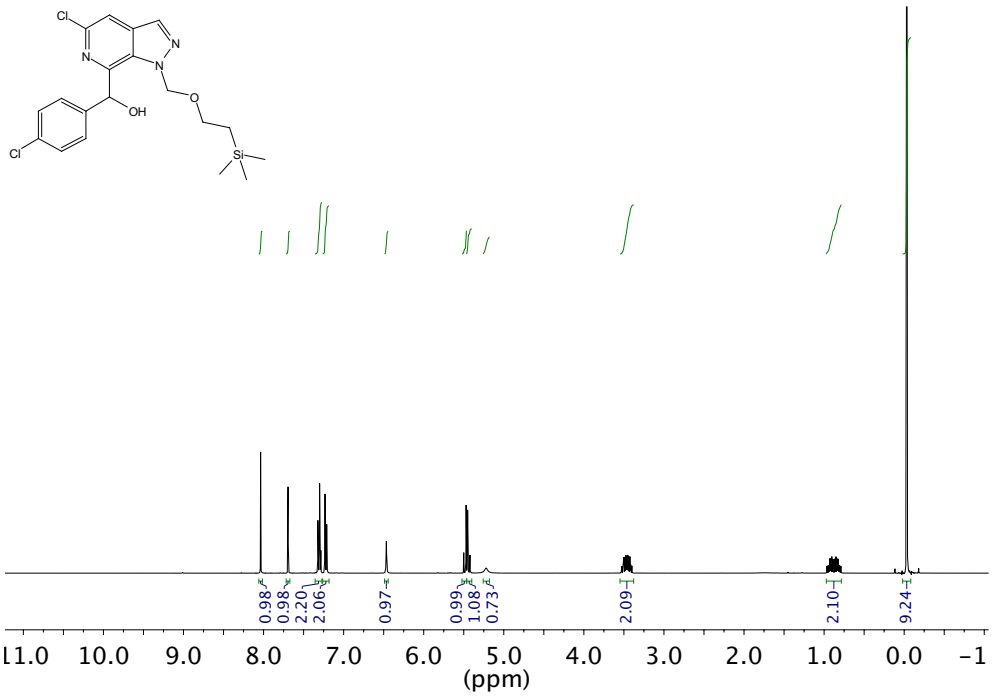

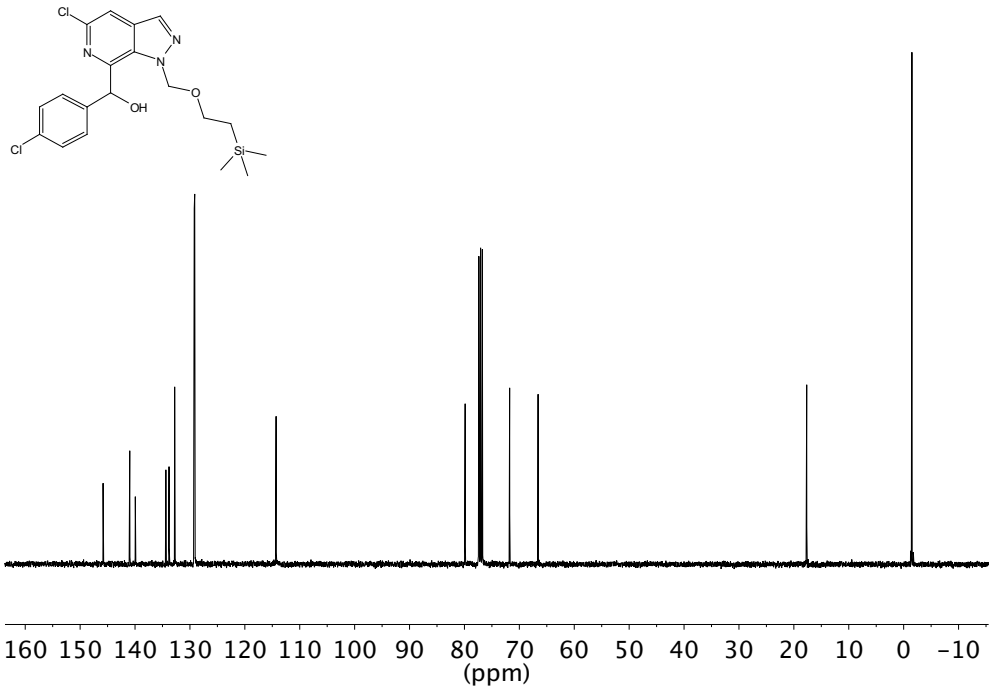

^{1}H NMR (600 MHz, $CDCl_3$) and ^{13}C NMR (151 MHz, $CDCl_3$) of compound **161**

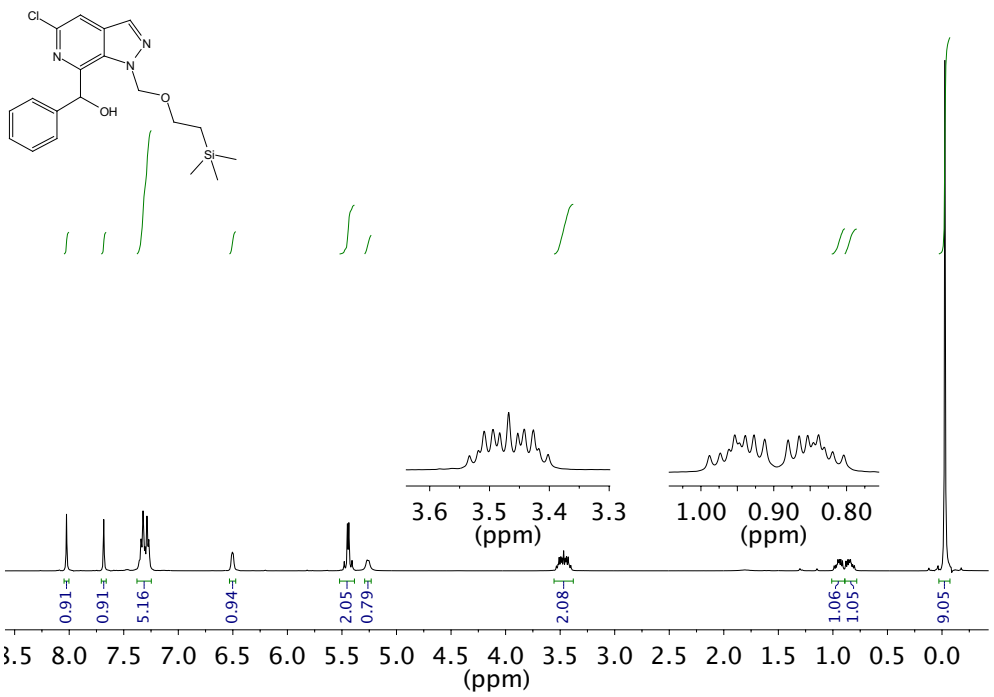

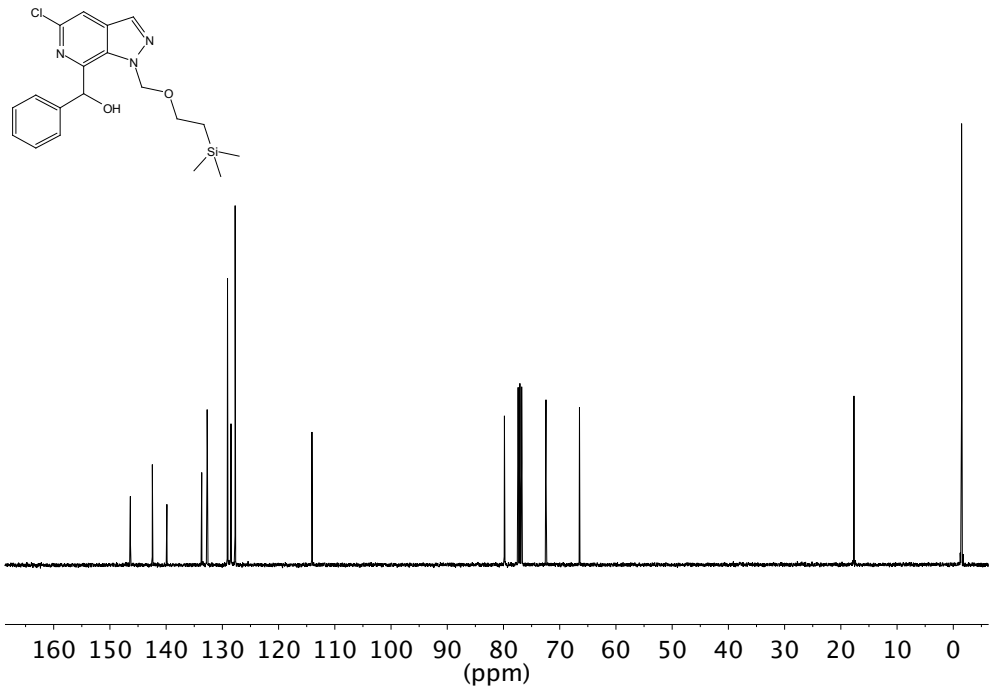

^{1}H NMR (600 MHz, $CDCl_3$) and ^{13}C NMR (151 MHz, $CDCl_3$) of compound **162**

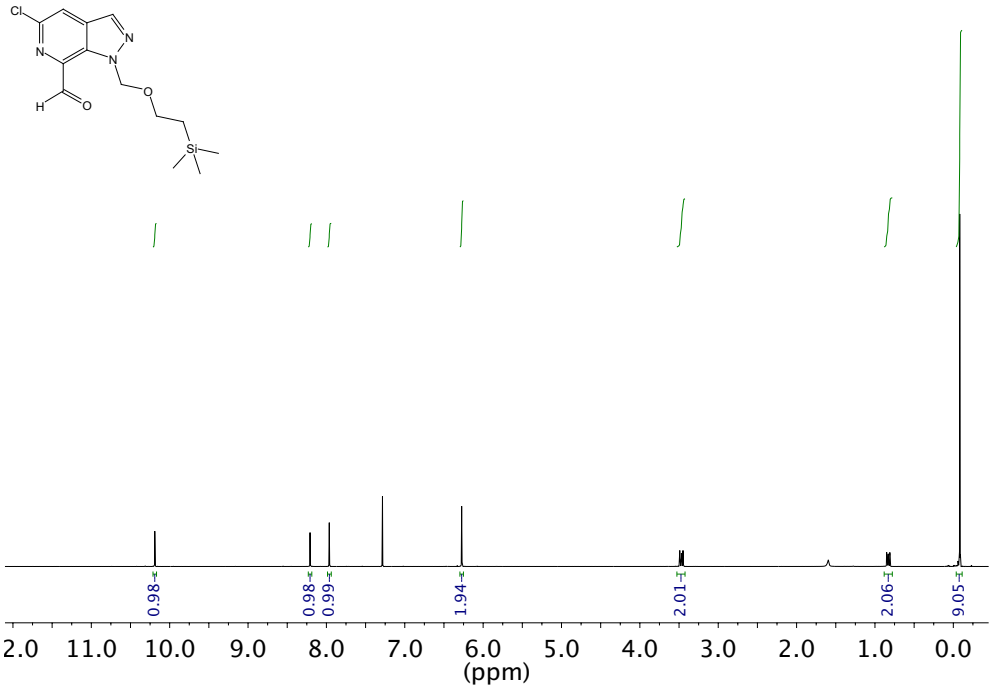

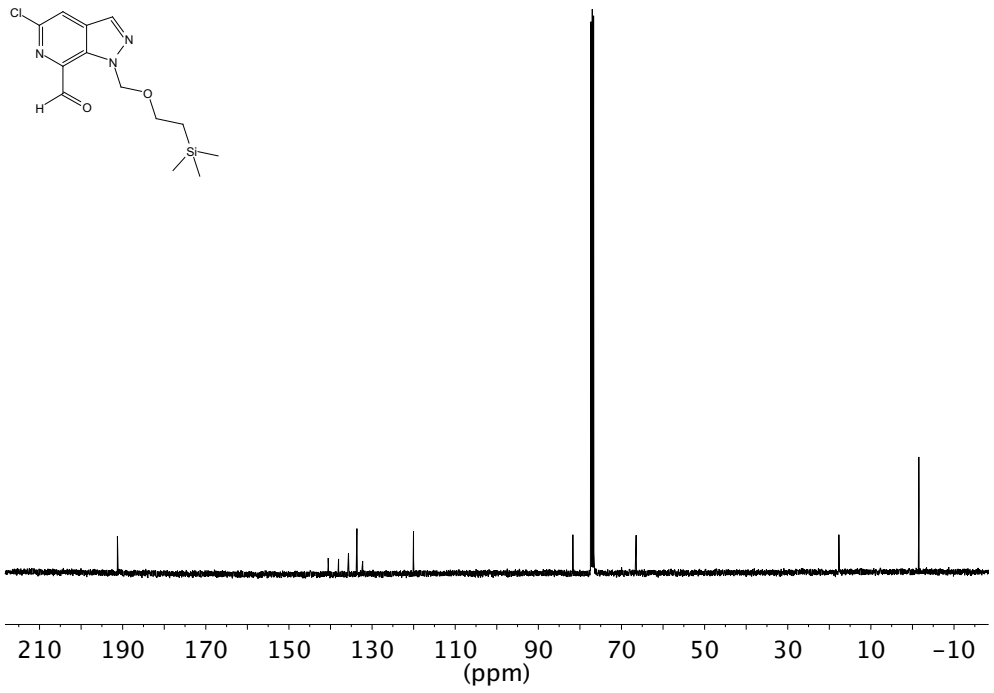

^{1}H NMR (600 MHz, $CDCl_3$) and ^{13}C NMR (151 MHz, $CDCl_3$) of compound **163**

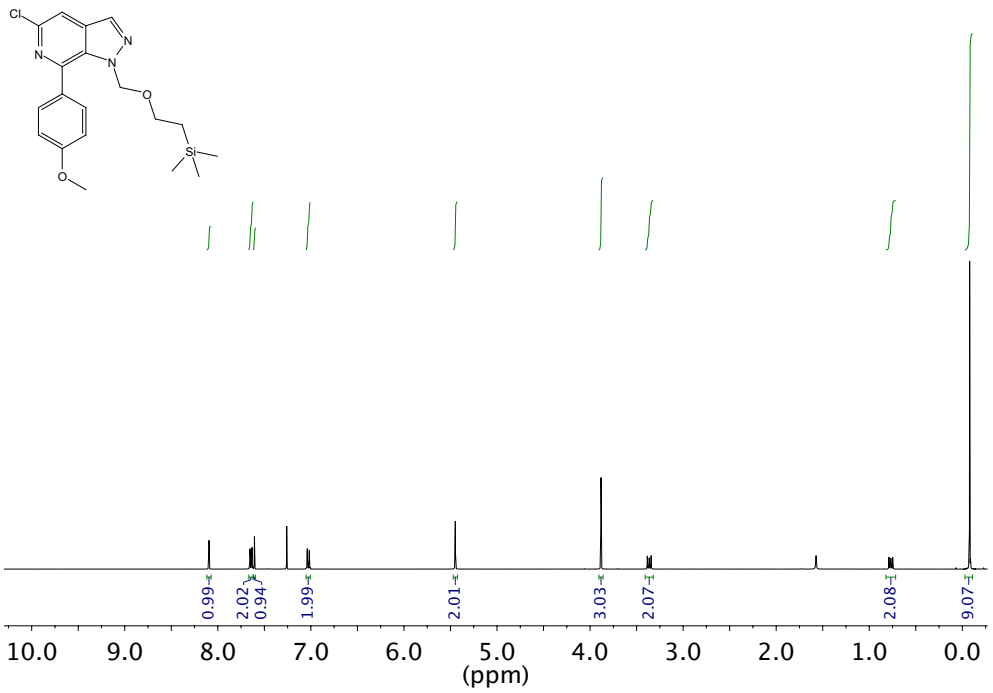

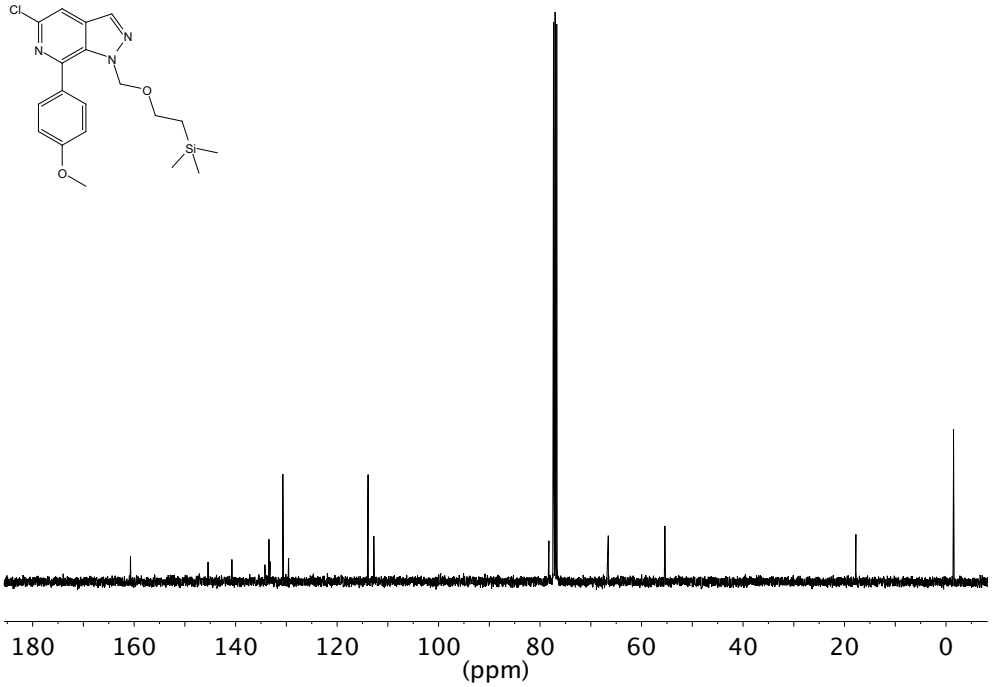

^{1}H NMR (600 MHz, $CDCl_3$) and ^{13}C NMR (151 MHz, $CDCl_3$) of compound **164**

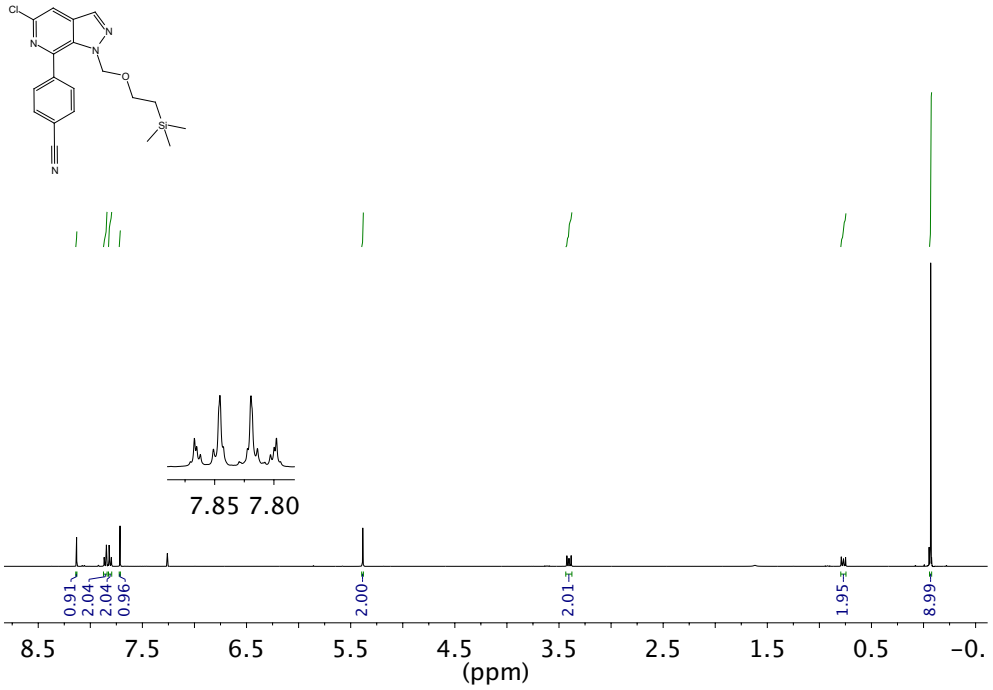

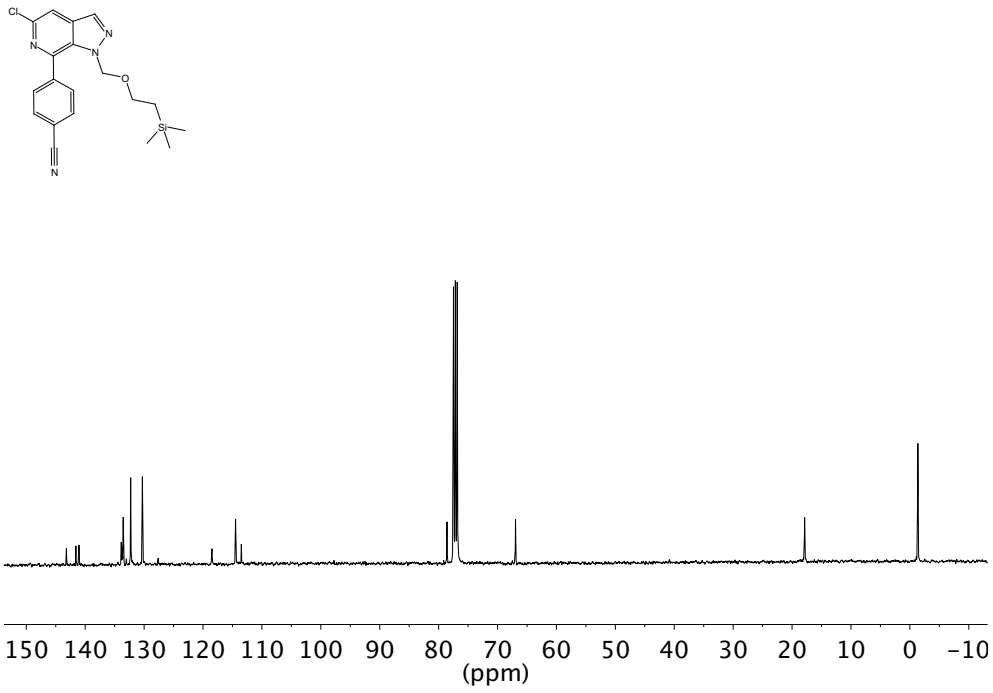

^{1}H NMR (700 MHz, $CDCl_3$) and ^{13}C NMR (176 MHz, $CDCl_3$) of compound **165**

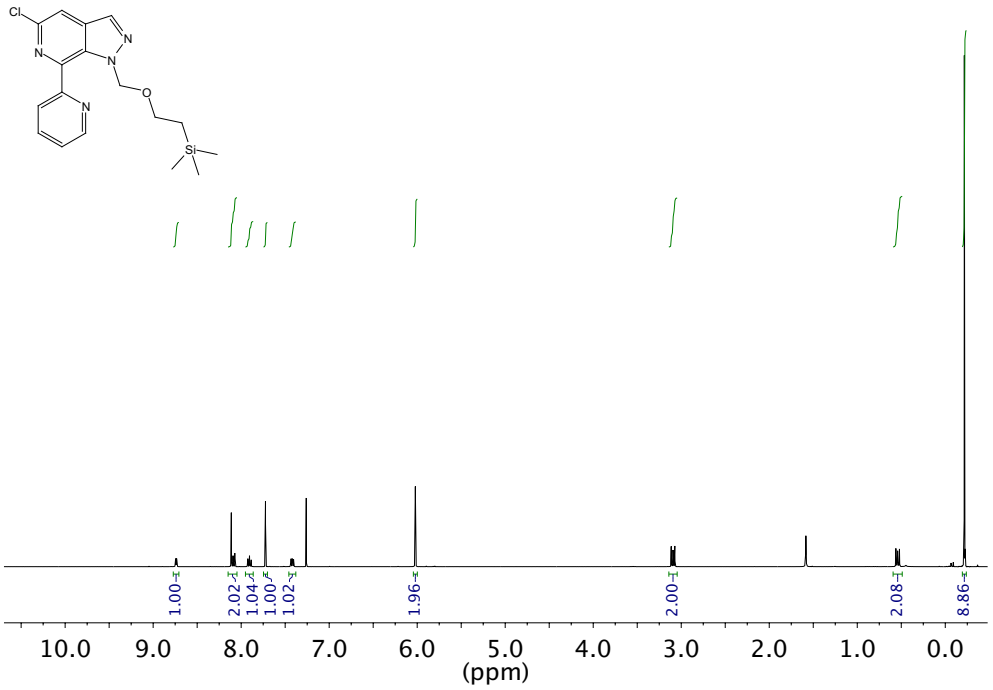

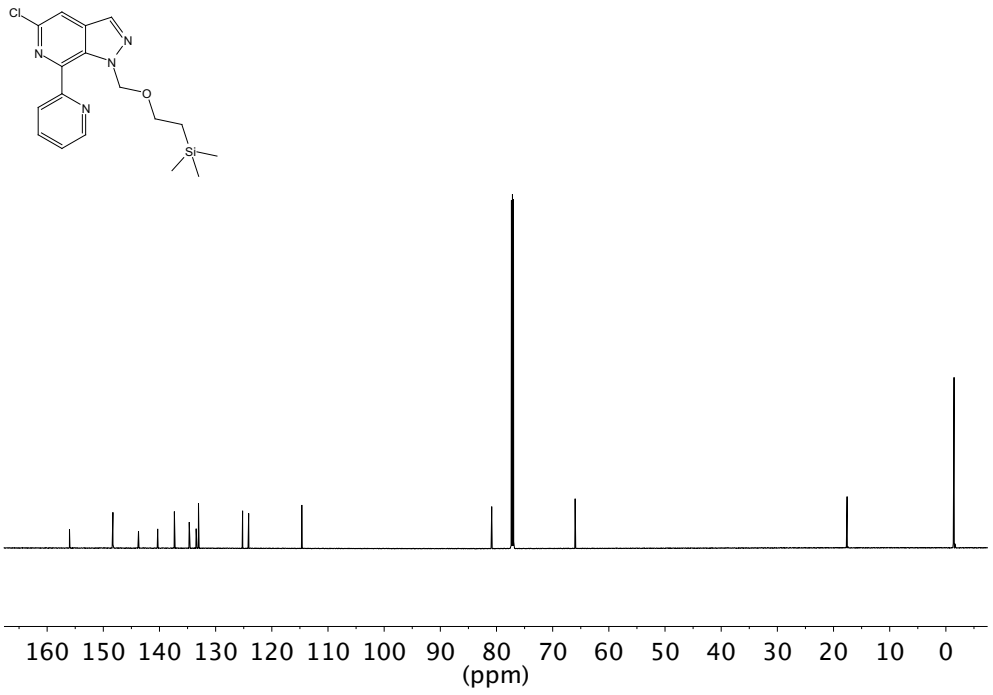

^{1}H NMR (600 MHz, $CDCl_3$) and ^{13}C NMR (151 MHz, $CDCl_3$) of compound **166**

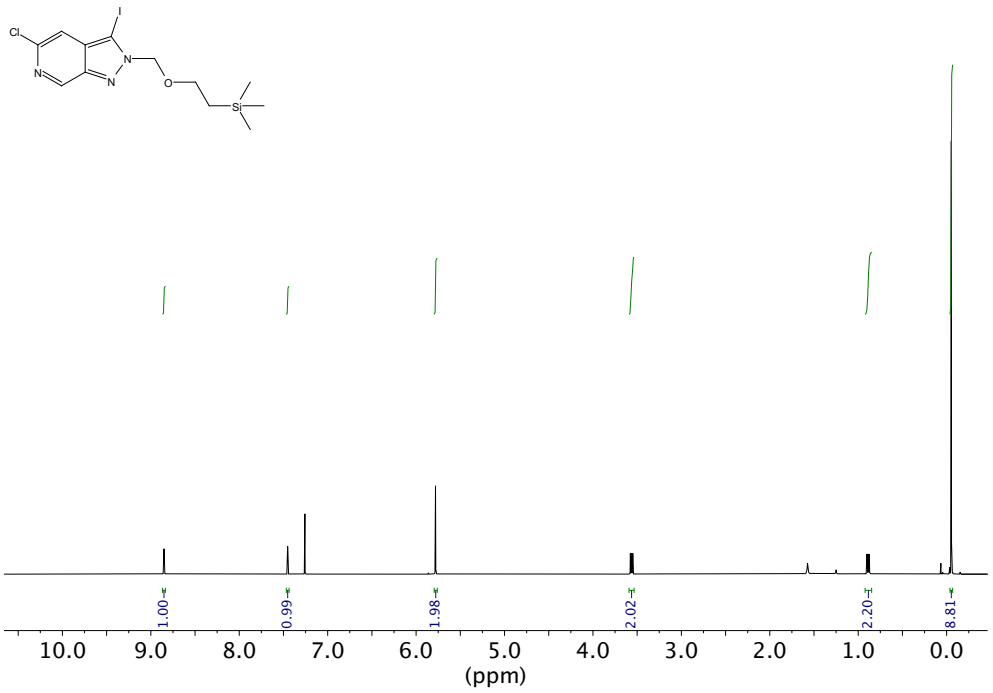

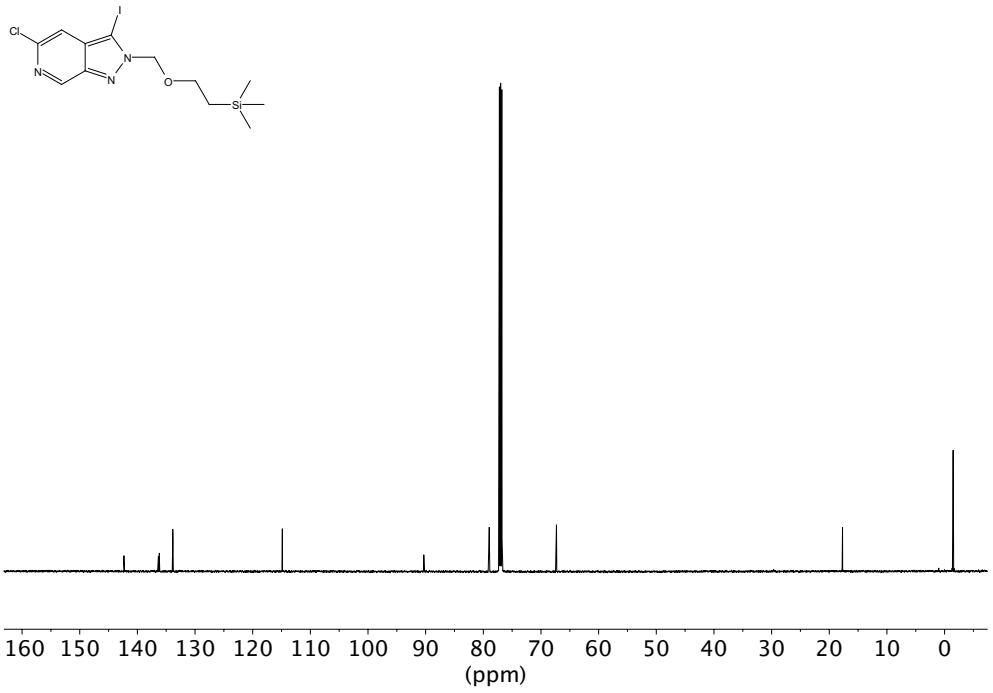

^{1}H NMR (600 MHz, $CDCl_3$) and ^{13}C NMR (151 MHz, $CDCl_3$) of compound **184**

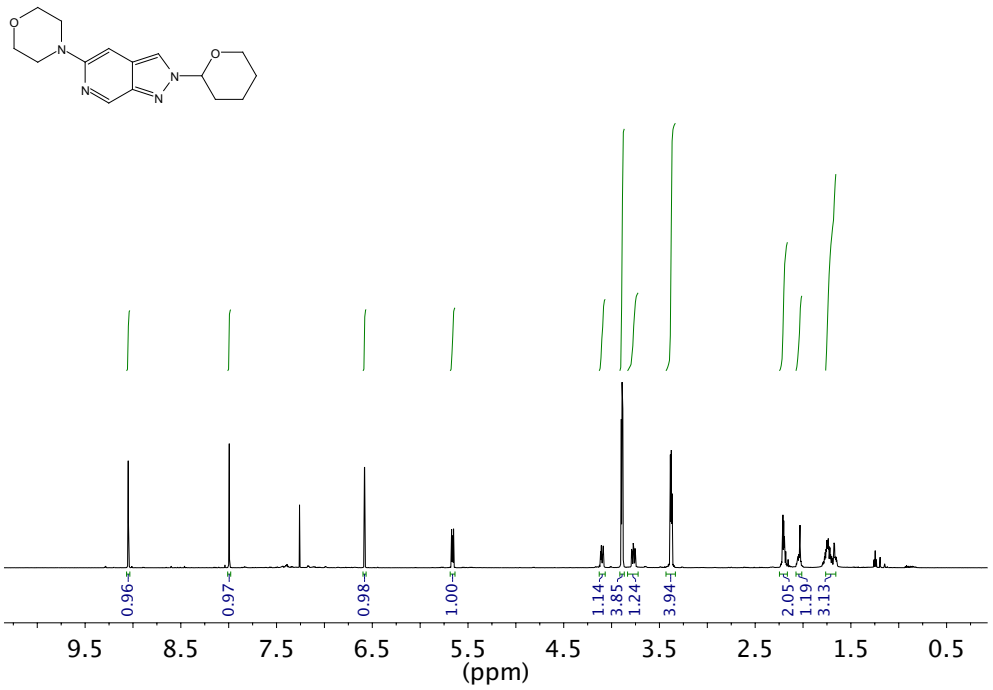

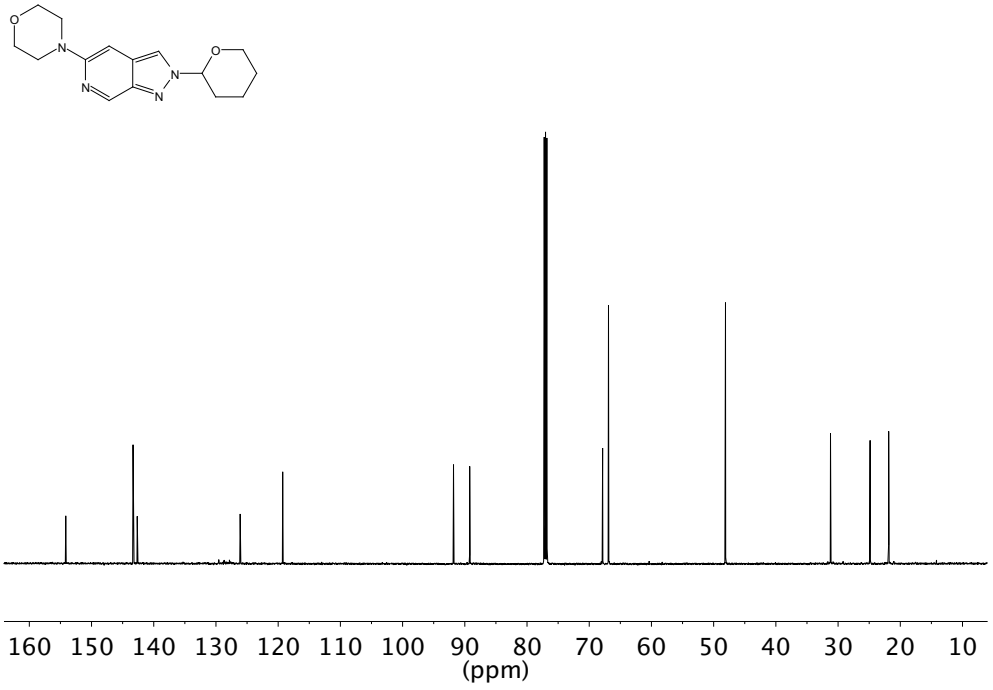

^{1}H NMR (600 MHz, $CDCl_3$) and ^{13}C NMR (151 MHz, $CDCl_3$) of compound **192**

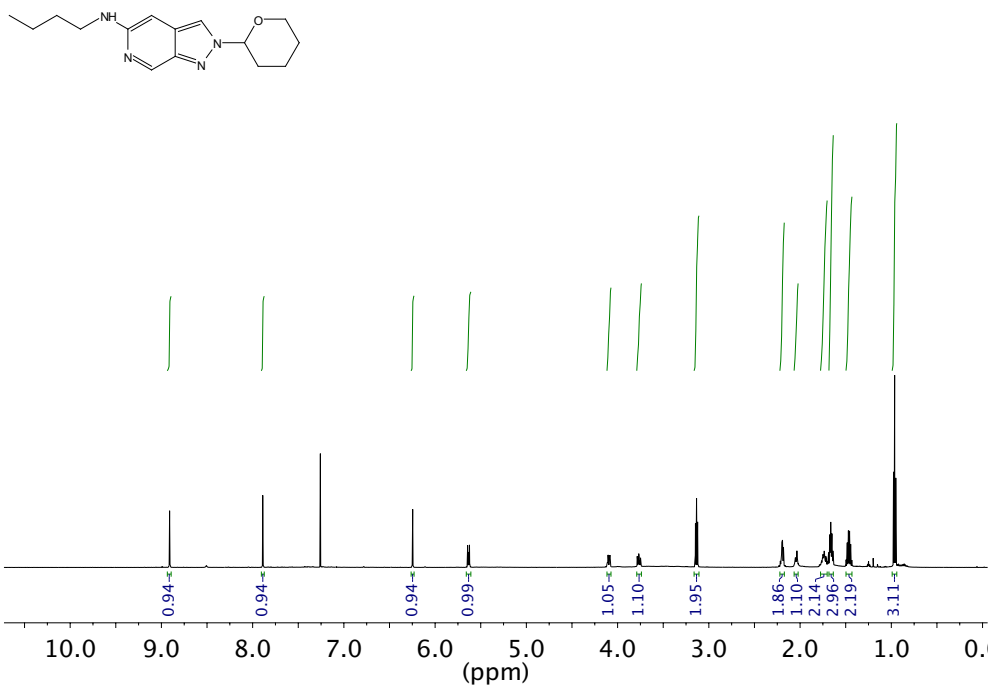

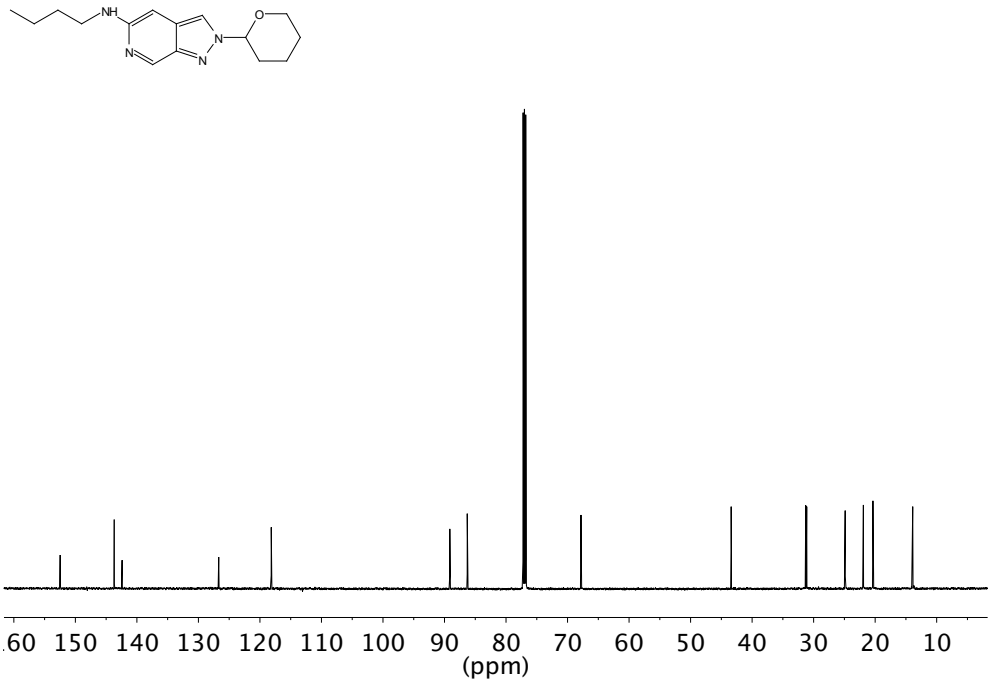

^{1}H NMR (600 MHz, $CDCl_3$) and ^{13}C NMR (151 MHz, $CDCl_3$) of compound **194**

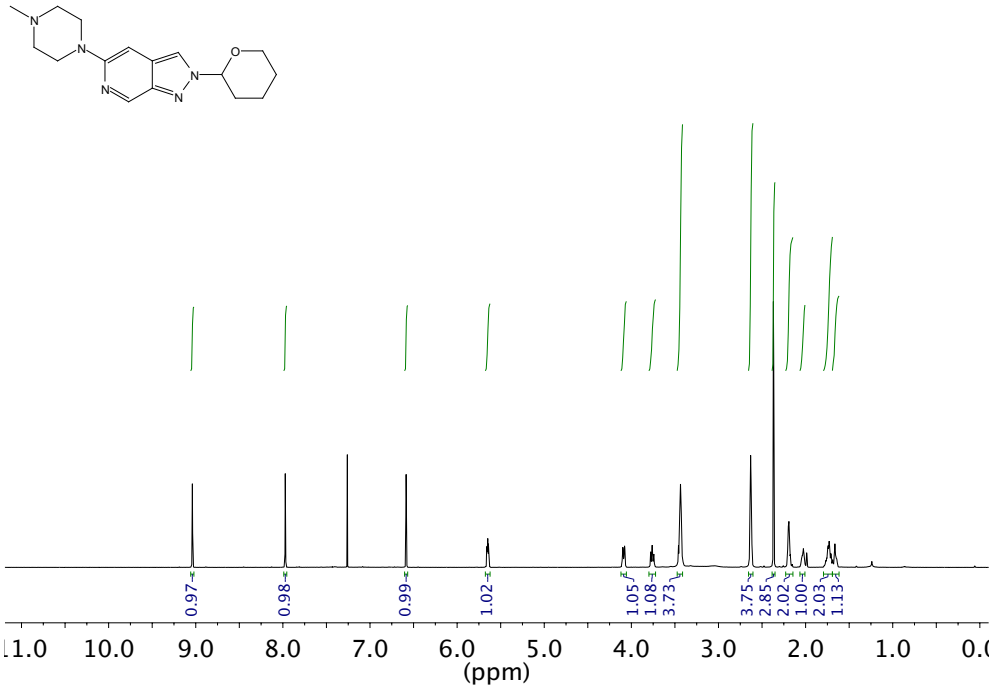

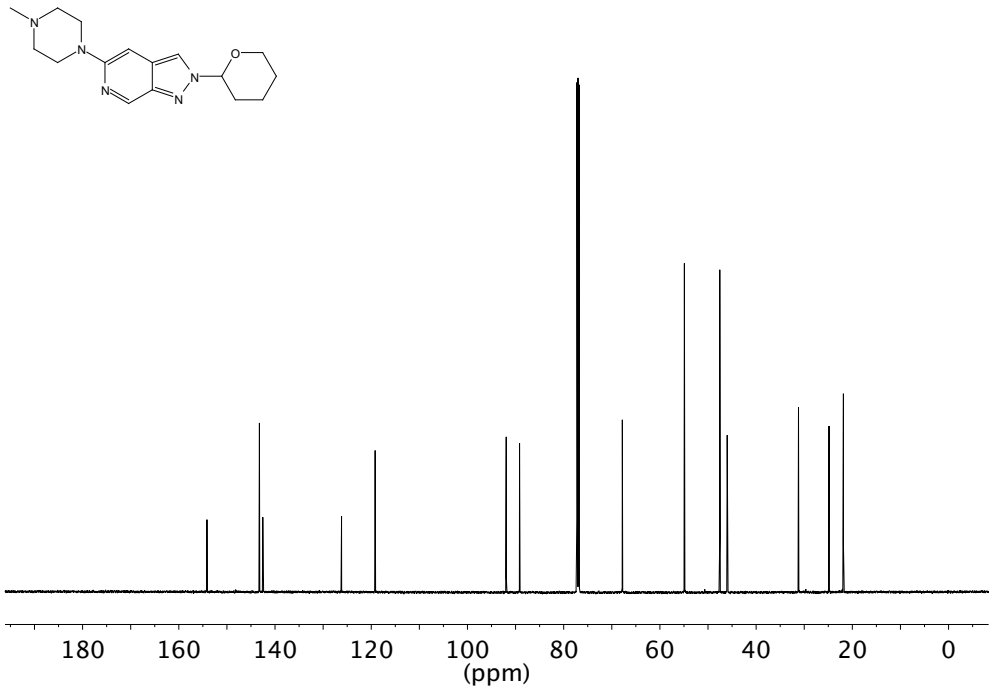

^{1}H NMR (600 MHz, $CDCl_3$) and ^{13}C NMR (151 MHz, $CDCl_3$) of compound **195**

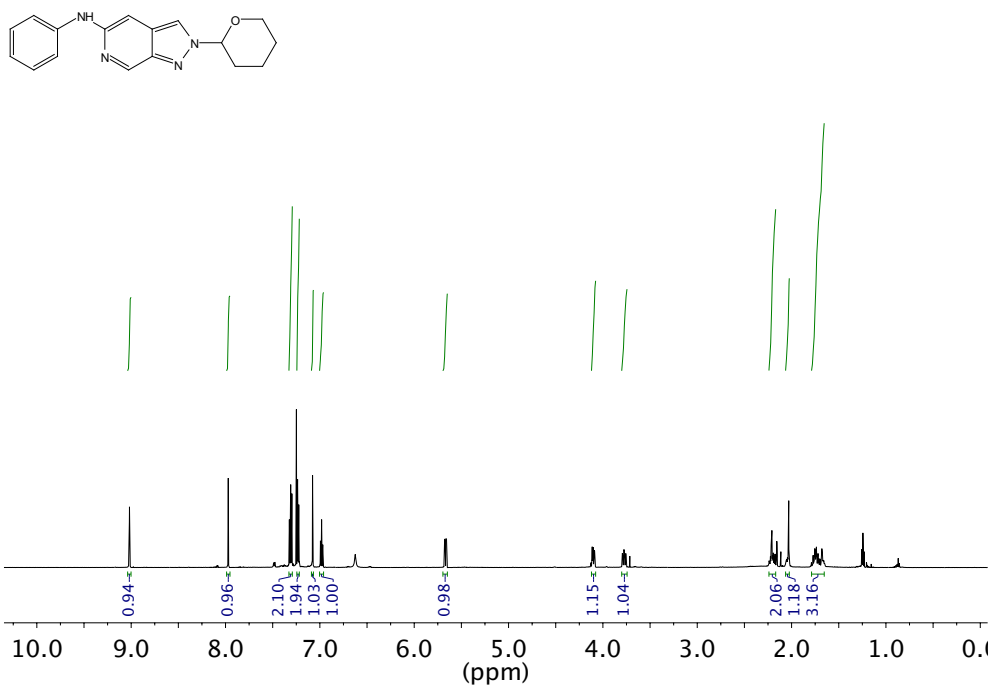

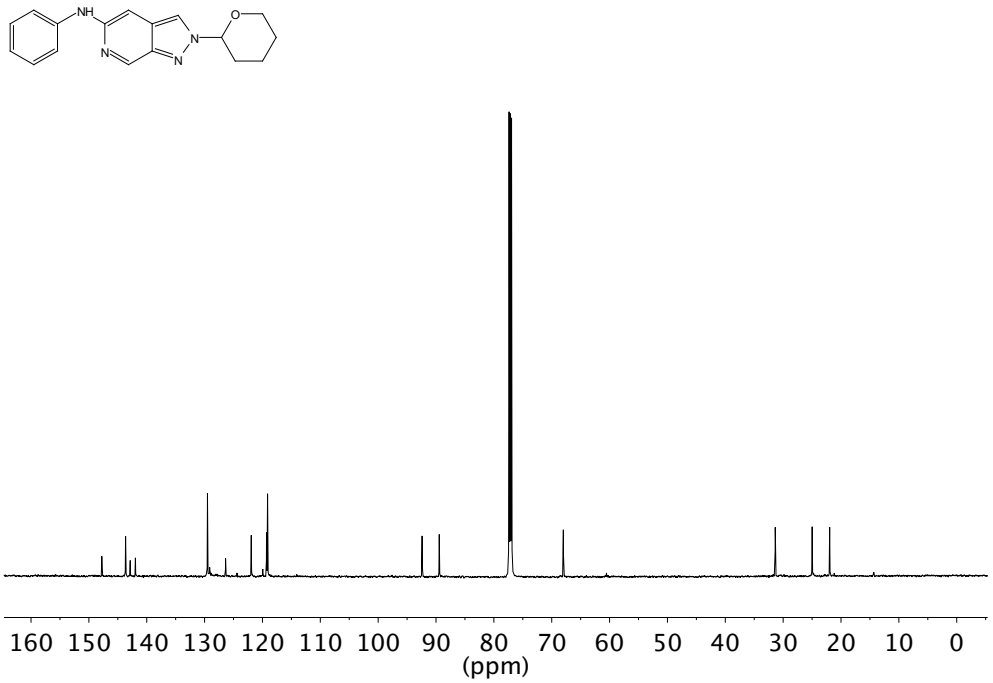

^{1}H NMR (600 MHz, $CDCl_3$) and ^{13}C NMR (151 MHz, $CDCl_3$) of compound **196**

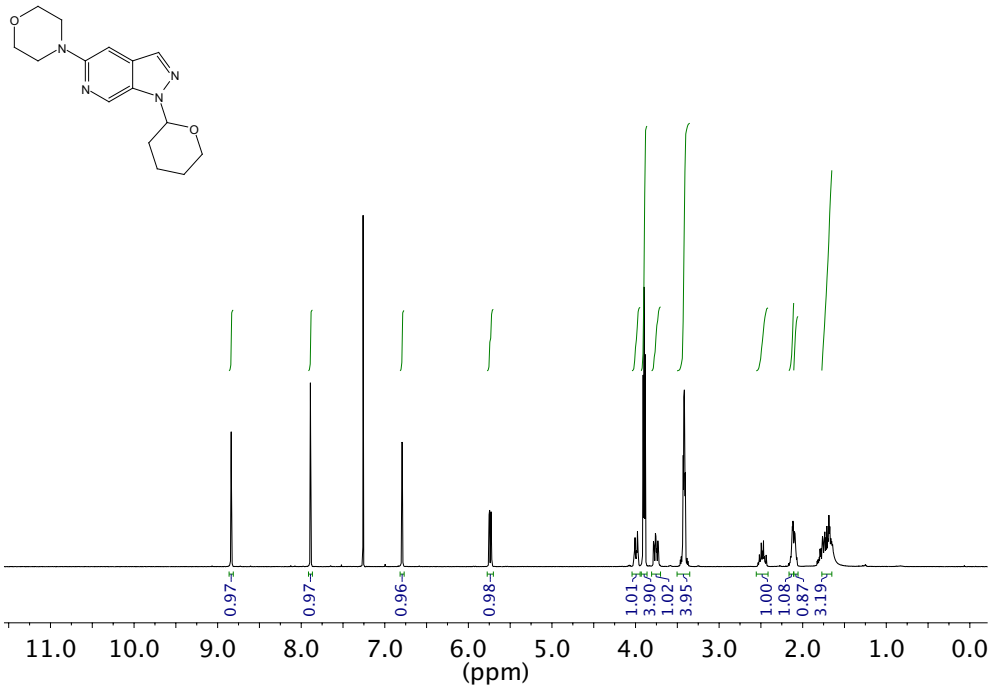

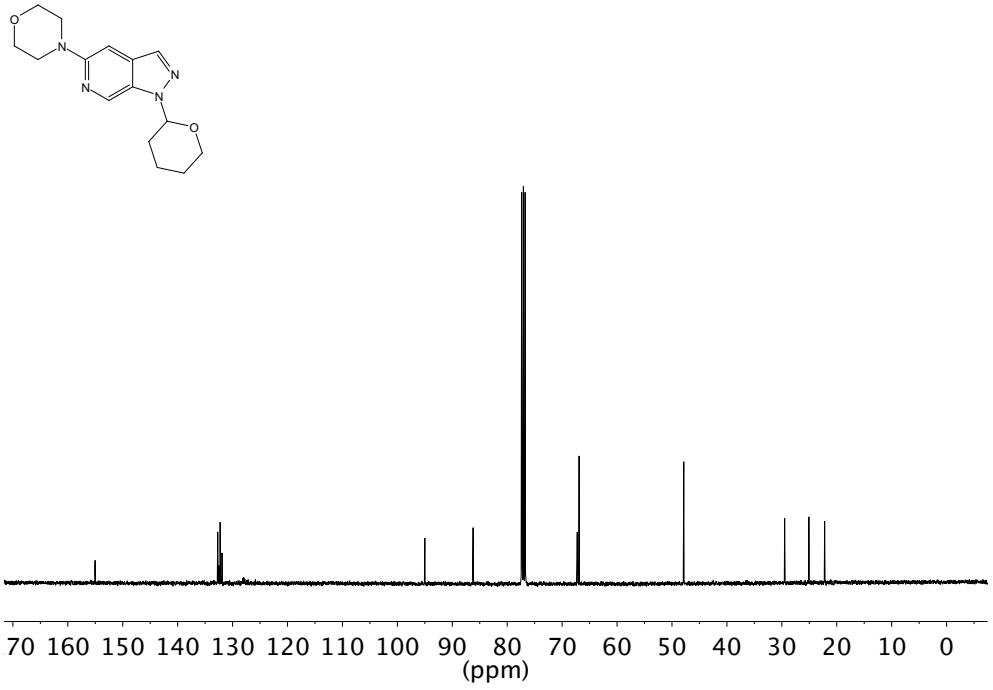

^{1}H NMR (600 MHz, $CDCl_3$) and ^{13}C NMR (151 MHz, $CDCl_3$) of compound **193**

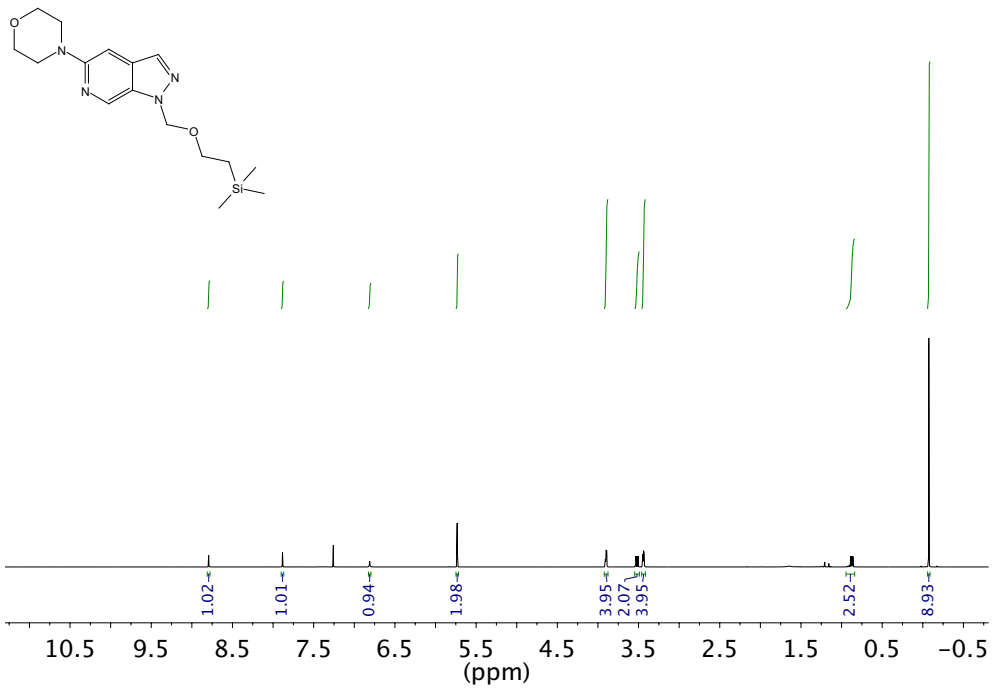

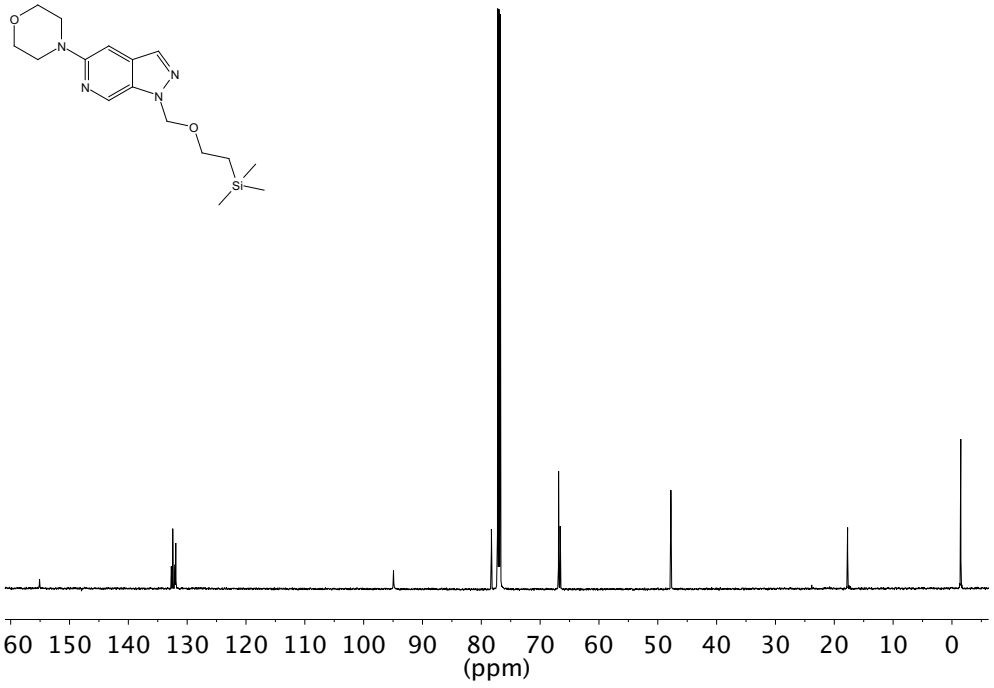

^{1}H NMR (600 MHz, $CDCl_3$) and ^{13}C NMR (151 MHz, $CDCl_3$) of compound **197**

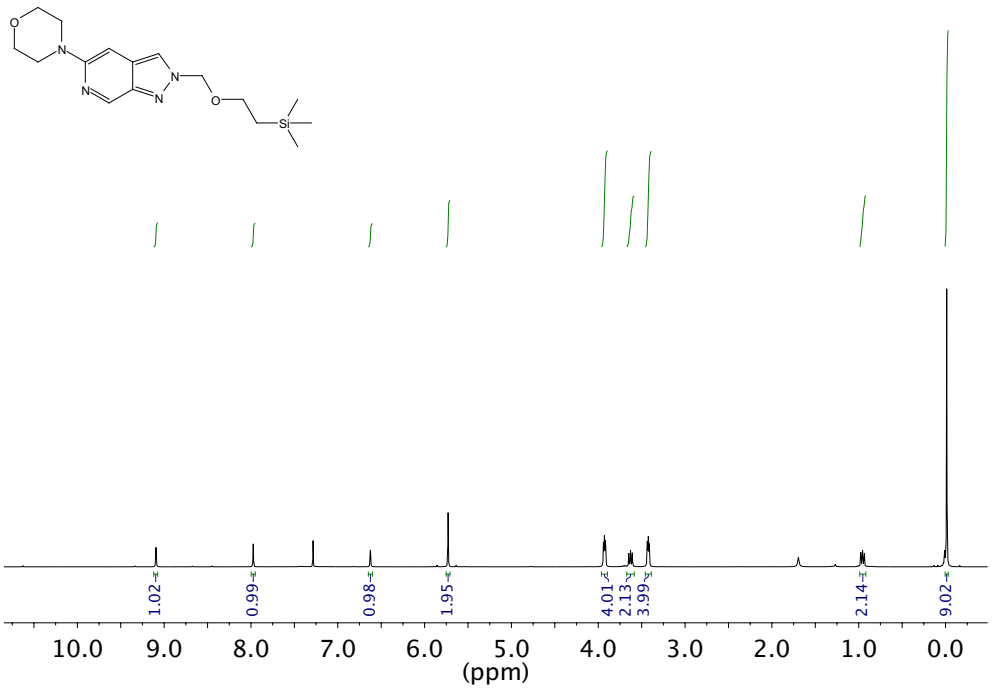

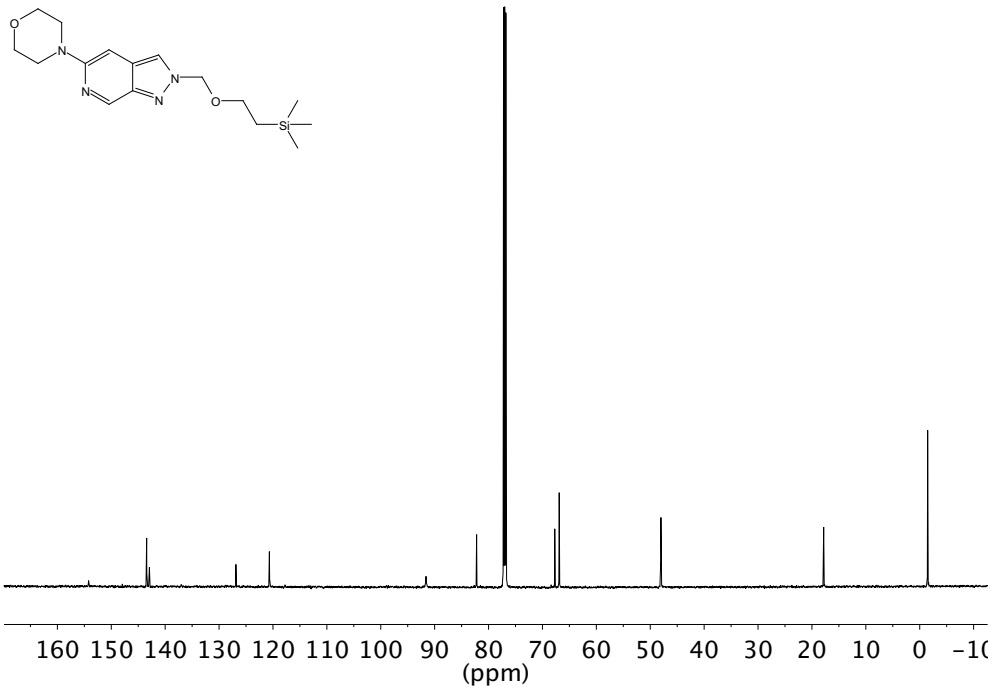

^{1}H NMR (600 MHz, $CDCl_3$) and ^{13}C NMR (151 MHz, $CDCl_3$) of compound **211**

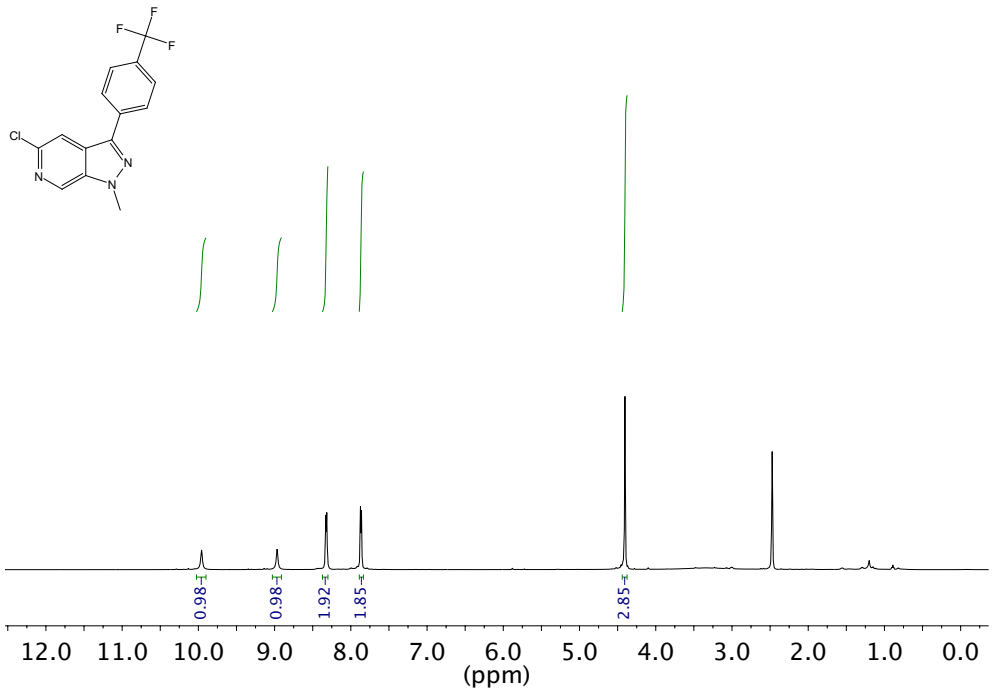

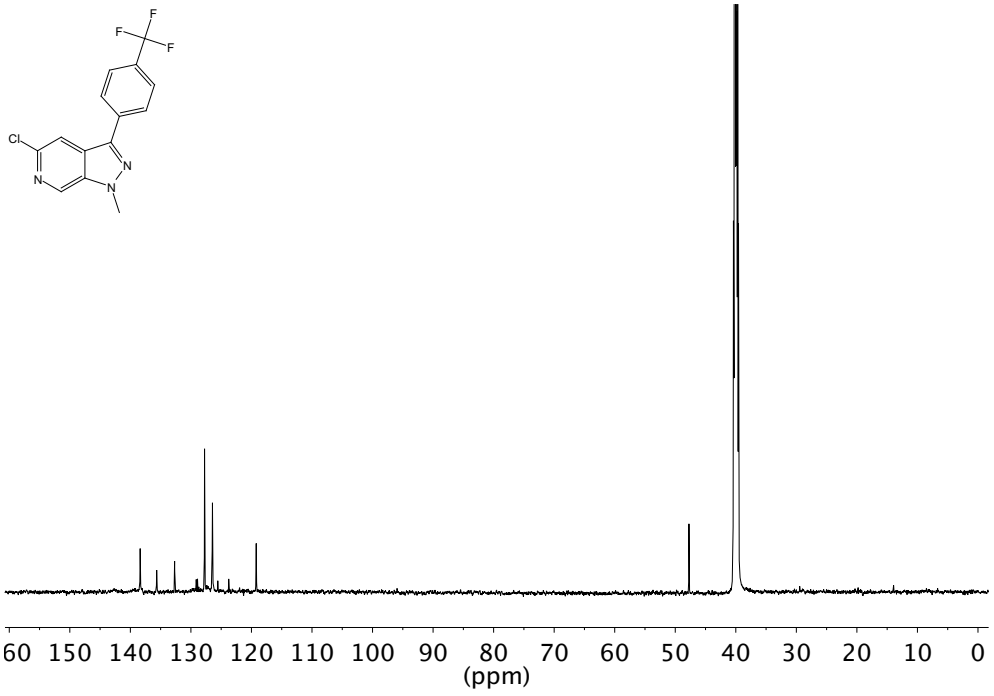

^{19}F NMR (376 MHz, $CDCl_3$) and ^{13}C NMR (151 MHz, $CDCl_3$) (VT = 90 ˚C) of compound **211**

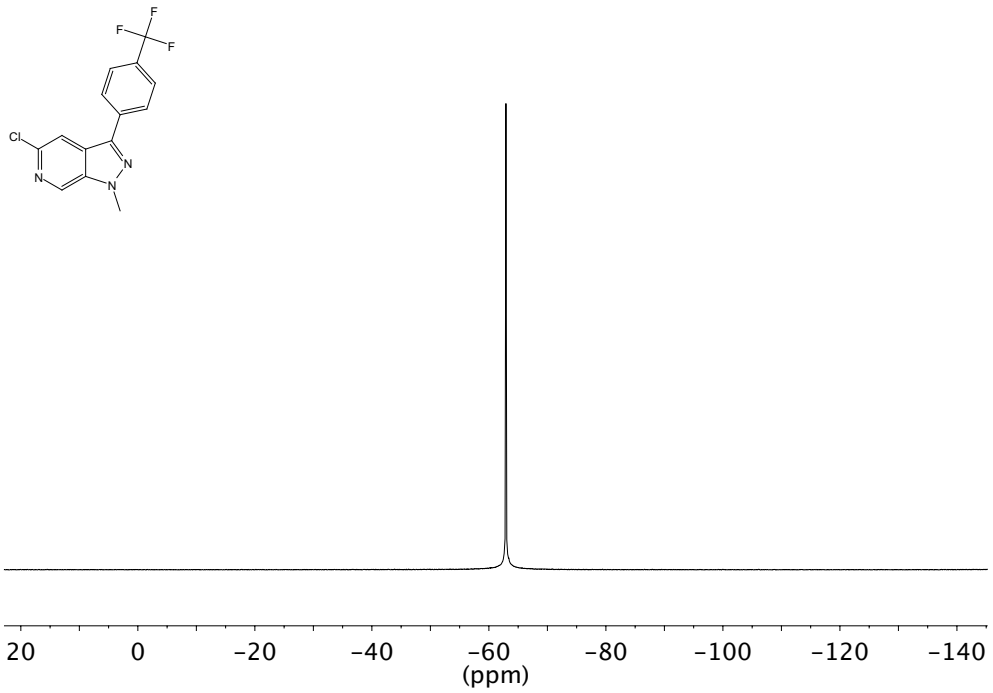

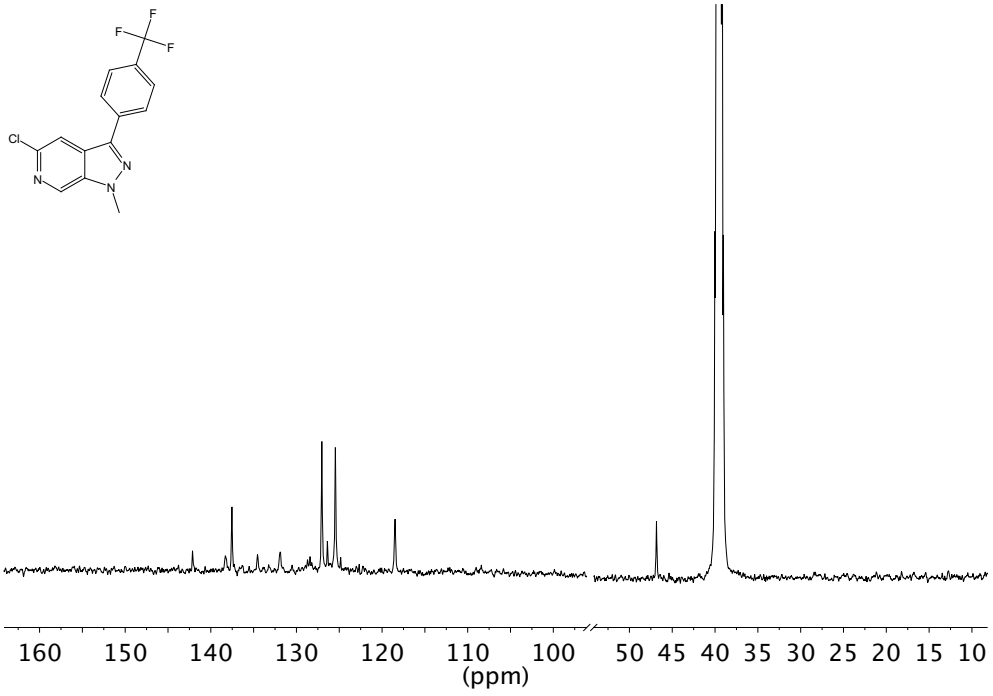

^{1}H NMR (400 MHz, DMSO) and ^{1}H NMR (600 MHz, DMSO+TFA) of compound **214**

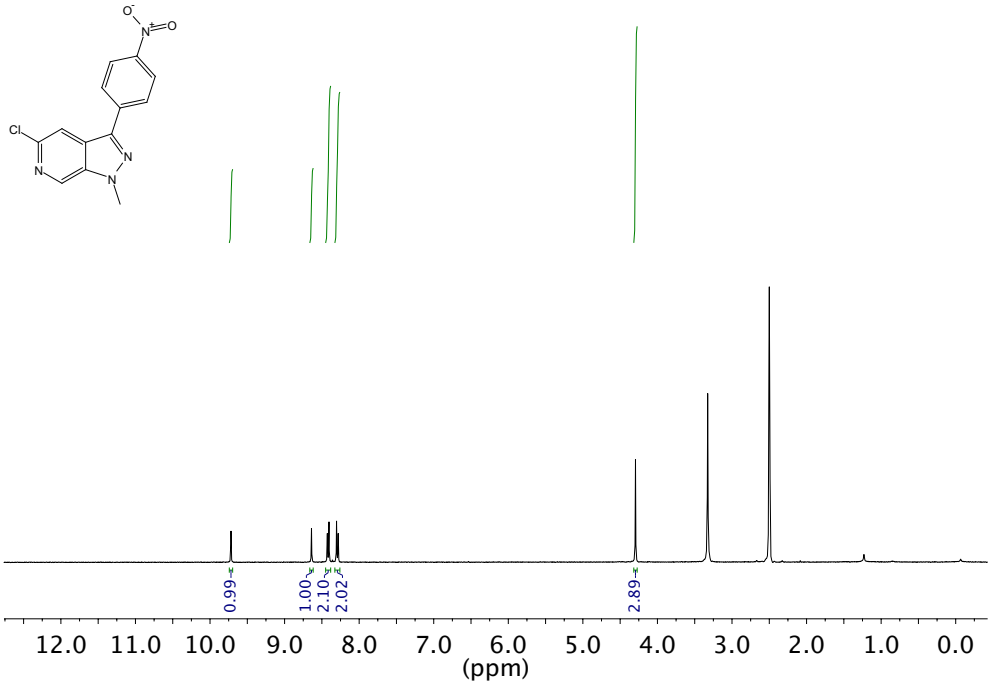

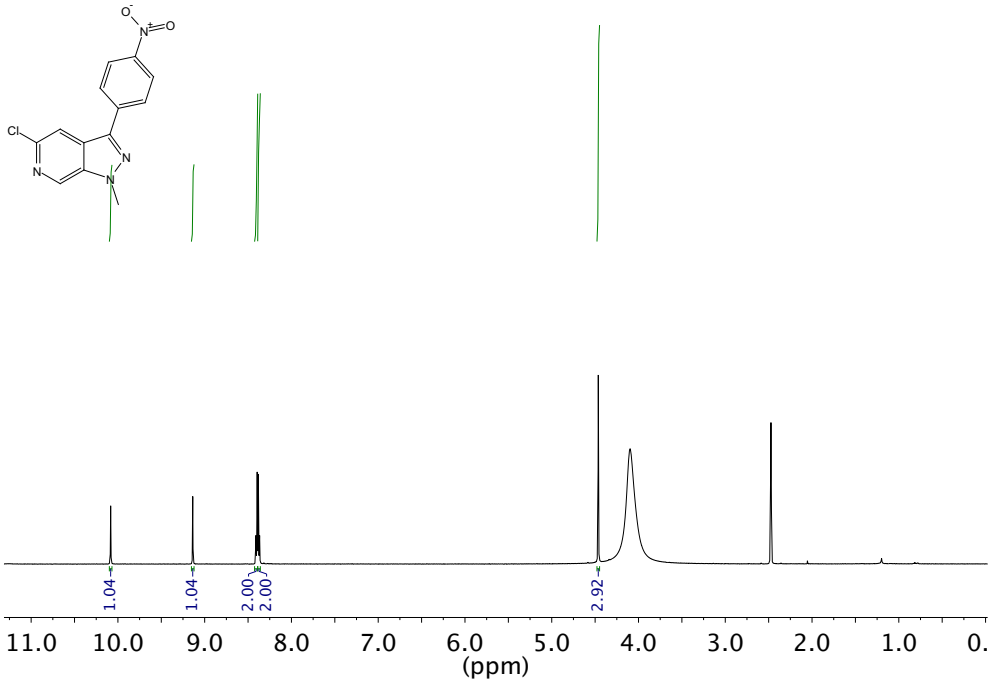

^{13}C NMR (151 MHz, DMSO+TFA) of compound **214**

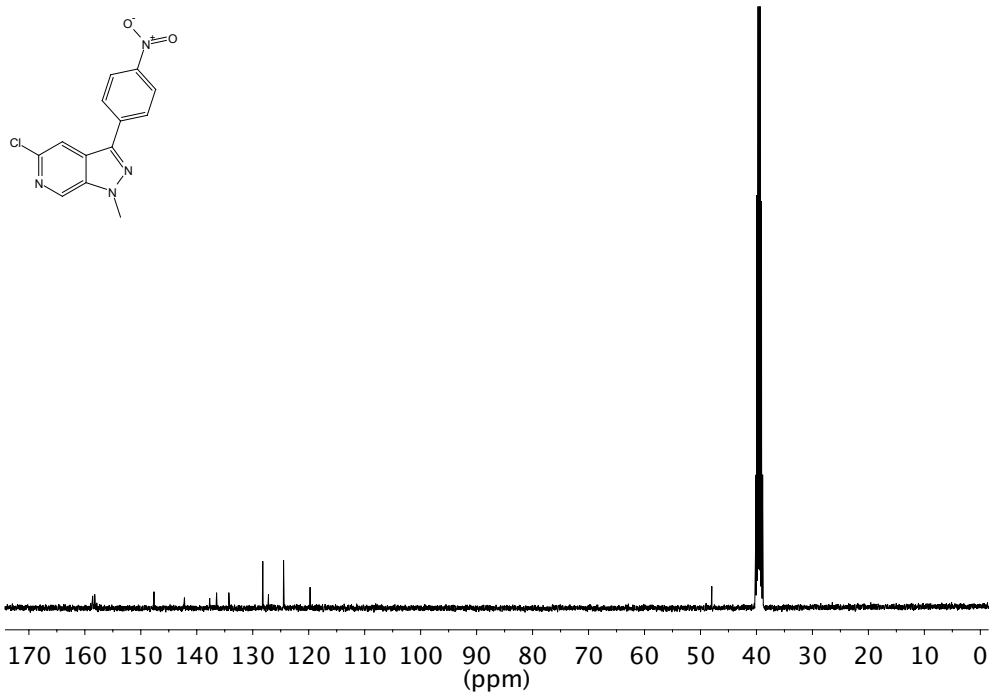

^{1}H NMR (700 MHz, $CDCl_3$) and ^{13}C NMR (176 MHz, $CDCl_3$) of compound **216**

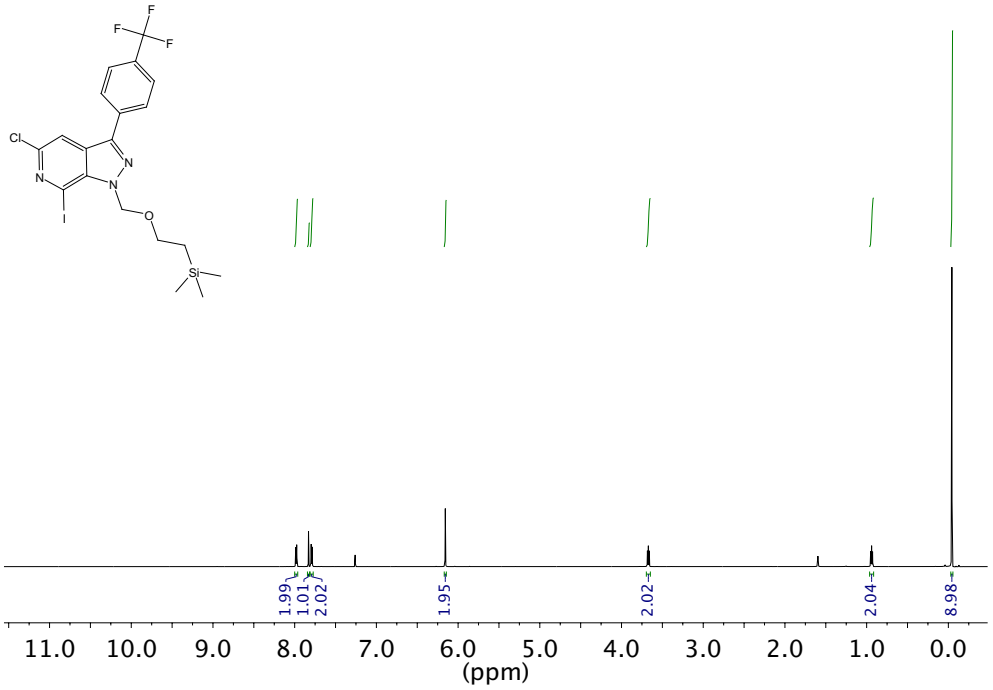

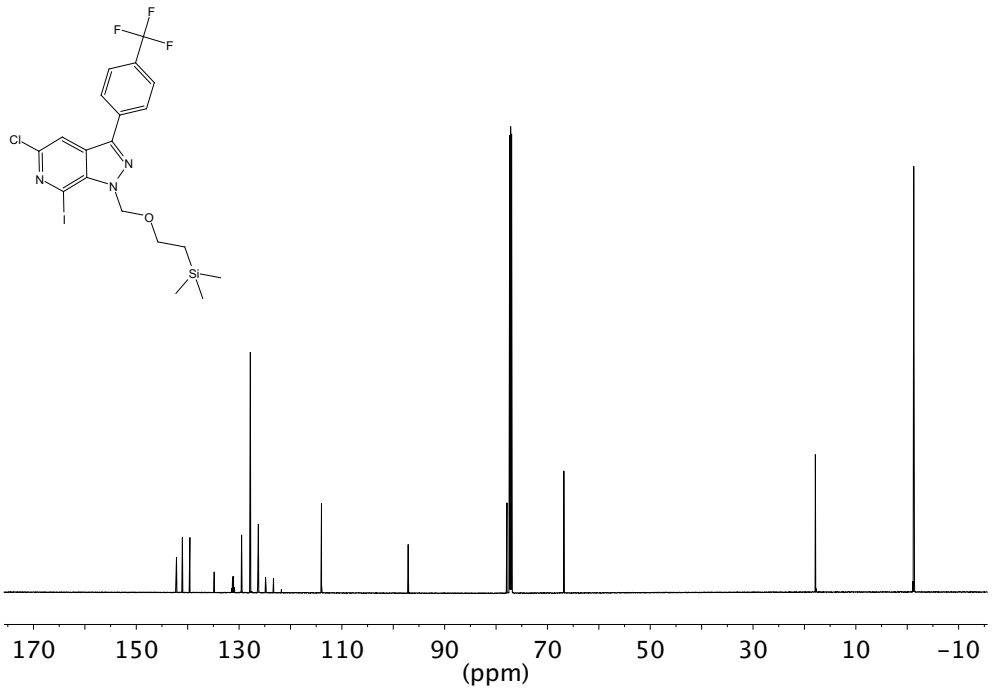

^{19}F NMR (376 MHz, $CDCl_3$) of compound **216**

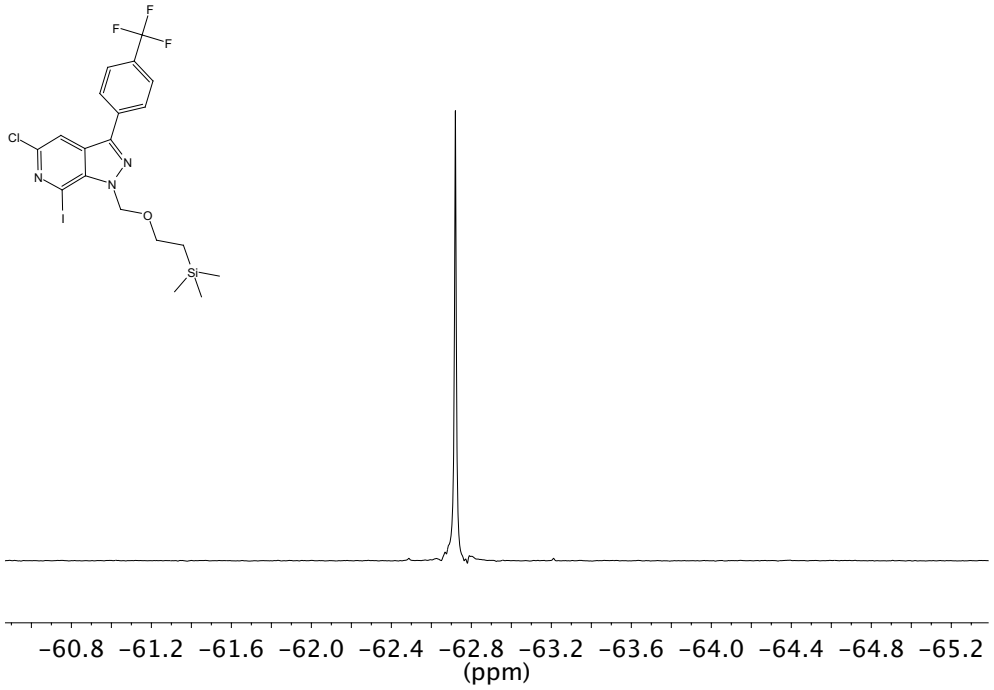

^{1}H NMR (600 MHz, $CDCl_3$) and ^{13}C NMR (151 MHz, $CDCl_3$) of compound **218**

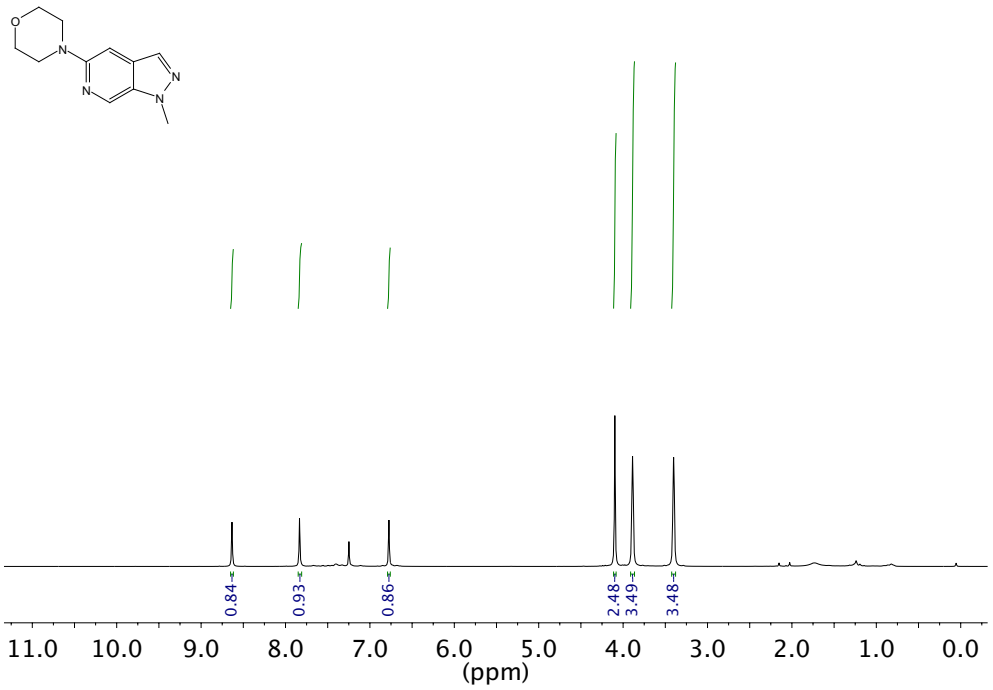

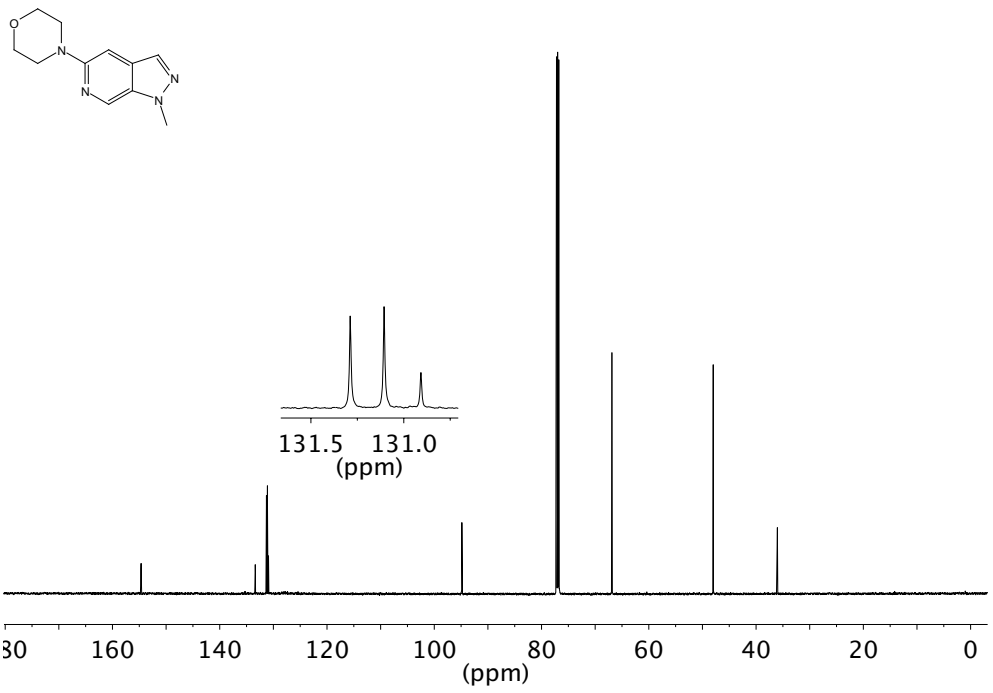

^{1}H NMR (700 MHz, $CDCl_3$) and ^{13}C NMR (176 MHz, $CDCl_3$) of compound **217**

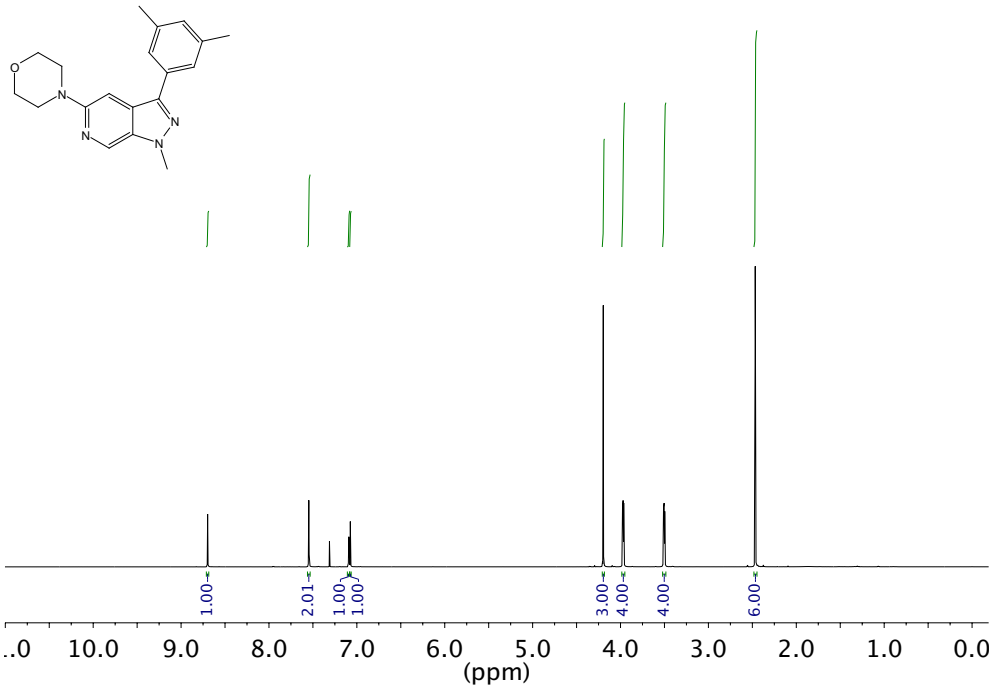

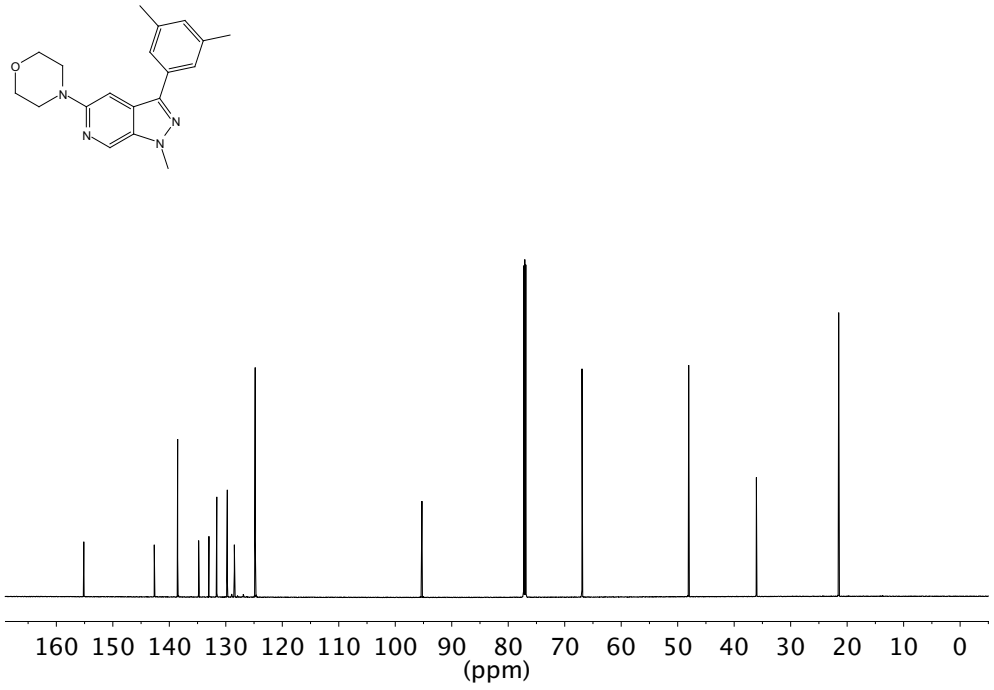

^{1}H NMR (600 MHz, $(CD_3)_2CO$) and ^{13}C NMR (151 MHz, $(CD_3)_2CO$) of **B1**

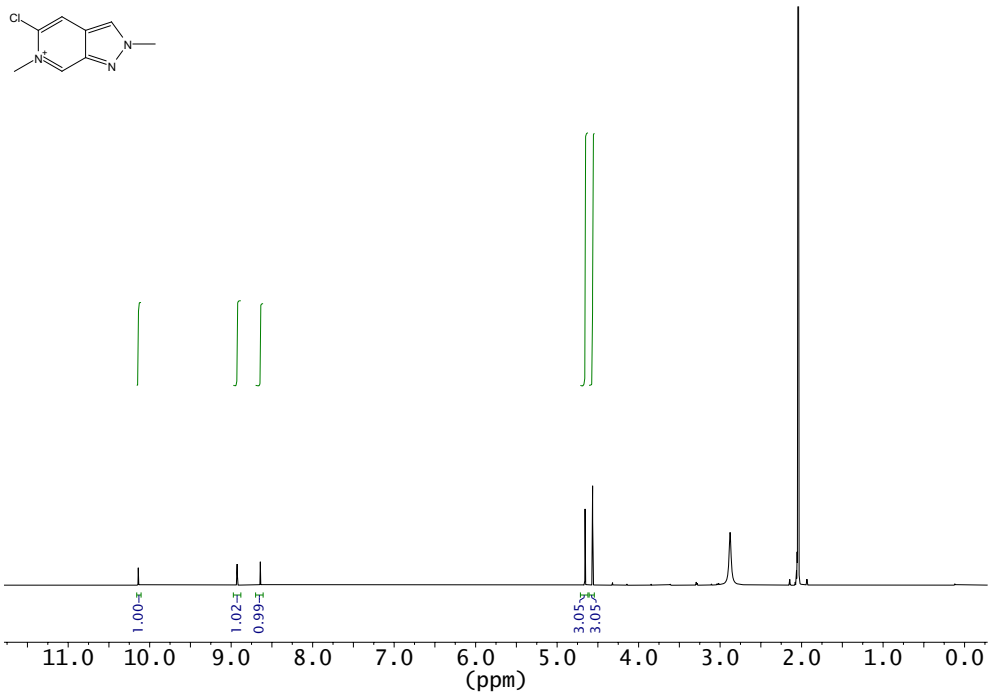

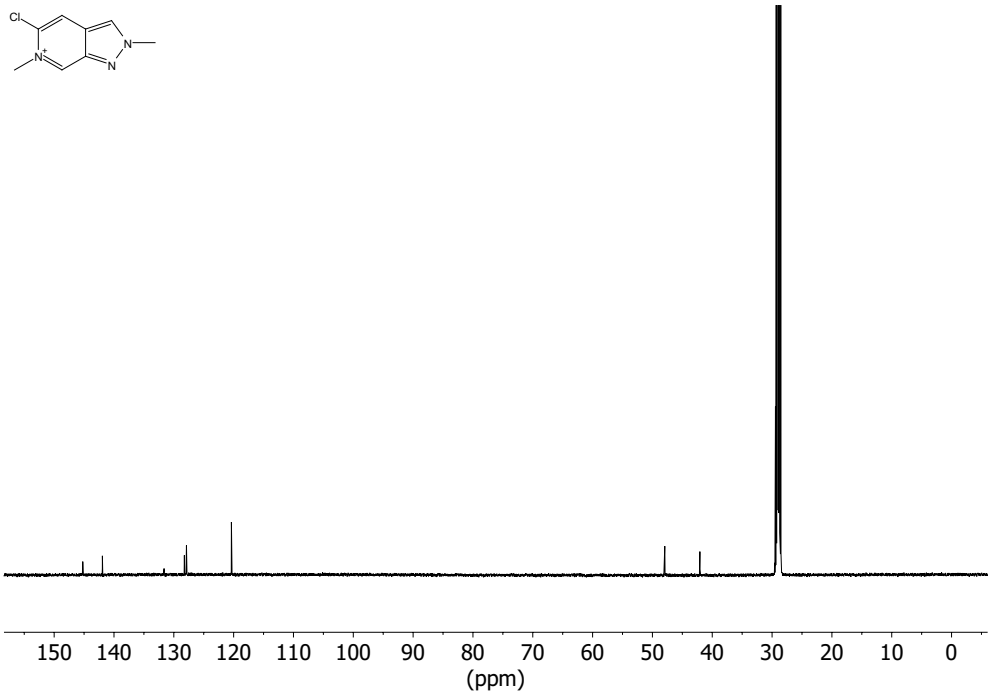

^{1}H NMR (600 MHz, $(CD_3)_2CO$) and ^{13}C NMR (151 MHz, $(CD_3)_2CO$) of **B2**

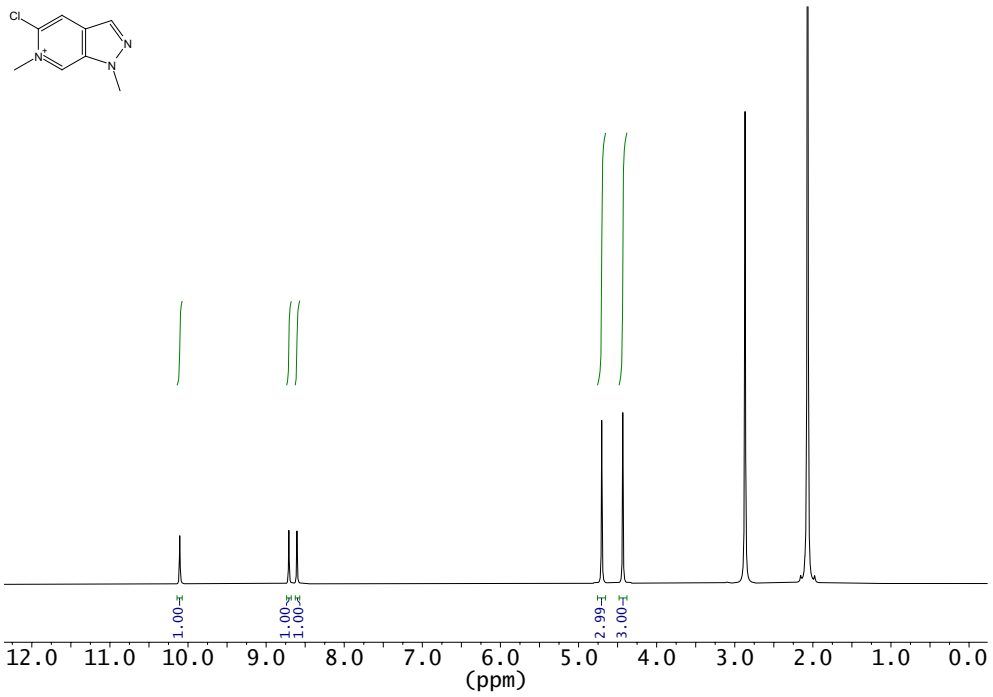

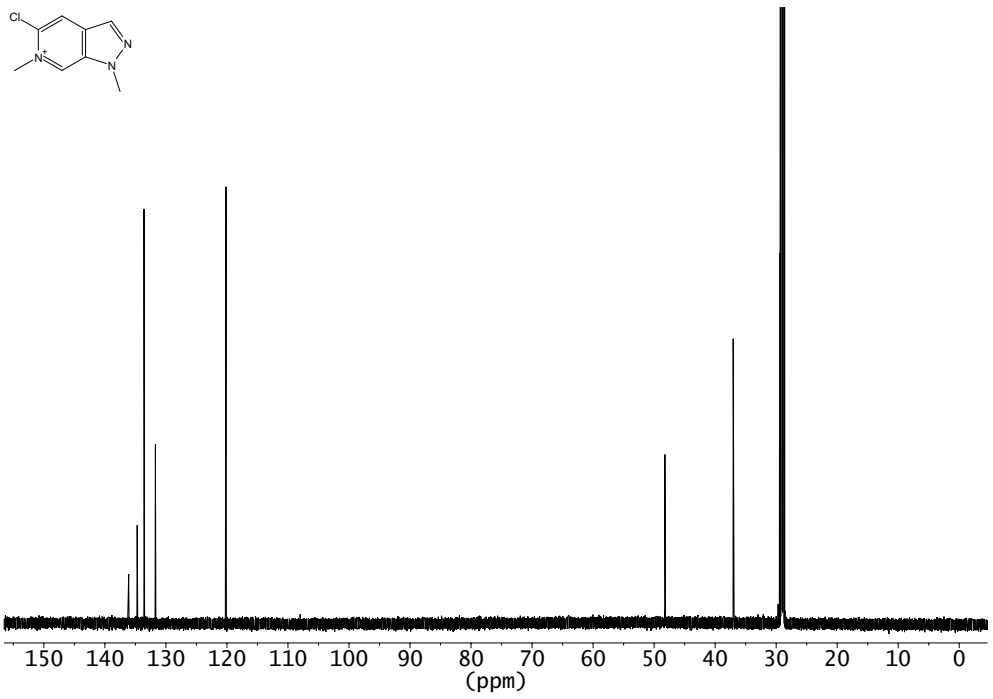

^{1}H NMR (600 MHz, $(CD_3)_2CO$) and ^{13}C NMR (151 MHz, $(CD_3)_2CO$) of **B3**

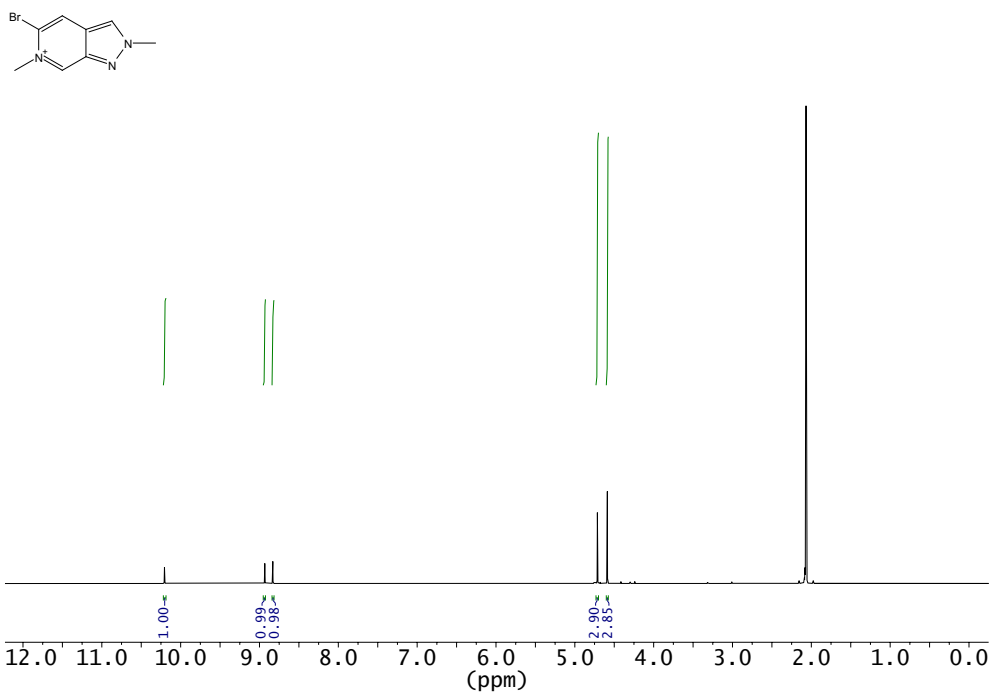

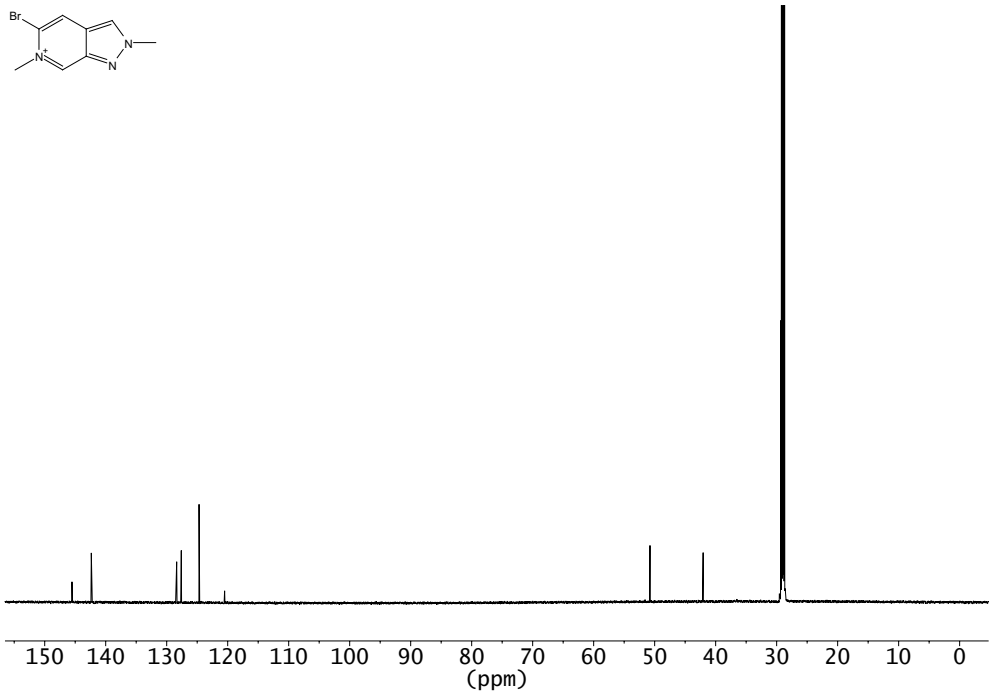

^{1}H NMR (600 MHz, $(CD_3)_2CO$) and ^{13}C NMR (151 MHz, $(CD_3)_2CO$) of **B4**

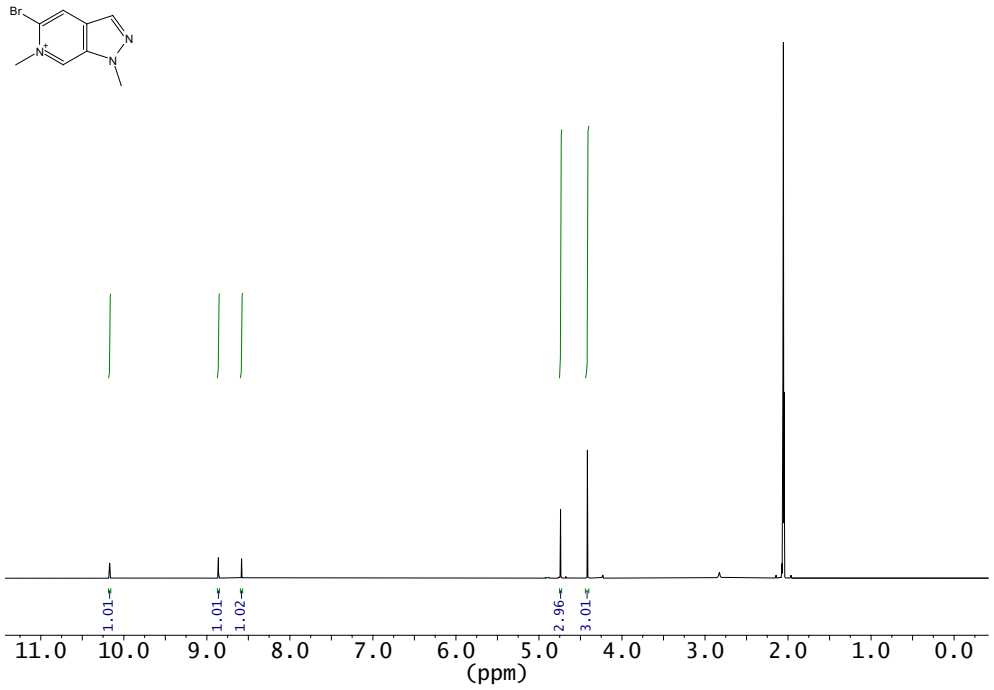

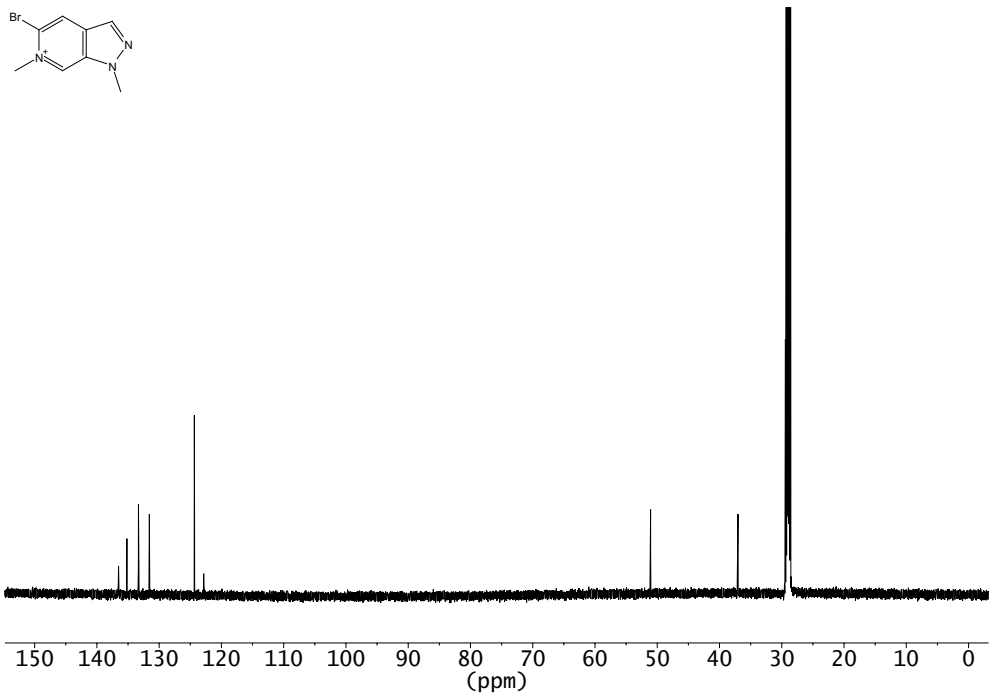

^{1}H NMR (400 MHz, $CDCl_3$) and ^{13}C NMR (101 MHz, $CDCl_3$) of compound **251**

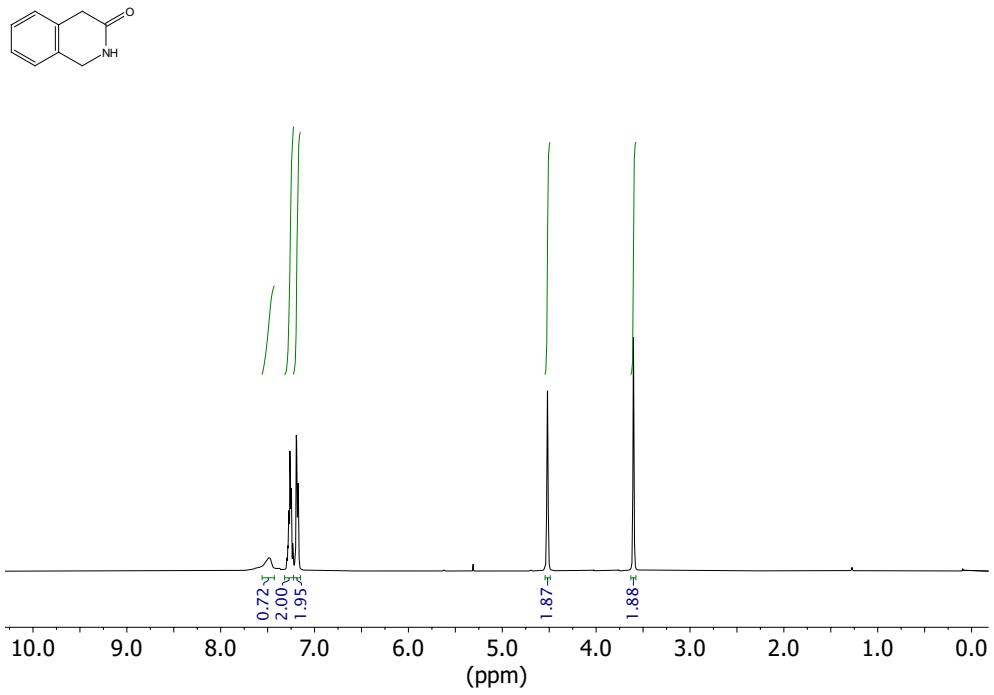

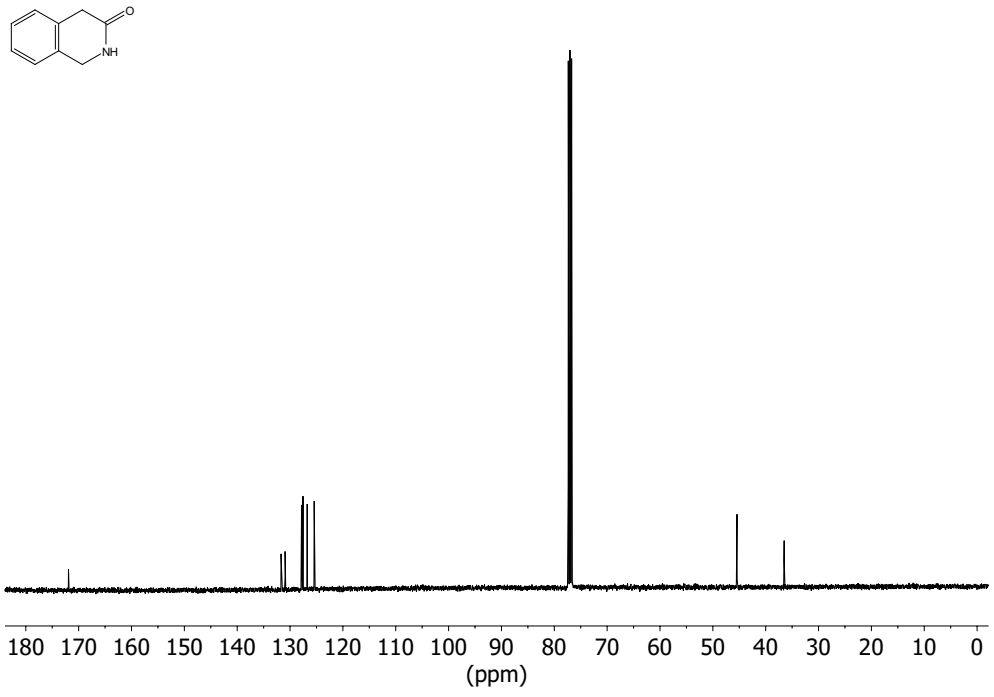

^{1}H NMR (400 MHz, $CDCl_3$) and ^{13}C NMR (101 MHz, $CDCl_3$) of compound **257**

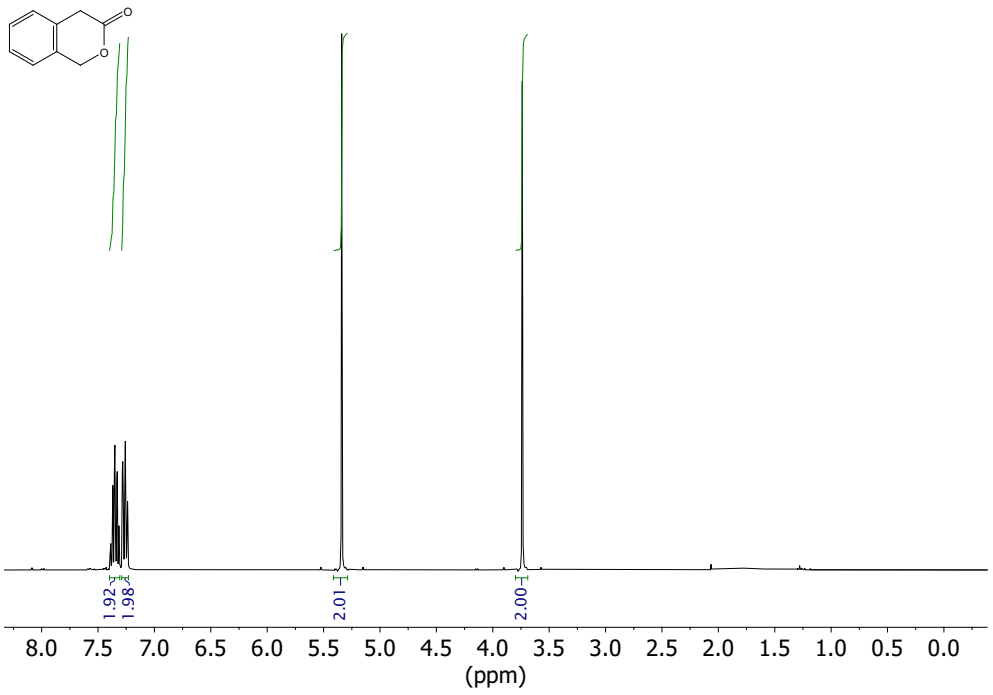

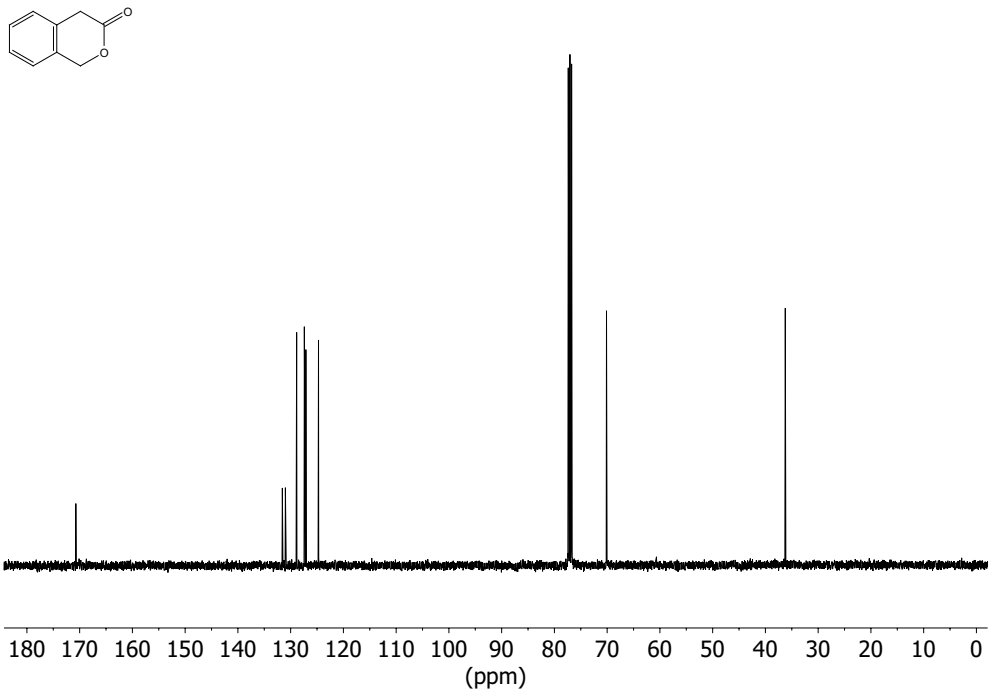

^{1}H NMR (700 MHz, $CDCl_3$) and ^{13}C NMR (176 MHz, $CDCl_3$) of compound **258**

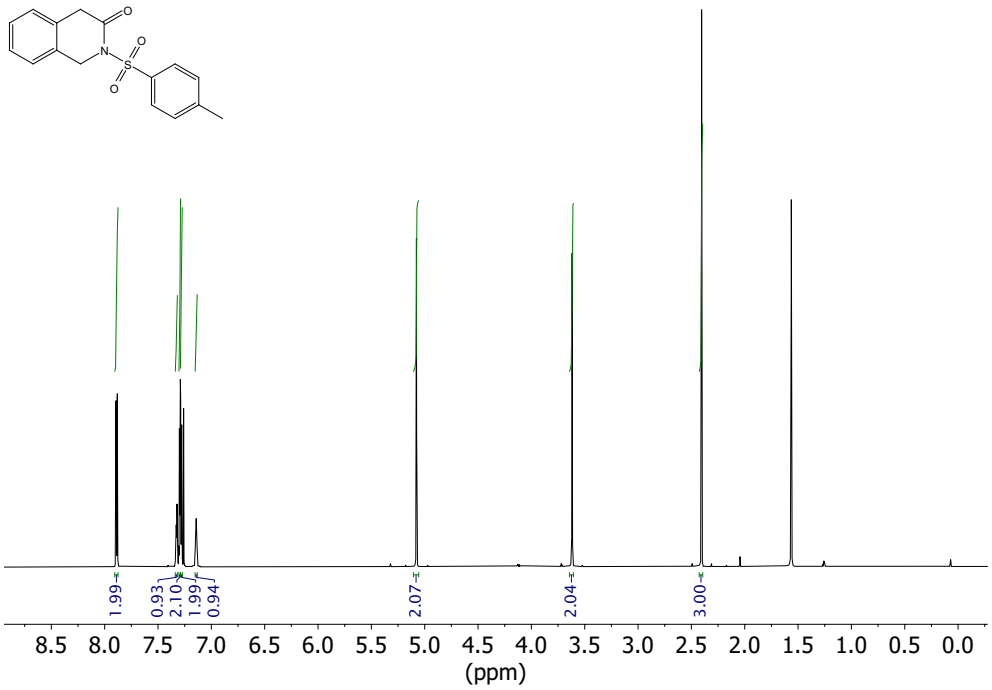

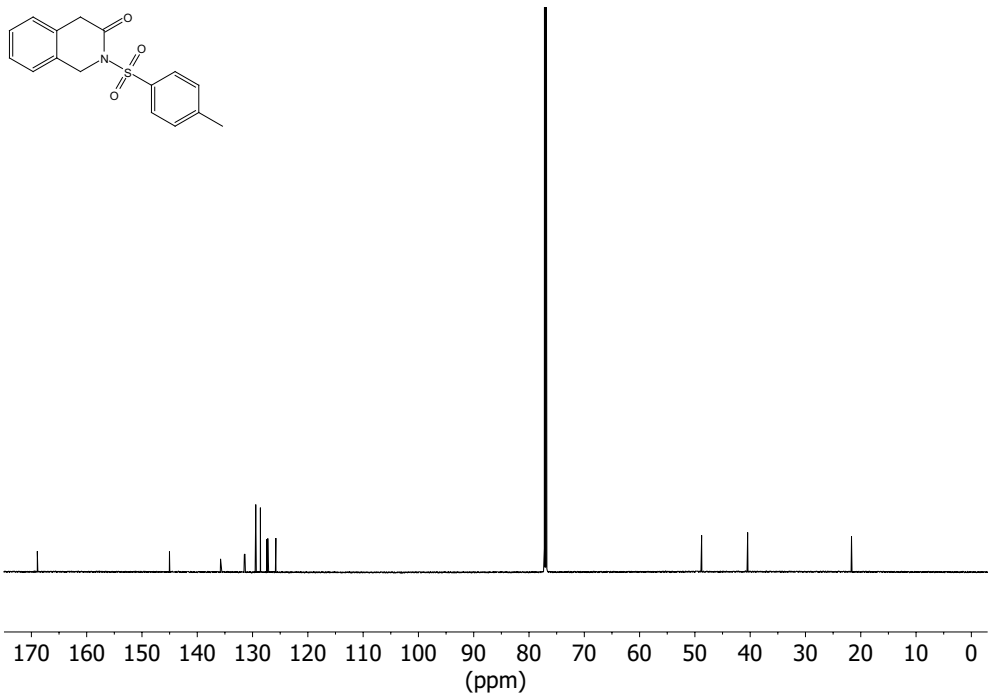

^{1}H NMR (600 MHz, $CDCl_3$) and ^{13}C NMR (151 MHz, $CDCl_3$) of compound **328**

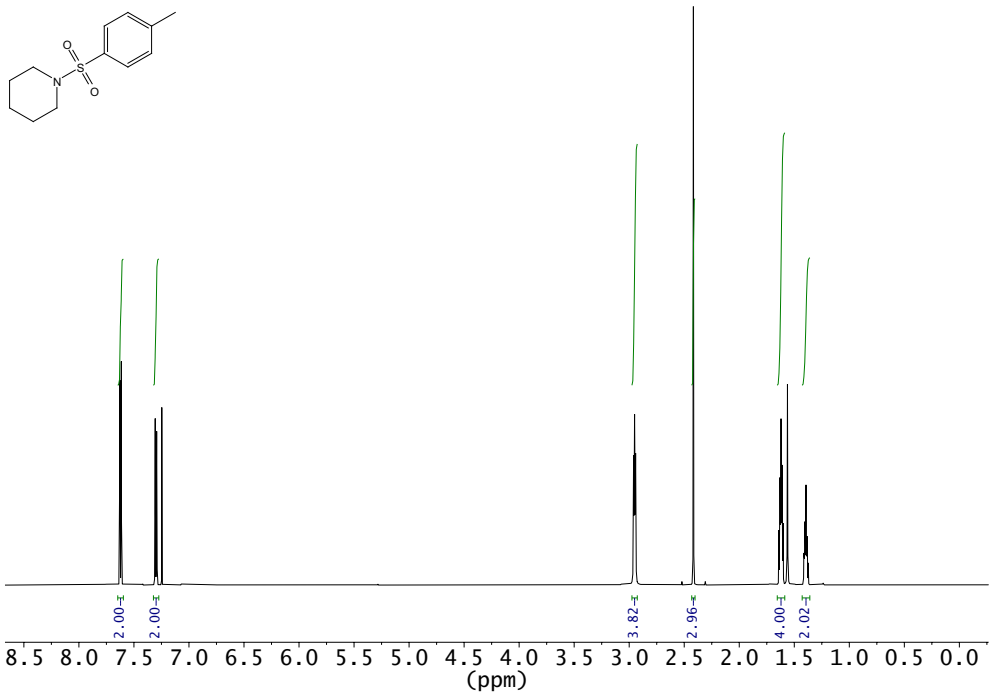

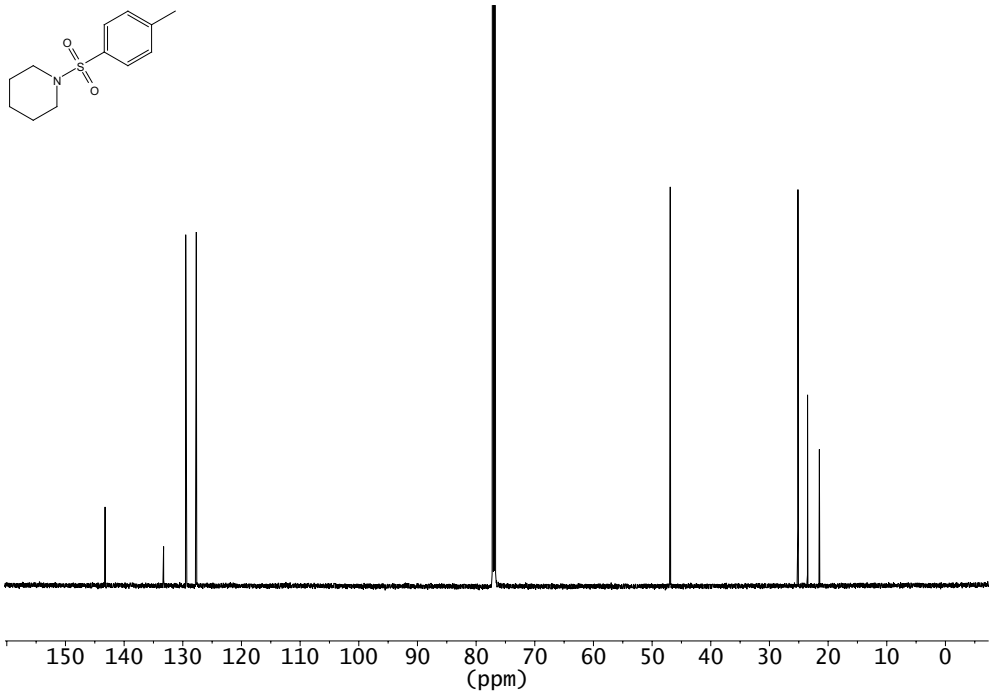

^{1}H NMR (400 MHz, $CDCl_3$) and ^{13}C NMR (101 MHz, $CDCl_3$) of compound **346**

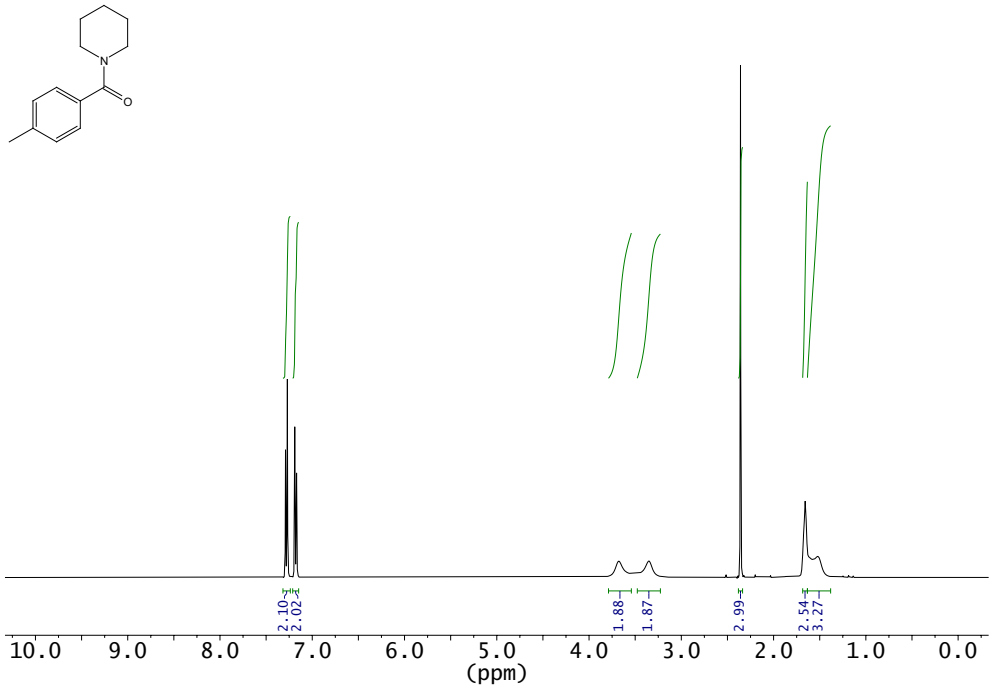

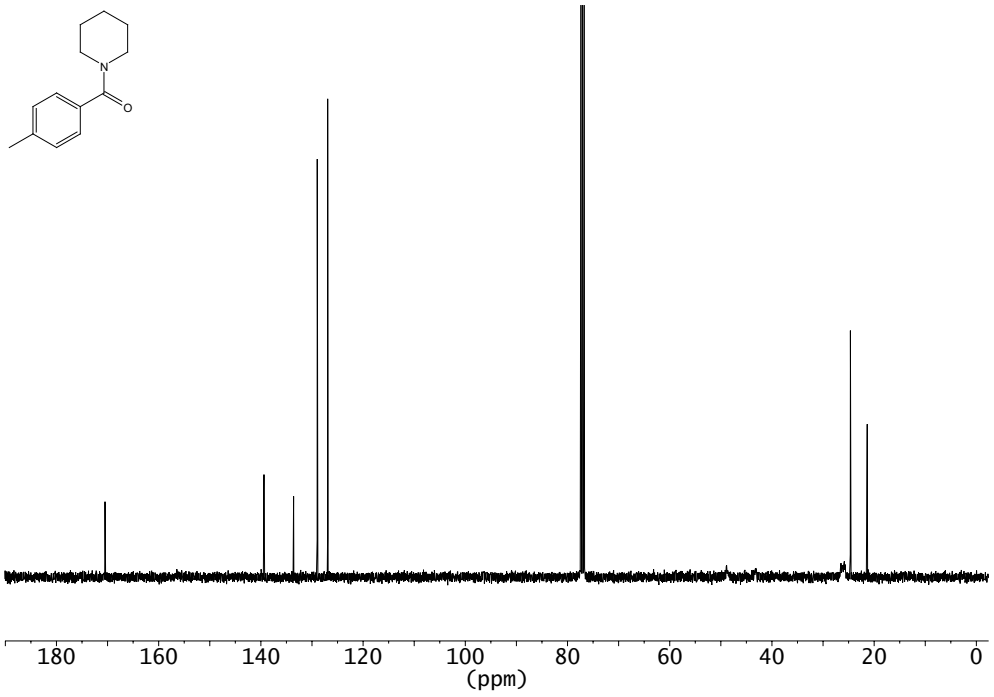

^{1}H NMR (600 MHz, $CDCl_3$) and ^{13}C NMR (151 MHz, $CDCl_3$) of compound **327**

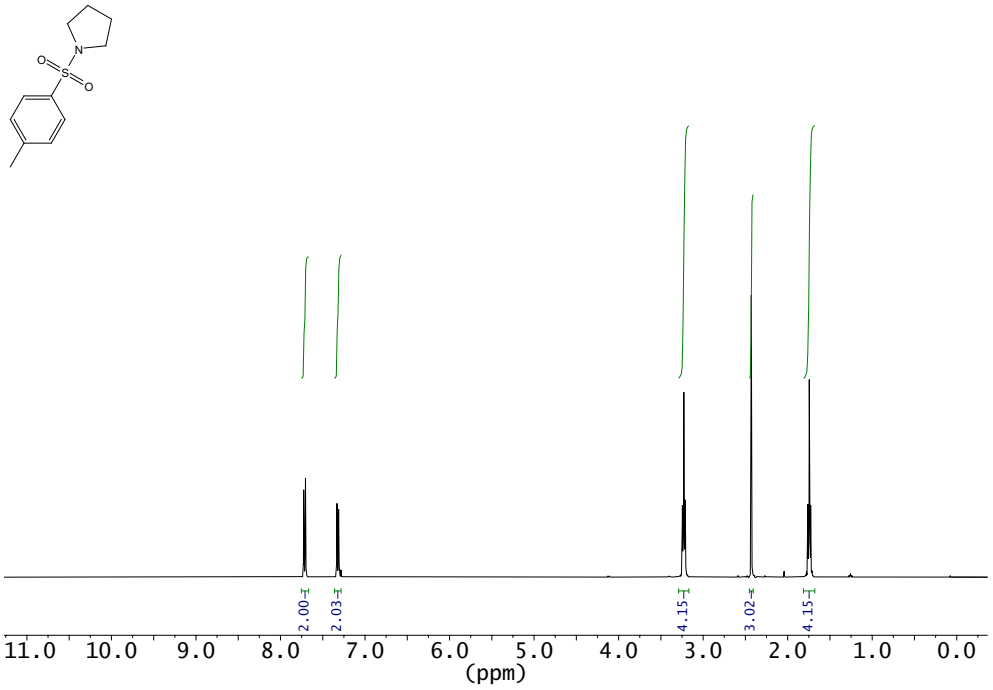

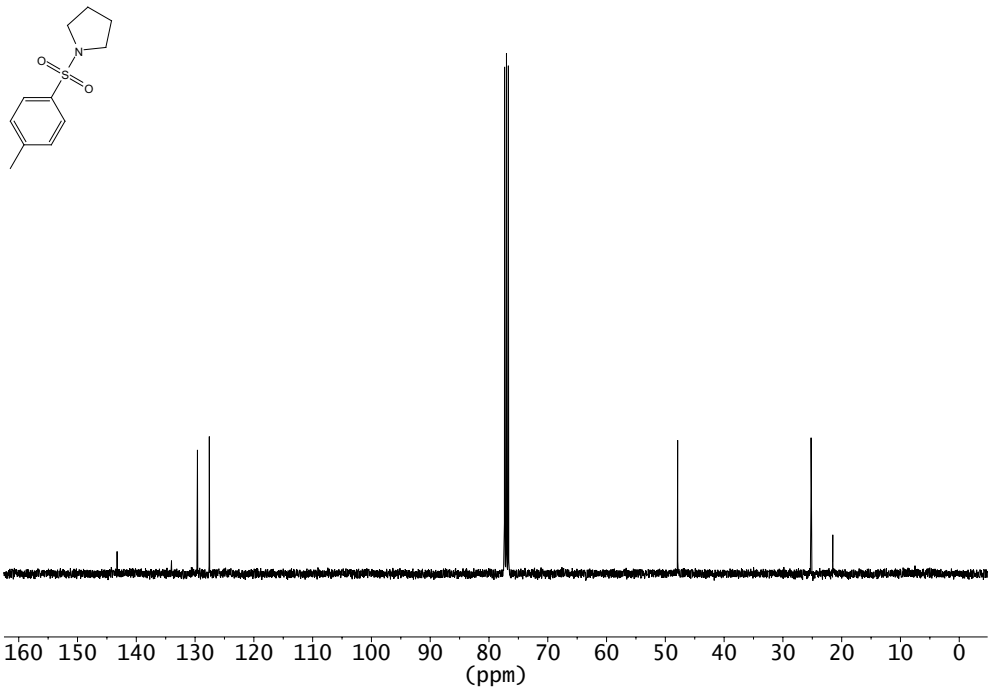

^{1}H NMR (700 MHz, $CDCl_3$) and ^{13}C NMR (176 MHz, $CDCl_3$) of compound **330**

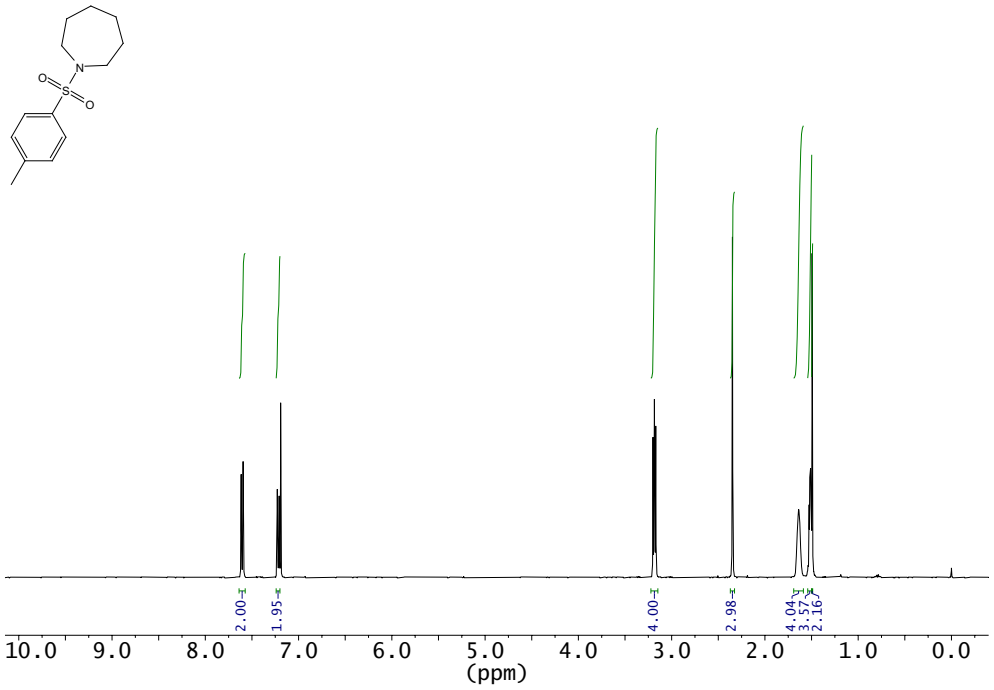

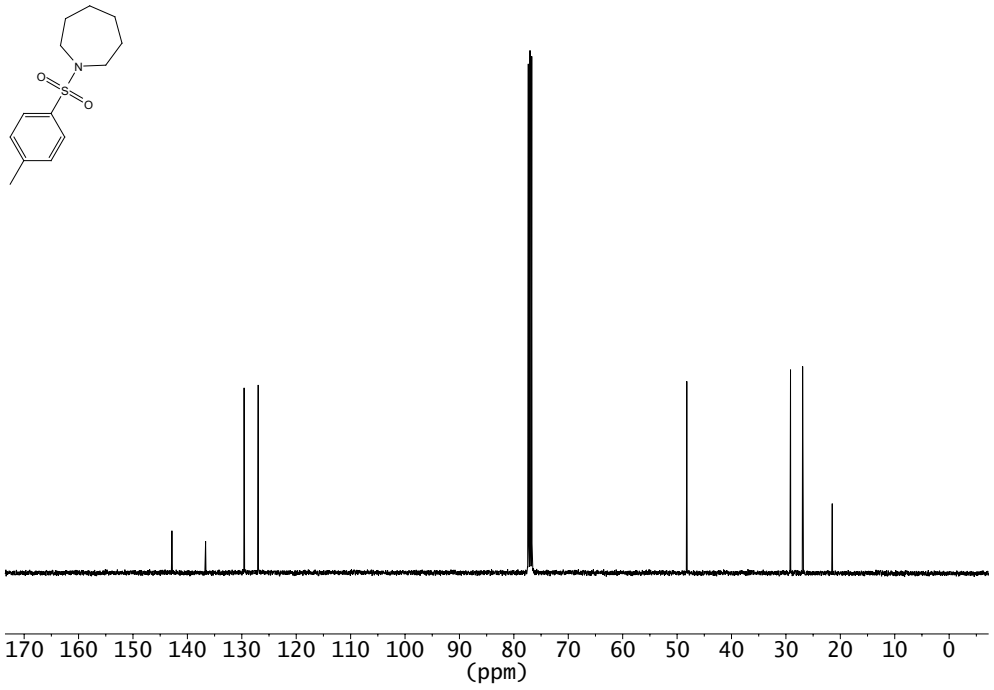

^{1}H NMR (700 MHz, $CDCl_3$) and ^{13}C NMR (176 MHz, $CDCl_3$) of compound **331**

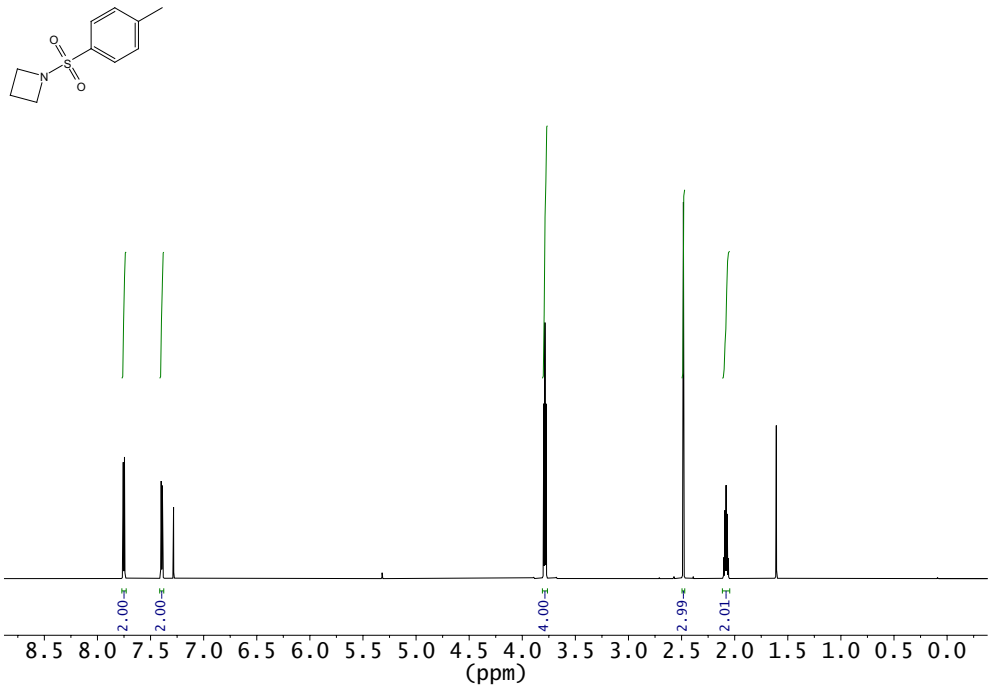

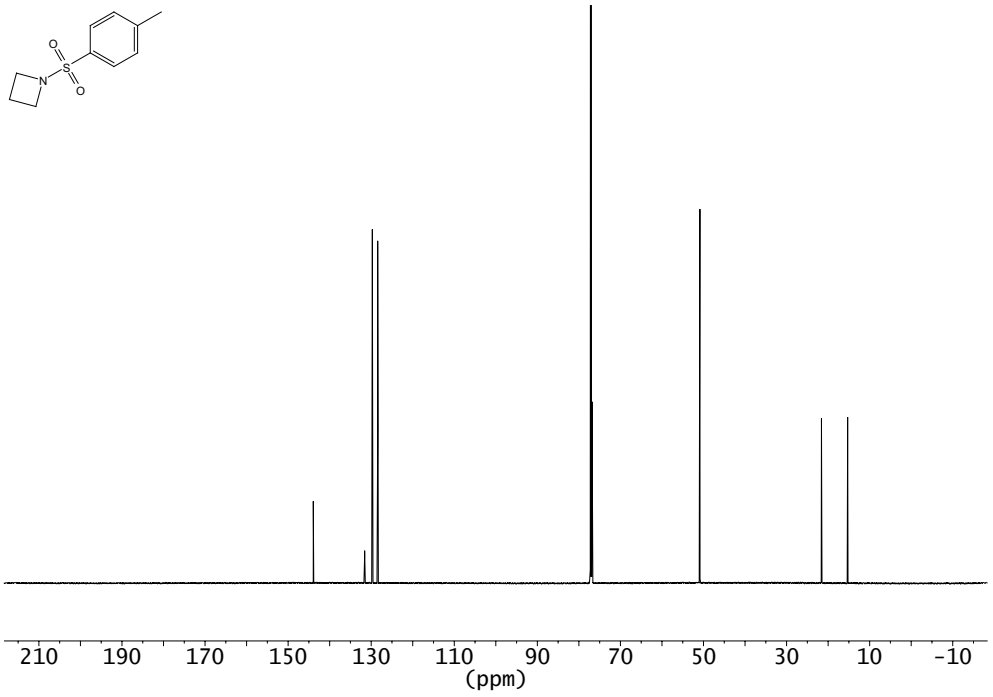

^{1}H NMR (700 MHz, $CDCl_3$) and ^{13}C NMR (176 MHz, $CDCl_3$) of compound **332**

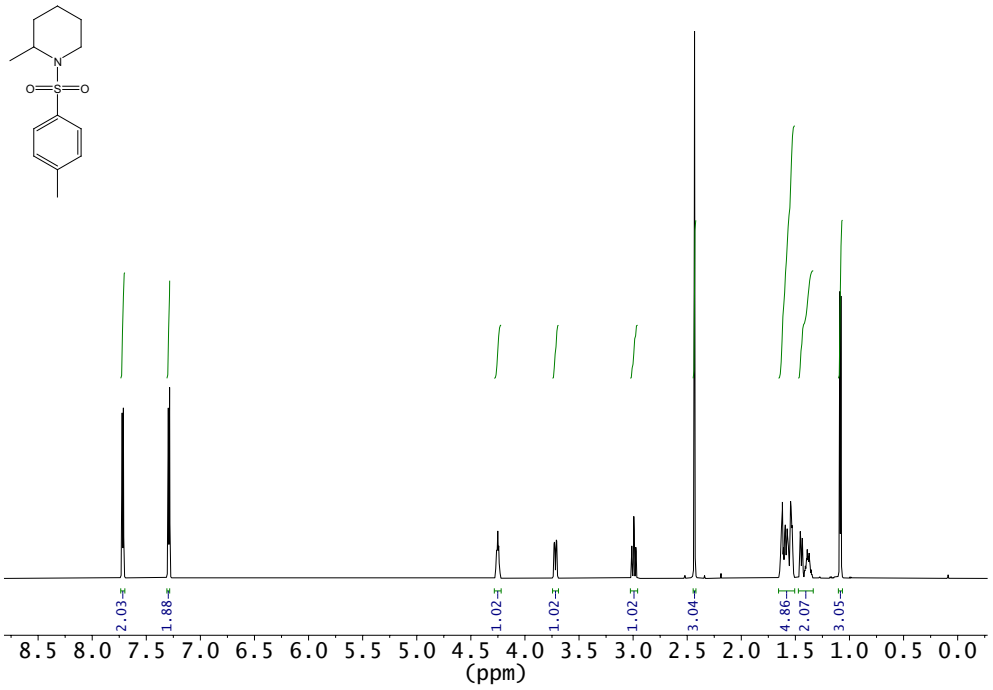

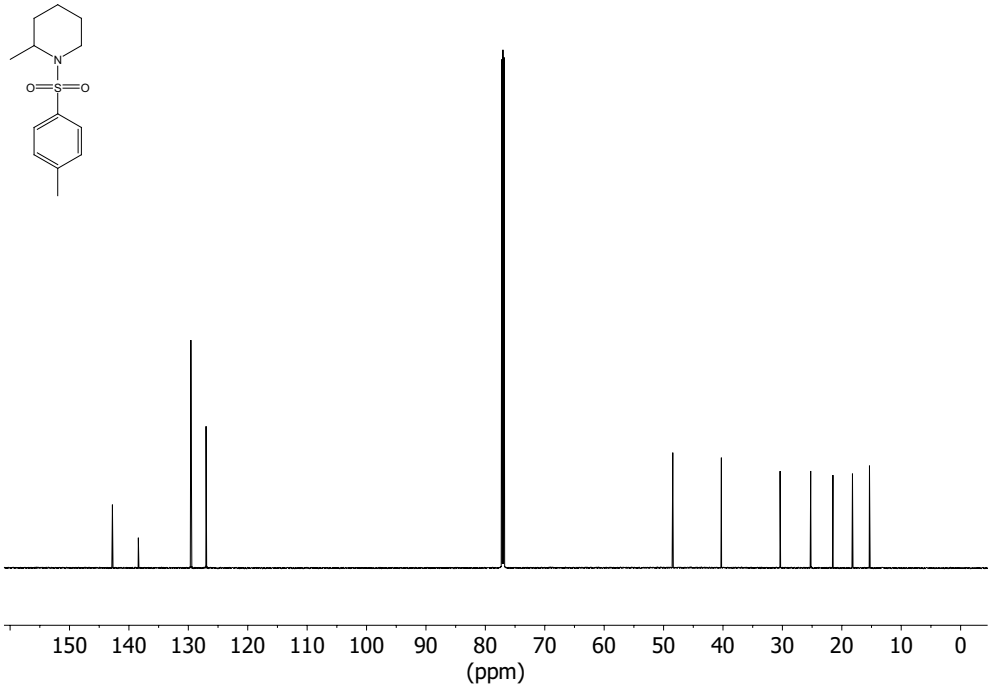

^{1}H NMR (700 MHz, $CDCl_3$) and ^{13}C NMR (176 MHz, $CDCl_3$) of compound **333**

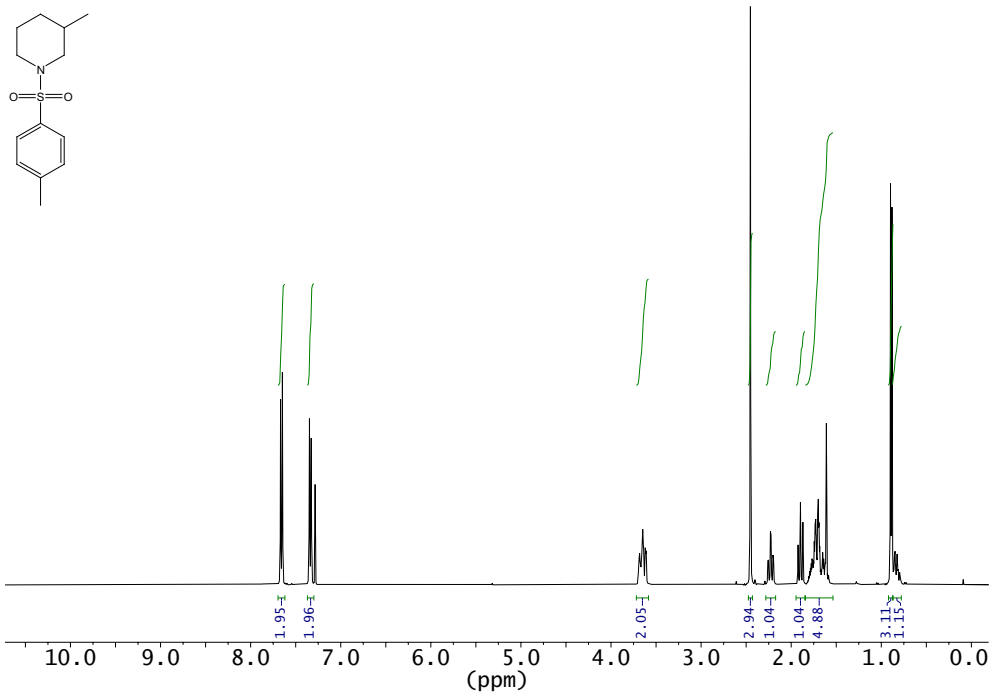

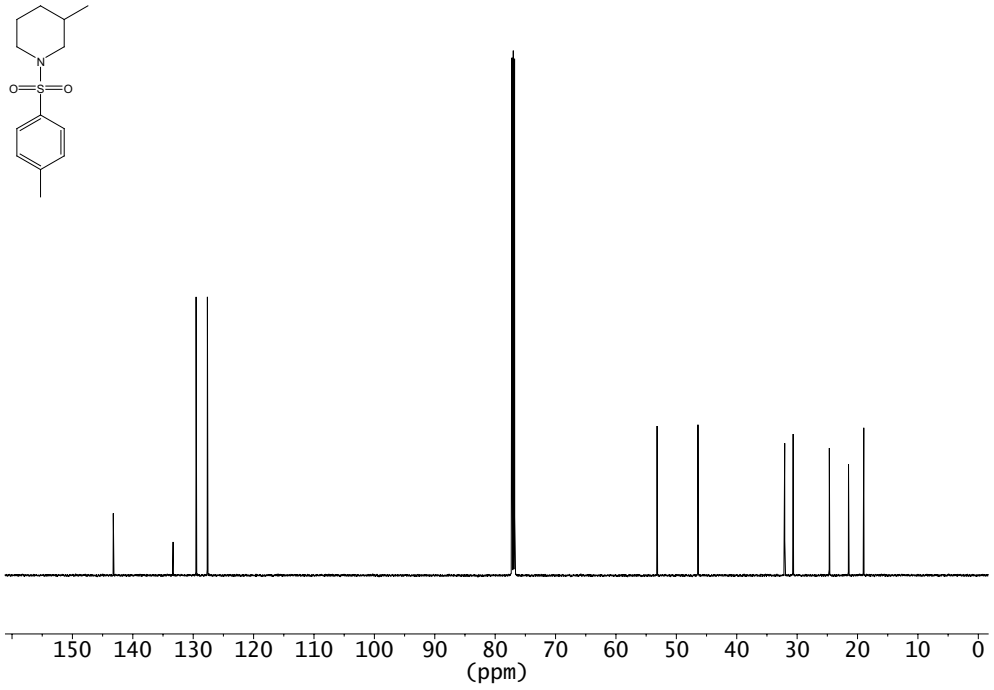

^{1}H NMR (600 MHz, $CDCl_3$) and ^{13}C NMR (151 MHz, $CDCl_3$) of compound **334**

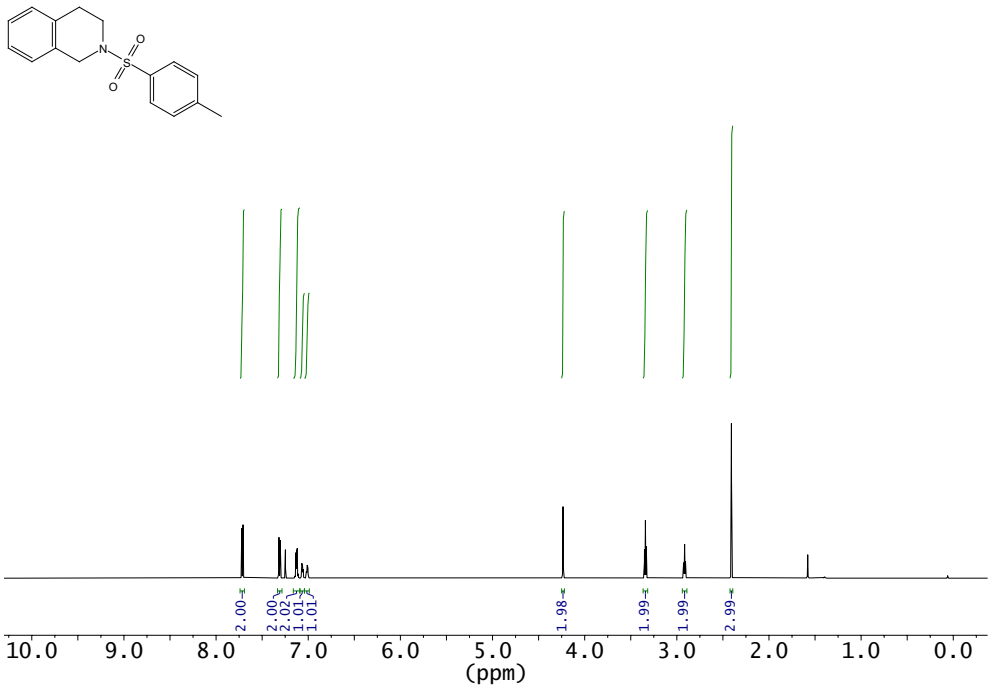

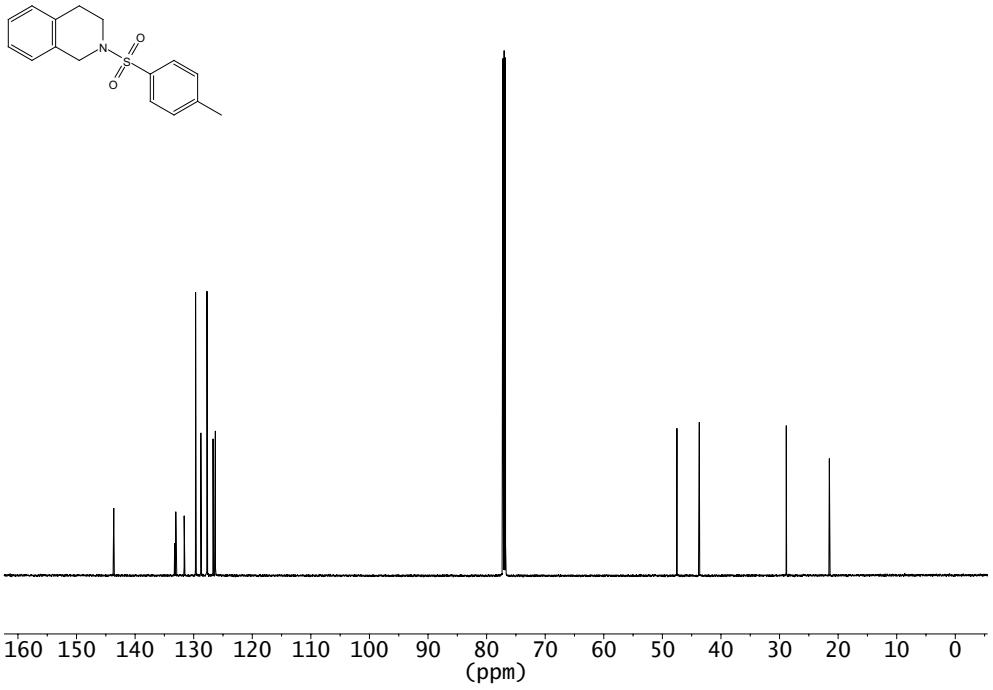

^{1}H NMR (600 MHz, $CDCl_3$) and ^{13}C NMR (151 MHz, $CDCl_3$) of compound **335**

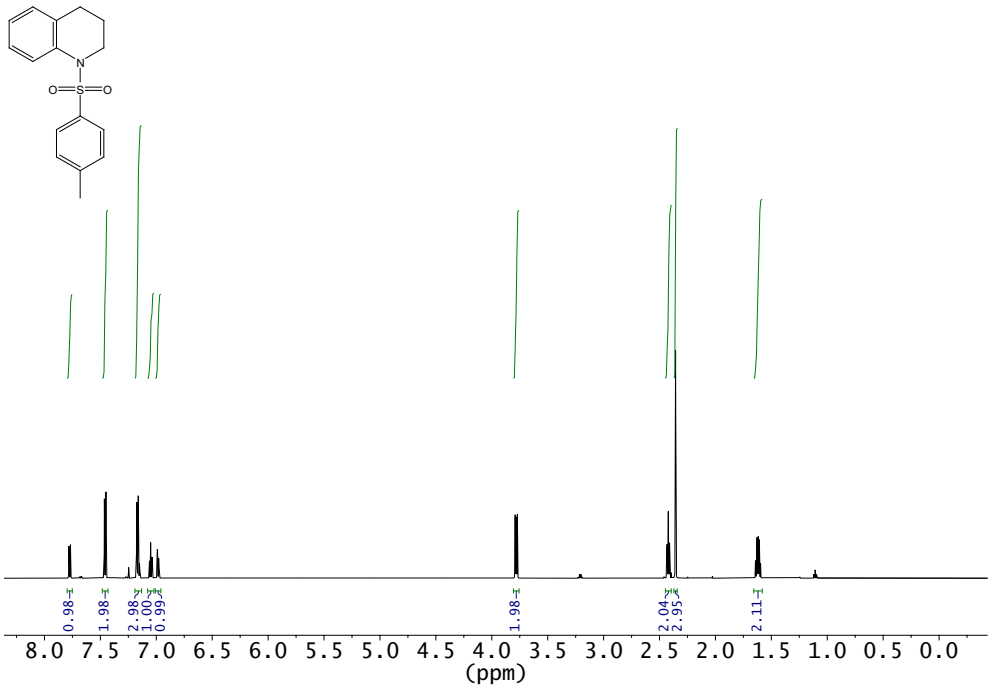

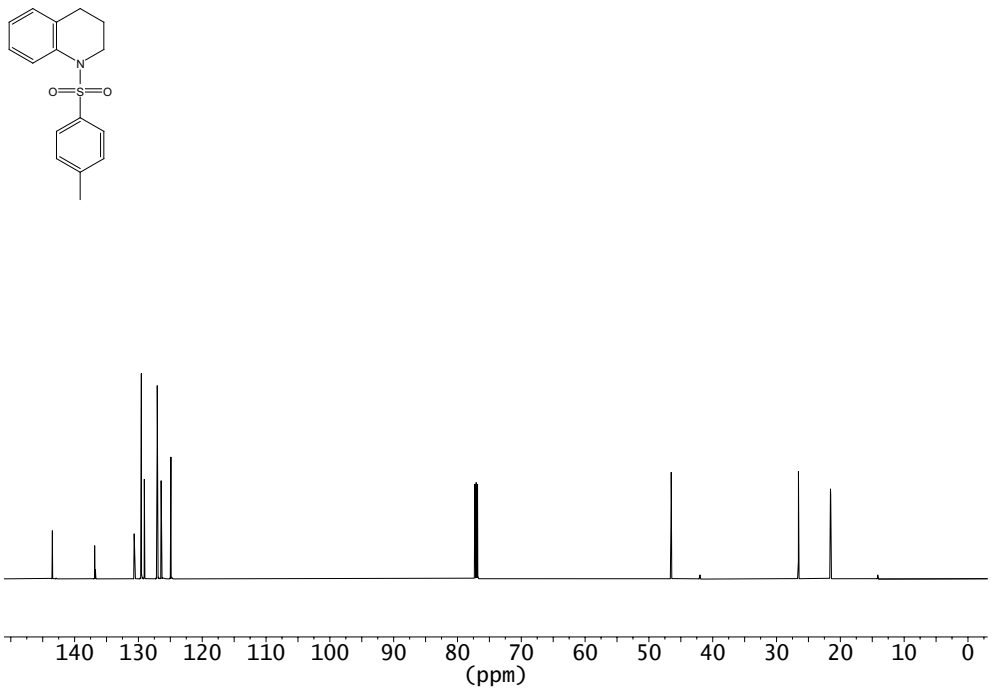

^{1}H NMR (700 MHz, $CDCl_3$) and ^{13}C NMR (176 MHz, $CDCl_3$) of compound **336**

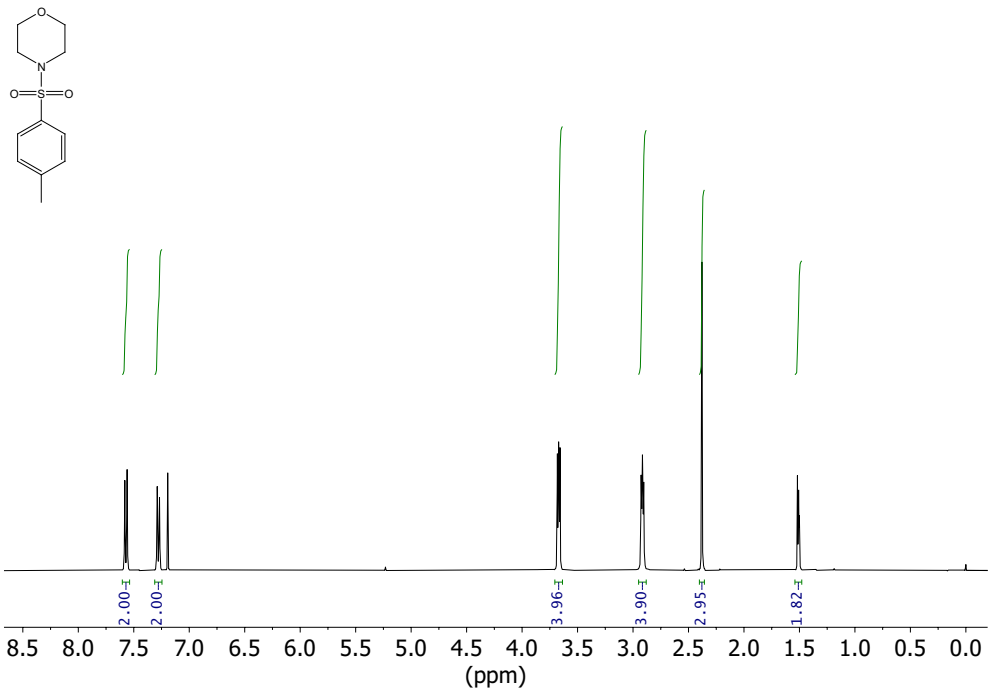

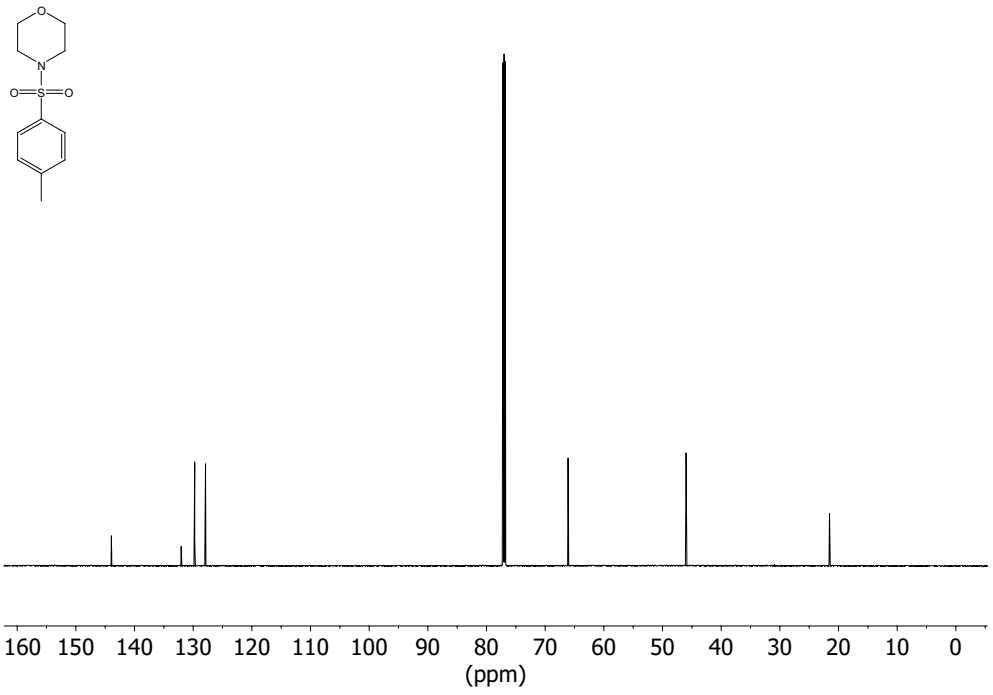

^{1}H NMR (600 MHz, $(CD_3)_2CO$) and ^{13}C NMR (151 MHz, $(CD_3)_2CO$) of compound **337**

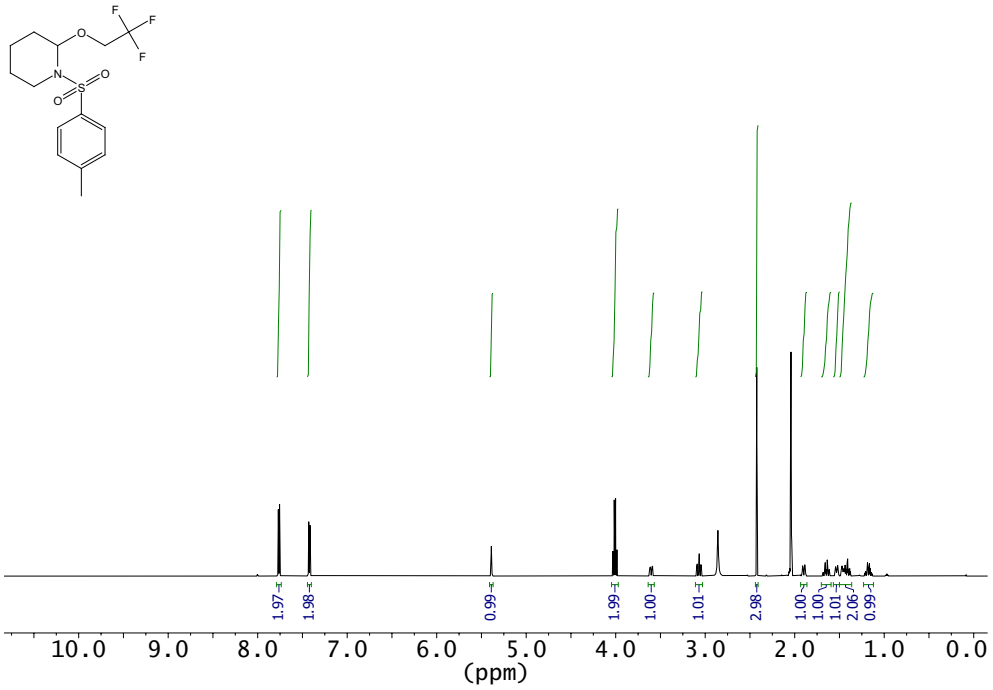

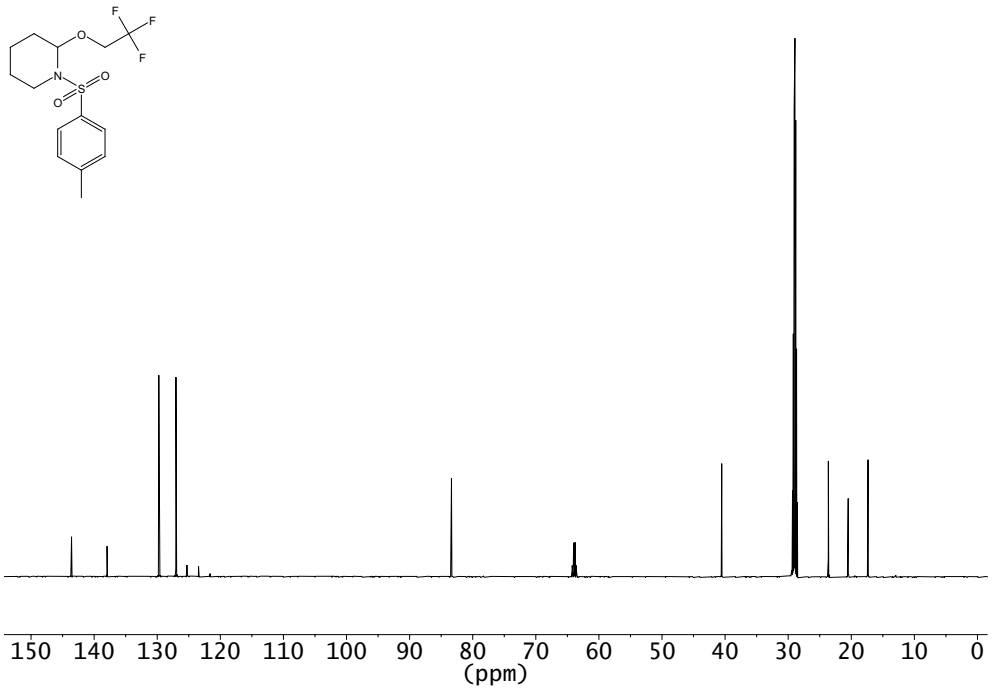

^{19}F NMR (376 MHz, $(CD_3)_2CO$) of compound **337**

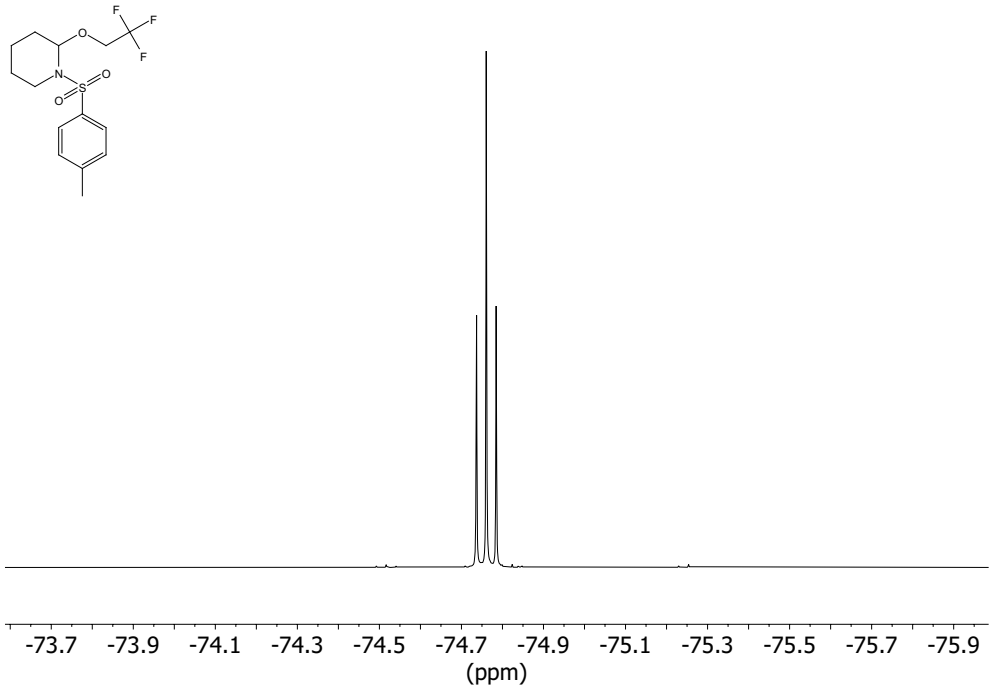

^{1}H NMR (500 MHz, $(CD_3)_2CO$)(VT = 80 ˚C) and ^{13}C NMR (126 MHz, $(CD_3)_2CO$)(VT = 80 ˚C) of compound **347**

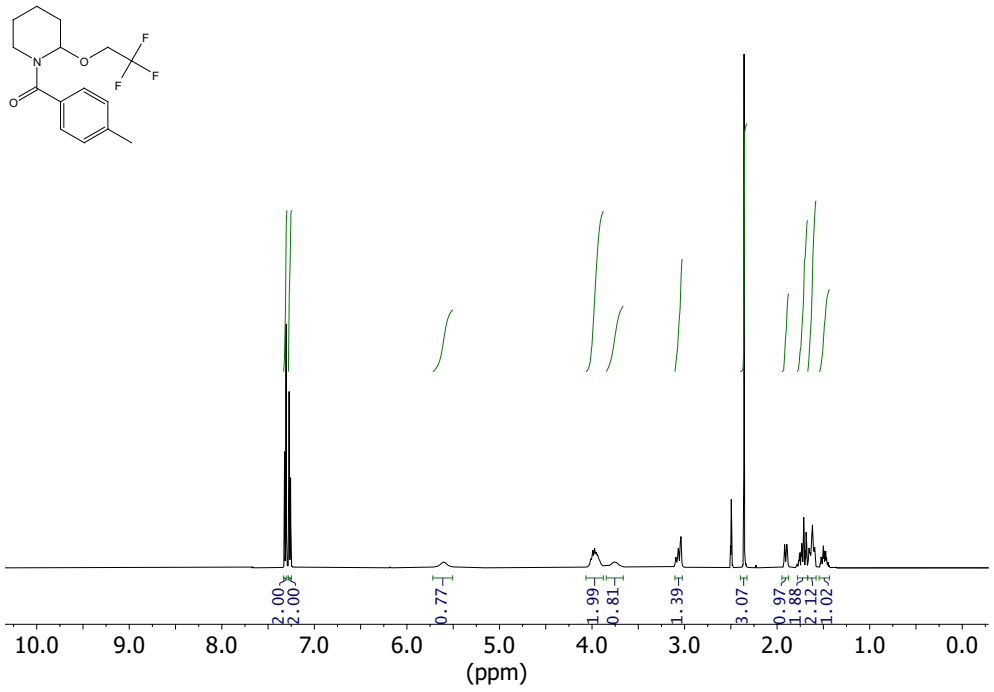

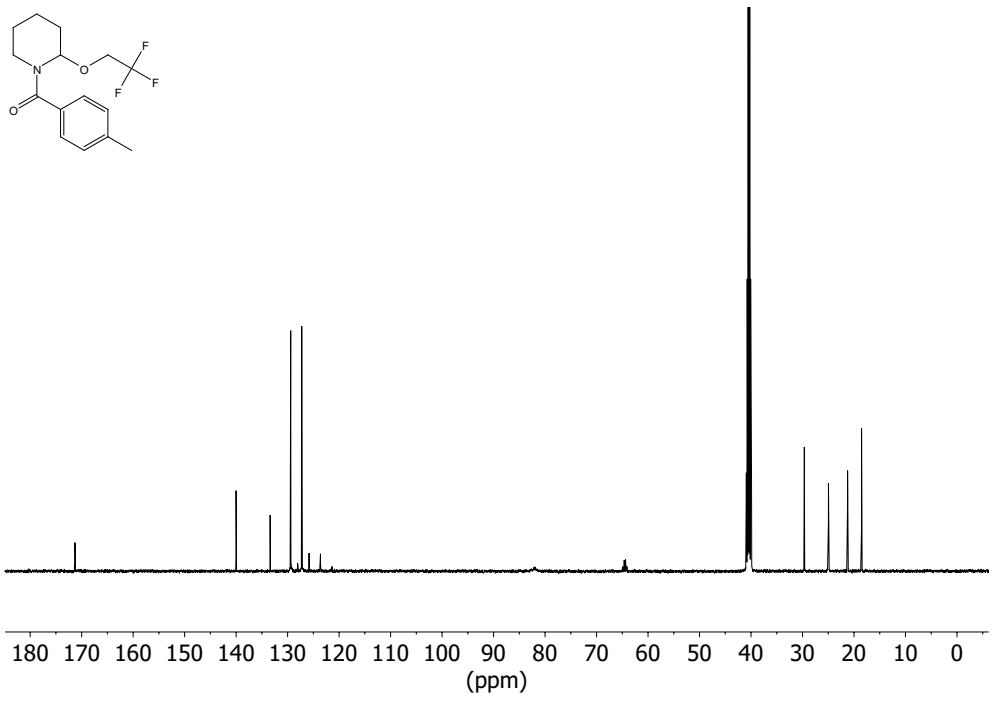

^{19}F NMR (376 MHz, $(CD_3)_2CO$) of compound **347**

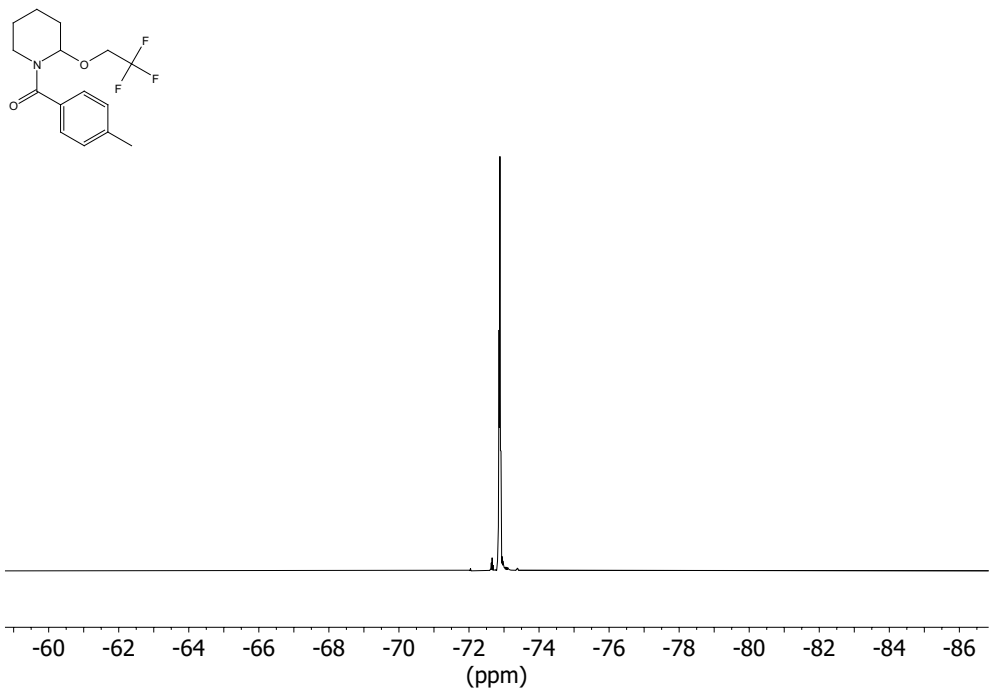

^{1}H NMR (600 MHz, $(CD_3)_2CO$) and ^{13}C NMR (151 MHz, $(CD_3)_2CO$) of compound **370**

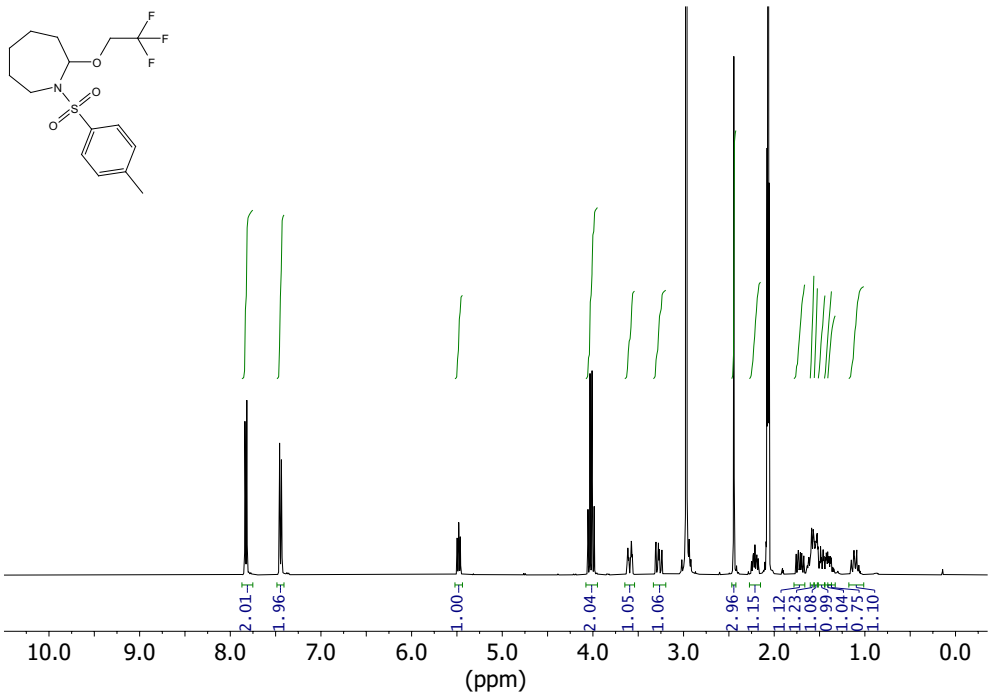

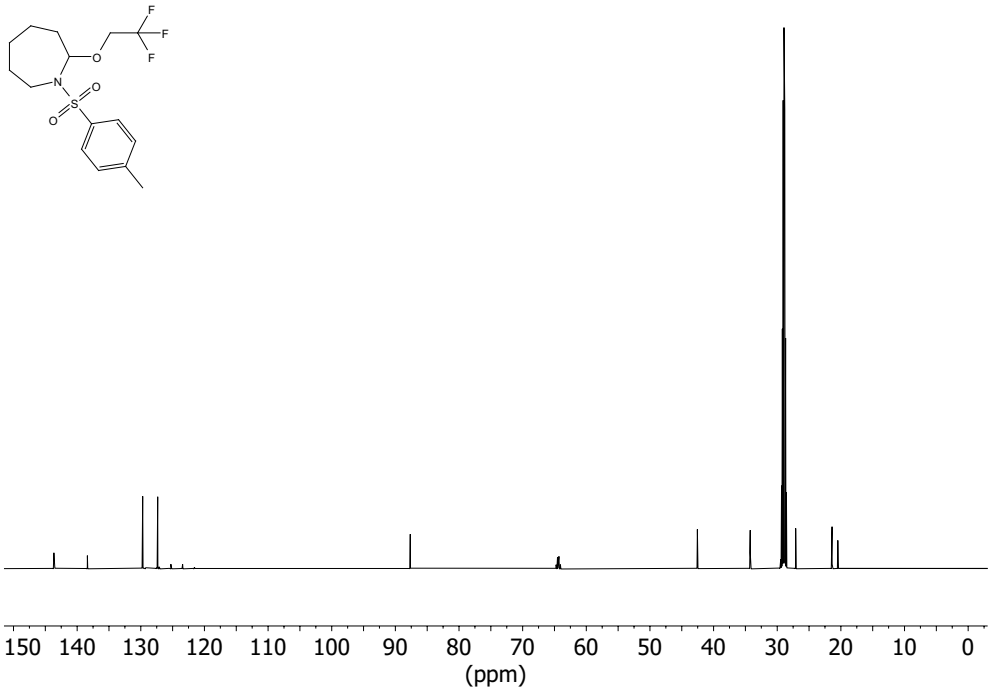

^{19}F NMR (376 MHz, $(CD_3)_2CO$) of compound **370**

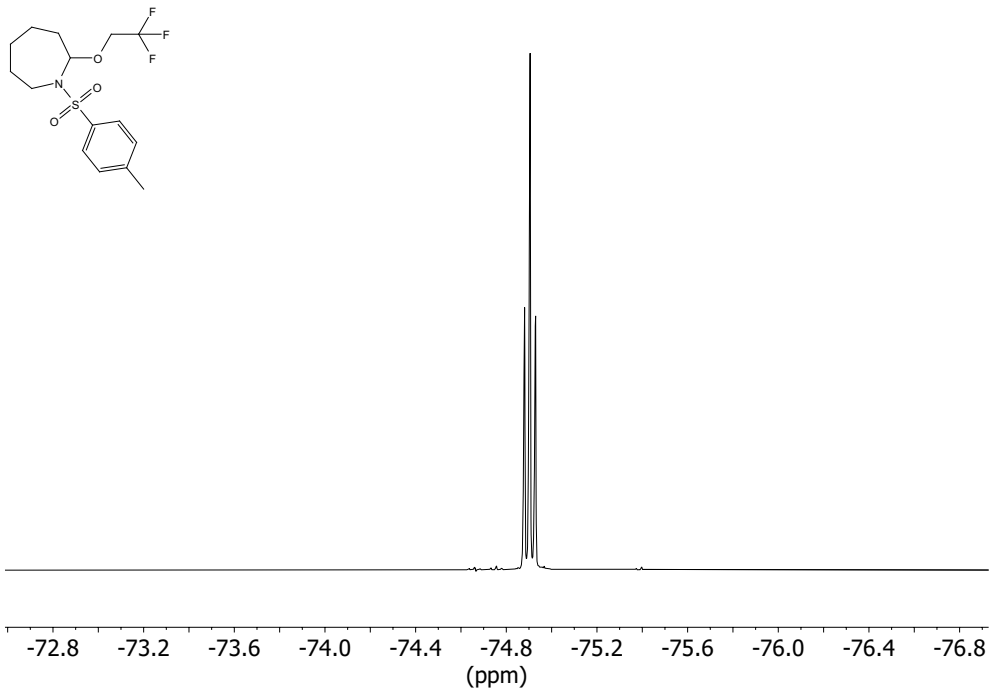

^{1}H NMR (600 MHz, $(CD_3)_2CO$) and ^{13}C NMR (151 MHz, $(CD_3)_2CO$) of compound **371**

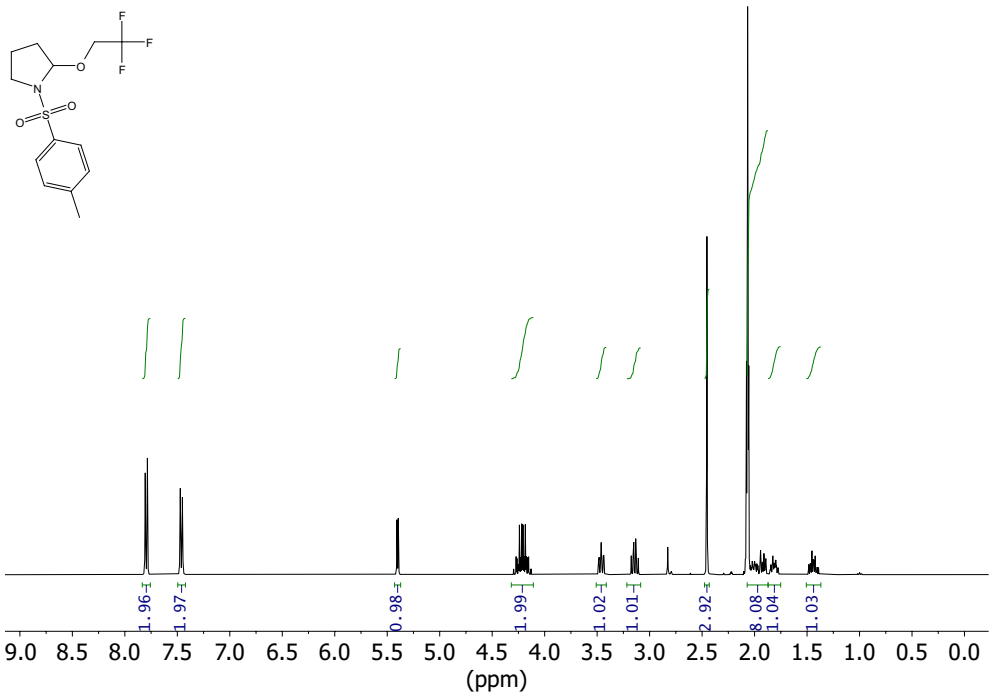

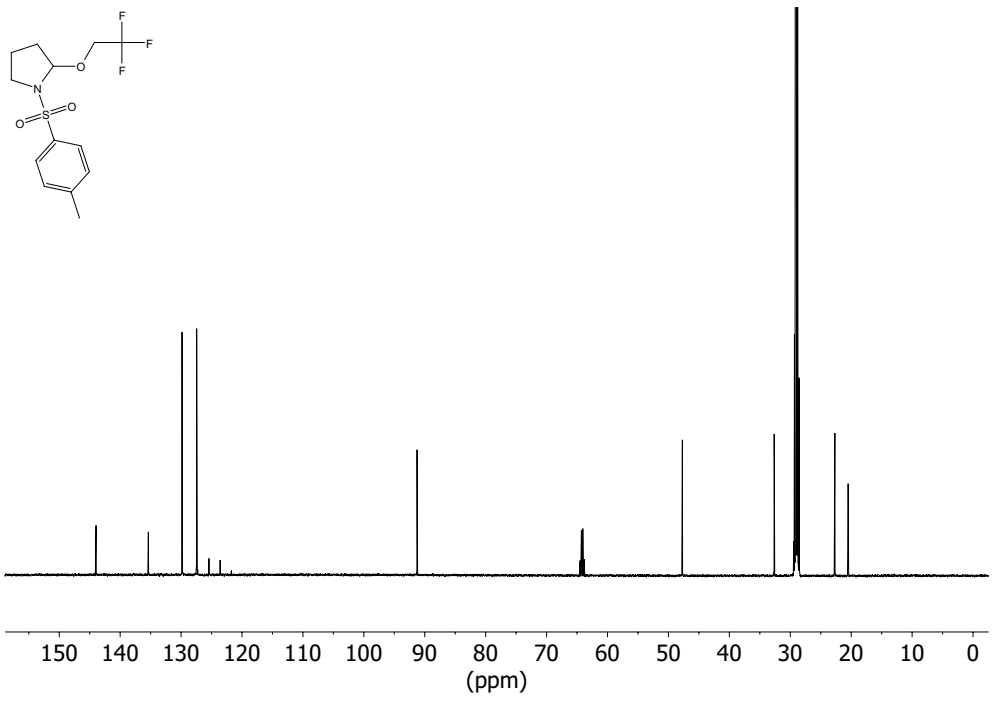

^{19}F NMR (376 MHz, $(CD_3)_2CO$) of compound **371**

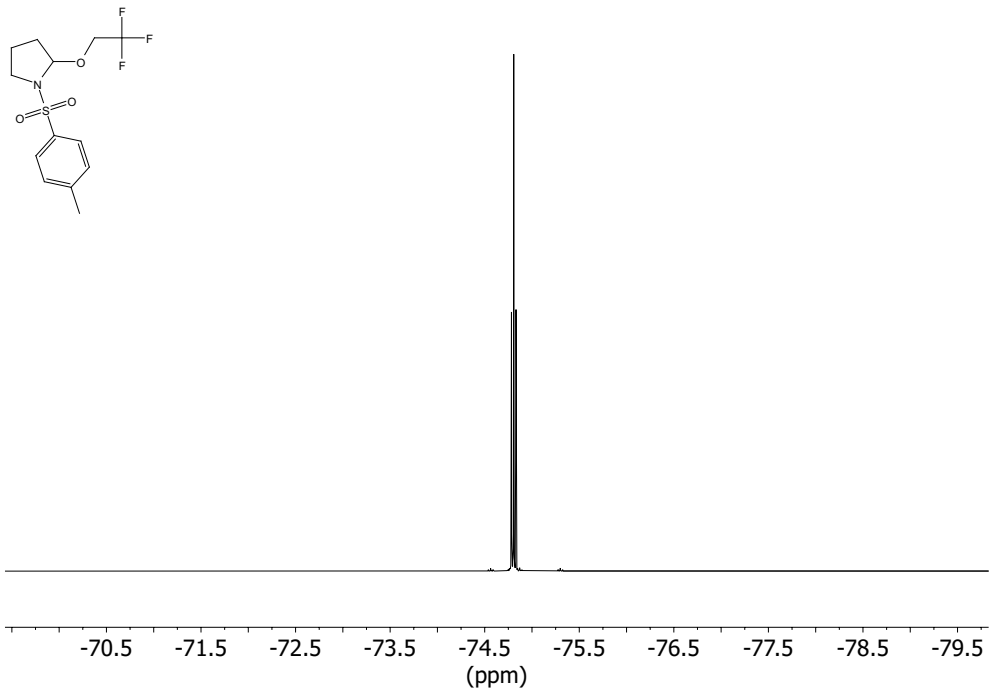

^{1}H NMR (600 MHz, $(CD_3)_2CO$) and ^{13}C NMR (151 MHz, $(CD_3)_2CO$) of compound **373**

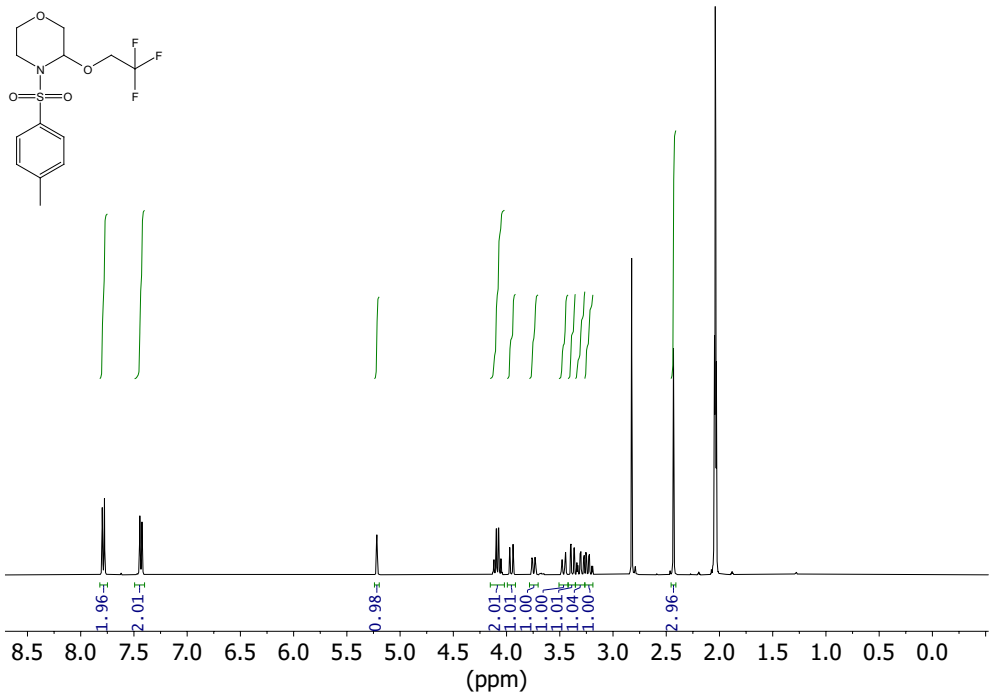

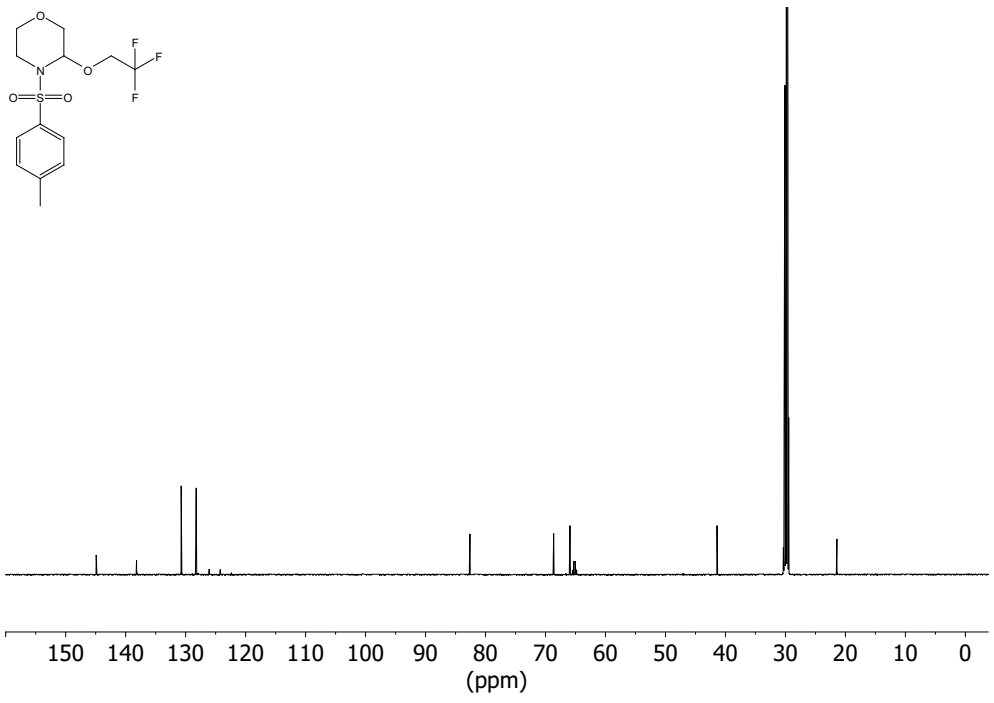

^{19}F NMR (376 MHz, $(CD_3)_2CO$) of compound **373**

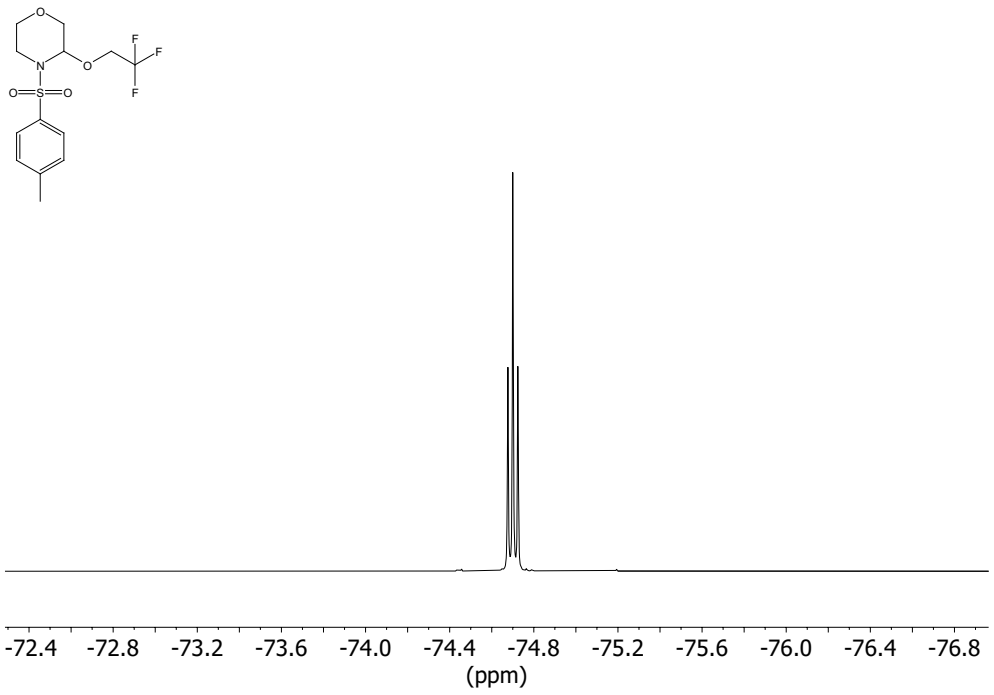

^{1}H NMR (600 MHz, $(CD_3)_2CO$) and ^{13}C NMR (151 MHz, $(CD_3)_2CO$) of compound **374**

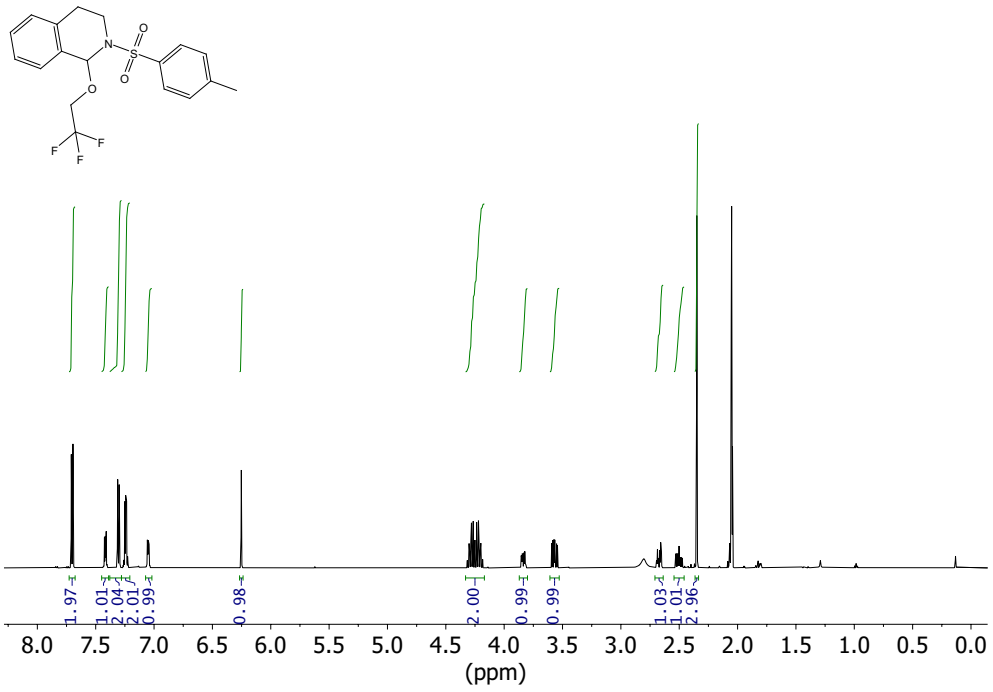

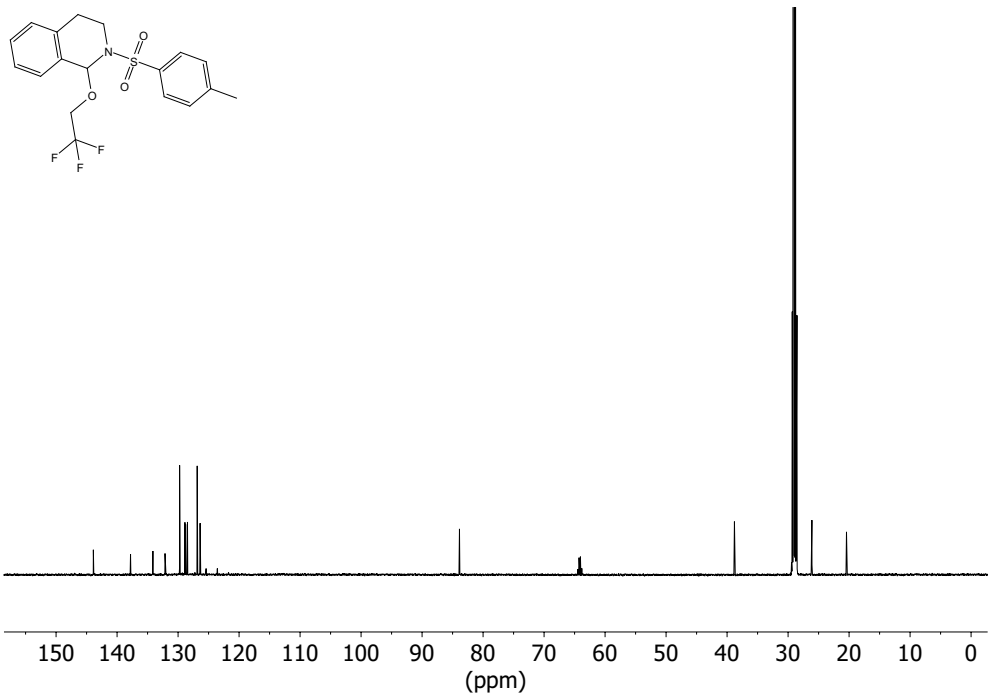

^{19}F NMR (376 MHz, $(CD_3)_2CO$) of compound **374**

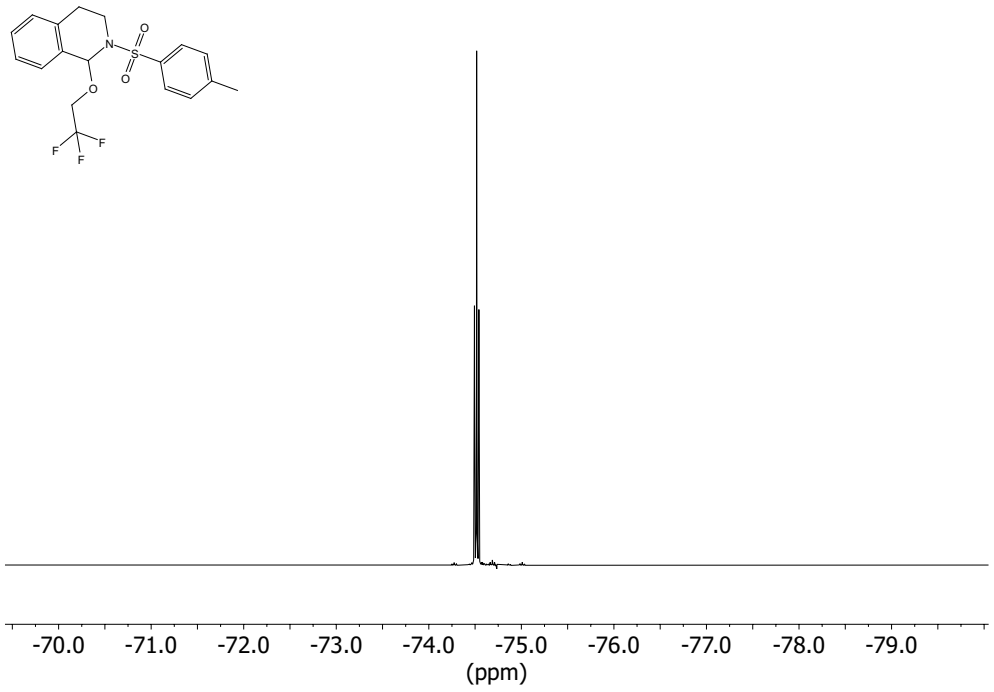

^{1}H NMR (700 MHz, $(CD_3)_2CO$) and ^{13}C NMR (176 MHz, $(CD_3)_2CO$) of compound **388**

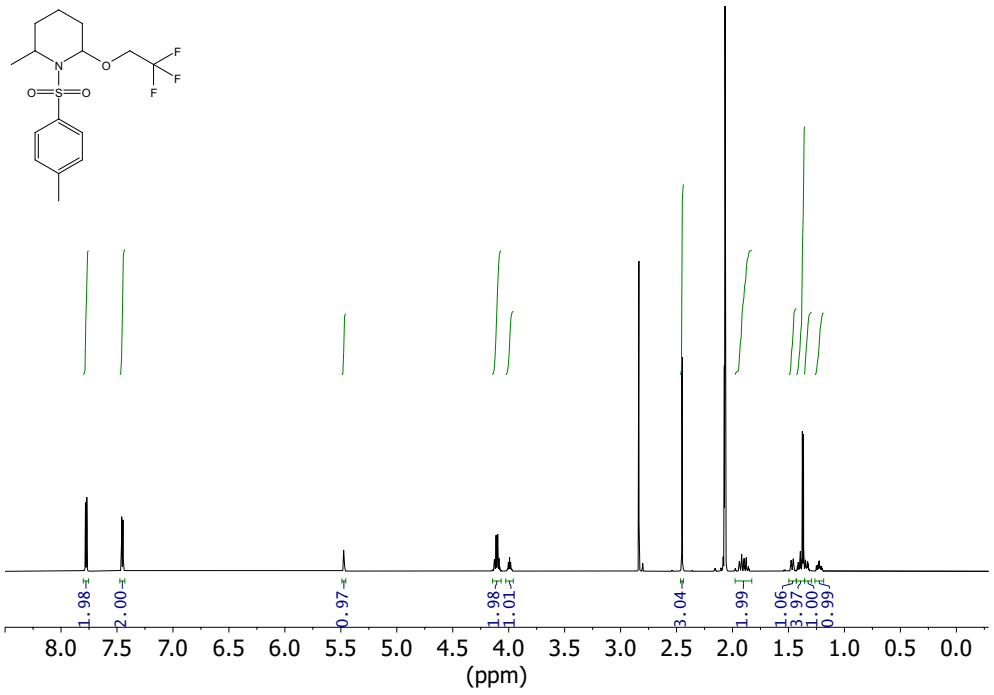

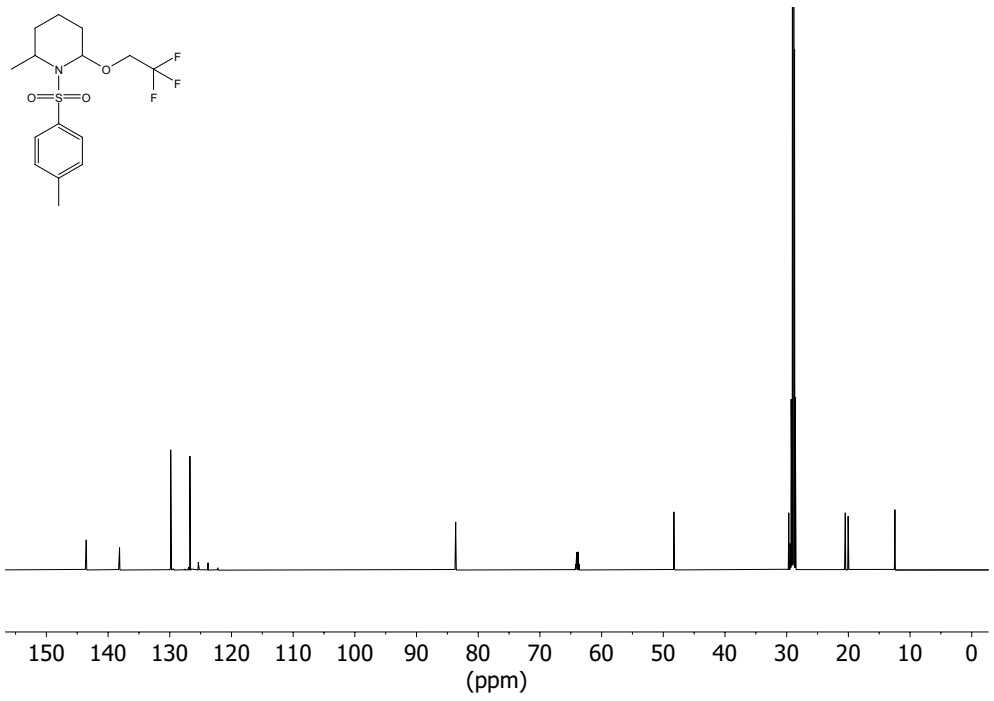

^{19}F NMR (376 MHz, $(CD_3)_2CO$) of compound **388**

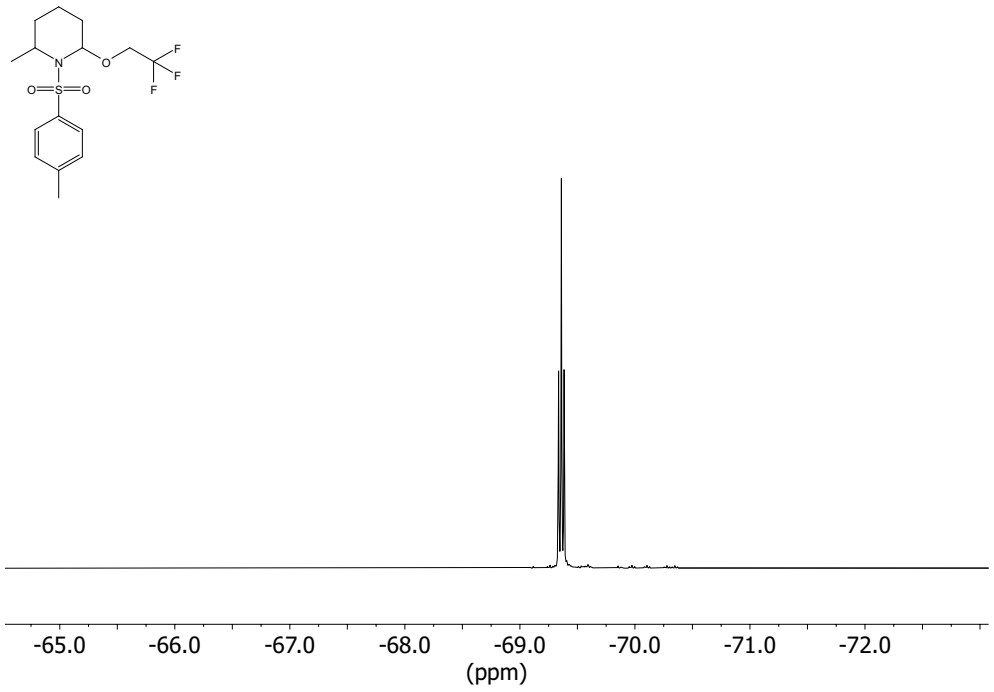

^{1}H NMR (400 MHz, $(CD_3)_2CO$) and ^{13}C NMR (101 MHz, $(CD_3)_2CO$) of compound **394** and **395**

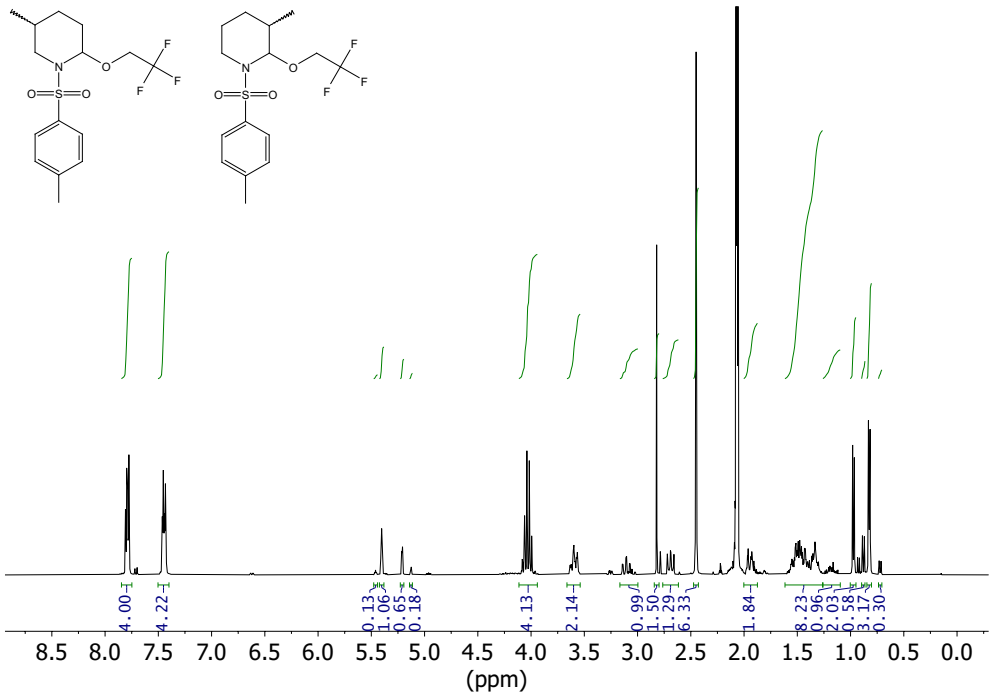

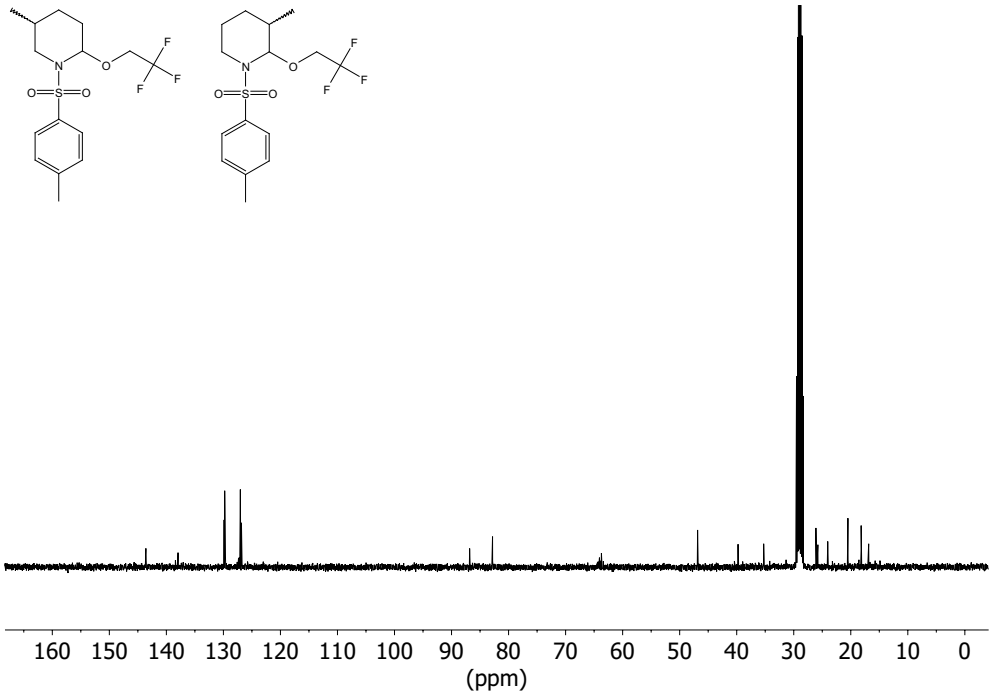

^{19}F NMR (376 MHz, $(CD_3)_2CO$) of compound **394** and **395**

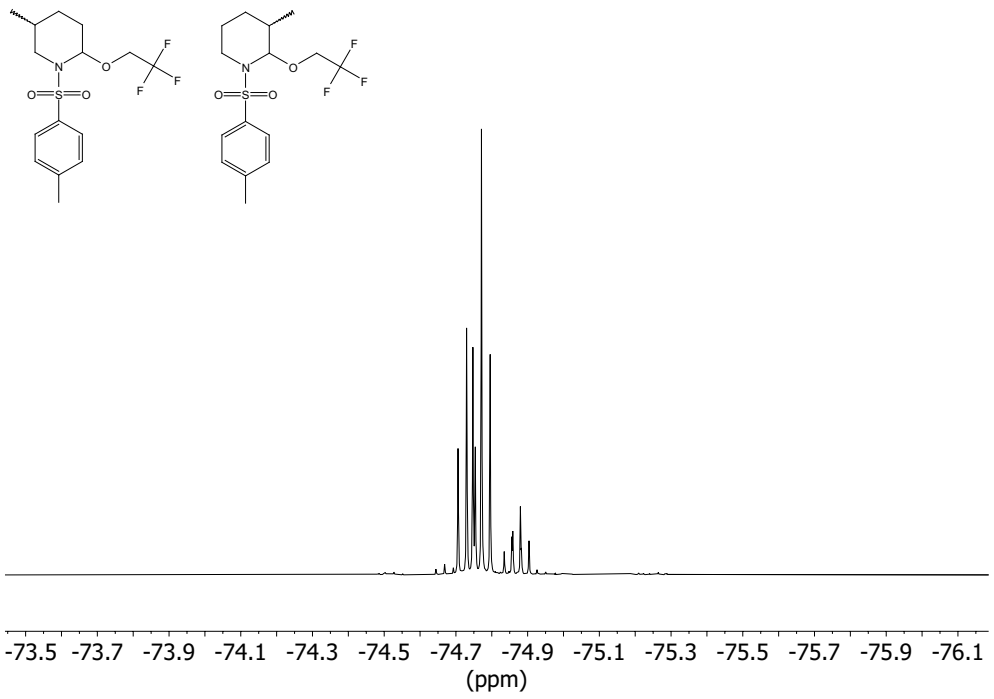

^{1}H NMR (700 MHz, $(CD_3)_2CO$) and ^{13}C NMR (176 MHz, $(CD_3)_2CO$) of compound **395**

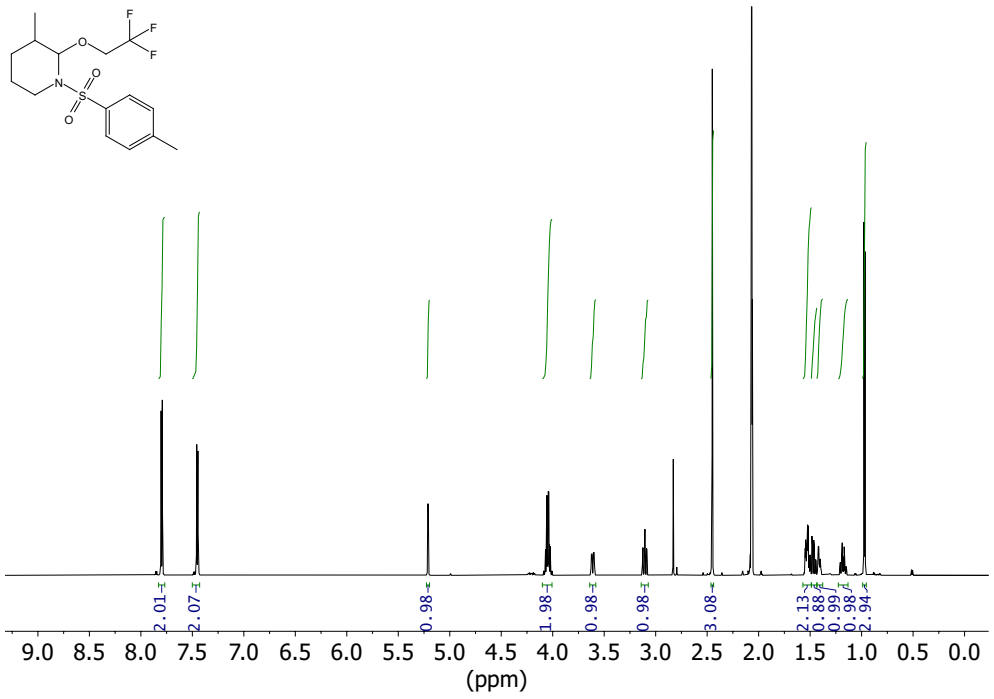

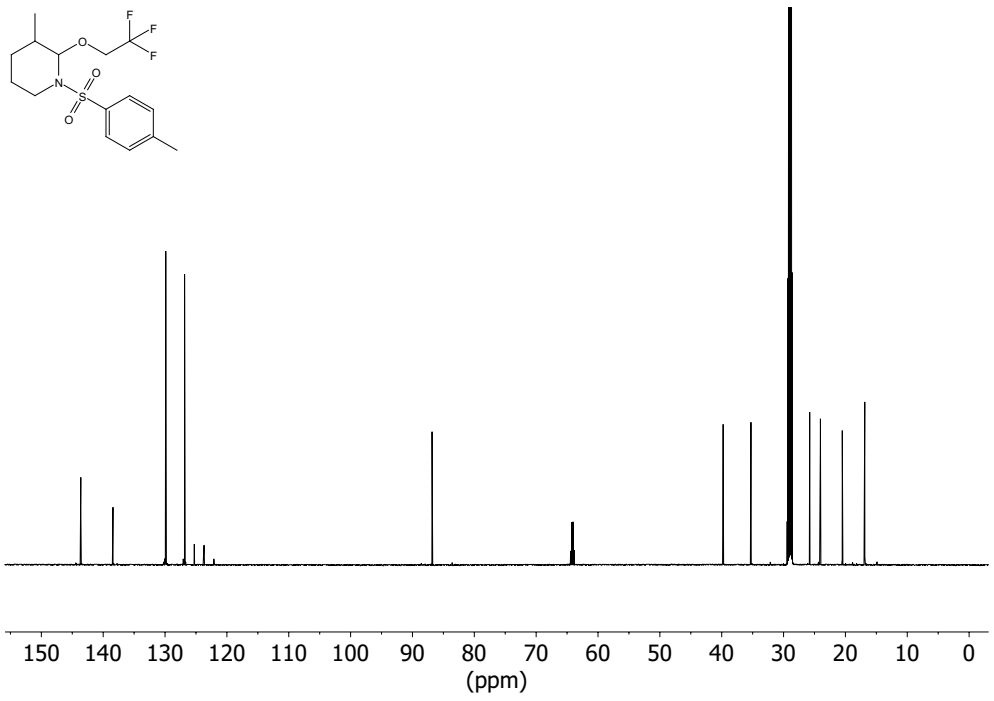

^{19}F NMR (376 MHz, $(CD_3)_2CO$) of compound **395**

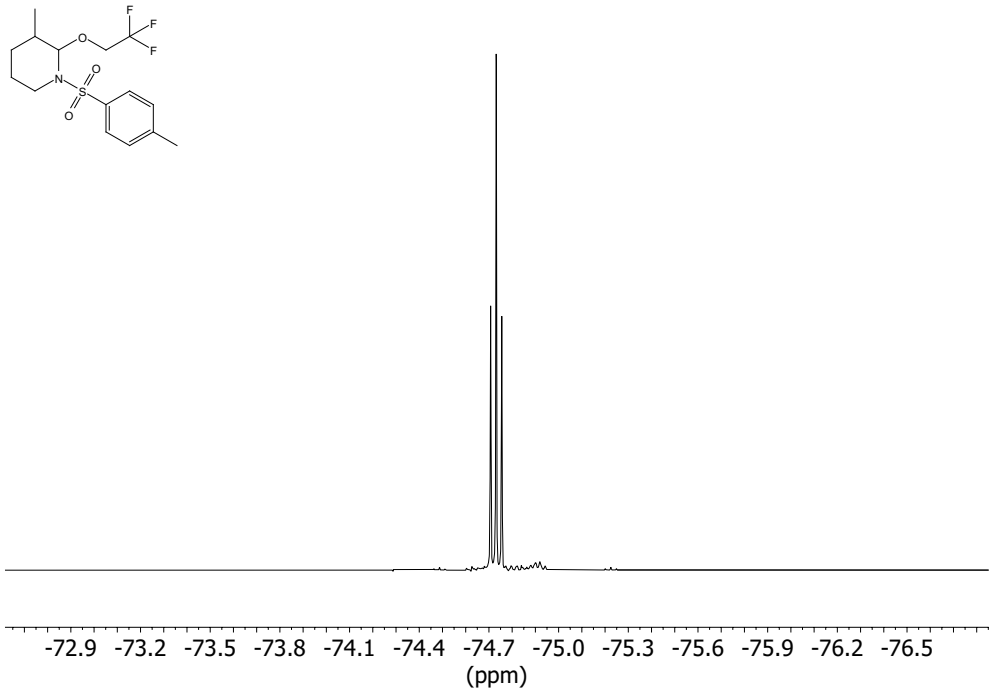

^{1}H NMR (600 MHz, $CDCl_3$) and ^{13}C NMR (151 MHz, $CDCl_3$) of compound **339**

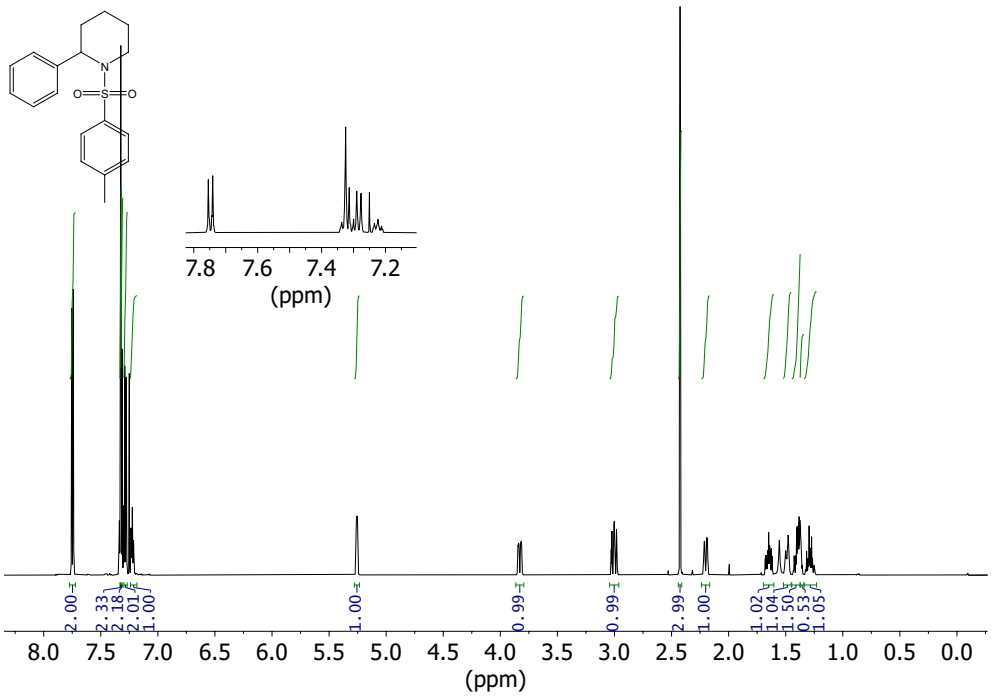

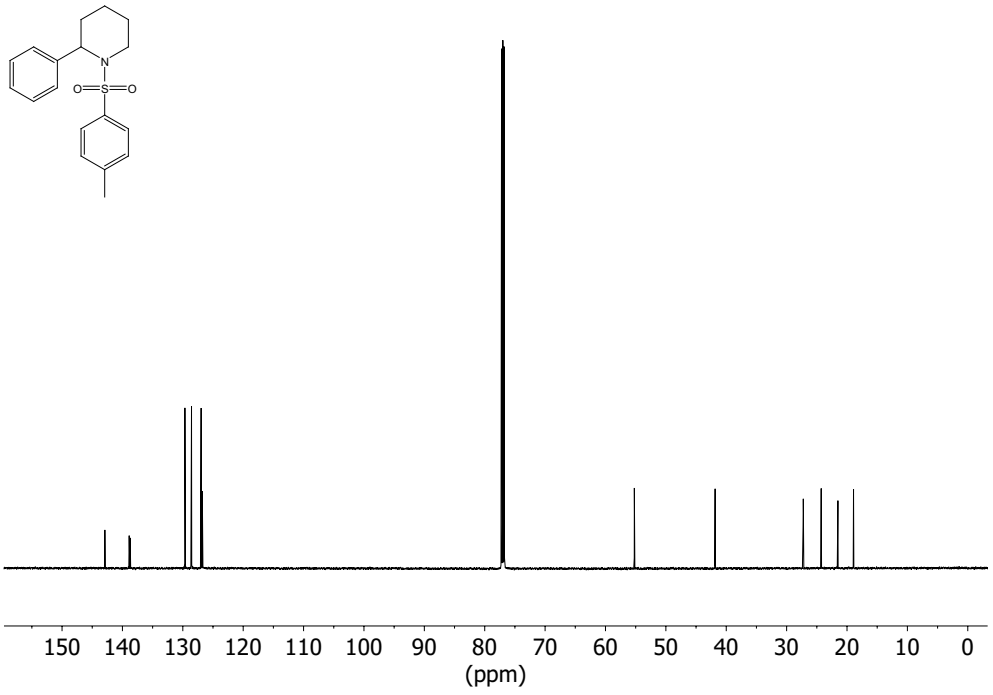

^{1}H NMR (600 MHz, $CDCl_3$) and ^{13}C NMR (151 MHz, $CDCl_3$) of compound **349**

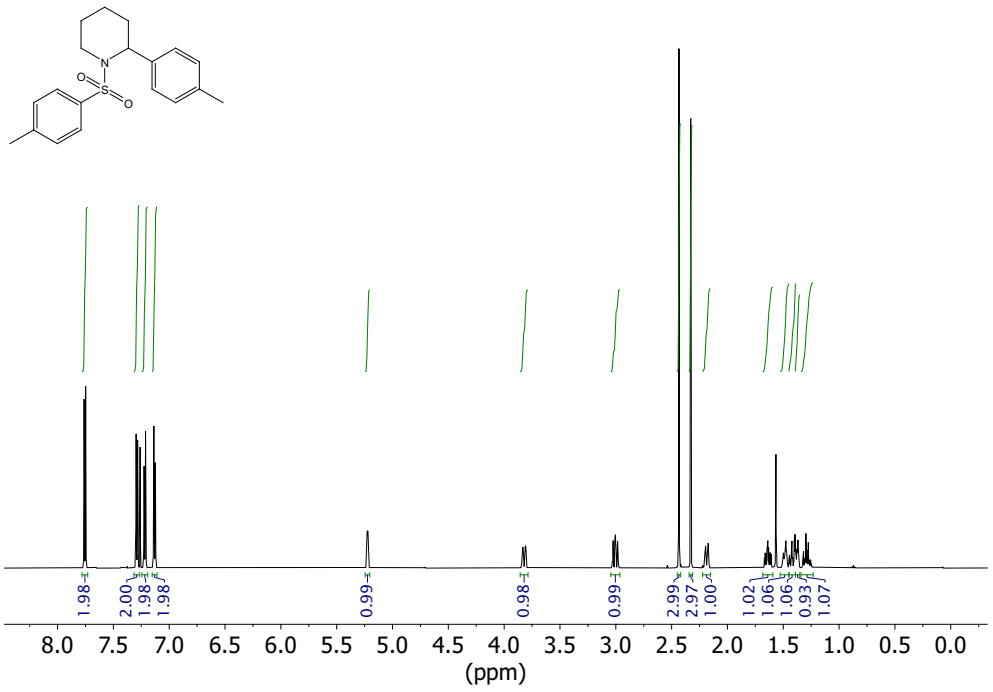

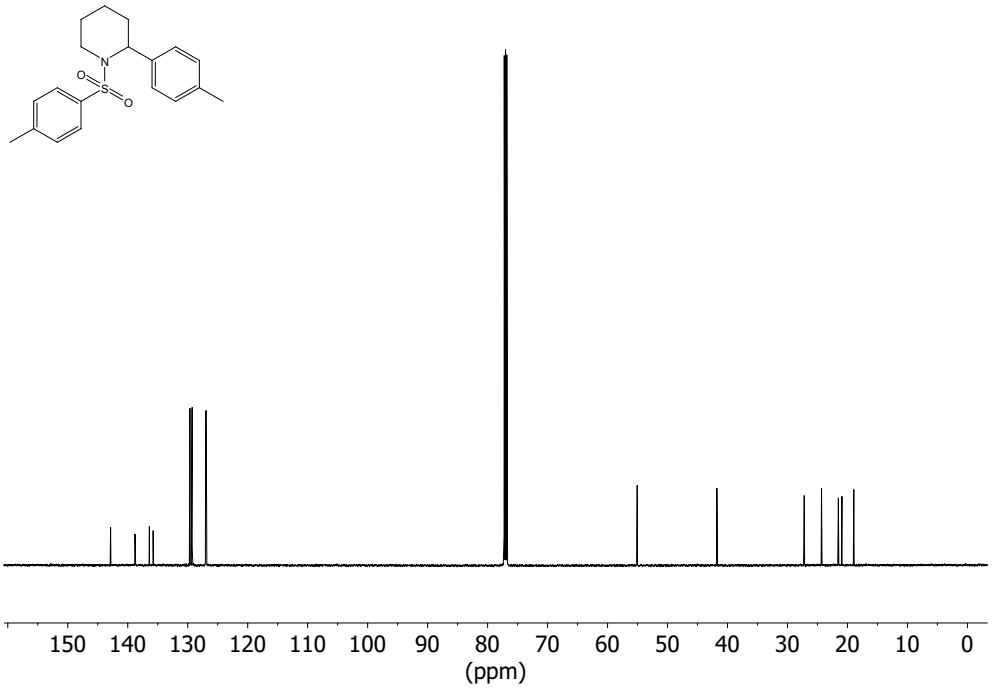

^{1}H NMR (600 MHz, $CDCl_3$) and ^{13}C NMR (151 MHz, $CDCl_3$) of compound **350**

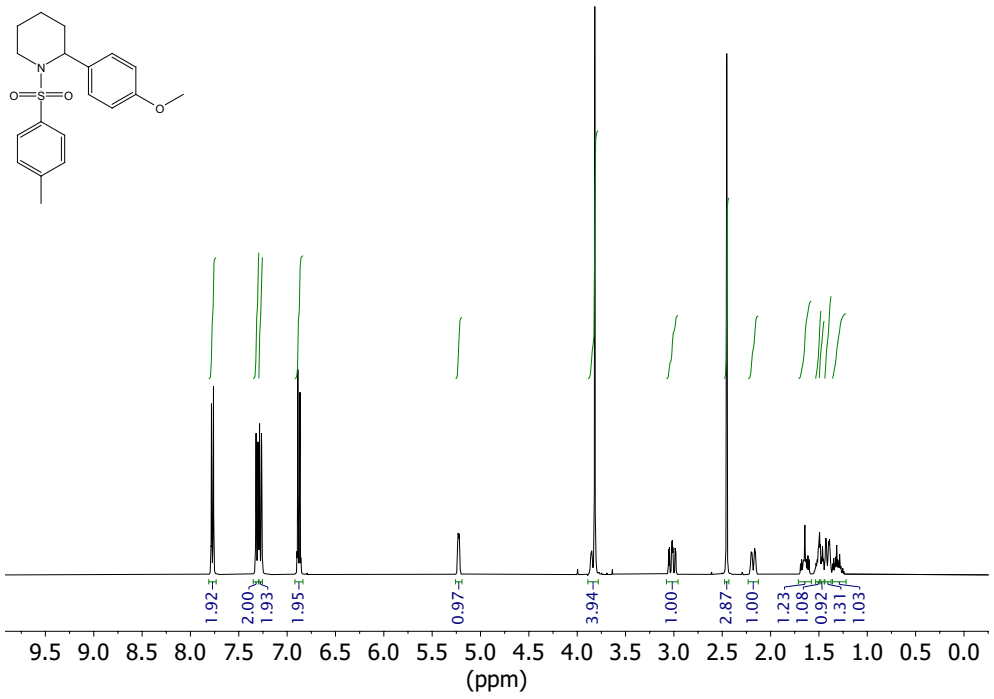

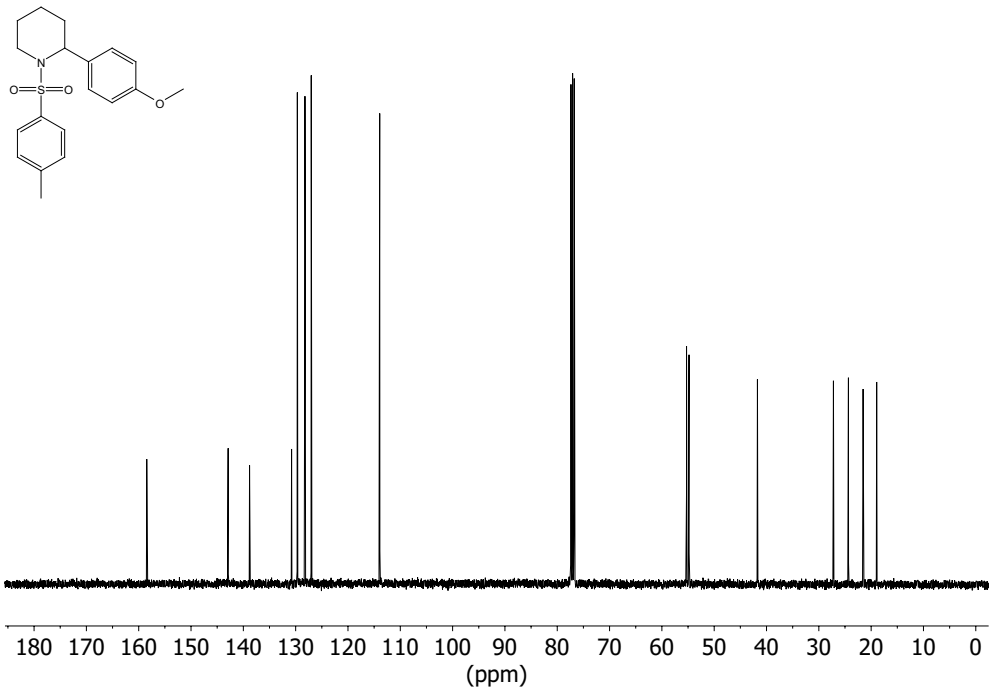

^{1}H NMR (700 MHz, $CDCl_3$) and ^{13}C NMR (176 MHz, $CDCl_3$) of compound **351**

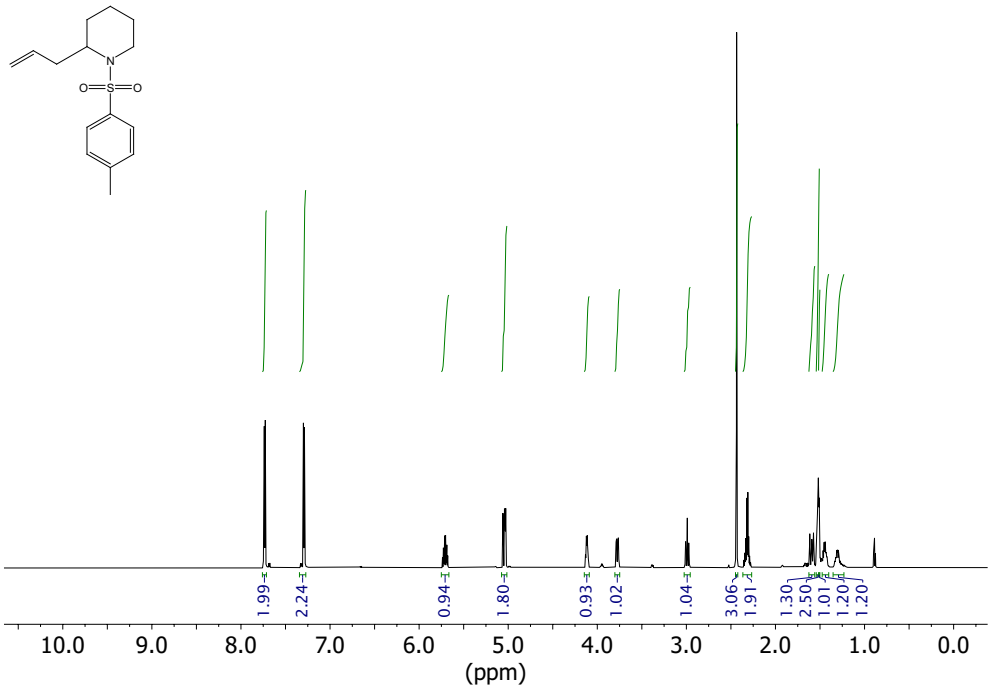

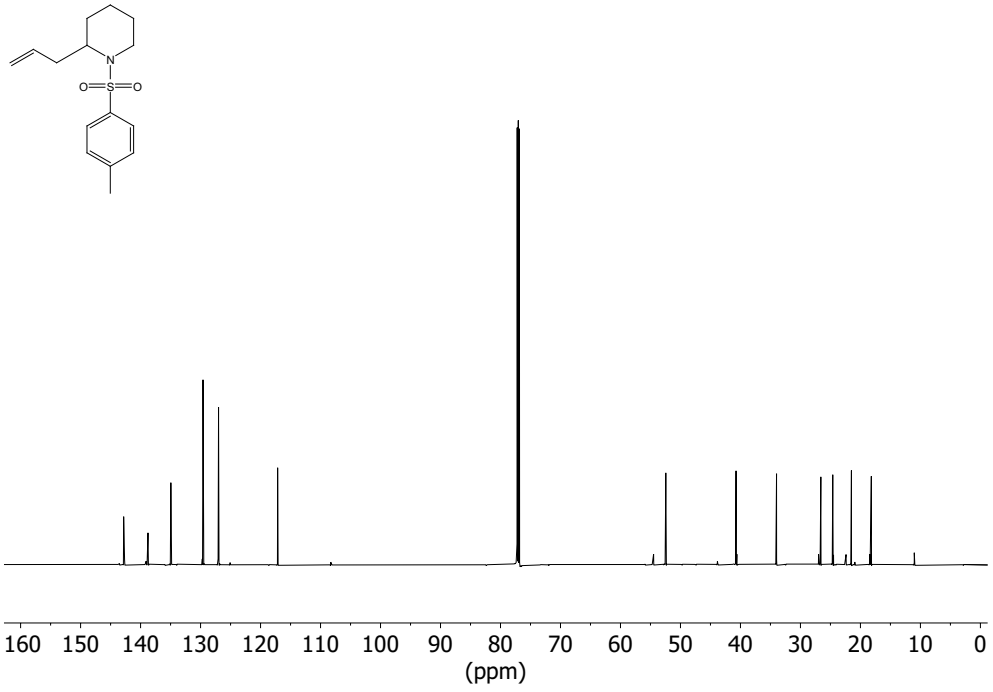

^{1}H NMR (700 MHz, $CDCl_3$) and ^{13}C NMR (176 MHz, $CDCl_3$) of compound **352**

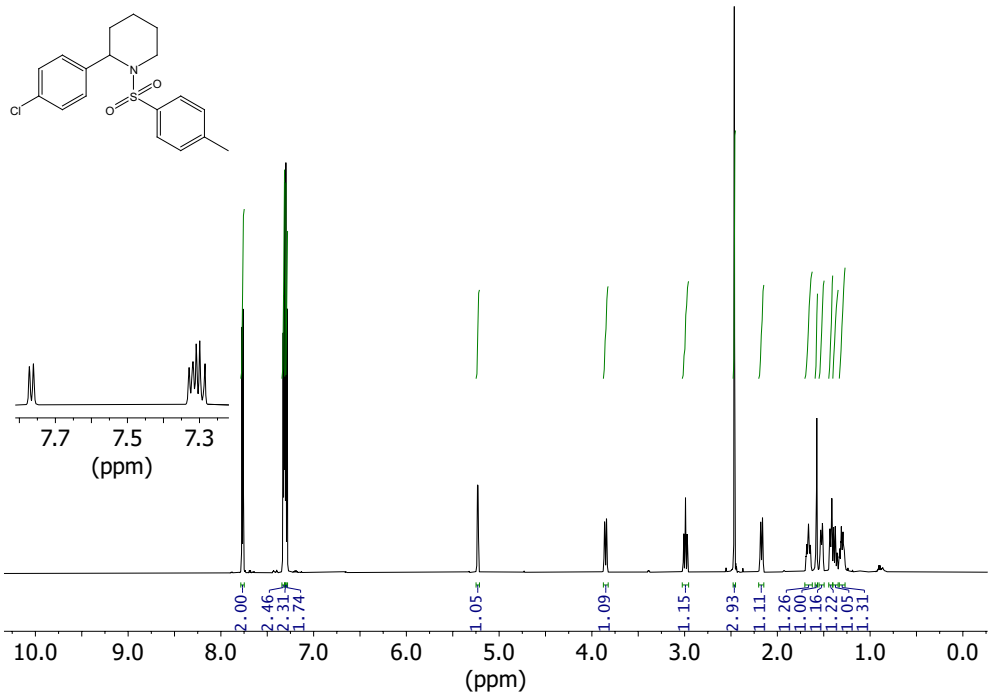

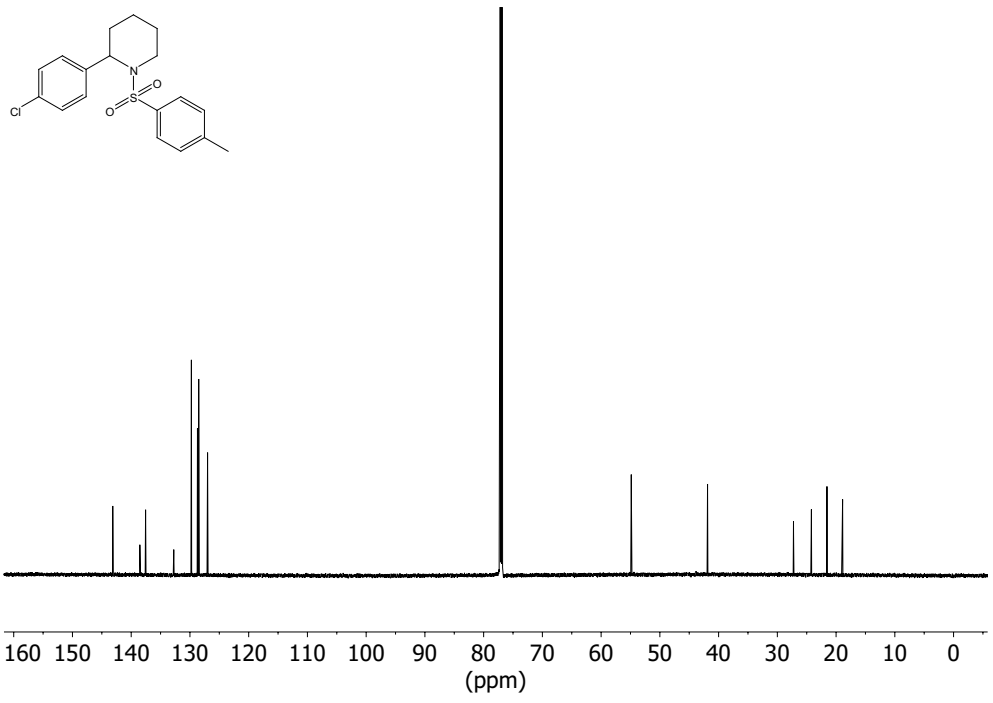

^{1}H NMR (500 MHz, $CDCl_3$) and ^{13}C NMR (126 MHz, $CDCl_3$)(VT = 80 ˚C) of compound **348**

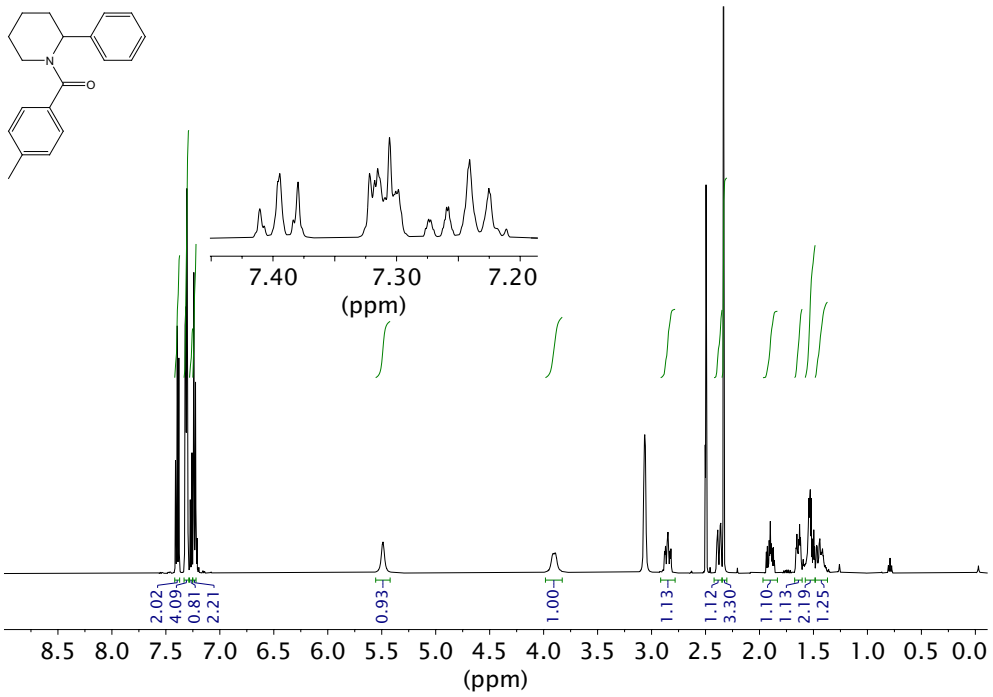

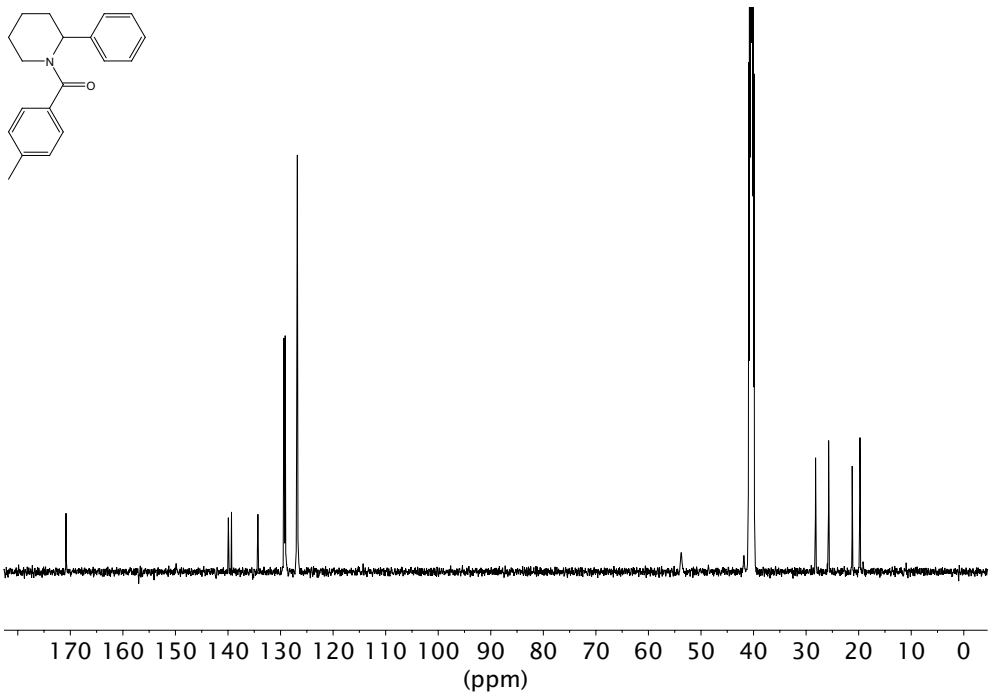

^{1}H NMR (700 MHz, $CDCl_3$) and ^{13}C NMR (176 MHz, $CDCl_3$) of compound **384**

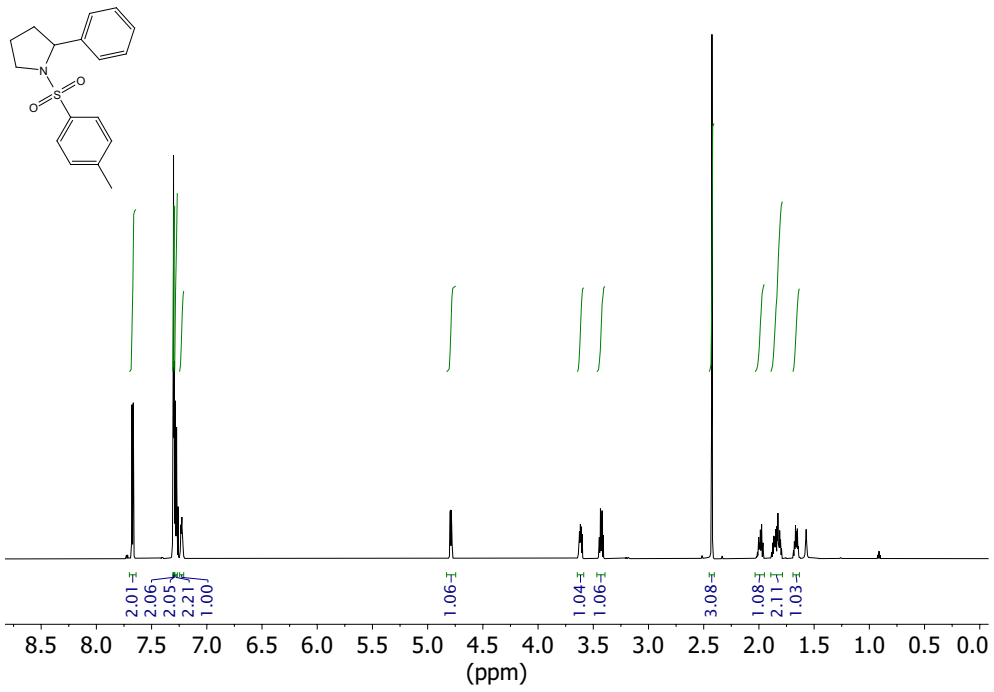

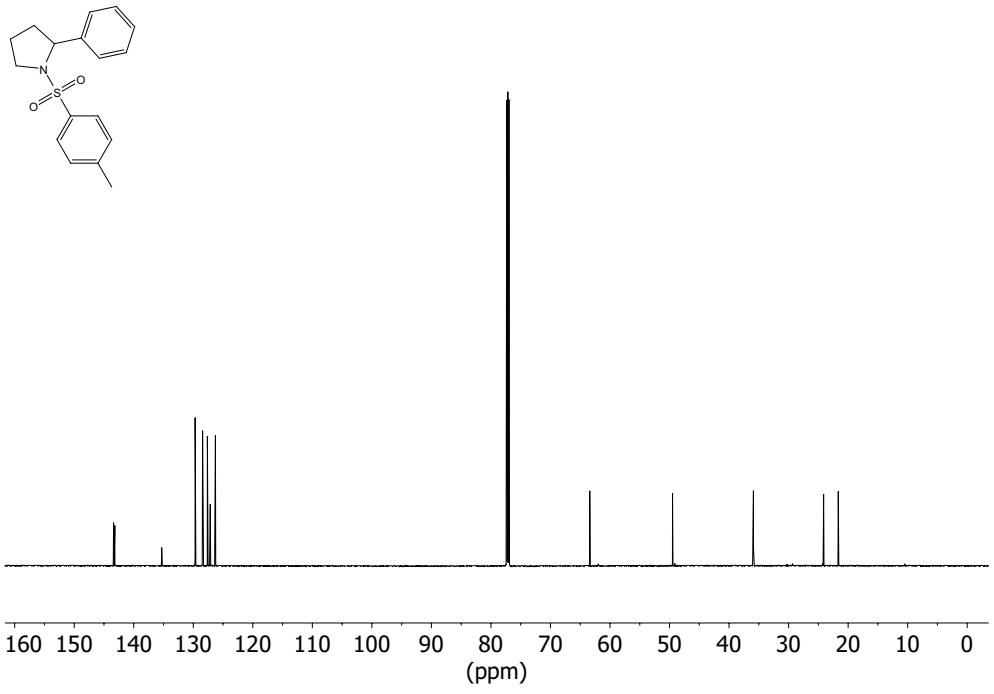

^{1}H NMR (700 MHz, $CDCl_3$) and ^{13}C NMR (176 MHz, $CDCl_3$) of compound **385**

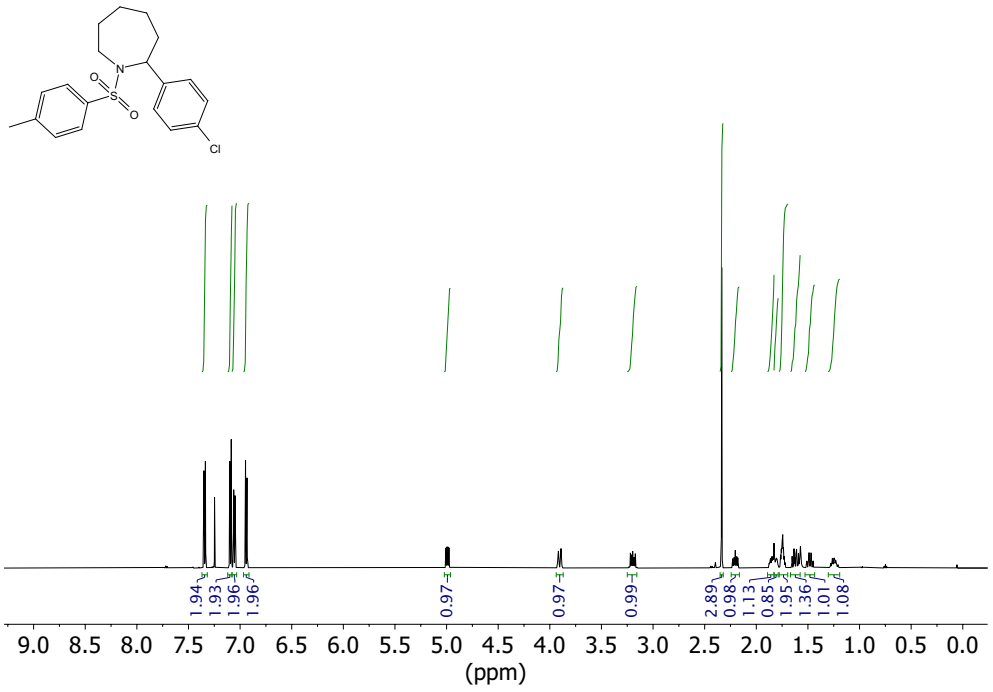

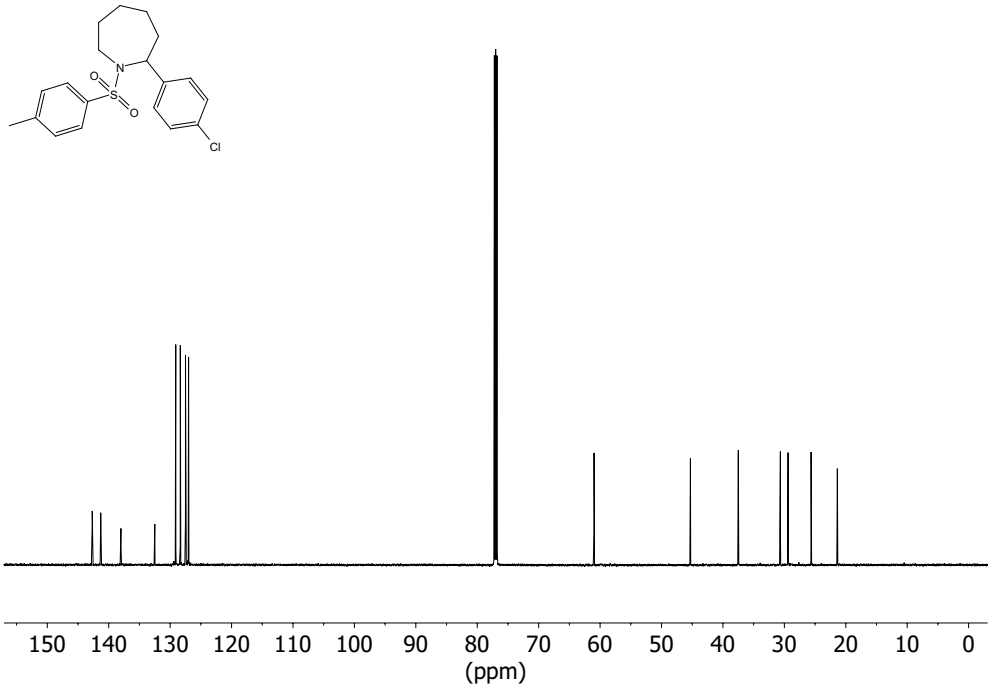

^{1}H NMR (700 MHz, $CDCl_3$) and ^{13}C NMR (176 MHz, $CDCl_3$) of compound **386**

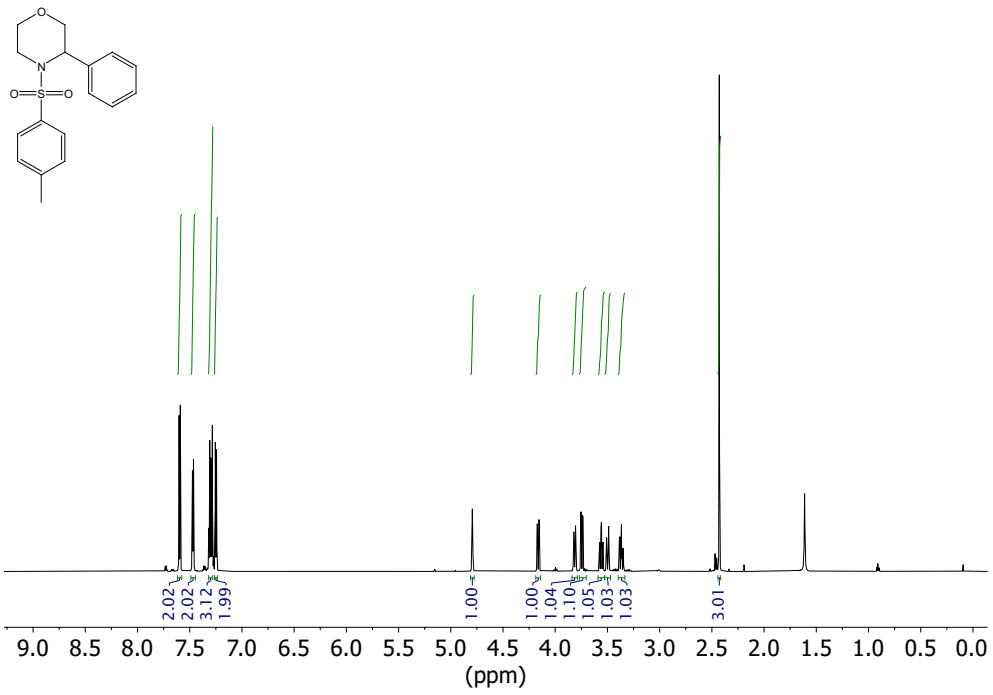

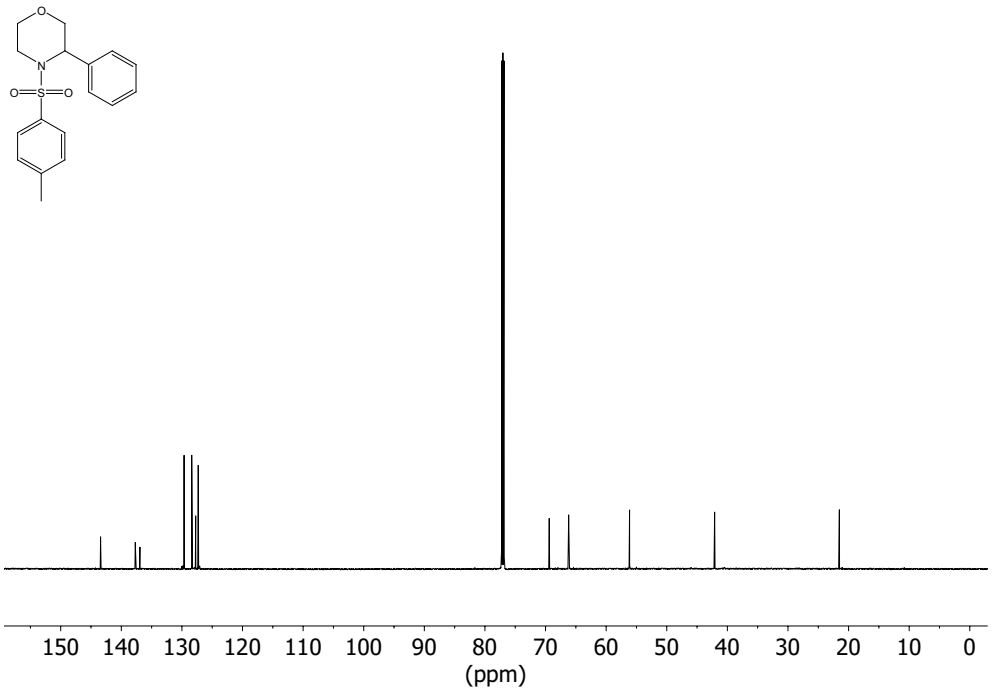

^{1}H NMR (600 MHz, $CDCl_3$) and ^{13}C NMR (151 MHz, $CDCl_3$) of compound **387**

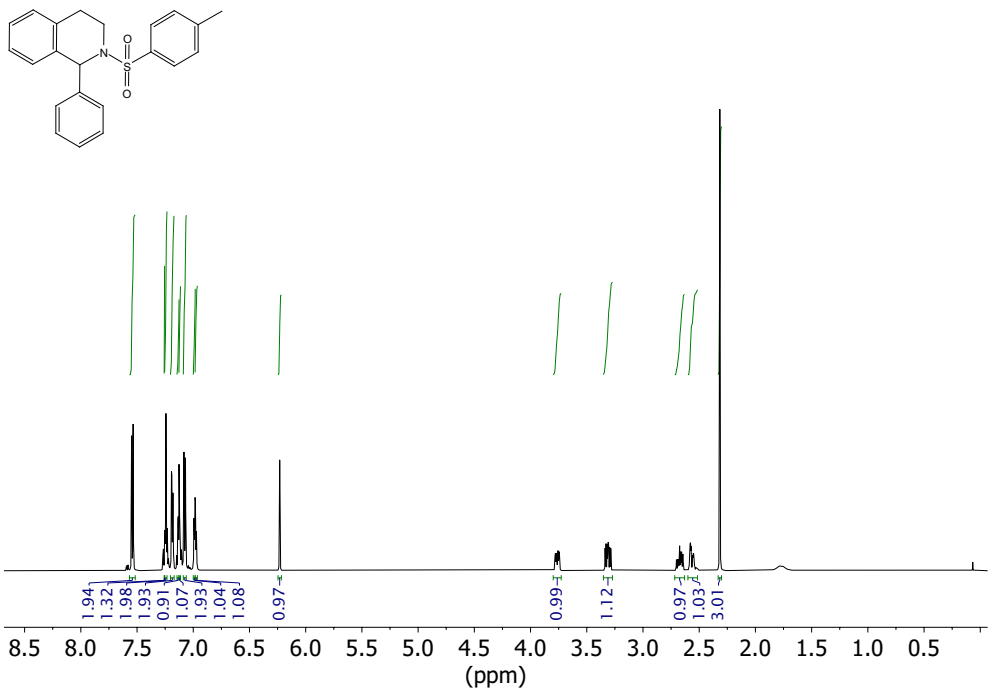

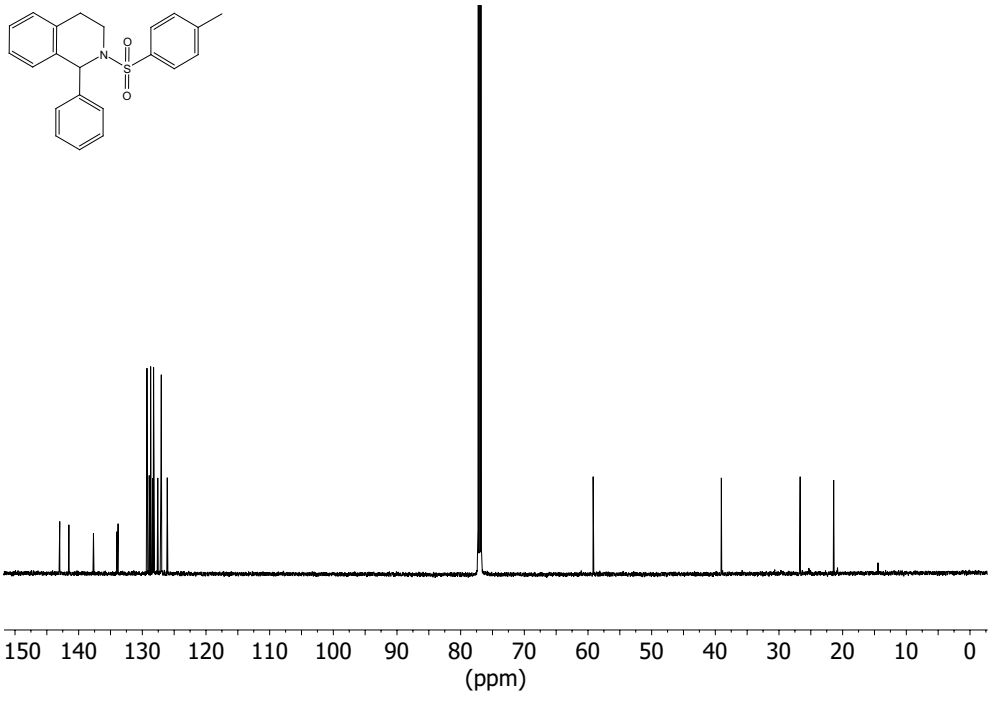

^{1}H NMR (600 MHz, $CDCl_3$) and ^{13}C NMR (151 MHz, $CDCl_3$) of **392** (major)

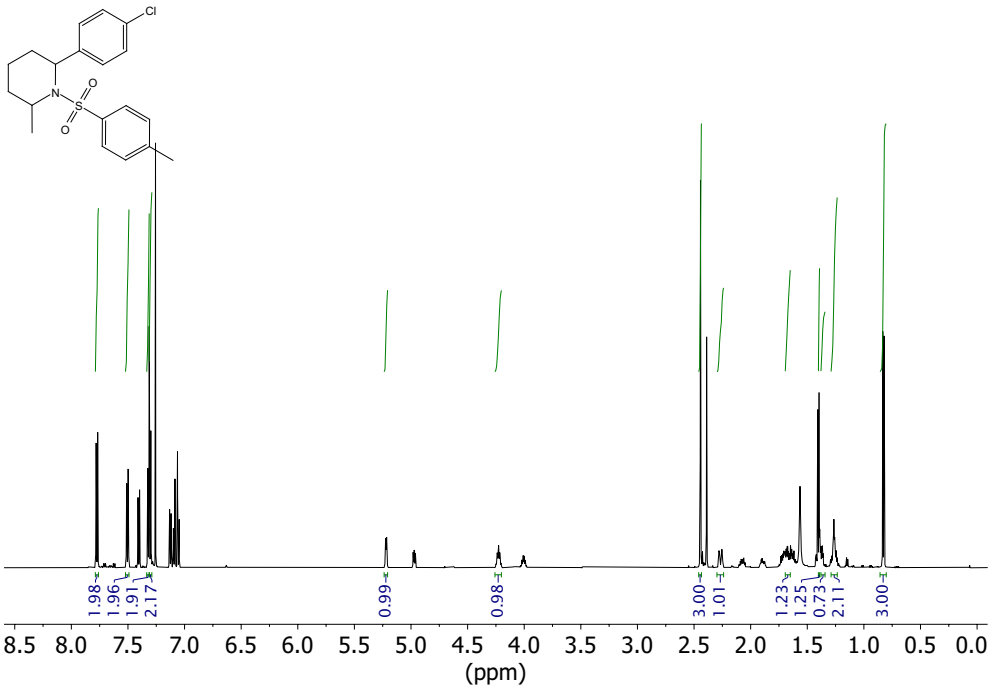

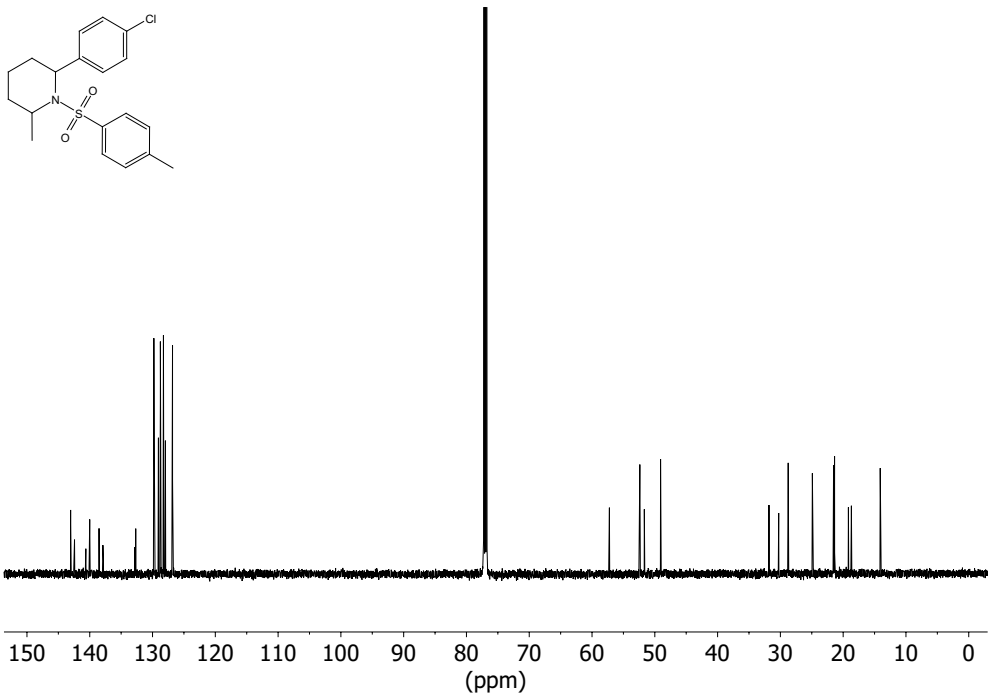

^{1}H NMR (600 MHz, $CDCl_3$) and ^{13}C NMR (151 MHz, $CDCl_3$) of **392** (minor)

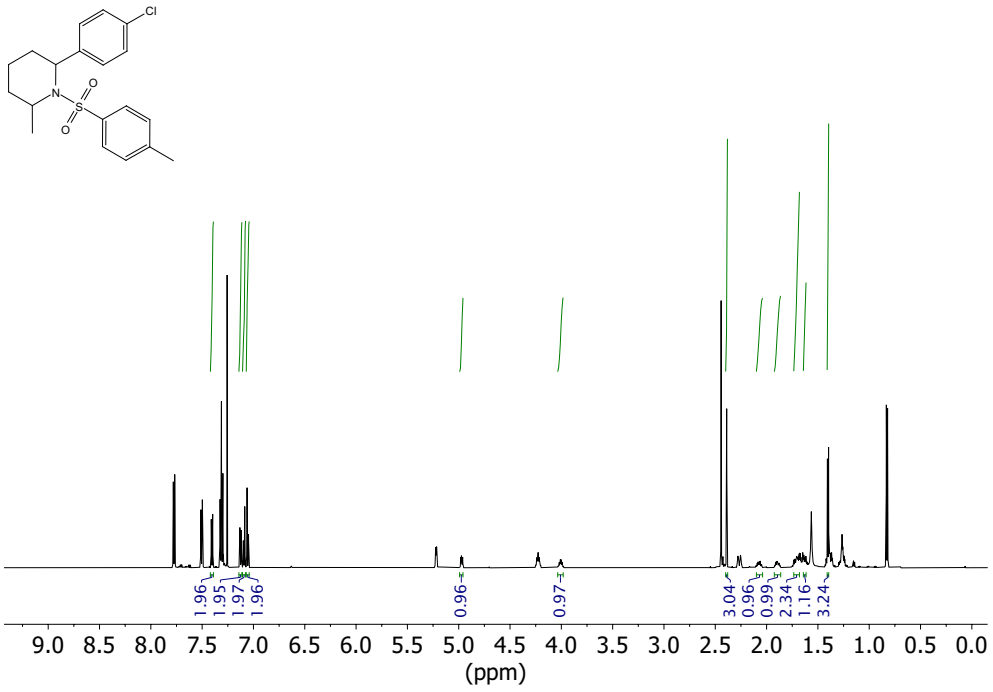

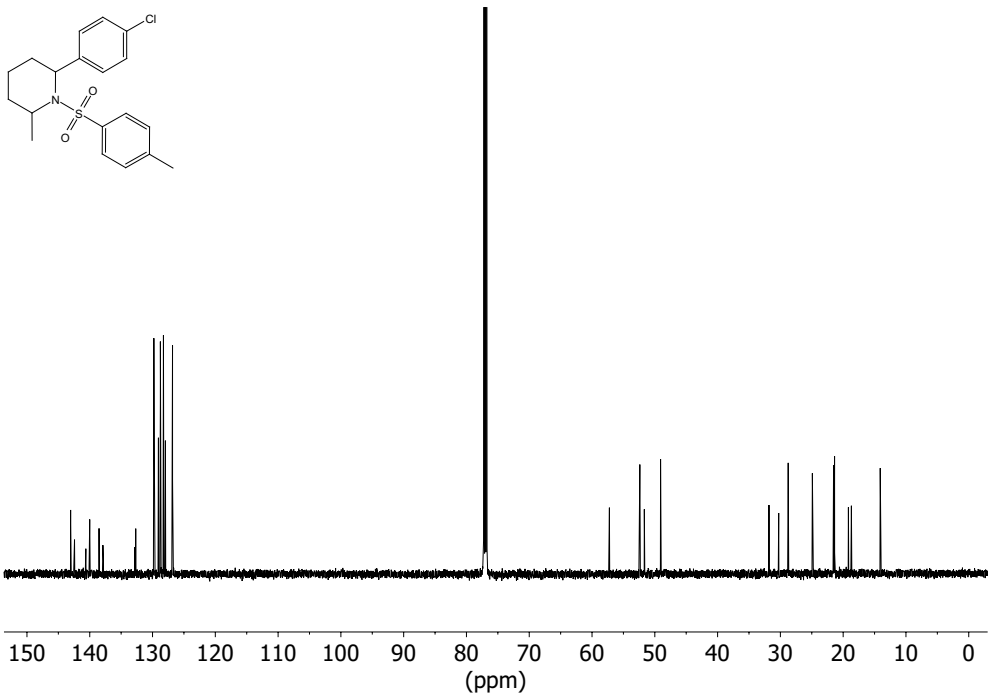

^{1}H NMR (600 MHz, $CDCl_3$) and ^{13}C NMR (151 MHz, $CDCl_3$) of compound **345**

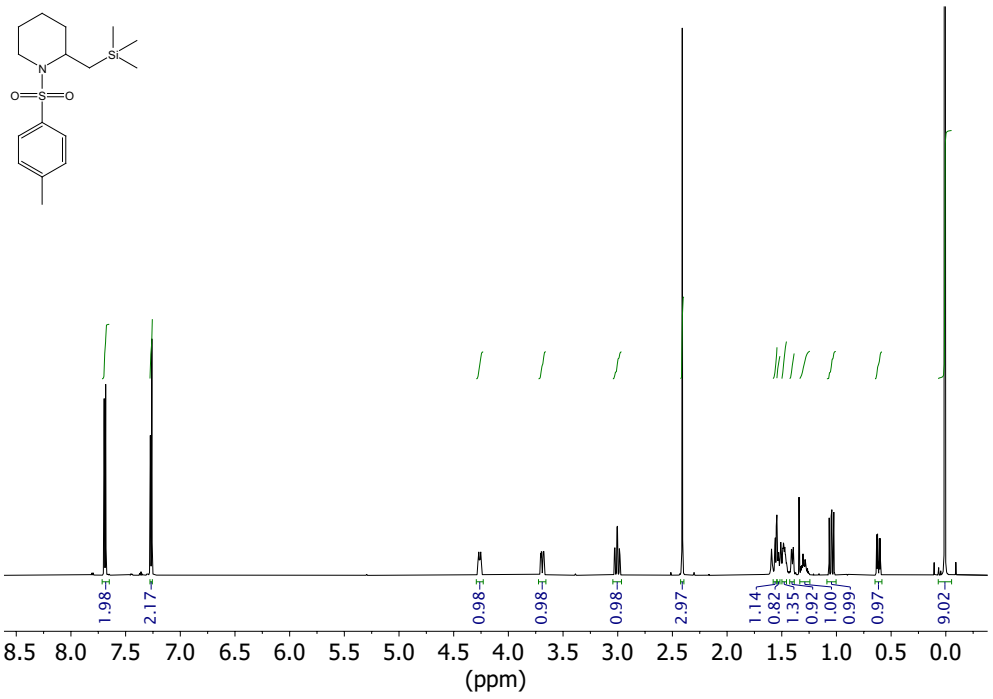

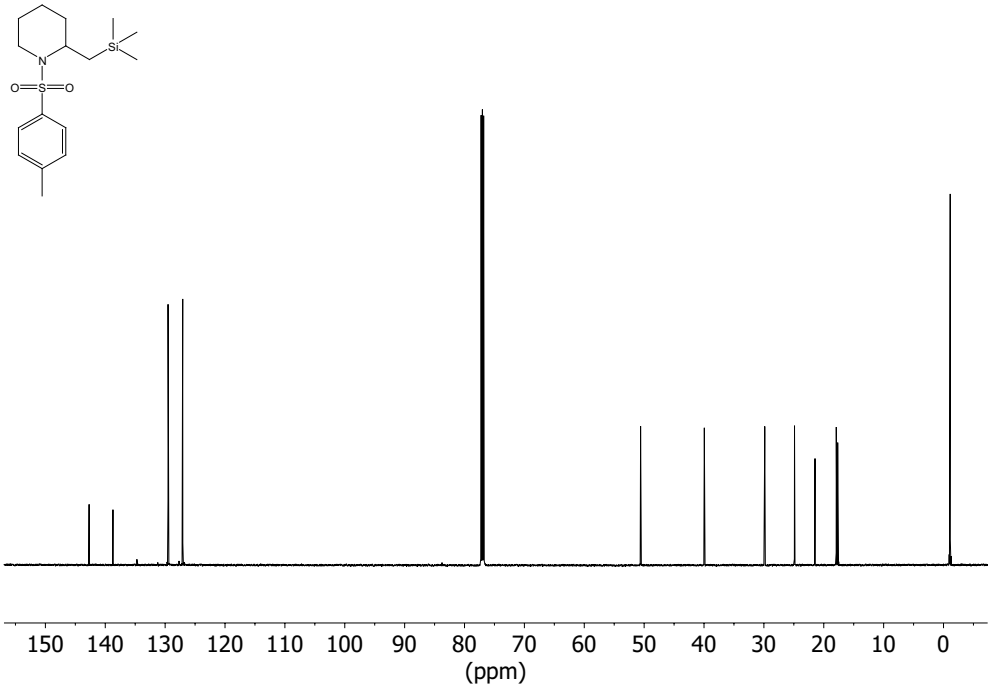

^{1}H NMR (700 MHz, $CDCl_3$) and ^{13}C NMR (176 MHz, $CDCl_3$) of compound **338**

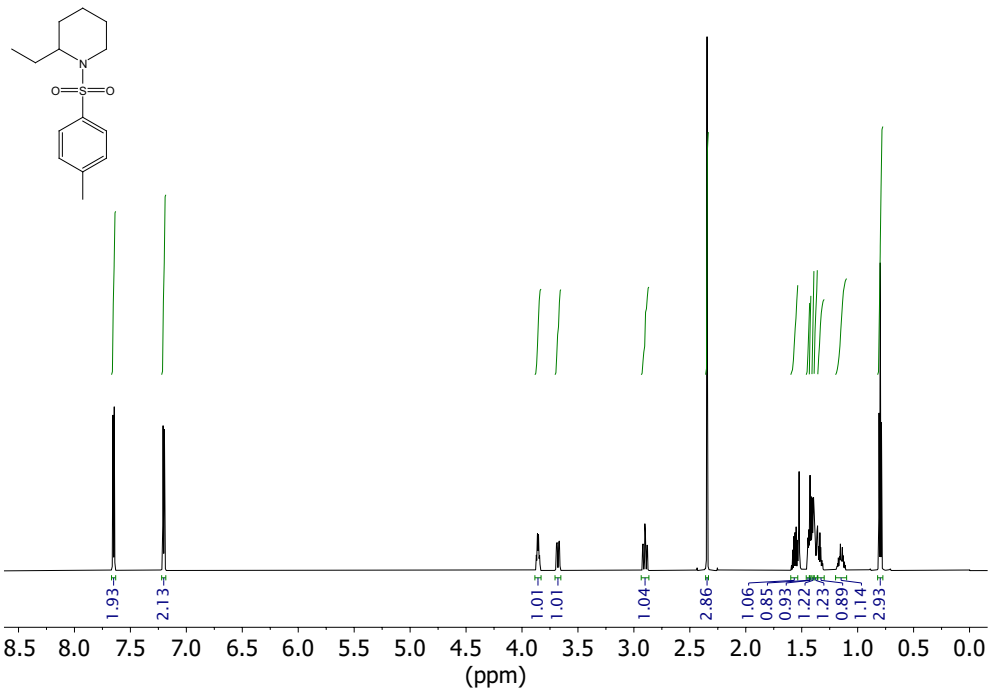

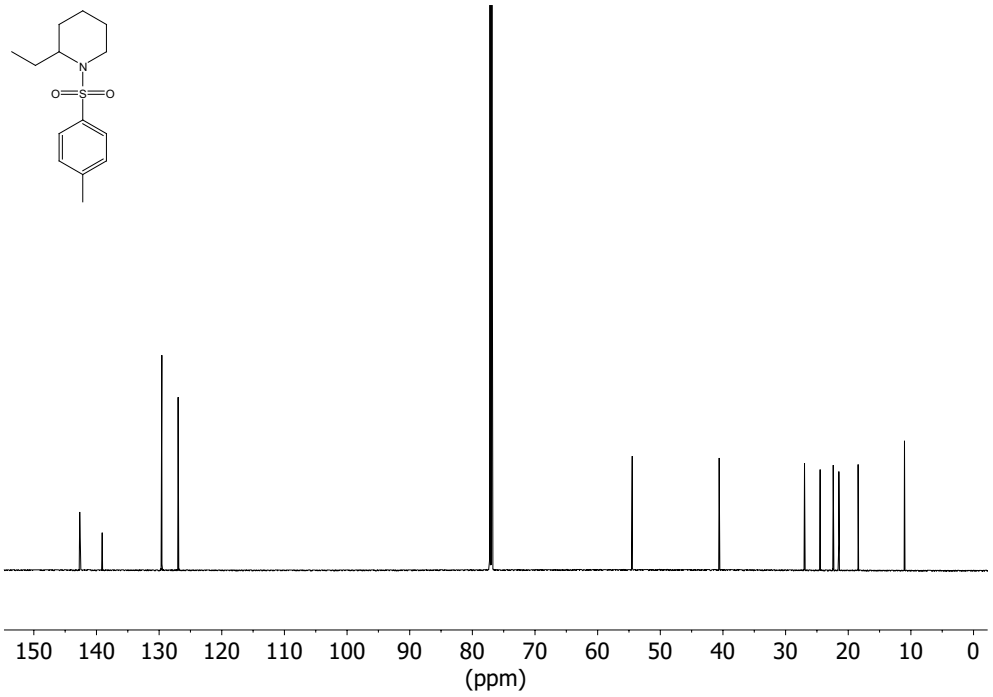

^{1}H NMR (700 MHz, $CDCl_3$) and ^{13}C NMR (176 MHz, $CDCl_3$) of compound **411**

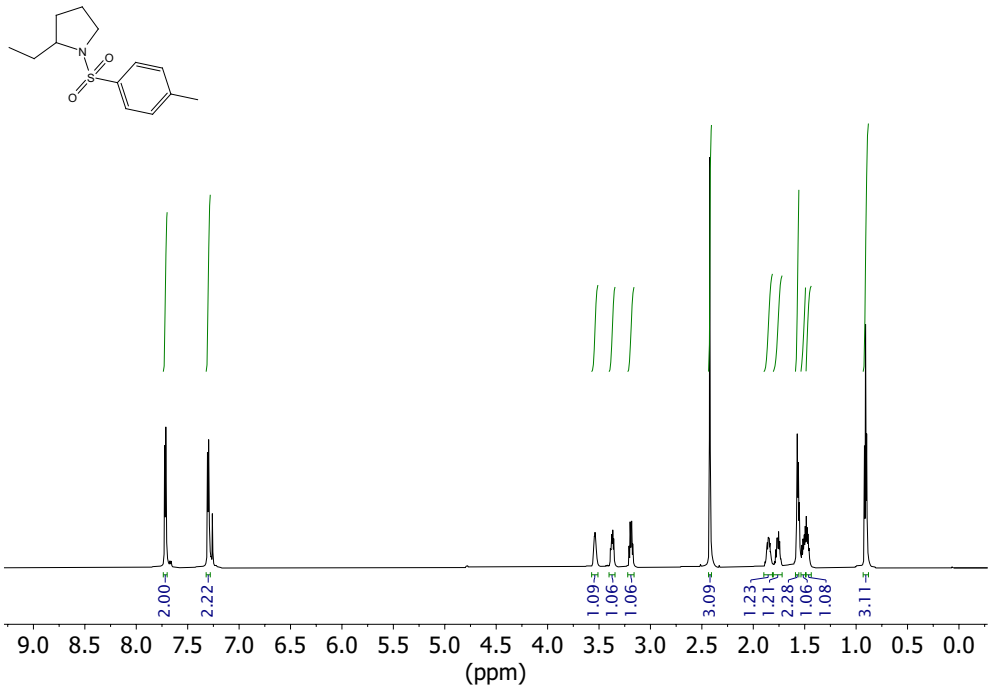

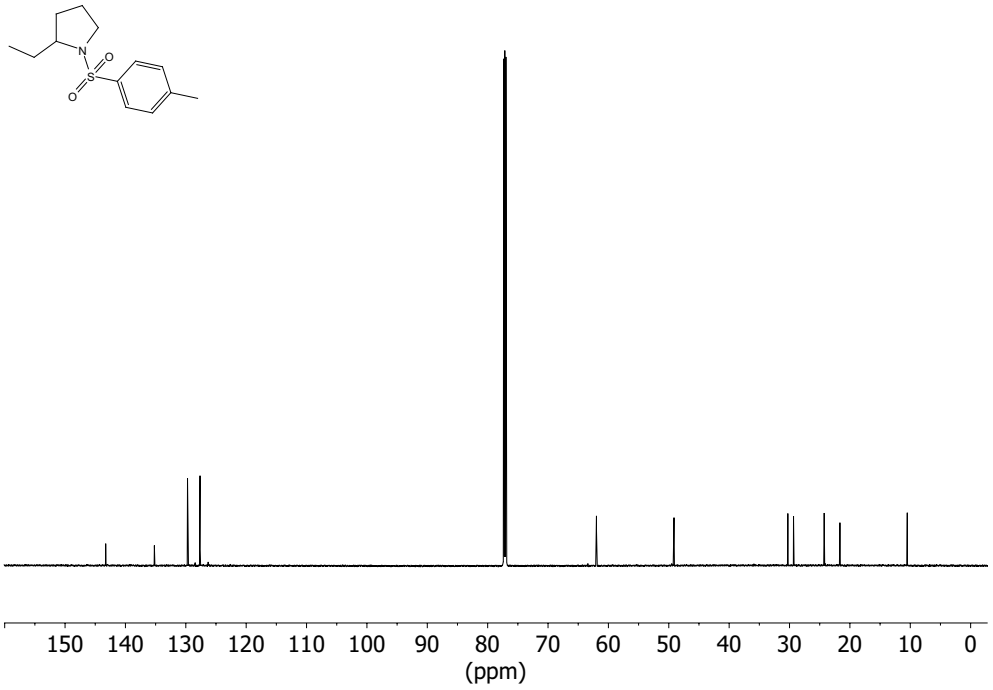

^{1}H NMR (600 MHz, $CDCl_3$) and ^{13}C NMR (151 MHz, $CDCl_3$) of compound **391**

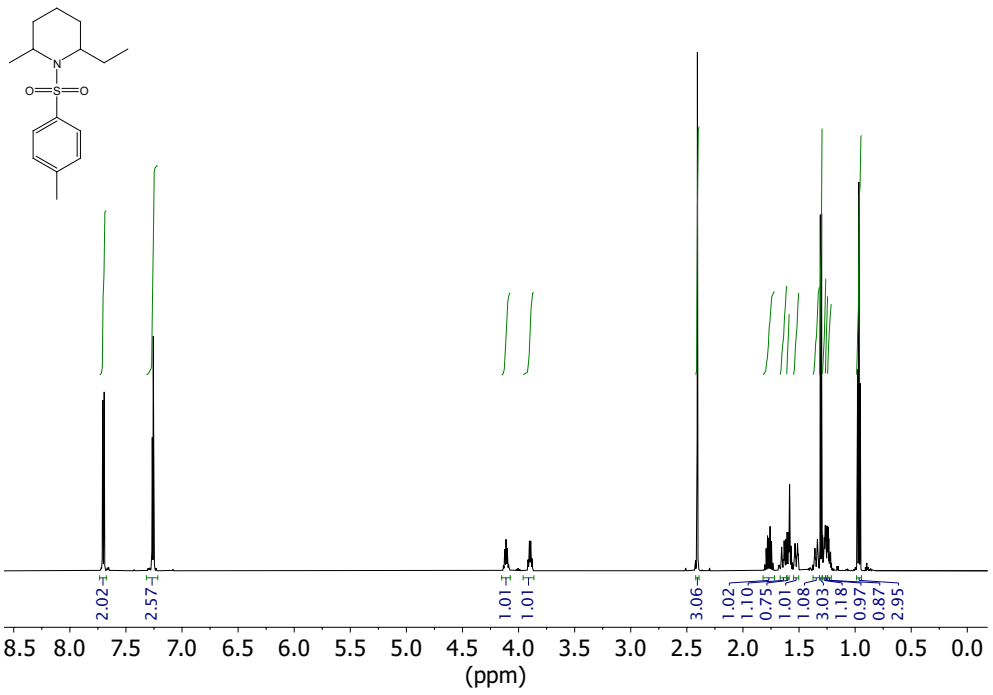

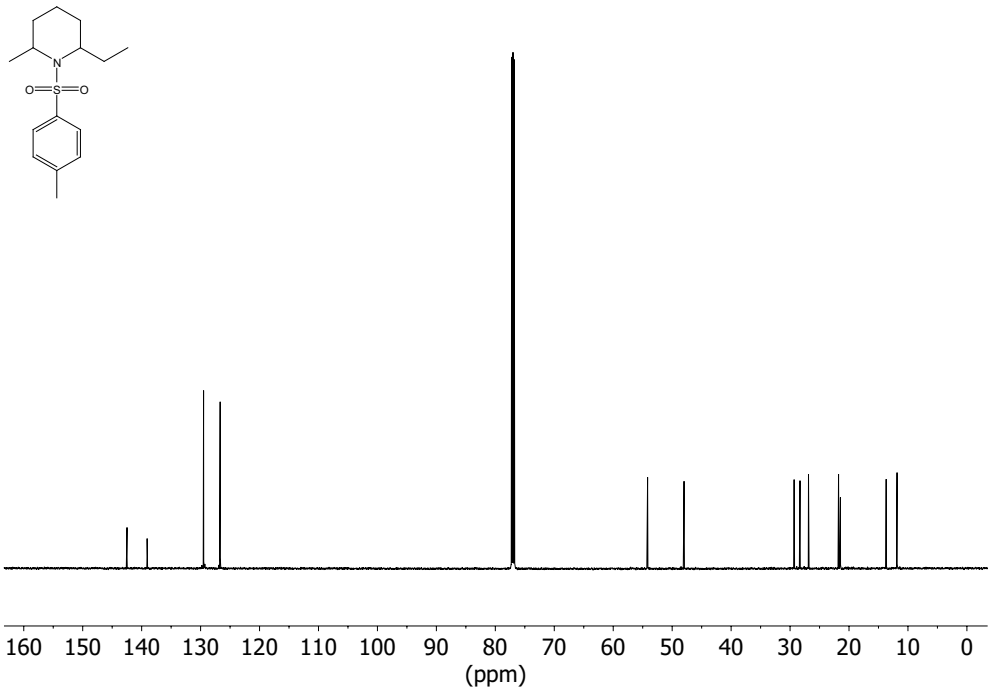

^{1}H NMR (600 MHz, $CDCl_3$) and ^{13}C NMR (151 MHz, $CDCl_3$) of compound **412**

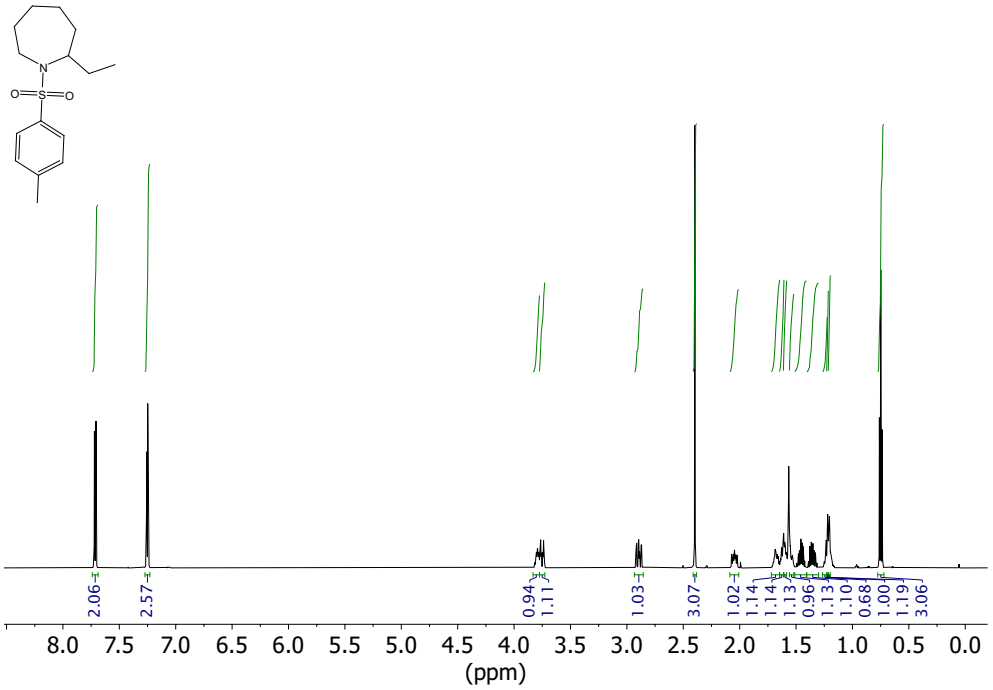

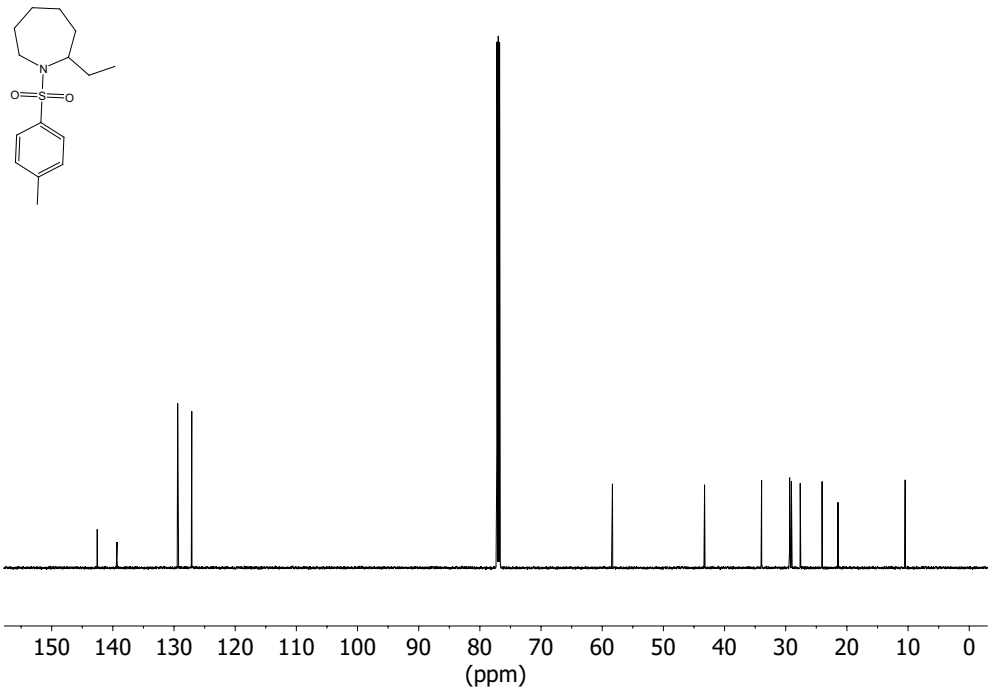

^{1}H NMR (600 MHz, $CDCl_3$) and ^{13}C NMR (151 MHz, $CDCl_3$) of compound **413**

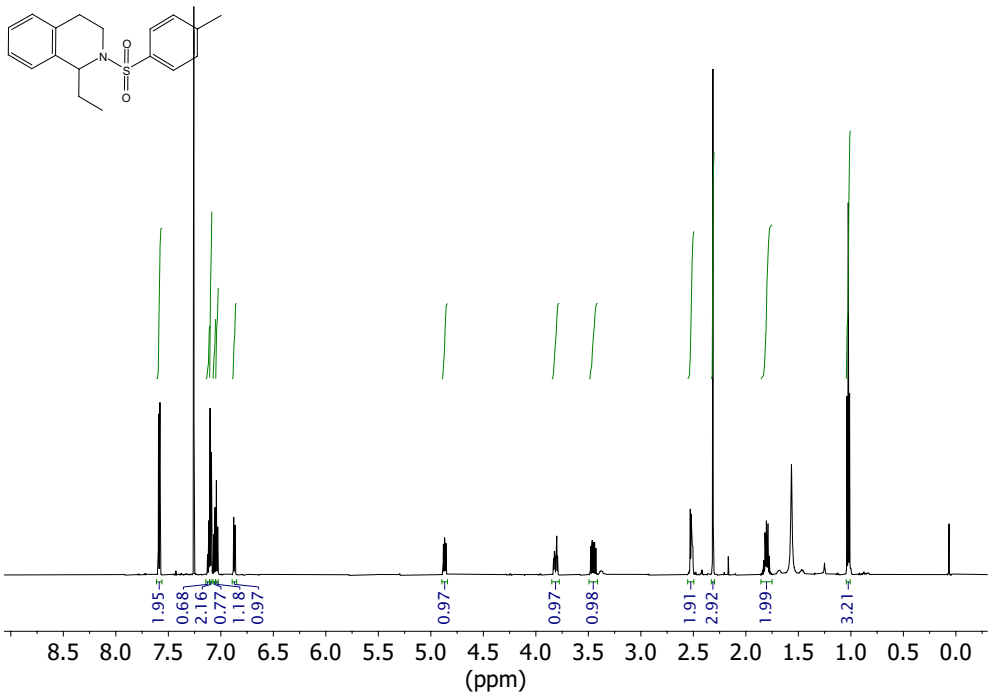

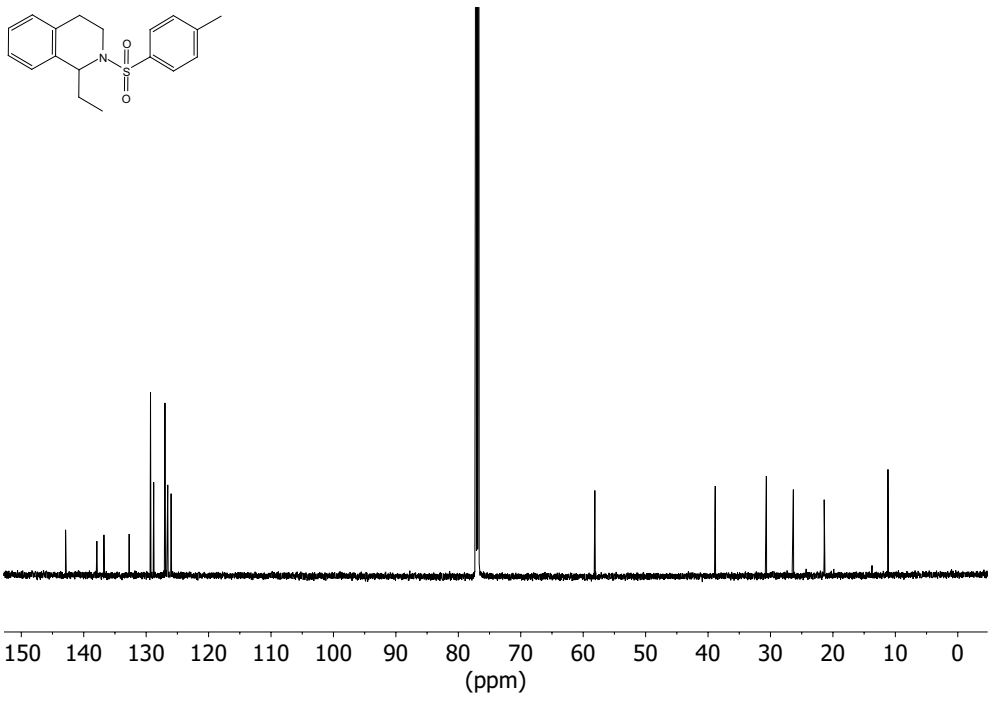

^{1}H NMR (700 MHz, $CDCl_3$) and ^{13}C NMR (176 MHz, $CDCl_3$) of compound **398** and **399**

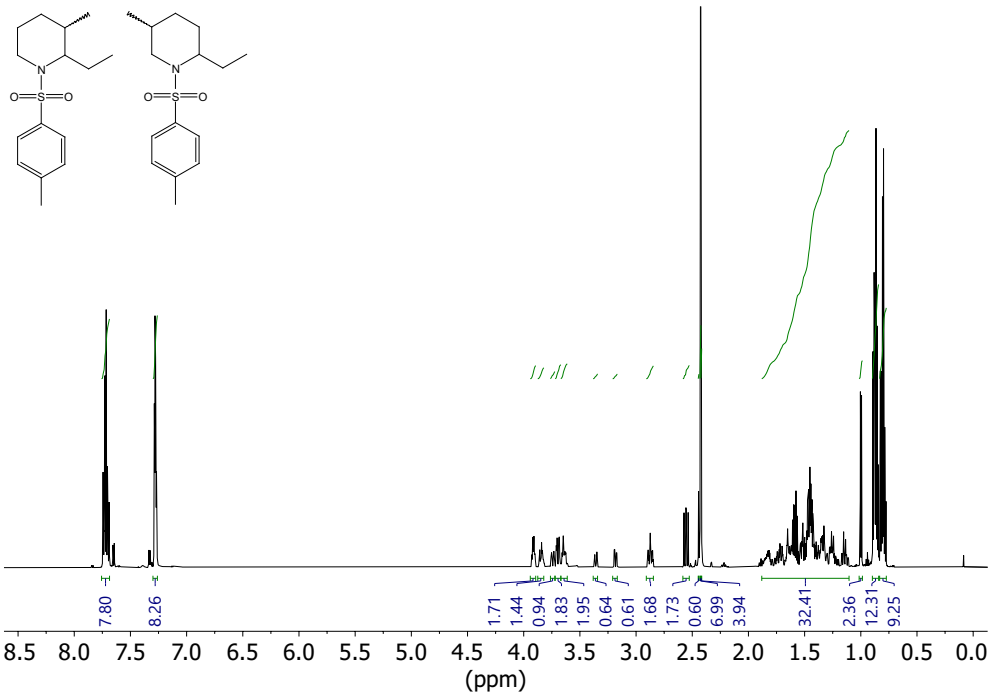

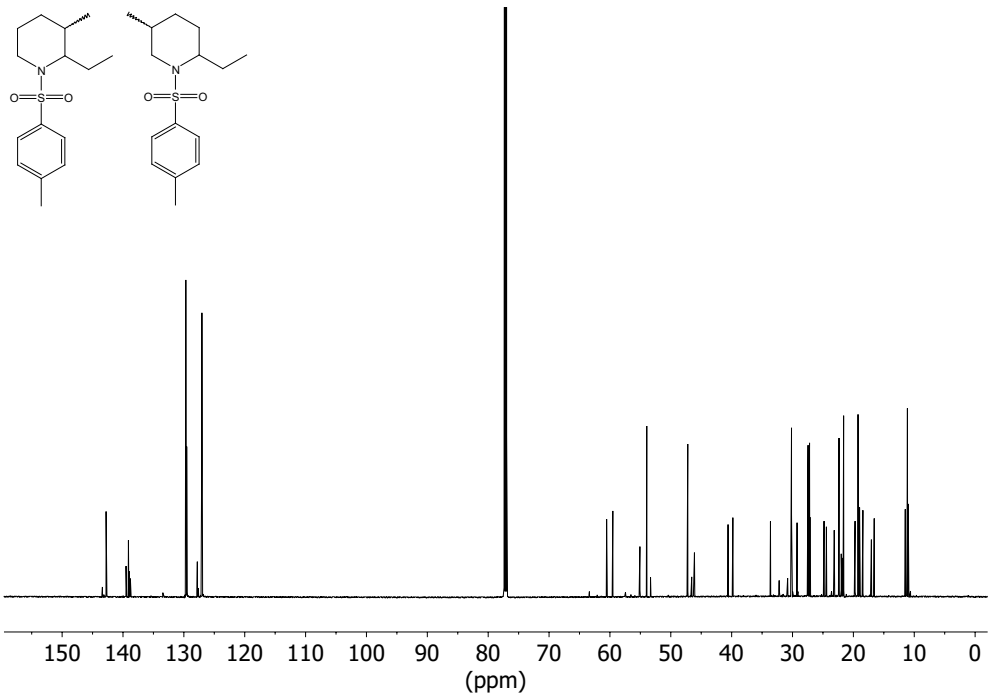

^{1}H NMR (400 MHz, $CDCl_3$) and ^{13}C NMR (101 MHz, $CDCl_3$) of compound **369**

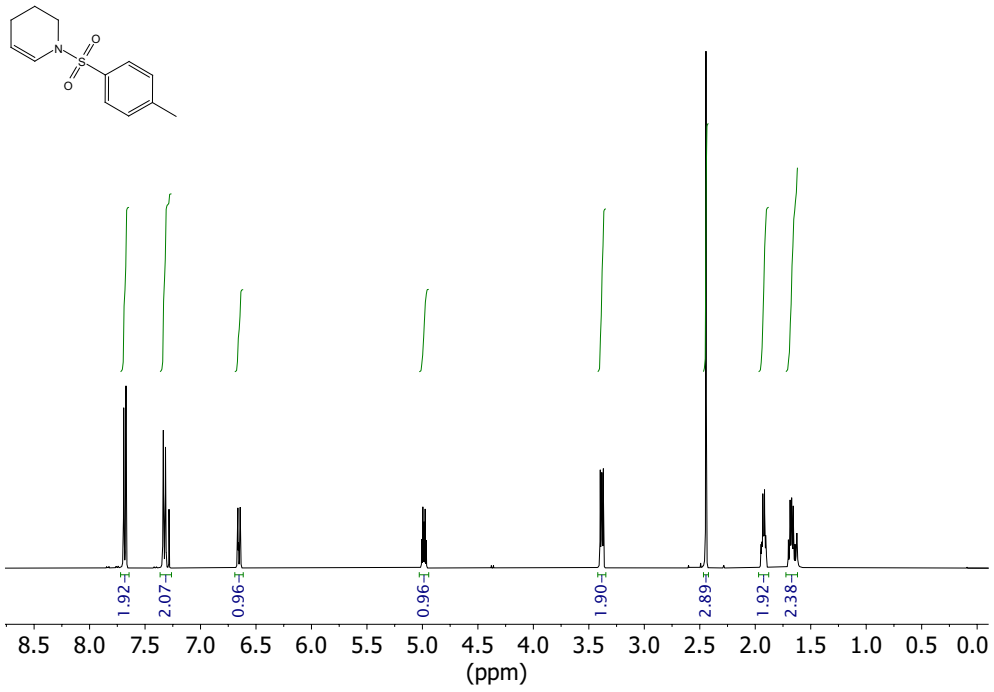

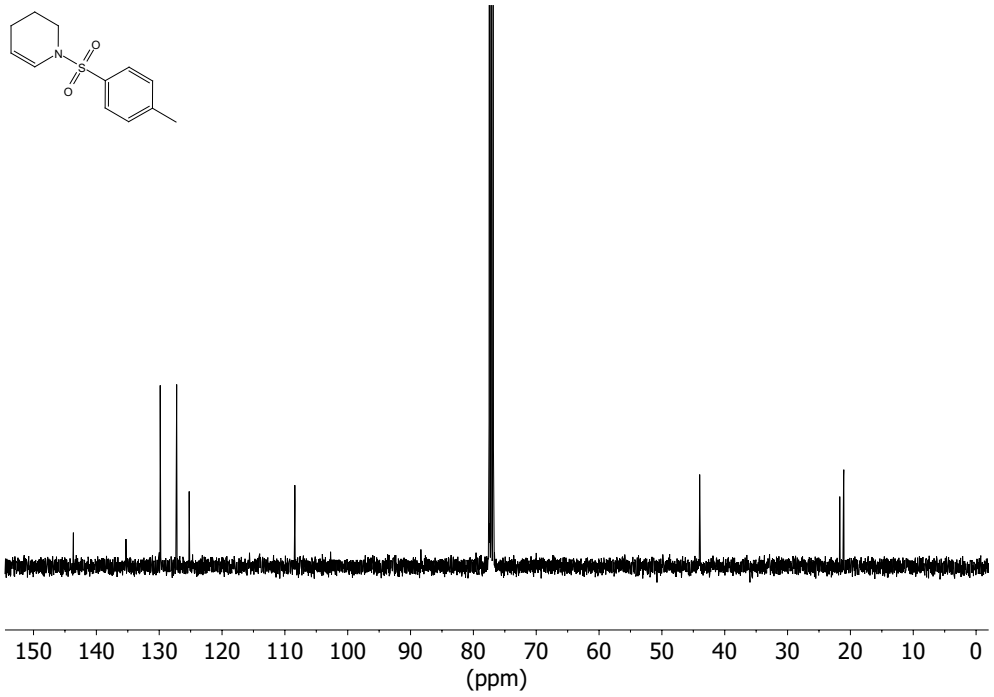

^{1}H NMR (600 MHz, $CDCl_3$) and ^{13}C NMR (151 MHz, $CDCl_3$) of compound **393**

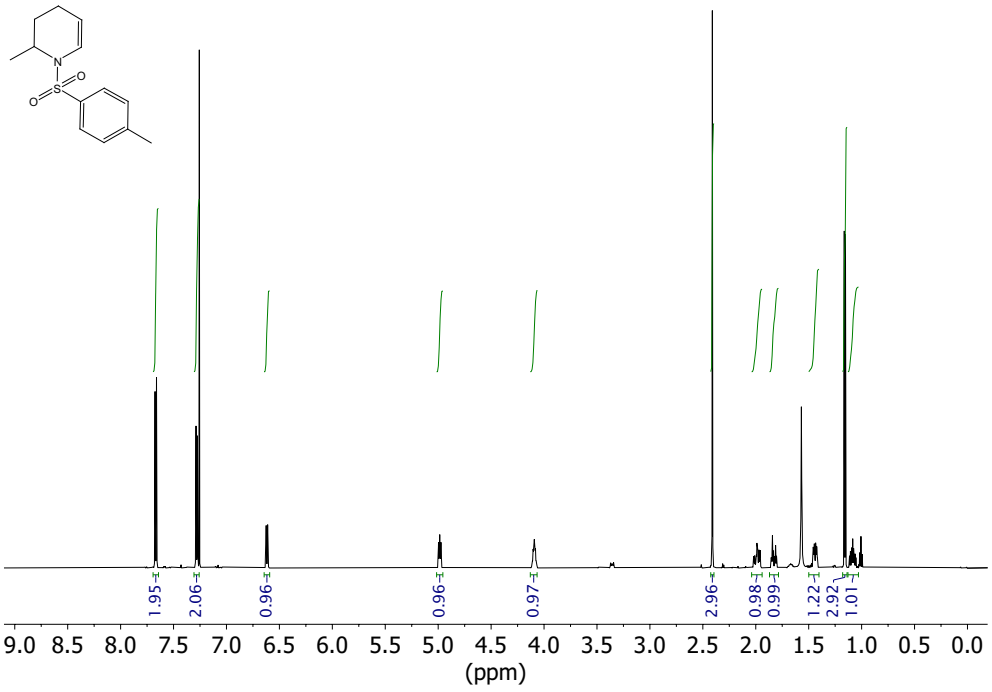

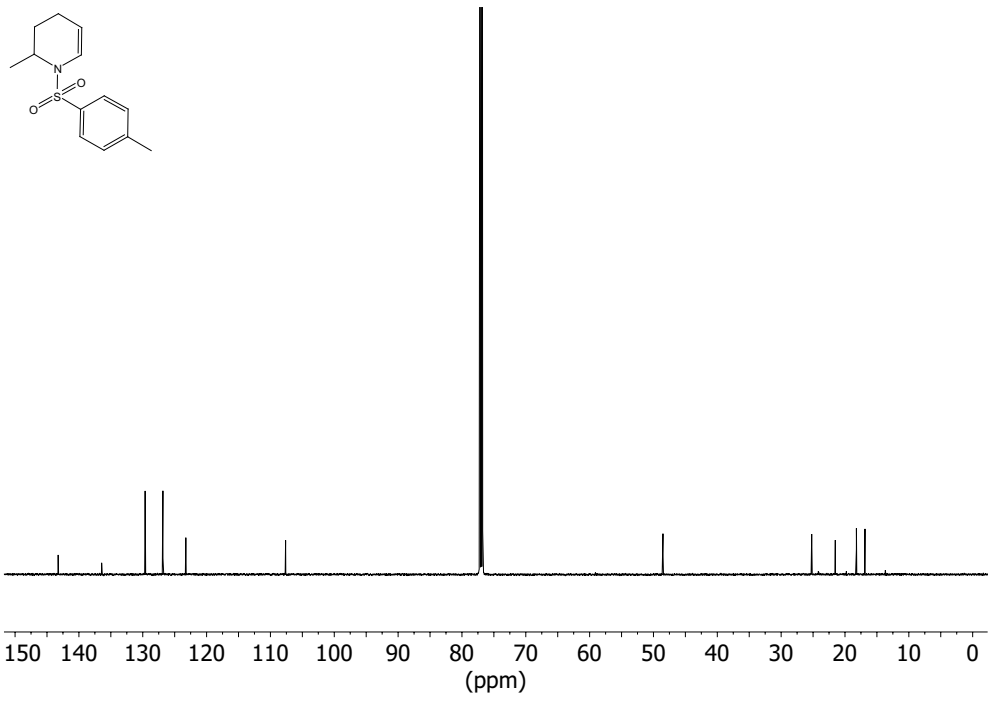

^{1}H NMR (700 MHz, $CDCl_3$) and ^{13}C NMR (176 MHz, $CDCl_3$) of compound **396**